

Challa S.S.R. Kumar *Editor*

Nanotechnology Characterization Tools for Tissue Engineering and Medical Therapy

MATERIALS.SPRINGER.COM

 Springer

Nanotechnology Characterization Tools for Tissue Engineering and Medical Therapy

Challa S. S. R. Kumar
Editor

Nanotechnology Characterization Tools for Tissue Engineering and Medical Therapy

With 144 Figures and 10 Tables

 Springer

Editor

Challa S. S. R. Kumar
Integrated Mesoscale Architectures for Sustainable Catalysis (IMASC)
Rowland Institute of Science
Harvard University
Cambridge, MA, USA

ISBN 978-3-662-59595-4 ISBN 978-3-662-59596-1 (eBook)
<https://doi.org/10.1007/978-3-662-59596-1>

© Springer-Verlag GmbH Germany, part of Springer Nature 2019

This work is subject to copyright. All rights are reserved by the Publisher, whether the whole or part of the material is concerned, specifically the rights of translation, reprinting, reuse of illustrations, recitation, broadcasting, reproduction on microfilms or in any other physical way, and transmission or information storage and retrieval, electronic adaptation, computer software, or by similar or dissimilar methodology now known or hereafter developed.

The use of general descriptive names, registered names, trademarks, service marks, etc. in this publication does not imply, even in the absence of a specific statement, that such names are exempt from the relevant protective laws and regulations and therefore free for general use.

The publisher, the authors, and the editors are safe to assume that the advice and information in this book are believed to be true and accurate at the date of publication. Neither the publisher nor the authors or the editors give a warranty, expressed or implied, with respect to the material contained herein or for any errors or omissions that may have been made. The publisher remains neutral with regard to jurisdictional claims in published maps and institutional affiliations.

This Springer imprint is published by the registered company Springer-Verlag GmbH, DE, part of Springer Nature.

The registered company address is: Heidelberger Platz 3, 14197 Berlin, Germany

Contents

1 Nanotechnology-Based Stem Cell Tissue Engineering with a Focus on Regeneration of Cardiovascular Systems	1
Srikanth Sivaraman, Arvind Sinha, Ki-Taek Lim, Jin-Woo Kim, Raj Rao, and Hanna Jensen	
2 Characterization Tools for Mechanical Probing of Biomimetic Materials	69
Silvia Caponi, Claudio Canale, Ornella Cavalleri, and Massimo Vassalli	
3 Open-Channel Separation Techniques for the Characterization of Nanomaterials and Their Bioconjugates for Drug Delivery Applications	113
Jiwon Lee, Roxana Coreas, and Wenwan Zhong	
4 Using Integrated Cancer-on-Chip Platforms to Emulate and Probe Various Cancer Models	151
Ziqiu Tong, Wing-Yin Tong, Bo Peng, Yingkai Wei, Arianna Oddo, and Nicolas H. Voelcker	
5 Design of Nanoparticles for Focused Ultrasound Drug Delivery	205
Paul Cressey, Weiqi Zhang, Mihnea Turcanu, Sandy Cochran, and Maya Thanou	
6 Magneto-Responsive Nanomaterials for Medical Therapy in Preclinical and Clinical Settings	241
Kheireddine El-Boubbou	
7 Superparamagnetic Nanoparticles for Cancer Hyperthermia Treatment	299
Dipak Maity and Ganeshlenin Kandasamy	

8	Quantitative Methods for Investigating Dissociation of Fluorescently Labeled Lipids from Drug Delivery Liposomes	333
	Rasmus Münter, Kasper Kristensen, Dennis Pedersbæk, Thomas L. Andresen, Jens B. Simonsen, and Jannik B. Larsen	
9	Integrated Multilayer Microfluidic Platforms with Silicon Architectures for Next-Generation Health Diagnostic Systems . . .	361
	Aditya Kasukurti, Hari Hara Sudhan Lakshmanan, Sarojini Tiwari, and Jeevan Maddala	
10	Characterization of ATP Nanoliposome Treatment for Regeneration of Injured Spinal Cord	397
	Girish J. Kotwal, Michael Martin, Eyas M. Hattab, and Sufan Chien	
11	An Insight into Characterizations and Applications of Nanoparticulate Targeted Drug Delivery Systems	417
	Ayan Kumar Barui, Batakrishna Jana, and Ja-Hyoung Ryu	
	Index	455

Contributors

Thomas L. Andresen Center for Nanomedicine and Theranostics, Technical University of Denmark, Lyngby, Denmark

Department of Health Technology (DTU Healthtech), Technical University of Denmark, Lyngby, Denmark

Ayan Kumar Barui Department of Chemistry, Ulsan National Institute of Science and Technology (UNIST), Ulsan, Republic of Korea

Claudio Canale Department of Physics, University of Genova, Genoa, Italy

Silvia Caponi Istituto Officina dei Materiali, National Research Council, Perugia, Italy

Ornella Cavalleri Department of Physics, University of Genova, Genoa, Italy

Sufan Chien Noveratech LLC, Louisville, KY, USA

Hiram Polk Department of Surgery, School of Medicine Louisville, University of Louisville, Louisville, KY, USA

Sandy Cochran School of Engineering, University of Glasgow, Glasgow, UK

Roxana Coreas Environmental Toxicology Graduate Program, University of California-Riverside, Riverside, CA, USA

Paul Cressey Department of Chemistry, King's College London, London, UK

Kheireddine El-Boubbou Department of Basic Sciences, College of Science & Health Professions (COSHP), King Saud bin Abdulaziz University for Health Sciences (KSAU-HS), King Abdulaziz Medical City, National Guard Health Affairs, Riyadh, Saudi Arabia

King Abdullah International Medical Research Center (KAIMRC), King Abdulaziz Medical City, National Guard Health Affairs, Riyadh, Saudi Arabia

Eyas M. Hattab Department of Pathology and Laboratory Medicine, School of Medicine Louisville, University of Louisville, Louisville, KY, USA

Batakrishna Jana Department of Chemistry, Ulsan National Institute of Science and Technology (UNIST), Ulsan, Republic of Korea

Hanna Jensen Department of Biomedical Engineering, University of Arkansas, Fayetteville, AR, USA

Ganeshlenin Kandasamy Department of Biomedical Engineering, Vel Tech Rangarajan Dr. Sagunthala R&D Institute of Science and Technology, Chennai, Tamil Nadu, India

Aditya Kasukurti Intel Corp, Portland, OR, USA

Jin-Woo Kim Department of Biological and Agricultural Engineering, University of Arkansas, Fayetteville, AR, USA

Institute for Nanoscience and Engineering, University of Arkansas, Fayetteville, AR, USA

Girish J. Kotwal Noveratech LLC, Louisville, KY, USA

Kasper Kristensen Center for Nanomedicine and Theranostics, Technical University of Denmark, Lyngby, Denmark

Department of Health Technology (DTU Healthtech), Technical University of Denmark, Lyngby, Denmark

Hari Hara Sudhan Lakshmanan OHSU, Portland, OR, USA

Jannik B. Larsen Center for Nanomedicine and Theranostics, Technical University of Denmark, Lyngby, Denmark

Department of Health Technology (DTU Healthtech), Technical University of Denmark, Lyngby, Denmark

Jiwon Lee Department of Chemistry, University of California-Riverside, Riverside, CA, USA

Ki-Taek Lim Department of Biosystems Engineering, Kangwon National University, Chuncheon, Republic of Korea

Jeevan Maddala WVU, Morgantown, WV, USA

Dipak Maity Department of Chemical Engineering, Institute of Chemical Technology Mumbai, IOC Campus, Bhubaneswar, Odisha, India

Michael Martin Noveratech LLC, Louisville, KY, USA

Micro/Nano Technology Center, University of Louisville, Louisville, KY, USA

Rasmus Münter Center for Nanomedicine and Theranostics, Technical University of Denmark, Lyngby, Denmark

Department of Health Technology (DTU Healthtech), Technical University of Denmark, Lyngby, Denmark

Arianna Oddo Drug Delivery, Disposition and Dynamics, Monash Institute of Pharmaceutical Sciences, Monash University, Parkville, VIC, Australia

Dennis Pedersbæk Center for Nanomedicine and Theranostics, Technical University of Denmark, Lyngby, Denmark

Department of Health Technology (DTU Healthtech), Technical University of Denmark, Lyngby, Denmark

Bo Peng Commonwealth Scientific and Industrial Research Organization (CSIRO), Clayton, VIC, Australia

Raj Rao Department of Biomedical Engineering, University of Arkansas, Fayetteville, AR, USA

Ja-Hyoung Ryu Department of Chemistry, Ulsan National Institute of Science and Technology (UNIST), Ulsan, Republic of Korea

Jens B. Simonsen Center for Nanomedicine and Theranostics, Technical University of Denmark, Lyngby, Denmark

Department of Health Technology (DTU Healthtech), Technical University of Denmark, Lyngby, Denmark

Arvind Sinha Department of Biological and Agricultural Engineering, University of Arkansas, Fayetteville, AR, USA

Institute for Nanoscience and Engineering, University of Arkansas, Fayetteville, AR, USA

Srikanth Sivaraman Department of Biomedical Engineering, University of Arkansas, Fayetteville, AR, USA

Maya Thanou School of Cancer and Pharmaceutical Sciences, King's College London, London, UK

Sarojini Tiwari WVU, Morgantown, WV, USA

Wing-Yin Tong Drug Delivery, Disposition and Dynamics, Monash Institute of Pharmaceutical Sciences, Monash University, Parkville, VIC, Australia

Ziqiu Tong Drug Delivery, Disposition and Dynamics, Monash Institute of Pharmaceutical Sciences, Monash University, Parkville, VIC, Australia

Mihnea Turcanu School of Engineering, University of Glasgow, Glasgow, UK

Massimo Vassalli Institute of Biophysics, National Research Council, Genoa, Italy

Nicolas H. Voelcker Drug Delivery, Disposition and Dynamics, Monash Institute of Pharmaceutical Sciences, Monash University, Parkville, VIC, Australia

Commonwealth Scientific and Industrial Research Organization (CSIRO), Clayton, VIC, Australia

Melbourne Centre for Nanofabrication, Victorian Node of the Australian National Fabrication Facility, Clayton, VIC, Australia

Yingkai Wei Drug Delivery, Disposition and Dynamics, Monash Institute of Pharmaceutical Sciences, Monash University, Parkville, VIC, Australia

Weiqi Zhang School of Cancer and Pharmaceutical Sciences, King's College London, London, UK

Wenwan Zhong Department of Chemistry, University of California-Riverside, Riverside, CA, USA

Environmental Toxicology Graduate Program, University of California-Riverside, Riverside, CA, USA



Nanotechnology-Based Stem Cell Tissue Engineering with a Focus on Regeneration of Cardiovascular Systems

1

Srikanth Sivaraman, Arvind Sinha, Ki-Taek Lim, Jin-Woo Kim, Raj Rao, and Hanna Jensen

Contents

1	Definition of the Topic	3
2	Overview	3
3	Introduction	4
4	Experimental and Instrumental Methodology Utilized in Nanotechnology-Based Stem Cell Tissue Engineering	5
4.1	Methodology and Techniques	5
4.2	Stem Cell Types for Nanotechnology-Based Tissue Engineering	8
5	Review and Analysis of Key Research Findings	13
5.1	Nanoparticles for Stem Cell-Based Tissue Engineering	13
5.2	Tissue Engineering Constructs and Scaffolds for Regenerative Nanomaterial Applications	25
5.3	Stem Cells in Research and Applications in the Cardiovascular System	35
6	Conclusion and Future Perspectives	47
	References	48

Funding/Disclosures: Partial funding was provided by NSF-CBET-1659244, and George M. and Boyce W. Billingsley Endowment Fund for Dr. Rao, as well as NSF-CMMI-1235100, NSF-OIA-1457888, and Arkansas Biosciences Institute for Dr. Kim.

S. Sivaraman · R. Rao (✉) · H. Jensen (✉)
Department of Biomedical Engineering, University of Arkansas, Fayetteville, AR, USA
e-mail: rajrao@uark.edu; hkjensen@uark.edu

A. Sinha · J.-W. Kim (✉)
Department of Biological and Agricultural Engineering, University of Arkansas, Fayetteville, AR, USA

Institute for Nanoscience and Engineering, University of Arkansas, Fayetteville, AR, USA
e-mail: jwkim@uark.edu

K.-T. Lim
Department of Biosystems Engineering, Kangwon National University, Chuncheon, Republic of Korea

Abbreviations

AFPC	Amniotic fluid progenitor cells
AgNP	Silver nanoparticle
AuNP	Gold particle
bFGF	Basic fibroblast growth factor
BM-MSC	Bone marrow-derived mesenchymal stem cells
CAD	Computer-aided software
CAFC	Cobblestone area formation assay
CFU	Colony formation unit assay
CM	Cardiomyocyte
CNC	Cellulose nanocrystals
CNT	Carbon nanotube
CRU	Competitive repopulating unit assay
CVD	Chemical vapor deposition
DNA	Deoxyribonucleic acid
EB	Embryoid body
EC	Endothelial cell
ECM	Extracellular matrix
ESC	Embryonic stem cells
FACS	Fluorescence-activated cell sorting
FDM	Fused deposition modeling
FGF	Fibroblast growth factor
GelMA	Carbon nanotube-gelatin methacrylate
GM	Gelatin microspheres
GO	Graphene oxide
HA	Hyaluronic acid
HAp/CS-Gel	Hydroxyapatite/chitosan-gelatin
hASCs	Human adipose mesenchymal stem cells
hESC	Human embryonic stem cells
HIPE	High internal phase emulsion
hNSCs	Human neural stem cells
HSCs	Hematopoietic stem cells
IGF	Insulin growth factor
iPSC	Induced pluripotent stem cells
KOSR	Knockout serum replacement
LIF	Leukemia inhibitory factor
LSPR	Localized surface plasma resonance
LT-IC	Long-term culture initiation assay
MI	Myocardial infarction
miRNA	Micro-RNA
MRI	Magnetic resonance imaging
MSC	Mesenchymal stromal cells
MWNT	Multi-walled carbon nanotube
NFC-X	Nanofibrillated cellulose
NF- κ B	Nuclear factor kappa-light-chain-enhancer of activated B cells

NPs	Nanoparticles
PBAE	Biodegradable poly (β -amino-ester)
PCL	Polycaprolactone
PEG-DA	Polyethylene (glycol) diacrylate
PEI	Polyethyleneimine
PGLA	Poly(lactic-co-glycolic acid)
PLA	Poly(lactic acid)
PS	Protamine sulfate
QD	Quantum dot
RBMSCs	Rat bone marrow stromal cells
RGO	Reduced graphene oxide
RNA	Ribonucleic acid
SCNT	Somatic cell nuclear transfer
SG	Single-layer graphene
SL	Stereolithography
SPIO	Superparamagnetic iron oxide nanoparticle
SWNT	Single-walled carbon nanotube
TCP	Tricalcium phosphate
TGF	Transforming growth factor
TiO ₂ NP	Titanium dioxide-based nanoparticle
UDSCs	Urine-derived stem cells
VEGF	Vascular endothelial growth factor
ZnONP	Zinc-oxide-based nanoparticle

1 Definition of the Topic

This chapter outlines the main stem cell lines and nanomaterials utilized in tissue engineering for regenerative medicine, with a distinct focus on the cardiovascular system, which is our research area of interest.

2 Overview

In the modern biomedical research enterprise, three buzz words that have garnered unforeseeable enthusiasm are *regenerative medicine*, *tissue engineering*, and *nanotechnology*. Each one of the concepts has seen a skyrocketing of available information in the last decade, with seemingly unending quests for a revolution of available medical tools. In this chapter, we aim to dwell at the intersection of these three concepts, to explore available information and new directions within research that in a compelling way brings forth advances within the joint field of nanotechnology-based stem cell tissue engineering.

The chapter has been written in a way that can provide an introduction or an overview of current technical and applied knowledge in the addressed field. The chapter will discuss the most common types of stem cells and nanoparticles utilized

in tissue engineering efforts, and provide examples of typical scaffolds or mediums popular in current applications. The focus among nanotechnology-based stem cell tissue engineering that is highlighted is the current knowledge in cardiovascular research; however, other biological applications are discussed as well.

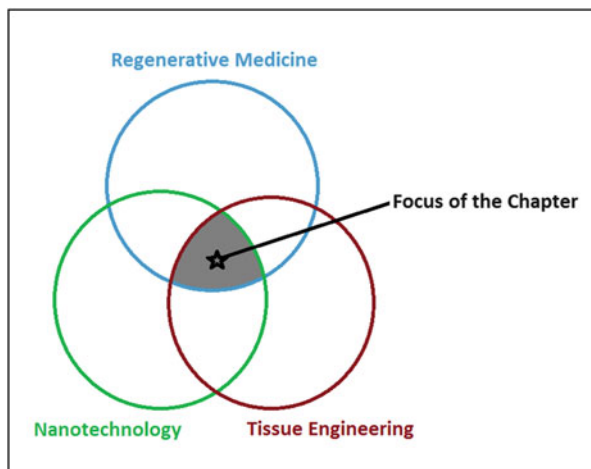
At the intersection of nanotechnology-based tissue engineering and regenerative stem cell therapy, promising results continue to be reported on a monthly basis. However, significant questions about effectiveness, safety, and sustainability of therapeutics based on this approach are still in the early stages of exploration. The wide variety of choices in terms of cell types, nanomaterials, supplementary materials, and biological constructs is bewildering, and pre-clinical testing platforms include important limitations that must be acknowledged prior to translation of these novel strategies. However, the potential is indisputable and titillating – at the convergence of nanotechnology, stem cell science and tissue engineering may lay the philosopher’s stone to human tissue regeneration.

3 Introduction

In the modern biomedical research enterprise, three buzz words that have garnered unforeseeable enthusiasm are *regenerative medicine*, *tissue engineering*, and *nanotechnology*. Each one of the concepts has seen a skyrocketing of available information in the last decade, with seemingly unending quests for a revolution of available medical tools. In this chapter, we aim to dwell at the intersection of these three concepts, as illustrated in Fig. 1.1, to explore available information and new directions within research that in a compelling way brings forth advances within the joint field of nanotechnology-based stem cell tissue engineering.

The chapter has been written in a way that can provide an introduction or an overview of current technical and applied knowledge in the addressed field. The

Fig. 1.1 Schematic about the focus area of chapter



chapter will discuss the most common types of stem cells and nanoparticles utilized in tissue engineering efforts, and provide examples of typical scaffolds or mediums popular in current applications. The focus among nanotechnology-based stem cell tissue engineering that is highlighted is the current knowledge in cardiovascular research; however, other biological applications are presented and discussed as well.

It is perhaps at this point intuitive that stem cell science combined with nanotechnology has the potential to revolutionize tissue regeneration and healing outcomes [1]. With tissue loss and organ failure as the most life-devastating and economically taxing problems in health care, the need for versatile biomaterials that restore, maintain, and/or improve tissue function has been painstakingly evident since the goals of tissue engineering were defined in 1993 by Langer and Vacanti [1–2]. The recent nano-revolution has allowed scientists to manipulate the small-scale architecture and topography of any tissue engineered construct, allowing for a better understanding and more effective therapies as these platforms can now enhance interaction between cells and their environment. Nanotechnology can better mimic the intricate biological structures that determine the fate of cells in the body, especially in the case of stem cells, whose appropriate differentiation as a part of any targeted therapy *in vivo* has proven much harder than what was initially thought.

The goal of applications of any type of stem cell therapy is ultimately biomimicry, with the hope of potentially recruiting the body's own regenerative pathways to initiate sustainable healing. Whether nanotechnology-driven tissue engineering can achieve this “philosopher's stone” in biomedicine, in a way that is safe for patients, remains a question at this junction. However, increasing evidence in various applications in, for example, dentistry [3–4], nephrology [5–6], neurology [7–8], musculoskeletal system [9–10], orthopedics [11–12], ophthalmology [13], and cardiovascular medicine [14–15], allows us to remain increasingly hopeful as we summarize these encouraging findings.

While several excellent review articles have been written on each of the three focus areas of nanotechnology and/or tissue engineering and/or stem cells [1, 16–19], this chapter is unique in focusing specifically at the intersection of these core concepts, and broadly exploring real-world applications in cardiovascular systems.

4 Experimental and Instrumental Methodology Utilized in Nanotechnology-Based Stem Cell Tissue Engineering

4.1 Methodology and Techniques

Methodology and techniques discussed in this chapter include the following.

4.1.1 Electrical Stimulation

Cells seeded on biomaterials are subjected to measured and sustained electric current using electrodes (e.g., graphite). The programmed electric pulses are delivered at a particular frequency at regular time intervals to resemble the level required for

exciting a normal ventricular tissue. This technique will be discussed in this chapter, and more information is available in previously published literature by Mooney [20] and Kai [21].

4.1.2 Electrospinning

The principle of electrospinning is that an electric field is used to overcome the surface tension of a polymer solution to shoot a jet of liquid out of a needle toward a conducting collector. The volatile solvent evaporates in the air leaving behind a polymer fiber with a diameter that can range from tens of nanometers to microns. Polymer properties, solvent properties, solution flow rate, voltage, distance from the needle to the collector, and polymer concentration, among other parameters, affect this process. While electrospinning will be discussed in the coming chapter, more details are available in articles by Jiang [22], Nair [23], Ramesh Kumar [24], Deitzel [25], and Jaworek [26].

4.1.3 Epicardial Surface Patch

Various nanostructured materials synthesized from either natural polymers (e.g., collagen) or electrospun synthetic materials (e.g., PLCL) have been implanted in the form of a patch onto cardiovascular tissue to aid in tissue growth, regeneration, or repair. Patch applications are discussed in this chapter, and more information is available in articles by Jin [27], Rane [28], Karam [29], and Ruvinov [30].

4.1.4 Fluorescence Spectroscopy

Fluorescence produced by NPs is used for tracking the cell growth, migration, proliferation, biosensing, immunohistochemistry, and bioimaging. Any change in fluorescence can easily be detected using an epi-fluorescence microscope, confocal microscope, fluorimeter, fluorescence spectrophotometer, and fluorescence-activated cell sorter. These methodologies will be discussed in this chapter, and for more details, the reader is directed to previously published literature [31–34].

4.1.5 Gene/Plasmid/miRNA Delivery

Various nanoparticles are tagged with genes/plasmids and miRNAs and injected into the bloodstream to target the delivery site and release the cargo at the site of delivery. The nanoparticle design enables the package to be protected from degradation by serum DNAases and avoid being taken up by phagocytic cells or the reticuloendothelial system. While these applications will be discussed in the forthcoming chapter, for more details the reader is directed to works by Tu [35], Yang [36], Lee [37], and Gomes [38].

4.1.6 Intra-myocardial Injection

Intra-myocardial injections are given directly into the heart muscle. The procedure is performed by inserting a long spinal needle into the ventricular wall. The needle is usually inserted in the fourth intercostal space between the ribs. While this procedure is mentioned in this chapter, more details of the clinical procedure are available in, for example, a recent previous publication by Mann and colleagues [39].

4.1.7 Magnetic Properties and Techniques

Supramagnetic properties of NPs are used for remote and non-invasive imaging (contrast agents), carrier molecules, enriching scarce molecules, smart actuators, and mechanical or heat stimuli for modulating different cellular functions. In addition to the information provided within this chapter, the reader is directed to previously published material [40–42].

4.1.8 Near-Infrared Imaging (NIR-Imaging)

The near-infrared photoluminescence properties of NPs are used for bioimaging, tracking, and identifying biomolecules inside the biological system owing to the low autofluorescence and deep tissue penetration of the near-infrared wavelength. For details beyond this chapter, please refer to works published by Frangioni [43], Guo [44], Hilderbrand [45], and Smith [46].

4.1.9 Photoacoustic and Photothermal Techniques

A non-invasive hybrid technique uses the high contrast of optics and the high-resolution acoustic properties of NPs for *in vivo* tracking of the stem cells, differentiation, growth, proliferation, and identifying morphological, functional, or molecular properties of biomolecules and cell ablation. More information is available in articles by Kim [47], Wang [48], and Zerda [49].

4.1.10 Production of Nanoparticle-Hybrids

NPs conjugate with various natural and biomolecules. The process can be used for creating biocompatible and multifunctional NPs composites or hybrids with tailored functions and physiochemical properties for stem cells attachment, growth, migration, differentiation, and proliferation. Information beyond this chapter is offered in previous works by Baron [50], Divya [51], and Portney [52].

4.1.11 Surface-Enhanced Raman Scattering (SERS)

Enhanced Raman activity in the presence of NPs is used for selective and sensitive detection and investigation of the stem cell differentiation, including undifferentiated single cells, embryoid bodies, and others. For more reading beyond this chapter, we suggest previous publications by Brauchle [53], Ghita [54], and Kudelski [55].

4.1.12 Synthesis of Nanoparticles

Nanoparticles are particles between 1 and 100 nanometers (nm) in size with a surrounding interfacial layer. There are several methods for creating nanoparticles, including gas condensation, attrition, chemical precipitation, ion implantation, pyrolysis, and hydrothermal synthesis, which will be described in this chapter. Some further reading about nanoparticle synthesis can be found in publications by Batista [56] and Ealias [57].

4.1.13 Surface Functionalization

NPs are modified to impart additional chemical functional groups on the surface. Added functionalities provide an additional site and opportunity for the conjugation

of different molecules, surface tuning, and topological manipulation. Beyond the material discussed in this chapter, more details can be found in publications by Daniel [58], Rana [59], and Sperling [60].

4.1.14 Three-Dimensional (3D) Bioprinting

Several bioprinting types have been newly established, including inkjet-based printing, extrusion-based printing, and laser-based printing. There are processes for patterning and assembling complex multi-functional living platforms through controlling layer by layer of some of the biological materials with viable cells. Inkjet-based printing has been employed to uniformly deposit 3D tissues with low-viscous biomaterials. Likewise, extrusion-based printing can be printed layer by layer in the form of solid filaments. The diameter of printed filaments is around the size of the nozzle tip, while laser-induced printing patterns cells by the force of the pressure of laser-induced vapor bubbles with high spatial resolution and precise control. These methods will be discussed in more detail in the coming chapter, and more information is available in comprehensive review articles by Sears [61], Do [62], and Layani [63].

4.2 Stem Cell Types for Nanotechnology-Based Tissue Engineering

The various stem cell types are broadly classified based on their origin. There are two broad types of stem cells: embryonic stem cells and adult stem cells. Embryonic stem cells (ESCs) originate from the inner cell mass of the embryo and are considered “pluripotent” with the ability to differentiate into all somatic lineages that comprise the entire body, including the germ line [64] and have an apparently limitless capacity to self-renew in vitro, whereas adult stem cells in situ are considered multipotent [64]. Only by studying all types of stem cells, namely ESCs, fetal cells, induced pluripotent stem cells, adult stem cells obtained from various tissue, as well as body fluids such as amniotic fluid, urine, and blood, we will be able to completely understand their utility for regenerative medicine [64].

4.2.1 Embryonic Stem Cells

The embryonic stem cells normally exist in the human embryo for 3–6 days after fertilization [65]. They can maintain their undifferentiated state for long periods of time and are always allogenic cells for the recipient as each human ESC (hESC) line has its own genome [65]. This makes them an excellent choice for various tissue engineering and regenerative medicine purposes. The pluripotency of ESCs is controlled at multiple levels by a core set of transcription factors that inhibit differentiation, a unique cell cycle that promotes proliferation and inhibits differentiation, a poised chromatin state with an open transcriptome, and extracellular signaling molecules that stimulate or inhibit key signal transduction pathways [66]. It has been established that three core transcription factors maintain the undifferentiated state of ESCs: Oct3/4 [67], Sox2 [67–68], and Nanog [69, 70].

The initial step in derivation of hESC lines is the ethical acquisition of supernumerary embryos from assisted reproductive technology clinics, which is the most commonly appropriate starting material. These are either frozen or non-cryopreserved embryos that have been judged to be genetically abnormal or cryopreserved embryos donated by couples that are no longer pursuing family building [71] for preimplantation genetic diagnosis [72] for single-gene disorders. hESCs are usually maintained in Dulbecco's Modified Eagle's Medium with knockout serum replacement (KOSR) and basic fibroblast growth factor (bFGF). The growth factor requirements for hESCs growth resemble those required for post-implantation epiblast stem cells such as the absence of leukemia inhibitory factor (LIF) and inclusion of FGF and activin [73–74]. A great deal of research has centered on developing xeno-free, feeder-free, defined conditions to expand and maintain hESCs and to enable adoption of good manufacturing practice standards [75–78].

hESCs are passaged mechanically by cutting larger colonies into smaller clumps though it is labor intensive and inhibitory to rapid expansion. During passage, the differentiated cells can also be eliminated from cultures. Various chemical or enzymatic agents used to passage hESCs have been shown to increase the risk of chromosomal instability [78–79], and hence, chemical and enzymatic passage methods are being used only sparingly [80]. Thus, mechanical dissection is currently the best way to maintain the bulk of an hESC line.

hESC lines need to be characterized to determine whether they are pluripotent [81] by immunocytochemistry or fluorescence-activated cell sorting (FACS) techniques to look for pluripotency markers such as Oct3/4 and Nanog as well as expression of surface antigens such as SSEA-3, SSEA-4, and/or TRA-1-60, TRA-1-81. Karyotyping is done to demonstrate chromosomal stability on early, middle, and late passages. hESCs spontaneously differentiate into all three germ layers: ectoderm, mesoderm, and endoderm when they are grown in suspension culture as embryoid bodies, floating aggregates of cells.

hESCs have protected their stem cell features such as pluripotency, immortality, and proliferation capacity after enhanced culture of 70 passages which is approximately 250 doublings [82–83]. Studies by Kehat et al. showed that human ESCs could differentiate into cardiomyocytes spontaneously when cultivated in suspension [84]. Extrinsic signals as well as basic FGF and transforming growth factor (TGF) family members are required for the self-renewal of hESCs [85]. The core pluripotency factors Nanog/Oct4/Sox2 are required for the self-renewal of hESCs, and modulators of the core transcriptional network are important to maintain self-renewal and pluripotency of hESCs [85]. The IGF/PI-3K/AKT pathways and the NF- κ B pathway promote and regulate the survival of hESCs, respectively. The genomic stability of hESCs is maintained by the tumor suppressor p53 gene [85].

Recent studies in the context of hESCs for cell-based therapies have aimed at improving the vision of patients with Stargardt's macular dystrophy and dry age-related macular degeneration [86]. The trials involved the patients' eyes being injected with retinal pigmented epithelial cells derived from hESCs. Results showed that after a period of 22 months, no evidence of rejection, adverse proliferation, or

serious ocular or systemic safety issues related to the transplanted tissue was observed [86]. Best-corrected visual acuity, improved in ten eyes, whereas the untreated eyes did not show similar improvements in visual acuity [86]. However, several questions still remain regarding immunosuppression dosage and extent of macular regeneration [86], which needs to be addressed in future studies.

4.2.2 Induced Pluripotent Stem Cells

A major limitation of adult somatic stem cells is that they exist at a very low frequency in almost all tissues of the body and are usually lineage-restricted to the subset of cell types from their tissue of origin [64]. However, seminal studies by Yamanaka and colleagues showed that the somatic cells can be “reprogrammed/induced” to confer ES cell-like pluripotency by introducing a cocktail of genes typically Klf4, Sox2, Oct4, and c-Myc [87]. Various types of somatic cells such as blood, amniotic fluid, bone marrow, fat, liver, brain, pancreas, tooth, skin, umbilical cord, and stomach have been reprogrammed to pluripotency to generate induced pluripotent stem cells (iPSC) [64] (Fig. 1.2). Recently, fibroblasts from neonatal foreskin tissues have been used for the generation of iPSCs. Studies have demonstrated the creation of iPSCs from human foreskin fibroblasts with the same factors as hESCs [4]. The concept of cell reprogramming has been applied to direct cell conversion, such as converting fibroblasts into neural progenitors [88], neurons [89–91], cartilage [92], hematopoietic progenitors [93], hepatocytes [94–95], and cardiomyocytes [96] using a combination of transcriptional factors. The

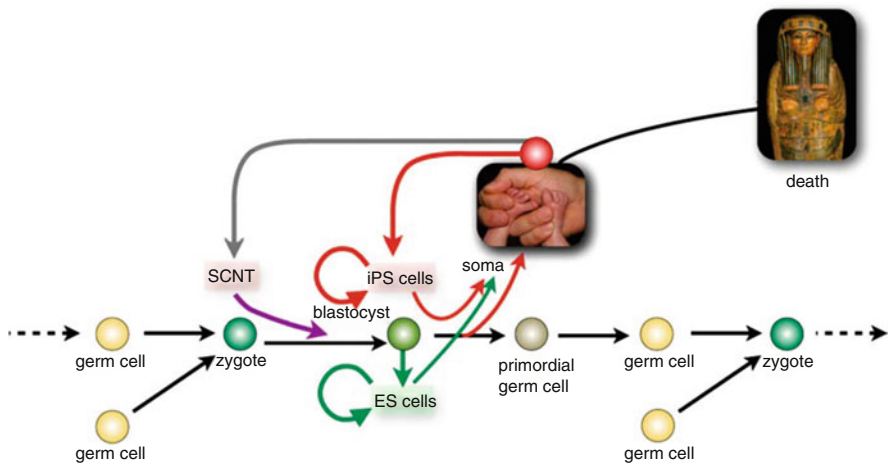


Fig. 1.2 Schematic representation of the journey of the ES, iPSC, and SCNT cell genome. The black arrows show the journey of the genome in the germ line. Red and green arrows show where iPSCs and ESCs could acquire genetic alterations, respectively. The semicircle arrows show the self-renewal/expansion of iPSCs and ESCs. Purple arrow represents the reprogramming after SCNT. **Abbreviations:** *ESCs* embryonic stem cells, *iPSCs* induced pluripotent stem cells, *SCNT* somatic cell nuclear transfer. (Figure reprinted with permission [107])

reprogramming was performed by using plasmids, lentiviruses, transposons, adenoviruses, and recombinant proteins to transfer candidate genes into somatic cells [97].

Studies by Zhang and colleagues have demonstrated the successful production of beating cardiomyocytes from hiPSCs [98]. Hayashi and colleagues mimicked whole eye development and presented a method of creating SEAM (self-formed ectodermal autonomous multi-zone) of ocular cells [99]. Basically, hiPSCs progressively formed a primordium spanning the ocular surface ectoderm, lens, neuro-retina, and retinal pigment epithelium when they were cultivated in differentiation medium [99].

However, studies show that iPSCs may be significantly different from other kinds of stem cells because they retain residual DNA methylation patterns similar to parental somatic cells [97]. Even in syngeneic hosts, aberrant gene expression in iPSCs may generate an immune response [100]. The developmental potential of iPSCs are restricted due to the variability in the pluripotency of iPSCs derived from different cell types as they retain some “cellular memory” [101–102]. However, there are several reports on deriving parental footprint-free iPSCs [103–105].

Thus, iPSCs are an excellent tool to further our understanding of pluripotency and differentiation [106]. Equally important is the application of iPSCs to serve as model systems for investigating diseases at the cellular level, based on derivation from people with genetic diseases. The discovery of iPSCs was initially heralded as justification for the elimination of funding and research with hESCs due to the controversy surrounding perceived destruction of human embryos. Ideally, generic iPSCs that have been optimally reprogrammed seem indistinguishable from ESCs in molecular and functional terms. However, in cases when multiple iPSCs are derived under suboptimal reprogramming conditions and from specific tissue types, epigenetic variations can influence the use of these cells and represent safety concerns for clinical applications [106]. Hence, future work should focus on (1) identification of molecular epigenetic markers that are indicative of the differentiation capacity for specific lineages and (2) application of high-throughput approaches to develop robust directed differentiation conditions for iPSCs [106].

4.2.3 Connective Tissue Stem Cells

Stem cells have been isolated from a long list of connective tissues and have been collectively termed “mesenchymal stem cells” or more recently “mesenchymal stromal cells” (MSCs), because of their fibroblastic morphology, adherence to tissue culture plastic, and expression of stem cell surface markers [108]. The isolation of stem cells from every connective tissue in the body generally fall into three types of techniques: (1) enzymatic release, (2) explantation, and (3) aspiration and lavage (bone marrow and bone) [109].

4.2.4 Fetal Stem Cells

Fetal stem cells are obtained from various fetal tissues, including amniotic fluid, blood, bone marrow, liver, primordial germ cells, as well as extra-embryonic tissues such as the placenta and umbilical cord (especially Wharton’s jelly) [110]. The use of fetal stem cells elicits no ethical concerns since their isolation does not put a

developing fetus at risk [111]. Fetal stem cells can be isolated in large numbers as extra-embryonic tissues are relatively large and discarded *en masse* after birth [112].

4.2.5 Amniotic Fluid Progenitor Cells

Amniotic fluid progenitor cells (AFPS) are isolated from amniotic fluid obtained from amniocentesis at the second trimester of pregnancy [113]. AFPS have been shown to express common markers, differentiate into all three germ layers, and preserve their telomere length [114]. Studies by Kaviani and colleagues showed that 2 ml of AF gives up to 20,000 cells with 80% viability [115]. The cells also have shown a 100% success rate in differentiation into various lineages such as hepatocytes, adipocytes, endothelial cells, myocytes, osteocytes, neuronal cells, and renal cells [114]. Unlike ES cells, AFPS are obtained without destruction of embryos and are less likely to raise ethical concerns and take less than 24 h to double their population [116]. AFPS have a low risk of tumorigenesis and do not differentiate into teratomas [114]. Osteogenically differentiated AFPS were embedded in a collagen/alginate scaffold and implanted subcutaneously in immunodeficient mice for 18 weeks in a study by Atala et al. [114]. The recipient mice displayed highly mineralized tissue and bone-like structures (with a density higher than mouse femoral bone) [114]. Human AFPS when injected into isolated murine embryonic kidneys have been shown to integrate into renal tissues [117] or that injection of AFPS could mediate a protective effect into damaged kidneys of mice with rhabdomyolysis-related acute tubular necrosis [118].

4.2.6 Urine-Derived Stem Cells

Urine-derived stem cells (UDSCs) are a noninvasive and easy-to-expand cell resource that has been induced into endodermal, mesodermal, and ectodermal lineages [119]. UDSCs have been applied in urological tissue engineering including urethral reconstruction and urinary bladder tissue engineering [120–127].

4.2.7 Hematopoietic Stem Cells

Hematopoietic stem cells (HSCs) can be isolated from multiple sources such as bone marrow, cord blood, and peripheral blood with bone marrow being the primary site of HSCs in adult mammals [128]. HSCs can produce approximately 500 billion cells per day in the bone marrow niche [129]. Three-dimensional (3D) cultures of HSCs have been reported to increase the expansion of HSCs in vitro as cells are arranged in a 3D structure in the HSC niche [130–135]. Some of these studies have included with capillaries of endothelial cells, in porous biomatrix Cellfoam, culturing of HSCs on collagen beads, on tantalum-coated porous biomaterial, in porous hydroxyapatite disks, on silk fiber matrices, on porous bovine collagen microspheres, on collagen-coated porous polyvinyl formal resin, and on 3D bone marrow spheroids [128, 131–132, 134–137].

HSC fate is regulated by several highly orchestrated pathways that determine the cell cycle status and gene expression profile [128]. The genes involved in HSC self-renewal are MPL, HOXB4, WNT proteins, p18, Notch-1, Sonic hedgehog, AML1, GATA2, STAT5, and p21 [138]. Apart from CD34, the most positive identifier of

human HSCs; HSCs can be enriched on the basis of CD49f [139], Thy1 (CD90) [140–141], CD45RA [142], and CD38 [143] expression. The stem cell activity of HSCs is detected by a variety of *in vitro* and *in vivo* assays, such as long-term culture initiation assay (LT-IC), cobblestone area formation assay (CAFC), colony-formation unit (CFU) assay, and competitive repopulating unit (CRU) assay, that measure proliferation of cells and their differentiation potential [128].

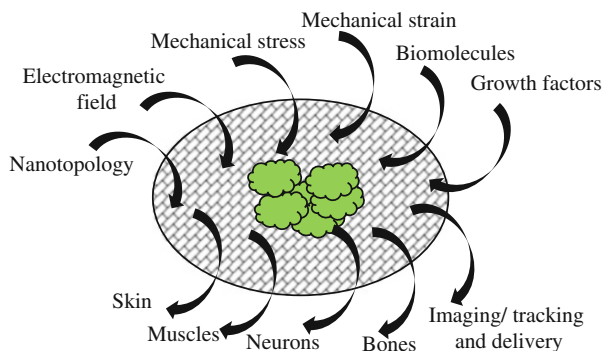
5 Review and Analysis of Key Research Findings

5.1 Nanoparticles for Stem Cell-Based Tissue Engineering

In the natural milieu, cells are surrounded by a highly complex and dynamic extracellular microenvironment constantly providing various biophysical and biochemical cues to the cells. It is the integrated response from the microenvironment including matrix-mediated signals, various growth factors, cytokines, and cell-cell interactions that modulates the final phenotypic expressions and functions of the stem cells [144]. The ultimate goal of the stem cell engineering is to replace the damage or derive the functionality of the biological system which have been lost due to any disease manifestations. However, the functionality to be achieved mostly relies on the bioactive scaffolds that provide the physical and chemical cues to the cells and guide their differentiation proliferation and assembly.

To construct a suitable and specific scaffold for explicit function is still a challenging task. Nanotechnology is bringing a new hope to the stem cell research and development. Because of the unique size-, shape-, and composition-dependent properties, NPs can be used to design and construct complex functional nanostructures. Such functional materials can be custom-made to exhibit significantly improved physical, chemical, and biological properties relevant to a particular condition. With tailored properties of nanomaterials, the integrated response of the cells with its surrounding environment can be better controlled. It has been found that morphological and mechanical properties of the matrix such as rigidity, strain, shear stress, topography, and geometrical and spatial patterns have remarkable effect on the growth, differentiation, and fate of the stem cells [145]. In this case, nanomaterials can effectively be used to modulate the morphological and mechanical properties of the respective matrices for tailored functions. Nanotechnology not only provides platform for effective and selective growth and differentiation of various stem cell types, but can also be used as non-invasive tracking or imaging system. The distribution, location, and persistence time of the transplanted cells can easily be evaluated with different kind of NP materials. While these are few examples, many other functionalities and properties can be obtained with different combinations of NPs (Fig. 1.3). The intimate combination of different nanoparticles in collaboration with synthetic or natural materials, biomolecules, or alone will ultimately lead to major advances in prevention, diagnosis, and treatment of diseases.

Fig. 1.3 Schematic showing some of the modulations of nanotechnology in stem cell engineering



This section will provide insight into some of the widely used nanotechnological platforms in stem cell/tissue engineering. Each section gives a unique opportunity of gaining basic and clear understanding about various NPs, their developments, and use into stem cell/tissue engineering.

5.1.1 Graphene

Graphene is a two-dimensional (2D) sheet-like nanostructure made up of sp^2 -bonded carbon atoms. The carbon atoms are arranged in a honeycomb-like lattice [146]. The carbon atoms in graphene lattice are joined together by three σ and one out-of-plane π -bond [147]. Graphene can be single, double, or multilayer based on the layers of the carbon sheets. Single-layer graphene (SG) consists of one layer of carbon sheet; double or bilayer layer consists of two layers of carbon sheets; whereas multilayer consists of few layers of carbon sheets (layers 10 or less in number) [148]. Graphene can be synthesized by many physical and chemical methods. The synthesis methods are micromechanical or chemical exfoliation of graphite, epitaxial growth on an insulator surface, solvothermal process, sonication, chemical vapor deposition (CVD), arc discharge of graphite, and unzipping of carbon nanotubes [149–150]. Various interesting physicochemical properties such as high specific surface area, high intrinsic mobility, high mechanical stiffness, high optical transmittance, as well as high thermal and electrical conductivity [151–152] are carried by graphene. These properties make graphene a very attractive material toward numerous applications such as electronics, sensors, high-end composite materials, transparent conducting films, energy generation and storage, and catalysis [153–154].

Technically, pristine graphene is hydrophobic and inert to various chemical reactions. On oxidation (with a mineral acid, ozone, or potassium permanganate), graphene can become oxygen-rich by acquiring chemical functionalities (Fig. 1.4) such as hydroxyl, carboxyl, carbonyl, and epoxides [157]. This oxygen-rich graphene is called as graphene oxide (GO). GO is hydrophilic and contains both sp^2 - and sp^3 -hybridized carbon atoms which further enlarge the scope of introducing chemical functionalities on its surface [158].

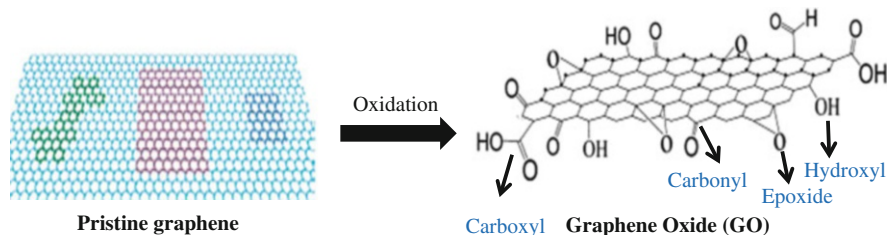


Fig. 1.4 Oxidation of pristine graphene. (Figure adopted and modified with permission from Fang et al. and Geim et al. [155–156])

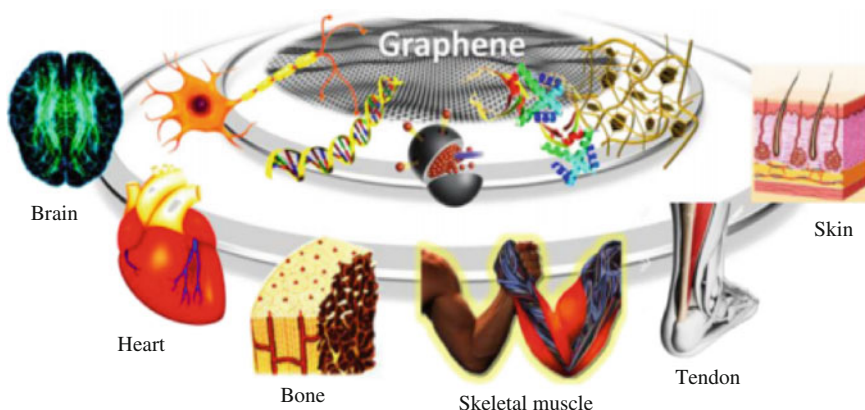


Fig. 1.5 Biomedical applications of graphene. (Adopted from Shen et al. [160], and printed under the terms of the Creative Commons Attribution (CC BY-NC) License [<http://ivyspring.com/terms>])

The flexibility of surface modification with various chemical functionality and hydrophilicity provides GO a multipurpose platform for different biomedical applications (Fig. 1.5). GO has shown encouraging potential in drug delivery, gene therapy, cancer therapy, biosensing, bioimaging, antibacterial materials, protein or biomolecule binding, and biocompatible scaffold for tissue and stem cell engineering [159–160]. Specially in the field of tissue and stem cell engineering, graphene and its chemically modified derivatives look promising. They can easily be attached with different biomolecules to tailor mechanical, physical, and electrical properties for customized applications.

The vital source of tissue engineering or regenerative medicine is stem cells, with applications requiring strict control over the cellular microenvironment. The physical and chemical properties of the materials profoundly affect the microenvironment of the surrounding and the cells, thus affecting overall differentiation, growth, and final fate of the cells [161]. To efficiently utilize the potential of stem cells, precise control over the biochemical and physical micro-environmental cues can be obtained with graphene due to its tenable physicochemical properties [162]. Graphene and graphene oxide can be

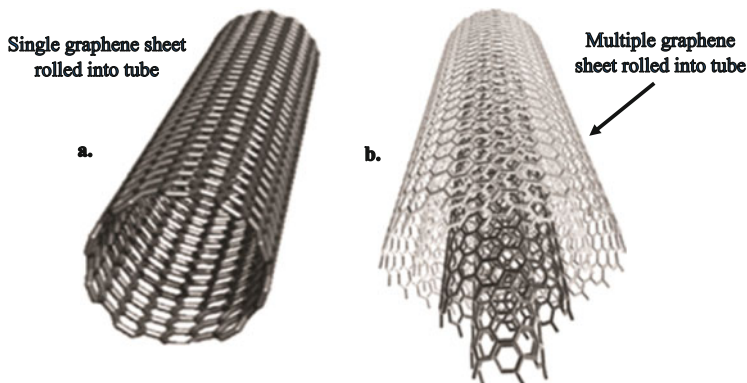


Fig. 1.6 Schematic presentation of (a) single-walled and (b) multi-walled carbon nanotube. (Adopted and modified with permission from Alshehri et al. [167] Copyright (2016) American Chemical Society)

used as preconcentration platform for the development and differentiation of stem cells toward different tissue lineages through molecular interactions with specific growth and differentiation factors [163]. Graphene was used as preconcentration platform for dexamethasone and β -glycerolphosphate for osteogenic differentiation, whereas GO can induce adipogenic differentiation of bone marrow-derived mesenchymal stem cells due to high affinity toward insulin [163]. Graphene alone or its conjugated materials can also be used for selectively guiding stem cell differentiation without any need of external differentiation inducers. For example, graphene was found to be an excellent substrate for long-term cell-adhesion and differentiation of human neural stem cells (hNSCs) toward neuronal growth rather than glial cells [164]. Graphene and polycaprolactone (PCL) hybrid scaffolds were found to offer instructive physical cues to neural stem cells for selective differentiation into mature oligodendrocytes without adding any differentiation inducers in the culture medium [165].

5.1.2 Carbon Nanotubes

Carbon nanotubes (CNTs) are hollow cylindrical molecules made up of a hexagonal lattice of carbon atoms similar to the structure of graphite or graphene [166]. If we roll a graphene sheet, a cylindrical tube-like shape can be crafted which will mimic CNTs. The tube ends of the CNTs can be closed or open. The carbon atoms in CNTs are joined together with sp^2 bonds and have perfect hexagonal lattice except at the end [168]. CNTs can be single walled (SWNTs), or multi walled; (MWNTs) depending upon the number of graphene sheets involved in rolling (Fig. 1.6). If a single graphene sheet is rolled into a tube, it forms SWNTs; however, if multiple graphene sheets are rolled together concentrically, they will form MWNTs. Length of SWNTs can be from 100 to few microns and width from 0.5 to >3 nm wherein MWNTs shows a wider range of diameters (2–100 nm) due to multilayer composition [169–170]. Aspect ratios of CNTs are large due to the huge difference between width and length ratio. CNTs can be synthesized using various methods such as

electric arc discharge, laser vaporization, chemical vapor deposition, pyrolysis of hydrocarbons, and decomposition of CO, and metal carbides [171–172].

Due to rolled tubular structure, CNTs show unique physicochemical properties such as high tensile strength, high Young's modulus, high surface area per unit weight, high electrical and thermal conductivity, and unique optical properties [173–174]. Most of the physicochemical properties of CNTs are governed by their aspect ratio and the chirality or the twist of the carbon tubes [175]. By nature, pristine CNTs are hydrophobic but can be suitably functionalized with various chemical groups to suit particular applications. These features make CNTs impressive for various biomedical applications. Some of the major applications comprise but not limited to designing of biosensors, bioimaging, targeted drug and gene delivery, photothermal therapy, photoacoustic therapy, tumor or cancer therapy, and source of extracellular matrix for tissue engineering and regenerative medicine [176].

In the context of tissue engineering, the unique mechanical, optical, and surface modification properties of CNTs have shown lots of promising results. The mechanical property of CNTs can be used for reinforcing the mechanical properties of the conjugated materials. CNTs are mixed with various natural or synthetic polymers (polylactic-co-glycolic acid; PGLA, polylactic acid; PLA, silk, and chitosan) to improve the mechanic strength of synthetic tissue scaffolds [177]. Surface modification, electrical conductivity, and alignment pattern of CNTs can be used for controlling the release and transport of different growth factors for simulated cell growth and differentiation. For example, the silk-CNT hybrid scaffold was used as 3D matrices for differentiation of hESCs into neuronal lineage [178]. This offers a great hope and opportunity for the repairing of damaged nerves (Fig. 1.7).

A highly biocompatible and multifunctional SWNT-PLGA composite was prepared and found to be promising in providing support and electrical stimulation to human neural stem cells (hNSCs) obtained from iPSCs for its neural differentiation and maturation [179]. MWNTs functionalized with fibroblast growth factor (FGF) were studied for the bone augmentation *in vitro* and *in vivo*. The FGF conjugated MWNTs enhanced the proliferation of rat bone marrow stromal cells (RBMSCs). In addition, after 14 days of implantation of FGF-CNT-coated sponges (between the parietal bone and the periosteum of rats), larger amount of newly formed bone was observed [180]. Functional cardiac patches with excellent mechanical integrity and advanced electrophysiological functions were successfully prepared by seeding neonatal rat cardiomyocytes onto CNT-gelatin methacrylate (GelMA) hydrogels [181]. As compared to myocardial tissues obtained from pristine GelMA hydrogels, myocardial tissues cultured on 50- μm -thick CNT-GelMA exhibited three times higher spontaneous synchronous beating rates and 85% lower excitation threshold. This shows CNTs composites could be a good choice for making multifunctional cardiac scaffolds for therapeutic use.

SWNTs also show very good optical activity in the near-infrared (NIR) region of electromagnetic radiation [182–183]. This means SWNTs can be used for high contrast detection of biomolecules or tracking the cells against biological optical interferences [184]. SWNTs also show unique Raman activity [185]. Since Raman activity lacks photo-bleaching and can avoid interference from background

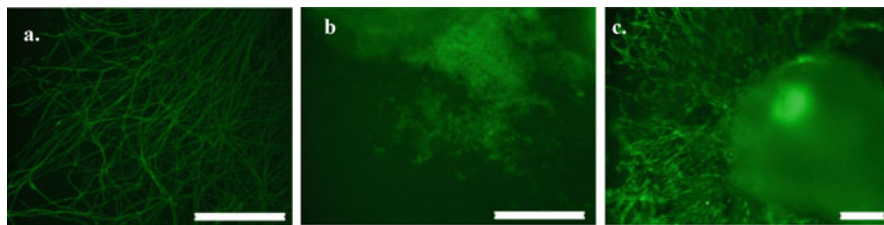


Fig. 1.7 Neuronal marker b-tubulin III expression of hESC during its differentiation into neuron cells on different scaffolds. Poly-L-ornithine; (a) exhibiting long two-dimensional axonal developments with lower density, silk; (b) exhibiting some cell migration along with negligible axonal projections, and silk-CNT scaffolds; (c) demonstrating 3D axonal elongation as well as cell migration. Scale bar, 200 μm . (Adopted and modified from Chen et al. [178]. This figure is used under the terms of the Creative Commons Attribution License [<http://creativecommons.org/licenses/by/2.0>])

autofluorescence from the biological system, SWNTs can be used for long-term imaging, tracking of differentiation processes, and abnormalities in different stem cell types [186]. For instance, SWNTs-PEG-PRO were used for imaging the hMSCs in living mice using Raman, photoacoustic, and magnetic resonance imaging techniques [187]. In vivo experiments with Deutschland, Denken, and Yoken mice (general purpose mice) provided evidence of induction of ectopic bone formation in the dorsal musculature [188]. The in vitro study with MWNTs, chitosan, and hydroxyapatite composite showed doubled cell proliferation of human osteosarcoma (MG-63) cells [189].

5.1.3 Cellulose Nanocrystals

Cellulose nanocrystals (CNCs) are whisker- or rod-shaped, crystalline nanoparticles extracted from the cellulosic elementary fibrils. The cellulosic elementary fibrils have highly ordered crystalline and amorphous regions (Fig. 1.8). The amorphous regions can be broken down by applying various mechanical, chemical, or enzymatic processes [190]. The remaining crystalline region is called CNCs. Cellulosic elementary fibrils could be obtained from various renewable natural sources such as algae, fungi, plants, bacteria, and even animals [191]. Depending upon the sources, origin, maturity, extraction process, CNCs with variable structural and geometric dimensions such as length, width, and aspect ratio can be obtained [192]. Typically average length, width, and aspect ratio of CNCs vary from few nm to several μm (L), 3–50 nm (W) and 10–70 nm (L/W), respectively [193].

As a nanomaterial, CNCs exhibit unique physicochemical properties. It has an impressive very high surface to volume ratio and mechanical properties similar to Kevlar [194]. CNCs barrier, rheological, hydrophilicity, unique self-assembly, and chiral nematic properties makes it a versatile material for different applications [195]. Because of glucosic origin of the structure, CNCs have abundant hydroxyl groups. Also, depending upon the synthesis procedures, CNCs can acquire negative charges from sulfate esters or carboxyl groups [196]. The abundant hydroxyl groups and high surface area provide an excellent combination for surface modification of

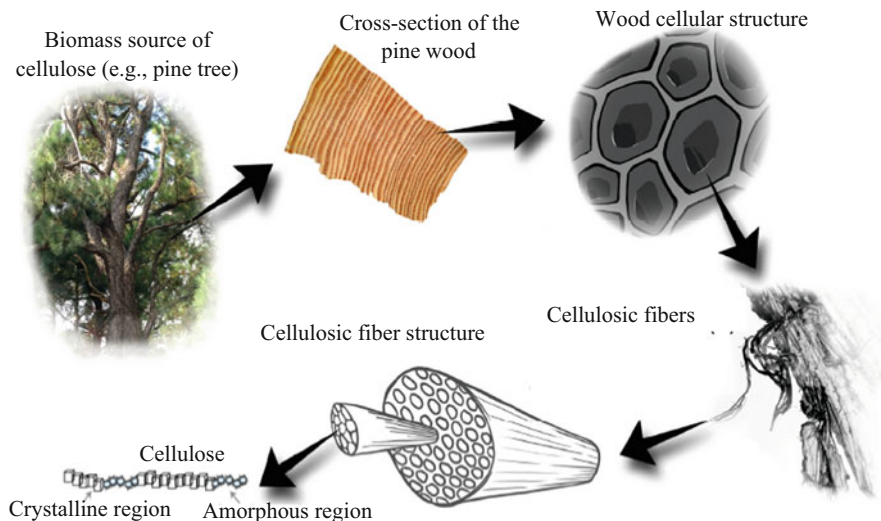


Fig. 1.8 Schematic showing structural and hierarchical arrangement of cellulose chain leading to the formation of CNCs. (Adopted and modified from Sinha et al. [200]. This figure is reprinted under the terms of the Creative Commons Attribution Non-Commercial License [<http://creativecommons.org/licenses/by-nc/3.0/>])

CNCs with different chemical functional groups [197]. The ample opportunities of modifying the surface with different chemical compositions can be harvested for tailoring the properties of CNCs for arbitrary functions. Green source, carbon-neutrality, biodegradability, biocompatibility, and non-toxic nature, make CNCs promising nanomaterials for many useful applications. Catalysis, antimicrobial activity, biosensors, bio-photonics, drug delivery, wound healing, tissue engineering, nanocomposite films, and bio-imaging are some of the leading applications, but there could be many more [198–200], particular, in case of tissue or stem cell (autologous or allogeneic) engineering, where the microcellular environment greatly influences the cell behaviour, fate, differentiation, and proliferation [201]. The physicochemical properties of CNCs can be utilized for modulating the cellular microenvironments and fabrication of bioactive 3D scaffolds similar to the tissue-specific natural extracellular matrix (ECM) [198]. This will help in guiding various types of cells attachment, migration, differentiation, and proliferation.

In an experiment with human adipose mesenchymal stem cells (hASCs), it was observed that when hASCs were administered on glutaraldehyde cross-linked nano-fibrillated cellulose (NFC-X), the cells adhered, migrated, and proliferated very well without showing toxicity [202]. The hASC attached on NFC-X retained their bioactivity, morphology, and undifferentiated state even after intradermal suturing. Injectable hydrogels are believed to be very useful in tissue engineering; however, weak mechanical strength has limited its applications. CNCs can be used for fabrication of different types of hydrogels with modified mechanical strength, gelation rate, swelling kinetics, and stability [203]. A new class of injectable

hydrogel composed of adipic acid dihydrazide-modified hyaluronic acid (HA) (ADH-HA), aldehyde-modified HA (a-HA), and aldehyde-modified CNCs (a-CNCs) was developed. Incorporation of a-CNCs increased the stiffness, and organized and compacted the network structure of the hydrogel. In vitro culture conditions, HA-CNCs nanocomposite hydrogels exhibited preferential cell support toward hASCs and increased its proliferative activity. It was believed to be due to higher structural integrity provided by CNCs and potential interaction of microenvironmental cues with CNC's sulfate groups [204]. A biocompatible 3D scaffold in situ was fabricated using nanofibrillar cellulose (NFC) hydrogels that helped in the differentiation of human hepatic cell lines HepaRG and HepG2 even in the absence of any external growth factors [205]. For the long-term release of growth factors in angiogenic applications, CNC and its conjugated structures can effectively be used. For example, gelatin microspheres (GMs) containing basic fibroblast growth factor (bFGF) can be incorporated into a porous collagen/cellulose nanocrystals (CNCs) scaffold [206], and used to augment cell proliferation of human umbilical vein endothelial cells. In vivo experiments using Sprague-Dawley rats has shown that the collagen/CNCs/bFGF-GMs scaffolds produced an expressively larger number of new and matured blood vessels. Recently, using high internal phase emulsion (HIPE) as a template, macroporous hybrid hydrogels were prepared using CNCs and 2-ureido-4[1H]-pyrimidone (UPy). The hybrid hydrogel exhibited excellent cytocompatibility and cell adhesion toward mouse bone mesenchymal stem cells (mBMSC) [207]. All these examples show that CNC can open a versatile generic platform for creating high-performance active biological scaffolds for tissue engineering and stem cell applications. This will pave a way toward the realization of creating artificial tissues or organs, such as nerve tissues, blood vessel, bones, skin, and many more.

5.1.4 Gold Nanoparticles

The attractive physicochemical properties of gold nanoparticles (AuNPs) have created remarkable interest in harvesting its potential for developing various functional nanomaterials. AuNPs have unique electronic, optical, and thermal properties mainly derived from its nanosize regime. Because of quantum size effect, AuNPs show interesting light scattering and localized surface plasma resonance (LSPR/SPR) phenomenon [208]. The physical origin of the LSPR in AuNPs is the interaction between conduction band electrons and the electromagnetic field. LSPR is an optical phenomenon caused when the incident photon frequency is in resonance with the collective oscillation of the conduction band electrons [209]. During this phenomenon, some of the incident photons are scattered and some of them cause vibrations of the lattice or transformed into phonons referred to as absorption [210]. The relative scattering and LSPR characteristics of AuNPs are greatly influenced by the shape, sizes, composition, core charge, surface ligand, dielectric property of surrounding, and the proximity of the other nanoparticles [208–209, 211], implying that the properties of AuNPs can be tuned for custom-made applications. LSPR phenomenon seizes to operate when the size of the AuNPs are either very small ($d < 2$ nm) or comparable to

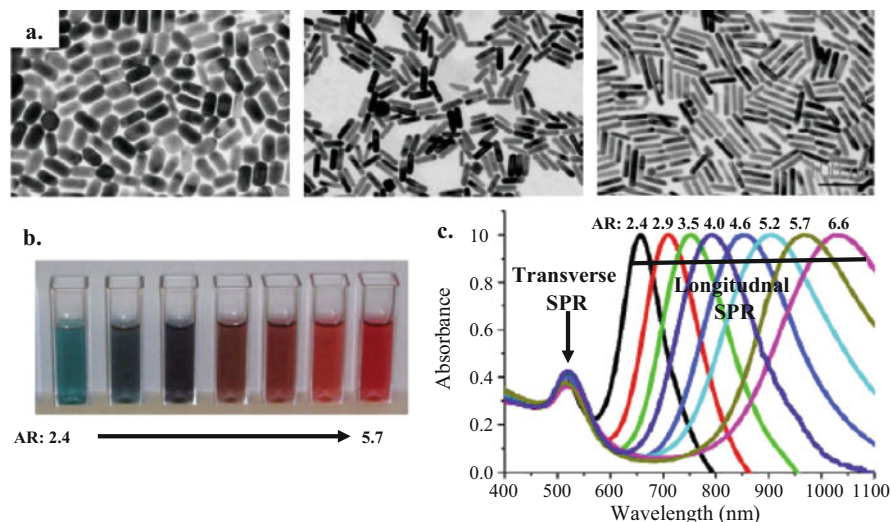


Fig. 1.9 Tunable SPR of gold nanorods. Gold nanorods of different aspect ratios (AR); (a) different color; and (b) different longitudinal and transverse SPR wavelength (c). (Adopted and modified with permission from Huang and El-Sayed [214])

bulk size [212–213]. With the increase in size, the LSPR is red shifted (red to purple) due to increased plasmonic coupling between the particles.

As the AuNPs becomes nonspherical, the surface plasmon resonance (SPR) band splits into two (Fig. 1.9) (i) a strong longitudinal band in visible-NIR region due to plasmonic oscillations along the long axis, (ii) and a transverse band in the visible wavelength of light due to plasmonic oscillation along the short axis [214]. Spherical AuNPs only show transverse LSPR and is dependent on the overall diameter of the particles. As the diameter increases, the transverse LSPR red shifts with broadening of the wavelength peak. The longitudinal LSPR depends mainly upon the aspect ratio of the AuNPs (length to width ratio). When the aspect ratio is increased, the longitudinal LSPR red-shifts from the visible to the NIR wavelength [215]. AuNPs of different shape (shell, cubes, and cages) and size can be synthesized by various methods such as Turkevich, Brust-Schiffrin, pulse radiolysis, seed-mediated, micellar, microbial, and many more [216]. For nanoshells, hollow nanocages and nanocubes visible-NIR LSPR can be tuned by modifying the shell thickness, wall thickness, void sizes, or the ratio of the core/shell radius [208, 217]. Other properties such as redox activity, high surface area to volume ratio, surface-enhanced Raman scattering (SERS), fluorescence quenching, photothermal effect, biocompatibility, and freedom of modifying surface with different molecules provide suitable platform for various state of art applications [58, 214, 218].

Due to biocompatibility, AuNPs have been a leading choice to explore its potential in the field of biosensors, bioimaging, catalysis, photothermal therapy, photoacoustic, immunoassay, single particle tracking, targeted drug, gene delivery, and many more applications [58, 218–219]. For example, SERS property of AuNPs

has been used to investigate the differentiation of mouse embryonic stem cells (mESC), including undifferentiated single cells, embryoid bodies (EBs), and terminally differentiated cardiomyocytes [220]. The study showed AuNPs can easily be administered into the cells without affecting cell viability or proliferation and used as fast and noninvasive molecular profiling technique for ES cell differentiation. AuNPs functionalized with polyethylene glycol can enhance MSCs migration, scaffold colonization, and regeneration. Internalized AuNPs by MSCs caused an increase in actin and tubulin protein expression, fibrin colonization, and osteoblastic differentiation [221].

Gold nanorods and spheres have also been used for *in vivo* tracking of the MSCs and macrophages activity using photoacoustic technique [222]. AuNPs and MSCs conjugates can also be used for targeting and killing of tumor cells. Intravenous administration of pH-sensitive gold nanoparticles (PSAuNPs) tagged with MSCs showed increased tumor targeting and heat generation, resulting in enhanced anticancer activity [223]. AuNPs can also promote and guide the differentiation of MSCs. In a study, it was found that AuNPs selectively enhanced the differentiation of MSCs toward osteoblast cells over adipocyte cells [224]. AuNPs were increasing the osteogenic transcriptional profile and decreasing the adipogenic transcriptional profile to achieve the selective differentiation. AuNPs-decellularized matrix hybrids were found to be very effective in cardiac tissue engineering. Hybrid scaffolds showed superior functions with respect to contraction forces, lower excitation threshold, and faster calcium transients than the pristine patches. The cardiac cells grown within the hybrid scaffolds showed lengthened and aligned morphology, substantial striation, and orderly connexin 43 electrical coupling proteins [224]. AuNPs can also be used for site-specific delivery of different growth factors. AuNPs-conjugated vascular endothelial growth factor (VEGF) was used for transdermal transport of VEGF, which could penetrate the skin barrier and allow VEGF to exert its biological activity subcutaneously, an important step toward wound repair or healing process [224].

5.1.5 Superparamagnetic Iron Oxide Nanoparticles

Superparamagnetic iron oxide nanoparticles (SPIOs) are nanosize iron-oxide particles. They exhibit interesting superparamagnetic property. Superparamagnetism is the phenomena of small crystallites (1–10 nm) wherein thermal energy changes the direction of magnetization of the entire crystallite even if the temperature is below the Curie or Neel temperature [225]. This causes the net average magnetic field to zero. These materials are similar to paramagnetic materials but with some differences. In superparamagnetic materials, instead of each discrete atomic magnetic dipoles being individually influenced by an external magnetic field, the magnetic moment of the whole crystallite tends to align with the direction of the external magnetic field [226]. SPIOs can be synthesized using various methods such as coprecipitation, microemulsions, sonochemical, or thermal decomposition of iron pentacarbonyl, reduction of iron salts, and oxides [227]. The SPIOs particles consist of two parts (i) iron-oxide core (magnetite, maghemite or hermatite) and hydrophilic coating [228]. The hydrophilic coating is achieved by providing a layer of synthetic or natural polymers (such as chitosan, dextran, gelatin, polyethylene-co-vinyl acetate, polyvinylpyrrolidone, polylactic-co-

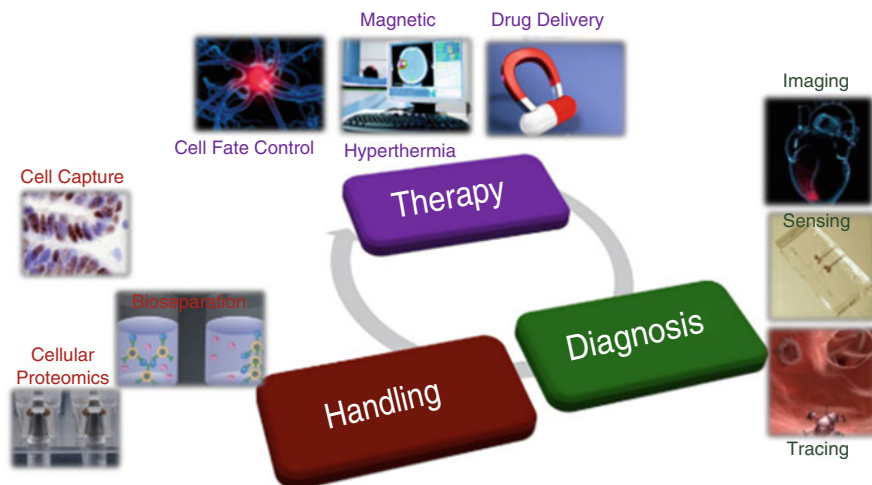


Fig. 1.10 Schematic showing applications of magnetic nanoparticles. (Adopted with permission from Angelakeris [230])

glycolic acid, and polyethyleneglycol) [226, 229]. Due to the superparamagnetic behavior, SPIOs provide a unique multifunctional platform for modern functional nanomaterials. They can be remotely and non-invasively used as imaging probes, carrier molecules, theranostics, enriching scarce molecules, smart actuators, and mechanical or heat stimuli for modulating different cellular functions [230]. In stem cell or tissue engineering, most of the applications are related to targeted delivery, imaging, separation, and scaffold development.

The hybrid magnetic scaffold can be developed for external magnetic field guided *in vivo* applications of growth factors, stem cells, gene delivery, and other biomolecules [230] (Fig. 1.10). A multifunctional magnetic nanoparticle was fabricated using polyethylenimine (PEI) and oxidized PEI/alginate; this hybrid system was found to be very effective in gene delivery to NSCs [231]. After transfection, real-time cell tracking of intracellular particles was carried out using magnetic resonance imaging (MRI). SPIOs derivatized with HIV-Tat can be internalized into hematopoietic and neural progenitor cells [232]. Following intravenous injection cells can easily be tracked and detected by MRI. Furthermore, magnetically labeled cells could be recovered by magnetic separation techniques. In another experiment, SPIOs tagged with specific monoclonal antibodies were used for separation of CD105+ and CD73+ mesenchymal stem cells from synthetic cell suspension comprising peripheral blood, human bone marrow cells, and fibroblastic cells [233]. The synergetic effect of magnetic nanoparticle hybrid scaffolds and magnetic field could be a promising tool for simulated tissue engineering. Polycaprolactone-magnetic nanoparticles conjugate system, when treated with the external static magnetic field, influenced the osteoblastic differentiation of primary mouse calvarium osteoblasts. Expression of bone-associated genes (Runx2 and Osterix), alkaline phosphatase activity, integrin signaling pathways, bone morphogenetic protein-2,

phosphorylation, and angiogenic responses of endothelial was found to be modulated [234]. Using magnetic particles and MSCs, 3D tissue can be constructed without using scaffolds. In a novel study, MSCs labeled with magnetite cationic liposomes were used to create a multilayered sheet-like structure. MSCs in the sheets preserved its ability to differentiate into osteoblasts, adipocytes, or chondrocytes. When the MSC sheets were transplanted into the bone defected in the crania of nude rat, new bone surrounded by osteoblast-like cells was formed after days of transplantation [235]. Polymeric nanofiber and SPIOs hybrids can also be used for cell differentiation and growth. In an experiment, poly- ϵ -caprolactone nanofibers and magnetic particles hybrid system was found to be enhancing cellular adhesion and proliferation of MSCs for osteogenic differentiation [231].

5.1.6 Quantum Dots

Quantum dots (QDs) are luminescent semiconductor nanomaterials. These nanomaterials are composed of 100–100,000 atoms per nanoparticle with an average diameter in the range of 2–20 nm [236–237]. Normally, QDs are binary systems made up of a core of semiconductor, surrounded by a shell of a different semiconductor material [236]. This shell is further coated with capping molecules to provide hydrophilicity and stability in the aqueous environment [238]. QDs can be synthesized by various methods such as hydrothermal, microwave, refluxing, micellar, and high-temperature colloidal synthesis process using group II (Zn, Cd, Hg)-VI (Se, S, and Te), III-V and IV-VI or mixture of group I-III-VI elements of the periodic table [239–240]. Due to nanometer size, QDs possess unique optical property arising from interactions between holes, electrons, and their surrounding environments [241]. Some of the interesting and unique properties of QDs are (i) size, shape, and composition-dependent narrow Gaussian emission bands, which can be tuned from blue to NIR region of the electromagnetic spectrum by varying the size and composition (Fig. 1.11);

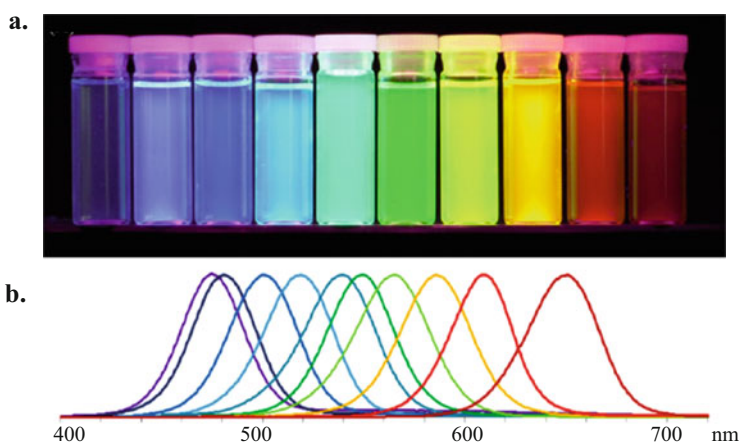


Fig. 1.11 Illustrative emission spectra of different QDs. Fluorescent color (a) and narrow emission spectra (b). (Adopted and modified with permission from Zrazhevskiy et al. [243])

(ii) high quantum yields of luminescence and molar extinction coefficients; (iii) high thermal and photostability; and (iv) luminescence blinking or intermittency [238–239, 241]. Unique tunable fluorescent properties of QDs make them a promising material for various biomedical applications including but not limited to multispectral imaging of cells, tissues, organs, biomolecules, photoinduced therapy, immunohistochemistry, real-time targeting, tracking, gene therapy, and biosensing [241–243].

In tissue and stem cell engineering, QDs used for tagging, tracking, and imaging of biomolecules or cells are advantageous in many senses. For example, long-term labeling of stem cells during self-replication and differentiation will help in understanding the fate and mechanism of tissue regeneration. The biological or biochemical phenomenon at the molecular or cellular level can be properly understood and elucidated. This can lead to the correct and optimized selection of a methodology for a personalized application. For example, QDs have been used for labeling hMSCs and remained active for 22 days [244]. Even after differentiation into chondrogenic, osteogenic, and adipogenic cells, QDs continued to exist in differentiated cells. This can be exploited in understanding the fate of the proliferated and differentiated stem cells under different conditions. In a study, hMSCs were found to be uniformly and completely loaded with QDs. QD-loaded cells can be distinctly imaged in histologic sections even after 8 weeks of delivery. Other important observations such as no negative effect on differentiation of hMSCs *in vivo*, no transfer of QDs to adjacent cells, and ability of being transfected to overexpress genes even after QDs treatment were also concluded [245]. Quantum dots were used to label orbital fat-derived stem cells (OFSCs) for determining their fate of differentiation toward corneal epithelial cells [246]. After 5 days of culture, expression of epithelial specific antigen can be seen for QD-labeled OFSCs. The fate of the stem cells, its proliferation, and differentiation profile can easily be imaged using different fluorescent modalities like light/confocal/two-photon microscopy. The tissue distribution of MSCs labeled with CdSe/ZnS (tagged and capped with Tat peptide and PEG) was visualized using fluorescence microscopy [247]. After subcutaneous administration of QDs tagged murine embryonic stem (ES) cells into mice, it was imaged using flow cytometry and fluorescent microscopy. QDs did not show negative effect on the cell viability, proliferation, and differentiation [248]. QDs tagged with adipose tissue-derived stem cells (ASCs) using the octa-arginine peptide (R8) cell-penetrating peptide (CPP) were found to be actively differentiating into adipogenic and osteogenic cells. The labeled ASCs were tracked using the Maestro *in vivo* imaging system after subcutaneous transplantation into the mice [249]. Undoubtedly, QDs tagging seems to be promising in identifying and imaging the fate of different biomolecules in both *in vivo* and *ex vivo*. However, its cytotoxicity and biocompatibility need more careful and systematic evaluation.

5.2 Tissue Engineering Constructs and Scaffolds for Regenerative Nanomaterial Applications

Micro- and nanoscale technologies are emerging as powerful enabling tools for tissue engineering and drug discovery. In tissue engineering, micro- and nanotechnologies

can be used to fabricate biomimetic scaffolds with increased complexity and vascularization. Furthermore, these technologies can be used to control the cellular micro-environment (i.e., cell–cell, cell–matrix, and cell–soluble factor interactions) in a reproducible manner and with high temporal and spatial resolution [250]. Tissue engineering approach is one of the key approaches for the treatment of damaged tissues and organs without limitations of the conventional therapies including technical, economic, and social obstacles. Artificial three-dimensional (3D) implantable nanomaterials composed of specific cells are employed to generate new tissues with natural histology and functions [251]. Therefore, this chapter treats the convergence of research at the interface of nanostructured bio-nanomaterials and tissue engineering for emerging biological technologies such as scaffolding/nano-platforms and tissue regeneration based on recent developments in the field of micro- and nanoscale technologies.

5.2.1 Nanostructured Tissue Engineering Constructs and Scaffolds for Bone Tissue Engineering

The use of nanostructured biomaterials in bone regeneration is an important issue. It is of great interest to develop biomimetic nanostructured scaffolds to mimic native bone [252]. Several researches showed that nano-CaP biomaterials exhibited physicochemical and biological characteristics better than conventional-sized CaPs, due to nano-CaPs being more similar to bone nanocrystals [253]. The fibers of the ECM and basement membrane (10–300 nm in diameter), their interconnecting nanopores, and hydroxyapatite crystals (4 nm) found in natural bone typically have nanoscaled dimensions (Fig. 1.12) [254].

5.2.2 Biomimetic Efforts in Bone Tissue Engineering

Bone is a remarkable organ playing key roles in critical functions in human physiology including protection, movement, and support of other critical organs, blood production, mineral storage and homeostasis, blood pH regulation, multiple progenitor cell (mesenchymal, hematopoietic) housing, and others [256]. Bone defects such as osteogenesis imperfecta, osteoarthritis, osteomyelitis, and osteoporosis represent a medical and socioeconomic challenge [257]. Different types of bone tissue engineering research are raising interest. The traditional biological methods of bone-defect management include autografting and allografting cancellous bone, applying vascularized grafts of the fibula and iliac crest, and using other bone transport techniques [258].

Bone scaffolds are typically made of porous degradable materials that provide the mechanical support during repair and regeneration of damaged or diseased bone [259]. Promising results have already been obtained with this approach, not only for bone tissue, but also for other organs and tissues [260]. One common approach is to isolate specific cells through a small biopsy from a patient to grow them on a three-dimensional (3D) scaffold under controlled culture conditions [261]. Subsequently, the construct is delivered to the desired site in the patient's body with the aim to direct new tissue formation into the scaffold that can be degraded over time [260, 262–263]. 3D internal geometry, similar to bone morphology, and the retention of

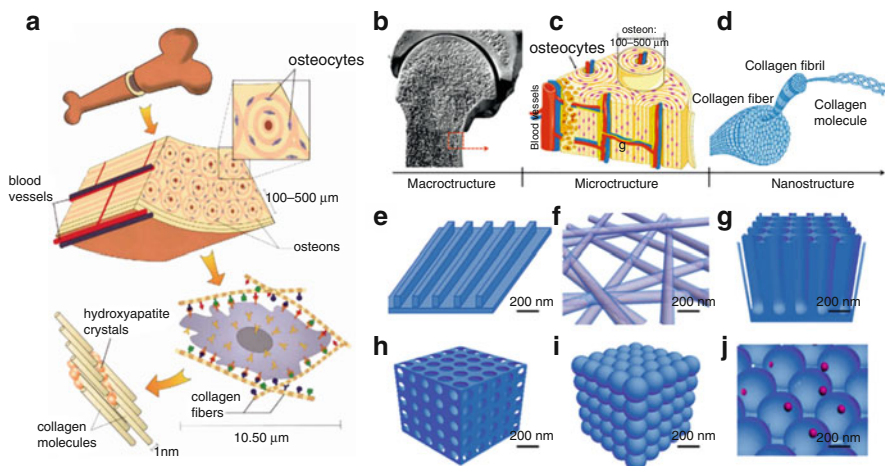


Fig. 1.12 (a) Hierarchical organization of bone over different length scales. The microstructure and nanostructure of bone and the nanostructured material used in bone regeneration [254]. (b) At the macroscopic level, bone consists of a dense shell of cortical bone with porous cancellous bone at both ends. (c) Repeating osteon units within cortical bone. In the osteons, 20–30 concentric layers of collagen fibers, called lamellae, are arranged at 90° surrounding the central canal, which contain blood vessels and nerves. (d) Collagen fibers (100–2 000 nm) are composed of collagen fibrils. The tertiary structure of collagen fibrils includes a 67 nm periodicity and 40 nm gaps between collagen molecules. The hydroxyapatite (HA) crystals are embedded in these gaps between collagen molecules and increase the rigidity of the bone. Nanostructures with features of nanopattern (e), nanofibers (f), nanotubers (g), nanopores (h), nanospheres (i), and nanocomposites (j) with structural components with a feature size in the nanoscale [255]

mechanical properties after implantation are required for scaffolds in order to maintain a tissue space of prescribed size and shape for tissue formation [264]. In the case of ceramic scaffolds, a macroporosity of 200–400 μm is needed to promote bone cell attachment, and a microporosity of less than 10 μm should promote ion and liquid diffusion [265]. Especially, Keaveny and Hayes reported that cancellous bone ranged in compressive modulus from 10 to 2,000 MPa [266]. In contrast to most man-made sandwich cores, trabecular bone has an optimized structural anisotropy due to the trabecular orientation along the principal stress trajectories [267–268]. On a nanometer scale bone is a composite consisting of 20–30% collagen fibers, about 1% of other proteinaceous material bonding about 70% of calcium phosphate in the form of hydroxyapatite which provides stiffness and strength [269]. As materials applied in bone grafting as well as guided tissue regeneration, highly porous microstructures with an interconnected, communicating network and a large surface area are desirable [270].

The scaffolds for bone tissue engineering should be fabricated from a biocompatible polymer, which does not have the potential to elicit an immunological or foreign body reaction [271]. One of the requirements is that the degradation products of scaffold should not be toxic and must be easily excreted by metabolic pathways. Polymers can serve as a matrix to support cell growth by having various properties

such as biocompatibility, biodegradability, porosity, charge, mechanical strength, and hydrophobicity [272]. Polymers can be easily modified and altered by changing the constituents of monomers, controlling polymerization conditions, or introducing functional groups to the polymers [273]. The poly- α -hydroxy-esters, namely polylactic acid (PLA), polyglycolic acid (PGA) and copolymers, poly(lactide-co-glycolide) (PLAGA), approved by the FDA for use in a number of applications have been widely investigated for tissue engineering applications [274]. High-molecular-weight poly(L-lactide) have been successfully investigated on the in vivo and in vitro degradation for bone fixation pins [275]. The composite sintered with poly-DL-lactide (PDLA) and tricalcium phosphate (TCP) ceramic particles healed the fractured bone and fixed on the fracture area during the implanted period, which provided a breeding environment for normal bone remodeling [276]. Hydroxyapatite/chitosan–gelatin network (HAp/CS-Gel) composite scaffold indicated that osteoblasts become securely attached to the material surfaces, express their functions, and maintain a good proliferation trend in the HAp/CS-Gel composite scaffolds [277]. Nano-HA/collagen/PLA composite scaffold has promise for the clinical repair of large bone defects according to the showing some features of natural bone both in main composition and hierarchy microstructure [278]. Recently, natural polymer-based composites such as polysaccharides (starch, alginate, chitin/chitosan, hyaluronic acid derivatives) and proteins (soy, collagen, fibrin gels, silk) have been focused with more attention than synthetic polymer composites for bone tissue engineering applications [272]. Consequently, a variety of polymers have been reported for their applications in bone tissue engineering.

In the light of the complexity of bone properties, various requirements must be met to produce a scaffold. Firstly, determining how or even if designer scaffolds can improve tissue-engineering treatment requires that these scaffolds can be first fabricated and then tested for mechanical function and tissue regeneration [279]. Hutmacher et al. [280] should have the following characteristics for ideal scaffold: (i) three-dimensional and highly porous with an interconnected pore network for cell growth and flow transport of nutrients and metabolic waste; (ii) biocompatible and bioresorbable with a controllable degradation and resorption rate to match cell/tissue growth in vitro and/or in vivo; (iii) suitable surface chemistry for cell attachment, proliferation, and differentiation; and (iv) mechanical properties to match those of the tissues at the site of implantation. An important property of scaffolds for replacement of bone tissue engineering was strength. If the scaffold cannot provide a mechanical modulus in the range of hard (10–1,500 MPa) [281] or soft tissues (0.4–350 MPa) [282], then any nascent tissue formation will probably also fail due to excessive deformation [279].

5.2.3 Nanoscaffolds in Dental Tissue Engineering Applications

It is perhaps unsurprising that curiosity in novel technologies in dental implant treatments is on the rise, as the American Academy of Implant Dentistry estimates half a million more Americans are getting dental implants each year for aesthetic and functional reconstruction. The most dire need for nanostructures and scaffolds lies within regeneration of missing or damaged oral tissues [3], as large defects due to

trauma or tooth loss limit the effectiveness of prosthodontic treatments [283]. However, regenerative medicine is not only targeting teeth and alveolar bone, but aiming to provide a platform to regenerate other oral tissues such as the salivary gland [284], tongue [285], and craniofacial skeletal muscles [286], as well as the cartilage of the temporomandibular joint [283, 287–288].

The stem cells most commonly used for bone regeneration in dental patients are still bone-marrow-derived multipotent mesenchymal stromal cells from the iliac crest [283]. However, it is becoming increasingly evident that stem cells obtained from the craniofacial area for autologous bone grafting provide better results and significantly higher resultant bone volume than bone generated from cells harvested from the iliac crest – indicating that skeletal donor tissues indeed have site-specific regenerative properties [283]. However, the collectable volume of orofacial bone marrow is much less than that of iliac crest; necessitating a reliable and safe cell expansion protocol if and when orofacial BMSCs are used for clinical trials [283].

The field of dentistry is very experienced in material/growth-factor-based approaches with several commercial scaffolds on the market with a wide variety of recombinant growth-factor approaches; for details, the reader is directed to a comprehensive review of the tissue engineering aspect by Egusa and colleagues [289]. Nanotechnology has entered the field primarily through the antimicrobial properties of silver nanoparticles (AgNPs), zinc-oxide-based nanoparticles (ZnONPs), titanium dioxide-based nanoparticles (TiO₂NPs), and chitosan nanoparticles; as well as polymeric nanoparticles and nanocomposites facilitating drug delivery, restoration, and biomodulation of dental tissues – as described in detail in a review by Padovani et al. [4]. The synthesis of nanoparticles with specific surface topography and biological properties, and their incorporation into composites and injectable biomaterials, afford a promising approach to repair dental tissues through biological responses [4].

At the intersection of nanotechnology-based tissue engineering and regenerative stem cell therapy, promising results have been published indicating, for example, that chitosan can be used as an effective calcium chelating agent for implants, facilitating the differentiation BM-MSCs [290]. Furthermore, it appears as though dental cements conjugated with nano-hydroxyapatite exhibit better biocompatibility when in contact with MSCs and more effectively induce mineralization-associated gene expression in osteoblasts, compared to conventional ceramic cements [291–292]. As tools and methodologies advance both in the field of nanodentistry and stem cell applications, it is evident that the combination of the two can be translated into highly impactful therapies within the oral cavity.

5.2.4 Main Types of Nano-scaffolds for Tissue Engineering

Nanopattern

The construction of synthetic ECMs inspired by tissue-specific niches for programmed stem cell fate and response, such as proliferation and differentiation, is a topic of interest in the field of tissue regeneration [255]. At the microstructure level, tissue exhibits both morphological and mechanical heterogeneity and varies greatly

at different anatomical and structural levels [293]. Using feature primitive approach, each primitive discrete volume can be represented by a specific design feature, such as different internal architecture patterns used in common tissue scaffold design, for example, the standard weave, braided, and knit geometric feature of textile fiber patterns can be used as scaffold architectures or muscular pattern in soft tissues [293]. Figure 1.13 shows diverse patterns of scaffold based on different feature primitives.

Using nanogrooved matrices mimicking the native tissues, Kim et al. found that the body and nucleus of human mesenchymal stem cells (hMSCs) with the sparser nanogrooved pattern elongated and orientated more along the direction of nanogrooves than those with the relatively denser nanogroove patterns [294]. In contrast, the effect of nano-topographical density on the osteo- or neurogenesis of hMSCs was significant at the 1:1 and 1:3 nanogrooved patterns, but not significant at 1:5 nanogrooved pattern compared to that at the flat substrate [255]. It is demonstrated the effects of nano-topographical density on the morphology and differentiation of mesenchymal stem cells [255].

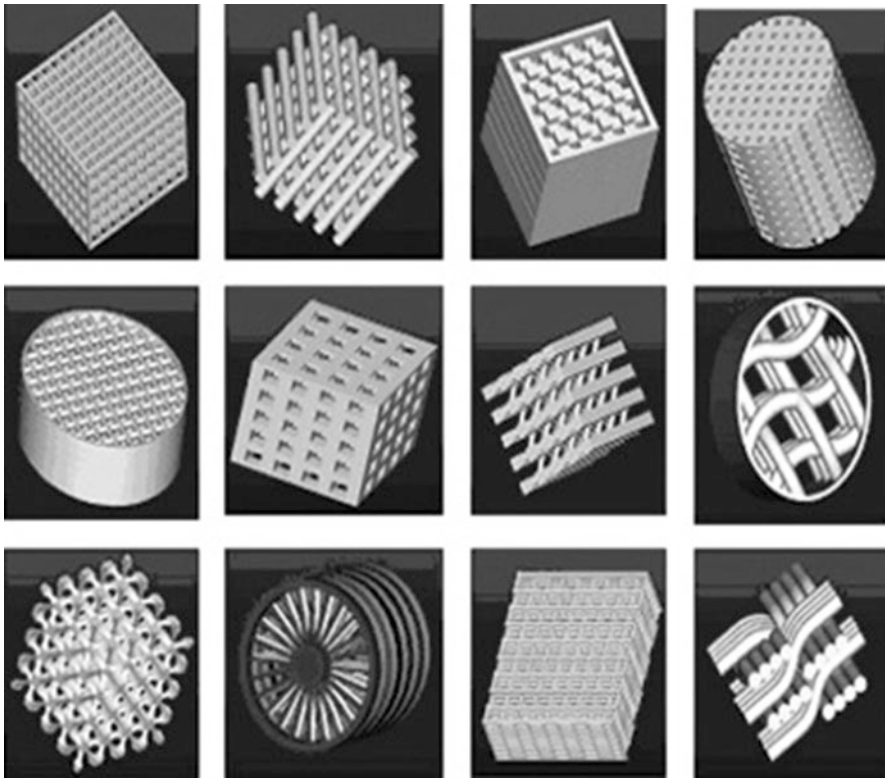


Fig. 1.13 A library of designed scaffold unit cells based on different feature primitives [295]. (Reprinted with permission)

Electrospinning

The principle of electrospinning is that an electric field is used to overcome the surface tension of a polymer solution to shoot a jet of liquid out of a needle toward a conducting collector [22–24]. The volatile solvent evaporates in the air leaving behind, under the right conditions, a polymer fiber with a diameter that can range from tens of nanometers to microns [255]. Many parameters affect this process including polymer properties, solvent properties, solution flow rate, voltage, distance from the needle to the collector, and polymer concentration, among others [25–26].

The wide range of polymers capable of being electrospun is appealing to bone tissue engineering and gives researchers flexibility in designing nanofibrous scaffolds [255]. Generally, there are two types of polymers that are chosen: synthetic polymers or natural polymers [255]. Synthetic polymers, such as poly(L-lactic acid) (PLLA), poly(glycolic acid) (PGA), and polycaprolactone (PCL), among others, provide great flexibility in synthesis, processing, and modification [255]. However, these polymers lack bioactivity and special care needs to be taken to ensure that newly synthesized polymers are biocompatible [255]. Many natural polymers, on the other hand, have inherent bioactivity with peptide sequences that affect cell adhesion, proliferation, and differentiation [255]. Since both synthetic and natural polymers have advantages and disadvantages, research has progressed to fabricate hybrid scaffolds in an effort to maximize the benefits of both [255].

Li et al. developed a new nanoparticle-embedded electrospun nanofiber scaffold for the controlled dual delivery of BMP-2 and dexamethasone (DEX) [296]. The *in vitro* studies showed that the bioactivity of DEX and BMP-2 was preserved in the dual-drug-loaded nanofiber scaffold, and a sequential release pattern in which most of the DEX was released in the original 8 days and the BMP-2 release lasted up to 35 days was achieved [296]. The *in vitro* osteogenesis study demonstrated that the drug-loaded groups exhibited a strong ability to induce differentiation toward osteoblasts [296].

Nanocomposites

Nanobiomaterials and nanocomposites represent promising platforms in bone tissue engineering with a capacity to recapitulate the organization of natural ECM and the generation of functional bone tissues through osteo-mimetic architecture [255]. The inherent properties of nanocomposites, such as increased wettability, roughness, and surface area, can also promote biomaterial-driven bone regeneration through increased protein adsorption, nutrient exchange, and porosity relative to macroscale biomaterials [255].

Nanoscale features have been shown to have regulatory effects over multiple aspects of osteoblast and bone derived stem-cell behavior including adhesion, migration, proliferation, cell signaling, genetic expression, and stem cell fate [255]. Consequentially, biomaterial design has focused on the introduction of nanoscale elements that elicit directed cellular behavior while imparting structural and mechanical advantages to the bone construct to induce the formation of functional tissues [255]. Current methodologies employed in the fabrication of nanocomposites include electrospinning and molecular self-assembly [255].

3D Printing of Nanomaterial Scaffolds

Three-dimensional printing is an emerging technique in the tissue engineering field [297]. The unique control offered by designed scaffolds opens up additional avenues for tissue engineers to take advantage of that were until recently not realistic [297]. In any form of 3D printing, the desired structure is precisely designed using computer-aided design (CAD) software [297]. The 3D design is then passed to a slicing program that parses the solid object into a stack of thin, axial cross sections [297]. Figure 1.14 and Table 1.1 show examples on application of 3D printing methods for tissue engineering.

Inkjet printers (also known as drop-on-demand printers) are the most commonly used type of printer for both nonbiological and biological applications [298]. Inkjet bioprinting (Fig. 1.14) uses a modified consumer grade inkjet printer to deposit cells and biomaterial, dubbed “bioink,” onto a substrate, dubbed “biopaper.” [297] Bioinks have poor mechanical strength [299]. In order to provide a suitable mechanically strong scaffold with nanofeatures suitable for stem cell performance, an inkjet bioprinter was used in conjunction with an electrospinning needle to simultaneously print scaffold and multiple cell populations into the three distinctive layers of the bladder [297].

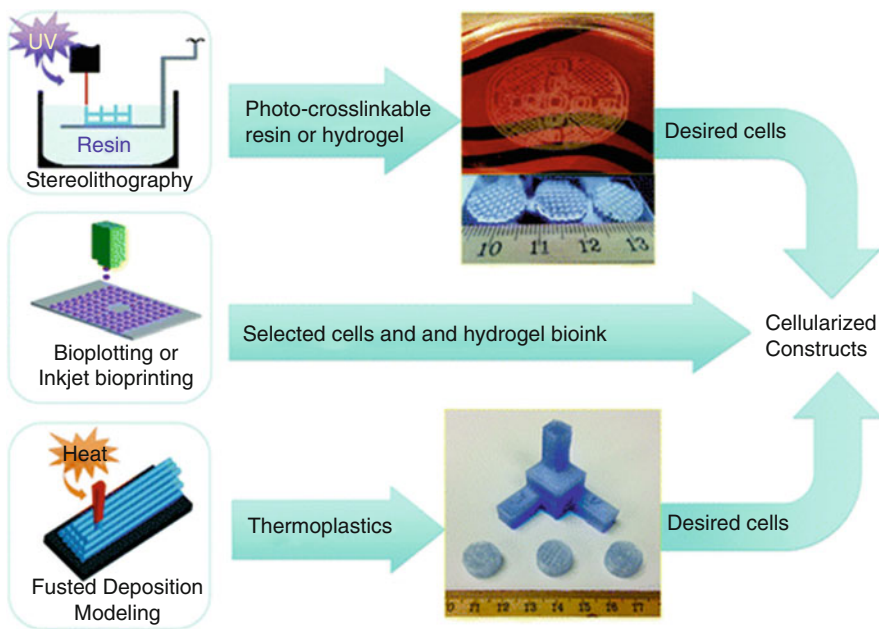


Fig. 1.14 Several 3D printing modalities discussed in this article with examples of the resulting scaffolds. The stereolithography printed scaffold is PEG-DA, and the FDM printed scaffold is polylactic acid. 3D three dimensional, FDM fused deposition modeling, PEGDA poly(ethylene glycol) diacrylate [297]. (This figure is reprinted under the terms of the Creative Commons Attribution Non-Commercial License [<http://creativecommons.org/licenses/by-nc/3.0/>])

Table 1.1 Several examples of 3D printing for various tissue and organ regeneration [297]. (This table is reprinted under the terms of the Creative Commons Attribution Non-Commercial License [<http://creativecommons.org/licenses/by-nc/3.0/>])

Tissue types	Printing methods	Printing materials	Description	References
Bone	FDM	Polymer and ceramic	PCL/CaP was printed into a 3D scaffold and seeded with MSC hydrogel. The scaffold can support MSC attachment and osteogenic differentiation	[300]
	SLS	TCP	Microwaves were used in a novel device to sinter particles into a biomimetic, porous scaffold that increased bone formation	[301]
Cartilage and osteochondral tissue	Inkjet bioprinting	Collagen-fibrin hydrogel	In conjunction with electrospun PCL, cartilage scaffolds were fabricated that supported the development of collagen-like structures both in vitro and in vivo.	[302]
	Bioplotting	Alginate hydrogel	Two layers of an osteochondral scaffold were fabricated, and evaluated both in vitro and in vivo. The scaffold developed distinctly different ECM morphologies in the corresponding bone and cartilage layers.	[303]
	FDM	Poly-lactic acid polymer and collagen	An osteochondral construct conjugated with collagen was created to enhance MSC growth and differentiation	[304]
Neural	Inkjet bioprinting	Fibrin hydrogel	NT2 neural cells were printed between layers of 3D fibrin hydrogel to create a neural mat. The cells adhered well, proliferated, and began to extend neuritis after 12 days of culture	[305]
	SL	Hyaluronic acid hydrogel	Biomimetic nerve conduits were fabricated and found to support	[306]

(continued)

Table 1.1 (continued)

Tissue types	Printing methods	Printing materials	Description	References
			neuronal growth and axonal extension in vitro	
Vascular	Bioplotting	Hyaluronangelatin hydrogel	Cellular constructs were fabricated that formed a vascular construct with excellent cellular viability. Aortic root sinus cells and aortic valve leaflet cells were printed in the same construct, in biomimetic form	[307]
Complex tissue and organ	Bioplotting	Alginate spheroids	Stem cells were printed in an organ mimetic fashion. Cell viability was high, and spheroids fused in time to a continuous geometry.	[308]
	Inkjet bioprinting	Calcium chloride/sodium alginate hydrogel	Three cell types were printed concurrently into a single scaffold. All cell types maintained viability and proliferative capacity, as well as phenotypic expression and physiological function. In vivo, vascularization was observed	[309]

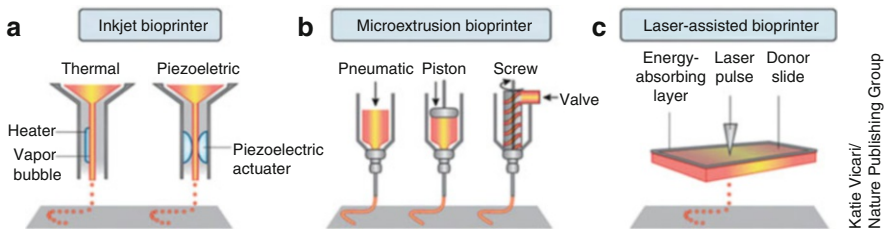


Fig. 1.15 (a) Thermal inkjet printers electrically heat the printhead to produce air-pressure pulses that force droplets from the nozzle, whereas acoustic printers use pulses formed by piezoelectric or ultrasound pressure. (b) Microextrusion printers use pneumatic or mechanical (piston or screw) dispensing systems to extrude continuous beads of material and/or cells. (c) Laser-assisted printers use lasers focused on an absorbing substrate to generate pressures that propel cell-containing materials onto a collector substrate [298]. (Reprinted with permission)

The main technologies used for deposition and patterning of biological materials are inkjet, microextrusion, and laser-assisted printing (Fig. 1.15) [298]. Different features of these technologies (Table 1.2) should be considered in light of the most

Table 1.2 Comparison of bioprinter types with different factors [298]. (Reprinted with permission)

Bioprinter type	Inkjet	Microextrusion	Laser assisted
Material viscosities	3.5–12 mPa/s	30 mPa/s to $>6 \times 10^7$ mPa/s	1–300 mPa/s
Gelation methods	Chemical, photo-crosslinking	Chemical, photo-crosslinking, shear thinning, temperature	Chemical, photo-crosslinking
Preparation time	Low	Low to medium	Medium to high
Print speed	Fast (1–10,000 droplets per second)	Slow (10–50 $\mu\text{m/s}$)	Medium-fast (200–1,600 mm/s)
Resolution or droplet size	<1 pl to >300 pl droplets, 50 μm wide	5 μm to millimeters wide	Microscale resolution
Cell viability	$>85\%$	40–80%	$>95\%$
Cell densities	Low, $<10^6$ cells/ml	High, cell spheroids	Medium, 10^8 cells/ml
Printer cost	Low	Medium	High

important factors in 3D bioprinting, which are surface resolution, cell viability, and the biological materials used for printing [298].

5.3 Stem Cells in Research and Applications in the Cardiovascular System

Cardiovascular diseases such as myocardial infarction (MI) or coronary artery complications account for over 40% of deaths and are among the major causes of morbidity and mortality in the developing and developed nations [310]. In the United States alone, an estimated \$555 billion was spent on cardiovascular disease treatment and medication in the year 2016 and the cost is estimated to reach 1.1 trillion by 2035 [311]. Myocardial infarction is a condition where interruption to the heart's blood supply leads to the death of resident cardiomyocytes (CMs) in a short period of time and subsequently leads to remodeling and dilation of ventricular wall, and the formation of non-contractile scar tissue [312]. Since the adult myocardium has limited regenerative capacity, MI ultimately results in catastrophic heart failure [21].

5.3.1 Nanofibrous Cardiovascular Scaffolds

Nanofibrous cardiovascular scaffolds (Fig. 1.16) have several advantages such as nanoscaled morphology mimicking the hierarchy of native ECM, high porosity which accelerates blood vessel formation, and high surface area for cell attachment and proliferation [21]. Most nanofibrous scaffolds are synthesized by electrospinning, which is a process to create nanofibers through an electrically charged jet of polymer solution/melt [21]. Electrospinning allows control of the

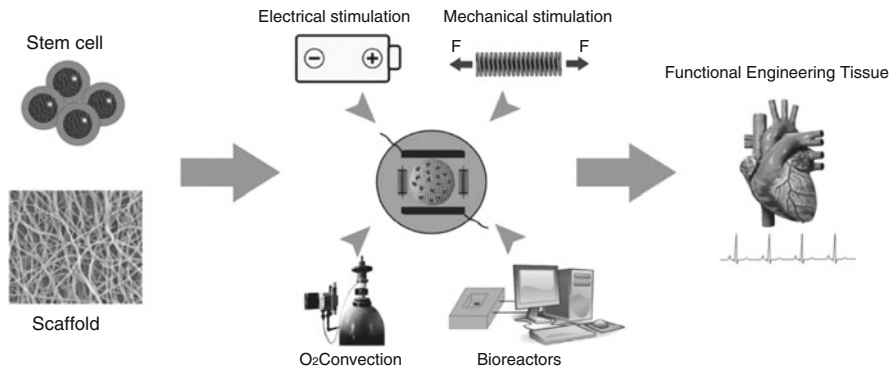


Fig. 1.16 Current approaches of using cells and scaffolds for cardiac tissue engineering [21]

Table 1.3 Myocardial tissue engineering with stem cells

Biomaterials	Physical form	Chemical/physical stimuli	Cells	Reference
Gelatin	Microsphere	–	ESC-CMs	Akasha et al. [313]
PU + gel/lam/coll	Film	–	ESC-CMs	Alperin et al. [314]
PLCL	Solid scaffold	Mechanical loading	ESC-CMs	Gwak et al. [314–315]
PGA	Patch	–	ESCs	Ke et al. [316]
ABP	Porous patch	–	MSCs	Wei et al. [317]
SF + chitosan/HA	Solid scaffold	5-Azacytidine	MSCs	Yang et al. [318]

PU polyurethane, *gel* gelatin, *lam* lam, *coll* collagen, *PLCL* poly(lactide-co-caprolactone), *PGA* polyglycolic acid, *ABP* acellular bovine pericardium, *SF* silk fibroin, *HA* hyaluronic acid, *CM* cardiomyocytes

diameters, mechanical properties, and even orientation of fibers, which all are significant for cardiac TE [21].

Scaffolds for cardiac TE (Table 1.3) should possess the features such as (1) the ability to deliver and foster cells, (2) biodegradability, (3) suitable mechanical property that suits the contraction of native myocardium, and (4) porous structure for vascularization. Several studies focused on developing nanofibrous cardiovascular scaffolds (Table 1.4).

Studies by Shin et al. showed that when cultured rat cardiomyocytes were cultured on electrospun PCL nanofibers, the cells attached on the scaffolds, started to beat after 3 days, and cardiac-specific proteins such as connexin 43, α -myosin heavy chain, and cardiac troponin I were expressed after 2 weeks [319]. The group also created thick cardiac grafts by overlapping up to five layers of the cell-nanofiber membranes [320], and demonstrated that after 1 week of culture *in vitro*, morphologic and electrical

Table 1.4 Results of biomaterials-integrated stem cell therapy for MI in *in vitro* studies [339]. Peptide sequence: R, arginine; A, alanine; D, aspartic acid. (Reprinted with permission)

Approach and materials	Cells or biomolecules	Model	Delivery method	Time point (in vivo)	Major observations (in vitro and in vivo)
<i>Protein or gene delivery materials</i> Chitosan-alginate nanoparticle [323]	PIGF	Rat	Intramyocardial injection	8 weeks	Heart function ↑ Vascular density ↑ Scar formation ↓ Inflammation ↓
Self-assembling peptide nanofiber [324] (AcN-RARADARARADADA-CN _H ₂)	PDGF-BB	Rat	Intramyocardial injection	2 weeks	CMC death ↓ Systolic function ↑ Infarct size ↓ Contractility ↑
Baculovirus nanocomplex [325]	Angiopoietin-1 with ASC	Rat	Intramyocardial injection	4 weeks	Capillary density ↑ Infarct size ↓ Heart function ↑
<i>Cell delivery materials</i> Self-assembling peptide [326] (AcN-RADARADARADADA-NH ₂)	CSC	Mouse	Intramyocardial injection	2 weeks	Heart function ↑ Fibrosis ↓ Capillary density ↑
Collagen patch [327]	MSC	Rat	Epicardial surface patch	4 weeks	MSC enlargement ↑ Wall thickness ↑ Heart function ↑
PLCL patch [27]	MSC	Rat	Epicardial surface patch	4 weeks	MSC cardiac differentiation ↑ Heart function ↑ Infarct size ↓
Self-assembling peptide [328] (AcN-RARADARADADA-NH ₂)	MNC	Pig	Intramyocardial injection	4 weeks	Heart function ↑ Enlargement ↓ Capillary density ↑
Self-assembling peptide [329] (AcN-RARADARADADA -NH ₂)	MSC	Rat	Intramyocardial injection	4 weeks	Heart function ↑ Infarct size ↓ Cardiac differentiation ↑

(continued)

Table 1.4 (continued)

Approach and materials	Cells or biomolecules	Model	Delivery method	Time point (in vivo)	Major observations (in vitro and in vivo)
Self-assembling peptide [330] (AcN-RADARADARADA-NH ₂)	CSC	Rat	Intramyocardial injection	4 weeks	Heart function ↑ Capillary density ↑ Vascular enlargement ↑
<i>Nanomaterials with topographical cues</i>					
Patterned PEG hydrogel [331]	CSC	Rat	Epicardial surface patch	3 weeks	Wall thickness ↑ Organized collagen deposition ↑ Surviving muscle cells ↑
Microelectrode arrays (in vitro study) [332]	MSC and CMC co-culture	N/A	N/A	N/A	MSC conduction velocity ↑ MSC gap junction protein ↑
PCL nanofiber [333]	MSC	Rat	Epicardial surface patch	4 weeks	Heart function ↑ Fibrosis ↓ Wall thickness ↑
<i>Nanomaterials with electrical conductivity</i>					
Carbon nanotube (in vitro study) [20]	MSC	N/A	N/A	N/A	MSC cardiac-specific and gap junction protein ↑
Gold nanoparticle embedded BSA/PVA scaffold [334] (in vitro study)	MSC with 5-azacytidine	N/A	N/A	N/A	MSC cardiac-specific and gap junction protein ↑
Reduced graphene oxide [335]	MSC spheroids	Mouse	Intramyocardial injection	2 weeks	MSC gap junction protein ↑, heart function ↑
<i>Nanomaterials with chemical cues</i>					
Iron oxide nanoparticle [336]	MSC and H9C2 co-culture	Rat	Intramyocardial injection	2 weeks	MSC cardiac-specific and gap junction protein ↑, MSC paracrine ↑, heart function ↑, capillary density ↑
Self-assembling peptide nanofiber (not specified) [337]	MSC-conditioned medium	Mouse	Intramyocardial injection	4 weeks	Contractility ↑, vascularization ↑, heart function ↑
Graphene (in vitro study) [335]	MSC	N/A	N/A	N/A	MSC cardiac-specific and gap junction protein ↑
Graphene (in vitro study) [338]	ESC	N/A	N/A	N/A	ESC cardiac differentiation ↑

communication between the intimately adhered layers was established, and synchronized contraction was also observed. Studies by Li et al. with electrospun PLGA-gelatin-elastin nanofibers found the scaffolds promoting rat cardiac myoblasts (H9c2) proliferation and assisting bone marrow-derived stem cells (BMSCs) to penetrate into the center of scaffolds [321]. Zong et al. were able to fabricate aligned biodegradable non-woven PLGA nanofibers membranes and cultured neonatal rat cardiomyocytes, and cell orientation and elongation were enhanced on aligned nanofibers [322]. Several such studies indicate that surface topography affects cell behavior and aligned nanostructure guides cell orientation.

Alignment of fibers on nanofibrous patches plays a major role in cardiac repair. Cardiomyocytes cultured on aligned nanofibrous electrospun patches displayed a higher amplitude and beating frequency compared to those cultured on randomly oriented fibrous patches [340]. The cardiomyocytes-seeded aligned cardiac patch improved cardiac function, unlike the cardiomyocytes-seeded randomly oriented patch which resulted in serious deterioration in the cardiac function upon implantation in vivo [341]. MSCs cultured on a directionally nanopatterned substrate have also significantly improved their cardiac differentiation and their functional integration with cardiomyocytes in the MSC-cardiomyocyte co-culture in a study by Pijnappels et al. [332]. The nanopatterned alignment increased MSC's conduction velocity and expression of connexin 43 (Cx43-gap junction protein) indicating cell behavior regulation and synchronous integration of MSCs with the surrounding cardiac tissue.

5.3.2 Cardiac Patches and Injectable Nanomaterials

Nanostructured cardiac patches and injectable nanomaterials were studied to improve stem cell retention after implantation in vivo [28–30]. Collagen has a nanofibrillar structure which mimics native cardiac extracellular matrix and studies by Simpson et al. demonstrated that collagen patches seeded with MSCs restored cardiac function after implantation [327]. MSCs delivered with collagen patches achieved a 23% cell engraftment and resulted in improved cardiac function. However, limitations such as an inflammatory microenvironment at the infarct region and the leakage of the implanted cells from the injection site still affect such cardiac patches. Studies also showed that when MSCs were seeded onto an elastic nanofibrous PLCL-based cardiac patches and implanted onto infarcted hearts, both MSC survival and cardiac function were significantly improved compared to the direct injection of MSCs [27] as the cardiac patch served as a mechanical extracellular matrix for MSC survival and allowed MSCs to differentiate into functional cardiomyocytes [27].

Cui et al. demonstrated that growth, survival, and differentiation of MSCs are enhanced by peptide nanofibers in vitro [329]. Nanopeptides have spontaneously assembled into nanofiber scaffolds that mimic the extra cellular matrix post-implantation. The MSCs mixed with self-assembling nano-peptides exhibited increased cell survival, retention at the infarct size in vivo, and improved cardiac function [329]. Guo et al. constructed self-assembling peptides tethered with the cell-adhesion motif RGDSP [330], implanted with CSCs and bundled into nanofiber

scaffolds which were successful in providing a suitable microenvironment for CSC adhesion and survival as it protected CSCs from apoptosis and necrosis (caused by anoxia). The combination led to enhanced cardiac differentiation, reduced collagen deposition, and resulted in better cardiac repair, compared to the groups treated with either CSCs or self-assembling peptides alone.

5.3.3 Advantageous Properties of Nanobiomaterials for Cardiovascular Applications

The anisotropic properties of nanobiomaterials have improved the paracrine action of stem cells. This was demonstrated by Kang et al. who cultured MSCs on anisotropic fibronectin-immobilized PCL nanofibers which significantly improved the cardiac function in rat MI model. Furthermore, fibronectin immobilization significantly improved angiogenesis, anti-inflammation, stem cell homing, and anti-apoptosis in MSCs [342].

Cx43 expression is of great significance for MI repair because it is essential for arrhythmic risk reduction, intercellular coupling, and functional cardiomyogenic differentiation of stem cells [310, 343–345]. Carbon nanofibers/nanotubes integrated with polymer scaffolds promoted the expression of Cx43 in cardiac cells and stimulated the electrical coupling between the cells as well as adhesion and proliferation of cardiomyocytes [346] and cardiac progenitor cells [347].

Cardiomyocytes seeded on a conductive nanobiomaterial-hybrid scaffold (chitosan matrix incorporated with carbon nanofibers [348] or poly (glycerol sebacate): gelatin scaffolds embedded with carbon nanotubes [349], respectively) increased expression of cardiac-specific genes involved in cardiac muscle contraction, exhibited a synchronous beating behavior and electrical coupling in studies by Kharaziha et al. and Martines et al. Thus, the studies demonstrated that conductive nanobiomaterials induced synchronous beating of the cardiac tissue due to enhanced the electrical coupling between the cells with Cx43 upregulation.

Gold nanomaterials have been used in several studies to improve the therapeutic effects of cell therapy. The integration of gold nanoparticles [350] or gold nanowires [351] with cardiomyocytes cultured in hydrogel scaffolds showed an increased Cx43 expression compared to cardiomyocytes cultured in hydrogels without gold nanomaterials. Other studies by Dvir et al. focused on bridging non-conducting alginate pore walls with conductive gold nanowires and demonstrated enhanced electrical signal propagation, and enabled electrical communication between the cardiomyocytes seeded on the scaffolds. Consequently, cardiomyocytes showed a better aligned tissue structure, and exhibited higher levels of the myogenic proteins when cultured on the conductive nanocomposite. Finally, the cells also demonstrated synchronous contraction under electric stimulation of the conductive nanocomposites [46].

In studies by Mooney et al., electrical stimulation augmented the expression of cardiac-specific biomarkers such as Cx43 and reoriented the cells perpendicular to the direction of the current [20]. However, electrical stimulation did not promote cardiac protein expression in MSCs in the absence of nano-materials. Crowder et al. observed that the electrically conductive nanobiomaterials alone promoted cardiac differentiation of the stem cells and their Cx43 expression without any electrical

stimulation [352]. Ravichandran et al. demonstrated that MSCs seeded onto conductive bovine serum albumin (BSA)-polyvinyl alcohol (PVA) nanofibrous scaffolds embedded with gold nanoparticles greatly stimulated the MSC differentiation toward cardiomyogenic lineage and enhanced Cx43 expression with 5-azacytidine treatment [334]. Thus, various studies could show that the electrical conductivity of nanobiomaterials can exert synergistic effects with conventional cardiac differentiation methods to provide a superior therapy for MI.

Peptide nanofibers that capture stem cell paracrine factors have been utilized for the treatment of MI [337] in a study by Webber et al. The presentation of heparin on the surface of self-assembling peptide nanofibers via heparin-binding domains enabled the binding of growth factors secreted from the stem cells in cell cultures [337]. The heparin-presenting self-assembling peptides were incubated with hypoxic stem cell conditioned medium and captured more than 58% of bFGF present in the medium. The growth factor-bound nanofibers successfully restored the hemodynamic function of the heart when implanted into the damaged heart by modulating the cardiac metabolism [337]. Integration of stem cells and nanobiomaterials for the treatment of MI is outlined in Fig. 1.17.

Several studies recently showed that graphene stimulated the MSC differentiation toward cardiomyogenic lineage [335]. The unique chemical nanostructure of graphene with a single layer of carbon atoms stimulated the expression of the extracellular matrix and signaling molecules related to cardiomyogenic differentiation, enhanced cardiomyogenic gene expression in MSCs and promoted the cardiac differentiation of ESCs [335, 338]. Compared to ESCs cultured on glass or matrigel, ESCs cultured on graphene exhibited significant changes in the focal adhesion kinase signaling and the extracellular signal-regulated kinase. Genetic analysis indicated ESCs cultured on graphene showed great increase in the expression of genes associated with early cardiomyocytes, late cardiomyocytes, cardiac transcription, and gap junctions [338].

Various *in vivo* studies by Park et al. demonstrated the therapeutic effect of conductive nanomaterials, in the presence of reduced graphene oxide (RGO) [353], which is composed mostly of carbon atoms. The incorporation of RGO flakes in MSC spheroids enhanced the Cx43 expression of MSCs due to the electrical conductivity and cell-extracellular matrix interactions via stacking and hydrophobic interactions generated by RGO flakes leading to reduction in tissue fibrosis and improvement in cardiac function (Fig. 1.18). Collectively, these studies showed that the integration of stem cells with nanobiomaterials improves the therapeutic outcomes of conventional stem cell therapy for MI treatment.

5.3.4 Nanocarriers for Cardiovascular Applications

NPs as protein carriers can deliver angiogenic growth factors into damaged cardiovascular tissue, reducing off-target effects and undesirable degradation, lowering the dosage requirements and increasing the effective drug concentration [35]. NPs as gene carriers can overcome the cell membrane barrier effectively and release their cargo inside cells with fewer safety concerns as compared to viral vectors.

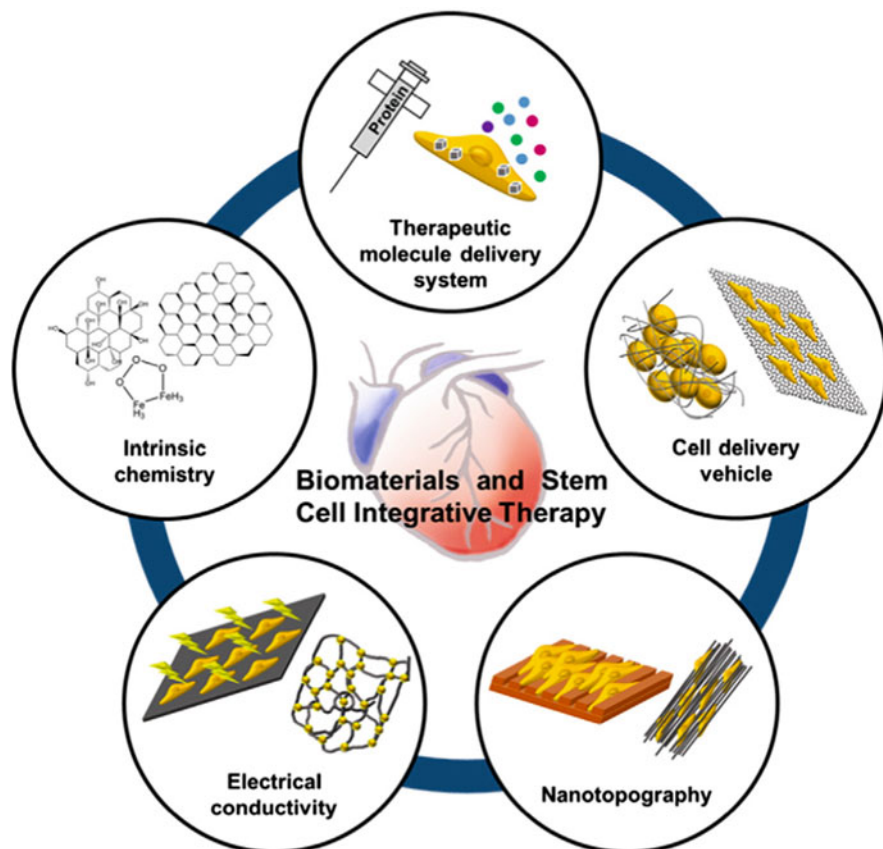


Fig. 1.17 Integration of stem cell with nanobiomaterials for the treatment of MI [339]. (Reprinted with permission)

The nanocarrier needs to navigate through the bloodstream, protect the DNA from degradation by serum DNases, avoid being taken up by phagocytic cells or the reticuloendothelial system (RES), target to the specific cell type at the specific site, enter the target cell through internalization, escape from the endosome into the cytoplasm, and eventually translocate into nucleus and release the cargo [35]. Additionally, other design targets also need to be met, including inexpensive synthesis, low toxicity, and ease of manufacturing [354].

Yang et al. delivered VEGF plasmids using biodegradable poly (β -amino-ester) (PBAE) NPs into MSCs. Compared to injection of non-transfected cells, intramuscular injection of these high VEGF expressing cells into a mouse hind limb ischemia model led to a markedly decreased tissue fibrosis and muscle degeneration and a two- to fourfold increase in vessel densities [36]. In vivo studies in a hind limb ischemia model showed that myoblast cell sheets that were genetically engineered with PBAE-VEGF plasmid NPs prevented the development of necrosis and successfully protected 5 out of 7 mice from limb loss [37].

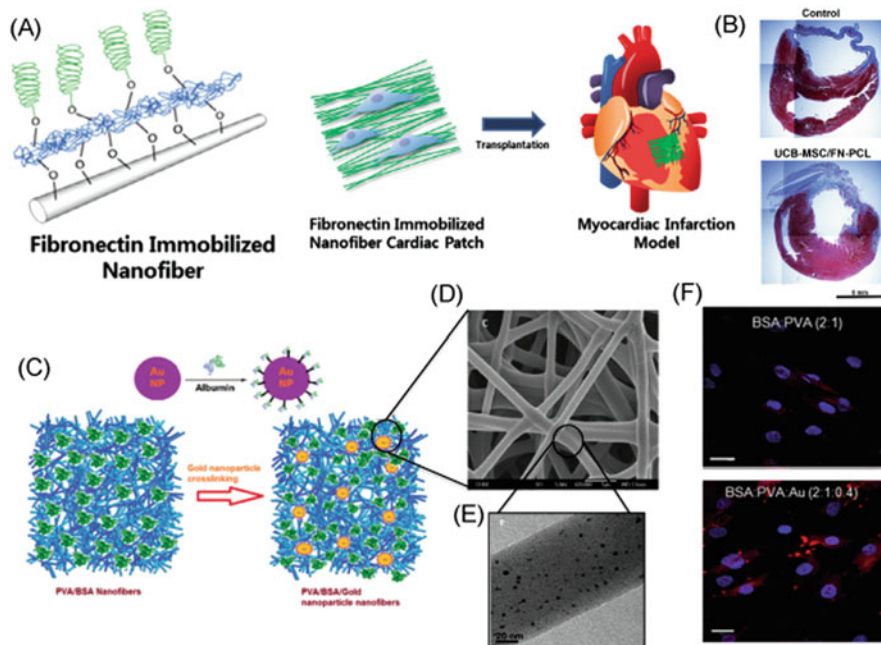


Fig. 1.18 (a) Schematic representation of fibronectin-functionalized PCL nanofibers seeded with MSCs and transplanted in a MI rat model. (b) Heart sections stained with Masson's trichrome demonstrating the wall thinning and fibrosis within the infarcted area. (Viable myocardium in red and fibrotic areas is colored in blue). (c) Schematic illustration of PVA nanofibrous constructs consisting of BSA crosslinked with Au nanoparticles. (d) FESEM and (e) TEM images of nanofibrous BSA/PVA/Au (2/1/0.4). (f) Immunocytochemical analysis showed enhanced expression of gap junction protein Cx43 on BSA/PVA/Au (2/1/0.4) compared to BSA/PVA scaffolds. (Scale bars = 20 μ m). (Reprinted with permission [15])

Nanobiomaterials can also be used for *in vitro* transfection of cells prior to implantation. Self-assembling peptide nanofibers were used for transfection of insulin growth factor-1 (IGF-1) into cardiac progenitor cells (prior to implantation) which promoted heart repair and enhanced cell survival in the infarcted heart [355]. Studies have shown that when PEI was used to transfect VEGF genes into skeletal myoblasts, implantation of these transfected cells into the infarcted myocardium showed significantly improved cardiac repair and better cell survival at the infarcted region compared to naïve skeletal myoblasts [356]. Other studies have shown promotion of angiogenesis via transfection of the angiopoietin-1 gene into adipose-derived stem cells using baculovirus nanocomplex prior to implantation the infarcted heart [325]. Overall, these studies show the promotion of efficient gene transfection of the cells via nanobiomaterials and aid in cardiac tissue engineering.

Several studies have looked at miRNA delivery with nanoparticles to enhance the angiogenic effects of cellular therapy. Gomes et al. formulated multilayered NPs (consisted of PLGA and per fluoro-1, 5 crown ether (PFCE) and the surface was coated with protamine sulfate (PS), a cationic peptide for miRNA adsorption) that

could be used simultaneously for miRNA delivery and cell tracking [38]. Pro-survival/angiogenic miRNAs (miR132 and miR424) were effectively delivered by these multifunctional NPs (up to 90% transfection efficiency) of into endothelial cells (ECs). Compared to limbs treated with cells alone, endothelial cells engineered with NP-miRNAs exhibited a 3.5-fold increase in blood perfusion of ischemic mouse limb and threefold increase in cell survival. Other studies have looked at using nanomaterials to guide the injected cells to the ischemic site. Polystyrene-copolymer NPs containing iron oxide engineered with intravenously injected EPCs could target to ischemic site under external magnetic forces and augment blood perfusion by 40% [357]. Similarly, transfection with magnetic NPs (isolated from *Magnetospirillum magneticum* strain AMB-1) led to an 80% improvement in in vivo homing of EPCs to ischemic site [358] leading to a 25% improvement in blood perfusion compared to untreated cells.

Piezoelectric materials such as Poly (vinylidene fluoride-trifluoroethylene) (PVDF-TrFE) are used in tissue engineering to stimulate cell proliferation and also in combination with nanoparticles such as Zinc oxide (ZnO) which possess antibacterial activity [359]. ZnO nanostructures are also endowed with piezoelectric features as well as the capacity to generate reactive oxygen species (ROS) [360–362]. In vivo research in rats using electrospun PVDF-TrFE/ZnO nanocomposite tissue engineering scaffolds pre-seeded with hMSCs confirmed the non-toxicity of the P(VDF-TrFE)/ZnO scaffolds, enhanced angiogenesis (due to the presence on ZnO nanoparticles), and favored more successful integration of the scaffold [363].

One- and two-dimensional (1D and 2D) carbon-based organic conductive nanomaterials [22] such as graphene and carbon nanotubes (CNTs) have been used in several cardiovascular tissue engineering studies. The unique chemical nanostructure of graphene was able to stimulate MSC cardiomyogenic differentiation via culturing MSCs on the graphene monolayers by providing signaling cues [335]. The incorporation of reduced graphene oxide (RGO) flakes with hMSCs spheroids by Park et al. [353] improved cardiac repair by changing the expression of cell signaling molecules and enhancing the expression of cardiac specific markers such as Cx43 (Fig. 1.19). The enhanced behavior of cardiac spheroids due to the high affinity of RGO toward fibronectin led to the improvement in cell-ECM interactions. When the hybrid RGO-hMSC spheroids were implanted in an in vivo mouse model of MI, the implantation led to improved cardiac repair and function compared to either hMSCs or RGO alone. Furthermore, the implantation of hybrid RGO-MSC spheroids [353] significantly enhanced therapeutic efficacy as only 10-folds lower dose of MSCs was required [338] to enhance the cardiomyogenic differentiation of (hESC)s. Incorporation of graphene within the vitronectin (VN) deposited on glass slide substrate to culture hESC)s promoted the gene expression of cardiac-specific ECM components in a study by Lee et al. [338].

Inorganic nanomaterials such as metals (e.g., silver and gold) and their oxides (e.g., iron, zinc and cerium oxides) synthesized using either liquid-solid or gas-solid transformations [364] are being increasingly used in cardiovascular tissue engineering [338]. In a study by Han et al., the IONP made from nanocubes sorted MSCs and

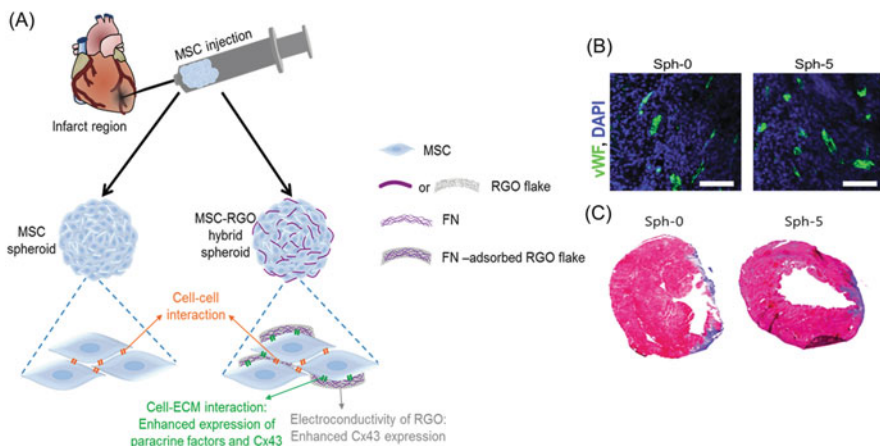


Fig. 1.19 (a) Schematic representation of electrically conductive RGO flakes incorporated in MSC spheroids for treatment of MI. (b and c) RGO could enhance cardiac function restoration via implantation in a MI animal model. (Sph-5: MSC-RGO hybrid spheroids Sph-0: MSC spheroids). (b) Enhanced capillary formation in Sph-5 compared to Sph-0 and (c) Reduced cardiac fibrosis (blue areas) as a result of incorporating RGO in the spheroids. (Scale bars = 100 μ m). (Reproduced with permission [15])

H9C2 co-cultures, improved paracrine profile and cardiac phenotype ultimately leading to enhanced functional recovery and myocardial repair in an *in vivo* MI rat model [339]. In another study, superparamagnetic iron oxide (SPIO) nanoparticles were infiltrated into the ECSs to detect the functionalities of the cardiac patch [365] and subsequently ESC differentiation to cardiac lineage was revealed after 6 weeks within the fibrin matrix [365]. Cerium oxide (nanoceria) metal in studies by Pagliari et al. could protect cardiac progenitor cells from reactive oxygen species and its induced cytotoxicity and demonstrated prolonged activity without affecting cell growth and function [366]. Among the widely applied metallic materials in cardiac tissue engineering is gold (Au) and in particular its forms such as nanoparticles, nanowires, and coating [338, 367]. Studies coating Au on microspheres and incorporation within hESC-derived EBs [338] led to improvement in the expression of cardiac-specific genes along with cardiomyogenic differentiation markers. Au-coated microspheres also promoted electrical coupling of the hESC-derived EBs through enhanced Cx43 expression with recipient myocardial cells [338]. Other inorganic nanoparticles made of europium [79], lanthanide [80], and graphene oxides [82] also have played a significant role in cardiovascular therapeutics through therapeutic angiogenesis [368].

5.3.5 3D Nanoengineered Hybrid Scaffolds

To overcome the electrically resistant structure of alginate, a study by the Langer group incorporated Au nanowires within alginate hydrogel for cardiac tissue engineering applications [351]. The nanowires were able to create conductive bridges across the scaffold matrix and subsequently connected neighboring pores, leading to

improved electrical communication of adjacent cardiac cells (i.e., Cx43) within the matrix. These results are highly conducive in engineering cardiac patches [351]. In a recent study, Li et al. reported that the single-wall CNTs (SWCNTs) promoted BASIC attachment, spreading, proliferation, and cardiac differentiation incorporated within PNIPAAm (SWCNTs/PNIPAAm) [369]. Furthermore, the enhanced nanoroughness, within the hydrogel in the presence of SWCNTs significantly improved the engraftment and the survival of the cells within MI region [369].

5.3.6 Nanostructured Surfaces for Controlling Stem Cell Behavior

Electrospinning technique has been used to develop nanofibrous constructs, to create suitable matrices to control cell function [349, 370]. PCL scaffolds incorporated with Au nanoparticle and vitamin B12 with appropriate stiffness (2.56 MPa) to direct MSCs into cardiac lineage [371]. In another study, the anisotropic properties of aligned nanofibrous fibronectin immobilized PCL constructs could enhance the angiogenic and cardioprotective gene expression in umbilical-cord-blood-derived MSCs (UCB-MSCs) [333].

Cardiac differentiation of hMSCs was promoted by electrically conductive nanocomposite fibrous scaffolds of PCL-CNTs [352]. The electrical stimulation (5 V cm⁻¹ for 5 ms duration, 1 Hz) of fibrous scaffolds resulted in upregulation of early cardiac markers (Nkx2.5). The promotion of cardiogenic differentiation of hMSCs using applied nanocomposites of PANI ultrafine short-fiber blended with PCL was shown in a study by Borriello et al. [372]. Orza et al. demonstrated enhanced growth and cardiac differentiation of hMSCs seeded on the scaffolds by coating collagen nanofibrous scaffolds with Au [373]. Furthermore, MSCs exposed to an electrical field improved expression of cardiac specific genes (troponin I, Nkx 2.5, and GATA-4) and displayed changes in cell morphology.

A composite scaffold composed of poly (methylglutarimide) (PMGI) nanofibers, PEGylated Au nanoparticles, RGD peptides, and heparin binding protein (HBP) was developed by Jung et al. demonstrated successful differentiation of PSCs to CMs [374]. Ex vivo pretreatment of hMSCs using 5-aza and Au nanoparticles (AuNPs) loaded novel hybrid nanofibrous albumin from bovine serum (BSA)/PVA scaffold led to functional improvements of infarcted myocardium and enhanced cardiomyogenic differentiation [334].

5.3.7 Recent Patents in Cardiovascular Therapeutics and Under Clinical Trial Investigation

There have been several nanotechnology-based patents filed for cardiovascular biomaterials in the past decade, few of which will be discussed in this section. A hydrogel based cardiac patch (Patent# US20170143871 A1) embedded with gold nanorods developed upon ultraviolet cross linking of gelatin methacrylate possessed high surface area with enhanced electrical conductivity [368]. The functional cardiomyocytes adhered and retained viability for a long duration in culture when seeded on these scaffolds. Another patent on the incorporation of gold nanowires in the tissue engineered scaffolds (US20170072109 A1) could control the cellular function through electronic circuits. Neonatal rat ventricular cardiomyocytes were

monitored remotely for its rhythmic contraction and relaxation when cultured in the nano-electronic scaffold (US20170072109 A1) [368]. Due to the severe regulations involved, only few cardiovascular therapeutics that have been patented undergo clinical trial investigation. Various bioengineered patches such as XenoSureVR biologic vascular patch (developed by LeMaitre Vascular, Inc. (NCT03176225)), and CorMatrixVR-ECM patch (developed from the small intestinal submucosa of porcine NCT02887768) have been selected for clinical trial investigation for treating cardiac repair and epicardial infarct treatment, respectively [375]. Autologous stem cells were used to prepare multi-layered cell sheets (UMIN000003273) and clinically tested in 27 patients to treat dilated cardiomyopathy and ischemia. The phase I clinical study showed safety of autologous stem cells for clinical testing and the recovery of cardiac function [375].

Thus, a lot of progress in research on nanotechnology based stem cell tissue engineering techniques has been happening throughout this past decade. However, a thorough understanding of the regulation of stem cell differentiation toward cardiac lineage has not been achieved. More specifically, the inability to robustly generate mature ventricular CMs (vCMs) from PSCs and the relative phenotypic immaturity of these resultant cell populations is a pressing research problem [376]. Furthermore, there is a need for the development of new methodologies to minimize or eliminate complications associated with allogenic immune responses in the use of PSC-derived CMs for regenerative medicine therapies [377]. Finally, there is urgent need in scaling up the cardiomyogenic differentiation of stem cells to industrial levels. Various emerging bio-fabrication techniques such as textile [378, 379] and 3D-printing [380] methods can be used to address these shortcomings. Further studies are also needed to investigate the integration of nanostructured patches/matrices within the host myocardium [381]. In particular, *in vivo* analysis is needed to assess whether the implantation of nano-engineered matrices leads to adverse outcomes within the host myocardium such as arrhythmic responses or fibrillation. Further studies are to be performed on the fate of nanoparticles upon injection/implantation. Future research using automated robotic interventions will be able to reduce time delay and production cost involved in the synthesis of biomaterial scaffolds. The next generation of cardiovascular therapeutics is expected to focus on custom-made nanotherapeutics with unique range of biomaterials/stem cells formulation to treat wide range of cardiovascular diseases.

6 Conclusion and Future Perspectives

At the intersection of nanotechnology-based tissue engineering and regenerative stem cell therapy, promising results continue to be reported on a monthly basis. Nanoparticles have played a significant role in the modification of biological and artificial scaffolds, and have boosted their capacity to simulate the intricate properties of bone and offer a suitable microenvironment for cell proliferation, adherence, and differentiation [16]. However, there are hurdles to cross before clinical translation of the combination of emerging nanotechnology and stem cell science, such as controlled and uniform stem cell seeding within nanofabricated scaffolds and

controlling subsequent cell survival, migration, and differentiation, and development of desired tissue type [1]. The complexity of the task to accurately recapitulate the spatial and temporal components of the extracellular environment including ECM, cell adhesion molecules, growth factors, and cytokines, particularly the stem cell niche, is a major challenge faced by regenerative engineering [1].

Standardizing culture techniques and conditions for the expansion and differentiation of stem cells, as well as narrowing down to a few material substrates from the plethora of material choices is a gargantuan task [12]. In vitro models, even dynamic ones, have a limited capacity of accurately mimicking the in vivo conditions often further complicated by individual variability among different patients. In addition, the obvious question of safety regarding the use of nanomaterials in the human body persists with no clear answers to date. The potential cyto- and genotoxicity of nanomaterials is a significant issue requiring thorough examination prior to translation of nano-regenerative tissue engineering. Similarly, any concerns regarding the intended or unintentional biodegradation of tissue-engineered constructs necessitate long-term controlled in vivo studies before their effectiveness in therapy can be established.

At the time of writing of this chapter, the United States Clinical Trial database shows 205 active clinical studies that incorporate the use of nanoparticles; the vast majority of them operating within the fields of dentistry, cancer, and cardiovascular disease. While only a fraction of them incorporate an element of regenerative medicine, it is evident that the near future will provide us more information about the potential, effectiveness, and safety of nanotherapeutic strategies. At this time, the intersection of nanotechnology, regenerative medicine, and tissue engineering holds exciting promises and clearly demonstrated potential and significant questions that we are thrilled to see so many attempting to clarify.

References

1. Vernekar VN, James R, Smith KJ, Laurencin CT (2016) Nanotechnology applications in stem cell science for regenerative engineering. *J Nanosci Nanotechnol* 16(9):8953–8965
2. Langer R, Vacanti JP (1993) Tissue engineering. *Science* 260(5110):920–926
3. Wang W, Zhao Q, Liao S, Zhu Y (2016) Application of stem cells and nanomaterials in prosthodontics. *J Nanosci Nanotechnol* 16(9):8935–8947
4. Padovani GC, Feitosa VP, Sauro S, Tay FR, Duran G, Paula AJ, Duran N (2015) Advances in dental materials through nanotechnology: facts, perspectives and toxicological aspects. *Trends Biotechnol* 33(11):621–636
5. Sciancalepore GA, Maria M, Simonetta C, Luigi R, Netti GS, Clelia P, Dario P (2016) Bioactive nanofiber matrices functionalized with fibronectin-mimetic peptides driving the alignment and tubular commitment of adult renal stem cells. *Macromol Chem Phys* 217(2):199–212
6. MacGregor-Ramiasa M, Hopp I, Bachhuka A, Murray P, Vasilev K (2017) Surface nanotopography guides kidney-derived stem cell differentiation into podocytes. *Acta Biomater* 56:171–180
7. Fabbro A, Prato M, Ballerini L (2013) Carbon nanotubes in neuroregeneration and repair. *Adv Drug Deliv Rev* 65(15):2034–2044
8. Akhavan O (2016) Graphene scaffolds in progressive nanotechnology/stem cell-based tissue engineering of the nervous system. *J Mater Chem B* 4(19):3169–3190

9. Holzapfel BM, Wagner F, Martine LC, Hutmacher DW, Holzapfel BM, Reppenhagen S, Rudert M, Wagner F, Wagner F, Schuetz M, Denham J, Schantz J-T, Schantz J-T, Hutmacher DW, Hutmacher DW (2016) Tissue engineering and regenerative medicine in musculoskeletal oncology. *Cancer Metastasis Rev* 35(3):475–487
10. Biazar E (2017) Application of polymeric nanofibers in medical designs, part III: musculoskeletal and urological tissues. *Int J Polym Mater Polym Biomater* 66(1):28–37
11. Pan S, Yu H, Yang X, Yang X, Wang Y, Liu Q, Jin L, Yang Y (2017) Application of nanomaterials in stem cell regenerative medicine of orthopedic surgery. *J Nanomater* 2017:12
12. Ngiam M, Nguyen LTH, Liao S, Chan CK, Ramakrishna S (2011) Biomimetic nanostructured materials: potential regulators for osteogenesis? *Ann Acad Med Singap* 40(5):213–222
13. Mi S, Khutoryanskiy VV, Jones RR, Zhu X, Hamley IW, Connon CJ (2011) Photochemical cross-linking of plastically compressed collagen gel produces an optimal scaffold for corneal tissue engineering. *J Biomed Mater Res A* 99(1):1–8
14. Lakshmanan R, Maulik N (2018) Development of next generation cardiovascular therapeutics through bio-assisted nanotechnology. *J Biomed Mater Res Part B Appl Biomater* 106:2072–2083
15. Kharaziha M, Memic A, Akbari M, Brafman DA, Nikkhah M (2016) Nano-enabled approaches for stem cell-based cardiac tissue engineering. *Adv Healthc Mater* 5(13):1533–1553
16. Dayem AA, Choi HY, Yang G-M, Kim K, Saha SK, Kim J-H, Cho S-G (2016) The potential of nanoparticles in stem cell differentiation and further therapeutic applications. *Biotechnol J* 11(12):1550–1560
17. Chen C, Dubin R, Kim MC (2014) Emerging trends and new developments in regenerative medicine: a scientometric update (2000–2014). *Expert Opin Biol Ther* 14(9):1295–1317
18. Borghi FF, Rider AE, Kumar S, Han ZJ, Haylock D, Ostrikov K (2013) Emerging stem cell controls: nanomaterials and plasma effects. *J Nanomater* 329139:16 pp
19. Teoh GZ, Klanrit P, Kasimatis M, Seifalian AM (2015) Role of nanotechnology in development of artificial organs. *Minerva Med* 106(1):17–33
20. Mooney E, Mackle JN, Blond DJP, O’Cearbhaill E, Shaw G, Blau WJ, Barry FP, Barron V, Murphy JM (2012) The electrical stimulation of carbon nanotubes to provide a cardiomimetic cue to MSCs. *Biomaterials* 33(26):6132–6139
21. Kai D, Prabhakaran MP, Liao S, Ramakrishna S (2010) Stem cells for myocardial tissue engineering. *Nano Biomed* 2(1):1–22
22. Jiang T, Carbone EJ, Lo KW-H, Laurencin CT (2015) Electrospinning of polymer nanofibers for tissue regeneration. *Prog Polym Sci* 46:1–24
23. Nair LS, Bhattacharyya S, Laurencin CT (2004) Development of novel tissue engineering scaffolds via electrospinning. *Expert Opin Biol Ther* 4(5):659–668
24. Ramesh Kumar P, Khan N, Vivekanandhan S, Satyanarayana N, Mohanty A, Misra M (2012) Nanofibers: effective generation by electrospinning and their applications. *J Nanosci Nanotechnol* 12(1):1–25
25. Deitzel JM, Kleinmeyer J, Harris D, Tan NB (2001) The effect of processing variables on the morphology of electrospun nanofibers and textiles. *Polymer* 42(1):261–272
26. Jaworek A, Sobczyk A (2008) Electro spraying route to nanotechnology: an overview. *J Electrostat* 66(3–4):197–219
27. Jin JY, Jeong SI, Shin YM, Lim KS, Shin HS, Lee YM, Koh HC, Kim KS (2009) Transplantation of mesenchymal stem cells within a poly(lactide-co-epsilon-caprolactone) scaffold improves cardiac function in a rat myocardial infarction model. *Eur J Heart Fail* 11(2):147–153
28. Rane AA, Christman KL (2011) Biomaterials for the treatment of myocardial infarction. *J Am Coll Cardiol* 58(25):2615–2629
29. Karam JP, Muscari C, Montero-Menei CN (2012) Combining adult stem cells and polymeric devices for tissue engineering in infarcted myocardium. *Biomaterials* 33(23):5683–5695
30. Ruvinov E, Harel-Adar T, Cohen S (2011) Bioengineering the infarcted heart by applying bio-inspired materials. *J Cardiovasc Transl Res* 4(5):559–574
31. Bright FV (1988) Bioanalytical applications of fluorescence spectroscopy. *Anal Chem* 60(18):1031A–1039A

32. Quinn KP, Sridharan GV, Hayden RS, Kaplan DL, Lee K, Georgakoudi I (2013) Quantitative metabolic imaging using endogenous fluorescence to detect stem cell differentiation. *Sci Rep* 3(3432):1–10
33. Sapoznik E, Niu G, Zhou Y, Murphy SV, Soker S (2016) Fluorescent cell imaging in regenerative medicine supplementary issue: image and video acquisition and processing for clinical applications. *Biomed Eng Comput Biol* 77(S1S1):29–33
34. Yukawa H, Baba Y (2017) In vivo fluorescence imaging and the diagnosis of stem cells using quantum dots for regenerative medicine. *Anal Chem* 89(5):2671–2681
35. Tu CY, Das S, Baker AB, Zoldan J, Suggs LJ (2015) Nanoscale strategies: treatment for peripheral vascular disease and critical limb ischemia. *ACS Nano* 9(4):3436–3452
36. Yang F, Cho SW, Son SM, Bogatyrev SR, Singh D, Green JJ, Mei Y, Park S, Bhang SH, Kim BS, Langer R, Anderson DG (2010) Genetic engineering of human stem cells for enhanced angiogenesis using biodegradable polymeric nanoparticles. *Proc Natl Acad Sci U S A* 107(8):3317–3322
37. Lee J, Jun I, Park HJ, Kang TJ, Shin H, Cho SW (2014) Genetically engineered myoblast sheet for therapeutic angiogenesis. *Biomacromolecules* 15(1):361–372
38. Gomes RSM, das Neves RP, Cochlin L, Lima A, Carvalho R, Korpisalo P, Dragneva G, Turunen M, Liimatainen T, Clarke K, Yla-Herttuala S, Carr C, Ferreira L (2013) Efficient pro-survival/angiogenic miRNA delivery by an MRI-detectable nanomaterial. *ACS Nano* 7(4):3362–3372
39. Mann I, Rodrigo SF, van Ramshorst J, Beeres SL, Dibbets-Schneider P, de Roos A, Wolterbeek R, Zwaginga JJ, Fibbe WE, Bax JJ, Schalij MJ, Atsma DE (2015) Repeated intramyocardial bone marrow cell injection in previously responding patients with refractory angina again improves myocardial perfusion, anginal complaints, and quality of life. *Circ Cardiovasc Interv* 8(8)
40. Accomasso L, Gallina C, Turinetti V, Giachino C (2016) Stem cell tracking with nanoparticles for regenerative medicine purposes: an overview. *Stem Cells Int* 2016:7920358
41. Bull E, Madani SY, Sheth R, Seifalian A, Green M, Seifalian AM (2014) Stem cell tracking using iron oxide nanoparticles. *Int J Nanomedicine* 9:1641–1653
42. Zhang L, Dong W-F, Sun H-B (2013) Multifunctional superparamagnetic iron oxide nanoparticles: design, synthesis and biomedical photonic applications. *Nanoscale* 5(17):7664–7664
43. Frangioni JV (2003) In vivo near-infrared fluorescence imaging. *Curr Opin Chem Biol* 7(5):626–634
44. Guo B, Wang Y, Peng C, Zhang H, Luo G, Le H, Gmachl C, Sivco D, Peabody M, Cho A (2004) Laser-based mid-infrared reflectance imaging of biological tissues. *Opt Express* 12(1):208–219
45. Hilderbrand SA, Weissleder R (2010) Near-infrared fluorescence: application to in vivo molecular imaging. *Curr Opin Chem Biol* 14(1):71–79
46. Smith AM, Mancini MC, Nie S (2009) Second window for in vivo imaging. *Nat Nanotechnol* 4(11):710–711
47. Kim J-W, Galanzha EI, Shashkov EV, Moon H-M, Zharov VP (2009) Golden carbon nanotubes as multimodal photoacoustic and photothermal high-contrast molecular agents. *Nat Nanotechnol* 4(10):688–694
48. Wang LV, Yao J (2016) A practical guide to photoacoustic tomography in the life sciences. *Nat Methods* 13(8):627–638
49. de la Zerda A, Kim J-W, Galanzha EI, Gambhir SS, Zharov VP (2011) Advanced contrast nanoagents for photoacoustic molecular imaging, cytometry, blood test and photothermal theranostics. *Contrast Media Mol Imaging* 6(5):346–369
50. Baron, R.; Willner, B.; Willner, I., Biomolecule-nanoparticle hybrids as functional units for nanobiotechnology. *Chem Commun* 2007, 0 (4), 323–332
51. Divya KP, Miroshnikov M, Dutta D, Vemula PK, Ajayan PM, John G (2016) In situ synthesis of metal nanoparticle embedded hybrid soft nanomaterials. *Acc Chem Res* 49(9):1671–1680

52. Portney NG, Singh K, Chaudhary S, Destito G, Schneemann A, Manchester M, Ozkan M (2005) Organic and inorganic nanoparticle hybrids. *Langmuir* 21(6):2098–2103
53. Brauchle E, Schenke-Layland K (2013) Raman spectroscopy in biomedicine – non-invasive in vitro analysis of cells and extracellular matrix components in tissues. *Biotechnol J* 8(3):288–297
54. Ghita A, Pascut FC, Sottile V, Denning C, Notingher I (2015) Applications of Raman microspectroscopy to stem cell technology: label-free molecular discrimination and monitoring cell differentiation. *EPJ Tech Instrum* 2(1):6–6
55. Kudelski A (2008) Analytical applications of Raman spectroscopy. *Talanta* 76(1):1–8
56. Batista CA, Larson RG, Kotov NA (2015) Nonadditivity of nanoparticle interactions. *Science* 350(6257):1242477
57. Anu Mary E, Saravanakumar MP (2017) A review on the classification, characterisation, synthesis of nanoparticles and their application. *IOP Conf Ser Mate Sci Eng* 263(3):032019
58. Daniel MCM, Astruc D (2004) Gold nanoparticles: assembly, supramolecular chemistry, quantum-size related properties and applications toward biology, catalysis and nanotechnology. *Chem Rev* 104:293–346
59. Rana D, Ramasamy K, Leena M, Jiménez C, Campos J, Ibarra P, Haidar ZS, Ramalingam M (2016) Surface functionalization of nanobiomaterials for application in stem cell culture, tissue engineering, and regenerative medicine. *Biotechnol Prog* 32(3):554–567
60. Sperling RA, Parak WJ (1915) Surface modification, functionalization and bioconjugation of colloidal inorganic nanoparticles. *Philos Trans R Soc A Math Phys Eng Sci* 2010(368):1333–1383
61. Sears NA, Seshadri DR, Dhavalikar PS, Cosgriff-Hernandez E (2016) A review of three-dimensional printing in tissue engineering. *Tissue Eng Part B Rev* 22(4):298–310
62. Do AV, Khorsand B, Geary SM, Salem AK (2015) 3D printing of scaffolds for tissue regeneration applications. *Adv Healthc Mater* 4(12):1742–1762
63. Layani M, Wang X, Magdassi S (2018) Novel materials for 3D printing by photopolymerization. *Adv Mater* 30:e1706344
64. Hotta A, Yamanaka S (2015) *Induced pluripotent stem cells*. Cambridge University Press, Cambridge, pp 19–33
65. Hovatta O, Rodin S, Antonsson L, Tryggvason K (2014) Concise review: animal substance-free human embryonic stem cells aiming at clinical applications. *Stem Cells Transl Med* 3(11):1269–1274
66. Slawny N, Smith GD (2015) *Embryonic stem cells*. Cambridge University Press, Cambridge, pp 3–18
67. Nichols J, Zevnik B, Anastassiadis K, Niwa H, Klewe-Nebenius D, Chambers I, Scholer H, Smith A (1998) Formation of pluripotent stem cells in the mammalian embryo depends on the POU transcription factor Oct 4. *Cell* 95(3):379–391
68. Avilion AA, Nicolis SK, Pevny LH, Perez L, Vivian N, Lovell-Badge R (2003) Multipotent cell lineages in early mouse development depend on SOX2 function. *Genes Dev* 17(1):126–140
69. Mitsui K, Tokuzawa Y, Itoh H, Segawa K, Murakami M, Takahashi K, Maruyama M, Maeda M, Yamanaka S (2003) The homeoprotein Nanog is required for maintenance of pluripotency in mouse epiblast and ES cells. *Cell* 113(5):631–642
70. Chambers I, Colby D, Robertson M, Nichols J, Lee S, Tweedie S, Smith A (2003) Functional expression cloning of Nanog, a pluripotency sustaining factor in embryonic stem cells. *Cell* 113(5):643–655
71. Harper JC, SenGupta SB (2012) Preimplantation genetic diagnosis: state of the art 2011. *Obstet Gynecol Surv* 67(6):347–348
72. Kuliev A, Rechitsky S (2011) Polar body-based preimplantation genetic diagnosis for Mendelian disorders. *Mol Hum Reprod* 17(5):275–285
73. Brons IGM, Smithers LE, Trotter MWB, Rugg-Gunn P, Sun BW, Lopes S, Howlett SK, Clarkson A, Ahrlund-Richter L, Pedersen RA, Vallier L (2007) Derivation of pluripotent epiblast stem cells from mammalian embryos. *Nature* 448(7150):191–197

74. Tesar PJ, Chenoweth JG, Brook FA, Davies TJ, Evans EP, Mack DL, Gardner RL, McKay RDG (2007) New cell lines from mouse epiblast share defining features with human embryonic stem cells. *Nature* 448(7150):196–U10
75. Ahrlund-Richter L, De Luca M, Marshak DR, Munsie M, Veiga A, Rao M (2009) Isolation and production of cells suitable for human therapy: challenges ahead. *Cell Stem Cell* 4(1):20–26
76. Unger C, Skottman H, Blomberg P, Dilber MS, Hovatta O (2008) Good manufacturing practice and clinical-grade human embryonic stem cell lines. *Hum Mol Genet* 17:R48–R53
77. Rajala K, Lindroos B, Hussein SM, Lappalainen RS, Pekkanen-Mattila M, Inzunza J, Rozell B, Miettinen S, Narkilahti S, Kerkela E, Aalto-Setälä K, Otonkoski T, Suuronen R, Hovatta O, Skottman H (2010) A defined and xeno-free culture method enabling the establishment of clinical-grade human embryonic, induced pluripotent and adipose stem cells. *PLoS One* 5(4)
78. Catalina P, Montes R, Ligeró G, Sanchez L, de la Cueva T, Bueno C, Leone PE, Menendez P (2008) Human ESCs predisposition to karyotypic instability: is a matter of culture adaptation or differential vulnerability among hESC lines due to inherent properties? *Mol Cancer* 7
79. Mitalipova MM, Rao RR, Hoyer DM, Johnson JA, Meisner LF, Jones KL, Dalton S, Stice SL (2005) Preserving the genetic integrity of human embryonic stem cells. *Nat Biotechnol* 23(1):19–20
80. Hasegawa K, Pomeroy JE, Pera MF (2010) Current technology for the derivation of pluripotent stem cell lines from human embryos. *Cell Stem Cell* 6(6):521–531
81. Englund MCO, Caisander G, Noaksson K, Emanuelsson K, Lundin K, Bergh C, Hansson C, Semb H, Strehl R, Hyllner J (2010) The establishment of 20 different human embryonic stem cell lines and subclones; a report on derivation, culture, characterisation and banking. *In Vitro Cell Dev Biol Anim* 46(3–4):217–230
82. Amit M, Margulets V, Segev H, Shariki K, Laevsky I, Coleman R, Itskovitz-Eldor J (2003) Human feeder layers for human embryonic stem cells. *Biol Reprod* 68(6):2150–2156
83. Hovatta O, Mikkola M, Gertow K, Stromberg AM, Inzunza J, Hreinsson J, Rozell B, Blennow E, Andang M, Ahrlund-Richter L (2003) A culture system using human foreskin fibroblasts as feeder cells allows production of human embryonic stem cells. *Hum Reprod* 18(7):1404–1409
84. Kehat I, Gepstein L (2003) Human embryonic stem cells for myocardial regeneration. *Heart Fail Rev* 8(3):229–236
85. Fu X, Xu Y (2011) Self-renewal and scalability of human embryonic stem cells for human therapy. *Regen Med* 6(3):327–334
86. Schwartz SD, Regillo CD, Lam BL, Elliott D, Rosenfeld PJ, Gregori NZ, Hubschman J-P, Davis JL, Heilwell G, Spirn M, Maguire J, Gay R, Bateman J, Ostrick RM, Morris D, Vincent M, Anglade E, Del Priore LV, Lanza R (2015) Human embryonic stem cell-derived retinal pigment epithelium in patients with age-related macular degeneration and Stargardt’s macular dystrophy: follow-up of two open-label phase 1/2 studies. *Lancet* 385(9967):509–516
87. Yamanaka S, Blau HM (2010) Nuclear reprogramming to a pluripotent state by three approaches. *Nature* 465(7299):704–712
88. Kim J, Efe JA, Zhu SY, Talantova M, Yuan X, Wang SF, Lipton SA, Zhang K, Ding S (2011) Direct reprogramming of mouse fibroblasts to neural progenitors. *Proc Natl Acad Sci U S A* 108(19):7838–7843
89. Vierbuchen T, Ostermeier A, Pang ZP, Kokubu Y, Sudhof TC, Wernig M (2010) Direct conversion of fibroblasts to functional neurons by defined factors. *Nature* 463(7284):1035–U50
90. Caiazzo M, Dell’Anno MT, Dvoretzkova E, Lazarevic D, Taverna S, Leo D, Sotnikova TD, Menegon A, Roncaglia P, Colciago G, Russo G, Carninci P, Pezzoli G, Gainetdinov RR, Gustincich S, Dityatev A, Broccoli V (2011) Direct generation of functional dopaminergic neurons from mouse and human fibroblasts. *Nature* 476(7359):224–U151

91. Pfisterer U, Kirkeby A, Torper O, Wood J, Nelander J, Dufour A, Bjorklund A, Lindvall O, Jakobsson J, Parmar M (2011) Direct conversion of human fibroblasts to dopaminergic neurons. *Proc Natl Acad Sci U S A* 108(25):10343–10348
92. Hiramatsu K, Sasagawa S, Outani H, Nakagawa K, Yoshikawa H, Tsumaki N (2011) Generation of hyaline cartilaginous tissue from mouse adult dermal fibroblast culture by defined factors. *J Clin Investig* 121(2):640–657
93. Szabo E, Rampalli S, Risueno RM, Schnerch A, Mitchell R, Fiebig-Comyn A, Levadoux-Martin M, Bhatia M (2010) Direct conversion of human fibroblasts to multilineage blood progenitors. *Nature* 468(7323):521–U191
94. Huang PY, He ZY, Ji SY, Sun HW, Xiang D, Liu CC, Hu YP, Wang X, Hui LJ (2011) Induction of functional hepatocyte-like cells from mouse fibroblasts by defined factors. *Nature* 475(7356):386–U142
95. Sekiya S, Suzuki A (2011) Direct conversion of mouse fibroblasts to hepatocyte-like cells by defined factors. *Nature* 475(7356):390–U148
96. Ieda M, Fu JD, Delgado-Olguin P, Vedantham V, Hayashi Y, Bruneau BG, Srivastava D (2010) Direct reprogramming of fibroblasts into functional cardiomyocytes by defined factors. *Cell* 142(3):375–386
97. Das AK, Pal R (2010) Induced pluripotent stem cells (iPSCs): the emergence of a new champion in stem cell technology-driven biomedical applications. *J Tissue Eng Regen Med* 4(6):413–421
98. Zhang JH, Wilson GF, Soerens AG, Koonce CH, Yu JY, Palecek SP, Thomson JA, Kamp TJ (2009) Functional cardiomyocytes derived from human induced pluripotent stem cells. *Circ Res* 104(4):E30–E41
99. Hayashi R, Ishikawa Y, Sasamoto Y, Katori R, Nomura N, Ichikawa T, Araki S, Soma T, Kawasaki S, Sekiguchi K, Quantock AJ, Tsujikawa M, Nishida K (2016) Co-ordinated ocular development from human iPS cells and recovery of corneal function. *Nature* 531(7594):376–380
100. Zhao TB, Zhang ZN, Rong ZL, Xu Y (2011) Immunogenicity of induced pluripotent stem cells. *Nature* 474(7350):212–U251
101. Hu QR, Friedrich AM, Johnson LV, Clegg DO (2010) Memory in induced pluripotent stem cells: reprogrammed human retinal-pigmented epithelial cells show tendency for spontaneous redifferentiation. *Stem Cells* 28(11):1981–1991
102. Kim K, Doi A, Wen B, Ng K, Zhao R, Cahan P, Kim J, Aryee MJ, Ji H, Ehrlich LIR, Yabuuchi A, Takeuchi A, Cunniff KC, Hongguang H, McKinney-Freeman S, Naveiras O, Yoon TJ, Irizarry RA, Jung N, Seita J, Hanna J, Murakami P, Jaenisch R, Weissleder R, Orkin SH, Weissman IL, Feinberg AP, Daley GQ (2010) Epigenetic memory in induced pluripotent stem cells. *Nature* 467(7313):285–U60
103. Yusa K, Rad R, Takeda J, Bradley A (2009) Generation of transgene-free induced pluripotent mouse stem cells by the piggyBac transposon. *Nat Methods* 6(5):363–U69
104. Jia FJ, Wilson KD, Sun N, Gupta DM, Huang M, Li ZJ, Panetta NJ, Chen ZY, Robbins RC, Kay MA, Longaker MT, Wu JC (2010) A nonviral minicircle vector for deriving human iPS cells. *Nat Methods* 7(3):197–U46
105. Kim D, Kim CH, Moon JI, Chung YG, Chang MY, Han BS, Ko S, Yang E, Cha KY, Lanza R, Kim KS (2009) Generation of human induced pluripotent stem cells by direct delivery of reprogramming proteins. *Cell Stem Cell* 4(6):472–476
106. Cahan P, Daley GQ (2013) Origins and implications of pluripotent stem cell variability and heterogeneity. *Nat Rev Mol Cell Biol* 14(6):357–368
107. Puri MC, Nagy A (2012) Concise review: embryonic stem cells versus induced pluripotent stem cells: the game is on. *Stem Cells* 30(1):10–14
108. Dominici M, Le Blanc K, Mueller I, Slaper-Cortenbach I, Marini FC, Krause DS, Deans RJ, Keating A, Prockop DJ, Horwitz EM (2006) Minimal criteria for defining multipotent mesenchymal stromal cells. The International Society for Cellular Therapy position statement. *Cytotherapy* 8(4):315–317

109. Robey PG (2015) Connective tissue stem and progenitor cells. Cambridge University Press, Cambridge, pp 34–43
110. Abdulrazzak H, Moschidou D, Jones G, Guillot PV (2010) Biological characteristics of stem cells from foetal, cord blood and extraembryonic tissues. *J R Soc Interface* 7:S689–S706
111. Mack D, Skardal A, Soker S, Atala A (2015) Using biomaterials for fetal stem cell isolation, expansion and directed-differentiation. Cambridge University Press, Cambridge, pp 64–79
112. Marcus AJ, Woodbury D (2008) Fetal stem cells from extra-embryonic tissues: do not discard. *J Cell Mol Med* 12(3):730–742
113. Hoehn H, Bryant EM, Fantel AG, Martin GM (1975) Cultivated cells from diagnostic amniocentesis in 2nd trimester pregnancies. 3. Fetal urine as a potential source of clonable cells. *Humangenetik* 29(4):285–290
114. Atala A (2012) Basic principles of amniotic fluid and placenta stem cells. Elsevier, Cambridge, pp 64–76
115. Kaviani A, Perry TE, Dzakovic A, Jennings RW, Ziegler MM, Fauza DO (2001) The amniotic fluid as a source of cells for fetal tissue engineering. *J Pediatr Surg* 36(11):1662–1665
116. Tsai MS, Lee JL, Chang YJ, Hwang SM (2004) Isolation of human multipotent mesenchymal stem cells from second-trimester amniotic fluid using a novel two-stage culture protocol. *Hum Reprod* 19(6):1450–1456
117. Perin L, Giuliani S, Jin D, Sedrakyan S, Carraro G, Habibian R, Warburton D, Atala A, De Filippo RE (2007) Renal differentiation of amniotic fluid stem cells. *Cell Prolif* 40(6):936–948
118. Perin L, Sedrakyan S, Giuliani S, Da Sacco S, Carraro G, Shirri L, Lemley KV, Rosol M, Wu S, Atala A, Warburton D, De Filippo RE (2010) Protective effect of human amniotic fluid stem cells in an immunodeficient mouse model of acute tubular necrosis. *PLoS One* 5(2)
119. Ji XL, Wang M, Chen F, Zhou JM (2017) Urine-derived stem cells: the present and the future. *Stem Cells Int*. <https://doi.org/10.1155/2017/4378947>
120. Zhang YY, McNeill E, Tian H, Soker S, Andersson KE, Yoo JJ, Atala A (2008) Urine derived cells are a potential source for urological tissue reconstruction. *J Urol* 180(5):2226–2233
121. Bharadwaj S, Liu GH, Shi YG, Wu RP, Yang B, He TC, Fan YX, Lu XY, Zhou XB, Liu H, Atala A, Rohozinski J, Zhang YY (2013) Multipotential differentiation of human urine-derived stem cells: potential for therapeutic applications in urology. *Stem Cells* 31(9):1840–1856
122. Ramsay S, Ringuelette-Goulet C, Langlois A, Bolduc S (2016) Clinical challenges in tissue-engineered urethral reconstruction. *Transl Androl Urol* 5(2):267–270
123. Liu Y, Ma WJ, Liu B, Wang YC, Chu JQ, Xiong G, Shen LJ, Long CL, Lin T, He DW, Butnaru D, Alexey L, Zhang YY, Zhang DY, Wei GH (2017) Urethral reconstruction with autologous urine-derived stem cells seeded in three-dimensional porous small intestinal submucosa in a rabbit model. *Stem Cell Res Ther* 8
124. Versteegden LRM, de Jonge P, Int'Hout J, van Kuppevelt TH, Oosterwijk E, Feitz WFJ, de Vries RBM, Daamen WF (2017) Tissue engineering of the urethra: a systematic review and meta-analysis of preclinical and clinical studies. *Eur Urol* 72(4):594–606
125. Chan YY, Sandlin SK, Kurzrock EA, Osborn SL (2017) The current use of stem cells in bladder tissue regeneration and bioengineering. *Biomedicine* 5(1):4
126. Bodin A, Bharadwaj S, Wu SF, Gatenholm P, Atala A, Zhang YY (2010) Tissue-engineered conduit using urine-derived stem cells seeded bacterial cellulose polymer in urinary reconstruction and diversion. *Biomaterials* 31(34):8889–8901
127. Tong ZC, Cao C, Rao MH, Lu J, Tan JM (2015) Potential cell source for cell-based therapy and tissue engineering applications: urine-derived stem cells. *J Biomater Tissue Eng* 5(2):150–156
128. Mehta G, Shiozawa Y, Taichman R (2015) Hematopoietic stem cells and their niches. Cambridge University Press, Cambridge, pp 44–63
129. Flidner TM, Graessle D, Paulsen C, Reimers K (2002) Structure and function of bone marrow hemopoiesis: mechanisms of response to ionizing radiation exposure. *Cancer Biother Radiopharm* 17(4):405–426

130. Rookmaaker MB, Verhaar MC, Loomans CJM, Verloop R, Peters E, Westerweel PE, Murohara T, Staal FJT, van Zonneveld AJ, Koolwijk P, Rabelink TJ, van Hinsbergh VWM (2005) CD34(+) cells home, proliferate, and participate in capillary formation, and in combination with CD34(-) cells enhance tube formation in a 3-dimensional matrix. *Arterioscler Thromb Vasc Biol* 25(9):1843–1850
131. Braccini A, Wendt D, Jaquiere C, Jakob M, Heberer M, Kenins L, Wodnar-Filipowicz A, Quarto R, Martin I (2005) Three-dimensional perfusion culture of human bone marrow cells and generation of osteoinductive grafts. *Stem Cells* 23(8):1066–1072
132. Kim HS, Lim JB, Min YH, Lee ST, Lyu CJ, Kim ES, Kim HO (2003) Ex vivo expansion of human umbilical cord blood CD34(+) cells in a collagen bead-containing 3-dimensional culture system. *Int J Hematol* 78(2):126–132
133. Li Y, Ma T, Kniss DA, Yang ST, Lasky LC (2001) Human cord cell hematopoiesis in three-dimensional nonwoven fibrous matrices: in vitro simulation of the marrow microenvironment. *J Hematother Stem Cell Res* 10(3):355–368
134. Banu N, Rosenzweig M, Kim H, Bagley J, Pykett M (2001) Cytokine-augmented culture of haematopoietic progenitor cells in a novel three-dimensional cell growth matrix. *Cytokine* 13(6):349–358
135. Bagley J, Rosenzweig M, Marks DF, Pykett MJ (1999) Extended culture of multipotent hematopoietic progenitors without cytokine augmentation in a novel three-dimensional device. *Exp Hematol* 27(3):496–504
136. de Barros A, Takiya CM, Garzoni LR, Leal-Ferreira ML, Dutra HS, Chiarini LB, Meirelles MN, Borojevic R, Rossi MID (2010) Osteoblasts and bone marrow mesenchymal stromal cells control hematopoietic stem cell migration and proliferation in 3D in vitro model. *PLoS One* 5(2)
137. Rossi MID, Barros A, Baptista LS, Garzoni LR, Meirelles MN, Takiya CM, Pascarelli BMO, Dutra HS, Borojevic R (2005) Multicellular spheroids of bone marrow stromal cells: a three-dimensional in vitro culture system for the study of hematopoietic cell migration. *Braz J Med Biol Res* 38(10):1455–1462
138. Seita J, Weissman IL (2010) Hematopoietic stem cell: self-renewal versus differentiation. *Wiley Interdiscip Rev Syst Biol Med* 2(6):640–653
139. Notta F, Doulatov S, Laurenti E, Poepl A, Jurisica I, Dick JE (2011) Isolation of single human hematopoietic stem cells capable of long-term multilineage engraftment. *Science* 333(6039):218–221
140. Majeti R, Park CY, Weissman IL (2007) Identification of a hierarchy of multipotent hematopoietic progenitors in human cord blood. *Cell Stem Cell* 1(6):635–645
141. Craig W, Kay R, Cutler RL, Lansdorp PM (1993) Expression of Thy-1 on human hematopoietic progenitor cells. *J Exp Med* 177(5):1331–1342
142. Mayani H, Dragowska W, Lansdorp PM (1993) Characterization of functionally distinct subpopulations of CD34+ cord-blood cells in serum-free long-term cultures supplemented with hematopoietic cytokines. *Blood* 82(9):2664–2672
143. Hao QL, Shah AJ, Thiemann FT, Smogorzewska EM, Crooks GM (1995) A functional comparison of CD34(+)CD38(-) cells in cord-blood and bone-marrow. *Blood* 86(10):3745–3753
144. Martínez E, Lagunas A, Mills CA, Rodríguez-Seguí S, Estévez M, Oberhansl S, Comelles J, Samitier J (2009) Stem cell differentiation by functionalized micro- and nanostructured surfaces. *Nanomedicine* 4(1):65–82
145. Huang NF, Li S (2011) Regulation of the matrix microenvironment for stem cell engineering and regenerative medicine. *Ann Biomed Eng* 39(4):1201–1214
146. Pumera M (2010) Graphene-based nanomaterials and their electrochemistry. *Chem Soc Rev* 39(11):4146–4146
147. Fuhrer MS, Lau CN, MacDonald AH (2010) Graphene: materially better carbon. *MRS Bull* 35(4):289–295
148. Rao CNR, Sood AK, Subrahmanyam KS, Govindaraj A (2009) Graphene: the new two-dimensional nanomaterial. *Angew Chem Int Ed Engl* 48(42):7752–7777

149. Bhuyan MSA, Uddin MN, Islam MM, Bipasha FA, Hossain SS (2016) Synthesis of graphene. *Int Nano Lett* 6(2):65–83
150. Park S, Ruoff RS (2009) Chemical methods for the production of graphenes. *Nat Nanotechnol* 4(4):217–224
151. Papageorgiou DG, Kinloch IA, Young RJ (2017) Mechanical properties of graphene and graphene-based nanocomposites. *Prog Mater Sci* 90:75–127
152. Zhu Y, Murali S, Cai W, Li X, Suk JW, Potts JR, Ruoff RS (2010) Graphene and graphene oxide: synthesis, properties, and applications. *Adv Mater* 22(35):3906–3924
153. Cui X, Zhang C, Hao R, Hou Y (2011) Liquid-phase exfoliation, functionalization and applications of graphene. *Nanoscale* 3(5):2118–2118
154. Huang Y, Liang J, Chen Y (2012) An overview of the applications of graphene-based materials in supercapacitors. *Small* 8(12):1805–1834
155. Fang M, Wang K, Lu H, Yang Y, Nutt S (2009) Covalent polymer functionalization of graphene nanosheets and mechanical properties of composites. *J Mater Chem* 19(38):7098–7098
156. Geim AK, Novoselov KS (2007) The rise of graphene. *Nat Mater* 6:183–191
157. Georgakilas V, Otyepka M, Bourlinos AB, Chandra V, Kim N, Kemp KC, Hobza P, Zboril R, Kim KS (2012) Functionalization of graphene: covalent and non-covalent approaches, derivatives and applications. *Chem Rev* 112:6156–6214
158. Georgakilas V, Tiwari JN, Kemp KC, Perman JA, Bourlinos AB, Kim KS, Zboril R (2016) Noncovalent functionalization of graphene and graphene oxide for energy materials, biosensing, catalytic, and biomedical applications. *Chem Rev* 116(9):5464–5519
159. Ryon Shin S, Yi-Chen L, Jang H, Khoshakhlagh P, Akbari M, Nasajpour A, Zhang YS, Tamayol A, Khademhosseini A (2016) Graphene-based materials for tissue engineering. *Adv Drug Deliv Rev* 105:255–274
160. Shen H, Zhang L, Liu M, Zhang Z (2012) Biomedical applications of graphene. *Theranostics* 2(3):283–294
161. Ikada Y (2006) Challenges in tissue engineering. *J R Soc Interface* 3(10):589–601
162. Reina G, González-Domínguez JM, Criado A, Vázquez E, Bianco A, Prato M (2017) Promises, facts and challenges for graphene in biomedical applications. *Chem Soc Rev*:4400–4416
163. Lee WC, Lim CHYX, Shi H, Tang LAL, Wang Y, Lim CT, Loh KP (2011) Origin of enhanced stem cell growth and differentiation on graphene and graphene oxide. *ACS Nano* 5(9):7334–7341
164. Park SY, Park J, Sim SH, Sung MG, Kim KS, Hong BH, Hong S (2011) Enhanced differentiation of human neural stem cells into neurons on graphene. *Adv Mater* 23(36):263–267
165. Shah S, Yin PT, Uehara TM, Chueng STD, Yang L, Lee KB (2014) Guiding stem cell differentiation into oligodendrocytes using graphene-nanofiber hybrid scaffolds. *Adv Mater* 26(22):3673–3680
166. Ajayan PM (1999) Nanotubes from carbon. *Chem Rev* 99(7):1787–1800
167. Alshehri R, Ilyas AM, Hasan A, Arnaout A, Ahmed F, Memic A (2016) Carbon nanotubes in biomedical applications: factors, mechanisms, and remedies of toxicity: miniperspective. *J Med Chem* 59(18):8149–8167
168. Harris PJF (2013) Carbon nanotube science. *Int Mater* 53:1689–1699
169. Baughman RH (2002) Carbon nanotubes – the route toward applications. *Science* 297(787):787–792
170. Coleman JN, Khan U, Blau WJ, Gun'ko YK (2006) Small but strong: a review of the mechanical properties of carbon nanotube-polymer composites. *Carbon* 44(9):1624–1652
171. Awasthi K, Srivastava A, Srivastava ON (2005) Synthesis of carbon nanotubes. *J Nanosci Nanotechnol* 5(10):1616–1636
172. Rakov EG (2000) Methods for preparation of carbon nanotubes. *Russ Chem Rev* 69(1):35–52
173. Dresselhaus MS, Dresselhaus G, Saito R (1995) Physics of carbon nanotubes. *Carbon* 33(7):883–891
174. Shah KA, Tali BA (2016) Synthesis of carbon nanotubes by catalytic chemical vapour deposition: a review on carbon sources, catalysts and substrates. *Mater Sci Semicond Process* 41:67–82

175. Harrison BS, Atala A (2007) Carbon nanotube applications for tissue engineering. *Biomaterials* 28(2):344–353
176. Alshehri R, Ilyas AM, Hasan A, Arnaout A, Ahmed F, Memic A (2016) Carbon nanotubes in biomedical applications: factors, mechanisms, and remedies of toxicity. *J Med Chem* 59(18):8149–8167
177. Stout DA, Webster TJ (2012) Carbon nanotubes for stem cell control. *Mater Today* 15(7–8):312–318
178. Chen C-S, Soni S, Le C, Biasca M, Farr E, Chen EYT, Chin W-C (2012) Human stem cell neuronal differentiation on silk-carbon nanotube composite. *Nanoscale Res Lett* 7(1):126–126
179. Landers J, Turner JT, Heden G, Carlson AL, Bennett NK, Moghe PV, Neimark AV (2013) Carbon nanotube composites as multifunctional substrates for in situ actuation of differentiation of human neural stem cells. *J Magn Reson* 236(11):47–56
180. Hirata E, Uo M, Takita H, Akasaka T, Watari F, Yokoyama A (2011) Multiwalled carbon nanotube-coating of 3D collagen scaffolds for bone tissue engineering. *Carbon* 49(10):3284–3291
181. Shin SR, Jung SM, Zalabany M, Kim K, Zorlutuna P, Kim SB, Nikkhah M, Khabiry M, Azize M, Kong J, Wan KT, Palacios T, Dokmeci MR, Bae H, Tang X, Khademhosseini A (2013) Carbon-nanotube-embedded hydrogel sheets for engineering cardiac constructs and bioactuators. *ACS Nano* 7(3):2369–2380
182. Berciaud S, Cognet L, Poulin P, Weisman RB, Lounis B (2007) Absorption spectroscopy of individual single-walled carbon nanotubes. *Nano Lett* 7(5):1203–1207
183. Connell MJO, Bachilo SM, Huffman CB, Moore VC, Strano MS, Haroz EH, Rialon KL, Boul PJ, Noon WH, Kittrell C, Ma J, Hauge RH, Weisman RB, Smalley RE (2002) Band gap fluorescence from individual single-walled carbon nanotubes. *Science* 297(5581):593–596
184. Shi Kam NW, O’Connell M, Wisdom JA, Dai H (2005) Carbon nanotubes as multifunctional biological transporters and near-infrared agents for selective cancer cell destruction. *Proc Natl Acad Sci* 102(33):11600–11605
185. Dresselhaus MS, Dresselhaus G, Saito R, Jorio A (2005) Raman spectroscopy of carbon nanotubes. *Phys Rep* 409(2):47–99
186. Gao Y, Cui Y, Chan JK, Xu C (2013) Stem cell tracking with optically active nanoparticles. *Am J Nucl Med Mol Imaging* 3(3):232–246
187. Wang C, Ma X, Ye S, Cheng L, Yang K, Guo L, Li C, Li Y, Liu Z (2012) Protamine functionalized single-walled carbon nanotubes for stem cell labeling and in vivo Raman/magnetic resonance/photoacoustic triple-modal imaging. *Adv Funct Mater* 22(11):2363–2375
188. Li X, Liu H, Niu X, Yu B, Fan Y, Feng Q, Cui FZ, Watari F (2012) The use of carbon nanotubes to induce osteogenic differentiation of human adipose-derived MSCs in vitro and ectopic bone formation in vivo. *Biomaterials* 33(19):4818–4827
189. Venkatesan J, Qian ZJ, Ryu B, Ashok Kumar N, Kim SK (2011) Preparation and characterization of carbon nanotube-grafted-chitosan – natural hydroxyapatite composite for bone tissue engineering. *Carbohydr Polym* 83(2):569–577
190. Kargarzadeh H, Ioelovich M, Ahmad I, Thomas S, Dufresne A (2017) Methods for extraction of nanocellulose from various sources. In: *Handbook of nanocellulose and cellulose nanocomposites*. Wiley, Weinheim, pp 1–49
191. Trache D, Hussin MH, Haafiz MKM, Thakur VK (2017) Recent progress in cellulose nanocrystals: sources and production. *Nanoscale* 9(5):1763–1786
192. Sacui IA, Nieuwendaal RC, Burnett DJ, Stranick SJ, Jorfi M, Weder C, Foster EJ, Olsson RT, Gilman JW (2014) Comparison of the properties of cellulose nanocrystals and cellulose nanofibrils isolated from bacteria, tunicate, and wood processed using acid, enzymatic, mechanical, and oxidative methods. *ACS Appl Mater Interfaces* 6(9):6127–6138
193. Tang J, Sisler J, Grishkewich N, Tam KC (2017) Functionalization of cellulose nanocrystals for advanced applications. *J Colloid Interface Sci* 494:397–409
194. Dufresne A (2013) Nanocellulose: a new ageless bionanomaterial. *Mater Today* 16(6):220–227

195. Habibi Y, Lucia LA, Rojas OJ (2010) Cellulose nanocrystals: chemistry, self-assembly, and applications. *Chem Rev* 110(6):3479–3500
196. Moon RJ, Martini A, Nairn J, Simonsen J, Youngblood J (2011) Cellulose nanomaterials review: structure, properties and nanocomposites. *Chem Soc Rev* 40:3941–3994
197. Lin N, Huang J, Dufresne A (2012) Preparation, properties and applications of polysaccharide nanocrystals in advanced functional nanomaterials: a review. *Nanoscale* 4(11):3274–3274
198. Domingues RMA, Gomes ME, Reis RL (2014) The potential of cellulose nanocrystals in tissue engineering strategies. *Biomacromolecules* 15(7):2327–2346
199. Jorfi M, Foster EJ (2015) Recent advances in nanocellulose for biomedical applications. *J Appl Polym Sci* 132(14):1–19
200. Sinha A, Martin EM, Lim K-T, Carrier DJ, Han H, Zharov VP, Kim J-W (2015) Cellulose nanocrystals as advanced “green” materials for biological and biomedical engineering. *J Biosyst Eng* 40(4):373–393
201. Lutolf MP, Hubbell JA (2005) Synthetic biomaterials as instructive extracellular microenvironments for morphogenesis in tissue engineering. *Nat Biotechnol* 23(1):47–55
202. Mertaniemi H, Escobedo-Lucea C, Sanz-Garcia A, Gandia C, Mäkitie A, Partanen J, Ikkala O, Yliperttula M (2016) Human stem cell decorated nanocellulose threads for biomedical applications. *Biomaterials* 82:208–220
203. De France KJ, Chan KJW, Cranston ED, Hoare T (2016) Enhanced mechanical properties in cellulose nanocrystal-poly(oligoethylene glycol methacrylate) injectable nanocomposite hydrogels through control of physical and chemical cross-linking. *Biomacromolecules* 17(2):649–660
204. Domingues RMA, Silva M, Gershovich P, Betta S, Babo P, Caridade SG, Mano JF, Motta A, Reis RL, Gomes ME (2015) Development of injectable hyaluronic acid/cellulose nanocrystals bionanocomposite hydrogels for tissue engineering applications. *Bioconjug Chem* 26(8):1571–1581
205. Bhattacharya M, Malinen MM, Lauren P, Lou YR, Kuisma SW, Kanninen L, Lille M, Corlu A, Guguen-Guillouzo C, Ikkala O, Laukkanen A, Urtti A, Yliperttula M (2012) Nanofibrillar cellulose hydrogel promotes three-dimensional liver cell culture. *J Control Release* 164(3):291–298
206. Li W, Lan Y, Guo R, Zhang Y, Xue W, Zhang Y (2015) In vitro and in vivo evaluation of a novel collagen/cellulose nanocrystals scaffold for achieving the sustained release of basic fibroblast growth factor. *J Biomater Appl* 29(6):882–893
207. Liu S, Jin M, Chen Y, Gao H, Shi X, Cheng W, Ren L, Wang Y (2017) High internal phase emulsions stabilised by supramolecular cellulose nanocrystals and their application as cell-adhesive macroporous hydrogel monoliths. *J Mater Chem B* 5(14):2671–2678
208. Jain PK, Lee KS, El-Sayed IH, El-Sayed MA (2006) Calculated absorption and scattering properties of gold nanoparticles of different size, shape, and composition: applications in biological imaging and biomedicine. *J Phys Chem B* 110(14):7238–7248
209. Ghosh SK, Nath S, Kundu S, Esumi K, Pal T (2004) Solvent and ligand effects on the localized surface plasmon resonance (LSPR) of gold colloids. *J Phys Chem B* 108(37):13963–13971
210. Hu M, Chen J, Li Z-Y, Au L, Hartland GV, Li X, Marquez M, Xia Y (2006) Gold nanostructures: engineering their plasmonic properties for biomedical applications. *Chem Soc Rev* 35(11):1084–1084
211. Kelly KL, Coronado E, Zhao LL, Schatz GC (2003) The optical properties of metal nanoparticles: the influence of size, shape, and dielectric environment. *J Phys Chem B* 107(3):668–677
212. Li J, Zhu JJ, Xu K (2014) Fluorescent metal nanoclusters: from synthesis to applications. *TrAC Trends Anal Chem* 58:90–98
213. Lin CAJ, Lee CH, Hsieh JT, Wang HH, Li JK, Shen JL, Chan WH, Yeh HI, Chang WH (2009) Synthesis of fluorescent metallic nanoclusters toward biomedical application: recent progress and present challenges. *J Med Biol Eng* 29(6):276–283
214. Huang X, El-Sayed MA (2010) Gold nanoparticles: optical properties and implementations in cancer diagnosis and photothermal therapy. *J Adv Res* 1(1):13–28

215. Cao J, Sun T, Grattan KTV (2014) Gold nanorod-based localized surface plasmon resonance biosensors: a review. *Sensors Actuators B Chem* 195:332–351
216. Zhao P, Li N, Astruc D (2013) State of the art in gold nanoparticle synthesis. *Coord Chem Rev* 257(3–4):638–665
217. Skrabalak SE, Chen J, Sun Y, Lu X, Au L, Copley CM, Xia Y (2008) Gold nanocages: synthesis, properties, and applications. *Acc Chem Res* 41(12):1587–1595
218. Yeh Y-C, Creran B, Rotello VM (2012) Gold nanoparticles: preparation, properties, and applications in bionanotechnology. *Nanoscale* 4(6):1871–1880
219. Sperling RA, Gil PR, Zhang F, Zanella M, Parak WJ (2008) 2008 Gold: Chemistry, Materials and Catalysis Issue. Please take a look at the full table of contents to access the. *Chem Soc Rev* 37(9):1909–1930
220. Sathuluri RR, Yoshikawa H, Shimizu E, Saito M, Tamiya E (2011) Gold nanoparticle-based surface-enhanced Raman scattering for noninvasive molecular probing of embryonic stem cell differentiation. *PLoS One* 6(8)
221. Encabo-Berzosa MDM, Sancho-Albero M, Crespo A, Andreu V, Sebastian V, Irusta S, Arruebo M, Martín-Duque P, Santamaria J (2017) The effect of PEGylated hollow gold nanoparticles on stem cell migration: potential application in tissue regeneration. *Nanoscale* 9(28):9848–9858
222. Ricles LM, Nam SY, Trevino EA, Emelianov SY, Suggs LJ (2005) A dual gold nanoparticle system for mesenchymal stem cell tracking. *Biophys Chem* 257(5):2432–2437
223. Kang S, Bhang SH, Hwang S, Yoon JK, Song J, Jang HK, Kim S, Kim BS (2015) Mesenchymal stem cells aggregate and deliver gold nanoparticles to tumors for photothermal therapy. *ACS Nano* 9(10):9678–9690
224. Yi C, Liu D, Fong C-C, Zhang J, Yang M (2010) Gold nanoparticles promote osteogenic. *ACS Nano* 4(11):6439–6448
225. Berman SC, Walczak P, Jeff WMB (2011) Tracking stem cells using magnetic nanoparticles. *Wiley Interdiscip Rev Syst Biol Med* 3:343–355
226. Thorek DLJ, Chen AK, Czupryna J, Tsourkas A (2006) Superparamagnetic iron oxide nanoparticle probes for molecular imaging. *Ann Biomed Eng* 34(1):23–38
227. Huber DL (2005) Synthesis, properties, and applications of iron nanoparticles. *Small* 1(5):482–501
228. Wahajuddin, Arora S (2012) Superparamagnetic iron oxide nanoparticles: magnetic nano-platforms as drug carriers. *Int J Nanomedicine* 7:3445–3471
229. Mohammed L, Gomaa HG, Ragab D, Zhu J (2017) Magnetic nanoparticles for environmental and biomedical applications: a review. *Particuology* 30:1–14
230. Angelakeris M (2017) Magnetic nanoparticles: a multifunctional vehicle for modern theranostics. *Biochim Biophys Acta Gen Subj* 1861(6):1642–1651
231. Adams C, Israel LL, Ostrovsky S, Taylor A, Poptani H, Lellouche JP, Chari D (2016) Development of multifunctional magnetic nanoparticles for genetic engineering and tracking of neural stem cells. *Adv Healthc Mater* 5(7):841–849
232. Lewin M, Carlesso N, Tung CH, Tang XW, Cory D, Scadden DT, Weissleder R (2000) Tat peptide-derivatized magnetic nanoparticles allow in vivo tracking and recovery of progenitor cells. *Nat Biotechnol* 18(4):410–414
233. Odabaş S, Sayar F, Güven G, Yanikkaya-Demirel G, Pişkin E (2008) Separation of mesenchymal stem cells with magnetic nanosorbents carrying CD105 and CD73 antibodies in flow-through and batch systems. *J Chromatogr B Anal Technol Biomed Life Sci* 861(1):74–80
234. Yun HM, Ahn SJ, Park KR, Kim MJ, Kim JJ, Jin GZ, Kim HW, Kim EC (2016) Magnetic nanocomposite scaffolds combined with static magnetic field in the stimulation of osteoblastic differentiation and bone formation. *Biomaterials* 85:88–98
235. Shimizu K, Ito A, Yoshida T, Yamada Y, Ueda M, Honda H (2007) Bone tissue engineering with human mesenchymal stem cell sheets constructed using magnetite nanoparticles and magnetic force. *J Biomed Mater Res B Appl Biomater* 83(2):340–344

236. Drummen GPC (2010) Quantum dots – from synthesis to applications in biomedicine and life sciences. *Int J Mol Sci* 11(1):154–163
237. Esteve-Turrillas FA, Abad-Fuentes A (2013) Applications of quantum dots as probes in immunosensing of small-sized analytes. *Biosens Bioelectron* 41(1):12–29
238. Rosenthal SJ, Chang JC, Kovtun O, McBride JR, Tomlinson ID (2011) Biocompatible quantum dots for biological applications. *Chem Biol* 18(1):10–24
239. Brichkin SB, Razumov VF (2016) Colloidal quantum dots: synthesis, properties and applications. *Russ Chem Rev* 85(12):1297–1312
240. Foubert A, Beloglazova NV, Rajkovic A, Sas B, Madder A, Goryacheva IY, De Saeger S (2016) Bioconjugation of quantum dots: review & impact on future application. *TrAC Trends Anal Chem* 83:31–48
241. Chan WCW, Maxwell DJ, Gao X, Bailey RE, Han M, Nie S (2002) Luminescent quantum dots for multiplexed biological detection and imaging. *Curr Opin Biotechnol* 13(1):40–46
242. Michalet X, Gambhir SS, Weiss S (2005) Quantum dots for live cells, in vivo imaging, and diagnostics. *Science* 307(January):538–544
243. Zrazhevskiy P, Gao X (2009) Multifunctional quantum dots for personalized medicine. *Nano Today* 4(5):414–428
244. Shah BS, Clark PA, Moiola EK, Stroschio MA, Mao JJ (2007) Labeling of mesenchymal stem cells by bioconjugated quantum dots. *Nano Lett* 7(10):3071–3079
245. Rosen AB, Kelly DJ, Schuldt AJT, Lu J, Potapova IA, Doronin SV, Robichaud KJ, Robinson RB, Rosen MR, Brink PR, Gaudette GR, Cohen IS (2007) Finding fluorescent needles in the cardiac haystack: tracking human mesenchymal stem cells labeled with quantum dots for quantitative in vivo three-dimensional fluorescence analysis. *Stem Cells* 25(8):2128–2138
246. Ho JH-C, Ma W-H, Tseng T-C, Chen Y-F, Chen M-H, Lee OK-S (2011) Isolation and characterization of multi-potent stem cells from human orbital fat tissues. *Tissue Eng A* 17(1–2):255–266
247. Lei Y, Tang H, Yao L, Yu R, Feng M, Zou B (2008) Applications of mesenchymal stem cells labeled with tat peptide conjugated quantum dots to cell tracking in mouse body. *Bioconjug Chem* 19(2):421–427
248. Lin S, Xie X, Patel MR, Yang Y-H, Li Z, Cao F, Gheysens O, Zhang Y, Gambhir SS, Rao J, Wu JC (2007) Quantum dot imaging for embryonic stem cells. *BMC Biotechnol* 7(1):67–67
249. Yukawa H, Kagami Y, Watanabe M, Oishi K, Miyamoto Y, Okamoto Y, Tokeshi M, Kaji N, Noguchi H, Ono K, Sawada M, Baba Y, Hamajima N, Hayashi S (2010) Quantum dots labeling using octa-arginine peptides for imaging of adipose tissue-derived stem cells. *Biomaterials* 31(14):4094–4103
250. Chung BG, Kang L, Khademhosseini A (2007) Micro-and nanoscale technologies for tissue engineering and drug discovery applications. *Expert Opin Drug Discovery* 2(12):1653–1668
251. Griffith LG, Naughton G (2002) Tissue engineering – current challenges and expanding opportunities. *Science* 295(5557):1009–1014
252. Wang P, Zhao L, Liu J, Weir MD, Zhou X, Xu HH (2014) Bone tissue engineering via nanostructured calcium phosphate biomaterials and stem cells. *Bone Res* 2:14017
253. Tadic D, Epple M (2004) A thorough physicochemical characterisation of 14 calcium phosphate-based bone substitution materials in comparison to natural bone. *Biomaterials* 25(6):987–994
254. Stevens MM, George JH (2005) Exploring and engineering the cell surface interface. *Science* 310(5751):1135–1138
255. Gong T, Xie J, Liao J, Zhang T, Lin S, Lin Y (2015) Nanomaterials and bone regeneration. *Bone Res* 3:15029
256. Porter JR, Ruckh TT, Popat KC (2009) Bone tissue engineering: a review in bone biomimetics and drug delivery strategies. *Biotechnol Prog* 25(6):1539–1560
257. Kneser U, Schaefer DJ, Polykandriotis E, Horch RE (2006) Tissue engineering of bone: the reconstructive surgeon's point of view. *J Cell Mol Med* 10(1):7–19

258. Burg KJ, Porter S, Kellam JF (2000) Biomaterial developments for bone tissue engineering. *Biomaterials* 21(23):2347–2359
259. Khan Y, Yaszemski MJ, Mikos AG, Laurencin CT (2008) Tissue engineering of bone: material and matrix considerations. *JBJS* 90:36–42
260. Shin H, Jo S, Mikos AG (2003) Biomimetic materials for tissue engineering. *Biomaterials* 24(24):4353–4364
261. Rezwan K, Chen Q, Blaker J, Boccaccini AR (2006) Biodegradable and bioactive porous polymer/inorganic composite scaffolds for bone tissue engineering. *Biomaterials* 27(18):3413–3431
262. Williams D (2004) Benefit and risk in tissue engineering. *Mater Today* 7(5):24–29
263. Mano JF, Sousa RA, Boesel LF, Neves NM, Reis RL (2004) Bioinert, biodegradable and injectable polymeric matrix composites for hard tissue replacement: state of the art and recent developments. *Compos Sci Technol* 64(6):789–817
264. Mathieu LM, Mueller TL, Bourban P-E, Pioletti DP, Müller R, Månson J-AE (2006) Architecture and properties of anisotropic polymer composite scaffolds for bone tissue engineering. *Biomaterials* 27(6):905–916
265. Boyan BD, Hummert TW, Dean DD, Schwartz Z (1996) Role of material surfaces in regulating bone and cartilage cell response. *Biomaterials* 17(2):137–146
266. Keaveny TM, Hayes WC (1993) Mechanical properties of cortical and trabecular bone. *Bone* 7:285–344
267. Li X, Wang L, Fan Y, Feng Q, Cui FZ, Watari F (2013) Nanostructured scaffolds for bone tissue engineering. *J Biomed Mater Res A* 101(8):2424–2435
268. Wolff J (1892) *Das Gesetz der Transformation der Knochen* (Berlin A. Hirschwild). Translated as: *The law of bone remodeling*. Springer, Berlin Google Scholar
269. Wegst U, Ashby M (2004) The mechanical efficiency of natural materials. *Philos Mag* 84(21):2167–2186
270. Hu Y, Grainger DW, Winn SR, Hollinger JO (2002) Fabrication of poly (α -hydroxy acid) foam scaffolds using multiple solvent systems. *J Biomed Mater Res A* 59(3):563–572
271. Liu X, Ma PX (2004) Polymeric scaffolds for bone tissue engineering. *Ann Biomed Eng* 32(3):477–486
272. Swetha M, Sahithi K, Moorthi A, Srinivasan N, Ramasamy K, Selvamurugan N (2010) Biocomposites containing natural polymers and hydroxyapatite for bone tissue engineering. *Int J Biol Macromol* 47(1):1–4
273. Lee KY, Yuk SH (2007) Polymeric protein delivery systems. *Prog Polym Sci* 32(7):669–697
274. Lu HH, Kofron MD, El-Amin SF, Attawia MA, Laurencin CT (2003) In vitro bone formation using muscle-derived cells: a new paradigm for bone tissue engineering using polymer–bone morphogenetic protein matrices. *Biochem Biophys Res Commun* 305(4):882–889
275. Leenslag JW, Pennings AJ, Bos RR, Rozema FR, Boering G (1987) Resorbable materials of poly (L-lactide): VII. In vivo and in vitro degradation. *Biomaterials* 8(4):311–314
276. Lin FH, Chen TM, Lin CP, Lee CJ (1999) The merit of sintered PDLLA/TCP composites in management of bone fracture internal fixation. *Artif Organs* 23(2):186–194
277. Zhao F, Yin Y, Lu WW, Leong JC, Zhang W, Zhang J, Zhang M, Yao K (2002) Preparation and histological evaluation of biomimetic three-dimensional hydroxyapatite/chitosan-gelatin network composite scaffolds. *Biomaterials* 23(15):3227–3234
278. Liao S, Cui F, Zhang W, Feng Q (2004) Hierarchically biomimetic bone scaffold materials: nano-HA/collagen/PLA composite. *J Biomed Mater Res B Appl Biomater* 69(2):158–165
279. Hollister SJ (2005) Porous scaffold design for tissue engineering. *Nat Mater* 4(7):518
280. Huttmacher DW (2006) Scaffolds in tissue engineering bone and cartilage. In: *The biomaterials: silver jubilee compendium*. Elsevier, Oxford, pp 175–189
281. Goulet RW, Goldstein SA, Ciarelli MJ, Kuhn JL, Brown M, Feldkamp L (1994) The relationship between the structural and orthogonal compressive properties of trabecular bone. *J Biomech* 27(4):379–389

282. Holzapfel GA, Ogden RW (2014) *Biomechanics of soft tissue in cardiovascular systems*, vol 441. Springer, Wien
283. Egusa H, Sonoyama W, Nishimura M, Atsuta I, Akiyama K (2012) Stem cells in dentistry – part I: stem cell sources. *J Prosthodont Res* 56(3):151–165
284. Lombaert IM, Knox SM, Hoffman MP (2011) Salivary gland progenitor cell biology provides a rationale for therapeutic salivary gland regeneration. *Oral Dis* 17(5):445–449
285. Luxamechanporn T, Hadlock T, Shyu J, Cowan D, Faquin W, Varvares M (2006) Successful myoblast transplantation in rat tongue reconstruction. *Head Neck* 28(6):517–524
286. Shah R, Sinanan AC, Knowles JC, Hunt NP, Lewis MP (2005) Craniofacial muscle engineering using a 3-dimensional phosphate glass fibre construct. *Biomaterials* 26(13):1497–1505
287. Dormer NH, Busaidy K, Berklund CJ, Detamore MS (2011) Osteochondral interface regeneration of rabbit mandibular condyle with bioactive signal gradients. *J Oral Maxillofac Surg* 69(6):e50–e57
288. Yu H, Yang X, Cheng J, Wang X, Shen SG (2011) Distraction osteogenesis combined with tissue-engineered cartilage in the reconstruction of condylar osteochondral defect. *J Oral Maxillofac Surg* 69(12):e558–e564
289. Egusa H, Sonoyama W, Nishimura M, Atsuta I, Akiyama K (2012) Stem cells in dentistry – part II: clinical applications. *J Prosthodont Res* 56(4):229–248
290. Kim SH, Park JK, Hong KS, Jung HS, Seo YK (2013) Immobilization of BMP-2 on a nano-hydroxyapatite-coated titanium surface using a chitosan calcium chelating agent. *Int J Artif Organs* 36(7):506–517
291. De-Deus G, Canabarro A, Alves G, Linhares A, Senne MI, Granjeiro JM (2009) Optimal cytocompatibility of a bioceramic nanoparticulate cement in primary human mesenchymal cells. *J Endod* 35(10):1387–1390
292. Yuan Z, Peng B, Jiang H, Bian Z, Yan P (2010) Effect of bioaggregate on mineral-associated gene expression in osteoblast cells. *J Endod* 36(7):1145–1148
293. Sun W, Starly B, Nam J, Darling A (2005) Bio-CAD modeling and its applications in computer-aided tissue engineering. *Comput Aided Des* 37(11):1097–1114
294. Kim J, Kim HN, Lim K-T, Kim Y, Seonwoo H, Park SH, Lim HJ, Kim D-H, Suh K-Y, Choung P-H (2013) Designing nanotopographical density of extracellular matrix for controlled morphology and function of human mesenchymal stem cells. *Sci Rep* 3:3552
295. Fang Z, Starly B, Sun W (2005) Computer-aided characterization for effective mechanical properties of porous tissue scaffolds. *Comput Aided Des* 37(1):65–72
296. Li L, Zhou G, Wang Y, Yang G, Ding S, Zhou S (2015) Controlled dual delivery of BMP-2 and dexamethasone by nanoparticle-embedded electrospun nanofibers for the efficient repair of critical-sized rat calvarial defect. *Biomaterials* 37:218–229
297. O’Brien CM, Holmes B, Faucett S, Zhang LG (2014) Three-dimensional printing of nano-material scaffolds for complex tissue regeneration. *Tissue Eng Part B Rev* 21(1):103–114
298. Murphy SV, Atala A (2014) 3D bioprinting of tissues and organs. *Nat Biotechnol* 32(8):773
299. Zhang T, Yan KC, Ouyang L, Sun W (2013) Mechanical characterization of bioprinted in vitro soft tissue models. *Biofabrication* 5(4):045010
300. Schantz J-T, Brandwood A, Huttmacher DW, Khor HL, Bittner K (2005) Osteogenic differentiation of mesenchymal progenitor cells in computer designed fibrin-polymer-ceramic scaffolds manufactured by fused deposition modeling. *J Mater Sci Mater Med* 16(9):807–819
301. Wagner DE, Jones AD, Zhou H, Bhaduri SB (2013) Cytocompatibility evaluation of microwave sintered biphasic calcium phosphate scaffolds synthesized using pH control. *Mater Sci Eng C* 33(3):1710–1719
302. Xu T, Binder KW, Albanna MZ, Dice D, Zhao W, Yoo JJ, Atala A (2012) Hybrid printing of mechanically and biologically improved constructs for cartilage tissue engineering applications. *Biofabrication* 5(1):015001
303. Fedorovich NE, Schuurman W, Wijnberg HM, Prins H-J, Van Weeren PR, Malda J, Alblas J, Dhert WJ (2011) Biofabrication of osteochondral tissue equivalents by printing topologically defined, cell-laden hydrogel scaffolds. *Tissue Eng Part C Methods* 18(1):33–44

304. Holmes B, Zhu W, Li J, Lee JD, Zhang LG (2014) Development of novel three-dimensional printed scaffolds for osteochondral regeneration. *Tissue Eng A* 21(1–2):403–415
305. Xu T, Gregory CA, Molnar P, Cui X, Jalota S, Bhaduri SB, Boland T (2006) Viability and electrophysiology of neural cell structures generated by the inkjet printing method. *Biomaterials* 27(19):3580–3588
306. Suri S, Han L-H, Zhang W, Singh A, Chen S, Schmidt CE (2011) Solid freeform fabrication of designer scaffolds of hyaluronic acid for nerve tissue engineering. *Biomed Microdevices* 13(6):983–993
307. Duan B, Kapetanovic E, Hockaday LA, Butcher JT (2014) Three-dimensional printed trileaflet valve conduits using biological hydrogels and human valve interstitial cells. *Acta Biomater* 10(5):1836–1846
308. Williams SK, Touroo JS, Church KH, Hoying JB (2013) Encapsulation of adipose stromal vascular fraction cells in alginate hydrogel spheroids using a direct-write three-dimensional printing system. *Biores Open Access* 2(6):448–454
309. Xu T, Zhao W, Zhu J-M, Albanna MZ, Yoo JJ, Atala A (2013) Complex heterogeneous tissue constructs containing multiple cell types prepared by inkjet printing technology. *Biomaterials* 34(1):130–139
310. Severs NJ (2000) The cardiac muscle cell. *BioEssays* 22(2):188–199
311. American Heart Association (2015) Cardiovascular disease: a costly burden for America – projections through 2035, p 10. http://www.heart.org/adc/groups/heart-public/@wcm/@adv/documents/downloadable/ucm_491543.pdf
312. Baig MK, Mahon N, McKenna WJ, Caforio ALP, Bonow RO, Francis GS, Gheorghiadu M (1998) The pathophysiology of advanced heart failure. *Am Heart J* 135(6):S216–S230
313. Akasha AA, Sotiriadou I, Doss MX, Halbach M, Winkler J, Baunach JJS, Katsen-Globa A, Zimmermann H, Choo Y, Hescheler J, Sachinidis A (2008) Entrapment of embryonic stem cells-derived cardiomyocytes in macroporous biodegradable microspheres: preparation and characterization. *Cell Physiol Biochem* 22(5–6):665–672
314. Alperin C, Zandstra PW, Woodhouse KA (2005) Polyurethane films seeded with embryonic stem cell-derived cardiomyocytes for use in cardiac tissue engineering applications. *Biomaterials* 26(35):7377–7386
315. Gwak S-J, Bhang SH, Kim I-K, Kim S-S, Cho S-W, Jeon O, Yoo KJ, Putnam AJ, Kim B-S (2008) The effect of cyclic strain on embryonic stem cell-derived cardiomyocytes. *Biomaterials* 29(7):844–856
316. Ke Q, Yang Y, Rana JS, Chen Y, Morgan JP, Xiao Y-F (2005) Embryonic stem cells cultured in biodegradable scaffold repair infarcted myocardium in mice. *Sheng Li Xue Bao* 57(6):673–681
317. Wei HJ, Chen SC, Chang Y, Hwang SM, Lin WW, Lai PH, Chiang HHK, Hsu LF, Yang HH, Sung HW (2006) Porous acellular bovine pericardia seeded with mesenchymal stem cells as a patch to repair a myocardial defect in a syngeneic rat model. *Biomaterials* 27(31):5409–5419
318. Yang MC, Wang SS, Chou NK, Chi NH, Huang YY, Chang YL, Shieh MJ, Chung TW (2009) The cardiomyogenic differentiation of rat mesenchymal stem cells on silk fibroin-polysaccharide cardiac patches in vitro. *Biomaterials* 30(22):3757–3765
319. Shin M, Ishii O, Sueda T, Vacanti JP (2004) Contractile cardiac grafts using a novel nanofibrous mesh. *Biomaterials* 25(17):3717–3723
320. Ishii O, Shin M, Sueda T, Vacanti JP (2005) In vitro tissue engineering of a cardiac graft using a degradable scaffold with an extracellular matrix-like topography. *J Thorac Cardiovasc Surg* 130(5):1358–1363
321. Li M, Mondrinos MJ, Chen X, Gandhi MR, Ko FK, Lelkes PI (2006) Co-electrospun poly (lactide-co-glycolide), gelatin, and elastin blends for tissue engineering scaffolds. *J Biomed Mater Res A* 79A(4):963–973
322. Zong XH, Bien H, Chung CY, Yin LH, Fang DF, Hsiao BS, Chu B, Entcheva E (2005) Electrospun fine-textured scaffolds for heart tissue constructs. *Biomaterials* 26(26):5330–5338

323. Binsalamah ZM, Paul A, Khan AA, Prakash S, Shum-Tim D (2011) Intramyocardial sustained delivery of placental growth factor using nanoparticles as a vehicle for delivery in the rat infarct model. *Int J Nanomedicine* 6:2667–2678
324. Hsieh PCH, Davis ME, Gannon J, MacGillivray C, Lee RT (2006) Controlled delivery of PDGF-BB for myocardial protection using injectable self-assembling peptide nanofibers. *J Clin Invest* 116(1):237–248
325. Paul A, Nayan M, Khan AA, Shum-Tim D, Prakash S (2012) Angiopoietin-1-expressing adipose stem cells genetically modified with baculovirus nanocomplex: investigation in rat heart with acute infarction. *Int J Nanomedicine* 7:663–682
326. Tokunaga M, Liu ML, Nagai T, Iwanaga K, Matsuura K, Takahashi T, Kanda M, Kondo N, Wang P, Naito AT, Komuro I (2010) Implantation of cardiac progenitor cells using self-assembling peptide improves cardiac function after myocardial infarction. *J Mol Cell Cardiol* 49(6):972–983
327. Simpson D, Liu H, Fan THM, Nerem R, Dudley SC (2007) A tissue engineering approach to progenitor cell delivery results in significant cell engraftment and improved myocardial remodeling. *Stem Cells* 25(9):2350–2357
328. Lin Y-D, Yeh M-L, Yang Y-J, Tsai D-C, Chu T-Y, Shih Y-Y, Chang M-Y, Liu Y-W, Tang ACL, Chen T-Y, Luo C-Y, Chang K-C, Chen J-H, Wu H-L, Hung T-K, Hsieh PCH (2010) Intramyocardial peptide nanofiber injection improves postinfarction ventricular remodeling and efficacy of bone marrow cell therapy in pigs. *Circulation* 122(11 suppl 1):S132
329. Cui XJ, Xie H, Wang HJ, Guo HD, Zhang JK, Wang C, Tan YZ (2010) Transplantation of mesenchymal stem cells with self-assembling polypeptide scaffolds is conducive to treating myocardial infarction in rats. *Tohoku J Exp Med* 222(4):281–289
330. Guo HD, Cui GH, Wang HJ, Tan YZ (2010) Transplantation of marrow-derived cardiac stem cells carried in designer self-assembling peptide nanofibers improves cardiac function after myocardial infarction. *Biochem Biophys Res Commun* 399(1):42–48
331. Kim DH, Kshitz, Smith RR, Kim P, Ahn EH, Kim HN, Marban E, Suh KY, Levchenko A (2012) Nanopatterned cardiac cell patches promote stem cell niche formation and myocardial regeneration. *Integr Biol* 4(9):1019–1033
332. Pijnappels DA, Schalijs MJ, Ramkisoensing AA, van Tuyn J, de Vries AAF, van der Laarse A, Ypey DL, Atsma DE (2008) Forced alignment of mesenchymal stem cells undergoing cardiomyogenic differentiation affects functional integration with cardiomyocyte cultures. *Circ Res* 103(2):167–176
333. Kang B-J, Kim H, Lee SK, Kim J, Shen Y, Jung S, Kang K-S, Im SG, Lee SY, Choi M, Hwang NS, Cho J-Y (2014) Umbilical-cord-blood-derived mesenchymal stem cells seeded onto fibronectin-immobilized polycaprolactone nanofiber improve cardiac function. *Acta Biomater* 10(7):3007–3017
334. Ravichandran R, Sridhar R, Venugopal JR, Sundarajan S, Mukherjee S, Ramakrishna S (2014) Gold nanoparticle loaded hybrid nanofibers for cardiogenic differentiation of stem cells for infarcted myocardium regeneration. *Macromol Biosci* 14(4):515–525
335. Park J, Park S, Ryu S, Bhang SH, Kim J, Yoon JK, Park YH, Cho SP, Lee S, Hong BH, Kim BS (2014) Graphene-regulated cardiomyogenic differentiation process of mesenchymal stem cells by enhancing the expression of extracellular matrix proteins and cell signaling molecules. *Adv Healthc Mater* 3(2):176–181
336. Han J, Kim B, Shin J-Y, Ryu S, Noh M, Woo J, Park J-S, Lee Y, Lee N, Hyeon T, Choi D, Kim B-S (2015) Iron oxide nanoparticle-mediated development of cellular gap junction crosstalk to improve mesenchymal stem cells' therapeutic efficacy for myocardial infarction. *ACS Nano* 9(3):2805–2819
337. Webber MJ, Han XQ, Murthy SNP, Rajangam K, Stupp SI, Lomasney JW (2010) Capturing the stem cell paracrine effect using heparin-presenting nanofibres to treat cardiovascular diseases. *J Tissue Eng Regen Med* 4(8):600–610

338. Lee TJ, Park S, Bhang SH, Yoon JK, Jo I, Jeong GJ, Hong BH, Kim BS (2014) Graphene enhances the cardiomyogenic differentiation of human embryonic stem cells. *Biochem Biophys Res Commun* 452(1):174–180
339. Han J, Park J, Kim BS (2015) Integration of mesenchymal stem cells with nanobiomaterials for the repair of myocardial infarction. *Adv Drug Deliv Rev* 95:15–28
340. Hsiao CW, Bai MY, Chang Y, Chung MF, Lee TY, Wu CT, Maiti B, Liao ZX, Li RK, Sung HW (2013) Electrical coupling of isolated cardiomyocyte clusters grown on aligned conductive nanofibrous meshes for their synchronized beating. *Biomaterials* 34(4):1063–1072
341. Lin YD, Ko MC, Wu ST, Li SF, Hu JF, Lai YJ, Harn HIC, Laio IC, Yeh ML, Yeh HI, Tang MJ, Chang KC, Su FC, Wei EIH, Lee ST, Chen JH, Hoffman AS, Wu WT, Hsieh PCH (2014) A nanopatterned cell-seeded cardiac patch prevents electro-uncoupling and improves the therapeutic efficacy of cardiac repair. *Biomater Sci* 2(4):567–580
342. Piao H, Kwon JS, Piao S, Sohn JH, Lee YS, Bae JW, Hwang KK, Kim DW, Jeon O, Kim BS, Park YB, Cho MC (2007) Effects of cardiac patches engineered with bone marrow-derived mononuclear cells and PGCL scaffolds in a rat myocardial infarction model. *Biomaterials* 28(4):641–649
343. Hwang HJ, Chang W, Song BW, Song H, Cha MJ, Kim IK, Lim S, Choi EJ, Ham O, Lee SY, Shim J, Joung B, Pak HN, Kim SS, Choi BR, Jang Y, Lee MH, Hwang KC (2012) Antiarrhythmic potential of mesenchymal stem cell is modulated by hypoxic environment. *J Am Coll Cardiol* 60(17):1698–1706
344. Song H, Hwang HJ, Chang W, Song BW, Cha MJ, Kim IK, Lim S, Choi EJ, Ham O, Lee CY, Park JH, Lee SY, Choi E, Lee C, Lee M, Lee MH, Kim SH, Jang Y, Hwang KC (2011) Cardiomyocytes from phorbol myristate acetate-activated mesenchymal stem cells restore electromechanical function in infarcted rat hearts. *Proc Natl Acad Sci U S A* 108(1):296–301
345. Chen HSV, Kim C, Mercola M (2009) Electrophysiological challenges of cell-based myocardial repair. *Circulation* 120(24):2496–2508
346. Stout DA, Basu B, Webster TJ (2011) Poly(lactic-co-glycolic acid): carbon nanofiber composites for myocardial tissue engineering applications. *Acta Biomater* 7(8):3101–3112
347. Wickham AM, Islam MM, Mondal D, Phopase J, Sadhu V, Tamas E, Poliseti N, Richter-Dahlfors A, Liedberg B, Griffith M (2014) Polycaprolactone-thiophene-conjugated carbon nanotube meshes as scaffolds for cardiac progenitor cells. *J Biomed Mater Res B Appl Biomater* 102(7):1553–1561
348. Martins AM, Eng G, Caridade SG, Mano JF, Reis RL, Vunjak-Novakovic G (2014) Electrically conductive chitosan/carbon scaffolds for cardiac tissue engineering. *Biomacromolecules* 15(2):635–643
349. Kharaziha M, Shin SR, Nikkha M, Topkaya SN, Masoumi N, Annabi N, Dokmeci MR, Khademhosseini A (2014) Tough and flexible CNT-polymeric hybrid scaffolds for engineering cardiac constructs. *Biomaterials* 35(26):7346–7354
350. You JO, Rafat M, Ye GJC, Auguste DT (2011) Nanoengineering the heart: conductive scaffolds enhance connexin 43 expression. *Nano Lett* 11(9):3643–3648
351. Dvir T, Timko BP, Brigham MD, Naik SR, Karajanagi SS, Levy O, Jin HW, Parker KK, Langer R, Kohane DS (2011) Nanowired three-dimensional cardiac patches. *Nat Nanotechnol* 6(11):720–725
352. Crowder SW, Liang Y, Rath R, Park AM, Maltais S, Pintauro PN, Hofmeister W, Lim CC, Wang XT, Sung HJ (2013) Poly(epsilon-caprolactone)-carbon nanotube composite scaffolds for enhanced cardiac differentiation of human mesenchymal stem cells. *Nanomedicine* 8(11):1763–1776
353. Park J, Kim YS, Ryu S, Kang WS, Park S, Han J, Jeong HC, Hong BH, Ahn Y, Kim BS (2015) Graphene potentiates the myocardial repair efficacy of mesenchymal stem cells by stimulating the expression of angiogenic growth factors and gap junction protein. *Adv Funct Mater* 25(17):2590–2600

354. Pack DW, Hoffman AS, Pun S, Stayton PS (2005) Design and development of polymers for gene delivery. *Nat Rev Drug Discov* 4(7):581–593
355. Padin-Iruegas ME, Misao Y, Davis ME, Segers VFM, Esposito G, Tokunou T, Urbanek K, Hosoda T, Rota M, Anversa P, Leri A, Lee T, Kajstura J (2009) Cardiac progenitor cells and biotinylated insulin-like growth factor-1 nanofibers improve endogenous and exogenous myocardial regeneration after infarction. *Circulation* 120(10):876–U115
356. Ye L, Haider HK, Tan R, Toh W, Law PK, Tan W, Su L, Zhang W, Ge R, Zhang Y, Lim Y, Sim EKW (2007) Transplantation of nanoparticle transfected skeletal myoblasts overexpressing vascular endothelial growth factor-165 for cardiac repair. *Circulation* 116(11):I113–I120
357. Koiwaya H, Sasaki K, Ueno T, Yokoyama S, Toyama Y, Ohtsuka M, Nakayoshi T, Mitsutake Y, Imaizumi T (2011) Augmented neovascularization with magnetized endothelial progenitor cells in rats with hind-limb ischemia. *J Mol Cell Cardiol* 51(1):33–40
358. Kang HJ, Kim JY, Lee HJ, Kim KH, Kim TY, Lee CS, Lee HC, Park TH, Kim HS, Park YB (2012) Magnetic bionanoparticle enhances homing of endothelial progenitor cells in mouse hindlimb ischemia. *Korean Circ J* 42(6):390–396
359. Zhu P, Weng ZY, Li X, Liu XM, Wu SL, Yeung KWK, Wang XB, Cui ZD, Yang XJ, Chu PK (2016) Biomedical applications of functionalized ZnO nanomaterials: from biosensors to bioimaging. *Adv Mater Interfaces* 3(1)
360. Liao QL, Zhang Z, Zhang XH, Mohr M, Zhang Y, Fecht HJ (2014) Flexible piezoelectric nanogenerators based on a fiber/ZnO nanowires/paper hybrid structure for energy harvesting. *Nano Res* 7(6):917–928
361. Kang Z, Yan XQ, Zhao LQ, Liao QL, Zhao K, Du HW, Zhang XH, Zhang XJ, Zhang Y (2015) Gold nanoparticle/ZnO nanorod hybrids for enhanced reactive oxygen species generation and photodynamic therapy. *Nano Res* 8(6):2004–2014
362. Yan ZQ, Zhao AD, Liu XP, Ren JS, Qu XG (2017) A pH-switched mesoporous nanoreactor for synergetic therapy. *Nano Res* 10(5):1651–1661
363. Augustine R, Dan P, Sosnik A, Kalarikkal N, Tran N, Vincent B, Thomas S, Menu P, Rouxel D (2017) Electrospun poly(vinylidene fluoride-trifluoroethylene)/zinc oxide nanocomposite tissue engineering scaffolds with enhanced cell adhesion and blood vessel formation. *Nano Res* 10(10):3358–3376
364. Irvani S, Korbekandi H, Mirmohammadi SV, Zolfaghari B (2014) Synthesis of silver nanoparticles: chemical, physical and biological methods. *Res Pharm Sci* 9(6):385–406
365. Vallee JP, Hauwel M, Lepetit-Coeffe M, Bei W, Montet-Abou K, Meda P, Gardier S, Zammaretti P, Kraehenbuehl TP, Herrmann F, Hubbell JA, Jaconi ME (2012) Embryonic stem cell-based cardiopatches improve cardiac function in infarcted rats. *Stem Cells Transl Med* 1(3):248–260
366. Pagliari F, Mandoli C, Forte G, Magnani E, Pagliari S, Nardone G, Licocchia S, Minieri M, Di Nardo P, Traversa E (2012) Cerium oxide nanoparticles protect cardiac progenitor cells from oxidative stress. *ACS Nano* 6(5):3767–3775
367. Shevach M, Fleischer S, Shapira A, Dvir T (2014) Gold nanoparticle-decellularized matrix hybrids for cardiac tissue engineering. *Nano Lett* 14(10):5792–5796
368. Lakshmanan RAMN (2018) Development of next generation cardiovascular therapeutics through bio-assisted nanotechnology. *J Biomed Mater Res B Appl Biomater* 106(5):2072–2083
369. Li X, Zhou J, Liu Z, Chen J, Lü S, Sun H, Li J, Lin Q, Yang B, Duan C, Xing M, Wang C (2014) A PNIPAAm-based thermosensitive hydrogel containing SWCNTs for stem cell transplantation in myocardial repair. *Biomaterials* 35(22):5679–5688
370. Capulli AK, MacQueen LA, Sheehy SP, Parker KK (2016) Fibrous scaffolds for building hearts and heart parts. *Adv Drug Deliv Rev* 96:83–102
371. Sridhar S, Venugopal JR, Sridhar R, Ramakrishna S (2015) Cardiogenic differentiation of mesenchymal stem cells with gold nanoparticle loaded functionalized nanofibers. *Colloids Surf B: Biointerfaces* 134:346–354

372. Borriello A, Guarino V, Schiavo L, Alvarez-Perez MA, Ambrosio L (2011) Optimizing PANi doped electroactive substrates as patches for the regeneration of cardiac muscle. *J Mater Sci Mater Med* 22(4):1053–1062
373. Orza A, Soritau O, Olenic L, Diudea M, Florea A, Ciuca DR, Mihu C, Casciano D, Biris AS (2011) Electrically conductive gold-coated collagen nanofibers for placental-derived mesenchymal stem cells enhanced differentiation and proliferation. *ACS Nano* 5(6):4490–4503
374. Jung D, Minami I, Patel S, Lee J, Jiang B, Yuan Q, Li L, Kobayashi S, Chen Y, Lee K-B, Nakatsuji N (2012) Incorporation of functionalized gold nanoparticles into nanofibers for enhanced attachment and differentiation of mammalian cells. *J Nanobiotechnol* 10:23–23
375. Miyagawa S, Domae K, Yoshikawa Y, Fukushima S, Nakamura T, Saito A, Sakata Y, Hamada S, Toda K, Pak K, Takeuchi M, Sawa Y (2017) Phase I clinical trial of autologous stem cell-sheet transplantation therapy for treating cardiomyopathy. *J Am Heart Assoc* 6(4)
376. Yang X, Pabon L, Murry CE (2014) Engineering adolescence: maturation of human pluripotent stem cell-derived cardiomyocytes. *Circ Res* 114(3):511–523
377. Rong Z, Wang M, Hu Z, Stradner M, Zhu S, Kong H, Yi H, Goldrath A, Yang Y-G, Xu Y, Fu X (2014) An effective approach to prevent immune rejection of human ESC-derived allografts. *Cell Stem Cell* 14(1):121–130
378. Tamayol A, Akbari M, Annabi N, Paul A, Khademhosseini A, Juncker D (2013) Fiber-based tissue engineering: progress, challenges, and opportunities. *Biotechnol Adv* 31(5):669–687
379. Akbari M, Tamayol A, Laforte V, Annabi N, Hassani Najafabadi A, Khademhosseini A, Juncker D (2014) Composite living fibers for creating tissue constructs using textile techniques. *Adv Funct Mater* 24(26):4060–4067
380. Bajaj P, Schweller RM, Khademhosseini A, West JL, Bashir R (2014) 3D biofabrication strategies for tissue engineering and regenerative medicine. *Annu Rev Biomed Eng* 16:247–276
381. Vunjak-Novakovic G, Lui KO, Tandon N, Chien KR (2011) Bioengineering heart muscle: a paradigm for regenerative medicine. *Annu Rev Biomed Eng* 13:245–267



Characterization Tools for Mechanical Probing of Biomimetic Materials

2

Silvia Caponi, Claudio Canale, Ornella Cavalleri, and Massimo Vassalli

Contents

1	Overview	69
2	Introduction	70
3	Experimental and Instrumental Methodology	71
3.1	Scanning Probe Microscopy	72
3.2	Brillouin Spectroscopy	80
4	Key Research Findings	89
4.1	Indentation Experiments on Hard/Soft Materials	90
4.2	Mechanical Properties of Porous Materials for Tissue Engineering	93
4.3	Noncontact Mechanical Analysis	95
5	Conclusions and Future Perspective	104
	References	105

1 Overview

The possibility to fully heal damaged or failing tissues and organs is one of the major challenges of modern medicine. Several approaches have been proposed, either using tissue engineered functional substitutes or inducing the body to self-repair, exploiting its innate regenerative potential. In any case, a crucial step for the success of therapy is provided by the design of a suitable scaffold, capable to sustain cellular growth and induce the differentiation towards the lineage of

S. Caponi
Istituto Officina dei Materiali, National Research Council, Perugia, Italy

C. Canale · O. Cavalleri
Department of Physics, University of Genova, Genoa, Italy

M. Vassalli (✉)
Institute of Biophysics, National Research Council, Genoa, Italy
e-mail: massimo.vassalli@cnr.it

interest. A growing body of evidence suggests that the most affordable way to design an effective scaffold is to exploit a biomimetic approach, trying to emulate the characteristics of the natural environment. Moreover, it has been pointed out that not only the chemical nature of the material is relevant to this process but also its physical and, in particular, mechanical properties. Mapping the elasticity of a living tissue is becoming more and more relevant in the rational design of next generation biomimetic scaffolds, and the exploitation of advanced tools is required to achieve sub- μm resolution, comparable to the length scale probed by a single living cell.

2 Introduction

Living beings are studied in the context of life science from different points of view, but they can also be observed from an engineering perspective. Having survived millions of years of evolutionary pressure, living organisms have developed very specialized and effective behaviors and structures that can be regarded as an efficient template for the rational design of advanced engineering solutions. Smart textiles [52], visionary buildings [44], or locomotion strategies for swimming robots [42], all are examples of such a biomimetic approach, but the field of science that more inherently benefits of this strategy is probably biomedical engineering and, in particular, tissue engineering and regenerative medicine (TERM) [63].

The aim of TERM is to assemble functional constructs able to recover failing tissues or whole organs. After more than 30 years of intense research activity over the world [116], some engineered tissues have been fully translated to medicine and approved for human application [51]. Nevertheless, complex organs, such as liver, pancreas, or kidney, are still out of reach for current approaches and an extremely vital community is working to address the main issues of current methodologies in TERM [56].

The main experimental approach, emerging as a de facto standard in TERM, requires the development of biomimetic materials able to harness the self-healing potential of the organism [28]. Engineered scaffolds mimicking the natural physical and chemical environment can be designed to induce a local recruitment of undifferentiated cells and to elicit the formation of neotissue of the desired type [90]. Single cells, in particular stem cells, are extremely dynamical, continuously adapting to the matrix they are embedded in, deciphering and reacting to the mechanical and chemical cues provided by the material [49]. To guide their behavior, effectively inducing the desired response, it is of paramount importance to finely control the properties of the local microenvironment [11, 120].

The technological challenge posed by modern TERM is the development of characterization tools able to measure the material properties of the original (healthy) tissue and the corresponding engineered scaffold on a sub- μm length scale. This is particularly true when the biomechanical properties of the scaffold are concerned. Stem cells feature a panel of sensors to interpret the mechanical environment, either exploiting mechanisms occurring at the boundary of the cell,

the membrane [7], or involving the whole cell body [106]. These cellular machineries are able to trigger several transduction pathways, influencing the cell phenotype and eventually inducing stem cells differentiation towards a specific lineage, depending on the local elasticity [37]. In order to design an optimal scaffold for TERM application, specifically tailored to direct stem cell phase, it is mandatory to accurately know and control the mechanical properties of the material [62].

The availability and effectiveness of nanotechnology tools to characterize mechanical properties of biological materials has been widely reviewed during last years [13, 14, 82] and the potential application to biomimetic materials has also been investigated [49]. In this chapter, we recapitulate the main state-of-the-art methods to physically map the mechanical properties of biological materials, emphasizing approaches able to achieve sub μm resolution (Sect. 3.1) and concentrating on some key research findings in the context of rational design of biomimetic materials (Sect. 3.1). Moreover, we will also present new and emerging noncontact mechanical imaging technology (Sect. 3.2), able to achieve unprecedented resolution and thus provide a potentially breakthrough contribution to the field (Sect. 4.2).

Finally, current limitations and future perspectives of in vitro biomechanical mapping will be presented, with a special attention to the translational potential towards biomedical applications (Sect. 5).

3 Experimental and Instrumental Methodology

Measuring the mechanical properties of a soft biological material can be generally obtained either exploiting contact mechanics or measuring the effect of local material properties on the propagation of a physical wave (remote mapping). Both approaches have been extended to achieve single-cell high-resolution sub- μm resolution, and they will be discussed in the next sections.

Indenting a material with a tip of known geometry while measuring the corresponding force is the standard approach to measure mechanical properties (either static or dynamic) of a material, and a robust literature exists to model and analyze the resulting experiments [80]. This approach has been translated to biological applications and scaled down to nanometer size by means of the so-called atomic force microscope (AFM). Section 3.1 will present the measuring principle and the specific implementation nowadays available on the market, while key applications of AFM mechanical mapping on living cellular systems and biological materials are reported in Sect. 4.

While the scaling down of standard nanoindentation approaches to the nanoscale mainly involves technological issues, the identification of a remote mapping method with sub- μm resolution also implies to overcome some physical limitations. In fact, remote elastometry, as deployed in medical context, is based on acoustic imaging that, even using recent super-resolution advancements, hardly goes under 1 mm [40]. Nevertheless, not only the propagation of sound is influenced by the material

properties of the medium but also light can be used to probe the local elasticity, and this is the topic of Sect. 3.2 in which the use of Brillouin spectroscopy to achieve high resolution elasticity mapping is presented.

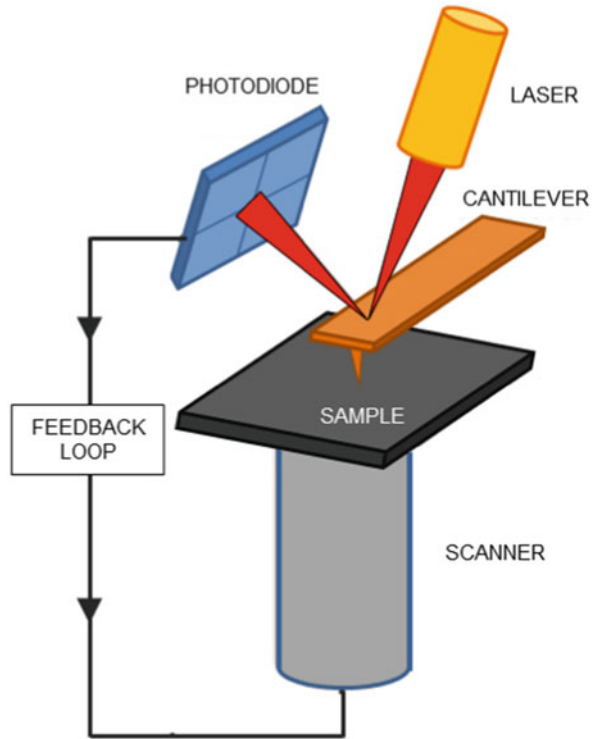
3.1 Scanning Probe Microscopy

Atomic Force Microscopy (AFM) is the second born member of the Scanning Probe Microscopy (SPM) family. The first scanning probe microscope, the Scanning Tunneling Microscope (STM), was invented in 1981 by Binnig e Rohrer [16]. Despite its extremely high spatial resolution, STM is not suitable for the analysis of biomaterials since it requires conductive samples. This limitation was overcome by the introduction in 1986 of the AFM [17] which can be used on insulating samples and is therefore well suited for the analysis of biological samples and bio-inspired materials. Other members of the SPM family followed over the years, like, to cite a few, Magnetic Force Microscopy (MFM) [48], Near-Field Scanning Optical Microscopy (NSOM) [12], and Scanning Thermal Microscopy (SthM) [130]. The key point of scanning probe microscopes is the use of a sharp tip which is placed in close proximity of the sample surface. The interaction between the tip and the sample is recorded while the tip scans over a selected area of the sample and the signal is used to build up a 3D image of the sample surface. In the case of AFM the signal of interest is the interaction force between the tip and the surface. As discussed below, AFM can be used not only as an imaging tool but also as a spectroscopic tool able to provide information on the mechanical properties of the samples under investigation.

3.1.1 The Microscope

A schematic of a typical AFM setup is shown in Fig. 2.1. The probe is based on a flexible μm -size cantilever fixed from one side and featuring a sharp tip at the free end. While the cantilever is scanned over the sample, the interaction force between tip and sample causes a deflection of the cantilever. The most commonly used method to measure the deflection of the cantilever is the so-called optical beam deflection method (OBDM). A laser beam is focused on the backside of the cantilever and the reflected beam is sent to a four quadrant photodiode. In this configuration, a deflection of the cantilever will cause a tilt of the reflected beam. Upon a proper calibration of the system, from the difference between the beam intensity on the upper and lower half of the photodiode the cantilever deflection can be evaluated, while from the difference between the beam intensity on the left and right half of the photodiode, the cantilever torsion can be evaluated. The high sensitivity of the optical method derives from the fact that the tip-photodiode distance is usually three order of magnitude larger than the cantilever length (millimeters vs micrometers), which greatly magnifies the tip displacements. When AFM is operated as an imaging tool, the tip is raster scanned over the sample (or the sample is raster scanned under the tip, depending on the microscope configuration) by using a piezoelectric scanner, which allows an extremely accurate motion of the

Fig. 2.1 Schematic diagram of a probe-scanned AFM including the main components

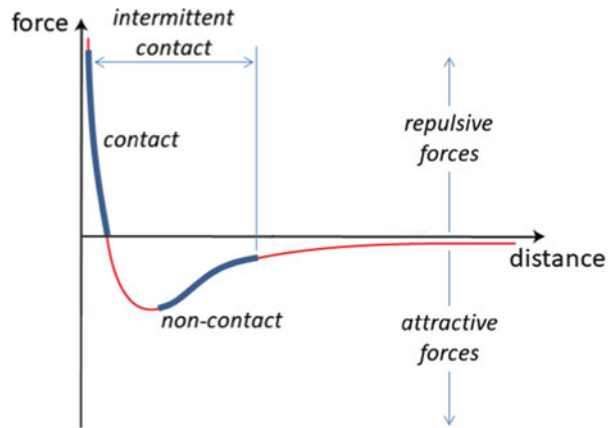


tip relative to the sample. The tip to sample distance, and therefore the interaction force, can be measured and controlled during scanning thanks to a feedback loop which tunes the position of the piezoelectric by changing its polarization.

3.1.2 AFM Operation Modes

The AFM can be operated in different modes, i.e., contact or DC mode and resonance or AC mode. In contact mode, the feedback system scans the AFM tip relative to the sample, with the tip kept in closest proximity with the surface and the static deflection of the cantilever is detected. In resonance modes, the cantilever is forced to oscillate at its resonance frequency and changes in its oscillation due to the interaction between the tip and the surface are detected. A schematic plot of the interaction force between tip and surface is reported in Fig. 2.2. In contact mode, short-range repulsive forces are involved in the interaction, while in resonance mode, long-range attractive forces come into play. In contact mode, the AFM is usually operated at constant force: the feedback loop modulates the z polarization of the piezo scanner in such a way to keep constant the cantilever deflection, i.e., the interaction force. The image is formed by recording the z polarization as a function of the (x,y) position of the tip and quantitative information on the surface morphology can be extracted from image analysis. The applied force, which can be modulated by the cantilever spring constant, can critically affect the image contrast,

Fig. 2.2 Schematic plot of the forces between tip and sample as a function of their distance. The regions of operation of the different imaging modes are shown



especially when soft samples like biological specimens are investigated. In this case, the use of very soft cantilevers and the possibility to image samples in liquid environment (to eliminate the effect of meniscus forces present in air imaging) can be successfully combined to achieve stable imaging on soft biological samples. By properly tuning the applied force it is even possible to switch from not perturbative soft imaging to high-load nanolithography modes [112].

Complementary information to sample morphology can be obtained in contact mode when the lateral force signal is recorded. As previously mentioned, the use of a four quadrant photodiode allows to monitor the torsion of the cantilever which is due to the friction between tip and surface. In this way, topographically uniform regions endowed with different chemical properties can be discriminated, as it is the case, for instance, of phase separated samples [122]. For the analysis of soft samples like biological ones, contact mode imaging can be advantageously complemented by resonant operational modes. In AC modes, the cantilever is oscillated close to its resonance frequency, depending on the cantilever oscillation amplitude and on the tip to surface distance intermittent or noncontact contact modes can be distinguished. As shown in Fig. 2.2, in intermittent contact mode, the tip oscillates from the contact region where it experiences repulsive forces to the noncontact region where it experiences attractive forces. The intermittent contact avoids the shear forces that the tip can exert on the sample in contact mode [27]. Images are formed by recording the piezo polarization signals set by the feedback loop in order to maintain selected cantilever oscillation amplitude. Very good vertical and lateral resolution can be achieved. Additional information on sample properties, like stiffness, viscosity, or adhesion, can be obtained by recording in a separate acquisition channel the phase difference between the cantilever oscillation and the driving signal [65]. Intermittent contact can be used in liquid, a favorable condition for biological or biomimetic samples. Noncontact mode differs from intermittent contact because during cantilever oscillation, the tip never touches the sample and experiences only long-range attractive forces; the oscillation amplitude is smaller than in intermittent contact. The interaction force between tip and sample is very low; this imaging mode is therefore

highly non perturbative, but the lateral resolution is lower compared to other modes. Further, noncontact can be operated only in air and, even on dry samples; because of the small-oscillation amplitude, the tip can be trapped by the thin condensed vapor layer on the surface.

3.1.3 Force Spectroscopy

Even if initially introduced as an imaging tool, over the years AFM has shown a huge potential as a spectroscopic tool, able to investigate at a very high-force resolution the interaction between the tip and the surface [25]. AFM spectroscopy can be exploited to get information on local chemical and mechanical properties like adhesion [81] or elasticity [83] as well as to investigate at the single-molecule level the interaction between specific molecular systems [79]. In the spectroscopic scheme, AFM is operated in a point mode, which means that the tip is not scanned over the surface, but, at a fixed lateral position, the cantilever deflection is recorded while the distance between tip and sample is changed from a large distance to contact and back to a large tip-sample separation. In this way a so-called force-distance curve is obtained. A general scheme is reported in Fig. 2.3. At large tip-sample separations, i.e., no interaction between tip and sample, the cantilever deflection is zero. Approaching the sample to the cantilever a point is reached when the gradient of the attractive force becomes larger than the cantilever elastic constant and the tip is captured by the sample, in the jump-to-contact point. The interaction force enters the repulsive regime and further approaching the sample results in larger cantilever deflections, with eventual sample indentation depending on the relative stiffness of the sample with respect to the cantilever. When reversing the sample displacement direction, the retraction curve is recorded. The sample is withdrawn until the tip is released from the surface, in the jump-off-contact point. Further retracting the sample from the jump-off-contact point, the tip-sample interaction vanishes and

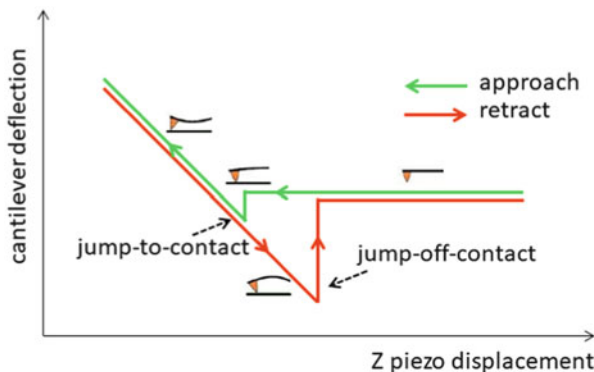


Fig. 2.3 Ideal Force-Distance (F-D) curve on a rigid sample. In the approach curve, starting from the right, the interaction between tip and surface is negligible until the jump-to-contact point, where the tip is captured by the surface. Moving further on, the deflection increases linearly in the contact region (rigid substrate). In the retract curve, the piezo is retracted until the tip is released from the surface in the jump-off-contact point

the deflection is zero. In order to derive quantitative data on interaction forces from the force distance curve, it is necessary to carefully calibrate the output of the photodiode system used to measure the cantilever deflection. To this end, a preliminary force curve has to be acquired on an ideally stiff sample (i.e., on a sample much stiffer of the cantilever used for the measurements). Under these conditions, the contact region of the curve must be linear with a unitary slope. Provided the piezoelectric scanner is properly calibrated, from the analysis of the preliminary curve, the photodiode signal can be converted into cantilever deflection calibrated values. In order to convert deflection values into force values through the Hooke's law:

$$F = -k\Delta z \quad (2.1)$$

the cantilever spring constant k has to be known. Nominal cantilever spring constants are provided by manufacturers, but for more accurate force evaluation, a direct measurement of the spring constant is desirable. Among the different methods, the thermal noise approach can be used to evaluate k [50].

3.1.4 Determination of Solid Elasticity by AFM Indentation Experiments

In the last two decades, the AFM in force spectroscopy mode has been widely employed in the analysis of the elastic/mechanical properties of biomaterials. By using soft cantilevers, materials with elastic moduli below 1 kPa can be tested. The AFM is able to discriminate variation of the local elasticity with a lateral resolution imposed by the tip size, hence, close to the molecular scale. In a typical indentation experiment, the AFM probe is pushed on the tested materials until the cantilever deflection reaches a pre-defined value (deflection setpoint). Increasing the applied force, the AFM probe gradually starts inducing a deformation of the sample (indentation). The shape of the resulting force versus distance curve contains information on the mechanical properties of the sample that should be further unravelled and quantified. After a tricky filtering and preprocessing phase (see [61] and Sect. 3.1.3), the force versus indentation experiment can be fitted on the expectations of a relevant descriptive model, to identify the corresponding material properties. Although different approaches have been proposed for AFM data interpretation [60], so far the most adopted model is based on the simple Hertz contact mechanics [123], eventually in the generalized Sneddon form that takes into account nonspherical indenters [111]. The Hertz model is theoretically valid under very special conditions, so that the sample could be treated as an isotropic and linear elastic body (viscous or plastic effects must be minimized), occupying an infinitely extended half plane (far larger than the tip size). Even though these requirements are considerably stringent, the Hertzian mechanics provides a reliable and effective first-order approximation of the mechanical properties of a biomaterial and special cases (such as thin layers or patterned substrates) can be treated as corrections to the general formulation (see Sect. 4.1 and [33]).

If the force F is measured as a function of the vertical displacement Z , as in an AFM experiment, it is possible to obtain the force versus indentation curve $F(\delta)$ by

taking into account the position Z_0 at which the tip contacts with the sample (contact point) and the resting deflection x of the cantilever during the penetration:

$$F(Z) \rightarrow F(\delta) \quad (2.2)$$

$$\delta = Z - Z_0 - x = Z - Z_0 - \frac{F(Z)}{\kappa} \quad (2.3)$$

where κ is the elastic constant of the cantilever (see Sect. 3.1.3). A generalized mechanical response can be expected in the form:

$$F = E^* \rho \delta^\beta \quad (2.4)$$

where E^* is the reduced Young's modulus accounting for the Poisson ratio:

$$E^* = \frac{E}{(1 - \nu^2)}$$

and ρ and β broadly depend on the indenter geometry; in the original Hertz theory of a spherical indenter of radius R , these parameters can be calculated as:

$$\rho = \frac{4}{3} \sqrt{R}; \beta = 3/2$$

while, in the conical approximation (more suitable for an AFM tip) if α is the apex aperture angle, the same parameters read as [111]:

$$\rho = \frac{2}{\pi} \tan \alpha; \beta = 2$$

3.1.5 AFM-Based Mechanical Mapping

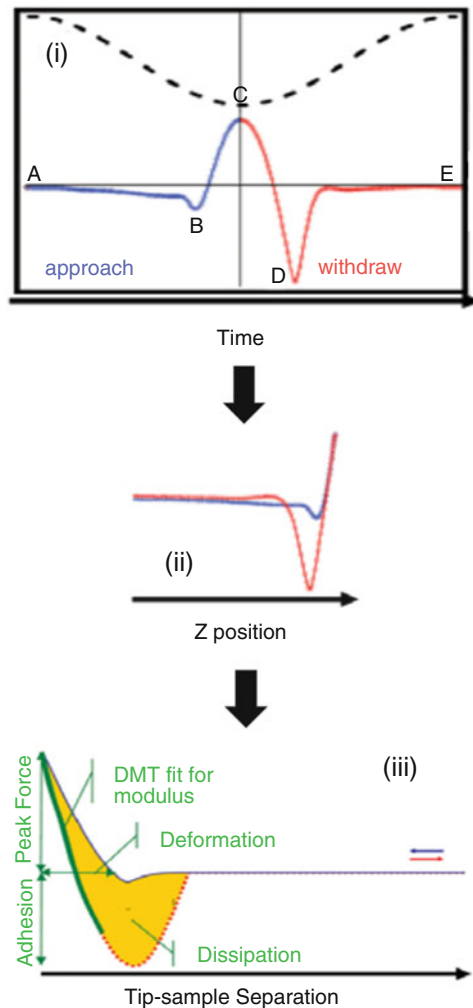
In the previous paragraph, we show how the AFM can be employed in the determination the local elastic properties of new materials for biomedical applications. In particular, we show how it is possible to work on small objects or to focus the analysis on a confined portion of the material. In spite of this, we didn't present any map of elasticity with a lateral resolution comparable with the typical lateral resolution of the AFM imaging mode. In the last decade, new technological approaches allowed for the acquisition of maps of elasticity formed by hundreds of thousands of points in a reasonable acquisition time. By using this new modalities, it is possible to obtain a distribution of elasticity that perfectly correlates with the topographical view of the sample, this means, on the exactly same area and with the same number of points. This technique paves the way for a new correlative approach in which all the feature displayed in the topography are also describe in terms of elasticity.

Among all the mechanical mapping approaches, one of the most successful implementations is the so-called PeakForce Tapping mode, marketed by Bruker since

2010. Here this technique will be briefly described and some application presented. PeakForce QNM is the further development of the pulsed force mode introduced some years in advance [92]. In PeakForce QNM mode, and similarly to Tapping mode, the AFM tip and the sample are intermittently brought in contact for a short period, minimizing the lateral forces (Fig. 2.4, see also Sect. 3.1.2). PeakForce is a dynamic mode, but unlike the traditional AC mode, PeakForce controls the position of the piezo to keep constant the maximum force (Peak Force) on the probe, instead of the vibration amplitude.

PeakForce QNM AFM mode allows the acquisition of maps of elastic modulus of a sample surface working as fast as standard tapping AFM imaging, i.e., acquiring a 512×512 points map in some minutes. The elastic modulus is calculated from the

Fig. 2.4 (a) A force curve is captured per each modulation cycle. The dashed line represents the Z-position of the piezo along a single period of the modulation. The solid line represents the measured force on the tip when the probe is approaching the sample (blue), and when the probe is moving away from the sample (red). Both quantities are plotted as a function of time. The point B is the jump-to-contact, C is the maximum applied force, controlled by the feedback loop, i.e., the peak force, while A is the maximum adhesion between tip and sample. (b) when the force is plotted as a function of the Z-displacement, the typical aspect of a force-distance curve is displayed. (c) The fit with the DMT model is performed on Force vs. Separation curves. The separation is calculated considering the Z-piezo position and the cantilever deflection [39].



force-indentation curves by using the Derjaguin-Muller-Toporov (DMT) model (Fig. 2.4) [113]. The PeakForce mode is capable of working with very small load forces, up to 0.1 nN, applying very small indentation depths, up to 1 nm. This unique feature of PeakForce makes the modality particularly suitable in the study of thin materials. PeakForce QNM is able to quantify Young's moduli in the range between 0.7 MPa and 70 GPa. To better exploit its capability, the choice of the cantilever is fundamental. In nanomechanical investigations, the maximum sensitivity is reached when the spring constant of the cantilever is equal to the effective spring constant of the sample [113]. When the spring constant of the cantilever is one order of magnitude higher or lower than that of the sample, the sensitivity is three times lower. For this reason, a rough estimate of the sample stiffness is important to set the correct experimental configuration. Here two examples on sample characterized by significantly different stiffness are reported.

Smolyakov and co-workers [110] investigated the nanomechanical properties of chitin-silica hybrid nanocomposites, employing stiff cantilever with a nominal spring constant $k = 200 \text{ N/m}$ to optimize the sensitivity of their experimental setup for Young's moduli in the order of the GPa.

Moreover, Sweers et al. [113] used cantilevers with a $k = 27 \text{ N/m}$ to test amyloid fibrils from α -synuclein, a biological material, but characterized by high-mechanical resistance (see Fig. 2.4a). In Fig. 2.5, the typical elasticity map of chitin nanorods deposited on silica substrate is shown. However, measuring the elasticity of objects with a cross-section in the order of few tens on nanometers is still challenging. In particular, the modulus significantly changes across the nanorod. An example of this variation is reported in Fig. 2.5b, while a cartoon explanation is provided in Fig. 2.5c. When the tip comes in contact with the nanorod side (in Fig. 2.5a the scan direction is from right to left), the contact is not spherical, and the DMT model is not applicable. Furthermore, the radius of contact is not correct in this case. Generally, these deviations from the ideal conditions bring to an overestimation of the elastic modulus. This artifact is called "edge effect." On the opposite side of the nanorod, an area is not accessible to the tip, due to the specific direction of its movement. This area is not tested; the authors called this area "shadow effect." Edge and shadow effects are present also inverting the scan direction, confirming the validity of the geometrical interpretation proposed by Smolyakov et al. [110]. The minimum value of the modulus, corresponding to the central area of the nanorods (see Fig. 2.5), was considered as the nanorod modulus, assuming that this value is less affected by geometric artefacts. The authors found a different behavior in the mechanical properties of textured chitin and chitin-silica films, measuring in both cases elastic moduli in the order of the GPa and optimizing the experimental condition in the study of these kind of samples.

Edge and shadow effects are also present in the elasticity maps acquired by Sweers et al. and clearly displayed in Fig. 2.5e, f. In this image, the mica background elastic modulus is underestimated, being about 1.5 GPa. This is likely due to the limited range of elastic moduli which can be explored by the cantilever employed in the work, demonstrating again the key role played by the probe in the PeakForce QNM mode.

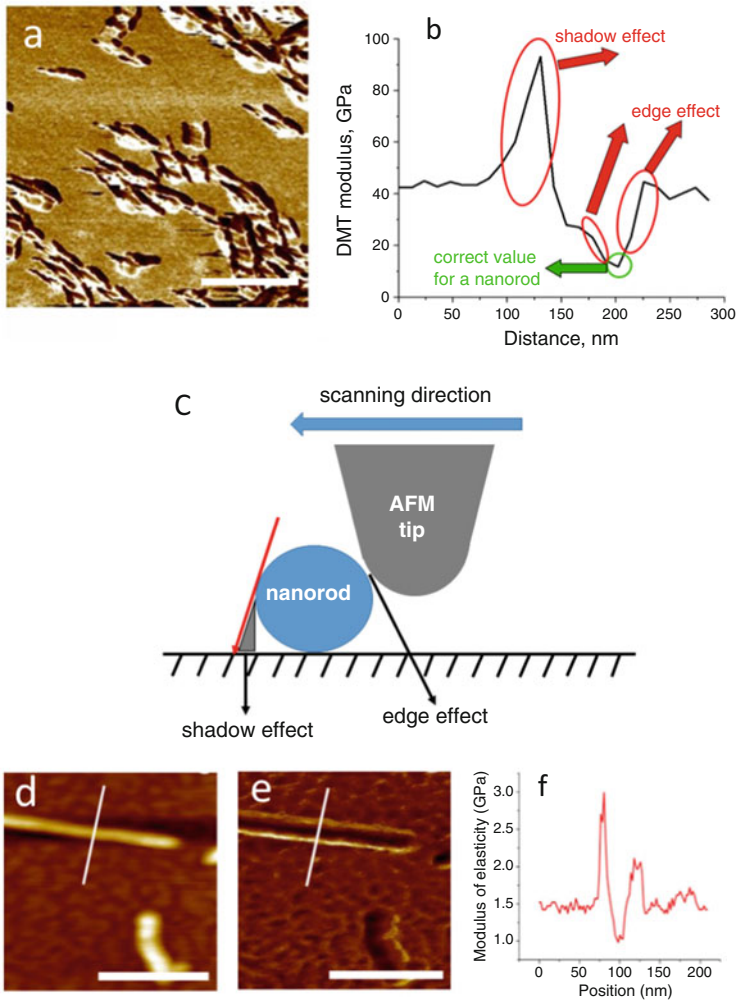


Fig. 2.5 (a) Maps of Young's modulus of chitin nanorods on silica substrate. The modulus image by PeakForce QNM ($3 \times \mu\text{m}^2$) was obtained by using a peak force of 150 nN. (b) Modulus variation along nanorod cross-section along the scan direction. (c) Graphical explanation of the artifacts induced in the modulus determination by edge and shadow effects.

3.2 Brillouin Spectroscopy

Brillouin light scattering (BLS) is a spectroscopic technique able to access the viscoelastic properties of the materials in the GHz frequency range.

For many years, this technique has been largely exploited in material science and condensed matter physics [26, 30, 32, 108, 118], but recently, thanks to its non-invasive character, new applications fields started to be explored [19, 54, 73].

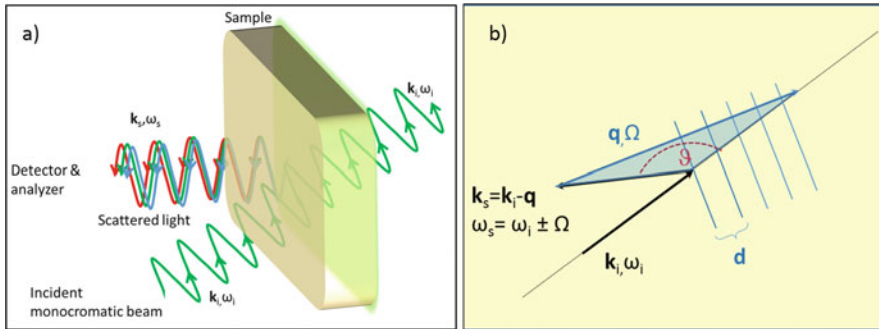


Fig. 2.6 (a) Schematic picture of inelastic light-scattering process. The incoming beam of given wave-vector \mathbf{k}_i and frequency ω_i interacts with the internal normal modes of the sample and diffuses in the space changing its frequency ω_s and wave-vector \mathbf{k}_s . The position of the analyzer fixes the scattering geometry. (b) Schematic picture of spontaneous Brillouin scattering process. The presence of sound wave in the sample of wave-vector \mathbf{q} and frequency Ω , shown as a series of parallel lines, induces the diffusion of the incoming monochromatic beam. In the scattered light, besides the incident frequency, two other components with frequency $\omega_s = \omega_i \pm \Omega$ and wave-vector \mathbf{k}_s are present. The scattering geometry is defined by the scattering angle ϑ , the angle between the vectors \mathbf{k}_i and \mathbf{k}_s on the scattering plane.

BLS is based on the inelastic scattering of photons from the long-wavelength acoustic phonons (~ 200 nm) naturally present at thermodynamic equilibrium in any material [32].

The interaction between light and the sound waves gives rise to the so-called Brillouin scattering, in honor to Leon Brillouin who first described this effect at theoretical level, almost a century ago [21].

In a typical BLS experiment, as schematized in Fig. 2.6a, a monochromatic beam of a given frequency ω_i and wave-vector \mathbf{k}_i is incident on a medium, whose spatial and temporal fluctuations of the local dielectric constant are responsible of light scattering processes [10, 29]. In particular, the light diffuses changing its wavevector when it goes through an optically heterogeneous material, if the material's heterogeneities are also time dependent, the light will change also its frequency.

Let us consider, for example, the inelastic light scattering generated by a 3D crystalline material; if p is the number of ions in the unit cell, we expect $3p$ normal vibrational modes: three of them are acoustic modes, one longitudinal (LA), and two mutually perpendicular transverse (TA1, TA2), the others $3(p - 1)$ are optical modes. All of these vibrations can induce dielectric constant fluctuations able to cause light scattering. In particular, if the scattering is generated by the propagating *acoustic waves* the process is called *Brillouin Light Scattering*, while if it is generated by optical modes, the process is called *Raman scattering*. Although these two spectroscopic techniques do not differ from the conceptual point of view, probing different frequency ranges, they have been developed as separate experimental methods able to obtain complementary information on mechanical and chemical properties of the materials, respectively.

In the following, we will focus on the Brillouin Light Scattering process, analyzing how it can represent a powerful tool to characterize the elastic constants in materials of biological strategic interest.

Let's consider a normal vibrational mode of wave-vector \mathbf{q} and frequency Ω . Avoiding the description referring to the microscopic structure of the material, the normal vibrational mode can be described as a wavelike modulation in a continuous medium. As schematized in Fig. 2.6b, at any given time, a density modulation with a periodicity $d = 2\pi/q$ is associated to the considered vibrational mode and can be regarded as a diffraction grating. The incoming light beam of frequency ω_i and wave-vector \mathbf{k}_i will diffuse approaching this grating with a well-defined wavevector given by the Bragg's law $2d \sin(\vartheta/2) = 2\pi m/k_s = 2m\pi/k_i$ (with m an integer), i.e., for $m = 1$ $q = 2k_i \sin(\vartheta/2)$ since $|\mathbf{k}_i| \sim |\mathbf{k}_f|$.

In the case of propagating acoustic modes, the density modulation moves in time with a constant phase velocity given by

$$v = \Omega/q \quad (2.5)$$

So the collective vibrations have to be considered as a moving diffraction grating in the material. The time evolution of the diffraction grating maintains unaltered the orientation and the distance d between two successive planes, conserving the relation 2.5 on the wavevector. On the contrary, the frequencies of the scattered light, ω_s , will be affected by the grating motion undergoing to the Doppler effect, i.e.,

$$\omega_s = \omega_i \pm \Omega \quad (2.6)$$

Brillouin light scattering process can be also explained from quantomechanical point of view, using corpuscular description. Considering the "photons" and the "phonons" as virtual particles corresponding to the normal modes of radiation field and ionic displacement field, respectively, the scattering process can be schematized as a photon-phonon collision. Imposing the conservation of energy, the relations in Eq. 2.6 are again obtained. Moreover imposing the conservation of the momentum, the relation

$$\mathbf{k}_i - \mathbf{k}_f = \pm \mathbf{q} \quad (2.7)$$

can be written.

Being $|\mathbf{k}_i| \sim |\mathbf{k}_f|$, the triangle highlight in Fig. 2.6b is nearly isosceles and the exchange wave-vector of the process will be $q = 2k_i \sin(\vartheta/2)$ where ϑ is the angle between \mathbf{k}_i and \mathbf{k}_f . It is worth to notice that the existence of the sign \pm in Eqs. 2.6 and 2.7 are linked to the phonon creation or annihilation.

Analyzing the frequency of the scattering light, two contributions have to be expected, i.e., the Stokes and anti-Stokes components of the Brillouin doublet, symmetrically shifted with respect to the elastic line at frequency $\pm \Omega$, respectively.

Moreover, considering that the modulus of the exchange wavevector q is of the order of 0.02 nm^{-1} , value very small compared to the typical dimension of the Brillouin zone ($\sim 10 \text{ nm}^{-1}$), the process gives information only for the long wavelength phonons for which (i) the linear dispersive relation as well as (ii) the approximation of the sample to continuous medium are well verified. Thus, by measuring the frequency shift of a scattered light, it is possible to achieve the local speed of sound v of the collective vibration which generated the scattering process.

Of course, the described effect occurs for each collective acoustic vibration present in the material. So, for example, the Brillouin spectrum of a 3D cubic crystal will be composed by three Stokes and three Anti-Stokes peaks. Measuring their frequency position, it is possible to estimate the longitudinal and the two transversal sound velocities characterizing the elastic tensor of the sample [117].

3.2.1 Elastic Constants Probed by BLS

If three independent monochromatic plane waves describe the collective oscillations in a 3D cubic crystal, in isotropic crystals (or amorphous materials), the symmetry relations reduce the number of independent elastic constants.

The transverse modes collapse one to the other, so the expected characteristic Brillouin spectrum is composed by two Stokes and two anti-Stokes peaks, symmetrically shifted with respect to the elastic line at frequencies:

$$\Omega_L = qv_L = q\sqrt{\frac{\left(B + \frac{4}{3}\mu\right)}{\rho}} = q\sqrt{\frac{M}{\rho}}$$

and

$$\Omega_T = qv_T = q\sqrt{\frac{\mu}{\rho}}$$

where Ω_L and Ω_T are the frequency position of the longitudinal and the transversal Brillouin peak, respectively, ρ is the mass density, B the bulk, and M the longitudinal and μ the shear modulus. The shape of the Brillouin spectrum will change due to the presence of particular selection rules related to the scattering angle ϑ , to the polarizations of both photons and phonons and to their relative orientations with respect to the scattering plane.

In general, the Brillouin scattering process is characterized by a low cross section. Furthermore, considering the low-frequency shift of the scattered light respect the elastic one $\Omega = \omega_s - \omega_i$ (in the range between 3 to 30 GHz in soft matter), high-resolution and high-contrast spectrometers are necessary to detect the tiny inelastic Brillouin signal. Different experimental set-ups are nowadays designed to achieve a good signal quality and in the following we describe their main features considering advantages and disadvantages of the more common types.

3.2.2 Experimental Set-up for Brillouin Scattering Experiments

After lasers advent, inelastic light scattering set-ups have been developed using spectrometers or interferometers able to detect the small-frequency variation (tens of GHz) and the weak intensity of the Brillouin signals (typically several orders of magnitude weaker than the elastic Rayleigh peak). In material science and condensed matter physics, the widest used instrument is the tandem Fabry-Pérot interferometer (TFP), in particular the 6-pass tandem Fabry-Pérot developed in the 1970s by John R. Sandercock [19, 26, 30, 108]. Its performance increased during the last two decades, and the last upgrade named TFP-2 HC, developed a few years ago, has drastically improved the set-up performance, widening the range of investigable samples. The internal optics of the instrument has been deeply modified obtaining an unprecedented contrast together with a high-frequency resolution (around 100 MHz). The contrast is the key parameter which defines in interferometric systems the peak-to-background ratio. The TFP-2 HC yields an instrumental contrast better than 150 dB [70, 103] opening the way for Brillouin scattering to study highly opaque or turbid media such as tissues of medical biopsies [68], biofilms grown on a metallic substrates [69, 103], or single living cells adhering to silicon slabs [70].

A recent proposed alternative to the TFP interferometer is offered by the VIPA (virtually imaged phase array) apparatus (a picture is shown in Fig. 2.7).

Using a nonscanning method for the light dispersion, VIPAs doubtless increase the acquisition speed of the spectrum allowing fast Brillouin imaging. However, several limitations characterize their use: the thickness of the etalon determines the spectral resolution which is limited to ~ 0.7 GHz and the spectral range restricted to some tens of GHz. Nevertheless, the most severe limitation is the low contrast which reaches the value of 30 dB in the single-pass setup. Different strategies have been developed to increase the VIPA contrast in order to detect the Brillouin signals: the use of equalization technique [5] or the multipass configurations [99], also in combination with a triple-pass Fabry-Pérot interferometer as a bandpass filter [41] or notch filters [71]. With these approaches, the spectral contrast reaches values good enough to allow the Brillouin scattering measurements of transparent or moderately turbid media [5, 41].

Anyway, whatever device is chosen, the most used experimental configuration is the backscattering geometry, i.e., $\vartheta = 180^\circ$ in which, even if the selection rules avoid the presence of the transverse mode in the spectrum, the light absorption of non-transparent samples does not prevent the focalization and the detection of the scattered light. Moreover, a relevant advantage of the back-scattering configuration is the possibility to use a microscope as focalizing and collecting optic. At $\vartheta = 180^\circ$, the maximum exchanged wave-vector $|q|$ is reached. In this condition: (i) the Brillouin peak associated to the longitudinal acoustic mode reaches the greatest frequency shift from to the elastic line, $\Omega_L = v_L q$, becoming more easily measurable also in the presence of high elastic scattering and (ii) the error in the evaluation of the exchanged wavevector, q , due to the finite dimension of the collection lens reaches its minimum value. This last condition allows the use of collection optics with high

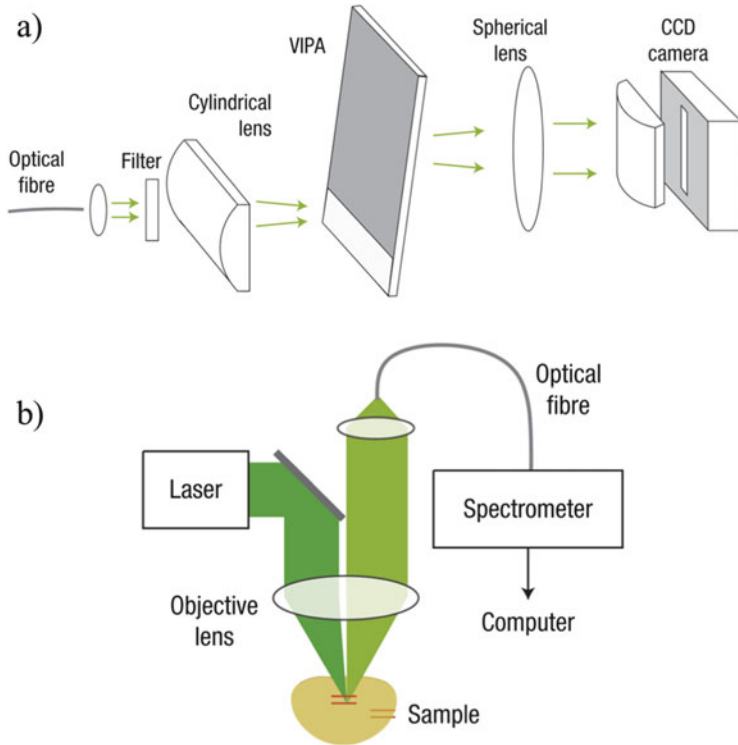


Fig. 2.7 VIPA-based optical setup: (a) Experimental setup of a single-stage VIPA spectrometer. (b) Schematic of the confocal Brillouin microscope system. (Reprinted with permission from [98])

numerical aperture, as microscope objectives, because the lineshape deformations are minimized [3]. However, also in backscattering condition, to analyze the Brillouin peak and in particular to correctly estimate its width, the asymmetric broadening related to the use of high numerical aperture objectives has to be taken into account [70].

The recent developments of Brillouin microscopes allow to measure the elastic properties of heterogeneous materials with a sub-micrometric spatial resolution, paving the way for high resolution mechanical imaging [5, 36, 53, 98, 104]. An innovative all-optical approach has been recently optimized in order to obtain the micro-mechanical analysis correlated with the local chemical composition [70, 73, 103, 115]. This approach has proved particularly useful for characterizing spatially heterogeneous materials such as biological cells and tissues. The inelastic light scattered from the same scattering volume is collected by a microscope and simultaneously analyzed by a Brillouin and a Raman spectrometers. The experimental set-up composed by a High-Contrast tandem Fabry-Pérot interferometer and a Raman spectrometer is reported as an example in Fig. 2.8.

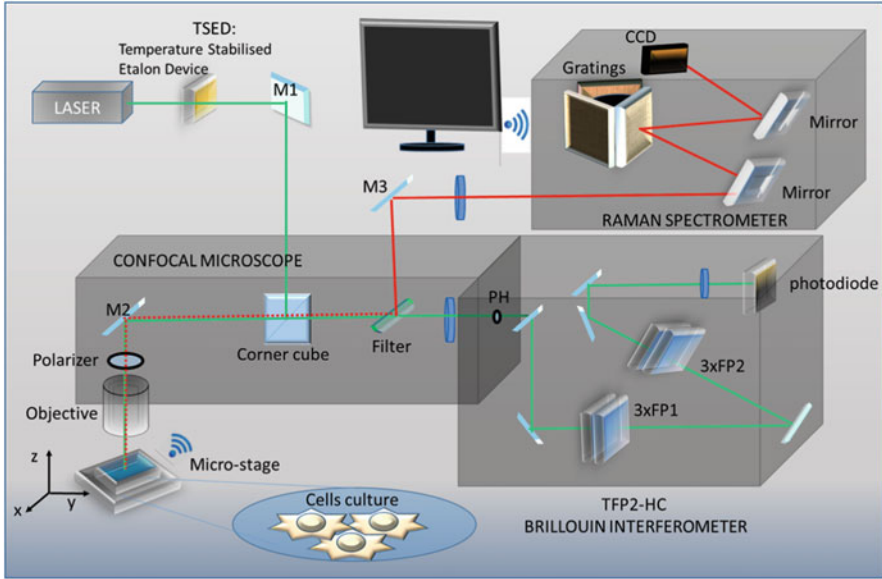


Fig. 2.8 Layout of the experimental setup composed by a High-Contrast tandem Fabry-Pérot interferometer (TFP-2 HC) and a Raman spectrometer. The laser beam is focused onto the sample by the same microscope objective used to collect the backscattered light. A short-pass tunable edge filter transmits the quasi-elastic scattered light (green beam) to the Brillouin spectrometer and reflects the inelastic scattered light (red beam) towards a Raman monochromator. Reprinted with permission from [70]

3.2.3 Key Time and Length Scales Probed by Brillouin Scattering

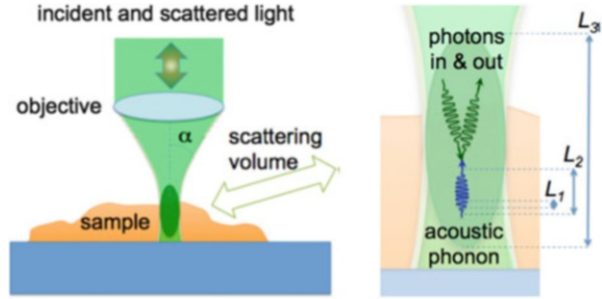
While planning a Brillouin experiment or comparing its results with those obtained by other techniques, a particular attention has to be paid to the relevant length and time scales probed by the spectroscopic approach.

In fact, being BLS an optical tool which directly probes material phonons, three different length scales have to be considered to explain the spectral shape and to estimate the effective spatial resolution obtained in the mechanical characterization [68, 70].

As schematically reported in Fig. 2.9, the smallest relevant length scale is represented by the wavelength of the probed acoustic modes, L_1 , which, in a typical light scattering experiment, is of the order of $\sim 0.1 \mu\text{m}$.

Elastic inhomogeneity much smaller than L_1 are not measurable from the acoustic field, which instead is sensitive to a mean value over the phonons wavelength. However, the presence of elastic spatial inhomogeneities of the order of $L_1/10$ or larger gives rise to the acoustic scattering effect, which in turn affects the propagation of the phonons and the Brillouin spectral shape. Their effect is well characterized in amorphous and porous glassy systems [22–24]: it originates attenuation processes of the acoustic field and anomalous dispersion of the acoustic modes [67].

Fig. 2.9 Schematic representation of the characteristic length scales in BLS. (Reprinted with permission from [68])



The second intermediate length scale to consider is the so-called mean free path of the acoustic modes. In fact, in non-crystalline materials, phonons cannot be considered as propagating plane waves any longer, but they are damped oscillations with a characteristic life time. The propagation length of acoustic phonons, L_2 , principally depends on two different factors: (i) the morphological disordered structure of the investigated material, responsible of the “static attenuation process” and (ii) the microscopic processes active in the materials associated to energy exchanges with the vibrational modes (dynamical attenuation processes). Due to the different origin of attenuation processes, L_2 can vary significantly among different materials, even spanning several orders of magnitude [9, 23, 74, 119]. However, as far as the investigation of biological samples is concerned, it has to be mentioned that the characteristic L_2 values measured in dry tissues [68], in living cells immersed in their buffer solution [70], or in extracellular matrix structures [85] are of the order of $\sim 1 \mu\text{m}$. So we refer to this value for L_2 in the following.

Finally, the last length scale L_3 takes into account the sizes of the scattering volume, i.e., the part of the sample enlightened by the laser beam and from which the scattered light is analyzed by the interferometer reaching the photo-detector. In the usual Brillouin configuration, L_3 is $\sim 10 \mu\text{m}$, but it can be reduced by almost one order of magnitude $L_3 \sim 1 \mu\text{m}$ in the more stringent confocal condition of the Brillouin microscopy. In spatially heterogeneous materials, such as cells or tissues, the scattering volume can be composed by homogeneous sub-regions with characteristic size greater than L_2 and characterized by different elastic constants. In this case, the measured spectrum is composed by the sum of the Brillouin peaks originating from the different subregions. As measured in living fibroblast immersed in their buffer solution, if the spectral spacing between the Brillouin peaks is larger than their width, the different contributions can be separated [70] obtaining the mechanical characterization of each subregion. Otherwise, the frequency position of the Brillouin peak will be a mean value between those of the subunits and an heterogeneous broadening characterize the width of the peak as measured in dry brain tissues [68]. From this simple analysis, it appears that the spatial resolution limiting the Brillouin mapping is L_2 since the acoustic modes would make an average of the mechanical properties over such a distance.

The second pivotal parameter for the understanding of the elastic moduli obtained by BLS is the frequency range analyzed by the technique. In fact, in the case of viscoelastic materials, the time scale plays a key role in the evaluation of their mechanical response.

Being a GHz spectroscopy, Brillouin probes the materials at higher frequency respect to AFM, quasistatic tensile testing or ultrasonic measurements. Comparing the high and the low frequency behavior for different biological materials such as collagen and elastin for the extracellular matrix proteins [31, 35], living fibroblast for cells [102] and the crystalline lenses and cornea for tissues [101], the existence of a dual biomechanical scale emerges from the measurements. In the GHz frequency region, the characteristic values of the elastic moduli are in the GPa range, while investigating these systems in the lower frequency range their value drastically decreases.

The reason for these apparently conflicting results is twofold.

- (i) From one hand, the different techniques probe different elastic moduli. In fact, Brillouin spectroscopy probes M , the longitudinal elastic modulus, defined as the ratio of axial stress to axial strain in a uniaxial strain state, i.e., the material deformation is limited only on the unique axis considered. On the contrary, probing the Young's modulus, the material deformations are allowed also in the others directions respect to one of the axial stress. It is worth to notice, however,, that a strict correlation between the elastic moduli obtained in the high (GHz) and low frequency (quasi-static or kHz) range has been obtained both in tissues and cells [35, 101, 102] proposing the existence of a scaling law (see Fig. 2.10).

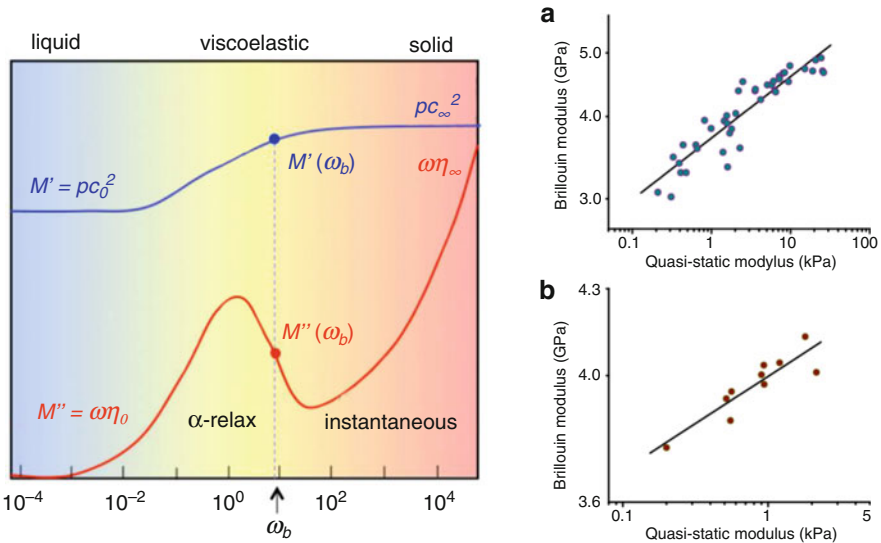


Fig. 2.10 Right panel: $M(\omega)$ behavior for the real (blue line) and an imaginary part (red line). The first one is related to the dispersion while the second to the absorption of the acoustic modes. ω_B indicated in figure is the frequency probed by the Brillouin techniques. Depending on the position of relaxation with respect to the frequency ω_B , different scenarios opened in the relation between $M'(\omega_B)$ and $M''(\omega_B)$. (Reprinted from [68]). Left panel: Comparison of Brillouin longitudinal and quasi-static Young's moduli for porcine lenses (a) and bovine lenses (b). Circles, experimental data; solid line, log-log linear fit. (Reprinted from [101])

This experimental observation, which deserves an in-depth phenomenological and theoretical investigation, confirms that both the techniques are sensitive, even if differently, to the same elastic modulations validating both as powerful tools for the biomechanics characterization.

- (ii) On the other hand, the elastic response of any viscoelastic material is strongly frequency dependent. This effect is largely characterized, for example, in glass forming materials [30, 57]. When a system undergoes the glass transition, its dynamics changes from the liquid-like behavior to the solid one increasing by orders of magnitude its viscosity and elastic moduli. Depending on the probed frequency range ω , the glass forming system appears as a liquid or as a solid. The characteristic frequency separating the two regimes is given in terms of the structural relaxation time τ_α , which is characteristic of any given material and changes its value as a function of temperature, pressure, or chemical modifications of the investigated sample. The structural relaxation defines the time scales which regulate the cooperative rearrangement processes by which the local structure reaches a new equilibrium after being perturbed.

Applying an external force or following the response to the spontaneous fluctuations in the low-frequency regime $\omega\tau_\alpha \ll 1$, the liquid-like behavior dominates: the system is able to follow the perturbation and it is in the so-called relaxed condition. On the contrary, when $\omega\tau_\alpha \gg 1$, the system is no more able to follow the time evolution of the perturbation. In this “unrelaxed state,” it shows a solid-like dynamics characterized by high viscosity and high elastic constants. A widely used approach to describe this behavior is introducing frequency dependence in the stress-to-strain relation which in the appropriate limits converges to the standard equations for a solid and a fluid [133].

In the generalized hydrodynamics framework, a complex frequency-dependent viscoelastic modulus is considered. The characteristic frequency behavior normalized to that of the α -relaxation is reported in Fig. 2.10 for the longitudinal elastic modulus $M(\omega)$ [18, 30]. To keep the model as simple as possible, we limit our discussions to the effect of the structural (or α -) relaxation process, neglecting the other relaxations eventually present in the system whose effect is described elsewhere (see for example [30]).

From the mechanical point of view, cells and tissues have been recently modelled as soft condensed matter near the glass or jamming transition [38, 64, 93, 94, 128]: the frequency dependence of their elastic moduli is a further confirmation of their similarity to glass forming materials.

4 Key Research Findings

Modern tissue engineering is exploiting the capability of new biomimetic materials to mediate cell response. An ideal biomimetic material is obtained by tuning not only the chemical and morphological but also mechanical properties of the material itself.

In particular, the development of soft tissue regeneration demonstrated that an effective physiological-like environment also requires the presence of physiological like mechanics. For example, the tuning of physical properties such as stiffness and topography has been used to control adsorption of specific proteins [75], driving the adhesion of monocytes and the polarization of macrophages. For drugs release purpose, the deformability of polymeric carriers is associated with a decreased recognition and interactions with specific cells of the immunosystem, thus to a reduction of their internalization and degradation [83]. Working on stem cells, field has been demonstrated that the mechanical properties of the extracellular matrix (ECM) regulate not only cell spreading but also the change of phenotypes in stem cells [127]. This limited number of examples, among the thousands in literature, is enough to demonstrate that the mechanical properties of a material are important, as much as the chemical and morphological properties, to define its interaction with biological cells. The characterization of biomimetic materials required the use of sensitive techniques, able to evaluate the mechanical properties of the material over a large range of elastic moduli, spanning from the GPa to the few hundreds of Pa, depending on the application, and possibly working in a physiological environment.

4.1 Indentation Experiments on Hard/Soft Materials

As already pointed out, single cells are able to sense local modulations of the mechanical properties, and the length scale on which this process occurs is comparable with single cell size (few μm) or even smaller. For this reason, in the last decades new materials have been proposed in which the mechanical properties were finely controlled at the microscale [45] or even at the nanoscale [109]. The leading characterization tool in this context is by far the AFM, being able to image the sample and test the mechanical properties with an unprecedented resolution (Fig. 2.11). In the following sections, few relevant examples of the AFM capabilities in this field are reported.

4.1.1 Assessing the Mechanics of Microparticles for Drug Delivery

A perfect example of the AFM potentiality is represented by the recent work of Palomba et al. [83] that developed and characterized a new class of polymer micro/nano-particles for drug-delivery applications. It was previously proposed that the stiffness of the drugs carrier could influence significantly the macrophages uptake of the carrier itself and, hence, influence the effectiveness of the treatment. In particular, the cellular uptake, by bone marrow-derived monocytes, of particles with different shapes (circular, elliptical, and quadrangular) and with two typical sizes (1,000 and 2,000 nm) was characterized as a function of the particles stiffness. Discoidal particles were obtained in a multistep process via replica molding [55]. Different experimental techniques can provide the morphological characterization of micro-size particles. In particular, the authors employed confocal microscopy and transmission electron microscopy to have a fast characterization of a high number of samples. The elasticity of the polymer disks is the key parameter in this

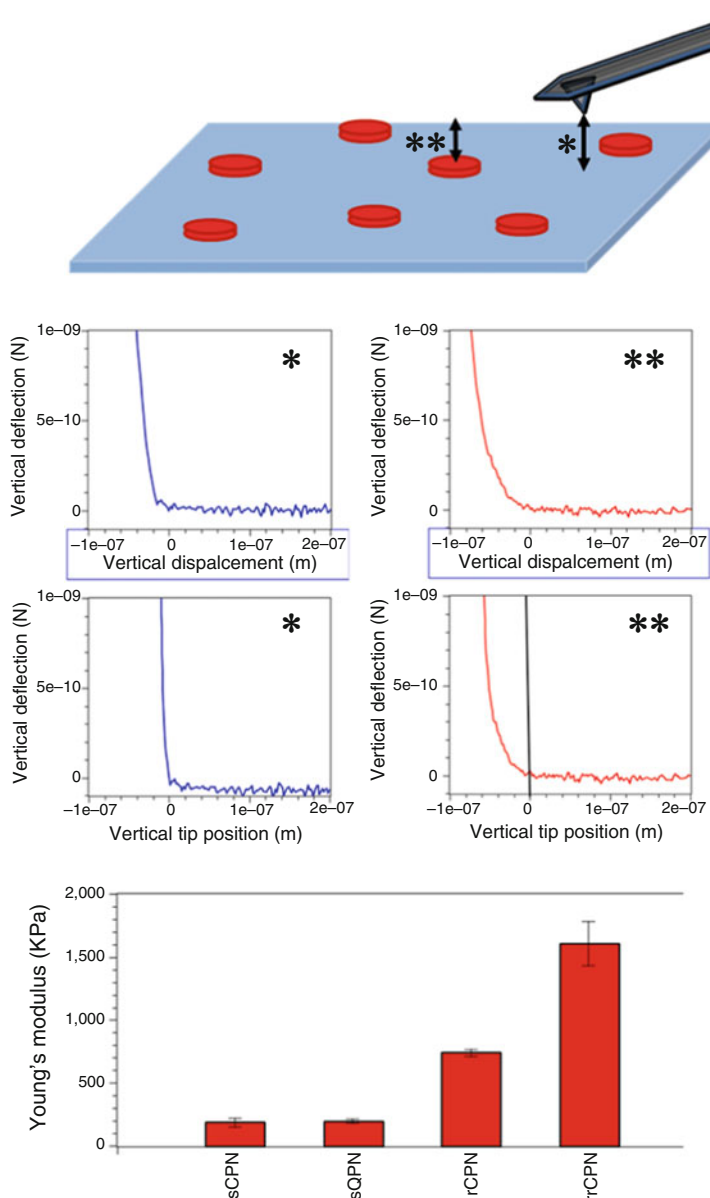


Fig. 2.11 A schematic representation of the experimental conditions is shown (top images). The soft disks, represented as red circular particles, are randomly distributed on the glass substrate. The sharp AFM tip can test the stiffness locally, and the analysis can be limited on the softer particles only. Two typical F-D curves and the correspondent F-I curves acquired on glass (*, left column) and on polymer disks (**, right column) are shown. A significant indentation is only present in **. The Young's moduli of CPN with three different composition (s, soft; r, rigid; and rr, very rigid) are shown in the bottom panel. The elasticity of soft square particle is also shown

investigation, and its experimental determination is fundamental, since the mechanical properties of the bulk polymer can be modified by the fabrication process and by the particle geometry itself. This characterization cannot be obtained using standard indentation methods that provide reproducible results only on extended samples and, generally, applying indentation forces that are not suitable for the study of a thin layer of soft material.

By using the AFM, the authors were able to identify the particles deposited on a standard glass slide, from the topographical reconstruction of the sample and to perform indentation experiments only on selected area (on the disk surface), applying a force load of 1 nN. All the analysis was performed in liquid environment, hence avoiding the stiffening effect induced by polymer dehydration. One of the main problems in the analysis of thin layers of soft materials lying on a rigid substrate is related to the influence of the stiffer substrate. In order to minimize the substrate contribution to Young's modulus determination, the authors applied small indentation depths, below the 10% of the particles thickness, also for the softer particles. The typical aspect of force vs. distance (F-D) curves obtained on soft, rigid, and overrigid substrates is shown in Fig. 2.11. F-D curves were corrected for the bending of the cantilever (36) to calculate the vertical tip position and to build force vs. indentation (F-I) curves (Fig. 2.11). Since the Hertz's model of contact mechanics is valid for spherical symmetry, the authors used the Bilodeau formula for pyramidal indenter [15], a generalization of the Hertz's model 4 that adapts it for square-shaped indenter putting $\rho = 0.7453tg\alpha$ and $\beta = 2$. F-I curves were thus fitted by using the following expression (Bilodeau's formula) 2.8,

$$F = 0.7453tg\alpha \frac{E}{1 - \nu^2} \delta^2 \quad (2.8)$$

where F is the force load, E is the Young's modulus, δ is the indentation depth, α is the face angle of the pyramid. Some manufacturer are not providing the angle α , but the angle measured at the corner edge, in this case, α can be deduced from trigonometric relations. Figure 2.11 shows an example of F-D curves acquired on the polymer disks and on the rigid substrate, and the correspondent F-I curves.

Palomba et al. demonstrated that the particle stiffness is not significantly affected by the particle shape, while changing the composition the stiffness can be reproducibly controlled (Fig. 2.11). The Young's moduli of circular (sCPN) and square (sQPN) particles with the same composition are shown in Fig. 2.11, as well as the elasticity of circular particles with a different composition (rCPN and rrCPN) are shown in figure (Fig. 2.11). For further details, also on other shape and composition particles, see [83]. The analysis performed by Palomba et al. [83] demonstrated particle stiffness can be tuned by varying the composition, in particular, softer disks are produced by increasing the PEG concentration. On the contrary, this work indicated that the geometry is just slightly affecting the mechanical properties of the particles. It was confirmed that, independently from the shape, softer particles interact less with macrophage, hence, they possess better biomimetic properties, being ideal candidates in drugs release applications.

4.2 Mechanical Properties of Porous Materials for Tissue Engineering

In the last decade, several applications focused on the use of soft porous and fibrous materials as cell scaffold for tissue regeneration [6, 63, 86, 109]. These materials are a valid 3D model of the extracellular matrix. They have interesting mechanical properties in terms of elasticity and stability upon compression. Furthermore, the presence of large and interconnected empty spaces provides an optimal environment for the ingrowth of cells and tissue formation and for an efficient vascularization. A great attention must be put in the characterization of porous and fibrous 3D materials since their mechanical properties depend on the spatial scale that is considered. Welzel et al. [126] investigated the elastic modulus of porous materials for cell scaffold application prepared by freezing glycosaminoglycan–poly(ethylene glycol). In particular, they employed AFM-based nanoindentation, by using a standard AFM tip as indenter. The AFM offers the possibility to test the stiffness of selected parts of the sample (Fig. 2.12). Starting from thin slices of materials, Welzel et al. concentrated the investigation on the scaffold wall, obtaining the elastic modulus of the material and avoiding the softening effect induced by porosity. Comparing these results with that obtained on the bulk hydrogel, they found that the process of pore formation induced by cryo-concentration significantly increased the elastic modulus of the material. This result was expected but still not confirmed experimentally.

Offeddu et al. [78] show a very explicative case by studying the multiscale mechanical properties of collagen scaffolds obtained through freeze-dried technique [78]. Freeze-drying is a consolidated technique for the fabrication of 3D polymer scaffold with controlled pore size and wall thickness [77, 87]. Previous work demonstrated that the scaffold pore size influence significantly adhesion, growth, and phenotype of cells [95, 124, 132].

Similarly, it has also been shown that Young's modulus of the bulk porous material increase with the concentration of collagen, i.e., with the concentration of solid in the material [47]. For tissue engineering and regeneration, the global stiffness of the porous 3D scaffold is essential, since this has to adapt to the stiffness of the host tissue/organ. On the other hand, the single cells are feeling the local stiffness, interacting with a limited portion of a pore wall with an area in the order of hundreds of μm^2 . The bulk stiffness is measured by standard indentation methods, by using large spherical indenter with a diameter of 1.2 mm and applying indentation of 0.5 mm (Fig. 2.12 c). The bulk stiffness increased quadratically by increasing the concentration of collagen, and this is due to the presence of a higher number of pores and an increased amount of material forming the walls (i.e., thicker walls). An interesting AFM approach was employed to evaluate the elasticity of single membrane of the material that forms the pore.

The analysis indicates that the mechanical properties of the single scaffold membranes, i.e., the mechanical environment felt by single cells seeded on this kind of scaffold, is the same, independently from collagen concentration (Fig. 2.12 f), on the contrary, the global stiffness of the device is influenced by

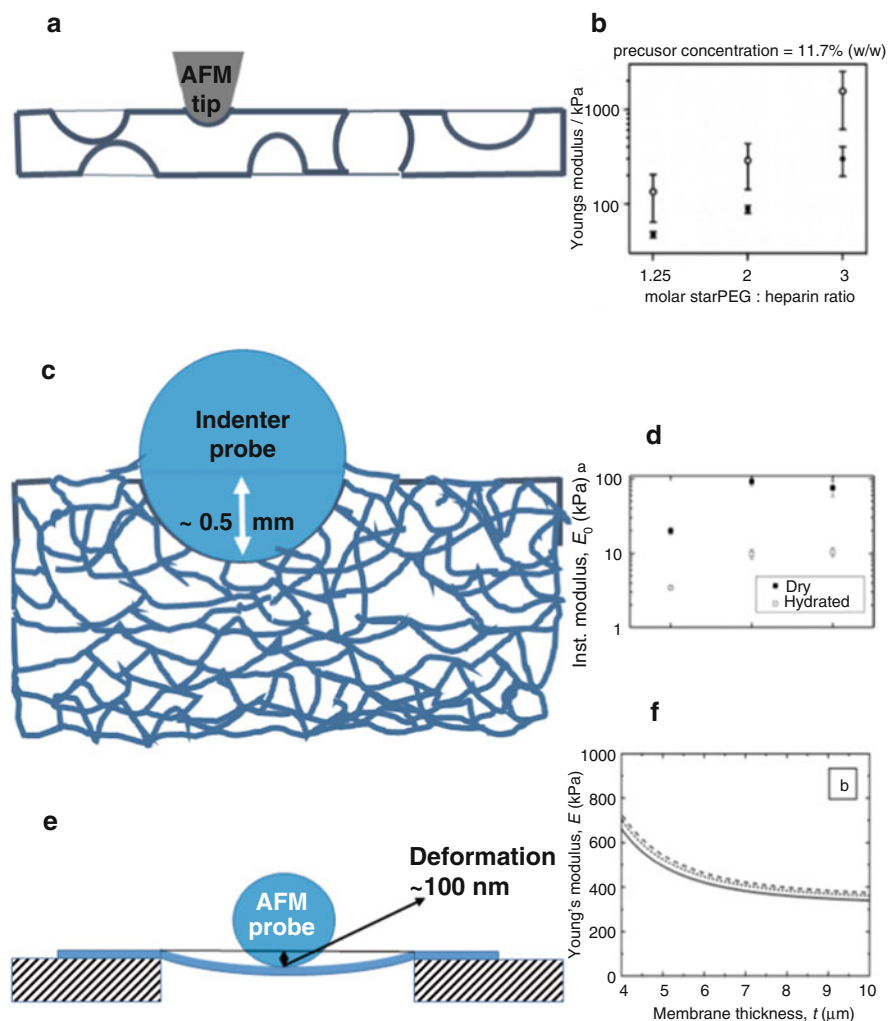


Fig. 2.12 (a) Schematic representation of the experimental design. A thin slice of porous material is prepared and deposited on a rigid substrate. By using a standard AFM tip only the walls are tested. The analysis is performed on hydrated samples. (b) Instantaneous Young's moduli calculated for the cryogel struts (open circles) and the corresponding bulk hydrogels (closed circles), modified from Welzel et al. [126]. The material that forms the wall of freezing-induced pores is stiffer than the bulk material. The stiffness is also dependent on the composition. Two approaches are proposed by Offeddu et al. [78], first, (c) large indentation with a standard indenter probe. The presence of the empty pores space decreases the stiffness of the bulk (d, modified from Offeddu et al. [78]). Dehydration is severely affecting the scaffold stiffness (d). The same kind of porous material is prepared differently for the AFM inspection. A thin slice is deposited on a copper grid with large pore (2.12 e). A microsize bead is pushed on the wall of a scaffold pore that stand above a grid pore. In this way not only the indentation but also a bending of the membrane of polymer is induce. The results derived from this experiment are shown in Fig. 2.12 f (modified from Offeddu et al. [78])

the concentration (Fig. 2.12 d), due to an increase of the scaffold wall thickness and this factor is important to adapt to the stiffness of the hosted organ.

Both papers here presented use standard AFM indentation methods, based on the acquisition of force-distance curves acquired in static mode (the AFM probe is not oscillating during the force-distance cycle), but the different experimental designs impose a different data treatment. Welzel et al. neglected the bending of the material and they applied the Bilodeau formula 2.8 for a pyramidal indenter, with α is the half-angle-to-face of the indenter (17.5° in this case).

On the contrary, Offeddu et al. tested the elasticity of relatively thin membranes that stand over the free space of a copper grid, hence, allowing membrane bending. In this case, the contribution of the deflection of the membrane must be considered, since it contributes, to define the correct elastic modulus of the membrane. A different model was chose to fit the experimental data, in particular, the author applied the model previously developed by Scott et al. [107], here shown in 2.9.

$$E = E_{\text{penetration}} + E_{\text{deflection}} = \sqrt[3]{\frac{9P^2(1-\nu^2)^2}{16rh^3}} + \frac{3Pa^2(1-\nu^2)}{4\phi t^3} \quad (2.9)$$

where E is the Young's modulus of the material, P is the measured load, t the thickness of the membrane, and ν the Poisson's ratio of the material.

Some of the primary results are summarized in Fig. 2.12. In particular, the discrepancy in the elastic moduli registered on collagen scaffolds (Fig. 2.12 d, f) is due to the different scale of analysis. The E of bulk porous materials results smaller, less than 10 KPa when hydrated, indicating that the scaffold is a very soft material, suitable for soft tissue regeneration purpose, while the local elasticity is more than one order of magnitude higher (Fig. 2.12). The interplay between local and bulk elasticity is an important parameter that can be controlled to create a good biomimetic environment.

4.3 Noncontact Mechanical Analysis

A complementary nondestructive, non-invasive and label free approach for the mechanical characterization of biomaterials is provided by Brillouin spectroscopy, which discovered in recent years new breakthroughs in instrumentation (see paragraph 2.2.1), enabling new applications areas [19, 73].

In the following we will focus our attention on two different application methods of the technique, exploiting BLS either to characterize the visco-elatic properties of homogeneous natural and/or artificial bio-materials, or as an imaging tool able to resolve bio-mechanical modulations with sub-cellular spatial resolution.

4.3.1 Brillouin Spectroscopy of Biomaterials

The first Brillouin applications for the bio-materials investigation appeared in the seventies, characterizing the elastic moduli of collagen, muscle [31, 46], eye

tissues such as crystalline lens and cornea [91, 121], aligned multilamella lipid samples [59] and DNA fibres [66].

After these pioneering studies which, for the first time, demonstrated the ability of the technique, many other studies have been addressed over time, analysing the link between morphology, composition, temperature and pressure conditions and elastic properties in bio-materials.

As a first relevant example, BLS has been successfully applied to study biomimetic materials with tunable elastic parameters, helping to design innovative bio-inspired samples aimed at mimicking different tissues stiffness. In brief, a platform based on chemically modified hydrogels from denaturalized collagen (GelMA) was adopted obtaining a photo-crosslinkable polymeric system responsive to UV exposure [76, 129]. Brillouin spectroscopy demonstrated its ability to follow the viscoelastic modulation obtained changing the concentration of the covalently crosslinked hydrogels. In fact, a good positive correlation has been found between the Brillouin frequency shift and the storage/loss modulus measured by shear-rheology in the different samples [73] (Fig. 2.12).

Moreover, BLS resulted to be effective also to characterize the interaction of biomembranes models with molecules potentially able to modify the lipid phase transitions. To analyze at molecular level the role of sugar in the protective action during drying or freezing in model membranes, the multi-lamellar lipidic assemblies has been studied as a function of temperature by infrared, Raman and Brillouin spectroscopies [96]. The collective dynamics measured by BLS evidenced the different temperature dependence measured in hydrated and dry samples with and without trehalose crossing the gel to liquid-crystalline phase transitions. The comparison with Raman and infrared spectroscopies links the collective dynamics with the molecular interactions.

BLS has been widely used also for natural biomaterials characterization, as occurred for example in the case of spider silk. This system has unique mechanical characteristics and analysing by BLS the different directions along the fibers, five independent elastic constants were determined [58]. Moreover, an intriguing and complex scenario of its dynamical properties has been revealed discovering the presence of a hypersonic phononic band-gap and a negatively dispersive region. The origin of these peculiar dynamical properties has been attributed to the link between non linearity in the mechanical response and the multilevel structural organization of the silk fiber [105]. These studies can give an important insight for the design of new bio-engineered meta-materials.

Recently, Brillouin studies has been performed using the innovative scattering geometry reported in Fig. 2.13 [34, 35, 85] which deserve a separate description. The experimental configuration has been used for the characterization of elastin and collagen, the principal fibrous, load-bearing components of the extracellular matrix.

Being the main components of bones, muscles and tendons the Extra Cellular Matrix (ECM) has a key role in the body functionality. It has a multidomain structure which starting from the nano-and micro-meter length scale develops on the macroscopic scale. The sophisticated ECM architecture and its role in the transmission of

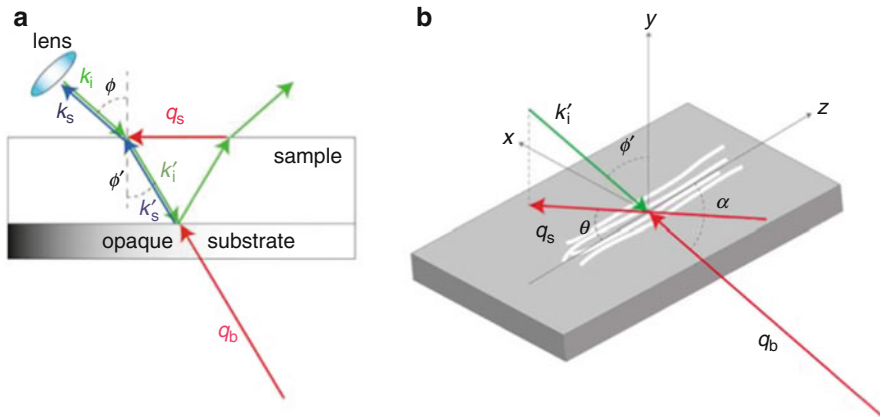


Fig. 2.13 Schematic diagram of the BLS geometry using the protein fibers in contact with the surface of a reflective silicon substrate. (Reprinted with permission from [85])

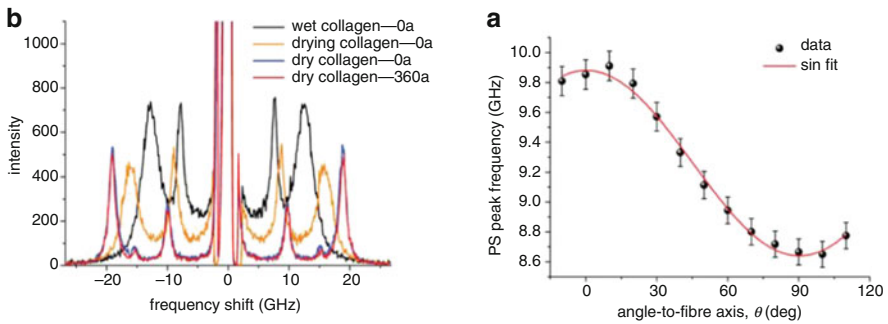


Fig. 2.14 Left panel: BLS spectra at different angle θ , in degrees, respect to the fibre axis. The letters ‘a’ and ‘r’ refer respectively to axial and radial directions of the exchanged wavevector respect to the fibre axis. Right panel: Plot of the frequency of the PS peak in a dry collagen fibre as a function of angle θ to the fibre axis. Data are fitted to a sinusoidal function. (Reprinted with permission from [85])

the mechanical stimuli to the cells attracted enduring interest of the scientific community [125].

In the new proposed experimental configuration the fibres, mainly aligned along a given direction, are in contact with a reflective silicon substrate which acts as a mirror for the incoming laser beam. In this way, two scattering processes occurs. The former is due to the usual interaction of the phonons with the incoming laser beam, giving rise to the so called bulk peak. The latter is due to the scattering of the phonons with the beam virtually generated by the reflective substrate. This second process probes the phonons travelling parallel to the substrate surface generating a second peak in the Brillouin spectrum (parallel-to-surface, PS mode) see Fig. 2.14a. Thanks to this configuration, it is possible (i) to evaluate the fibres elastic moduli

regardless of the accurate estimation of the refractive index of the medium and (ii) rotating the sample, to reveal both longitudinal and transverse acoustic waves travelling at different angles along the fiber axis assuring the complete acoustic characterization of the system. As suggested in the earliest studies [31], the fibres can be modelled as hexagonal symmetric elastic solid. The frequency position of the PS Brillouin peak measured at different angles changes as shown in Fig. 2.14b, and, from this modulation, four of the five elastic constants that characterize its elasticity tensor can be obtained. Imposing the relation between the elastic moduli, the axial and transverse Young's, the shear and the bulk moduli of the fibres has been evaluated finding 10.2, 8.3, 3.2 and 10.9 GPa, and 6.1, 5.3, 1.9 and 8 GPa for dehydrated type I collagen and elastin, respectively. These values, especially in the elastin case, are much higher than those obtained by the low frequency investigations [20, 97].

Moreover, the well known difference [20, 43] of two orders of magnitude between the elastin and collagen fibres elastic modulus is no more present analysing the system in the GHz frequency range. As already noted by Cusack and Miller in their pioneering work [31], the data disclose the presence of relaxation process with a characteristic time much slower than the time scale probed by BLS. In fact, this behaviour can be explain, as previously introduced in the paragraph 2.2.3, in term of the visco-elastic nature of the materials and to the different elastic moduli probed by the techniques.

4.3.2 Bio-Mechanical BLS Imaging

In the analysis of spatially heterogeneous materials such as cells and tissues, the evaluation of mechanical properties has to be addressed passing from single point analysis to a scanning mode approach. The increased spatial resolution obtained coupling Brillouin spectroscopy with microscopy, the drastic reduction in acquisition time and the increase of the experimental contrast obtained by the implementation of the spectrometers, as reported in paragraph 2.2.2, paved the way to new application possibilities.

BLS spectroscopy has been recently used to map the elastic heterogeneity in tissues [1, 4] recognising distinct anatomical structures living organisms [104]. The first studies of the in-situ 3D mechanical mapping of a mouse eye [98] further developed achieving the ability to obtain the in vivo Brillouin map of the full human eye in 2012 [100] anticipate the potential impact in ophthalmology [54, 131]. The modifications of the tissues elasticity in human pre-cancerous epithelial tissue studied in Barrett's oesophagus biopsies [84] or in Sinclair miniature swine, an accepted animal model for the human melanoma [71], highlighted the possibility to use BLS for the cancer diagnostics or therapeutics.

A correlative Brillouin and Raman approach has been also used to study the hippocampal part of the brain of transgenic mouse affected by amyloidopathy [68].

Both the experimental techniques proved to successfully differentiate the amyloid plaques and the healthy tissue highlighting the strict relation between the modifications of mechanical properties and chemical composition with the development of this pathology. In fact, the Brillouin imaging of the brain reported in

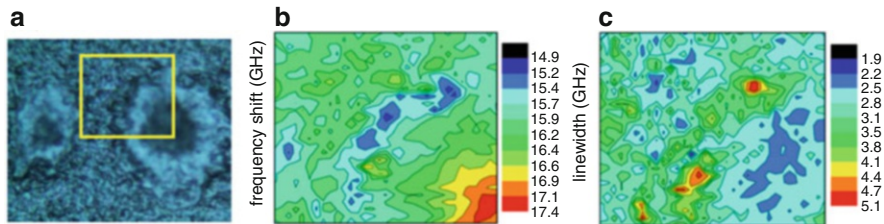


Fig. 2.15 (a) Image of the hippocampal section of a transgenic mouse brain containing two amyloid plaques. (Yellow box denotes a $50 \times 43 \mu\text{m}^2$ area where a Brillouin map was acquired using a $1.5 \mu\text{m}$ step-size. (b) Maps of the frequency shift and (c) linewidth of the Brillouin peak. (Reprinted from [68])

Fig. 2.15 shows an increase in the Brillouin shift investigating the core of the plaque. This region is more rigid than the surrounding tissue: the increase of about 10% found in the Brillouin frequency corresponds, neglecting density and refractive index changes, to an increase of about 20% in the longitudinal elastic modulus. The comparison with the Raman maps obtained investigating the same tissue region, shows that chemical modifications correspond to mechanical changes. In particular, the amyloid plaques structure presents a rigid core rich of protein in β -sheet conformation surrounded by a softer region rich in lipid and proteins in other conformational structures. In fact, it has been already observed that different types of protein aggregates correspond to different rigidity in particular random coil structures are softer than α -helix, which in turn are softer than aggregates in β -sheet conformation [88].

An other interesting aspect to underline in this study is the clear relationship between the width, $\Gamma_b(\Omega_b)$, and the frequency, Ω_b , of the Brillouin peak as showed in Fig. 2.15. Leaving the core of the plaque, the Brillouin frequency shift decreases, reaching its minimum value in the region of the lipid ring while the opposite behaviour has been found for the width of the Brillouin peak. The reduction of Ω_b , related with the real part of the longitudinal elastic modulus

$$M'(\Omega_b) = \rho\Omega_b^2/q^2$$

(where ρ is the density and q the exchanged wavevector, defined in Eq. 2.5), correlates quite strictly with an increase of $\Gamma_b(\Omega_b)$, related with $M''(\Omega_b)$, the imaginary part of the longitudinal elastic modulus, and with $\eta_L(\Omega_b)$ the longitudinal apparent viscosity as

$$\eta_L(\Omega_b) = M''(\Omega_b)/\omega = \rho\Gamma_b/q^2$$

A part from the key role played by the different chemical compositions in the modulation of the elastic properties, this experimental result could hide a possible viscoelastic origin. In fact, in the framework of the viscoelastic description in presence of relaxation phenomena, the direct correlation between the real and the

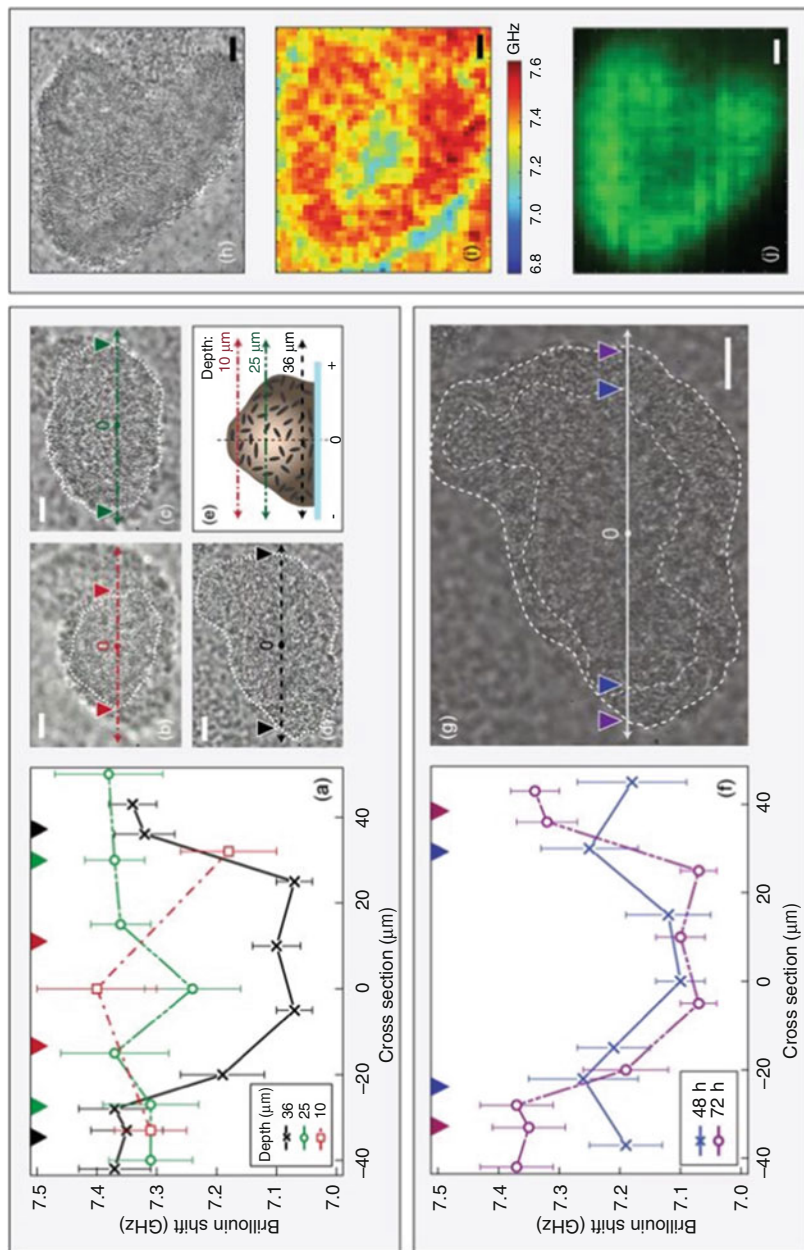


Fig. 2.16 (continued)

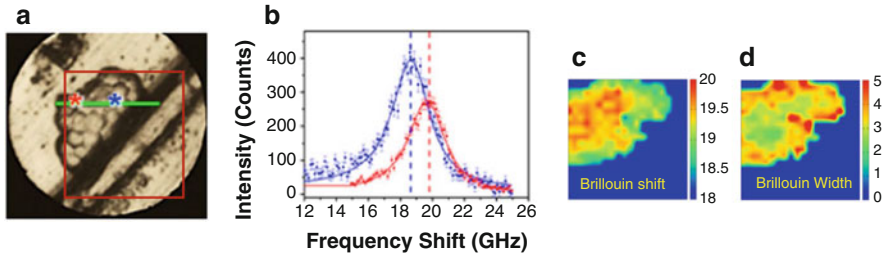


Fig. 2.17 (a) Optical micrograph of a *Candida albicans* biofilm. The red box denotes the $20 \times 20 \mu\text{m}^2$ area where Brillouin raster-scan maps are performed with $1 \mu\text{m}$ step-size. (Reprinted from [69, 103]). (b) Brillouin spectra (dots) measured in the points indicated by asterisks in (a). The full lines are the fitting curves obtained by a damped harmonic oscillation, DHO, model $I(\omega) = I_0 \Gamma_B \Omega_B^2 / \pi \left((\omega^2 - \Omega_B^2)^2 + (\Gamma_B \omega)^2 \right)$. (Reprinted from [69]). (c) and (d) Brillouin maps respectively based on the characteristic frequency Ω_b (GHz) and linewidth Γ (GHz) of the Brillouin peak. (Reprinted from [103])

imaginary part of the elastic modulus is expected if the frequency probed by the technique is lower than the characteristic frequency of the structural relaxation time. Otherwise the opposite behaviour is expected (see Fig. 2.10).

Besides the bio-mechanical mapping of tissues, applications at smaller length scales are recently performed, analysing for example biofilms as complex cells aggregates [53, 103]. Biofilms, the so called “city of microbes” is composed by microbial cells able to reach high level of resistance to antibiotics, anti-fungal drugs and extreme conditions. This ability is in part related to the solid surfaces surrounding the cells consisting of eso-polysaccharides (EPS) a cross-linked polymeric structure produced by the cells themselves. The mechanical characteristics of the biofilm appear of key importance for the understanding of its resistance ability or the mechanisms governing its lifecycle, which includes cells adhesion on surfaces, growth and maturation of the colony and dispersion of new cells to build a new biofilm.

Being a spectroscopic technique, Brillouin spectroscopy is able to provide a mechanical characterization not limited to the surface, allowing the detection of



Fig. 2.16 Brillouin study of *Pseudomonas aeruginosa* biofilms colonies. (a) Frequency shift of the Brillouin peak measured along cross-sections of a single colony (thickness $38 \mu\text{m}$, taken at 72 h post inoculation), depths are indicated. The coloured triangles on the top border denotes the colony boundaries at each depth corresponding to panels from (b) to (d) where the wide field images of the studied colony taken at different depths of 10, 25 and $36 \mu\text{m}$ are reported. The white dashed lines define the boundaries of the colony at each depth. (e) Schematic picture of the cross-sections. (f) Time evolution of the Brillouin shifts measured along the cross-section of a single colony at 48 and 72 h post inoculation. (g) Wide field image of the same colony, taken at 48 and 72 h post inoculation. (h) Wide field, (i) Brillouin, and (j) Fluorescence images of a different colony imaged 100 h post inoculation taken at a depth of $15 \mu\text{m}$ inside a $35\text{-}\mu\text{m}$ thick biofilm. Scale bars: $10 \mu\text{m}$. (Reprinted from [53])

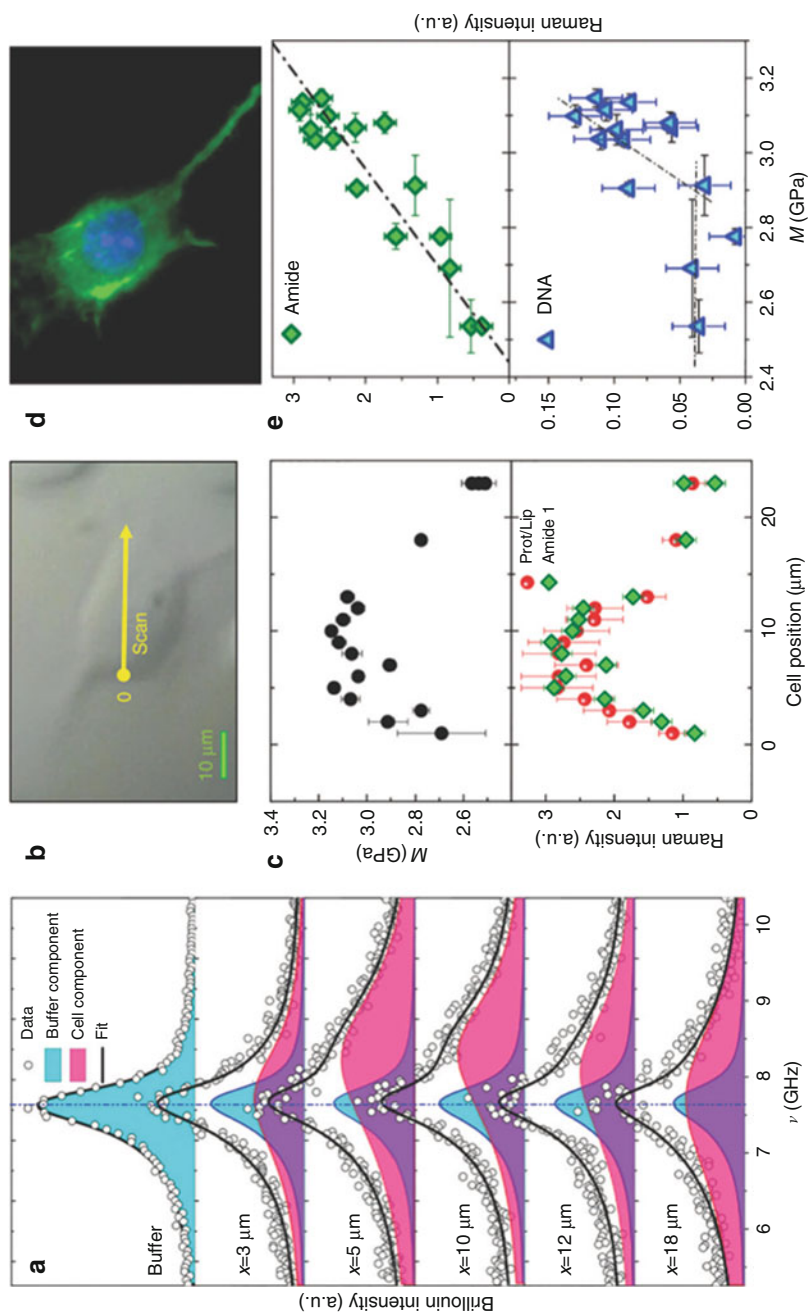


Fig. 2.18 (continued)

the bulk mechanical properties, well below the EPS matrix or the first cells layer of the biofilm. This ability is a clear advantage with respect to other techniques, like for example atomic force microscopy, able to reach higher spatial resolution, but mainly on the sample surface. Changing the position of the laser beam focus, different depths into the intact and live colony can be analyzed. The data [53] show a modification in mechanical properties at different times post inoculation showing how the mechanical properties can be used as marker to characterize the life-cycle of the colony (see Fig. 2.16).

The study of biofilms has been recently approached also by a correlative Brillouin and Raman spectroscopy [69, 103]. The Brillouin image of a dry sample of *Candida albicans* biofilm grown on a metallic substrate is reported in Fig. 2.17.

Using the Raman peaks as spectroscopic markers of modification in the cell status and/or in the biofilm composition, the study evidences the potential presence of still alive *Candida* cells in a dried sample maintained at room temperature for 1 week before the analysis. The existence of a softer region revealed by Brillouin scattering correlated with a region where the Raman signals drastically change revealing also the presence of residual water. These results confirm the microbiological properties of biofilms, which are able to preserve water and to protect cells acting as a defence structure against adverse external agents.

The Brillouin imaging even reached the sub-micrometric spatial resolution achieving the possibility to analyse mechanical modulations of subcellular compartments in living cells. The technique holds the promise to unveil new aspects of the cell biology since it is able to perform in situ analysis without the use of any fixation procedure and the presence of the buffer does not hamper the signal detection. The clear discrimination of the sub-cellular elastic heterogeneities are obtained in several cases [2, 36, 70, 72, 102], together with the evidences of elastic properties modifications in the cells after oncogenic transfection [70], after osmotic shock [102], after the exposure to latrunculin-A, a toxin that prevents polymerisation of actin filament [2]. Recently BLS has been



Fig. 2.18 (a) Brillouin spectra and their deconvolution into cell and buffer components. The fit was performed by considering a fixed shape of the buffer contribution (sound velocity and kinematic viscosity of the corresponding DHO function). Leaving these parameters as free, or even adding a further DHO function, would not lead to an increase in R^2 . (b) Cell image. The yellow point is the initial investigated point for the illustrated measurements. The straight arrow along the cell shows the direction in which the measurements were performed. (c) Upper panel Longitudinal elastic modulus M' as a function of the position. Lower panel relative variation of the protein concentration as obtained by the area of the amide 1 Raman peak and by the deconvolution of the carbon – hydrogen (CH) stretching vibrational mode. (d) Fluorescence microscopy image of NIH/3 T3 cell seeded onto glass cover slips. The average value of the nuclei size is $(14 \pm 2) \mu\text{m}$, in good agreement with the Raman spectroscopic signatures of the cell nucleus. (e) Raman peak intensities of the protein estimated by the intensity of the amide 1 peak and the DNA vs the longitudinal elastic modulus. (Reprinted from [70])

also used to analyse the roles for mechanotransduction in embryonic development [89]. A recent correlative Raman and Brillouin investigation has been performed analyzing single living fibroblasts cells [70]. The Brillouin line shape visibly changes probing different sub-cellular compartments, see Fig. 2.18a, highlighting the technique sensitivity to the local mechanical properties. In these measurements, the presence of the buffer inside the scattering volume is revealed analysing the shape of the Brillouin peak, which appears composed by a superposition of two contributions. The former, which changes its frequency position due to the signal of the cell, and the latter which instead remains at the same frequency changing only its intensity due to the buffer. Using an innovative fitting procedure the two components has been easily separated thereby obtaining the local longitudinal elastic modulus and viscosity. Both the obtained viscoelastic parameters appear modified analysing different positions inside the cell. The correlative analysis lets to link the mechanical evolution found by BLS measurements with the corresponding biochemical composition obtained by Raman spectroscopy. The data highlights the link between the protein concentration and the cell elasticity confirming the key role of protein structures in conferring rigidity to the cells.

5 Conclusions and Future Perspective

Measuring and mapping mechanical properties of biomimetic materials with a resolution below 1 μm is one of the key technological challenges in characterization tools for tissue engineering and regenerative medicine. Nowadays, the most effective approaches are based either on atomic force microscopy or exploiting Brillouin spectroscopy. The former has the highest resolution and a quite robust literature background, but it requires to enter in contact with the sample to probe its elasticity, thus inducing several issues in the wide application of AFM in every day practice and translation to medicine. On the other side, BLS is a very promising remote elasticity mapping technique, but several technical limitations have still to be overcome, among which the speed and the resolution.

Moreover, besides all the discussed experimental tricky points still present in AFM and BLS, a crucial theoretical and phenomenological question is also open. In fact, AFM and BLS not only exploit a different approach, but they intrinsically address different dynamical regions: the AFM probes the mechanical properties in the quasistatic regime (below 1–10 kHz, but often few Hz), while BLS attain the high frequency region (in the range of GHz). Some tentatives have already been done to recapitulate the two domains [35, 101, 102], also proposing the existence of a scaling law (see Fig. 2.10). Nevertheless, this experimental observation still deserves an in-depth phenomenological and theoretical investigation, requiring to combine the two approaches in order to assess the underlying theoretical framework. In addition, this consideration also points out that a multi-scale approach is an essential requirement to have the complete characterization of any viscoelastic material [8, 97, 114]. This is particularly important, in

the characterization of biomimetic materials designed to interface with cells or tissues, whose dynamical processes span over several decades in length and time. The combined use of experimental techniques which in complementary way cover the system dynamics is an important requirement to provide novel insights in their design and to modulate the structure-function relationships.

References

1. Akilbekova D, Ogay V, Yakupov T, Sarsenova M, Umbayev B, Nurakhmetov A, Tazhin K, Yakovlev VV, Utegulov ZN (2018) Brillouin spectroscopy and radiography for assessment of viscoelastic and regenerative properties of mammalian bones. *J Biomed Opt* 23(9):097004
2. Antonacci G, Braakman S (2016) Biomechanics of subcellular structures by non-invasive Brillouin microscopy. *Sci Rep* 6:37217. <https://doi.org/10.1038/srep37217>
3. Antonacci G, Foreman MR, Paterson C, Török P (2013) Spectral broadening in Brillouin imaging. *Appl Phys Lett* 103(22):221105. <https://doi.org/10.1063/1.4836477>. <http://adsabs.harvard.edu/abs/2013ApPhL.103v1105A>
4. Antonacci G, Pedrighi RM, Kondiboyina A, Mehta VV, De Silva R, Paterson C, Krams R, Török P (2015) Quantification of plaque stiffness by Brillouin microscopy in experimental thin cap fibroatheroma. *J R Soc Interface* 12(112):20150843
5. Antonacci G, De Panfilis S, Di Domenico G, DelRe E, Ruocco G (2016) Breaking the contrast limit in single-pass fabry-pérot spectrometers. *Phys Rev Appl* 6(5):054020. <https://doi.org/10.1103/PhysRevApplied.6.054020>. <http://adsabs.harvard.edu/abs/2016PhRvP..6e4020A>
6. Barenghi R, Beke S, Romano I, Gavazzo P, Farkas B, Vassalli M, Brandi F, Scaglione S (2014) Elastin-coated biodegradable photopolymer scaffolds for tissue engineering applications. *Biomed Res Int* 2014:624645
7. Bavi N, Nikolaev YA, Bavi O, Ridone P, Martinac AD, Nakayama Y, Cox CD, Martinac B (2017) Principles of mechanosensing at the membrane interface. In: Epanand R., Ruyschaert JM. (eds) *The Biophysics of Cell Membranes*. Springer Series in Biophysics, vol 19. Singapore: Springer
8. Bechtle S, Ang S, Schneider G (2010) On the mechanical properties of hierarchically structured biological materials. *Universitätsbibliothek der Technischen Universität Hamburg-Harburg, Hamburg*. <https://books.google.it/books?id=nW5QuwEACAAJ>
9. Benassi P, Caponi S, Eramo R, Fontana A, Giugni A, Nardone M, Sampoli M, Viliani G (2005) Sound attenuation in a unexplored frequency region: Brillouin ultraviolet light scattering measurements in v -si o_2 . *Phys Rev B* 71(17):172201. <https://doi.org/10.1103/PhysRevB.71.172201>. <http://adsabs.harvard.edu/abs/2005PhRvB.71q2201B>
10. Berne BJ, Pecora R (1977) *Dynamic Light Scattering with Applications to Chemistry, Biology, and Physics*. Courier Corporation, 54(10):A430 <https://doi.org/10.1021/ed054pA430.1>
11. Bettinger CJ, Langer R, Borenstein JT (2009) Engineering substrate topography at the micro- and nanoscale to control cell function. *Angew Chem Int Ed Engl* 48:5406–5415. <https://doi.org/10.1002/anie.200805179>
12. Betzig E, Trautman J, Harris T, Weiner J, Kostelak R (1991) Breaking the diffraction barrier: optical microscopy on a nanometric scale. *Science* 251(5000):1468–1470
13. Bhushan B (ed) (2010) *Scanning probe microscopy in nanoscience and nanotechnology*, vol 2. Springer, Berlin/Heidelberg
14. Bhushan B, Fuchs H (eds) (2008) *Applied scanning probe methods*, vol XIII. Springer, Berlin/Heidelberg
15. Bilodeau GG (1992) Regular pyramid punch problem. *J Appl Mech* 59:519. <https://doi.org/10.1115/1.2893754>

16. Binnig G, Rohrer H, Gerber C, Weibel E (1982) Surface studies by scanning tunneling microscopy. *Phys Rev Lett* 49(1):57
17. Binnig G, Quate CF, Gerber C (1986) Atomic force microscope. *Phys Rev Lett* 56:930–933. <https://doi.org/10.1103/PhysRevLett.56.930>
18. Boon J, Yip S (1991) *Molecular hydrodynamics*. Dover Publications, New York
19. Bottani CE, Fioretto D (2018) Brillouin scattering of phonons in complex materials. *Adv Phys: X* 3(1):1467281
20. Bracalello A, Santopietro V, Vassalli M, Marletta G, Del Gaudio R, Bochicchio B, Pepe A (2011) Design and production of a chimeric resilin-, elastin-, and collagen-like engineered polypeptide. *Biomacromolecules* 12:2957–2965. <https://doi.org/10.1021/bm2005388>
21. Brillouin L (1922) Diffusion of light and x-rays by a transparent homogeneous body. *Ann Phys* 17(2):88–122
22. Caponi S, Fontana A, Montagna M, Pilla O, Rossi F, Terki F, Woignier T (2003) Acoustic attenuation in silica porous systems. *J Non Cryst Solids* 322:29–34. [https://doi.org/10.1016/S0022-3093\(03\)00167-4](https://doi.org/10.1016/S0022-3093(03)00167-4). <http://adsabs.harvard.edu/abs/2003JNCS..322...29C>
23. Caponi S, Benassi P, Eramo R, Giugni A, Nardone M, Fontana A, Sampoli M, Terki F, Woignier T (2004a) Phonon attenuation in vitreous silica and silica porous systems. *Philos Mag* 84(13–16):1423–1431
24. Caponi S, Carini G, D'angelo G, Fontana A, Pilla O, Rossi F, Terki F, Tripodo G, Woignier T (2004b) Acoustic and thermal properties of silica aerogels and xerogels. *Phys Rev B* 70(21):214204
25. Cappella B, Dietler G (1999) Force-distance curves by atomic force microscopy. *Surf Sci* 34(1–3):1–3, 5–104
26. Carlotti G (2018) Elastic characterization of transparent and opaque films, multilayers and acoustic resonators by surface Brillouin scattering: a review. *Appl Sci* 8(1):124
27. Cavalleri O, Natale C, Stroppolo ME, Relini A, Cosulich E, Thea S, Novi M, Gliozzi A (2000) Azurin immobilisation on thiol covered au(111). *Phys Chem Chem Phys* 2:4630–4635
28. Chen C, Bang S, Cho Y, Lee S, Lee I, Zhang S, Noh I (2016) Research trends in biomimetic medical materials for tissue engineering: 3d bioprinting, surface modification, nano/micro-technology and clinical aspects in tissue engineering of cartilage and bone. *Biomater Res* 20(1):1. <https://doi.org/10.1186/s40824-016-0057-3>
29. Chu B (1976) *Laser spectroscopy*. (Book reviews: dynamic light scattering. With applications to chemistry, biology, and physics). *Science* 194:1155–1156. <https://doi.org/10.1126/science.194.4270.1155>. <http://adsabs.harvard.edu/abs/1976Sci...194.1155B>
30. Comez L, Masciovecchio C, Monaco G, Fioretto D (2012) Progress in liquid and glass physics by Brillouin scattering spectroscopy. *Solid State Phys* 63:1–77. Elsevier
31. Cusack S, Miller A (1979) Determination of the elastic constants of collagen by Brillouin light scattering. *J Mol Biol* 135:39–51
32. Dil J (1982) Brillouin scattering in condensed matter. *Rep Prog Phys* 45(3):285
33. Dimitriadis EK, Horkay F, Maresca J, Kachar B, Chadwick RS (2002) Determination of elastic moduli of thin layers of soft material using the atomic force microscope. *Biophys J* 82(5):2798–2810. [https://doi.org/10.1016/s0006-3495\(02\)75620-8](https://doi.org/10.1016/s0006-3495(02)75620-8)
34. Edginton RS, Mattana S, Caponi S, Fioretto D, Green E, Winlove CP, Palombo F (2016) Preparation of extracellular matrix protein fibers for Brillouin spectroscopy. *J Vis Exp*. <https://doi.org/10.3791/54648>
35. Edginton RS, Green EM, Winlove CP, Fioretto D, Palombo F (2018) Dual scale biomechanics of extracellular matrix proteins probed by Brillouin scattering and quasistatic tensile testing. In: *Society of photo-optical instrumentation engineers (SPIE) conference series*, vol 10504, p 105040J. <https://doi.org/10.1117/12.2290183>. <http://adsabs.harvard.edu/abs/2018SPIE10504E..0JE>
36. Elsayad K, Werner S, Gallemi M, Kong J, Guajardo ERS, Zhang L, Jaillais Y, Greb T, Belkhadir Y (2016) Mapping the subcellular mechanical properties of live cells in tissues with fluorescence emission–Brillouin imaging. *Sci Signal* 9(435):rs5–rs5
37. Engler AJ, Sen S, Sweeney HL, Discher DE (2006) Matrix elasticity directs stem cell lineage specification. *Cell* 126(4):677–689

38. Fabry B, Maksym GN, Butler JP, Glogauer M, Navajas D, Fredberg JJ (2001) Scaling the microrheology of living cells. *Phys Rev Lett* 87:148102. <https://doi.org/10.1103/PhysRevLett.87.148102>
39. Ferrera D, Canale C, Marotta R, Mazzaro N, Gritti M, Mazzanti M, Capellari S, Cortelli P, Gasparini L (2014) Lamin b1 overexpression increases nuclear rigidity in autosomal dominant leukodystrophy fibroblasts. *FASEB J* 28(9):3906–3918. <https://doi.org/10.1096/fj.13-247635>
40. Fink M, Tanter M (2010) Multiwave imaging and super resolution. *Phys Today* 63(2):28–33. <https://doi.org/10.1063/1.3326986>
41. Fiore A, Zhang J, Shao P, Yun SH, Scarcelli G (2016) High-extinction virtually imaged phased array-based Brillouin spectroscopy of turbid biological media. *Appl Phys Lett* 108:203701. <https://doi.org/10.1063/1.4948353>
42. Franz MO, Mallot HA (2000) Biomimetic robot navigation. *Robot Auton Syst* 30:133–153. [https://doi.org/10.1016/s0921-8890\(99\)00069-x](https://doi.org/10.1016/s0921-8890(99)00069-x)
43. Fung Y (1993) *Biomechanics: mechanical properties of living tissues*. Springer, New York
44. Gruber P (2008) The signs of life in architecture. *Bioinspir Biomim* 3:023001. <https://doi.org/10.1088/1748-3182/3/2/023001>
45. Hadden WJ, Young JL, Holle AW, McFetridge ML, Kim DY, Wijesinghe P, Taylor-Weiner H, Wen JH, Lee AR, Bieback K, Vo BN, Sampson DD, Kennedy BF, Spatz JP, Engler AJ, Choi YS (2017) Stem cell migration and mechanotransduction on linear stiffness gradient hydrogels. *Proc Natl Acad Sci U S A* 114:5647–5652. <https://doi.org/10.1073/pnas.1618239114>
46. Harley R, James D, Miller A, White JW (1977) Phonons and the elastic moduli of collagen and muscle. *Nature* 267:285–287
47. Harley BA, Leung JH, Silva ECCM, Gibson LJ (2007) Mechanical characterization of collagen-glycosaminoglycan scaffolds. *Acta Biomater* 3:463–474. <https://doi.org/10.1016/j.actbio.2006.12.009>
48. Hartmann U (1988) Magnetic force microscopy: some remarks from the micromagnetic point of view. *J Appl Phys* 64(3):1561–1564
49. Huang G, Li F, Zhao X, Ma Y, Li Y, Lin M, Jin G, Lu TJ, Genin GM, Xu F (2017) Functional and biomimetic materials for engineering of the three-dimensional cell microenvironment. *Chem Rev* 117(20):12764–12850. <https://doi.org/10.1021/acs.chemrev.7b00094>. PMID: 28991456
50. Hutter JL, Bechhoefer J (1993) Calibration of atomic-force microscope tips. *Rev Sci Instrum* 64(7):1868–1873. <https://doi.org/10.1063/1.1143970>
51. Ikada Y (2006) Challenges in tissue engineering. *J R Soc Interface* 3:589–601. <https://doi.org/10.1098/rsif.2006.0124>
52. Kapsali V (2013) 7 – Biomimetic approaches to the design of smart textiles for protection. In: Chapman R (ed) *Smart textiles for protection*. Wood-head Publishing series in textiles. Woodhead Publishing, Cambridge, UK, pp 214–226. <https://doi.org/10.1533/9780857097620.1.214>. <http://www.sciencedirect.com/science/article/pii/B9780857090560500078>
53. Karampatzakis A, Song CZ, Allsopp LP, Filloux A, Rice SA, Cohen Y, Wohland T, Török P (2017) Probing the internal micromechanical properties of *Pseudomonas aeruginosa* biofilms by Brillouin imaging. *NPJ Biofilms Microbiomes* 3:20. <https://doi.org/10.1038/s41522-017-0028-z>
54. Kennedy BF, Wijesinghe P, Sampson DD (2017) The emergence of optical elastography in biomedicine. *Nat Photonics* 11:215–221. <https://doi.org/10.1038/nphoton.2017.6>. <http://adsabs.harvard.edu/abs/2017NaPho..11..215K>
55. Key J, Palange AL, Gentile F, Aryal S, Stigliano C, Mascolo DD, Rosa ED, Cho M, Lee Y, Singh J, Decuzzi P (2015) Soft discoidal polymeric nanoconstructs resist macrophage uptake and enhance vascular targeting in tumors. *ACS Nano* 9(12):11628–11641. <https://doi.org/10.1021/acs.nano.5b04866>
56. Kim JH, Yoo JJ (2018) Current developments and future perspectives of tissue engineering and regenerative medicine. In: *Clinical regenerative medicine in urology*. Springer, Singapore

57. Klieber C, Hecksher T, Pezeril T, Torchinsky DH, Dyre JC, Nelson KA (2013) Mechanical spectra of glass-forming liquids. II. Gigahertz-frequency longitudinal and shear acoustic dynamics in glycerol and dc704 studied by time-domain Brillouin scattering. *J Chem Phys* 138:12A544. <https://doi.org/10.1063/1.4789948>
58. Koski KJ, Akhnenblit P, McKiernan K, Yarger JL (2013) Non-invasive determination of the complete elastic moduli of spider silks. *Nat Mater* 12:262–267. <https://doi.org/10.1038/nmat3549>
59. Lepesant JP, Powers L, Pershan PS (1978) Brillouin light scattering measurement of the elastic properties of aligned multilamella lipid samples. *Proc Natl Acad Sci U S A* 75:1792–1795
60. Lim C, Zhou E, Quek S (2006) Mechanical models for living cells – a review. *J Biomech* 39(2):195–216. <https://doi.org/10.1016/j.jbiomech.2004.12.008>
61. Lin DC, Dimitriadis EK, Horkay F (2007) Robust strategies for automated AFM force curve analysis – II: adhesion-influenced indentation of soft, elastic materials. *J Biomech Eng* 129(6):904. <https://doi.org/10.1115/1.2800826>
62. Lutolf MP, Gilbert PM, Blau HM (2009) Designing materials to direct stem-cell fate. *Nature* 462(7272):433
63. Ma PX (2008) Biomimetic materials for tissue engineering. *Adv Drug Deliv Rev* 60:184–198. <https://doi.org/10.1016/j.addr.2007.08.041>
64. Mandadapu KK, Govindjee S, Mofrad MRK (2008) On the cytoskeleton and soft glassy rheology. *J Biomech* 41:1467–1478. <https://doi.org/10.1016/j.jbiomech.2008.02.014>
65. Mapelli L, Canale C, Pesci D, Averaimo S, Guizzardi F, Fortunati V, Falasca L, Piacentini M, Gliozzi A, Relini A, Mazzanti M, Jodice C (2012) Toxic effects of expanded ataxin-1 involve mechanical instability of the nuclear membrane. *Biochim Biophys Acta* 1822:906–917. <https://doi.org/10.1016/j.bbadis.2012.01.016>
66. Maret G, Oldenbourg R, Winterling G, Dransfeld K, Rupprecht A (1979) Velocity of high frequency sound waves in oriented DNA fibres and films determined by Brillouin scattering. *Colloid Polym Sci* 257(10):1017–1020
67. Masciovecchio C, Baldi G, Caponi S, Comez L, Di Fonzo S, Fioretto D, Fontana A, Gessini A, Santucci S, Sette F et al (2006) Evidence for a crossover in the frequency dependence of the acoustic attenuation in vitreous silica. *Phys Rev Lett* 97(3):035501
68. Mattana S, Caponi S, Tamagnini F, Fioretto D, Palombo F (2017a) Viscoelasticity of amyloid plaques in transgenic mouse brain studied by Brillouin microspectroscopy and correlative Raman analysis. *J Innov Opt Health Sci* 10:1742001. <https://doi.org/10.1142/S1793545817420019>
69. Mattana S, Cardinali MA, Caponi S, Pierantoni DC, Corte L, Roscini L, Cardinali G, Fioretto D (2017b) High-contrast Brillouin and Raman micro-spectroscopy for simultaneous mechanical and chemical investigation of microbial biofilms. *Biophys Chem* 229:123–129
70. Mattana S, Mattarelli M, Urbanelli L, Sagini K, Emiliani C, Dalla Serra M, Fioretto D, Caponi S (2018) Non-contact mechanical and chemical analysis of single living cells by micro-spectroscopic techniques. *Light: Sci Appl* 7(2):17139
71. Meng Z, Traverso AJ, Yakovlev VV (2014) Background clean-up in Brillouin micro-spectroscopy of scattering medium. *Opt Express* 22:5410–5415. <https://doi.org/10.1364/OE.22.005410>
72. Meng Z, Bustamante Lopez SC, Meissner KE, Yakovlev VV (2016a) Subcellular measurements of mechanical and chemical properties using dual Raman-Brillouin microspectroscopy. *J Biophotonics* 9:201–207. <https://doi.org/10.1002/jbio.201500163>
73. Meng Z, Traverso AJ, Ballmann CW, Troyanova-Wood MA, Yakovlev VV (2016b) Seeing cells in a new light: a renaissance of Brillouin spectroscopy. *Adv Opt Photon* 8(2):300–327
74. Monaco G, Caponi S, di Leonardo R, Fioretto D, Ruocco G (2000) Intramolecular origin of the fast relaxations observed in the Brillouin light scattering spectra of molecular glass formers. *Phys Rev E* 62:R7595–R7598. <https://doi.org/10.1103/PhysRevE.62.R7595>. <http://adsabs.harvard.edu/abs/2000PhRvE..62.7595M>

75. Murphy SV, Atala A (2013) Organ engineering—combining stem cells, biomaterials, and bioreactors to produce bioengineered organs for transplantation. *BioEssays* 35:163–172. <https://doi.org/10.1002/bies.201200062>
76. Nichol JW, Koshy ST, Bae H, Hwang CM, Yamanlar S, Khademhosseini A (2010) Cellladen microengineered gelatin methacrylate hydrogels. *Biomaterials* 31(21):5536–5544
77. O'Brien FJ, Harley BA, Yannas IV, Gibson L (2004) Influence of freezing rate on pore structure in freeze-dried collagen-gag scaffolds. *Biomaterials* 25:1077–1086
78. Offeddu GS, Ashworth JC, Cameron RE, Oyen ML (2015) Multi-scale mechanical response of freeze-dried collagen scaffolds for tissue engineering applications. *J Mech Behav Biomed Mater* 42:19–25. <https://doi.org/10.1016/j.jmbbm.2014.10.015>
79. Oh YJ, Sekot G, Duman M, Chtcheglova L, Messner P, Peterlik H, Schäffer C, Hinterdorfer P (2013) Characterizing the s-layer structure and anti-s-layer antibody recognition on intact tannerella forsythia cells by scanning probe microscopy and small angle x-ray scattering. *J Mol Recognit* 26:542–549. <https://doi.org/10.1002/jmr.2298>
80. Oliver WC, Pharr GM (2004) Measurement of hardness and elastic modulus by instrumented indentation: advances in understanding and refinements to methodology. *J Mater Res* 19(1):3–20
81. Oropesa-Nuñez R, Keshavan S, Dante S, Diaspro A, Mannini B, Capitini C, Cecchi C, Stefani M, Chiti F, Canale C (2018) Toxic hypf-n oligomers selectively bind the plasma membrane to impair cell adhesion capability. *Biophys J* 114:1357–1367. <https://doi.org/10.1016/j.bpj.2018.02.003>
82. Oyen M (2011) Nanoindentation of biological and biomimetic materials. *Exp Tech* 37(1):73–87. <https://doi.org/10.1111/j.1747-1567.2011.00716.x>
83. Palomba R, Palange AL, Rizzuti IF, Ferreira M, Cervadoro A, Barbato MG, Canale C, Decuzzi P (2018) Modulating phagocytic cell sequestration by tailoring nanoconstruct softness. *ACS Nano* 12:1433–1444. <https://doi.org/10.1021/acsnano.7b07797>
84. Palombo F, Madami M, Stone N, Fioretto D (2014a) Mechanical mapping with chemical specificity by confocal Brillouin and Raman microscopy. *Analyst* 139:729–733. <https://doi.org/10.1039/c3an02168h>
85. Palombo F, Winlove CP, Edginton RS, Green E, Stone N, Caponi S, Madami M, Fioretto D (2014b) Biomechanics of fibrous proteins of the extracellular matrix studied by Brillouin scattering. *J R Soc Interface* 11:20140739. <https://doi.org/10.1098/rsif.2014.0739>
86. Pastorino L, Dellacasa E, Scaglione S, Giulianelli M, Sbrana F, Vassalli M, Ruggiero C (2014) Oriented collagen nanocoatings for tissue engineering. *Colloids Surf B: Biointerfaces* 114:372–378
87. Pawelec KM, Husmann A, Best SM, Cameron RE (2014) Understanding anisotropy and architecture in ice-templated biopolymer scaffolds. *Mater Sci Eng C Mater Biol Appl* 37:141–147. <https://doi.org/10.1016/j.msec.2014.01.009>
88. Peticaroli S, Nickels JD, Ehlers G, Sokolov AP (2014) Rigidity, secondary structure, and the universality of the boson peak in proteins. *Biophys J* 106(12):2667–2674
89. Pukhlyakova E, Aman AJ, Elsayad K, Technau U (2018) β -Catenin-dependent mechanotransduction dates back to the common ancestor of Cnidaria and Bilateria. *Proc Natl Acad Sci U S A* 115:6231–6236. <https://doi.org/10.1073/pnas.1713682115>
90. Qi C, Yan X, Huang C, Melerzanov A, Du Y (2015) Biomaterials as carrier, barrier and reactor for cell-based regenerative medicine. *Protein Cell* 6:638–653. <https://doi.org/10.1007/s13238-015-0179-8>
91. Randall JT, Vaughan JM (1979) Brillouin scattering in systems of biological significance. *Philos Trans R Soc Lond A* 293(1402):341–348
92. Rezende CA, Lee LT, Galembeck F (2009) Surface mechanical properties of thin polymer films investigated by AFM in pulsed force mode. *Langmuir* 25:9938–9946. <https://doi.org/10.1021/la9010949>
93. Rigato A, Miyagi A, Scheuring S, Rico F (2017) High-frequency microrheology reveals cytoskeleton dynamics in living cells. *Nat Phys* 13:771–775. <https://doi.org/10.1038/nphys4104>

94. Sadati M, Nourhani A, Fredberg JJ, Taheri Qazvini N (2014) Glass-like dynamics in the cell and in cellular collectives. *Wiley Interdiscip Rev Syst Biol Med* 6:137–149. <https://doi.org/10.1002/wsbm.1258>
95. Salem AK, Stevens R, Pearson RG, Davies MC, Tendler SJB, Roberts CJ, Williams PM, Shakesheff KM (2002) Interactions of 3T3 fibroblasts and endothelial cells with defined pore features. *J Biomed Mater Res* 61:212–217. <https://doi.org/10.1002/jbm.10195>
96. Sassi P, Caponi S, Ricci M, Morresi A, Oldenhof H, Wolkers WF, Fioretto D (2015) Infrared versus light scattering techniques to monitor the gel to liquid crystal phase transition in lipid membranes. *J Raman Spectrosc* 46:644–651. <https://doi.org/10.1002/jrs.4702>. <http://adsabs.harvard.edu/abs/2015JRSp...46..644S>
97. Sbrana F, Fotia C, Bracalello A, Baldini N, Marletta G, Ciapetti G, Boichicchio B, Vassalli M (2012) Multiscale characterization of a chimeric biomimetic polypeptide for stem cell culture. *Bioinspir Biomim* 7(4):046007
98. Scarcelli G, Yun SH (2007) Confocal Brillouin microscopy for three-dimensional mechanical imaging. *Nat Photonics* 2:39–43. <https://doi.org/10.1038/nphoton.2007.250>
99. Scarcelli G, Yun SH (2011) Multistage viba etalons for high-extinction parallel Brillouin spectroscopy. *Opt Express* 19(10):913–10922. <https://doi.org/10.1364/OE.19.010913>
100. Scarcelli G, Yun SH (2012) In vivo Brillouin optical microscopy of the human eye. *Opt Express* 20:9197–9202. <https://doi.org/10.1364/OE.20.009197>
101. Scarcelli G, Kim P, Yun SH (2011) In vivo measurement of age-related stiffening in the crystalline lens by Brillouin optical microscopy. *Biophys J* 101:1539–1545. <https://doi.org/10.1016/j.bpj.2011.08.008>
102. Scarcelli G, Polacheck WJ, Nia HT, Patel K, Grodzinsky AJ, Kamm RD, Yun SH (2015) Noncontact three-dimensional mapping of intracellular hydromechanical properties by Brillouin microscopy. *Nat Methods* 12:1132–1134. <https://doi.org/10.1038/nmeth.3616>
103. Scarponi F, Mattana S, Corezzi S, Caponi S, Comez L, Sassi P, Morresi A, Paolantoni M, Urbanelli L, Emiliani C et al (2017) High-performance versatile setup for simultaneous Brillouin-Raman microspectroscopy. *Phys Rev X* 7(3):031015
104. Schlüßler R, Möllmert S, Abuhattum S, Cojoc G, Müller P, Kim K, Möckel C, Zimmermann C, Czarnecki J, Guck J (2018) Mechanical mapping of spinal cord growth and repair in living Zebrafish larvae by Brillouin imaging. *Biophys J* 115(5):911–923
105. Schneider D, Gomopoulos N, Koh CY, Papadopoulos P, Kremer F, Thomas EL, Fytas G (2016) Nonlinear control of high-frequency phonons in spider silk. *Nat Mater* 15(10):1079
106. Schwarz US, Gardel ML (2012) United we stand – integrating the actin cytoskeleton and cell–matrix adhesions in cellular mechanotransduction. *J Cell Sci* 125:3051. <https://doi.org/10.1242/jcs.093716>. <http://jcs.biologists.org/content/early/2012/07/10/jcs.093716>
107. Scott ON, Begley MR, Komaragiri U, Mackin TJ (2004) Indentation of freestanding circular elastomer films using spherical indenters. *Acta Mater* 52:4877–4885. <https://doi.org/10.1016/j.actamat.2004.06.043>
108. Sebastian T, Schultheiss K, Obry B, Hillebrands B, Schultheiss H, Obry B (2015) Micro-focused Brillouin light scattering: imaging spin waves at the nanoscale. *Front Phys* 3:35. <https://doi.org/10.3389/fphy.2015.00035>. <http://adsabs.harvard.edu/abs/2015FrP.....3...35S>
109. Smith L, Ma P (2004) Nano-fibrous scaffolds for tissue engineering. *Colloids Surf B: Biointerfaces* 39(3):125–131
110. Smolyakov G, Pruvost S, Cardoso L, Alonso B, Belamie E, Duchet-Rumeau J (2016) AFM PeakForce QNM mode: evidencing nanometre-scale mechanical properties of chitin-silica hybrid nanocomposites. *Carbohydr Polym* 151:373–380. <https://doi.org/10.1016/j.carbpol.2016.05.042>
111. Sneddon IN (1965) The relation between load and penetration in the axisymmetric boussinesq problem for a punch of arbitrary profile. *Int J Eng Sci* 3(1):47–57. [https://doi.org/10.1016/0020-7225\(65\)90019-4](https://doi.org/10.1016/0020-7225(65)90019-4)
112. Solano I, Parisse P, Gramazio F, Ianeselli L, Medagli B, Cavalleri O, Casalis L, Canepa M (2017) Atomic force microscopy and spectroscopic ellipsometry combined analysis of small ubiquitin-like modifier adsorption on functional monolayers. *Appl Surf Sci* 421:722–727. <https://doi.org/10.1016/j.apsusc.2016.10.195>

113. Sweers K, van der Werf K, Bennink M, Subramaniam V (2011) Nanomechanical properties of α -synuclein amyloid fibrils: a comparative study by nanoindentation, harmonic force microscopy, and peakforce QNM. *Nanoscale Res Lett* 6(1):270. <https://doi.org/10.1186/1556-276x-6-270>
114. Tomar V, Qu T, Dubey DK, Verma D, Zhang Y (2015) Introduction. In: Multiscale characterization of biological systems. New York: Springer-Verlag <https://doi.org/10.1007/978-1-4939-3453-9>
115. Traverso AJ, Thompson JV, Steelman ZA, Meng Z, Scully MO, Yakovlev VV (2015) Dual Raman-Brillouin microscope for chemical and mechanical characterization and imaging. *Anal Chem* 87:7519–7523. <https://doi.org/10.1021/acs.analchem.5b02104>
116. Vacanti CA (2007) The history of tissue engineering. *J Cell Mol Med* 10(3):569–576. <https://doi.org/10.1111/j.1582-4934.2006.tb00421.x>. <https://onlinelibrary.wiley.com/doi/abs/10.1111/j.1582-4934.2006.tb00421.x>
117. Vacher R, Boyer L (1972) Brillouin scattering: a tool for the measurement of elastic and photoelastic constants. *Phys Rev B* 6(2):639
118. Vacher Sussner H, Schmidt M, Hunklinger S (1980) High resolution studies of Brillouin scattering in amorphous materials, Chap. 13. In: Maris HJ (ed) *Phonon scattering in condensed matter*. Springer, Boston, pp 61–64
119. Vacher R, Pelous J, Courtens E (1997) Mean free path of high-frequency acoustic excitations in glasses with application to vitreous silica. *Phys Rev B* 56(2):R481
120. Vassalli M, Sbrana F, Laurita A, Papi M, Bloise N, Visai L, Bochicchio B (2013) Biological and structural characterization of a naturally inspired material engineered from elastin as a candidate for tissue engineering applications. *Langmuir* 29(15):898–15906. <https://doi.org/10.1021/la403311x>
121. Vaughan J, Randall J (1980) Brillouin scattering, density and elastic properties of the lens and cornea of the eye. *Nature* 284(5755):489–491
122. Vezenov DV, Noy A, Rozsnyai LF, Lieber CM (1997) Force titrations and ionization state sensitive imaging of functional groups in aqueous solutions by chemical force microscopy. *J Am Chem Soc* 119(8):2006–2015
123. Vinckier A, Semenza G (1998) Measuring elasticity of biological materials by atomic force microscopy. *FEBS Lett* 430(1–2):12–16. [https://doi.org/10.1016/s0014-5793\(98\)00592-4](https://doi.org/10.1016/s0014-5793(98)00592-4)
124. Wake MC, Patrick CW, Mikos AG (1994) Pore morphology effects on the fibrovascular tissue growth in porous polymer substrates. *Cell Transplant* 3:339–343
125. Wang N, Tytell JD, Ingber DE (2009) Mechanotransduction at a distance: mechanically coupling the extracellular matrix with the nucleus. *Nat Rev Mol Cell Biol* 10(1):75
126. Welzel PB, Friedrichs J, Grimmer M, Vogler S, Freudenberg U, Werner C (2014) Cryogel micromechanics unraveled by atomic force microscopy-based nanoindentation. *Adv Health Mater* 3(11):1849–1853
127. Wen JH, Vincent LG, Fuhrmann A, Choi YS, Hribar KC, Taylor-Weiner H, Chen S, Engler AJ (2014) Interplay of matrix stiffness and protein tethering in stem cell differentiation. *Nat Mater* 13:979–987. <https://doi.org/10.1038/nmat4051>
128. Wolff L, Fernández P, Kroy K (2012) Resolving the stiffening-softening paradox in cell mechanics. *PLoS One* 7:e40063. <https://doi.org/10.1371/journal.pone.0040063>
129. Xavier JR, Thakur T, Desai P, Jaiswal MK, Sears N, Cosgriff-Hernandez E, Kaunas R, Gaharwar AK (2015) Bioactive nanoengineered hydrogels for bone tissue engineering: a growth-factor-free approach. *ACS Nano* 9(3):3109–3118
130. Xu J, Lauser K, Dransfeld K, Wilson I (1994) Thermal sensors for investigation of heat transfer in scanning probe microscopy. *Rev Sci Instrum* 65(7):2262–2266
131. Yun SH, Chernyak D (2018) Brillouin microscopy: assessing ocular tissue biomechanics. *Curr Opin Ophthalmol* 29:299–305. <https://doi.org/10.1097/ICU.0000000000000489>
132. Zeltinger J, Sherwood JK, Graham DA, Mueller R, Griffith LG (2001) Effect of pore size and void fraction on cellular adhesion, proliferation, and matrix deposition. *Tissue Eng* 7:557–572. <https://doi.org/10.1089/107632701753213183>
133. Zwanzig R, Mountain RD (1965) High-frequency elastic moduli of simple fluids. *J Chem Phys* 43(12):4464–4471



Open-Channel Separation Techniques for the Characterization of Nanomaterials and Their Bioconjugates for Drug Delivery Applications

Jiwon Lee, Roxana Coreas, and Wenwan Zhong

Contents

1	Definition of the Topic	114
2	Overview	114
3	Introduction	114
4	Experimental and Instrumental Methodology	117
4.1	Field Flow Fractionation	117
4.2	Capillary Electrophoresis	121
5	Key Research Findings	126
5.1	Field Flow Fractionation for Characterization of Nanomaterials and Their Bioconjugates for Drug Delivery Applications	126
5.2	Capillary Electrophoresis for Characterization of Nanomaterials and Their Bioconjugates for Drug Delivery Applications	133
6	Conclusions and Future Perspective	143
	References	144

Jiwon Lee and Roxana Coreas contributed equally to this work, with J. Lee contributing mainly to the discussion of CE related technology and development, and R. Coréas to the content about FFF.

J. Lee

Department of Chemistry, University of California-Riverside, Riverside, CA, USA

e-mail: jiwon.lee@email.ucr.edu

R. Coreas

Environmental Toxicology Graduate Program, University of California-Riverside, Riverside, CA, USA

e-mail: roxana.coreas@email.ucr.edu

W. Zhong (✉)

Department of Chemistry, University of California-Riverside, Riverside, CA, USA

Environmental Toxicology Graduate Program, University of California-Riverside, Riverside, CA, USA

e-mail: wenwan.zhong@ucr.edu

1 Definition of the Topic

Open-channel separation techniques can separate samples without reliance on column packing, minimizing sample loss due to adsorption onto the packing materials and reducing damage to samples, in particular, the complexes held together by non-chemical interactions. Field flow fractionation (FFF) and capillary electrophoresis (CE) are two representative open-channel separation techniques. In this chapter, we discuss the use of FFF and CE to separate and characterize various nanomaterials widely applied in biomedical research.

2 Overview

Nanoparticles (NPs) have facilitated advancements in disease cure and diagnosis, by enabling drug delivery, tumor imaging, and marker detection as well as other aspects of biomedical research. Thus, it is imperative to adequately access their biocompatibility and to investigate how the properties of nanomaterials, such as size, shape, charge, and composition, influence the functionality and behaviors of the nanomaterials in biosystems, which is governed by their interactions with the diverse biomolecules and biological surfaces. Many techniques have been used to characterize the biological relevant nanomaterials and study the nano-bio interface, including the open-channel separation techniques, FFF and CE. Because FFF and CE can analyze a wide range of nanomaterials composed of different chemical cores, including metals, metal oxides, semiconductors, polymers, and liposomes and exhibiting various morphology, sizes, and shapes, an assortment of separation modes and subtechniques of these two open-channel techniques have been utilized for the analysis of such materials and their bioconjugates to better assess their functionality in biosystems. Hence, in this chapter, we discuss the different approaches used in FFF and CE for such purposes.

3 Introduction

Nanomaterials have garnered appreciable significance over the years as imaging agents [1, 2], drug delivery tools [3–5], and biosensing resources [6]. Having such prodigious roles, investigating their behaviors in biological environments is of utmost importance. This is due to their potential interactions with certain biological entities such as proteins [7, 8], DNA [9], and cells [10], which greatly impacts the functionality of nanomaterials as well as raises toxicity concerns. Understanding molecular interactions and binding behaviors of nanomaterials to biological constituents have great implications in the advancement of developing nanomaterials as tools for medical research. Therefore, we begin by succinctly introducing the concepts of NP protein coronas, one example of bioconjugated NPs, and NPs for drug delivery.

Proteins and other macromolecules can adhere onto the surfaces of engineered nanomaterials (ENMs), and the resulting protein adsorption layer is termed protein corona [11–13]. In biological matrices, proteins compete to nonspecifically bind to the nanoparticle surface and lead to the formation of a protein corona [7, 14]. This corona can affect the physiochemical properties, alter the adsorption, distribution, metabolism, and excretion (ADME) profile and limit the targeting and detection capacity of NPs. Therefore, it is important to study protein corona formation on diverse nanomaterials in different biological matrices. However, the adsorption process can be quite complex in that the size, zeta potential, and surface chemistry of nanoparticles can affect the composition of the corona; in addition, the protein types and concentrations in the biological matrix also affect corona formation [7, 8]. Furthermore, there are two coronas that can adsorb onto nanoparticle surfaces: a soft corona of proteins with low binding affinity towards the nanomaterial and a hard corona with proteins that have low exchange kinetics and tend to persist longer on the nanoparticle surface. Studying the binding equilibrium of both coronas can lead to a better understanding of the toxicological mechanisms of bioconjugated nanoparticles.

The recent review by Ulbrich et al. on nanoparticles for drug delivery systems comprehensively covers the various types of NPs used, the types of drugs that have been loaded onto these particles, as well as their application in clinical trials. In this work, they address the advantages of using nanomaterials for drug delivery. Essentially, drugs that are sensitive to activation by nonspecific targets or lack water solubility can be loaded onto nanoparticles to mitigate these limitations. Additionally, nanoparticles can target specific organs or cells that the respective delivered drug cannot reach alone. For example, nanoparticles can accumulate through the leaky vasculature of tumors via an enhanced permeability and retention effect (EPR). Once these drug-loaded particles reach the targeted tumors, the drug can either be deposited or site-selectively activated and the nanoparticle itself can then be excreted [15]. The applicability of nanomaterials in medicine is extensive, thus characterization of these drug-delivery systems is indispensable.

Multiple techniques can analyze various nanomaterial characteristics. Morphology and size can be determined by microscopy techniques, such as transmission electron microscopy (TEM) and atomic force microscopy (AFM). However, sample preparation or analysis can be laborious and time-consuming. Dynamic light scattering (DLS) and nanoparticle tracking analysis (NTA) are other common techniques to evaluate the size distribution. These are nondestructive techniques, which make them ideal for analyzing nanomaterials; on the contrary, DLS may suffer in resolution [16], and both DLS and NTA have a bias towards larger particles.

On the other hand, separation techniques can be used to analyze complex biological samples, preconcentrate sample targets, and resolve sample contents, which enable them to provide a more comprehensive examination. They are also appropriate for investigating interactions since any change will be manifested in the retention time differences or shifts. Chromatography [17, 18] and gel electrophoresis [19, 20] are commonly used to separate nanomaterials. In chromatography, the efficiency of separation may be limited by the interactions of nanomaterials with

Table 3.1 Forces applied in respective field flow fractionation (FFF) subtechniques

FFF subtechniques	Force
<i>Flow FFF (F4)</i>	Cross flow; a second flow perpendicular to the channel flow
<i>Sedimentation FFF (SFFF)</i>	Centrifugal, gravitational
<i>Thermal FFF (Th-FFF)</i>	Thermal gradient
<i>Electrical FFF (El-FFF)</i>	Electrical gradient

the column packing material and the size of the packing material. In gel electrophoresis, issues of band broadening are apparent. FFF and CE are open-channel separation techniques that can overcome these complications.

More than half a century ago, J. Calvin Giddings proposed FFF as a separation tool for large analytes [21]. FFF consists of a family of flow elution techniques, which all use open channels and applied fields to achieve differential retention of the solutes. Alteration of the force applied in FFF has resulted in multiple flexible subtechniques [22], a few of which have been listed in Table 3.1, that can separate and measure analytes simultaneously. Since its invention, FFF has been used to separate and characterize a range of samples, including but not limited to, proteins [23, 24], DNA [25], DNA-protein interactions [26], viruses [27, 28], microRNA [29], polymers [30], and more recently bioconjugated nanoparticles. FFF is an ideal tool for fractionation of complex mixtures because of its gentle interface during separations [31] and its wider analyte size range compared to other separation techniques [32]. In addition, recent developments in instrumentation and miniaturization that couple FFF with orthogonal separation or analytical techniques, like inductively coupled plasma mass spectrometry (ICP-MS), nuclear magnetic resonance spectroscopy (NMR), and multi-angle light scattering (MALS), have significantly improved the resolution of various FFF techniques and their capability in providing in-depth information of the analytes [33–35].

As pioneers, Stellan Hjertén first introduced electrophoresis in tubes in the 1970s while James W. Jorgenson and Krynne DeArman Lukacs brought capillary electrophoresis to recognition in the 1980s. Now it is a standard technique with numerous developments over the years. CE has multiple advantages over column chromatography, which include high resolution, minimal sample and reagent usage, and fast analysis; furthermore, these attributes have made CE a widely used technique in many instances for the analysis of small molecules [36], anti-cancer drugs and their metabolites [37], proteins [38], DNA [39], and enzymes [40]. In addition to the analysis of bioconjugates, drug delivery systems have been studied via CE. Various studies utilized CE to characterize the size and charge of drug delivery nanomaterials as well as assessing drug entrapment and release efficiencies.

While both open-channel separation techniques play important roles in characterization of nanomaterials employed in biomedical research and applications, including the materials employed for drug delivery, no review articles or book chapters can be found to discuss the particular contributions from both. For the ones that are dedicated to the discussion of either CE or FFF, their particular focus was on environmental, engineered, or food-related nanomaterials [41–45].

4 Experimental and Instrumental Methodology

Because our chapter involves two separation techniques, FFF and CE, they are introduced in parallel in the following sections with equal importance, i.e., discussion order is not relevant to the importance of contribution by each technique to the field.

4.1 Field Flow Fractionation

4.1.1 Flow Field Flow Fractionation

There are several advantages of applying FFF for separation of bioconjugated nanomaterials and the analysis of nanoparticles used in drug delivery. Firstly, FFF can separate analytes that range in size, from 1 nm to 100 μm , matching well with the dimensions of nanomaterials and their bioconjugates employed in biomedical research. Second, comprehensive analysis can be performed on the analyte using hyphenated instrumentation (i.e., light scattering detectors and mass spectrometers) or offline techniques after fractionation. Third, due to a lack of a stationary phase in FFF, there are no shear forces that are applied directly on the analytes. This results in a “soft” separation, which is especially ideal for proteins that may be susceptible to structural changes. Additionally, FFF channels are compatible with a range of both aqueous and organic solvents, which, in most cases, permits the analyte to retain a native state.

The most commonly used FFF technique in the analysis of nanomaterials and their bioconjugates is flow field flow fractionation (F4), because its instrumentation and implementation are simpler and relatively more mature than other FFF techniques. In addition, it is able to fractionate analytes that come in a wide size range. Thus, this part of our book chapter will focus on this particular FFF technique.

F4 instrumentation is comprised of fluid pumps, a channel, flow control units, and a sample introduction system. The basic set-up of F4 is schematically represented in Fig. 3.1. Typical F4 channel dimensions are 20–50 cm long, 2–3 cm wide, and 0.01–0.05 cm deep [46]. The channel is made by fastening a semipermeable membrane, which is permeable to the carrier but not the analyte, and a spacer between blocks that can either contain metal or ceramic semipermeable frits or are constructed of nonpermeable solid Plexiglass plate. The thickness and shape of the spacer determine the dimensions of the separation channel [24, 47]. Samples are introduced into the channel through manual injection or through an autosampler that is also typically used in high-performance liquid chromatography (HPLC).

F4 uses an axial channel flow and a perpendicular cross flow to separate analytes by hydrodynamic radii in two steps. In the first step, an external force is applied to the solute zones in the ribbon-shaped channel forcing the analytes into a narrow band on the bottom channel wall, known as the accumulation wall. This focusing step overall has no net flow of fluid along the channel and is essential to achieve good resolution. In the second step, a laminar flow, delivered by a standard HPLC pump, is applied. Common flow rates range from 0.5–5 mL/min [46]. A portion of the fluid entering the channel

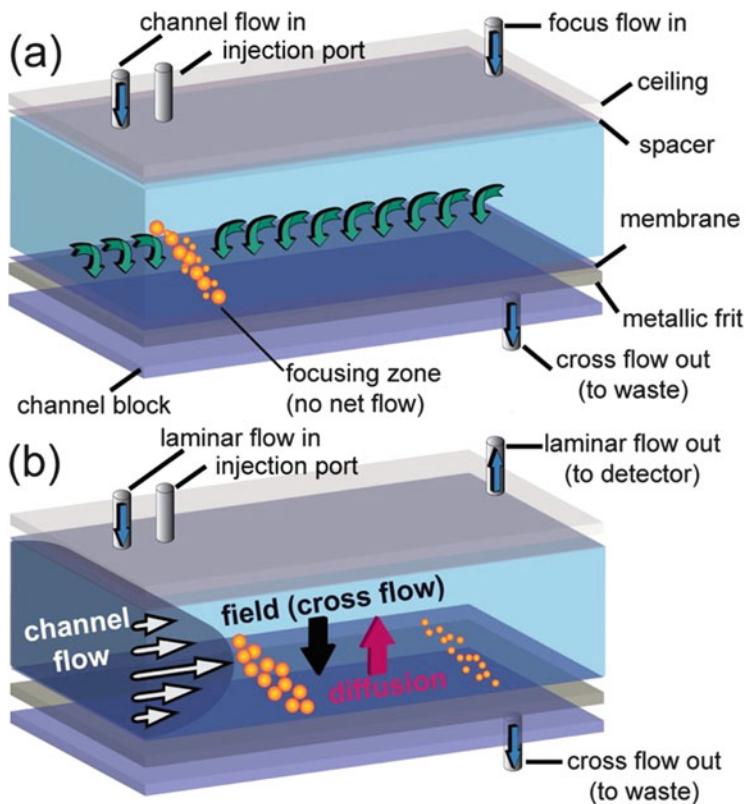


Fig. 3.1 The AF4 principle in which the eluent is pumped from the inlet to the outlet and the cross flow is applied perpendicular to the eluent flow. The first step (a) is known as the focusing step. The second step (b) is the separation process. (Reprinted with permission from Ref. [48]. Copyright 2015 American Chemical Society)

passes through the membrane to create a downward crossflow that pushes the analytes toward the membrane. The analytes then migrate back toward the channel center via Brownian motion. The remaining channel fluid flows in a laminar fashion from inlet to outlet, resulting in a parabolic elution profile. Hence, the center of this parabolic flow has a faster flow velocity whereas the edges of the channel are slower. The mass center of the analyte within this parabolic flow profile depends on the balance between its diffusion motion and the strength of the flow force: things diffusing more towards the center of the flow would be eluted earlier than those located closer to the accumulation wall. Therefore, analytes with the smallest sizes or the highest diffusion coefficients will be eluted earliest [35, 48].

Currently, there are three subtechniques of F4, which include asymmetric flow field flow fractionation (AF4), symmetric flow field flow fractionation (SF4), and hollow fiber flow field flow fractionation (HF5) [33]. Of these, AF4 is the most

developed [34]. Typical SF4 channels are symmetrical in shape, with the inlet and outlet opening in the same direction; but the most common modern instrumentation of F4 uses a trapezoidal-shaped spacer to maintain a constant axial flow velocity, and thus, is termed asymmetrical F4 (AF4) [49]. Moreover, in SF4 both of the external blocks of the channel are constructed with semipermeable porous frits, and in AF4, the bottom block contains semipermeable frits while the top block is a nonpermeable Plexiglass plate [46, 50]. HF5 is a cost-effective miniaturized FFF technique in which a hollow semipermeable polymeric or ceramic membrane serves as a cylindrical channel. HF5 can be coupled to detectors for analyte characterization.

Giddings' group explains the theory of F4 in depth [22, 23]. Briefly, the ratio between the retention time (t_r) and dead time (t_0), described by Eq. 3.1, is used to calculate the analyte retention (R) [22, 23, 50].

$$R = \frac{t_0}{t_r} \cong 6\lambda \quad (3.1)$$

The time it takes for a particle to travel through the channel without crossflow retention is referred to as the dead time and is solved by the following Eq. 3.2, in which V_0 refers to the channel void volume and V represents the flowrate of the channel [22, 50].

$$t_0 = \frac{V_0}{V} \quad (3.2)$$

The retention parameter, λ , which is related to the crossflow rate, V_c , the channel thickness, w , and the particle diffusion coefficient, D , [23] can be calculated using the following equation:

$$\lambda = \frac{DV_0}{V_c w^2} \quad (3.3)$$

At high retention levels (i.e., $R < 0.15$), t_r can be approximated with Eq. 3.4 [23]:

$$t_r = \frac{t_0 V_c w^2}{6DV_0} = \frac{t_0}{6\lambda} \quad (3.4)$$

Furthermore, using the Stokes-Einstein equation, the diffusion coefficient for spherical nanoparticles in a fluid with viscosity η , at an absolute temperature T , can be calculated by Eq. 3.5. The diffusion coefficients for proteins and other biomolecules can be acquired from literature values. The hydrodynamic radius is denoted as r_h and k_B denotes the Boltzmann's constant [32].

$$D = \frac{k_B T}{6\pi\eta r_h} \quad (3.5)$$

In order to calculate the relative recovery (RR) of nanoparticles in various carrier fluids used in FFF, Eq. 3.6 can be used, where A is the peak area of the nanoparticle in the studied carrier fluid and A^* is the peak area in the reference run.

$$RR = \frac{A}{A^*} \times 100\% \quad (3.6)$$

A deterring issue of F4 is sample loss due to analyte-membrane interactions. This can lead to inaccurate quantitation, and the collection of the fractions can be challenging. In order to minimize this loss while maximizing size resolution, extensive optimization is required of the carrier fluid composition and flow rates [51]. Therefore, for separation and characterization of bioconjugated nanoparticles with F4, carrier fluid compositions must be optimized for suitability by considering the separation of the nanoparticles as well as maintaining the integrity and native structures of the biomolecules.

Schachermeyer et al. studied the membrane adsorption of polystyrene nanoparticles and two proteins (IgG and HSA) when the carrier fluid contained various types of ionic species at high concentrations and biologically relevant pH values. Our group found that maintaining high electrostatic repulsion in F4 is essential for high recovery of NPs in high ionic strength buffers. Additionally, using weakly dissociated anions or particles conjugated with weak anions as functional groups can improve the recovery of porous nanoparticles at high ionic strengths. This phenomenon is due to the Donnan exclusion effect in which nanoparticles with higher crosslinking capacity have more occluded liquid-phase inside and are more resistant to adsorption in the carrier fluid with high ionic strength induced by weakly ionized anions [52].

With regards to the separation of proteins from nanoparticle surfaces, the protein conformation needs to be taken into consideration since the proteins ultimately determine the surface property of the nanoparticles as well as the electrostatic or hydrophobic interactions with the membrane used in FFF. Ashby et al. determined that the kinetic properties of nanoparticle-protein interactions can be probed with F4 by taking into consideration the effect of the carrier fluid on dissociation rates of proteins off of NPs, as illustrated in Fig. 3.2. Briefly, our group used F4 and LC-MS/MS to screen for proteins that bind to NPs with fast association/dissociation rates, a feature which is not possible with traditional centrifugation methods. To accomplish this feat, our group used 10 mM phosphate buffer at $\text{pH } 7.5 \pm 0.1$ with 0.025% FL-70 for the carrier fluid and 10 mM phosphate buffer at biological pH ($\text{pH } 7.4$) was used to incubate the NPs with the proteins before separation with F4 [53].

Ashby et al. used asymmetric flow field flow fractionation to separate miRNA carriers (i.e., proteins, lipoprotein particles, and exosomes) in serum and RT-qPCR to screen miRNA distributions in the carriers as a possible method to profile miRNA biomarkers for cancer diagnosis. The AF4 carrier fluid used in this study was $1 \times \text{PBS}$ (10 mM phosphate at $\text{pH } 7.4$, 137 mM NaCl, 2.7 mM KCl, and 1.0 mM MgCl_2). Extensive optimization was done on flow profiles in order to efficiently

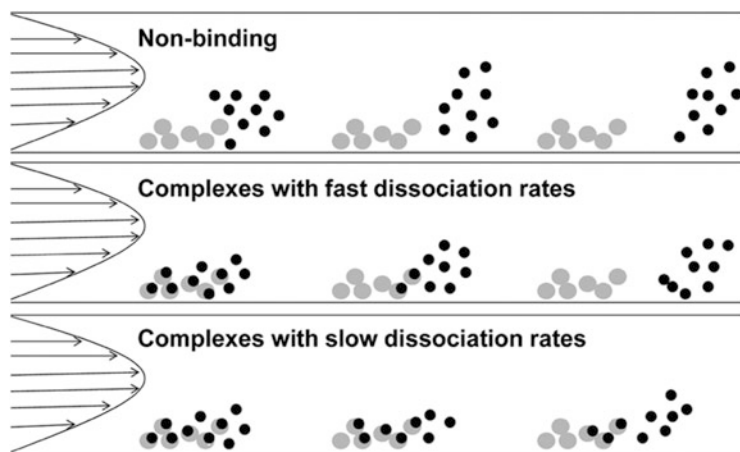


Fig. 3.2 Dissociation of proteins from nanoparticles (NPs) in AF4 allows for differentiation between the slowly and rapidly dissociating NP-protein complexes. The gray circles represent the NPs and the black circles symbolize proteins. (Reprinted with permission from Ref [53]. Copyright 2013 American Chemical Society)

separate the carriers. Ramp down of the crossflow from 3.0 mL/min to zero crossflow was analyzed over the course of 30, 20, and 15 min with the latter having better resolution and quicker elution of the analytes with little peak tailing. Also, to further improve the resolution, the crossflow was kept at 3.0 mL/min for 5 min before the 15-min ramp down, as shown in Fig. 3.3. More detail on the flow profile can be found in the article [54].

4.2 Capillary Electrophoresis

4.2.1 Capillary Zone Electrophoresis

Capillary electrophoresis (CE) consists of a bare fused silica capillary with an inner diameter typically ranging from 20 μm to 150 μm . The inlet and outlet are submerged into the background electrolyte to complete the circuit, and injection is via hydrodynamic or electrokinetic injection on the nanoliter scale. After the application of a high voltage to this system, the injected sample will be separated based on the size and charge. Each ion has its own apparent mobility, which can be calculated by the following equation:

$$\mu_{app} = \frac{L_d / t_m}{V / L_t} \quad (3.7)$$

L_d is the effective length from the inlet to the detector, L_t is the total length of the capillary, t_m is the migration time, and V is the voltage applied.

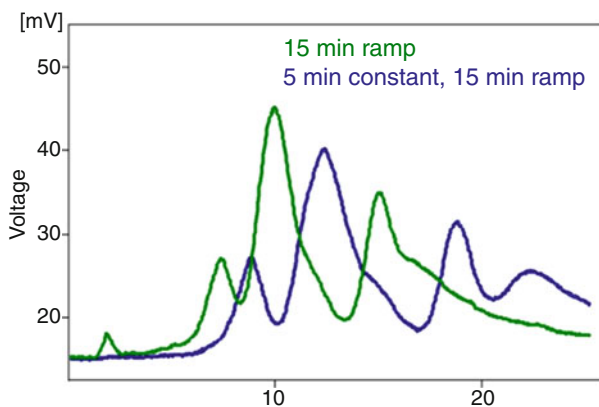


Fig. 3.3 To improve resolution of analytes, a 5-min constant crossflow was used before the AF4 separation which was performed over a 15-min ramp down from 3.0 mL/min to zero crossflow. (Reprinted with permission from Ref [54]. Copyright 2014 American Chemical Society)

The electroosmotic flow (EOF) is another component critical to CE, and it is caused by the bulk movement of the double diffuse layer, electrostatically attracted to the negatively charged silanol wall, in the background electrolyte after voltage application. The following equation explains the calculation of the EOF.

$$\mu_{eof} = \frac{\varepsilon\zeta}{4\pi\eta} = \frac{L_d / t_{\text{marker}}}{V / L_t} \quad (3.8)$$

ε is the relative permittivity of the buffer, ζ is the zeta potential of the capillary wall, and η is the viscosity of the buffer electrolyte. EOF can also be calculated using the same equation for the electrophoretic mobility, except t_{marker} is used to denote the time of an internal standard or marker. The internal standard chosen should be a neutral marker or a molecule that is only affected by the EOF. From the apparent mobility and the electroosmotic flow, each analyte's electrophoretic mobility can be obtained.

$$\mu_{em} = \mu_{app} - \mu_{eof} \quad (3.9)$$

Capillary zone electrophoresis (CZE) is the standard mode of CE. The migration order is according to the charge to size ratio in which the most positive ion with the smallest hydrodynamic diameter migrates first, and the most negative ion with the smallest hydrodynamic diameter migrates last. Figure 3.4 shows the general migration order. However, there are variations in the modes of CE as discussed in the following sections.

4.2.2 Affinity Capillary Electrophoresis

Affinity CE (ACE) is another mode of CE to study nanoparticles, and it can be applied to observe the interaction with proteins [55, 56]. Li et al. was able to

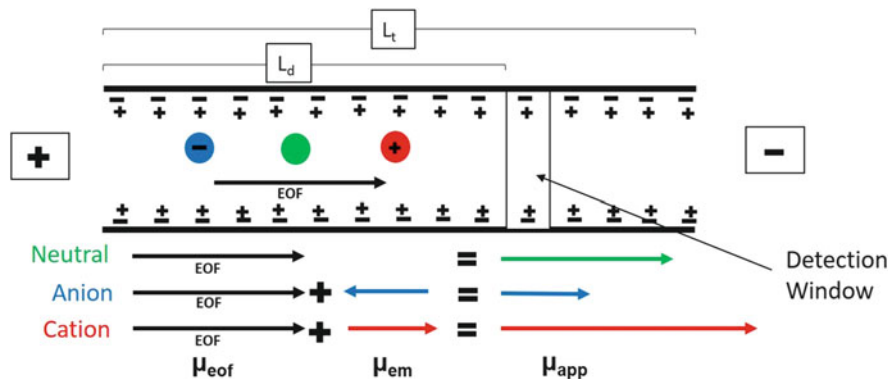


Fig. 3.4 Schematic of the separation order in CE.

differentiate between fast and slow dissociation kinetics by using both CZE and ACE to analyze the interaction between bovine serum albumin (BSA) with Fe_3O_4 nanoparticles and with Au nanoparticles [57].

Slow dissociation and fast dissociation kinetics can be analyzed using this system. For slow dissociation reactions, the nanoparticle-protein complex can be seen, and the peak area varies with the concentration of ligand in the background electrolyte. In this case, CZE is used. On the other hand, fast dissociation reactions can be monitored by observing the mobility shift of the receptor instead of the formation of a nanoparticle-protein complex. In the case of fast dissociation, ACE is used. The ratio of bound nanoparticles to total nanoparticles in CZE, θ , or the ratio of $\Delta\mu$ to $\Delta\mu_{max}$ in ACE (see Eq. 3.9), can be plotted against the ligand concentration to fit the Hill equation.

$$\theta = \frac{NP_{bound}}{NP_{total}} = \frac{(\mu - \mu_{free})}{(\mu_{max} - \mu_{free})} = \frac{\Delta\mu}{\Delta\mu_{max}} \quad (3.10)$$

μ , μ_{free} , and μ_{max} are the electrophoretic mobilities when there is a certain concentration of protein, when there is no protein, and when there is a saturated amount of protein in the background electrolyte, respectively.

Using the Hill equation, dissociation equilibrium constants and the binding cooperativity of a NP-protein complex can be calculated.

$$\theta = \frac{[protein]^n}{K_D^n + [protein]^n} \quad (3.11)$$

θ is the protein-bound nanoparticle fraction (bound nanoparticles/total nanoparticles), n is the binding cooperativity, and K_D is the dissociation equilibrium constant. The protein-bound nanoparticle fraction is based on the peak area ratio of the protein-bound and total nanoparticles. A flow chart to determine the appropriate

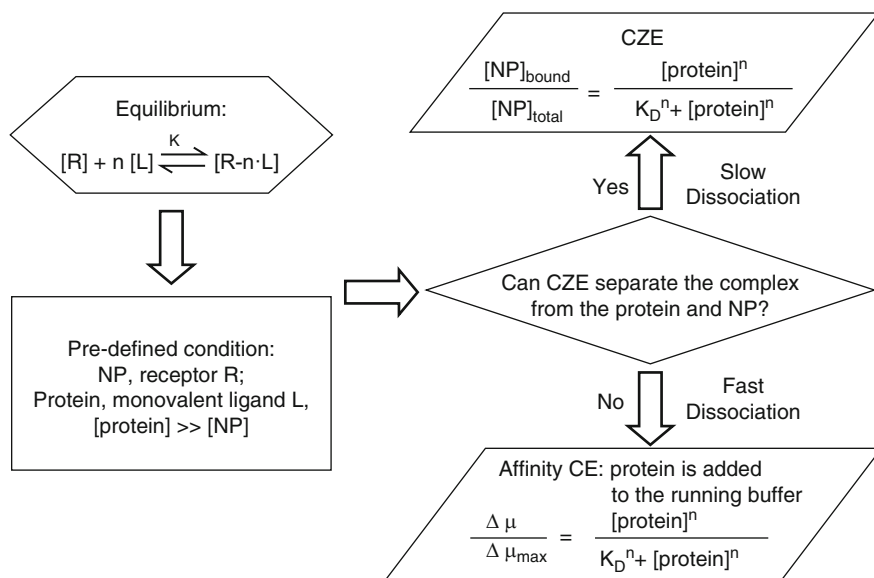


Fig. 3.5 Flowchart of CE methods for studying NP-protein interactions. (Reprinted with permission from Ref. [57]. Copyright 2010 American Chemical Society)

CE mode depending on the application is shown in Fig. 3.5 [57]. CZE and ACE can be used to understand the interactions between nanoparticles and proteins as well as extracting kinetic information.

4.2.3 Micellar Electrokinetic Chromatography

To separate neutral compounds or study an analyte with low mobility in normal polarity mode, Micellar Electrokinetic Chromatography (MEKC) is a technique commonly used for these purposes. In MEKC, surfactants are included in the background electrolyte above their critical micellar concentration. Micelles act as a pseudostationary phase, and analytes can partition between this pseudostationary phase and the aqueous phase.

Various surfactants can be used in the separation of analytes via MEKC. All surfactants have their own sizes and charges that affect their own electrophoretic mobility and their inclusion in the background electrolyte can affect the EOF. Thus, the charge and the size of the surfactant should be considered when designing MEKC methods. The most commonly used surfactant is sodium dodecyl sulfate (SDS), which was also notably used in the first development of MEKC [58]. SDS carries a negative charge to create a delay in the migration time of the analyte. Other common surfactants include positive ones, such as cetrimonium bromide (CTAB) and tetradecyltrimethylammonium bromide (TTAB), as well as nonionic ones, such as Brij-35 and Tween 20. Depending on the purpose, the most suitable surfactant can be chosen for separation in CE. For application to nanomaterial separations, SDS has been the prevalent option.

The use of SDS can improve the separation of metal nanoparticles. Liu et al. found that 5.3 and 19 nm AuNPs could not be separated with good resolution when the background electrolyte did not include SDS. SDS can adhere to the surface of AuNPs, affecting their surface chemistry, and act as their stabilizers as well. Due to the adsorption of SDS molecules, the concentration of the surfactant can affect the electrophoretic mobility of AuNPs; furthermore, the trend of change in electrophoretic mobility depended on the size of the nanoparticles. At lower surfactant concentrations, the charge-to-size ratio of small nanoparticles is larger. On the contrary, the charge-to-size ratio of larger nanoparticles is larger at higher surfactant concentrations. This is due to the charge of the nanoparticle not being limited by the number of SDS molecules allowed to attach to the surface at higher concentrations of SDS, and larger nanoparticles have more surface area to link to SDS molecules [59].

Ciriello et al. used a stabilizer, poly(sodium4-styrenesulfonate) (PSS), for the separation of AuNPs with sizes ranging from 5 to 20 nm. Similar to the behavior of SDS, PSS can adhere to the surface of AuNPs and induce an electrophoretic mobility difference and a modification of the EOF. This polyelectrolyte contains a hydrophobic and negatively charged hydrophilic portion, providing an electrostatic and steric stabilization and prevention of aggregation when adsorbed onto AuNPs. They found a saturation percentage of 1% PSS in which AuNPs are fully covered by the PSS molecules. They validated their technique by comparing with the sizes of nanoparticles found in transmission emission microscopy. In addition, the addition of PSS creates an electrophoretic drag that can improve separation of AuNPs [60]. In general, several parameters, such as buffer concentration, buffer pH, buffer type, voltage, and injection type (hydrodynamic vs. electrokinetic), need to be considered for CE analysis as these can affect separation.

4.2.4 Separation Efficiency

Assessment of CE performance and separation efficiency is important, and the sharpness and distance between peaks need to be optimized. They can be evaluated based on the resolution of peaks and the theoretical plate number. Plate height number is used in the evaluation of other chromatographic techniques as well, and it is defined by the relationship where L = length of the column and N = theoretical plate number.

$$H = L/N \quad (3.12)$$

The number of theoretical plates is defined as the following:

$$N = \frac{L_d^2}{2Dt_m} = \frac{(\mu_{em} + \mu_{eof})VL_d}{2DL_t} \quad (3.13)$$

where L_d is the effective length from the inlet to the detection window, D is the diffusion coefficient of the solute, t_m is the migration time, μ_{em} is the electrophoretic mobility, μ_{eof} is the electroosmotic flow, V is the voltage applied, and L_t is the total length of the capillary.

Peak resolution is defined by the ratio of the difference in migration times and the average of the width of the two peaks.

$$R = \frac{t_A - t_B}{W_{b,avg}} \quad (3.14)$$

t_A = migration time of peak A , t_B = migration time of peak B , and $w_{b,avg}$ is the average peak width of the two peaks at baseline. By calculating these variables, the separation performance in CE can be evaluated and validated.

5 Key Research Findings

Apart from the electrical, optical, and magnetic properties that nanomaterials individually possess, which allot their use as effective biomedical tools, conjugation with proteins, oligonucleotides, drugs, and other biomolecules is a critical step that facilitate their applications in biomolecular assays, in vivo imaging, and cancer targeting therapeutics [61, 62]. In the following sections, we will review analytical studies on the separation and characterization of bioconjugated as well as drug-loaded nanomaterials via FFF and CE.

5.1 Field Flow Fractionation for Characterization of Nanomaterials and Their Bioconjugates for Drug Delivery Applications

Many of the applications of SF4 or AF4 have been centered on characterizing nanomaterials prepared for biomedical purposes, such as drug delivering nanoparticles and nano-sized materials for target imaging. These nanoparticles are mainly metal oxide, metal, quantum dots, liposomes, and the bioconjugated entities. The works reviewed below will prove the utility of this technique in analysis of nanomaterials and their bioconjugates including medicinal molecules.

5.1.1 Metallic Nanoparticles

Metallic nanoparticles are becoming more frequent in medical applications and in sensors because of their reactive surfaces and unique optical properties. For example, gold nanoparticles (AuNPs) have been used optimized as nanozymes for aptasensor applications [63] and silver nanoparticles (AgNPs) have been complexed as highly selective fluorescent nanosensors for dopamine [64]. Herein we present articles that have applied FFF for the characterization of metal-based nanomaterials conjugated with biomolecules.

Safenkova et al. conjugated eight distinct antibodies from immunoglobulin G (IgG) to AuNPs, which were separated with AF4 and characterized by MALS, UV-Vis, and DLS. These bioconjugated AuNPs were prepared in three different ways: with a single conjugate, in a mixture of all eight antibodies, and in a

concentrated solution of all eight antibodies. They found that the mixtures of the eight conjugates had equal average radii compared to the single conjugated sample and that the concentration of the conjugate did not influence the size. In addition, they found that the AuNPs alone had a different distribution compared to the bioconjugated materials. Essentially, the AuNPs alone were monomodally distributed and the bioconjugated AuNPs were bimodally distributed with the second population of the latter being a structural influence from the conjugate during synthesis [65].

Although AgNPs have been separated by AF4 extensively [66, 67], their separation with hollow fiber F4 (HF5) has only recently been studied. HF5 was coupled to MALS for the characterization of AgNPs coated with either polyvinylpyrrolidone (PVP) or PVP with SiO₂. PVP is a water-soluble polymer used as a binder in the production of medical drugs. Regardless of coating, the fractograms displayed no void peak and showed that these types of coatings did not influence the elution time of the AgNP peak. Surprisingly, dilution of the coated AgNPs changed the overall shape of the particle from rod- and chain-like to spherical morphologies due to agglomeration events which were measured through the release of Ag⁺ ions [68]. The authors have also separated solid AgNPs from dissolved Ag⁺ ions with HF5 [69].

AF4, hyphenated to UV-Vis and ICP-MS, has also been used to determine the protein corona formed on AgNPs after incubation with plasma proteins. Wimuktiwan et al. found that within 5 min of incubation, a stable protein corona was formed, shown in Fig. 3.6. Additionally, after 24 h, they were able to identify the protein-corona stabilized AgNPs with AF4. However, the group did not assess the corona formation after incubation with protein-rich plasma itself [70].

Selenium nanoparticles (SeNPs), which can catalyze the generation of superoxide anions, have been applied in nanomedicine as drug carriers [71] and potential chemotherapeutic agents [72]. Their use as delivery agents has been supported due to the fact that these materials do not induce toxicity at low doses. Although most characterization of SeNPs occurs during synthesis, this method does not account for the alteration stabilizers, biomolecules, or biological matrices have on the sizes of SeNPs.

Pornwilard et al. studied the effect of gastrointestinal conditions (shifting the pH of the solutions to pH 2 for gastric and to pH 7 for intestinal conditions) on SeNPs through characterization with AF4-ICP-MS. They used biomolecules (pectin, alginate/pectin, ovalbumin, and β -lactoglobulin) to coat SeNPs before incubation in the two solutions that mimic gastrointestinal fluids. They found that there were shifts in the fractograms of SeNPs after incubation in the GI conditions, due to the chemistry of the conjugates. At pH 2, all four coating molecules were negatively charged, while at pH 7 only the two proteins were negatively charged. They found that the GI conditions, as well as the bioconjugates, stabilized the SeNPs. Additionally, they looked at the effects of adding enzymes into the two GI-conditioned SeNPs. For the polysaccharide coated particles at pH 2, there was a decrease in size after the introduction of pepsin (an enzyme to mimic the GI conditions of the stomach) to the pectin coated particles but no size change in the alginate/pectin conjugated

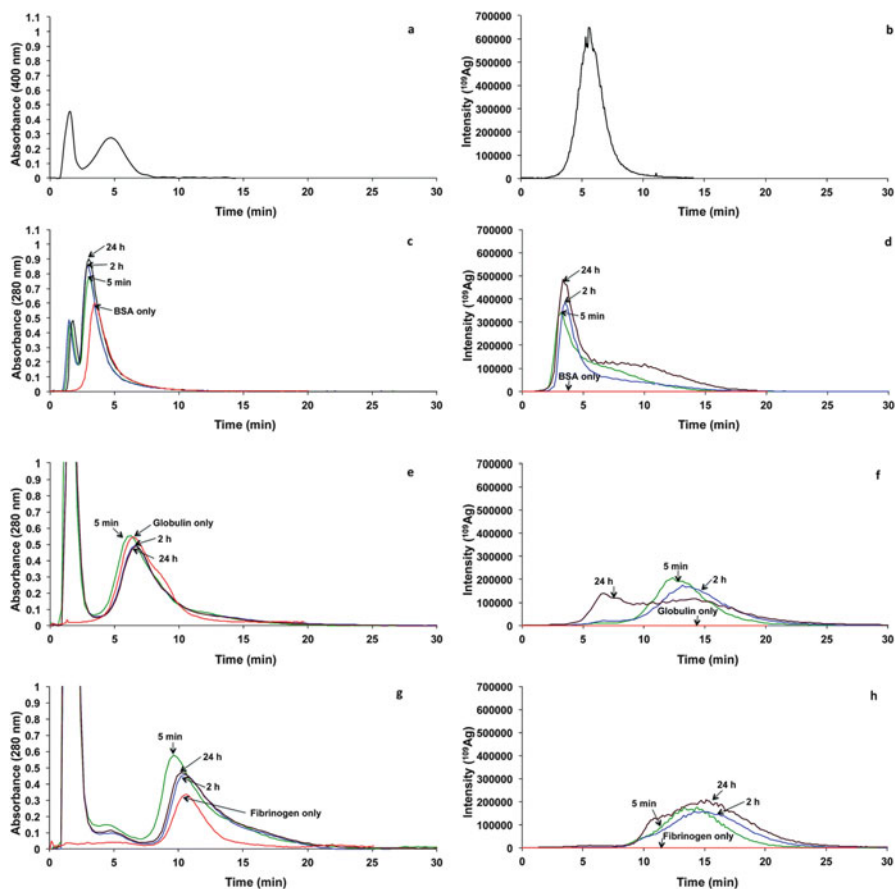


Fig. 3.6 Fractograms of 2.6 nm tannic stabilized AgNPs with UV-Vis (a, c, e, g) and ICP-MS detection (b, d, f, h). The AgNPs were incubated with BSA (c and d, red), globulin (e and f, red), and fibrinogen (g and h, red) for 5 min (green), 120 min (blue), and 24 h (brown). (Reproduced from Ref. [70]. Copyright 2015 The Royal Society of Chemistry)

particles. For the protein coated materials, incubation with pepsin resulted in a size increase for ovalbumin coated particles and the loss of the second peak seen in β -lactoglobulin coated SeNPs. At pH 7, they used pancreatin-bile extract as the enzyme to mimic the GI conditions of the intestine. They observed a decrease in size for all materials regardless of coating due to an increase in electrostatic repulsions. Regardless of the shifts they observed, more than 90% of SeNPs were present after the GI digestion and fractionation with AF4 [73].

5.1.2 Metal Oxide Nanoparticles

Metal oxide nanoparticles are extensively used in industry, agricultural products, medicine, and cosmetics [74]. For example, superparamagnetic iron oxide

nanoparticles (SPION) have been modified for chemotherapeutic applications [75]. Zinc oxide (ZnO) and titanium dioxide (TiO₂), which can be dispersed in a variety of materials, from personal care products to sensors, possess antimicrobial and disinfecting properties. Therefore, these materials have been increasingly used in nanomedicine as drug carriers with antibacterial capacities [76, 77]. The following articles used FFF for the separation of bioconjugated metal oxide nanoparticles.

Our group studied the formation of the protein corona on SPIONs after incubation in depleted human serum with AF4 by screening SPION-protein interactions based on dissociation rates [53], and we isolated the SPIONs with the intact hard corona [78]. The size of the SPIONs clearly increased after incubation with the serum, as inspected by AF4. The proteins in the hard corona were digested and analyzed with 2-dimensional nano-LC-MS/MS to determine the protein composition of both the soft and hard coronas, which is schematically represented in Fig. 3.7. We found that increasing the NP core size as well as using hydrophobic surface ligands attracted more proteins to form a more dynamic corona. These studies demonstrate the utility of an open-channel separation technique like AF4 in elucidating the formation of the protein corona, which can be useful in guiding the design of biocompatible nanomaterials for medical applications.

5.1.3 Polymeric Nanoparticles

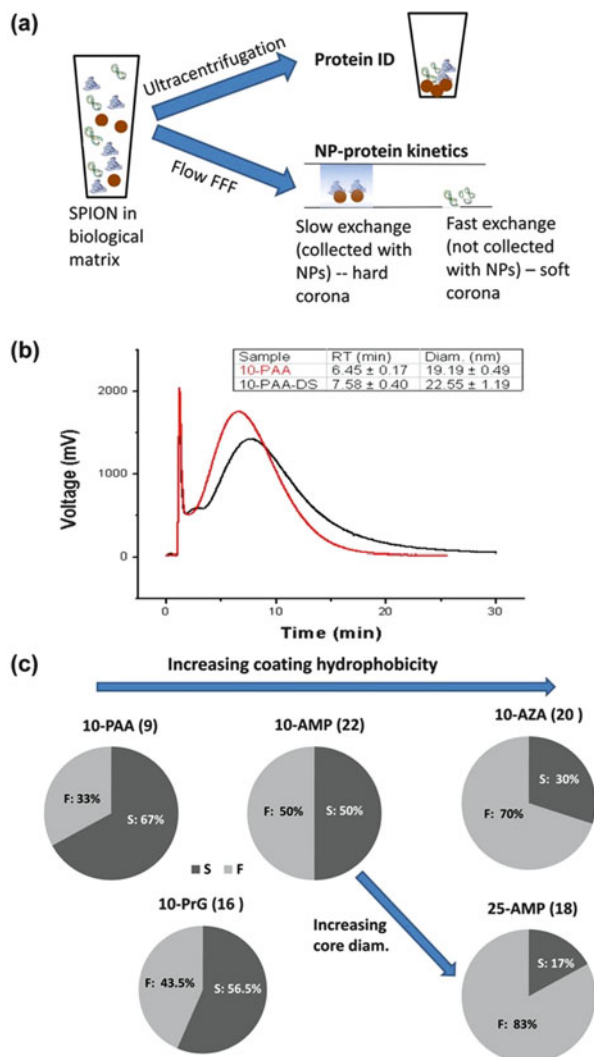
Polystyrene nanoparticles are versatile materials due to their stability in simple dispersants and complex matrices as well as their low toxicity and ability to be effortlessly functionalized. Here we introduce studies that have applied FFF for characterization of bioconjugated nanomaterials as well as drug-loaded particles for drug delivery.

Weber et al. used AF4 to separate free plasma proteins, without disturbing the weak interactions of low affinity proteins, from the surfaces of polystyrene nanoparticles. After incubation in serum, this group used centrifugation to separate the hard corona proteins and used AF4 for the soft corona which contains the low affinity proteins. This conclusion contradicts with what we have found in our work [53, 78] probably due to differences in the flow conditions, channel thickness, and membrane pore size used in these two studies. The authors confirmed the corona compositions with SDS-PAGE and LC-MS and found that the principal component that adsorbed onto the particles was the low-binding affinity protein, human serum albumin [79].

An evolving category of nanoparticles are metal organic framework (MOF) materials which exhibit very large surface areas. These particles are 3D porous inorganic polymer clusters or crystals composed of metal ions and are assembled together with organic ligands. Due to their ability to be modified readily, MOFs can be used in multiple applications ranging from sensors to drug delivery [80].

Recently, Roda et al. loaded MOFs with nucleoside reverse transcriptase inhibitors (NRTIs) for drug delivery in HIV therapy. The direct administration of NRTIs is complicated; poor stability of these types of drugs in biological media limits cellular uptake while the inefficiency of intracellular kinases to metabolize the drugs into the correct derivatives reduces the drugs ability to act as a therapeutic. Not only do

Fig. 3.7 (a) The scheme for determination of the hard and soft corona formed around SPIONs. (b) Fractograms of SPIONs functionalized with the surface ligand 10-PAA (red) and 10-PAA incubated with depleted serum (black). (c) The pie charts quantify the percentage of proteins identified in the hard (dark gray) and soft (light gray) corona. S stands for slow exchange and F for fast exchange. The number in parentheses, following the name of the nanomaterial, represents the total number of proteins identified in the corona. (Reprinted with permission from Ref. [78]. Copyright 2014 ACS Applied Materials & Interfaces)



MOFs overcome these two issues, due to their ability to stabilize the drugs and their derivatives, but also their nontoxic nature makes them optimal drug delivering nanoparticles [81]. Roda et al. examined empty MOFs and correlated the size changes after loading the MOFs with azidothymidine (AZT, a commonly used NRTI drug) azidothymidine monophosphate (AZT-MP) and azidothymidine triphosphate (AZT-TP) with the AF4-MALS results. They measured the particle size distribution (PSD), obtained with the AF4-MALS root mean square (rms) radius values. Both the empty MOF and the MOF-AZT samples had identical PSD values at approximately 81 nm while the MOF-AZT-MP and MOF-AZT-TP had radii of 90 and 97 nm, respectively. These size increases for the phosphorylated drug

MOF-delivering samples were attributed to the binding and bridging effects of the drug to the MOFs. Interestingly, this group found that, although the theory of FFF suggests that smaller particles elute first, the smaller unloaded MOFs eluted slower than the larger drug-loaded MOFs. They found that the zeta potential of their samples played a critical role in this elution order due to the two phosphorylated drug-loaded MOFs having negative zeta potentials; therefore, these particles would be repelled away readily from the negatively charged polyethersulfone membrane channel compared to the empty MOF which is smaller in size but has a positive zeta potential. Additionally, this group studied the morphological stability of the loaded MOFs after 24 h. Ultimately, each of the loaded MOFs as well as the empty MOF were stable over time. The tri-phosphorylated drug was more stable in the MOF, compared to the monophosphorylated drug, and this could be due to the binding constant of the drug to the MOF being higher for the tri-phosphorylated drug [81].

5.1.4 Liposomes

Liposomes are biocompatible drug delivering carriers due to their hydrophobic interactions with cellular receptors. The subsequent articles focus on the analysis of bioconjugated NPs and drug delivery NPs through the application of FFF.

Hinna et al. used AF4 to measure the exchange between small-drug-loaded liposomes with large acceptor liposomes that mimic the interactions between the carrier liposomes and “biological sinks.” The drug they used was p-THPP (5,10,15,20-tetrakis(4-hydroxyphenyl)21H,23H-porphine). After preparing the liposomes, they used AF4 to determine the size distribution of both donor and acceptor liposomes and they were able to reproducibly separate these two species, depicted in Fig. 3.8. They then coupled AF4 with UV-Vis and off-line HPLC to quantify the model drug content in the donor and acceptor fraction; they simultaneously quantified drug transfer and release to an aqueous phase and determined the transfer kinetics of p-THPP to be first order with a half-life of 300 min [82].

Targeted alpha (α)-particle therapy (TAT) is a form of radioimmunotherapy in which nuclides decay into radioactive daughters emitting α -particles that kill tumor cells, via short 70–100 μm energy paths, while evading surrounding normal cells [83]. TAT is considered to be both highly potent and specific in the therapeutic application for ovarian, breast, colon, and prostate cancers. Nanomaterials have recently been considered as vectors capable of transporting α -emitting particles to cancer cells. However, a limitation in using these vectors is keeping the daughter isotope bound to the nanomaterial after the parent nucleoside decays and emits the α -particle.

Huclier-Markai et al. monitored the stability of lead-212 (parent nuclide)/bismuth-212(daughter isotope) radionuclide pair encapsulated by liposomes in vitro using AF4 coupled to MALS and a gamma (γ) ray detector. This group began their analysis by preparing liposomes with an average diameter of 109 nm and a polydispersity index of 0.119, optimal for use in TAT. They then labeled the liposomes in two different manners. One set of the liposomes were labeled with indium and the other set was labeled with indium and also encapsulated ^{212}Pb . Using AF4 with a cellulose membrane, coupled to MALS and a UV-VIS detector, they found that there

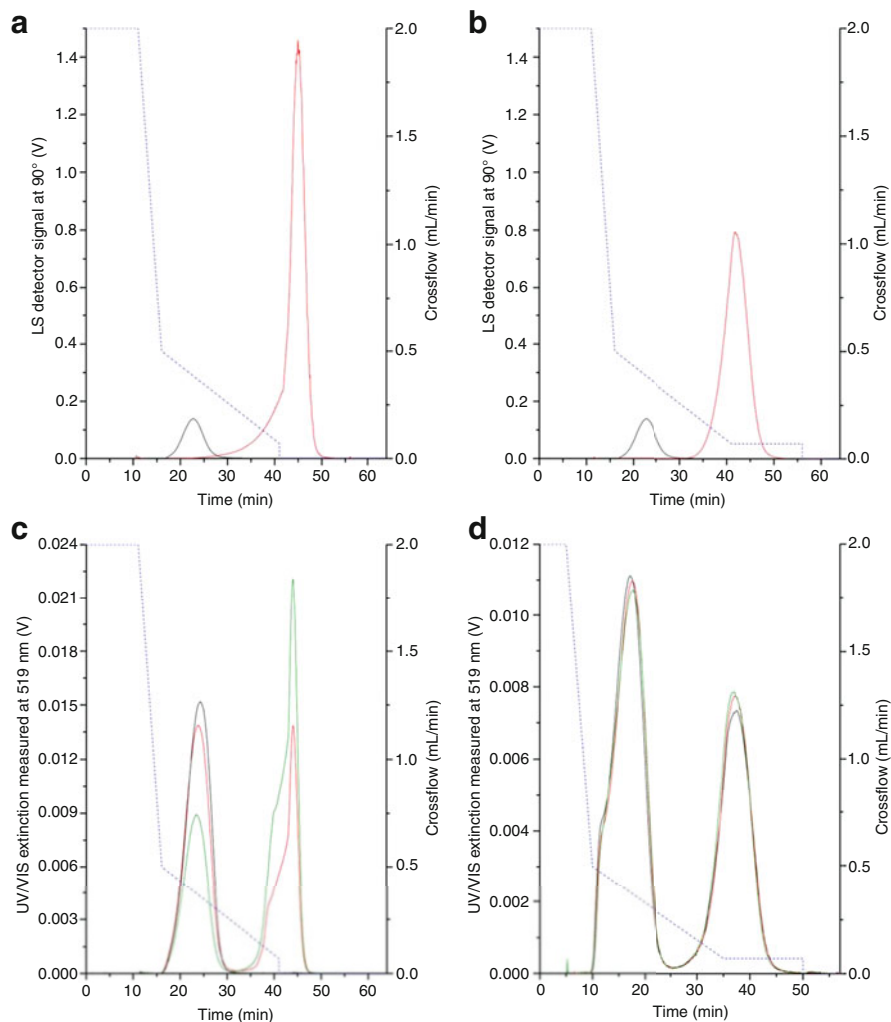


Fig. 3.8 (a and b) Fractograms of (black) donor liposomes were overlaid with those of (red) acceptor liposomes. The dashed blue lines represent the applied crossflow gradients. (a) Donor and acceptor liposomes were prepared by slow extrusion through polycarbonate membranes and were fractionated using a method where zero crossflow was attained around 41–42 min. (b) Donor and acceptor liposomes were prepared by extrusion, freeze-thaw, centrifugation, and fractionated over non-zero crossflow. (c) Fractograms of overlaid (black) donor liposomes with transfer experiment aliquots at (red) 0 min and (green) at equilibrium. (d) Overlaid fractograms of liposomes incubated within channel under low focus flow for (black) 10, (red) 30, and (green) 60 min. (Reprinted with permission from Ref. [82] Copyright 2016 Journal of Pharmaceutical and Biomedical Analysis)

was no significant size increase between the unlabeled liposomes, the indium-labeled liposomes, and the ^{212}Pb encapsulating liposomes and the three different liposome samples eluted at approximately 11 min. Additionally, through the use of the γ -ray detector, the group observed a signal at the 11 min retention time for the

^{212}Pb encapsulating liposomes and calculated 86% efficiency in radiolabeling the liposomes. They measured the stability of ^{212}Pb in liposomes after these species were incubated in human serum for 20 h and found that more than 85% of the liposomes encapsulating ^{212}Pb were stable in the matrix and did not release the daughter isotope. These results are notable due to the fact that the liposomes have a biological period of 14 h in mice and therefore there is both sufficient time for the ^{212}Pb encapsulating liposomes to reach cancerous cells, decay (the half-life of ^{212}Pb is 10.6 h), and release α -particles that can kill cancer cells [84].

5.1.5 Quantum Dots

Quantum dots (QDs) are luminescent semiconductor nanoparticles. Due to their optical properties, QDs are used in multiple applications including sensors and drug delivery. In biological applications, QDs are conjugated with a specific antibody or aptamer for therapeutic and in-vivo applications in complex matrices. The studies mentioned below use FFF for the separation and analysis of bioconjugated QDs.

Moquin et al. investigated the effects of cell culture media on the stability of QDs as well as the time-dependent effects on the hydrodynamic diameters using AF4 coupled to MALS, DLS, and UV-Vis detectors. They coated the CdSe (CdZnS) nanomaterials with three negatively charged ligands and then incubated the QDs in cell culture media. They found that after 24 h, the sizes of the QDs incubated in cell culture media were larger than those of QDs dispersed in water when the QDs were capped with mercaptopropionic acid (MPA) or dihydrolipoic acid (DHLA). The latter had the most dramatic size increase indicating hefty agglomeration, illustrated in Fig. 3.9. This was slightly observed in QDs coated with α -carboxyl- ω -mercapto poly(ethylene glycol) (PEG-COOH) denoting that this ligand was influential in the QDs stability in cell culture media [85].

Bouzas-Ramos et al. coupled AF4 to an ICP-MS to investigate the purification of one-pot synthesized QDs. These materials were separated with AF4 after being capped with ligands that can functionalize to antibodies [86]. This technique can be used to assess the integrity of these materials before their applications in biomedicine.

Menéndez-Miranda et al. used AF4 with on-line ICP-MS to measure conjugation effectiveness between monoclonal IgG antibody and CdSe/ZnS core shell QDs. In order to calculate the bioconjugation efficiency, they used four different molar ratios for analysis with AF4. They found that increasing the QD: antibody ratio would result in an increase in bioconjugation with a 75% efficiency using a 3:1 ratio [87].

5.2 Capillary Electrophoresis for Characterization of Nanomaterials and Their Bioconjugates for Drug Delivery Applications

CE is also quite comprehensive in its analysis of nanomaterials, and separation can be enhanced by selecting the optimal CE mode as described in the experimental section. CE can be applied to the separation of metallic nanoparticles, metal oxide

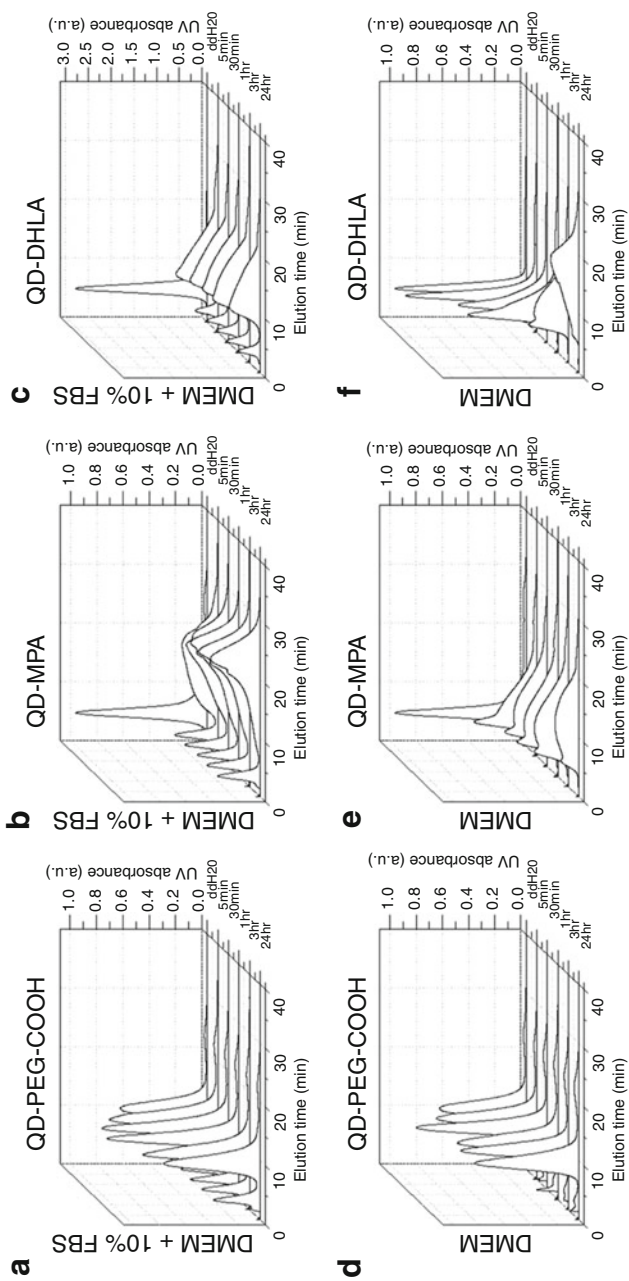


Fig. 3.9 Fractograms of the agglomeration phenomenon of QDs suspended in DMEM (bottom) and DMEM with 10% FBS (top) over 5 min, 30 min, 60 min, 3 h, and 24 h. (Reprinted with permission from Ref. [85]. Copyright 2015 European Journal of Pharmaceutics and Biopharmaceutics)

nanoparticles, polymeric nanoparticles, and quantum dots for the use as imaging tools, delivery agents, and biosensor components. In the following section, we will discuss the most recent revelations for various nanomaterial types.

5.2.1 Metallic Nanoparticles

Many recent key findings for metallic nanoparticles have focused on protein binding. When administering drug delivery nanomaterials into biological systems, it is imperative to understand nanoparticle-protein interactions and how they affect the process of targeting to specific sites. Matczuk et al. studied AuNPs and their interaction with proteins using CE coupled to ICP-MS. The authors first optimized the conditions for CE in order to analyze their samples. They found the best buffer to be 40 mM HEPES at a pH of 7.4 to ensure physiological conditions as well as optimal separation. 15 kV separation voltage and a sample loading pressure of 20 mbar for 5 s were chosen to reduce peak broadening and analysis time as well as prevent protein adsorption to the wall from sample overloading, which shows that optimization of the conditions is highly imperative to CE separation. The method was validated and found to be reproducible by comparing the migration time of AuNPs to that of AuNP-albumin conjugates and comparing the peak areas for intraday and interday analysis. After they calculated capillary recovery values, they found that there was a decrease in the capillary recovery with their largest AuNP at 50 nm due to adsorption of larger proteinaceous conjugates to the capillary wall [88], which can be avoided by a dynamic or permanent coating of the wall [89].

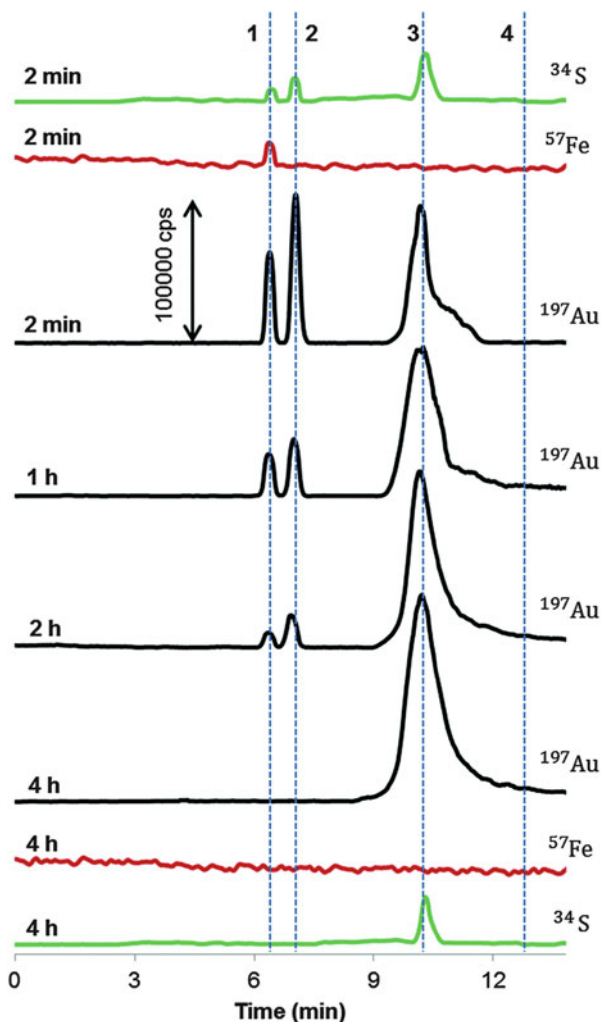
After optimization, Matczuk et al. explored the interactions between individual proteins and AuNPs. First, they found that the interaction between albumin and AuNPs is fast for 10-, 20-, and 50 nm sized particles in that binding was complete after 5 min. However, with 5 nm particles, the interaction is fast in the first 5 min but decelerates afterwards. They explained this mechanism as the change in albumin's structure after binding to nanoparticles over time [88].

Matczuk et al. then observed the interaction of AuNPs with two forms of transferrin: holo-transferrin and apo-transferrin. Again, the kinetics were fast in that equilibrium was attained after 5 min; however, there were more unbound nanoparticles at equilibrium. The authors then proceeded to study the interaction between different proteins in human serum to mimic a real biological system. As seen in Fig. 3.10, they found that albumin was the only protein participating in corona formation, and it eventually displaced the two forms of transferrin due to the contents in the serum matrix [88]. The paper emphasizes the interesting phenomenon of protein-NP interaction, which can depend on parameters such as protein type.

In another study, Matczuk et al. quantified the binding stoichiometry between AuNPs and albumin using CE-ICP-MS. Based on the initial concentrations of albumin and AuNPs and the peak area ratio of the total AuNPs to conjugated AuNPs, they calculated the binding stoichiometries for various-sized nanoparticles [90].

Legat et al. did an extension of the previous study by Matczuk et al. and compared the binding behaviors of spherical and rod-shaped AuNPs, denoted as sAuNPs and rAuNPs, respectively. Furthermore, they found the surface functionalization of

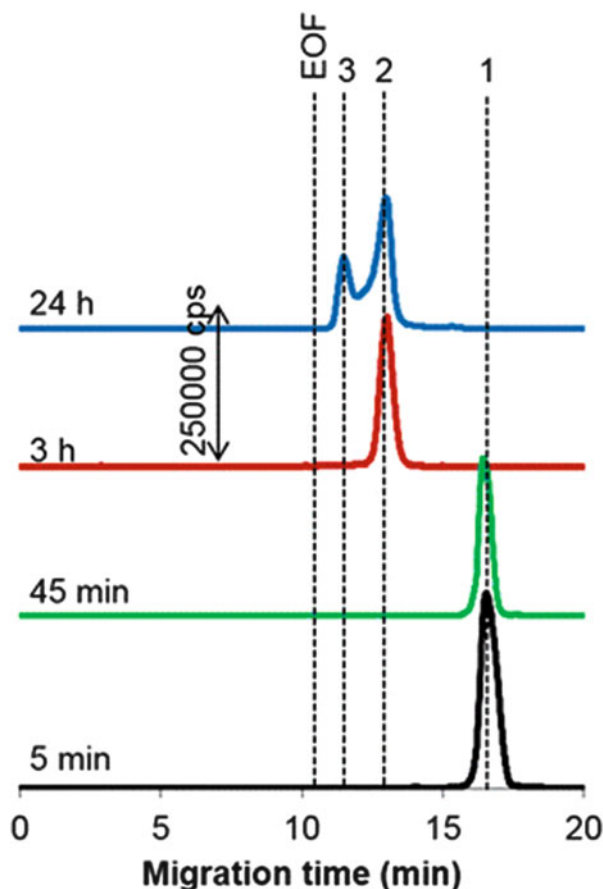
Fig. 3.10 Protein binding after incubation of 19 mg/L of 20 nm AuNPs in diluted human serum. Lines: 1 – holo-transferrin conjugate; 2 – apo-transferrin conjugate; 3 – albumin conjugate; 4 – indication of the migration time for AuNPs. (Reprinted with permission from Ref. [88]. Copyright 2015 Metallomics)



AuNPs affects the binding efficiencies to serum proteins. This work highlights the importance in the effect of AuNPs' characteristics on their functionality. Finally, they introduced sAuNPs and rAuNPs to a mixture of albumin, apo-transferrin, and holo-transferrin. sAuNPs completely changed to the conjugated form with only albumin; on the other hand, rAuNPs underwent slow association with both forms of transferrin proteins of which the apo-transferrin conjugate formed first as seen in Fig. 3.11 [91].

Boulos et al. conducted steady-state fluorescence quenching titration and ACE to extract kinetic information from the interaction between BSA and AuNPs with various surface charges. Polyacrylic acid (PAA), polyallylamine hydrochloride (PAH), and methoxy-polyethylene glycol (PEG) were the anionic, cationic, and

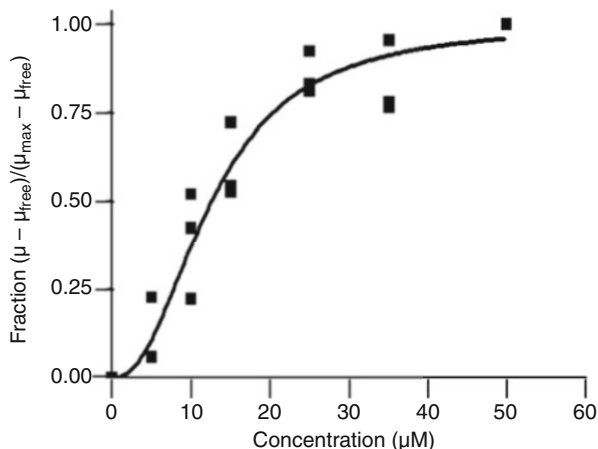
Fig. 3.11 ^{197}Au electropherograms of carboxy-rAuNPs with transferrin and albumin proteins at various incubation times. Peaks: 1 – free nanoparticles, 2 – apotransferrin conjugate, 3 – holo-transferrin conjugate. (Reprinted with permission from Ref. [91]. Copyright 2017 Chromatographia)



neutral polymer surface coatings on the AuNPs, respectively. They included BSA, which has been used as an inner wall coating in CE [92], in the background electrolyte; in effect, this reduced the EOF. By using dimethylformamide as a neutral marker, they normalized the electrophoretic mobility by EOF subtraction. Plotting the ratio of bound nanoparticle to total nanoparticle against the concentration of BSA allowed for derivation of association equilibrium constants from the Hill equation as shown in Fig. 3.12. Overall, they found that BSA adheres to PEG-functionalized AuNPs with similar affinity to charged AuNPs. Compared to the other modified AuNPs, PAH-modified AuNPs had higher affinity to BSA [93].

Nanoparticle modifications, such as those based on thiol derivatives, can improve the stability and reduce aggregation of nanoparticles [94]. López-Lorente et al. studied the effect of two thiol derivative buffer additives on the electrophoretic mobility and separation of Au and AgNPs. In their study, derivatization was performed in capillary via incorporation of thiocetic acid (TA) and thiomalic acid (TMA) in the electrophoretic buffer, which consisted of 40 mM SDS and 10 mM

Fig. 3.12 Plot of the ratio of bound nanoparticles to total nanoparticles against the concentration of BSA. The dissociation constant is calculated via the Hill equation, which was fitted to the curve plotted from pooled data. The data was obtained for PAA-GNRs with increasing concentration of BSA in 5 mM MOPS buffer. (Reprinted with permission from Ref. [93]. Copyright 2013 Langmuir)



3-(cyclohexylamino)-1-propanesulfonic acid (CAPS). The structures of the two thiol-based buffer additives are shown in Fig. 3.13. With TA in the buffer solution, the migration time of AuNPs increased; whereas, the migration time of both Au and AgNPs increased with TMA in the buffer solution as shown in the contour graph in Fig. 3.14. Furthermore, AgNPs had a higher increase in their migration time [95]. The overall structure and other functional groups of the acids seem to alter the strength of the metal-sulfur bond, especially since gold has a higher proclivity than silver to interact with H_2S [96]. The study on thiol derivative buffer additives exemplifies the applicability of CE on the characterization of nanoparticles with SAMs. Furthermore, the characterization of surface-modified nanoparticles can lead to the understanding of the potential effects of these modifications on protein adsorption.

5.2.2 Metal Oxide Nanoparticles

Metal oxide nanoparticles have been directly incorporated into drug delivery systems, and this has been studied by the use of CE to determine the delivery and encapsulation efficiencies. Doxorubicin (DOX) is a drug used in the treatment of various cancer types and the efficiency of this drug is improved by delivery in a carrier system. Gautier et al. loaded DOX- Fe^{2+} onto the surface of PEGylated superparamagnetic iron oxide nanoparticles (SPION). After analyzing the interaction and distribution of doxorubicin-loaded PEGylated SPION (DLPS) via fluorescence confocal spectral imaging (FCSI), the authors optimized the CE conditions for separation of DOX derivative molecules to overcome the challenge of differentiating chemical structure similarities. They found that modification of the capillary wall with the CEofix kitTM from Analis improved the peak shape and use of MEKC enhanced resolution. The group treated MCF-7 breast cancer cells with DOX or DLPS and obtained subcellular fractions via liquid-liquid extraction. These fractions were then analyzed by capillary electrophoresis-laser induced fluorescence (CE-LIF) to differentiate DOX and its metabolites. Along with the FCSI results, the lack of DOX metabolites detected in CE indicated that DLPS delivered DOX into the cell [97].

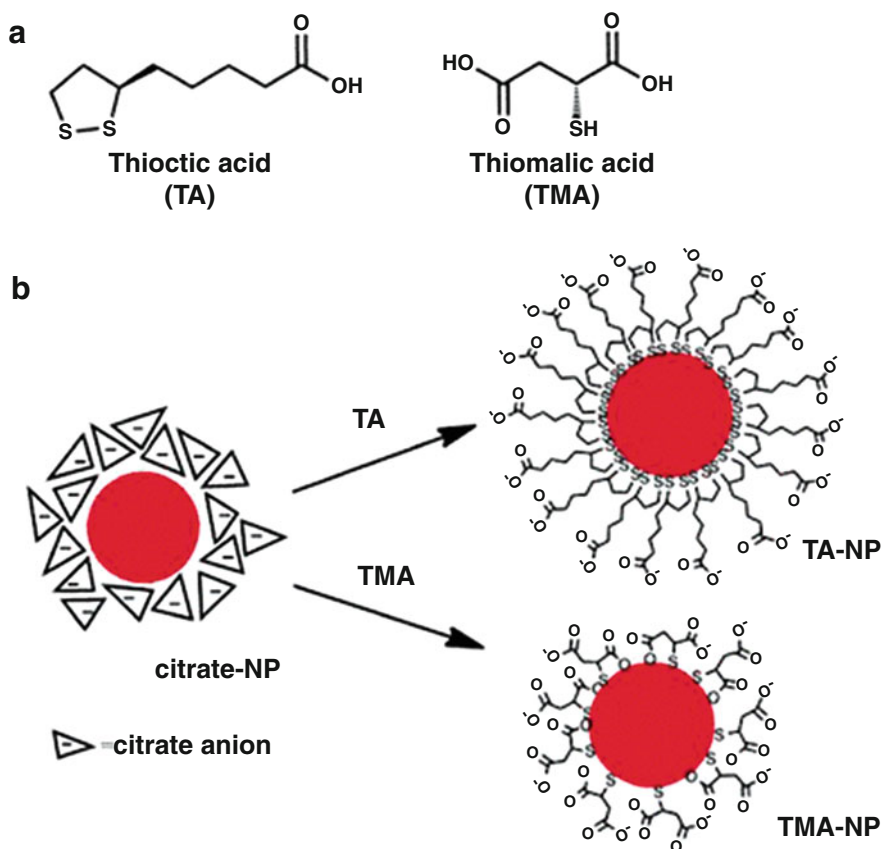


Fig. 3.13 (a) Structures of thioctic acid (TA) and thiomalic acid (TMA), which were the buffer additives used to resolve AuNPs and AgNPs. (b) Functionalization scheme for: (1) TA-NPs; (2) TMA-NPs (drawings are not to scale). (Reprinted with permission from Ref. [95]. Copyright 2014 *Microchimica Acta*)

Blazkova et al. also studied the use of DOX carriers for cancer treatment. They encapsulated DOX into apoferritin cages and conjugated this structure to magnetic nanoparticles. As shown in Fig. 3.15a, they found one peak corresponding to encapsulated DOX and the other corresponding to free DOX, which the authors attributed to the lack of success in eliminating free DOX during dialysis. The group explained that DOX molecules adhered to the surface of the apoferritin cage and were separated during electrophoresis. The correlation between the peak height and the concentration of DOX was found to be linear in Fig. 3.15b. In Fig. 3.15c, d, the amount of desorbed DOX increased while the amount of encapsulated DOX increased almost two times as much with a larger application of DOX amount. Through CE, they monitored the magnetic particle-mediated APODOX transport involving the following steps: separating the free DOX and encapsulated DOX using magnetic pull down and pH-mediated release of DOX from APODOX and APODOX-conjugated magnetic nanoparticles [98].

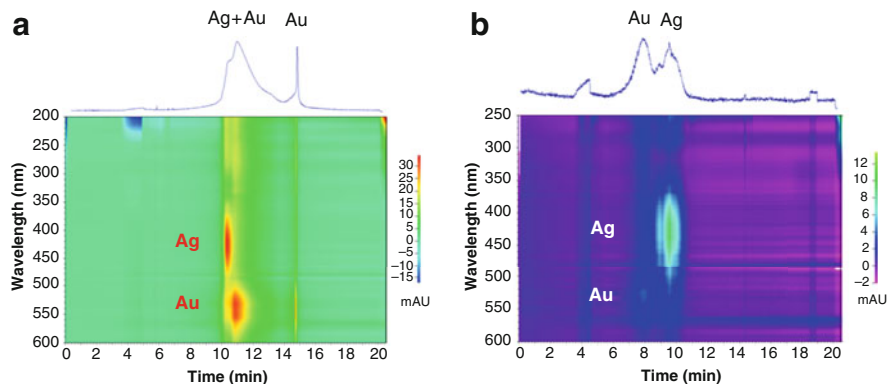


Fig. 3.14 Contour graph demonstrating the relationship between the absorbance at each wavelength and the migration time for the AuNP and AgNP mixture (a) in a buffer electrolyte with 0.1% (v/w) TA; detection wavelength at 539 nm, and (b) in a buffer electrolyte with 0.1% (v/w) of TMA; detection wavelength at 539 nm. (Reprinted with permission from Ref. [95]. Copyright 2014 Microchimica Acta)

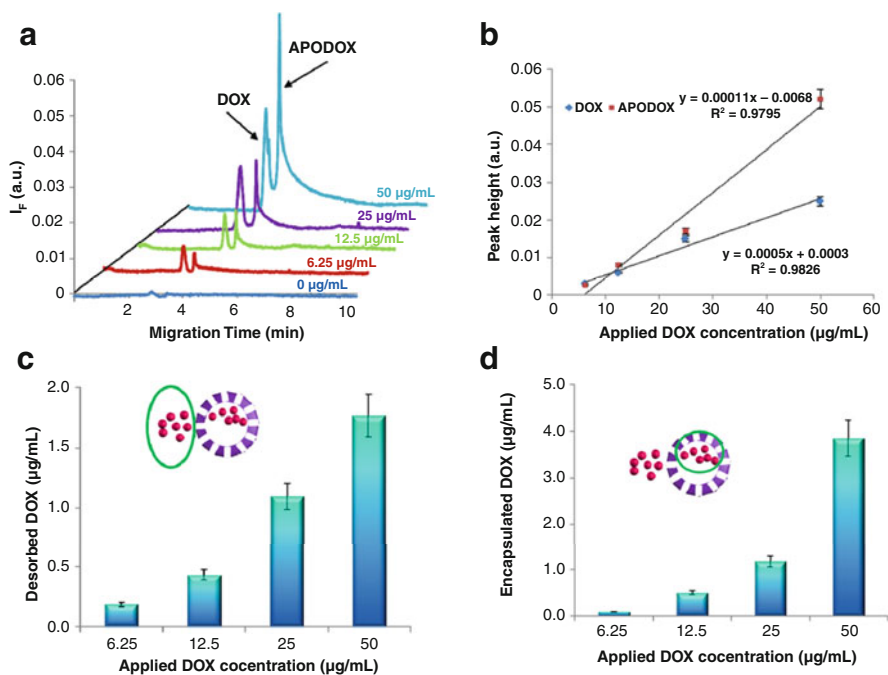


Fig. 3.15 (a) Electropherograms of APODOX solutions with the following concentrations of DOX: 0, 6.25, 12.5, 25, and 50 µg/mL. (b) Relationship between peak heights of DOX and APODOX peaks and the applied concentration of DOX. (c) Relationship between the concentration of desorbed DOX and the applied concentration of DOX. (d) Relationship between the concentration of encapsulated DOX and the applied concentration of DOX. (Reprinted with permission from Ref. [98]. Copyright 2013 International Journal of Molecular Sciences)

5.2.3 Polymeric Nanoparticles

As exemplified by the previous reports on the involvement of metal oxide nanoparticles in drug carrier systems, other literature sources assessed the usage of polymeric nanoparticles in drug delivery in addition to the study of polymeric nanoparticles and their biomolecular interactions. Oukacine et al. studied the hydrophobic properties of PEG-b-PGlu, which are the diblock copolymers that make up (1,2-diamino-cyclohexane)platinum(II) ((DACH)Pt)-loaded micelles, by using MEKC with SDS molecules in the buffer electrolyte. The electrophoretic mobility of the diblock copolymer decreases with high levels of negatively charged SDS molecules that adhere to PEG. Figure 3.16a shows the degradation of (DACH)Pt-loaded polymeric micelles, affected by a highly concentrated NaCl solution and 25 °C temperature conditions, over time. The authors observed the formation and increase of a second peak, which they suspected to be the smaller aggregates from the polymeric micelles. The peak area ratio of the degradation product to the original polymeric micelles was plotted in Fig. 3.16b [99].

Molecularly imprinted polymer nanoparticles (MIP NPs) are included in the repertoire of drug delivery tools. Although they have not been extensively studied for drug delivery purposes using CE, they have been studied for their interaction with biomolecules. Musile et al. studied the interaction of molecularly imprinted polymer nanoparticles (MIP NPs) with CE. After confirmation of the lack of MIP NPs' adsorption to the capillary wall, the group compared the interactions of MIP NPs and nonimprinted polymer nanoparticles. MIP NPs were incubated with increased concentrations of template in order for the group to obtain the binding isotherm for the complex and a dissociation equilibrium constant of $66 \pm 1 \mu\text{M}$. Selectivity was tested using angiotensin, a nonspecific ligand peptide, and it was found that there was no significant binding between MIP NPs and angiotensin [100].

Properties, such as hydrodynamic diameter and even polydispersity index, can be obtained using the theory of "Taylor dispersion," which is a result of nonuniform

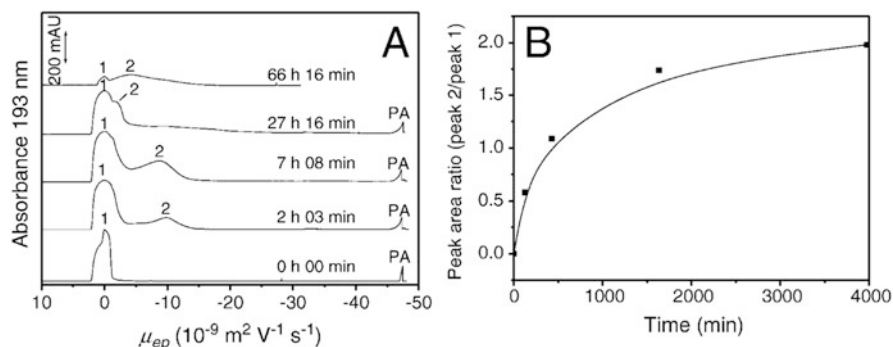


Fig. 3.16 Monitoring the decomposition of polymeric micelles in NaCl solution at 25 °C via CZE. Separation conditions: 30 mM phosphate buffer, pH 7.2, + 15 kV. Peaks: 1 – (DACH)Pt-loaded polymeric micelles; 2 – (DACH)Pt-loaded aggregates; PA phthalic acid. (Reprinted with permission from Ref. [99]. Copyright 2014 Journal of Controlled Release)

fluid velocity and molecular diffusion [101]. Ibrahim et al. used CE with Taylor Dispersion Analysis (TDA) to assess the hydrodynamic diameter and effective charge of polyglutamate backbone grafted with hydrophobic vitamin E (pGVE) hydrogels and polyglutamate (pGlu) hydrogels, which do not include vitamin E. They found a decrease in the effective charge number per nonmodified glutamate with inclusion of vitamin E in the hydrogel due to the influence of hydrophobic groups on the dissociation of glutamate molecules [102].

5.2.4 Liposomes

Liposomes can also be considered nanoparticles, and they have been a dominant option as a drug delivery tool. CE has been often used for the characterization of liposome properties, such as size, charge, and permeability, in drug delivery systems [103]. Nguyen et al. investigated PEGylated liposomes with CE-ICP-MS for the use of cisplatin anti-cancer drug delivery. They were able to separate liposome-encapsulated cisplatin from free cisplatin and hydrolysis products of cisplatin in human plasma. Coupling CE to ICP-MS allowed for simultaneous monitoring of phosphorus from phospholipids and platinum from cisplatin. Increasing the plasma amount caused a decrease in the signal of cisplatin; in addition, cisplatin and hydrolysis products co-migrated as one peak when the matrix was 50% plasma. They found that reducing the plasma amount to 20% was necessary to improve resolution and sensitivity during separation. The group speculated that the addition of SDS to the background electrolyte improved separation efficiency possibly due to the surfactant reducing adsorption to the capillary wall [104].

Nguyen et al. also studied the release of cisplatin from liposomes, which was induced by sonication. Based on reduction of peaks for free cisplatin and hydrolysis products, the amount of release cisplatin was calculated [105]. Otarola et al. analyzed the entrapment efficiency of their prepared nanostructured lipid carrier (NLC) with incorporated piroxicam, a nonsteroidal anti-inflammatory drug (NSAID) using CE. They obtained the entrapment efficiency by calculating the difference between the amount of piroxicam used for NLC suspensions and the amount of piroxicam not entrapped in the NLCs [106].

5.2.5 Quantum Dots

In general, quantum dots have been important tools for drug delivery, bioimaging, and sensors. In CE, they have been conjugated with biomolecules in interaction and detection studies. Janu et al. capped CdTe-QDs with heptapeptides (HWRGWVC) to conjugate to human immunoglobulin. They observed that HWR peptide has affinity towards IgG but not IgY. The IgG complex was separated from the IgY complex as well as the HWR peptide-capped QDs. HWR-QD conjugation was confirmed by magnetic particles coated with IgG and IgY in differential pulse voltammograms. The same binding phenomenon occurred in gel electrophoresis and ELISA results as well [107].

Zhou et al. also used quantum dots in a capillary electrophoresis-chemiluminescence (CE-CL) detection system, but their goal was to detect the presence of carcinoembryonic antigen (CEA) with their method. Their HRP-DNA_{A-B}-QD probe

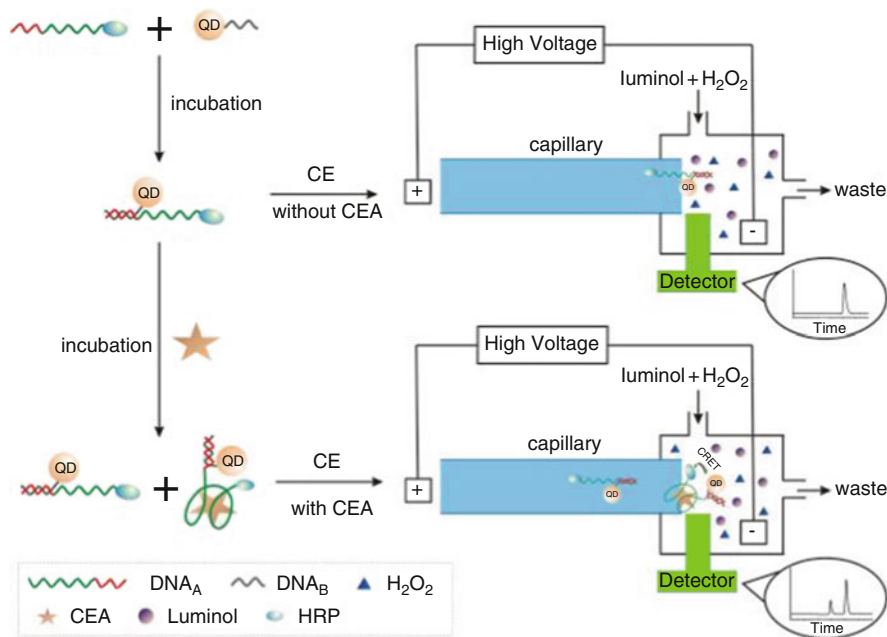


Fig. 3.17 Detection of CEA antigen with an aptamer-labeled QD probe by CE-CL detection system. CEA-probe complex can be separated from the free probe. (Reprinted with permission from Ref. [108]. Copyright 2015 Sensors and Actuators B: Chemical)

was designed to enable chemiluminescence resonance energy transfer (CRET) when bound to the target antigen. With CEA in the mixture, the CEA/HRP-DNA_{A-B}-QD complex was present and could be separated from the free probe in CE, as shown in Fig. 3.17. When compared to the calibration values for quantification of CEA in human serum by the standard LIAISON chemiluminescence immunoassay system, the authors' results from using their probe combined with the CE-CL detection system were similar [108].

6 Conclusions and Future Perspective

Open channel separation including FFF and CE are unique approaches for the study of nanomaterials and their bioconjugates as well as their application to drug delivery systems. They provide fast separation and sufficient resolution between the non-conjugated and conjugated nanomaterials for rapid characterization of the nanomaterial itself and biological layer formation. The different separation modes in each technique also provide superior tools for analysis of different physicochemical properties of the nanomaterials, including size, shape, and surface potential. Still, there is a deficiency in applications on the newer generation of nanomaterials, the 1D and 2D materials, like fibers and sheets. Lack of theory to guide separation optimization of

such materials is the main challenge behind this gap. In addition, hyphenation with more detectors or other separation techniques are desired to improve the amounts of information obtained upon separation. Sample throughput and collection recovery are to be improved for FFF, which is more prominent in recovering samples for down-stream analysis than CE. However, with the advancement in the instrumentation of CE-MS, more applications in this area are to be expected. Moreover, the previous efforts are all focused on protein conjugates. Future applications on analyzing adsorption of other biomolecules, like nucleic acids and lipids, are expected to explore contribution of other adsorbed or conjugated biomolecules on nanomaterials that could alter their biological behaviors. In addition, more analysis on drug delivery systems using open channel separation is a possibility, and potential avenues include studies with other nanomaterial types aside from polymeric and lipid-based ones, which have been dominant in FFF and CE research. Overall, while open channel separation techniques have shown strong power in the study of nanomaterials, more instrumentation developments and wider application scopes are expected in the coming years to improve their capability in characterization of diverse new nanomaterials and their bioconjugates and to meet the accompanying challenges in the fast development of nanotechnology.

Acknowledgments The authors thank the support from the National Institute of Environmental Health Sciences of the National Institutes of Health under the Award #U01ES027293 (to W. Z.) and T32ES018827 (to R. C.).

References

1. Kim S, Lim YT, Soltesz EG, De Grand AM, Lee J, Nakayama A, Parker JA, Mihaljevic T, Laurence RG, Dor DM, Cohn LH, Bawendi MG, Frangioni JV (2004) Near-infrared fluorescent type II quantum dots for sentinel lymph node mapping. *Nat Biotechnol* 22:93–97. <https://doi.org/10.1038/nbt920>
2. So M-K, Xu C, Loening AM, Gambhur SS, Rao J (2006) Self-illuminating quantum dots aid in vivo imaging. *Nat Biotechnol* 24:339–343. <https://doi.org/10.1038/nbt1188>
3. Yu MK, Jeong YY, Park J, Park S, Kim JW, Min JJ, Kim K, Jon S (2008) Drug-loaded superparamagnetic iron oxide nanoparticles for combined cancer imaging and therapy in vivo. *Angew Chemie – Int Ed* 47:5362–5365. <https://doi.org/10.1002/anie.200800857>
4. Alexiou C, Arnold W, Klein RJ, Parak FG, Hulin P, Bergemann C, Erhardt W, Wagenpfeil S, Lübbe AS (2000) Locoregional cancer treatment with magnetic drug targeting. *Cancer Res* 60:6641–6648
5. Wang Y, Sun Y, Wang J, Yang Y, Li Y, Yuan Y, Liu C (2016) Charge-reversal APTES-modified mesoporous silica nanoparticles with high drug loading and release controllability. *ACS Appl Mater Interfaces* 8:17166–17175. <https://doi.org/10.1021/acsami.6b05370>
6. Zhang CY, Yeh HC, Kuroki MT, Wang TH (2005) Single-quantum-dot-based DNA nanosensor. *Nat Mater* 4:826–831. <https://doi.org/10.1038/nmat1508>
7. Lundqvist M, Stigler J, Elia G, Lynch I, Cedervall T, Dawson KA (2008) Nanoparticle size and surface properties determine the protein corona with possible implications for biological impacts. *Proc Natl Acad Sci* 105:14265–14270. <https://doi.org/10.1073/pnas.0805135105>
8. Tenzer S, Docter D, Kuharev J, Musyanovych A, Fetz V, Hecht R, Schlenk F, Fischer D, Kiouptsi K, Reinhardt C, Landfester K, Schild H, Maskos M, Knauer SK, Stauber RH (2013)

- Rapid formation of plasma protein corona critically affects nanoparticle pathophysiology. *Nat Nanotechnol* 8:772–781. <https://doi.org/10.1038/nnano.2013.181>
9. An H, Jin B (2012) Prospects of nanoparticle-DNA binding and its implications in medical biotechnology. *Biotechnol Adv* 30:1721–1732. <https://doi.org/10.1016/j.biotechadv.2012.03.007>
 10. Villanueva A, Cañete M, Roca AG, Calero M, Veintemillas-Verdaguer S, Serna CJ, del Puerto Morales M, Miranda R (2009) The influence of surface functionalization on the enhanced internalization of magnetic nanoparticles in cancer cells. *Nanotechnology* 20:115103. <https://doi.org/10.1088/0957-4484/20/11/115103>
 11. Westmeier D, Stauber RH, Docter D (2016) The concept of bio-corona in modulating the toxicity of engineered nanomaterials (ENM). *Toxicol Appl Pharmacol* 299:53–57. <https://doi.org/10.1016/j.taap.2015.11.008>
 12. Wang F, Yu L, Monopoli MP, Sandin P, Mahon E, Salvati A, Dawson KA (2013) The biomolecular corona is retained during nanoparticle uptake and protects the cells from the damage induced by cationic nanoparticles until degraded in the lysosomes. *Nanomed Nanotechnol Biol Med* 9:1159–1168. <https://doi.org/10.1016/j.nano.2013.04.010>
 13. Ke PC, Lin S, Parak WJ, Davis TP, Caruso F (2017) A decade of the protein corona. *ACS Nano* 11:11773
 14. Cedervall T, Lynch I, Lindman S, Berggard T, Thulin E, Nilsson H, Dawson KA, Linse S (2007) Understanding the nanoparticle-protein corona using methods to quantify exchange rates and affinities of proteins for nanoparticles. *Proc Natl Acad Sci* 104:2050–2055. <https://doi.org/10.1073/pnas.0608582104>
 15. Ulbrich K, Holá K, Šubr V, Bakandritsos A, Tuček J, Zbořil R (2016) Targeted drug delivery with polymers and magnetic nanoparticles: covalent and noncovalent approaches, release control, and clinical studies. *Chem Rev* 116:5338–5431. <https://doi.org/10.1021/acs.chemrev.5b00589>
 16. Filipe V, Hawe A, Jiskoot W (2010) Critical evaluation of nanoparticle tracking analysis (NTA) by NanoSight for the measurement of nanoparticles and protein aggregates. *Pharm Res* 27:796–810. <https://doi.org/10.1007/s11095-010-0073-2>
 17. Wei GT, Liu F-K, Wang CRC (1999) Shape separation of nanometer gold particles by size-exclusion chromatography. *Anal Chem* 71:2085–2091. <https://doi.org/10.1021/ac990044u>
 18. Wilcoxon JP, Martin JE, Provencio P (2000) Size distributions of gold nanoclusters studied by liquid chromatography. *Langmuir* 16:9912–9920. <https://doi.org/10.1021/la000669j>
 19. Hanauer M, Pierrat S, Zins I, Lotz A, Sönnichsen C (2007) Separation of nanoparticles by gel electrophoresis according to size and shape. *Nano Lett* 7:2881–2885. <https://doi.org/10.1021/nl071615y>
 20. Xu X, Caswell KK, Tucker E, Kabisatpathy S, Brodhacker KL, Scrivens WA (2007) Size and shape separation of gold nanoparticles with preparative gel electrophoresis. *J Chromatogr A* 1167:35–41. <https://doi.org/10.1016/j.chroma.2007.07.056>
 21. Giddings JC (1966) A new separation concept based on a coupling of concentration and flow nonuniformities. *Sep Sci* 1:123–125. <https://doi.org/10.1080/01496396608049439>. Published
 22. Giddings JC (1993) Field-flow fractionation – analysis of macromolecular, colloidal, and particulate materials. *Science* (80-) 260:1456–1465. <https://doi.org/10.1126/science.8502990>
 23. Liu MK, Li P, Giddings JC (1993) Rapid protein separation and diffusion coefficient measurement by frit inlet flow field-flow fractionation. *Protein Sci* 2:1520–1531. <https://doi.org/10.1002/pro.5560020917>
 24. Giddings JC, Yang FJ, Myers MN (1977) Flow field-flow fractionation as a methodology for protein separation and characterization. *Anal Biochem* 81:395–407. [https://doi.org/10.1016/0003-2697\(77\)90710-2](https://doi.org/10.1016/0003-2697(77)90710-2)
 25. Liu MK, Giddings JC (1993) Separation and measurement of diffusion coefficients of linear and circular DNAs by flow field-flow fractionation. *Macromolecules* 26:3576–3588. <https://doi.org/10.1021/ma00066a016>
 26. Ashby J, Schachermeyer S, Duan Y, Jimenez LA, Zhong W (2014) Probing and quantifying DNA-protein interactions with asymmetrical flow field-flow fractionation. *J Chromatogr A* 1358:217–224. <https://doi.org/10.1016/j.chroma.2014.07.002>

27. Bousse T, Shore DA, Goldsmith CS, Hossain MJ, Jang Y, Davis CT, Donis RO, Stevens J (2013) Quantitation of influenza virus using field flow fractionation and multi-angle light scattering for quantifying influenza A particles. *J Virol Methods* 193:589–596. <https://doi.org/10.1016/j.jviromet.2013.07.026>
28. Giddings JC, Yang FJ, Myers MN (1977) Flow field-flow fractionation – new method for separating, purifying, and characterizing diffusivity of viruses. *J Virol* 21:131–138. <https://doi.org/10.1007/s11664-014-3204-4>
29. Flack K, Jimenez LA, Zhong W (2017) Analysis of the distribution profiles of circulating microRNAs by asymmetrical flow field flow fractionation. In: Rani S. (eds) *MicroRNA profiling. Methods in molecular biology*, vol 1509. Humana Press, New York, NY, pp 161–168
30. Wagner M, Pietsch C, Tauhardt L, Schallon A, Schubert US (2014) Characterization of cationic polymers by asymmetric flow field-flow fractionation and multi-angle light scattering—a comparison with traditional techniques. *J Chromatogr A* 1325:195–203. <https://doi.org/10.1016/j.chroma.2013.11.049>
31. Giddings JC (1973) The conceptual basis of field-flow fractionation. *J Chem Educ* 50:667. <https://doi.org/10.1021/ed050p667>
32. Kowalkowski T, Buszewski B, Cantado C, Dondi F (2006) Field-flow fractionation: theory, techniques, applications and the challenges. *Crit Rev Anal Chem* 36:129–135. <https://doi.org/10.1080/10408340600713702>
33. Contado C (2017) Field flow fractionation techniques to explore the “nano-world”. *Anal Bioanal Chem* 409:2501–2518. <https://doi.org/10.1007/s00216-017-0180-6>
34. Bednar AJ, Poda AR, Mitrano DM, Kennedy AJ, Gray EP, Ranville JF, Hayes CA, Crocker FH, Steevens JA (2013) Comparison of on-line detectors for field flow fractionation analysis of nanomaterials. *Talanta* 104:140–148. <https://doi.org/10.1016/j.talanta.2012.11.008>
35. Schachermeyer S, Ashby J, Zhong W (2012) Advances in field-flow fractionation for the analysis of biomolecules: instrument design and hyphenation. *Anal Bioanal Chem* 404:1151–1158. <https://doi.org/10.1007/s00216-012-6069-5>
36. Szolar OHJ, Brown RS, Luong JHT (1995) Separation of PAHs by capillary electrophoresis with laser-induced fluorescence detection using mixtures of neutral and Anionic.β-cyclodextrins. *Anal Chem* 67:3004–3010. <https://doi.org/10.1021/ac00113a039>
37. Cheng HL, Liao YM, Chiou SS, Wu SW (2008) On-line stacking capillary electrophoresis for analysis of methotrexate and its eight metabolites in whole blood. *Electrophoresis* 29:3665–3673. <https://doi.org/10.1002/elps.200800029>
38. Sun L, Zhu G, Zhang Z, Mou S, Dovichi NJ (2015) Third-generation electrokinetically pumped sheath-flow nanospray interface with improved stability and sensitivity for automated capillary zone electrophoresis-mass spectrometry analysis of complex proteome digests. *J Proteome Res* 14:2312–2321. <https://doi.org/10.1021/acs.jproteome.5b00100>
39. Han F, Huynh BH, Ma Y, Lin B (1999) High-efficiency DNA separation by capillary electrophoresis in a polymer solution with ultralow viscosity. *Anal Chem* 71:2385–2389. <https://doi.org/10.1097/JCP.0b013e3182549d2d>
40. Nehme H, Nehme R, Lafite P, Routier S, Morin P (2012) New development in in-capillary electrophoresis techniques for kinetic and inhibition study of enzymes. *Anal Chim Acta* 722:127–135. <https://doi.org/10.1016/j.aca.2012.02.003>
41. Mattarozzi M, Suman M, Cascio C, Calestani D, Weigel S, Undas A, Peters R (2017) Analytical approaches for the characterization and quantification of nanoparticles in food and beverages. *Anal Bioanal Chem* 409:63–80. <https://doi.org/10.1007/s00216-016-9946-5>
42. Bandyopadhyay S, Peralta-Videa JR, Gardea-Torresdey JL (2013) Advanced analytical techniques for the measurement of nanomaterials in complex samples: a comparison. *Environ Eng Sci* 30:118–125. <https://doi.org/10.3920/QAS2014.0410>
43. Sadik OA, Du N, Kariuki V, Okello V, Bushlyar V (2014) Current and emerging technologies for the characterization of nanomaterials. *ACS Sustain Chem Eng* 2:1707–1716. <https://doi.org/10.1021/sc500175v>

44. Meermann B, Laborda F (2015) Analysis of nanomaterials by field-flow fractionation and single particle ICP-MS. *J Anal At Spectrom* 30:1226–1228. <https://doi.org/10.1039/c5ja90019k>
45. Chetwynd A, Guggenheim E, Briffa S, Thorn J, Lynch I, Valsami-Jones E (2018) Current application of capillary electrophoresis in nanomaterial characterisation and its potential to characterise the protein and small molecule corona. *Nanomaterials* 8. <https://doi.org/10.3390/nano8020099>
46. Yohannes G, Jussila M, Hartonen K, Riekkola ML (2011) Asymmetrical flow field-flow fractionation technique for separation and characterization of biopolymers and bioparticles. *J Chromatogr A* 1218:4104–4116. <https://doi.org/10.1016/j.chroma.2010.12.110>
47. Giddings JC, Yang FJF, Myers MN (1976) Flow field-flow fractionation: a versatile new separation method. *Science* (80-) 193:1244–1245
48. Mudalige TK, Qu H, Sánchez-Pomales G, Sisco PN, Linder SW (2015) Simple functionalization strategies for enhancing nanoparticle separation and recovery with asymmetric flow field flow fractionation. *Anal Chem* 87:1764–1772. <https://doi.org/10.1021/ac503683n>
49. Rambaldi DC, Reschiglian P, Zattoni A (2011) Flow field-flow fractionation: recent trends in protein analysis. *Anal Bioanal Chem* 399:1439–1447. <https://doi.org/10.1007/s00216-010-4312-5>
50. Wahlund KG, Giddings JC (1987) Properties of an asymmetrical flow field-flow fractionation channel having one permeable wall. *Anal Chem* 59:1332–1339. <https://doi.org/10.1021/ac00136a016>
51. Mudalige TK, Qu H, Van Haute D, Ansar SM, Linder SW (2018) Capillary electrophoresis and asymmetric flow field-flow fractionation for size-based separation of engineered metallic nanoparticles: a critical comparative review. *TrAC – Trends Anal Chem* 106:202–212. <https://doi.org/10.1016/j.trac.2018.07.008>
52. Schachermeyer S, Ashby J, Kwon M, Zhong W (2012) Impact of carrier fluid composition on recovery of nanoparticles and proteins in flow field flow fractionation. *J Chromatogr A* 1264:72–79. <https://doi.org/10.1016/j.chroma.2012.09.050>
53. Ashby J, Schachermeyer S, Pan S, Zhong W (2013) Dissociation-based screening of nanoparticle-protein interaction via flow field-flow fractionation. *Anal Chem* 85:7494–7501. <https://doi.org/10.1021/ac401485j>
54. Ashby J, Flack K, Jimenez LA, Duan Y, Khatib AK, Somlo G, Wang SE, Cui X, Zhong W (2014) Distribution profiling of circulating MicroRNAs in serum. *Anal Chem* 86:9343–9349. <https://doi.org/10.1021/ac5028929>
55. Chu YH, Avila LZ, Biebuyck HA, Whitesides GM (1992) Use of affinity capillary electrophoresis to measure binding constants of ligands to proteins. *J Med Chem* 35:2915–2917. <https://doi.org/10.1021/jm00093a027>
56. Chu Y-H, Avila LZ, Gao J, Whitesides GM (1995) Affinity capillary electrophoresis. *Acc Chem Res* 28:461–468. <https://doi.org/10.1021/ar00059a004>
57. Li N, Zeng S, He L, Zhong W (2010) Probing nanoparticle– protein interaction by capillary electrophoresis. *Anal Chem* 82:7460–7466
58. Terabe S, Otsuka K, Ichikawa K, Tsuchiya A, Ando T (1984) Electrokinetic separations with micellar solutions and open-tubular capillaries. *Anal Chem* 56:111–113. <https://doi.org/10.1021/ac00265a031>
59. Liu FK, Wei GT (2004) Adding sodium dodecylsulfate to the running electrolyte enhances the separation of gold nanoparticles by capillary electrophoresis. *Anal Chim Acta* 510:77–83. <https://doi.org/10.1016/j.aca.2003.12.064>
60. Ciriello R, Ialorenzi PT, Laurita A, Guerrieri A (2017) Improved separation and size characterization of gold nanoparticles through a novel capillary zone electrophoresis method using poly(sodium4-styrenesulfonate) as stabiliser and a stepwise field strength gradient. *Electrophoresis* 38:922–929. <https://doi.org/10.1002/elps.201600478>
61. Kairdolf BA, Qian X, Nie S (2017) Bioconjugated nanoparticles for biosensing, in vivo imaging, and medical diagnostics. *Anal Chem* 89:1015–1031. <https://doi.org/10.1021/acs.analchem.6b04873>

62. Bazak R, Hourri M, El Achy S, Kamel S, Refaat T (2015) Cancer active targeting by nanoparticles: a comprehensive review of literature. *J Cancer Res Clin Oncol* 141:769–784. <https://doi.org/10.1007/s00432-014-1767-3>
63. Hizir MS, Top M, Balcioglu M, Rana M, Robertson NM, Shen F, Sheng J, Yigit MV (2016) Multiplexed activity of perAoxidase: DNA-capped AuNPs act as adjustable peroxidase. *Anal Chem* 88:600–605. <https://doi.org/10.1021/acs.analchem.5b03926>
64. Li H, Shen J, Cui R, Sun C, Zhao Y, Wu X, Li N, Tang B (2017) A highly selective and sensitive fluorescent nanosensor for dopamine based on formate bridged Tb(iii) complex and silver nanoparticles. *Analyst* 142:4240–4246. <https://doi.org/10.1039/c7an00961e>
65. Safenkova IV, Slutskaya ES, Panferov VG, Zherdev AV, Dzantiev BB (2016) Complex analysis of concentrated antibody-gold nanoparticle conjugates' mixtures using asymmetric flow field-flow fractionation. *J Chromatogr A* 1477:56–63. <https://doi.org/10.1016/j.chroma.2016.11.040>
66. Poda AR, Bednar AJ, Kennedy AJ, Harmon A, Hull M, Mitrano DM, Ranville JF, Steevens J (2011) Characterization of silver nanoparticles using flow-field flow fractionation interfaced to inductively coupled plasma mass spectrometry. *J Chromatogr A* 1218:4219–4225. <https://doi.org/10.1016/j.chroma.2010.12.076>
67. Tadjiki S, Montañó MD, Assemi S, Barber A, Ranville J, Beckett R (2017) Measurement of the density of engineered silver nanoparticles using centrifugal FFF-TEM and single particle ICP-MS. *Anal Chem* 89:6056–6064. <https://doi.org/10.1021/acs.analchem.7b00652>
68. Marassi V, Roda B, Casolari S, Ortelli S, Blosi M, Zattoni A, Costa AL, Reschiglian P (2018) Hollow-fiber flow field-flow fractionation and multi-angle light scattering as a new analytical solution for quality control in pharmaceutical nanotechnology. *Microchem J* 136:149–156. <https://doi.org/10.1016/j.microc.2016.12.015>
69. Marassi V, Casolari S, Roda B, Zattoni A, Reschiglian P, Panzavolta S, Tofail SAM, Ortelli S, Delpivo C, Blosi M, Costa AL (2015) Hollow-fiber flow field-flow fractionation and multi-angle light scattering investigation of the size, shape and metal-release of silver nanoparticles in aqueous medium for nano-risk assessment. *J Pharm Biomed Anal* 106:92–99. <https://doi.org/10.1016/j.jpba.2014.11.031>
70. Wimuktiwan P, Shiowatana J, Siripinyanond A (2015) Investigation of silver nanoparticles and plasma protein association using flow field-flow fractionation coupled with inductively coupled plasma mass spectrometry (FIFFF-ICP-MS). *J Anal At Spectrom* 30:245–253. <https://doi.org/10.1039/c4ja00225c>
71. Yu B, Zhou Y, Song M, Xue Y, Cai N, Luo X, Long S, Zhang H, Yu F (2016) Synthesis of selenium nanoparticles with mesoporous silica drug-carrier shell for programmed responsive tumor targeted synergistic therapy. *RSC Adv* 6:2171–2175. <https://doi.org/10.1039/c5ra21460b>
72. Zheng S, Li X, Zhang Y, Xie Q, Wong YS, Zheng W, Chen T (2012) PEG-nanolized ultrasmall selenium nanoparticles overcome drug resistance in hepatocellular carcinoma HepG2 cells through induction of mitochondria dysfunction. *Int J Nanomedicine* 7:3939–3949. <https://doi.org/10.2147/IJN.S30940>
73. M-M P, Somchue W, Shiowatana J, Siripinyanond A (2014) Flow field-flow fractionation for particle size characterization of selenium nanoparticles incubated in gastrointestinal conditions. *Food Res Int* 57:208–209. <https://doi.org/10.1016/j.foodres.2014.01.040>
74. Seabra A, Durán N (2015) Nanotoxicology of metal oxide nanoparticles. *Metals (Basel)* 5:934–975. <https://doi.org/10.3390/met5020934>
75. Peng N, Wu B, Wang L, He W, Ai Z, Zhang X, Wang Y, Fan L, Ye Q (2016) High drug loading and pH-responsive targeted nanocarriers from alginate-modified SPIONs for anti-tumor chemotherapy. *Biomater Sci* 4:1802–1813. <https://doi.org/10.1039/c6bm00504g>
76. Martínez-Carmona M, Gun'ko Y, Vallet-Regí M (2018) ZnO nanostructures for drug delivery and theranostic applications. *Nanomaterials* 8. <https://doi.org/10.3390/nano8040268>
77. Bogdan J, Plawinska-Czarnak J, Zarzynska J (2017) Nanoparticles of titanium and zinc oxides as novel agents in tumor treatment: a review Janusz. *Nanoscale Res Lett* 12:225. <https://doi.org/10.1186/s11671-017-2007-y>

78. Ashby J, Pan S, Zhong W (2014) Size and surface functionalization of iron oxide nanoparticles influence the composition and dynamic nature of their protein corona. *ACS Appl Mater Interfaces* 6:15412–15419. <https://doi.org/10.1021/am503909q>
79. Weber C, Simon J, Mailänder V, Morsbach S, Landfester K (2018) Preservation of the soft protein corona in distinct flow allows identification of weakly bound proteins. *Acta Biomater* 76:217–224. <https://doi.org/10.1016/j.actbio.2018.05.057>
80. Wang S, McGuirk CM, d’Aquino A, Mason JA, Mirkin CA (2018) Metal-organic framework nanoparticles. *Adv Mater* 30:1800202. <https://doi.org/10.1002/adma.201800202>
81. Roda B, Marassi V, Zattoni A, Borghi F, Anand R, Agostoni V, Gref R, Reschiglian P, Monti S (2018) Flow field-flow fractionation and multi-angle light scattering as a powerful tool for the characterization and stability evaluation of drug-loaded metal-organic framework nanoparticles. *Anal Bioanal Chem* 410:5245–5253. <https://doi.org/10.1007/s00216-018-1176-6>
82. Hinna AH, Hupfeld S, Kuntsche J, Brandl M (2016) The use of asymmetrical flow field-flow fractionation with on-line detection in the study of drug retention within liposomal nano-carriers and drug transfer kinetics. *J Pharm Biomed Anal* 124:157–163. <https://doi.org/10.1016/j.jpba.2016.02.037>
83. Elgqvist J, Frost S, Pouget J-P, Albertsson P (2014) The potential and hurdles of targeted alpha therapy – clinical trials and beyond. *Front Oncol* 3:1–9. <https://doi.org/10.3389/fonc.2013.00324>
84. Huclier-Markai S, Grivaud-Le Du A, N’tsiba E, Montavon G, Mougin-Degraef M, Barbet J (2018) Coupling a gamma-ray detector with asymmetrical flow field flow fractionation (AF4): application to a drug-delivery system for alpha-therapy. *J Chromatogr A* 1573:107–114. <https://doi.org/10.1016/j.chroma.2018.08.065>
85. Moquin A, Neibert KD, Maysinger D, Winnik FM (2015) Quantum dot agglomerates in biological media and their characterization by asymmetrical flow field-flow fractionation. *Eur J Pharm Biopharm* 89:290–299. <https://doi.org/10.1016/j.ejpb.2014.12.019>
86. Bouzas-Ramos D, García-Cortes M, Sanz-Medel A, Encinar JR, Costa-Fernández JM (2017) Assessment of the removal of side nanoparticulated populations generated during one-pot synthesis by asymmetric flow field-flow fractionation coupled to elemental mass spectrometry. *J Chromatogr A* 1519:156–161. <https://doi.org/10.1016/j.chroma.2017.08.068>
87. Menéndez-Miranda M, Encinar JR, Costa-Fernández JM, Sanz-Medel A (2015) Asymmetric flow field-flow fractionation coupled to inductively coupled plasma mass spectrometry for the quantification of quantum dots bioconjugation efficiency. *J Chromatogr A* 1422:247–252. <https://doi.org/10.1016/j.chroma.2015.10.012>
88. Matczuk M, Anecka K, Scaletti F, Messori L, Keppler BK, Timerbaev AR, Jarosz M (2015) Speciation of metal-based nanomaterials in human serum characterized by capillary electrophoresis coupled to ICP-MS: a case study of gold nanoparticles. *Metallomics* 7:1364–1370. <https://doi.org/10.1039/c5mt00109a>
89. Belder D, Deege A, Husmann H, Kohler F, Ludwig M (2001) Cross-linked poly(vinyl alcohol) as permanent hydrophilic column coating for capillary electrophoresis. *Electrophoresis* 22:3813–3818. [https://doi.org/10.1002/1522-2683\(200109\)22:17<3813::AID-ELPS3813>3.0.CO;2-D](https://doi.org/10.1002/1522-2683(200109)22:17<3813::AID-ELPS3813>3.0.CO;2-D)
90. Matczuk M, Legat J, Shtykov SN, Jarosz M, Timerbaev AR (2016) Characterization of the protein corona of gold nanoparticles by an advanced treatment of CE-ICP-MS data. *Electrophoresis* 37:2257–2259. <https://doi.org/10.1002/elps.201600152>
91. Legat J, Matczuk M, Scaletti F, Messori L, Timerbaev A, Jarosz M (2017) Erratum to: CE separation and ICP-MS detection of gold nanoparticles and their protein conjugates. *Chromatographia* 80:1719. <https://doi.org/10.1007/s10337-017-3410-3>
92. Man Y, Lv X, Iqbal J, Jia F, Xiao P, Hasan M, Li Q, Dai R, Geng L, Qing H, Deng Y (2013) Adsorptive BSA coating method for CE to separate basic proteins. *Chromatographia* 76:59–65. <https://doi.org/10.1007/s10337-012-2337-y>
93. Boulos SP, Davis TA, Yang JA, Lohse SE, Alkilany AM, Holland LA, Murphy CJ (2013) Nanoparticle-protein interactions: a thermodynamic and kinetic study of the adsorption of bovine serum albumin to gold nanoparticle surfaces. *Langmuir* 29:14984–14996. <https://doi.org/10.1021/la402920f>

94. Gao J, Huang X, Liu H, Zan F, Ren J (2012) Colloidal stability of gold nanoparticles modified with thiol compounds: bioconjugation and application in cancer cell imaging. *Langmuir* 28:4464–4471. <https://doi.org/10.1021/la204289k>
95. López-Lorente ÁI, Soriano ML, Valcárcel M (2014) Analysis of citrate-capped gold and silver nanoparticles by thiol ligand exchange capillary electrophoresis. *Microchim Acta* 181:1789–1796. <https://doi.org/10.1007/s00604-014-1218-5>
96. Pakiari AH, Jamshidi Z (2010) Nature and strength of M-S bonds (M = Au, Ag, and Cu) in binary alloy gold clusters. *J Phys Chem A* 114:9212–9221
97. Gautier J, Munnier E, Soucé M, Chourpa I, Douziech Eyrolles L (2015) Analysis of doxorubicin distribution in MCF-7 cells treated with drug-loaded nanoparticles by combination of two fluorescence-based techniques, confocal spectral imaging and capillary electrophoresis. *Anal Bioanal Chem* 407:3425–3435. <https://doi.org/10.1007/s00216-015-8566-9>
98. Blazkova I, Nguyen HV, Dostalova S, Kopel P, Stanisavljevic M, Vaculovicova M, Stiborova M, Eckschlagler T, Kizek R, Adam V (2013) Apoferritin modified magnetic particles as doxorubicin carriers for anticancer drug delivery. *Int J Mol Sci* 14:13391–13402. <https://doi.org/10.3390/ijms140713391>
99. Oukacine F, Bernard S, Bobe I, Cottet H (2014) Physico-chemical characterization of polymeric micelles loaded with platinum derivatives by capillary electrophoresis and related methods. *J Control Release* 196:139–145. <https://doi.org/10.1016/j.jconrel.2014.09.022>
100. Musile G, Cenci L, Andreetto E, Ambrosi E, Tagliaro F, Bossi AM (2016) Screening of the binding properties of molecularly imprinted nanoparticles via capillary electrophoresis. *Anal Bioanal Chem* 408:3435–3443. <https://doi.org/10.1007/s00216-016-9418-y>
101. Taylor G (1953) Dispersion of soluble matter in solvent flowing slowly through a tube. *Proc R Soc A Math Phys Eng Sci* 219:186–203. <https://doi.org/10.1098/rspa.1953.0139>
102. Ibrahim A, Meyrueix R, Pouliquen G, Chan YP, Cottet H (2013) Size and charge characterization of polymeric drug delivery systems by Taylor dispersion analysis and capillary electrophoresis. *Anal Bioanal Chem* 405:5369–5379. <https://doi.org/10.1007/s00216-013-6972-4>
103. Franzen U, Østergaard J (2012) Physico-chemical characterization of liposomes and drug substance-liposome interactions in pharmaceuticals using capillary electrophoresis and electrokinetic chromatography. *J Chromatogr A* 1267:32–44. <https://doi.org/10.1016/j.chroma.2012.07.018>
104. Nguyen TTTN, Østergaard J, Stürup S, Gammelgaard B (2013) Metallomics in drug development: characterization of a liposomal cisplatin drug formulation in human plasma by CE-ICP-MS. *Anal Bioanal Chem* 405:1845–1854. <https://doi.org/10.1007/s00216-012-6355-2>
105. Nguyen TTTN, Østergaard J, Stürup S, Gammelgaard B (2013) Determination of platinum drug release and liposome stability in human plasma by CE-ICP-MS. *Int J Pharm* 449:95–102. <https://doi.org/10.1016/j.ijpharm.2013.03.055>
106. Otarola J, Lista AG, Fernández Band B, Garrido M (2015) Capillary electrophoresis to determine entrapment efficiency of a nanostructured lipid carrier loaded with piroxicam. *J Pharm Anal* 5:70–73. <https://doi.org/10.1016/j.jpha.2014.05.003>
107. Janu L, Stanisavljevic M, Krizkova S, Sobrova P, Vaculovicova M, Kizek R, Adam V (2013) Electrophoretic study of peptide-mediated quantum dot-human immunoglobulin bioconjugation. *Electrophoresis* 34:2725–2732. <https://doi.org/10.1002/elps.201300088>
108. Zhou ZM, Feng Z, Zhou J, Fang BY, Ma ZY, Liu B, Zhao YD, Hu XB (2015) Quantum dot-modified aptamer probe for chemiluminescence detection of carcino-embryonic antigen using capillary electrophoresis. *Sensors Actuators B Chem* 210:158–164. <https://doi.org/10.1016/j.snb.2014.12.087>



Using Integrated Cancer-on-Chip Platforms to Emulate and Probe Various Cancer Models

4

Ziqiu Tong, Wing-Yin Tong, Bo Peng, Yingkai Wei, Arianna Oddo, and Nicolas H. Voelcker

Contents

1	Definition of Topic	152
2	Overview	152
3	Introduction	152
3.1	Cancer Biology	152
3.2	Microfluidic Systems	154
4	Experimental Methodology	157
4.1	Microfluidic Chip Fabrication	157
4.2	Microfluidic Device Assembly and ECM Coating	159
4.3	Cell Culture in Microfluidic Devices	160
5	Key Research Findings	161
5.1	Microfluidic Models for Cancer Metastasis	161
5.2	Microfluidic Model Systems for Specific Cancer Organ Types	172
5.3	Integration of CoC Systems with Advanced Technologies	181
6	Conclusions and Future Perspectives	196
	References	197

Z. Tong · W.-Y. Tong · Y. Wei · A. Oddo

Drug Delivery, Disposition and Dynamics, Monash Institute of Pharmaceutical Sciences, Monash University, Parkville, VIC, Australia

B. Peng

Commonwealth Scientific and Industrial Research Organization (CSIRO), Clayton, VIC, Australia

N. H. Voelcker (✉)

Drug Delivery, Disposition and Dynamics, Monash Institute of Pharmaceutical Sciences, Monash University, Parkville, VIC, Australia

Commonwealth Scientific and Industrial Research Organization (CSIRO), Clayton, VIC, Australia

Melbourne Centre for Nanofabrication, Victorian Node of the Australian National Fabrication Facility, Clayton, VIC, Australia

e-mail: nicolas.voelcker@monash.edu

1 Definition of Topic

Organ-on-chip platforms are engineered microfluidic systems that are capable of mimicking basic pathophysiological units of human organs. A number of organ-on-chip models have already been developed for emulating functional human healthy organs and their cancer counterparts, for example, lung (cancer), liver (cancer), brain (cancer), and breast (cancer). In the context of applications in cancer research, organ-on-chip systems are also referred to as cancer-on-a-chip (CoC). Recently, CoC has become an emerging in vitro model that can foster an innovative way of conducting cancer research and promote advances in cancer diagnostics and therapy. CoC systems are suitable models for cancerous tissues in both 2D and 3D microenvironments and can recapitulate pathophysiological phenomena, such as cancer cell extravasation, immune system responses, and also to provide a new platform for personalized medicine. Such systems can help us gain a deeper understanding of the cancer disease etiology and development, as well as, provide a high throughput screening tool to test and evaluate the safety and efficacy of new cancer therapies, including nanomedicines, ultimately aiding their clinical translation.

2 Overview

Recent advances in nano- and microfabrication have enabled the development of a new generation of in vitro platforms suitable for cancer research, disease modeling, and advanced diagnostics. In this chapter, a brief background on cancer biology and microfluidic system will be covered first. Secondly, the design and fabrication of microfluidic devices will be introduced in the Experimental Methodology section. Subsequently, a comprehensive overview of innovative CoC devices will be presented for modeling cancer metastatic cascades and organ-specific tumors (e.g., brain, breast, liver, and lung). The following section will focus on the discussion of the integration of advanced technologies with CoC for cancer cell imaging, monitoring, and manipulations. For example, selected super resolution imaging techniques will be reviewed. The integration of biosensors in CoC will also be discussed, as they allow to monitor changes in pH, oxygen, glucose, lactate level, and other cancer biomarkers. Finally, conclusions and future perspectives will be presented in relation to the opportunities and maturation of the recently developed CoC field, which in our view holds great potential to revolutionize in vitro drug testing and for personalized medicine.

3 Introduction

3.1 Cancer Biology

Cancer is the second leading cause of death globally and was responsible for 8.8 million deaths in 2015 [1]. Despite recent advancements in cancer treatment, overall 5-year survival rate still remains surprisingly low [2]. Cancer represents an

enormous societal burden, both in terms of human suffering and socioeconomical costs [3]. For example, the total cost for cancer treatment in 2010 alone was estimated at 1.16 trillion US dollars [4]. Nevertheless, these burdens could be greatly reduced through early cancer detection and intervention based on a better understanding of cancer etiology [5].

Healthy normal cells are transformed into cancerous cells in the process of tumorigenesis and including events such as: deregulated cell proliferation, angiogenesis, and metastasis [6]. Risk factors such as heredity, exposure to carcinogenic substances, or chronic inflammation are linked to genetic mutations [7]. However, the underlying mechanisms that drive many of those events still remain unknown. For example, cancer metastasis contributes to 90% of cancer-related deaths and, while molecular signatures of metastasis are widely studied, factors that drive metastasis are multifactorial and complex [8]. Clinically, cancer metastasis appears with an organ-specific pattern, but its process remains largely unidentified. One of the most accredited theories is the “seed and soil” hypothesis, which states that some types of cancer cells preferentially interact with the microenvironment of some specific organs [9]. The cancer microenvironment is a heterogenic and dynamic molecular “ecosystem,” where cancer cells orchestrate cell-to-cell communication leading to cancer progression [10]. More specifically, this complex tumor microenvironment consists of a heterogeneous mixture of cells in complex spatial arrangement, including tumor cells (such as carcinoma), cancer stem cells, inflammatory immune cells, assorted fibroblasts, pericytes, and endothelial cells of blood vessels [11]. Elucidating the role of each of these biological players is crucial but difficult, as the combination of these factors are interconnecting and complex in vivo.

In fact, early detection of cancer can greatly increase the chances for successful treatments of certain cancer types. Clinically, cancer detection is typically performed via tissue biopsy or the use of potentially harmful contrast agents for various clinical imaging techniques such as computed tomography (CT) or magnetic resonance imaging (MRI). However, these methods are generally considered invasive, require extensive technical expertise and complicated instrumentations [12]. On the other hand, detection of specific circulation cancer biomarkers has been demonstrated as promising alternatives [13]. For example, circulating cancer biomarkers, including circulating tumor cells (CTCs), vesicles (exosomes), proteins, and circulating tumor nucleic acids (ctNA) have been identified that are secreted by tumor cells into the bloodstream and other body fluids [13]. In particular, isolated CTCs can provide extremely valuable information in disease characteristics without the need to directly access tumor sites [14]. Cancerous cells indeed express certain proteins, such as epithelial cell adhesion molecule (EpCAM) at higher level than normal cells, exhibiting different morphology (such as cell size). Exosomes are small membrane-bound vesicles shed from cells for signaling and contain a number of biomolecules including nucleic acids and proteins which act as alternative biomarkers for cancer detection and diagnostics [13].

Metastatic animal models have been routinely used for cancer research, especially suitable for studying late stage of cancer progression. However, those animal models fall short to resolve modern theories such as parallel progression of cancer [14, 15].

The inherent genetic differences of animal models to human, the technical challenges of high-content molecular imaging *in vivo*, and the conventional *in vitro* models being overly simplistic and not resembling the tumor microenvironment highlight the dire need of more advanced cancer research models.

3.2 Microfluidic Systems

Microfluidic systems manipulate extremely small amounts of liquids (nanoliter), with channel dimensions range from tens to hundreds of micrometers [16]. Using microfluidics, traditional large-scale experiments can be conducted in a compact, high throughput manner in what is termed “lab-on-a-chip” opening up a plethora of applications in biological and biomedical fields [17]. Common biological assays, such as polymerase chain reaction (PCR) and cell-based assays have been integrated in such devices. Important advantages of using microfluidic systems include short analysis time and low cost, compact size, ease of use, and ultra-low sample volume requirements [17]. Moreover, such system allows fine-tuning of cell microenvironments and enable fast readout [18].

Until recently, research laboratories have started to culture mammalian cells in an intricate manner inside microfluidic devices to form the basic “functional” organ units that can closely mimic human tissues, hence coining the term “organ-on-a-chip” [19]. Those organ-on-a-chip units allow for the modeling of basic physiological functions of organs to be studied *in vitro* but still maintain the important basic *in vivo* functions [20]. A wide range of on-chip models have already been developed for emulating different human organs, including lung, liver, kidney, brain, gut, and bone. In the case of the cancer-affected organ counterparts, the term “cancer-on-a-chip” (CoC) has emerged (Fig. 4.1a) [21, 22]. Although organ-on-a-chip systems have been reviewed extensively in a number of articles [17, 19, 20], CoC model reviews still remain fairly limited and mainly cover the “biological” aspects of such systems [21, 23]. In contrast to the existing reviews, we provide here a comprehensive summary that covers experimental and technical details, a wide range of applications for cancer metastasis, and an overview of the most current state-of-the-art CoC models. Finally, we explain how innovative tools such as biosensors and advanced super-resolution imaging techniques can be incorporated into CoCs.

CoC platforms combine the advantages from both *in vitro* and *in vivo* models and represent a promising tool to study cancer at the “organ” level [24]. CoC can be used to evaluate the efficacy of cancer therapy, monitoring responses to external drug stimuli, while allowing for rapid, real-time, and multi-sample analysis [24]. Furthermore, these versatile, non-invasive tools can provide quantitative information regarding cell viability, microenvironment, molecular signaling and cancer cytomics [25]. When used in combination with patient-derived cells, CoC devices promise to revolutionize cancer diagnosis and help clinicians to predict efficacy and side effects of different therapeutic approaches, while monitoring the development of the

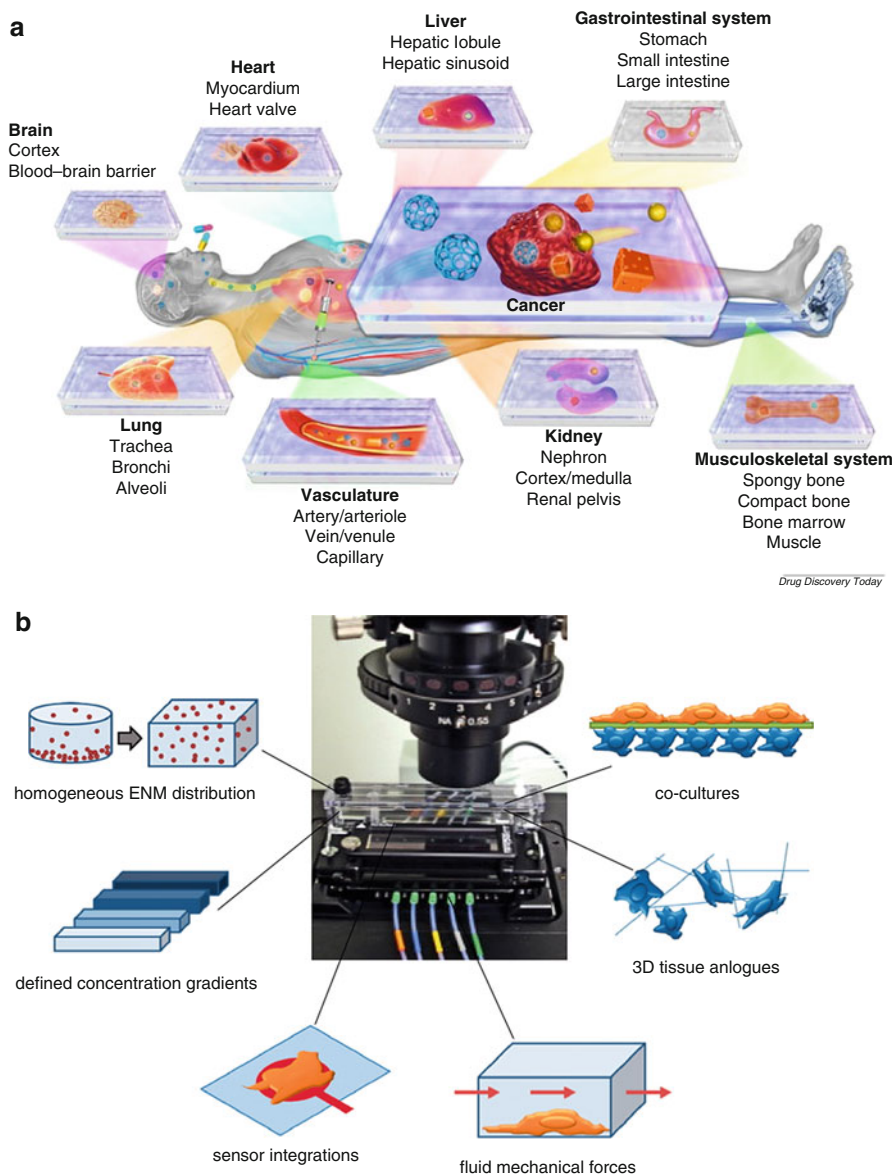


Fig. 4.1 (a) To date, most organ types have been replicated on microfluidic devices, including their cancer-affected counterparts (e.g., healthy brain-on-chip vs. brain tumor-on-chip). (Reprinted with permission from Ref. [21]. Copyright © 2017, Elsevier.) (b) Microfluidic technology enables the precise control over fine-tuning of chemical concentrations, integration of biosensors, co-culturing, and monitoring cellular responses to chemicals including anticancer therapeutics and nano-medicines under flow. (Adapted from Ref. [22]. Copyright © 2010, Elsevier, and from Ref. [17]. Copyright © 2015, Taylor & Francis)

disease. Applying imaging-based diagnosis in a microfluidic device allows the measurement of parameters such as cell size and stiffness, together with electrical responses detectable in cancer cells [26].

Using CoC systems as cancer models offers several advantages over traditional well plate 2D culture model or in vivo animal models. Unlike an animal model, a CoC system can “isolate” individual diseased organ type to be studied. Furthermore, CoC devices are capable of the co-culture of different cell types and the integration of sensors to modulate cancer cell functions in real time (Fig. 4.1b). CoC devices have the great potential to be applied in early stage anti-drug discovery, toxicology studies, and also to advance our understanding of cancer biology and its complex mechanisms. However, some limitations still need to be addressed (Table 4.1). For example, while CoC platforms can recapitulate the in vivo-like microenvironments such as induced shear flow which the traditional well plate format culture cannot achieve (Fig. 4.1b), they still lack the automation to enable high throughput screening (HTS).

Table 4.1 Summary of advantages and limitations of different systems: animal models, conventional in vitro systems (well-plates) and innovative in vitro microfluidic systems (cancer-on-a-chip, CoC). (Adapted from Ref. [17]. Copyright © 2015, Taylor & Francis)

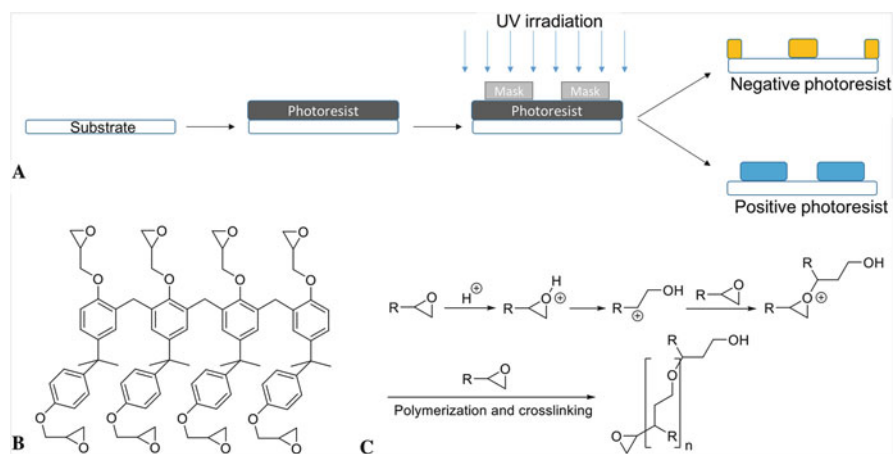
Parameter	In vivo systems (animal models)	Conventional in vitro systems (well plates)	Microfluidic systems (cancer-on-a-chip)
Physiological relevance	High complexity of living systems, although interspecies variability limits physiological relevance	Advantage of using human cells, but the setup (static conditions, gravitational settling) limits its physiological relevance	Human-derived cells, improved physiological relevance (e.g., flow, co-culture)
System fine-tuning	Tunable parameters are limited (usually to administered formulation)	Changes are limited to cell type, media and administered formulation	High versatility, systems can be optimized for different purposes (e.g., tissue-response, co-culture, gradient testing, dynamic vs. static conditions)
HTS/parallelization/automation	Not possible	State-of-the-art screening systems, implemented through robotics	Great potential, not yet fully exploited (still at an early stage)
Read-out	Animal sacrifice often needed, specialized training and facility required	Well-established analysis methods, although interferences with colorimetric assays often occur	Suitable for label-free sensor integration, microscopy-based readouts
Time/cost	Time and resource intensive	Generally fast and relatively cheap (depending on the degree of automation)	Medium financial input, but fairly comparable with conventional in vitro systems

4 Experimental Methodology

4.1 Microfluidic Chip Fabrication

Microfluidic technology offers flexibility in chamber design and choice of materials, which is an important aspect to mimic different organ microenvironment. The most commonly used materials for the fabrication of microfluidic device are polydimethylsiloxane (PDMS) and poly(methyl methacrylate) (PMMA) [27]. While the former is predominantly used for the fabrication and prototyping of microfluidic devices in the research community, the latter is often preferred material in commercial products. Advantages related to the use of PDMS include biocompatibility (gas permeability), low auto-fluorescence, and low cost. On the other hand, PMMA and other thermoplastics are more suitable for the mass production of microfluidics. Various techniques have been developed to fabricate microfluidic devices, such as print and peel methods, micro-milling, direct laser printing, micro-wire molding, and hot embossing [28]. Nonetheless, soft lithography is still by far the most popular fabrication method for biomedical microfluidic devices, especially in research laboratory settings [28]. In this section, photolithography and PDMS-based soft lithography will be discussed.

Photolithography is a process that a geometric pattern from a photomask is transferred to a photoresist on a flat surface. Due to the differences in chemical properties of photoresists, UV light exposure can either make the photoresist more soluble in a developer (positive photoresist) or can cross-link the photoresist and making the exposed region insoluble (negative photoresist) (Scheme 4.1a). For example, SU8 is an acid-catalyzed, epoxy-based negative photoresist (Scheme 4.1b) in an organic solvent with 10% triarylsulfonium hexafluoroantimonate salt as a photo-initiator (Scheme 4.1c). SU8 photoresist offers several advantages in



Scheme 4.1 (a) Positive and negative photoresists used in photolithography. (b) Chemical structure of SU8 resist. (c) Reaction mechanism of SU8 polymerization and crosslinking

photolithography process, such as the simplicity to form patterns with submicron resolution and offering a reasonable combination of mechanical strength and chemical tolerance [29, 30].

In a photolithography process, UV exposure transfers the desired patterns from a mask to a photoresist. According to the required resolution, there are two main types of photomasks commonly used: “hard” glass mask (made in quartz or borosilicate glass) and “soft” transparency plastic mask (made in plastic). The “hard” glass mask is fabricated via a direct-write technique through the use of a focused laser beam. This type of glass mask can provide a submicron resolution and is stable against different solvents and substrates [31]. On the other hand, “soft” masks can be easily fabricated from a high-resolution printer, which can offer a cheaper alternative, but with poor feature resolution (5–10 μm). For those microfluidic devices that contain “large” features, “soft” transparency photomask can be a better choice [32].

The protocols for the fabrication of SU8-based molds can differ in different applications; here we will use a dual-layer SU8 mold as an example to demonstrate the SU8 fabrication (Fig. 4.2). A spin coater is used for spreading SU8 photoresists onto a silicon wafer or a glass substrate. For creating a 3 μm thick feature, SU8 2002 is used and exposed at 90 mJ/cm^2 . Alignment marks (e.g., crossed shape) are very important for fabrication of multilayer molds that require precise alignments. After UV exposure, the substrate with SU8 2002 is baked at 95 $^{\circ}\text{C}$ for 2 min, followed by developing with SU8 developer for 1 min to resolve the first layer feature. For the second layer fabrication, a photoresist with different thickness can be used. For example, to create a thickness of 100 μm , SU8 3050 could be used. To note, with the increase of the resist thickness, the UV exposure dose needs to be increased (250 mJ/cm^2). After the second UV irradiation, the wafer is further baked at 95 $^{\circ}\text{C}$ for 5 min, followed by developing with SU8 developer for 20 min to obtain the second layer feature. To confirm that the resolved SU8 features on silicon wafer possess the desired dimensions (as the fabrication procedure such as UV over-exposure or under-

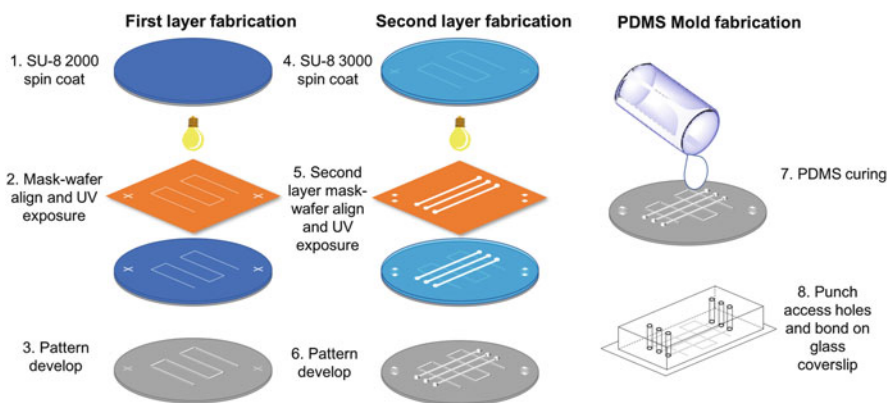


Fig. 4.2 A schematic illustration of a photolithographic procedure to fabricate a two-layer microfluidic device via SU8 negative photoresists and soft lithography via PDMS casting

exposure can affect the final size), several characterization techniques are performed. For example, a Stylus surface profilometer can be used, although this technique can be invasive to the SU8 features as the Stylus tip is in direct contact with SU8 patterns. The alternative noninvasive technique that one can use is the light interferometry which uses light interference fringes to determine the geometry size.

The final step is to silanize the silicon wafer mold to prevent adhesion to subsequent PDMS casting and ensure that the cured PDMS mold can be peeled off easily. Briefly, the fabricated silicon mold is placed inside a vacuum desiccator, where a droplet of 20 μL of hexamethyldisilazane is introduced in the desiccator. The desiccator is then sealed and connected to a vacuum pump for 5 min to create silane vapor to be deposited onto the mold surface overnight. To characterize if the hexamethyldisilazane has been deposited properly on the silicon wafer surface, common techniques such as contact angle measurement, X-ray photoelectron spectroscopy (XPS), or Fourier-transform infrared spectroscopy (FTIR) are suitable for surface functionality analysis.

4.2 Microfluidic Device Assembly and ECM Coating

Since its initial introduction in the late 1990s as a building material for microfluidic devices, PDMS is still the most popularly used material in many research laboratories [33]. PDMS fabrication is a rapid process, and multiple layers of PDMS can be covalently bonded. In brief, PDMS is mixed at a 10:1 ratio (monomer to catalyst), degassed, poured onto the passivated SU8 containing silicon wafer mold, and cured in an oven for 12 h at 80 °C. The cured PDMS mold is then carefully released from the silicon wafer mold, and the inlet and outlet ports are created using Haris Uni-Core biopsy punches with appropriate sizes. A glass cover slide and a PDMS mold are first cleaned by sonication in ethanol and are then loaded into an oxygen plasma chamber for surface activation for 30 s at 50 W. The oxygen plasma treated PDMS mold is then gently pressed against the cover slide for an irreversible covalent bonding. Sterilization is performed to make it suitable for subsequent cell culture. Typically, UV irradiation is a common and effective method (30–60 min of 254 nm UV irradiation) than the autoclaving approach.

In order to facilitate cell attachment and growth inside the microfluidic devices, channel surface functionalization and extracellular matrix (ECM) coating are usually performed. Here, we will introduce two methods for type I collagen immobilization: noncovalent and covalent approaches. To this end, for the noncovalent immobilization procedure, a working solution of 100 $\mu\text{g}/\text{ml}$ of type I collagen in MilliQ water is injected directly into the assembled microfluidic device (after plasma treatment and bonding) and incubated at 37 °C for 30 min or 4 °C overnight. After the incubation step, the device is washed thoroughly with MilliQ water and dried. The coated device can then be used for cell culture after equilibration with phosphate-buffered saline (PBS) or cell culture medium for 1 h. Alternatively, the coated devices can be stored at 4 °C until future use. In fact, this physisorption method has been used as a common practice for flask or microplate surface coating. On the other hand, a

covalent immobilization procedure can anchor ECM strongly onto the microfluidic channel surface, especially important for long-term cell cultures. The following protocol describes an adapted method from the Ingber group [34]. A microfluidic device is treated with oxygen plasma at 50 W for 30 s, immediately followed by injection of 10% (v/v) of (3-aminopropyl)-trimethyloxysilane (APTMS) in absolute ethanol and is incubated at room temperature for 15 min. The device is then washed with ethanol and water sequentially, and dried at 80 °C for 2 h. Subsequently the device is then filled with 2.5% glutaraldehyde in water and incubated at room temperature for 15 min and further washed with water and ethanol, and then dried at 80 °C for 2 h. In the final step, ECM (e.g., type I collagen) is injected and incubated in the device for 1 h, allowing the amine groups from the ECM to form Schiff bases with the aldehyde groups on the surface of the chip [34]. To confirm even ECM coating, fluorescence labeling of the proteins with fluorophores such as FITC or Cy5 can be performed and the coated channels can be imaged using a fluorescence microscope. An alternative method to characterize the coating is immunostaining.

4.3 Cell Culture in Microfluidic Devices

Microfluidic devices can be used to seed different types of cells depending on the nature of the research interests. Here, we will introduce the seeding protocol for hCMEC/D3 blood–brain barrier microvascular endothelial cell as an example. An assembled microfluidic device is initially washed with PBS and cell culture media. hCMEC/D3 cells at a concentration of 1×10^7 cells/ml in EBM-2 media are then injected and allowed to attach onto collagen-precoated microfluidic channel. The cell-loaded device is then placed in an inverted position for 1 h inside an incubator to seed the cells onto the upper surface of the microchannel. Subsequently, another batch of freshly isolated cells is injected into the device and incubated at the upright position for 1 h to facilitate cell attachment onto the lower surface. Afterwards, 100 μ l fresh EBM-2 media is delivered to the chip inlet and outlet reservoirs and then the chip is transferred inside an incubator. Starting on day 2, a culture media flow rate at 2 μ l/min is initiated using a syringe pump to induce shear flow to mimic in vivo hemodynamic flow condition.

A key step to validate if an “organ” is phenotypically desirable and functional after maturation inside the microfluidic chip is to check for specific surface biomarkers using appropriate bioassays (e.g., immunofluorescence staining). Here, we will introduce the protocol for immunostaining assay of endothelial cells inside a microfluidic chip as an example. The cells are cultured for 4 days inside a microfluidic device, and the microchannel containing cells is washed with PBS, followed by fixation with 4% paraformaldehyde for 20 min at room temperature. The cells are further permeabilized with 0.25% Triton X-100 for 10 min, and blocked with 5% BSA in PBS for 1 h at room temperature. FITC conjugate anti-zona occludens-1 antibody, at 1 μ g/ml in 1% BSA, is then added to the chip, and incubated for 3 h. The chip is further washed gently with PBS and injected with ProLong antifade mountant

with DAPI. The immunostained chip can then be imaged using either an epifluorescence or confocal fluorescence microscope (e.g., Leica SP8 inverted laser scanning confocal microscope).

5 Key Research Findings

5.1 Microfluidic Models for Cancer Metastasis

Cancer metastasis is a multistep process of the formation of secondary loci from a primary tumor. This process involves firstly the tumor cells infiltration into the surrounding stroma (invasion), followed by transendothelial migration into (intravasation) and out of vasculatures (extravasation), and the formation of a secondary tumor at the distance sites (colonization) [35]. Following colonization, secondary loci will develop into micrometastasis after dormancy [36]. Certain events within this cascade have long been studied in murine models. However, recent development of miniaturized in vitro systems, such as CoCs, has enabled a full-spectrum interrogation at each step of those events by allowing the individual features to be decoupled. Figure 4.3 represents an overview of the metastatic cascade, and a summary of the corresponding microfluidic model systems that recapitulate different stages of cancer metastasis. In this section, we will provide a comprehensive review of those microfluidic model systems.

5.1.1 Cancer Cell Invasion Modeling

In order for cancer cells to detach from the original tumor mass and to invade surrounding tissues, they undergo epithelial-mesenchymal transition (EMT), a hallmark of cancer metastasis which denotes the loss of epithelial characteristics and

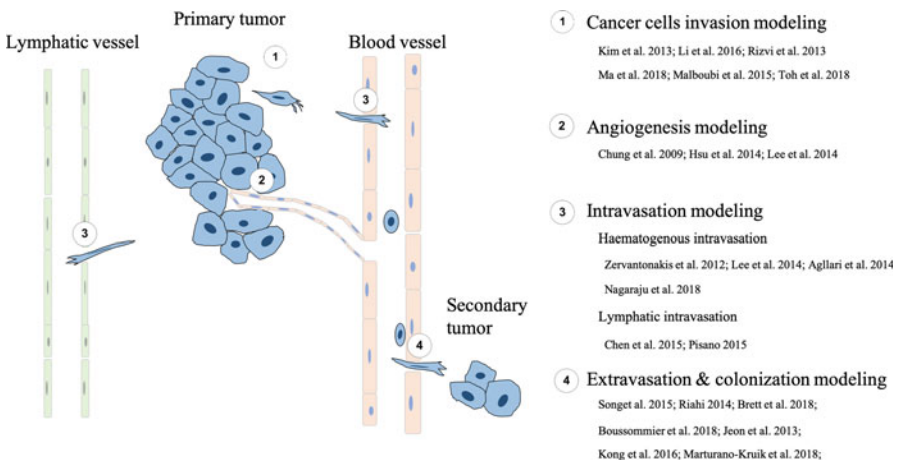


Fig. 4.3 Schematic representation of cancer metastasis cascade and summary of selected microfluidic models emulating each process

acquires mesenchymal phenotypes [37]. The EMT process involves a cascade of signaling events such as the downregulation of E-cadherin (E-cad) and the upregulation of N-cadherin (N-cad), which is referred to as “cadherin switch” [38]. Transforming growth factor β (TGF β) is known to contribute to EMT activation by upregulating transcriptional repressor of E-cad. The *in vivo* study of the EMT process in metastasis, which involves the use of transgenic murine models, has demonstrated the pro-metastatic roles of TGF β [39, 40].

Transgenic mice models are difficult to generate as knock-out mice with deletion of certain EMT genes may result in the premature animal death due to the dual roles of those genes in embryogenesis [41]. On the other hand, novel *in vitro* CoC systems have been developed to recapitulate those molecular hallmarks, offering a more robust means to study cancer metastasis. For example, Kim et al. developed a PDMS-based microfluidic device consisted of two interconnected microchannels where TGF β gradient was created (Fig. 4.4a) [42]. This platform enabled the precise detection of EMT cellular responses of A549 lung cancer cells to TGF β stimulation, such as elevated expression levels of vimentin and downregulation level of E-cad (Fig. 4.4a). The effect of TGF β on cell attachment, and on EMT, was also demonstrated by flow stimulation in a microfluidic chamber as reported by Li and coworkers [43]. By combining 3D cell culture and microfluidics, more EMT signatures have been reproduced. Rizvi and coworkers reported using a microfluidic chip to grow 3D ovarian cancer nodules that could mimic the interstitial fluid flow of ovary (Fig. 4.4b) [44]. They demonstrated that such fluid flow facilitated vimentin and integrin $\alpha 5$ upregulations as well as E-cad and β catenin downregulations in ovarian nodules (Fig. 4.4b).

After the activation of EMT, tumor cells gain the migratory ability to squeeze through the ECM barrier in the surrounding stroma to reach intravasation site. Therefore, techniques for characterizing this migratory ability would be instrumental in defining the efficacy of anti-metastasis drugs, and dissecting the role of certain aspects in tumor microenvironment. Ma and coworkers reported a microfluidic system to recapitulate the mechanical confinement features of the ECM barrier by incorporating vertical constrictions [45]. Under the effect of a chemoattractant, cells could squeeze through those constrictions (Fig. 4.5a). They discovered that the cell migratory ability (velocity and distance) was directly proportional to the number of contractions in the ECM. Ras homolog protein A (RhoA) and Rho-associated protein kinase (ROCK) gene expressions, related to cytoskeleton formation and contraction, were found to be upregulated. To interrogate the limit of cell migration in tight spaces, Malboubi and coworkers utilized a microfluidic system with microchannels of varying cross-sectional area, from larger than the dimension of a cell to smaller than the diameter of a nuclei [46]. They deduced that the limiting factor for cell migration was the size of cell nucleus. Breast cancer cells failed to migrate into a microchannel with cross-section area below $7 \times 5 \mu\text{m}^2$ (Fig. 4.5b). Apart from physical constrictions, other aspects of the tumor microenvironment on cancer cell migration and invasion can also be tested in microfluidic chips, such as cellular cross-talk and hypoxia [47, 48]. These studies via microfluidic systems provide

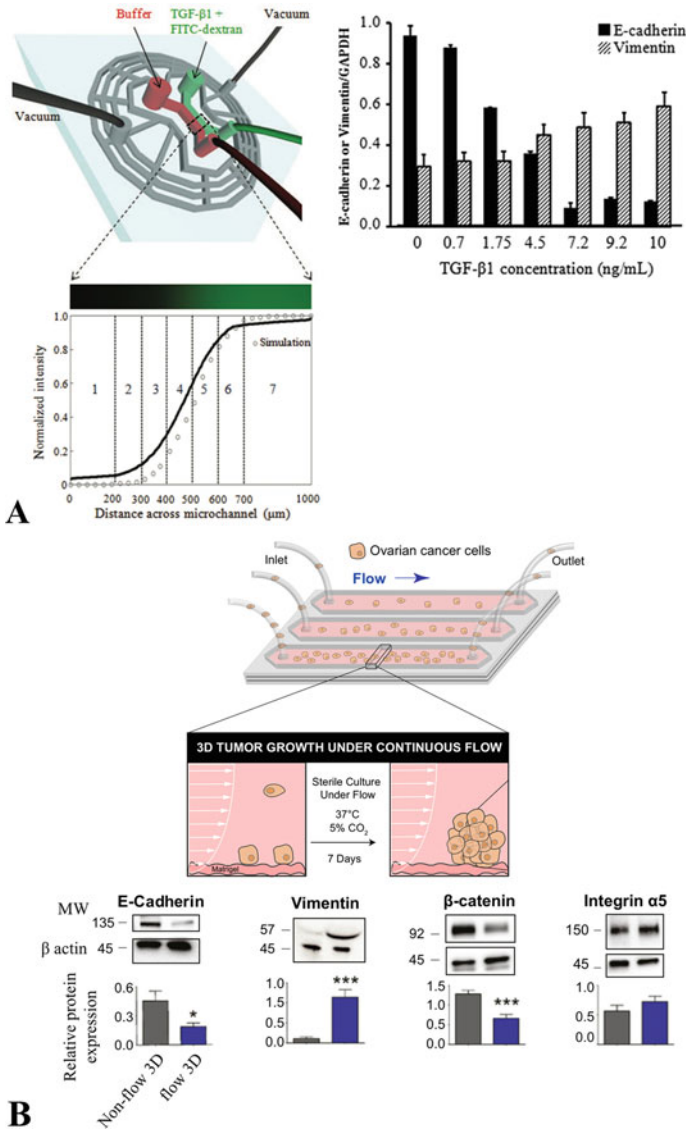


Fig. 4.4 Microfluidic models recapitulating microenvironmental cues in promoting EMT of cancer cells. (a) A microfluidic system created a gradient of TGFβ stimulation on lung cancer cells A549, and their E-cad and vimentin expressions were measured. (Reprinted from Ref. [41]. Copyright © 2013, Wiley.) (b) 3D ovarian nodules cultured with or without flow condition under microfluidics. EMT-related protein expressions in ovarian nodules cultured with or without simulated interstitial flow were assayed. (Reprinted from Ref. [43]. Copyright © 2013, Proceedings of the National Academy of Sciences)

insights that the ECM indeed partially supports cancer cell migration. Some of those aspects are difficult to test in *in vivo* models.

Not only can the individual cell invasion and migration events be tracked using microfluidic systems, collectively cell mass invasion events have also been modeled in a way that resembles more the *in vivo* situation [49]. Toh and colleagues reported a microfluidic device consisting of a cell culture channel and a perfusion channel, separated by elliptical pillar arrays with a gap size of 20 μm (Fig. 4.5c) [50]. This design permitted breast cancer cells to form 3D cellular aggregates that resemble tumor mass, followed by embedding the cell aggregates with collagen matrix resembling the ECM barrier. Collective invasion was initiated by local contact and degradation of the ECM barrier without breaking of cell-cell contacts. Other advanced microfluidic models, such as real-time quantification of cell migrations based on impedance measurements, and on-chip siRNA knockdown prior to migration study have also been reported [51, 52].

5.1.2 Angiogenesis Modeling

Angiogenesis in cancer progression stipulates that the tumor cells, together with the neighboring stroma, induce vessel development to support the tumor growth [53]. Using microfluidic systems to model angiogenesis has recently been reported. For instance, Chung et al. engineered a microfluidic platform to quantify the interactions between endothelial cells and cancer cells [54]. This device consisted of three independent flow channels inter-connected by collagen matrix (Fig. 4.6a). By perfusion of vascular endothelial growth factor (VEGF) through a side channel, endothelial cells were able to sprout into the 3D collagen scaffold in the direction towards the side channel. The system was further utilized to compare the capability to induce angiogenesis across different cell types: invasive breast cancer cells, glioblastoma, and smooth muscle cells. Interestingly, breast cancer cells were found to be able to induce higher endothelial cell sprouting than the other two cell types investigated, indicating higher angiogenesis induction ability (Fig. 4.6a). In another implementation, a microfluidic cytokine gradient has been used to study tumor cell induced angiogenesis [55].

Lee and coworkers have used a microfluidic chip to house a co-culture of lung fibroblasts and endothelial cells [56]. It was reported that the endothelial cells were stimulated by the lung fibroblasts to form differentiated micro-vessels, as evidenced by the observed tight junctions (Fig. 4.6b). By integrating glioblastoma cells into the microfluidic chip, they have observed and quantified the effect of cancer cells in promoting angiogenic sprout formations, which were subsequently abolished by anti-angiogenic treatment using bevacizumab. The close approximation of *in vivo* angiogenesis progression and respective drug response indicates the promise of these microfluidic system models to be used in the drug discovery pipeline.

5.1.3 Intravasation (Hematogenous and Lymphatic) Modeling

The entry of cancer cells into circulation can be through blood vessels (hematogenous intravasation) or lymph vessels (lymphatic intravasation). Hematogenous intravasations are often studied *in vivo* using chick embryo, murine, and zebra fish

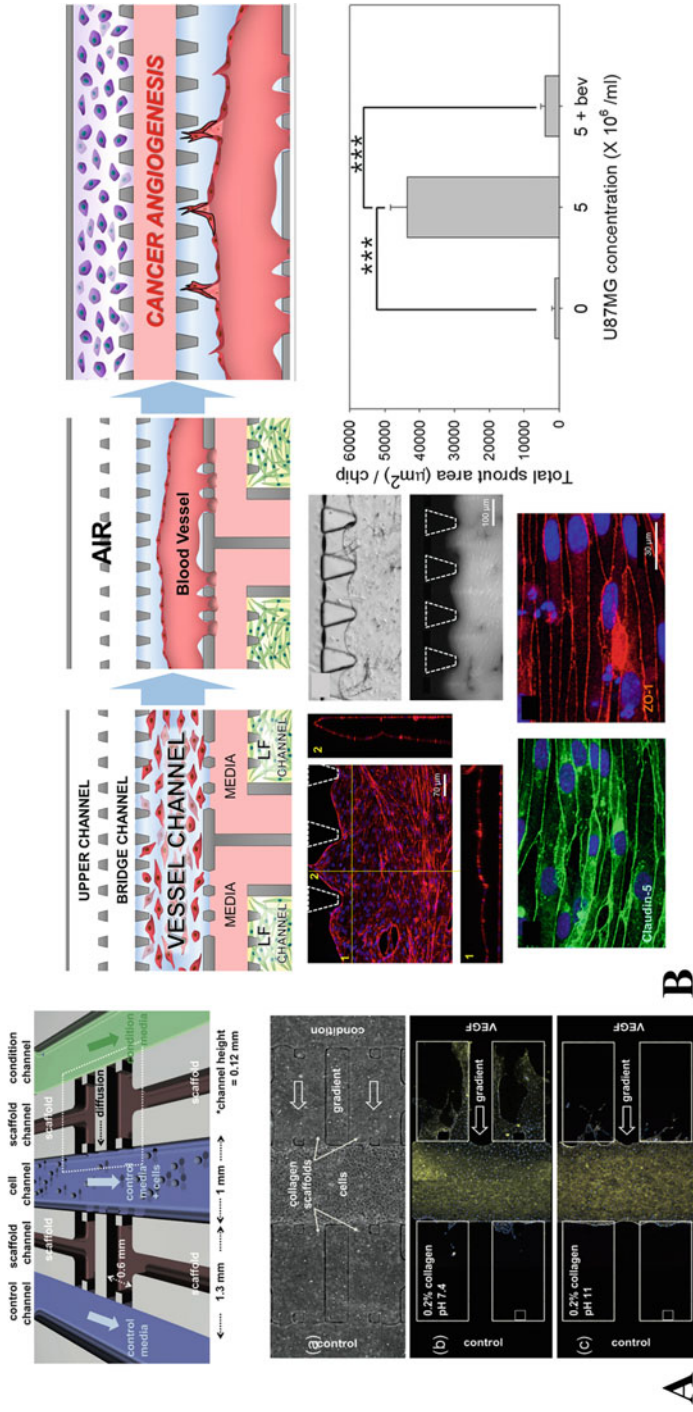


Fig. 4.6 Microfluidic angiogenesis models. (a) Three-channel microfluidic system to probe the ability of different cancer cell types in inducing angiogenesis. (Reprinted from Ref. [54]. Copyright © 2009, Royal Society of Chemistry.) (b) Microfluidic system housing lung microvasculature for cancer-induced angiogenesis study. Lung microvasculature showing cell-cell junctions by immunostaining. Sprouting of microvasculature influenced by the induction of glioblastoma and anti-angiogenic drug. (Reprinted from Ref. [56]. Copyright © 2014, AIP Publishing)

models [57]. The readouts of these models rely heavily on the counting of the number of CTCs [58]. Imaging the invadopodia of metastasizing cancer cells at the vasculature was also another commonly exercised method [59, 60]. However, those *in vivo* models are usually technically challenging and cannot fulfill the increased demand for high throughput drug screening. Conversely, *in vitro* microfluidic models have been used for cancer cell intravasation model studies and may enable drug HTS approaches.

To recreate the vasculature intravasation in microfluidic devices, two parallel microchannels are usually designed to house endothelial cells and cancer cells at each channel and are separated by a compartment of ECM. For instance, Zervantonakis and coworkers reported using such microfluidic design to culture breast cancer cells and macrovascular endothelial cells to study the effect of macrophages on breast cancer cell intravasation (Fig. 4.7a). Tumor necrosis factor α (TNF α) secreted by macrophages was responsible for increased cancer cell intravasation and vessel permeability [61]. This supportive effect of TNF α on cancer cell intravasation was also confirmed by Lee et al. using a similar parallel design of a microfluidic system [56]. Other immune-cancer cell interactions, such as the migratory responses of leukocytes to cancer cells, have also been modeled using microfluidic devices that mimic vasculatures and the tumor mass [62]. In an interesting study by Nagaraju and coworkers, both invasion and intravasation processes were realized in a single microfluidic system [63]. Their system combined the side-by-side organization of 3D tumor cells, stroma, and vasculature with physiologically relevant matrices (Fig. 4.7b). They visualized the breast cancer cell invasion and intravasation, delineating the effect of tumor microenvironment, such as the cross-talk between endothelia and cancer cells via angiogenic cytokines, on cancer intravasation (Fig. 4.7b). Their results are in agreement with *in vivo* observations [64].

Although the major pathway for cancer metastasis is via intravasation into blood vessels, intravasation via lymphatic vessel has also been observed [65, 66]. For example, Chen et al. reported using a microfluidic system to simulate lymphatic vessels with anatomical accuracy to study cancer cell intravasation events [67]. This system contained choke points ($6\ \mu\text{m} \times 10\ \mu\text{m}$) which were used to assess cancer cell intravasation ability by rating their migration through these choke points, mimicking lymphatic vessel entry (Fig. 4.8a). Moreover, this chip design also incorporated cell capture sites and serpentine channels, allowing for single cell analysis. It was shown that breast cancer cells with p38 γ gene knockdown could not navigate through the choke points. This reduced capability in metastasizing via lymph route is in agreement with the known associations between elevated p38 γ expression and lower survival rate of breast cancer patients [68].

To increase the high throughput and the ease of operation in the study of lymphatic intravasation, Pisano et al. combined the transwell approach with a microfluidic system [69]. In this “meso-scale microfluidics,” lymphatic endothelial cells were first cultured at the bottom of a transwell insert, and cancer cells embedded in 3D matrix were then put on the other side of the insert. The transwell with functional lymphatic endothelium and embedded cancer cells was then inserted

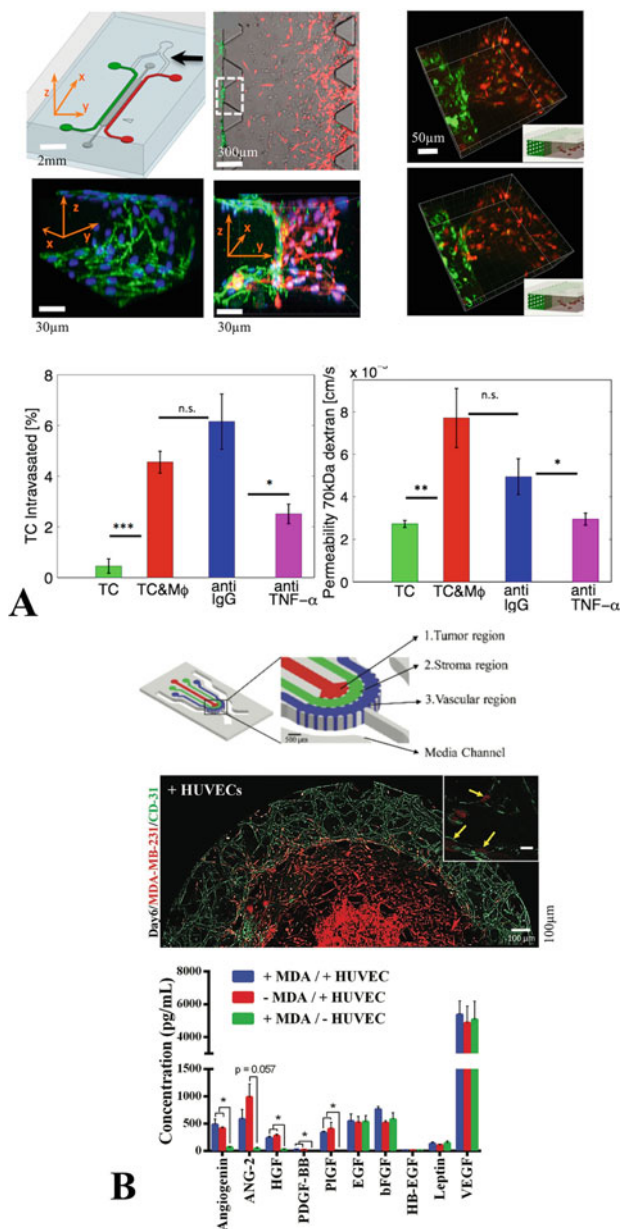


Fig. 4.7 Microfluidic hematogenous intravasation models. (a) ECM separated endothelium and breast tumor 3D culture in microfluidic channels. Cancer cells intravasation into ECM gel was imaged via confocal microscopy, and the effect of treatment using anti-TNF α antibody was quantified. (Reprinted from Ref. [61]. Copyright © 2012, Proceedings of the National Academy of Sciences.) (b) Invasion and intravasation model recapitulating tumor, stroma, and vascular tissues. Microscopy image shows the interaction of invading breast cancer cells with endothelium and angiogenic cytokine expressions were shown. (Reprinted from Ref. [63]. Copyright © 2018, Wiley)

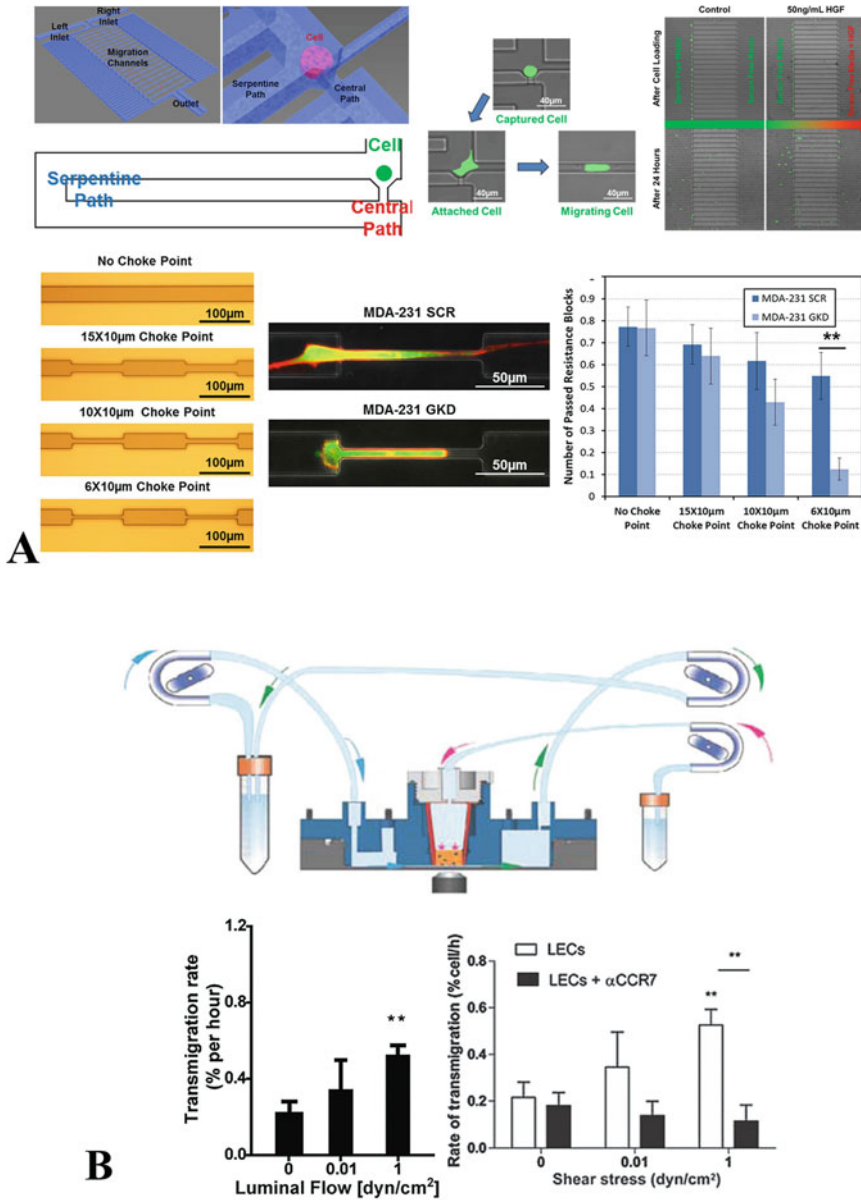


Fig. 4.8 Microfluidic lymphatic intravasation models. (a) Lymphatic migration channels with cell capture sites and serpentine channels. Migration ability of p38γ knocked down cells (MDA-231 GKD) and control cells (MDA-231 SCR) was assessed by their navigation event through choke points with different dimensions. (Reprinted from Ref. [67]. Copyright © 2015, Springer Nature.) (b) Microfluidics with Boyden chamber setup for invasion and intravasation modeling. Transmigration rate of breast cancer cells in the presence of CCR7 blocking antibody, at various lymphatic flow rate, was quantified. (Reprinted from Ref. [69]. Copyright © 2015, Royal Society of Chemistry)

into the microfluidic channels to complete the lymphatic intravasation model (Fig. 4.8b). It was demonstrated that luminal flow over the endothelium could facilitate cancer cell transmigration by regulating chemokine (CCL21) expressed by lymphatic endothelial cells. In another example of lymphatic vessel mimicry, Sato et al. designed a membrane incorporating a microfluidic co-culture of microvascular endothelial cells on one side of the membrane and lymphatic endothelial cells on the opposite side to mimic the physiological microenvironment of blood and lymphatic vessel junction. The permeability between blood and lymphatic vessels was increased upon exposure to snake venom [70].

5.1.4 Extravasation and Colonization Modeling

Extravasation is a key event in forming a secondary tumor, which involves CTC attaching to a vessel wall, followed by endothelium transmigration and colonization of the secondary site [60, 71–73]. Microfluidic systems enabling the perfusion of CTCs have been explored in detail to study the extravasation process. For instance, Song et al. developed a sandwiched design of a microfluidic chip with upper and lower compartments separated by a polyester membrane (Fig. 4.9a) [74]. Breast CTC cells perfused at a physiological flow rate in the upper channel were attracted towards the endothelial cells (grown on a polyester membrane) by responding to chemoattractant in the bottom compartment. It was shown that chemokine receptors, CXCR4 and CXCR7, expressed on cancer cells, were involved in the enhanced cancer cell adhesion onto endothelial cells. They also demonstrated that CXCL12-treated endothelial cells promoted CTC adhesion to endothelium (Fig. 4.9a). These *in vitro* results coincided with *in vivo* evidence that CXCR4 promotes cancer cells attachment to endothelial cells via integrin $\beta 1$ [75]. In a similar study, Riahi et al. reported a different microfluidic design where a concentration gradient of CXCL12 was created along a microfluidic channel lined with endothelial cells [76]. This gradient approach mimics more closely the organ specific microenvironment of blood vessels and demonstrated that the breast cancer cells (MDA-MB-231) preferentially extravasated at the high CXCL12 concentration section of the microfluidic channel.

Enhanced hyaluronic acid (HA) metabolism has been a known pro-metastatic extracellular microenvironmental factor. However, it was also speculated that the pericellular HA coat could also promote cancer metastasis [77]. An assay work flow using a microfluidic model has been applied to test this hypothesis [78]. Briefly, a dual-channel microfluidic device was used for the formation of a 3D stroma in one channel, and the circulation of breast cancer CTCs in the other channel (Fig. 4.9b). An array of pillars separating those two channels could support the formation of endothelium. CTCs treated with hyaluronidase to digest the pericellular HA coat were shown to be less capable in transendothelial migration and the treated CTCs migrated shorter distances than the control cells [78]. Microfluidic models could indeed allow the researchers to decouple various features in the vasculatures and the cells to dissect their roles in extravasation. Other examples, such as the effects of the presence of immune cells and the CTCs on the extravasation rate and vessel permeability have also been explored [79, 80].

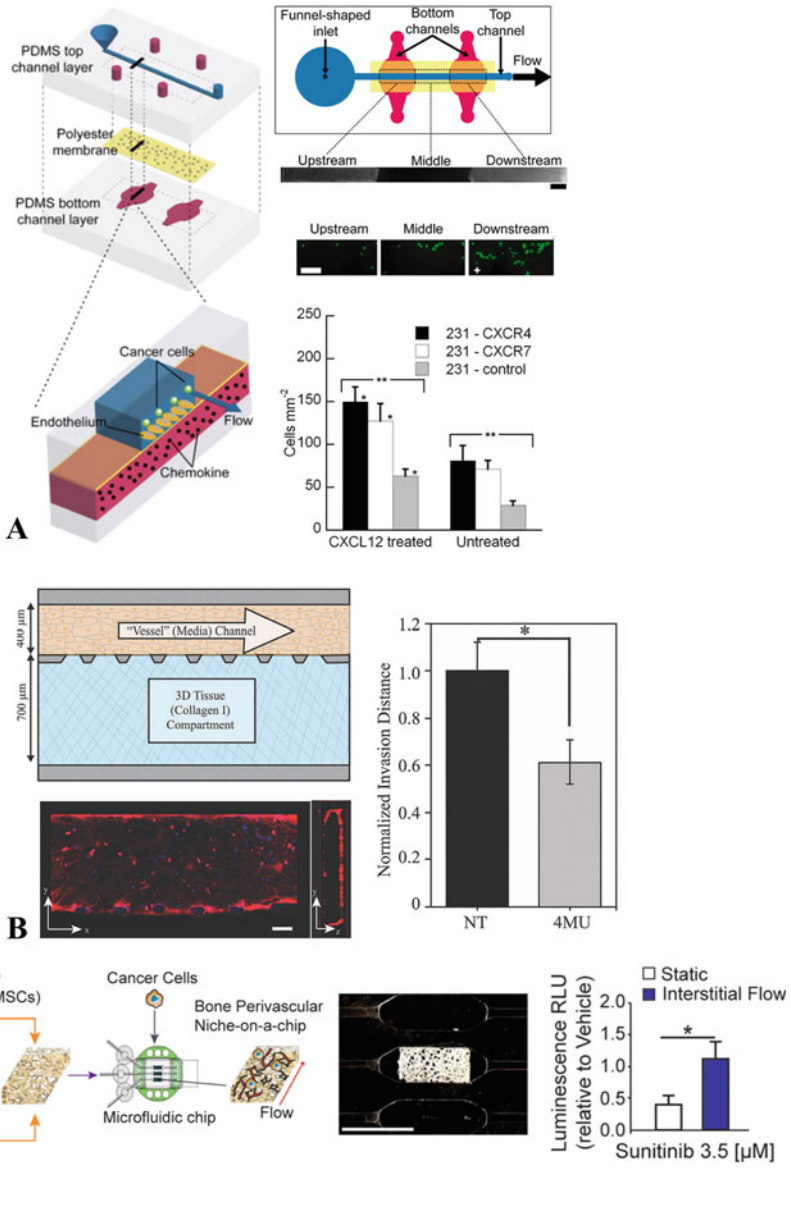


Fig. 4.9 Microfluidic extravasation models. (a) Schematic of breast CTC extravasation microfluidic model with dermal endothelial cells as the vessel model. Perfusion at bottom channels with chemokines promoted CTC attachment on the endothelial cells above. The attachment of three breast cell lines on the endothelial cell compartment which were treated, or not, with chemokine CXCL12. Scale bar, 200 μ m. (Reprinted from Ref. [74]. Copyright © 2009, PLOS.) (b) Schematics of extravasation and invasion model in microfluidics. Endothelium layer was formed expressing tight junctions. The invasion distance of breast carcinoma cells was recorded for cells with or without hyaluronic acid (HA) inhibitor

An advanced microfluidic model in mimicking the niche for CTC bone colonization has been developed by Marturano-Kruik and coworkers [81]. This model consisted of a single microfluidic channel encasing decellularized bone matrix (Fig. 4.9c). Bone marrow mesenchymal stem cells and endothelial cells were seeded inside the chip to complete the bone perivascular niche. It has been successfully demonstrated the formation of bone matrix and the vascularization under interstitial flow [81]. Measuring the attachment of perfused breast CTCs, the attached CTCs entered a slower proliferative state triggered by interstitial flow. Furthermore, a significantly lower number of viable CTCs were observed in static compared to flow conditions when both systems were exposed to Sunitinib (a drug that targets proliferative cancer cells), indicating the slow proliferative state of the bone-residing CTCs protected them from the effect of the chemotherapeutic. Such a microfluidic based model has significant implication on current models in anti-metastasis drug screening and discovery.

5.2 Microfluidic Model Systems for Specific Cancer Organ Types

Conventional methods used in cancer drug discovery and disease modeling, such as 2D cell cultures and animal cancer models, often fail to predict the outcomes of clinical trials and their practical efficacy [26, 82]. The advent of advanced cancer-on-a-chip (CoC) platforms suggests a new direction in overcoming such limitation [26]. Tumor pathophysiology can be partially simulated in CoC to recapitulate specific tumor microenvironment. Moreover, cell-cell interactions, biological, physical, and mechanical cues which are unique to each cancer cell types can also be modeled with high accuracy using CoC technology [21]. This dynamic system has the potential to become an important tool to screen for anticancer drugs at high throughput and to study cancer progression [21]. In this section, representative CoC models for brain cancer, breast cancer, liver cancer, and lung cancer will be discussed.

5.2.1 Brain CoC

According to the American Cancer Society, brain cancer is the second most common form of cancer in children and teenagers, and is the cause of the most pediatric cancer-related deaths [83]. Among all brain cancers, glioblastoma multiforme (GBM) is the most malignant with a median survival rate of 12–15 months [83]. Poor treatment efficacy and high recurrence rate are often encountered due to



Fig. 4.9 (continued) treatment using 4-methylumbelliferone (4MU). Scale bar, 100 μm . (Reprinted from Ref. [78]. Copyright © 2018, Royal Society of Chemistry.) (c) Bone perivascular niche in microfluidics for breast cancer colonization modeling. Viability of Sunitinib-treated breast cancer cells under static and interstitial flow conditions. (Reprinted from Ref. [81] Copyright © 2018, Proceedings of the National Academy of Sciences)

the following challenges: poor understanding of disease progression and underlying mechanisms, drug resistance, and the existence of blood-brain barrier (BBB) blocking therapeutics from reaching the tumors.

To overcome these challenges, researchers have explored extensively brain CoC systems to mimic the physiological environment of GBM for robust mechanistic studies and drug discovery. For example, Huang and coworkers reported using a dual-channeled microfluidic device for monitoring the migratory ability of brain tumor stem cells through microchannels [84]. Park et al. developed a CoC chip to house doxorubicin (DOX) resistant glioblastoma cells (U87) for studying GBM drug resistance in vitro [85]. This device developed by Park and coworkers contained 488 hexagonal micro-compartment which were surrounded by two opposing microfluidic channels for long-term cancer cell monitoring (Fig. 4.10a). Cell culture media with and without DOX were perfused through the two channels in opposing directions creating a range of drug concentration gradient. A subpopulation of U87 cells that survived at an intermediated concentration of DOX after 7 days of treatment were isolated and sequenced. They successfully identified 77 upregulated genes and 6 downregulated genes and elucidated key molecular signaling pathways related to drug resistance [85].

Cancer cells cultured in 3D format inside a CoC can better mimic physiological microenvironment of GBM. Fan and colleagues reported a CoC system fabricated in poly(ethylene) glycol diacrylate hydrogels to create microfluidic channel networks [86]. Similarly, this device was used to generate a drug concentration gradient by injecting drug and PBS from two inlets (Fig. 4.10b). A key difference to previous models was that in each subchannel of this device, U87 cells were seeded and cultured as 3D spheroids, which better captured phenotypic changes upon drug treatments. The authors performed combinatorial treatment of two anticancer drugs, Pitavastatin and Irinotecan, and identified the optimized combinatory concentrations.

Replicating an in vitro brain tumor model with a single cell type (i.e., monoculture) sometimes cannot fully recapitulate the complexity of brain tumor physiological microenvironment. More importantly, anticancer therapeutics need to pass through the BBB in vivo in order to reach tumor site to take effect [87]. Similarly, circulating tumor cells need to transmigrate through BBB to colonize distance sites. It is, therefore, appropriate and representative to fabricate brain CoC with functional BBB integrated to better understand the role of BBB in brain tumor development and treatment. For example, Qin and coworkers designed a 3D CoC with integrated BBB, where endothelial cells and astrocytes were co-cultured in 3D ECM [88]. Brain tumor metastasis was monitored on chip by tracking the invasion and migration of fluorescently labeled U87 cells. It was demonstrated that despite being an aggressive phenotype of glioma, U87 cells were unable to cross the BBB. The authors further utilized this CoC system to screen up to eight anticancer drugs and showed only the Temozolomide (a known GBM therapeutic) was able to pass through BBB and inhibited U87 growth. Another GBM CoC model integrated with BBB was reported by Ciofani and coworkers [89]. Porous microtubes resembling the brain capillaries were fabricated via two-photon lithography and used as

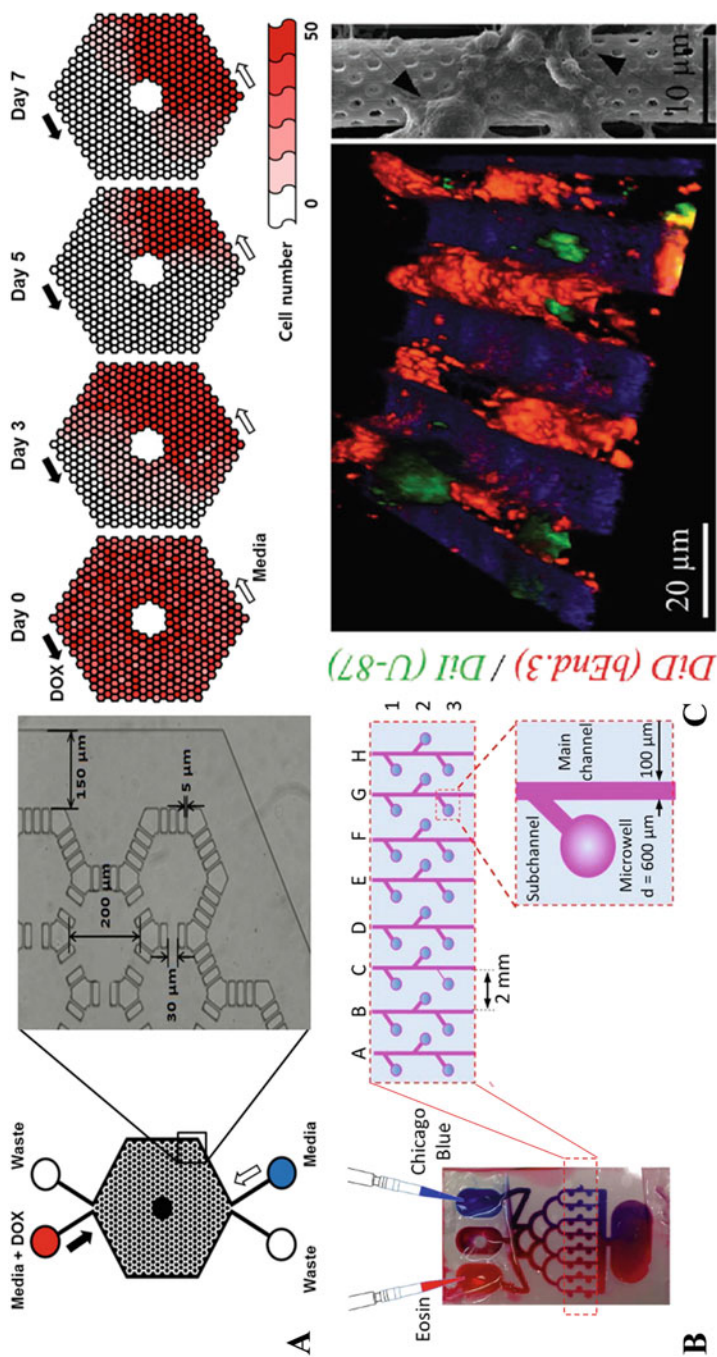


Fig. 4.10 Design of different brain CoCs. (a) Schematic diagram of the drug-resistant microfluidic chip with 488 micro-chambers and distribution of viable cells in the chip over a period of 7-day culture. (Reprinted from Ref. [85]. Copyright © 2016, Proceedings of the National Academy of Sciences.) (b) CoC chip fabricated in poly(ethylene) glycol diacrylate hydrogels to house U87 in 3D format for testing combinatory treatment of anticancer drugs. (Reprinted from Ref. [86]. Copyright © 2016, Springer Nature.) (c) Co-culture of endothelial (bEnd.3) and glioblastoma cells (U87) on the porous microtubes. Confocal image of bEnd.3 (red) and U87 cells (green) grow on the outer surface of the porous microtubes (SEM image). (Reprinted from Ref. [89]. Copyright © 2018, Wiley)

scaffolds for the co-culturing of endothelial cells and U87 cells. The authors showed that cancer cells were able to grow on the endothelial cell barrier and maintain their corresponding morphology (Fig. 4.12c).

5.2.2 Breast CoC

The pathophysiology of breast cancer begins with the proliferation of abnormal epithelial cells within the mammary duct, forming pre-invasive ductal carcinoma in situ (DCIS) lesions. As time progresses, cancerous cells within those DCIS develop invasive ability to penetrate the basement membrane and spread into surrounding tissues as invasive ductal carcinoma [90, 91]. In recent years, several studies have suggested that the tumor microenvironment is the critical determinant in cancer progression, as well as future metastasis towards distal organs [92, 93]. By applying microfluidic CoC technology, complex microenvironmental features in DCIS, such as ECM and cross-talk among various cell types (e.g., mammary fibroblast, adipocytes, and endothelial cells), can be partially recapitulated. In these breast CoCs, the phenotypes of breast cancer cells and their responses to drug treatment would resemble those in vivo, and thus allowing better prediction of anticancer drug efficacy [92].

Huh and co-workers developed a two-compartmentalized microfluidic system consisting an upper and lower microchannel to mimic the microenvironment of ductal carcinoma in early stage of breast cancer (Fig. 4.11a) [92]. In the upper channel, DCIS spheroids derived from MCF-10 cells were co-cultured with a monolayer of human mammary epithelial cells. DCIS spheroids with a relative diameter of 150 μm were selected to resemble early stage lesions [92]. A thin layer of ECM-coated porous membrane was used to separate the top culture chamber from the lower compartment, where a 3D stroma layer was formed by embedding mammary fibroblasts in type I collagen gel. The upper compartment was perfused with mammary epithelial growth medium to mimic the in vivo ductal lumen. Meanwhile, the lower channel resembling the vascular component of the stroma was maintained by mammary fibroblast media. A flow rate range of 30–40 $\mu\text{L}/\text{h}$ was selected to align with physiological interstitial flow rates [94]. Using this breast CoC device as a drug screening platform, they evaluated the anticancer effect of Paclitaxel and found the anticancer drug to have specific toxicity towards DCIS spheroid but not on epithelial cells.

Gioiella et al. also designed a similar platform to investigate the correlation between tumor epithelial cells and the activation of stroma tissue during cancer progression which would lead to ECM remodeling [93]. This CoC system consisted of an inner tumor chamber and an outer extracellular chamber, separated by micropillars with a diameter of 300 μm to prevent physical interaction among the seeded cells (Fig. 4.11b). 3D micro-tissues of MCF-7 breast cancer cells and fibroblasts were injected, respectively, into the two-compartment model. A flow rate of 3 $\mu\text{L}/\text{min}$ was used to mimic the physiological blood flow in the tumor environment [95]. By means of multiphoton microscopy, the stroma ECMs were monitored in real-time and both HA and fibronectin were found to be upregulated in the ECM remodeling during invasion. In addition, overexpression of alpha-smooth muscle actin ($\alpha\text{-SMA}$) and

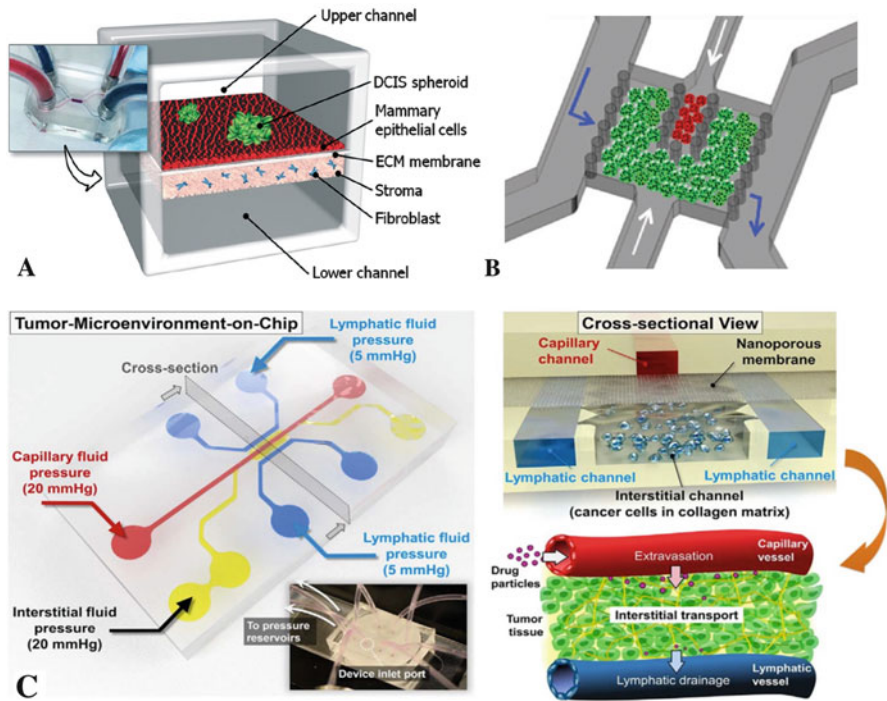


Fig. 4.11 Design of different breast CoC models. (a) Schematic diagram of dual-compartmentalized DCIS spheroid-on-chip mimicking early stage breast cancer. (Reprinted from Ref. [92]. Copyright © 2015, Royal Society of Chemistry.) (b) Micro-tissue model investigating stroma activation during breast cancer progression. Red dots represent tumor cells and green dots represent stroma cells. (Reprinted from Ref. [93]. Copyright © 2016, Wiley.) (c) Systemic flow model involving capillary, interstitial and lymphatic channels using different hydrostatic pressure. (Reprinted from Ref. [96]. Copyright © 2017, Elsevier)

platelet-derived growth factor (PDGF) receptor proteins were detected, indicating stroma fibroblasts were also activated during cancer cell invasion. Both α -SMA and PDGF are often used as an indicator in tumor progression [95].

Although the aforementioned CoC models provide an insight into the relationship between breast cancer cell and the local tumor microenvironment, the lack of systemic circulation and the absence of *in vitro* endothelium limit the full potential of those models [92]. Ozcelikkale et al. developed a comprehensive system which incorporated capillary, interstitial, and lymphatic channels (Fig. 4.11c) [96]. The upper capillary channel was separated from lower interstitial channel by a porous membrane of 400 nm pore size [97]. To mimic the elevated interstitial fluid pressure and passive drainage in the breast tumor environment, the capillary and interstitial channel were kept at 20 mmHg pressures while in the lymphatic compartment a lower pressure of 5 mmHg was maintained [98]. MCF-7 or the drug resistant breast cancer cell line, MDA-MB-231, was cultured within a 3D collagen matrix inside the

interstitial channel. To assess the efficiency of delivery of different drug formulations, DOX or doxorubicin nanoparticle were perfused through the capillary channel. Interestingly, it was found that both cancer cell lines proliferated slower and displayed elevated drug resistance when cultured within 3D microfluidic device as compared to conventional 2D culture. In addition, MCF-7 cell line exhibited a faster drug uptake than MDA-MB-231 cell line, a result that is in agreement with animal xenograft models [96].

5.2.3 Liver CoC

Liver cancer is the third leading cause of cancer death world-wide [99]. Hepatocellular carcinoma is one of the more common cancer form mainly caused by risk factors such as hepatitis infections and alcohol [100]. The prognosis of the disease is relatively poor as the main treatment options are resection surgery and radiation therapies [101]. Given the unique physiology of the organ, the liver contains a complex network of vascular circulations for hepatic metabolism [101]. It poses a critical challenge in discovery of new effective chemotherapies which have to overcome the obstacle of first pass drug metabolism.

Patra and coworkers reported a combinatorial approach of using flow cytometry and microfluidic platform to test anticancer drugs on 5,000 uniformly sized hepatocellular (HepG2) tumor spheroids (Fig. 4.12a) [102]. A dual-layer microfluidic chip was constructed which incorporated arrays of micro-wells in the bottom compartment to house 3D tumor spheroids and a top layer channel for media exchange and drug perfusion. Three different anticancer drugs, Cisplatin, Resveratrol, and Tirapazamine, were independently perfused through the top channel against two populations of tumor spheroids of different diameters on the bottom channel. It was found that tumor spheroids in the 3D microfluidic cultures were more resistant to anticancer drugs as compared to 2D cell cultures.

A similar investigation was performed by Brzozka and co-workers for assessing anticancer drugs using microfluidic CoC systems [103]. Instead of using single microchannel for drug testing, the authors developed a triple microchannel design to examine the cytotoxicity of 5-fluorouracil (5-FU) on HepG2 tumor spheroids. The three parallel microchannels were individually connected to four micro-chambers which consisted of 18 identical micro-wells in each micro-chamber (Fig. 4.12b). This configuration allowed two different concentrations of 5-FU along with a control condition to be tested. Interestingly, it was demonstrated that tumor spheroids with the smallest diameter were more resistant to 5-FU treatment than the larger ones. Furthermore, a lower concentration (0.5 mM) of 5-FU displayed a higher cytotoxicity effect towards HepG2 tumor spheroids as compared to 1 mM concentration [103].

It is very important to also test systemic toxicity when testing new cancer chemotherapeutics. Zhang and coworkers developed a dual-organ platform which incorporated the heart and liver CoC [104]. Human induced pluripotent stem cell-derived cardiomyocytes (iPSC-CMs) were used to mimic the heart organ while HepG2/C3A hepatocellular tumor cells were used to reconstitute the hepatic compartment (Fig. 4.12c). DOX was administered to examine the cytotoxic effects

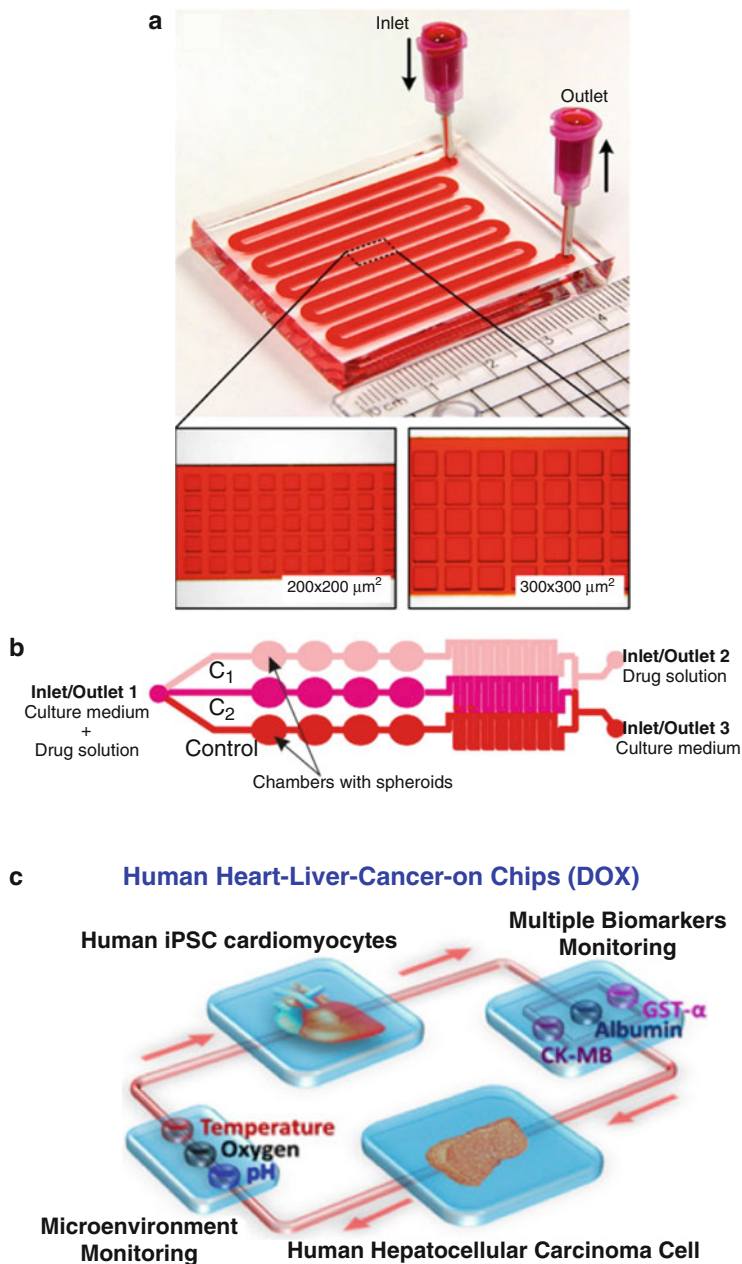


Fig. 4.12 Design of different liver CoC models. (a) Schematic diagram of microfluidic platform with 5000 micro-wells for anticancer drug testing. (Reprinted from Ref. [102]. Copyright © 2016 Springer Nature.) (b) Three-channel model composed of micro-chambers and micro-wells. (Reprinted from Ref. [103]. Copyright © 2017, Wiley.) (c) Integrated dual-organ platform involving human heart-on-chip and liver cancer-on-chip. (Reprinted from Ref. [104]. Copyright © 2017, Proceedings of the National Academy of Sciences)

towards liver cancer cells while potential acute cardiac toxicity was evaluated on the cardiac organoids. After administering DOX at dosages of 5 and 10 μM , significant liver cancer organoid death was observed while iPSC-CMs also underwent detachment and cell death which demonstrated cardiotoxicity.

5.2.4 Lung CoC

Non-small-cell lung cancer (NSCLC) accounts for approximately 40% of the 150,000 lung cancer deaths per year in the United States [3]. With the advancement of genome technology, patients with NSCLC were found to often have mutation in epidermal growth factor receptor (EGFR) gene and mostly show initial response to tyrosine kinase inhibitors (TKIs) [105]. CoC models were used to recapitulate the lung cancer microenvironment to enable the study of cancer mutations, disease progression, and mechanism of drug responses [106–108].

One of the first generation of lung CoC model was reported by Aref and coworkers to investigate the significance of 3D microenvironment on lung cancer progression, specifically during EMT [106]. The device consisted of a central matrix gel area lined by two parallel side channels containing permeable holes and PDMS pillars (Fig. 4.13a). To form NSCLC spheroids, A549 cells were suspended and embedded in a 3D gel matrix while a monolayer of HUVECs were co-cultured in the side channels forming a barrier to mimic the vascular structure. Twelve drug candidates including EGFR inhibitors were introduced via the vascular channel and their EMT inhibition (dispersion assay) effects examined. The effective doses to inhibit EMT (prevent spheroid dispersion) for all 12 drugs were significantly lower as compared to 2D culture, some even showing a difference of up to 3 orders of magnitude [106].

A more comprehensive NSCLC model was developed by Ingber and colleagues [107]. A two-compartment microfluidic device was fabricated and separated by a porous membrane where epithelial and endothelial cells were seeded in each compartment (Fig. 4.13b). This platform also incorporated two side vacuum chambers which could be imposed with cyclic stretching (10% strain, 0.2 Hz) to mimic breathing motion. Human NSCLC cells, H1975 (activated mutation at L858R), were plated at low density together with either primary lung alveolar or small airway epithelial cells on the upper surface of the ECM-coated membrane. Human lung microvascular endothelial cells were used to line the bottom vascular channel. The study aimed at examining the cancer progression on small airway versus alveolar microenvironment and to recapitulate the development of the T790 M mutation. Interestingly, H1975 cells displayed a preferential growth in alveolar as compared to airway microenvironment, which correlates well with observations on lung cancer patients [109, 110]. More importantly, the authors observed that although the TKI inhibitor, Rociletinib, was effective towards T790 M mutated cells in the static alveolus chip at low dose, an opposite result was shown in the presence of breathing motion.

To more accurately mimic the structure of alveolar respiratory interface and the effect of cell-cell crosstalk, Yang and coworkers designed a lung CoC model which incorporated a PLGA membrane with a thickness of 3 μm by means of electrospinning [108]. The influence of human fetal lung fibroblast (HFL1) on NSCLC was

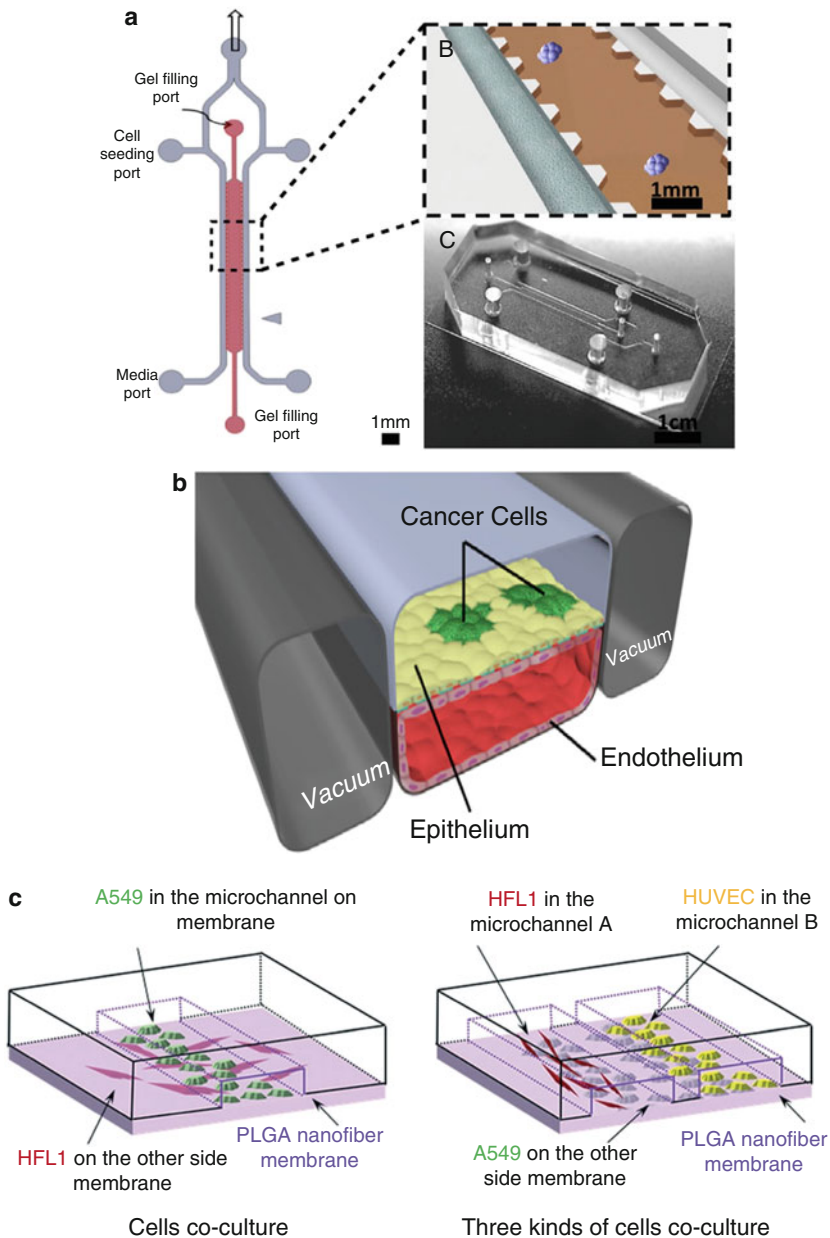


Fig. 4.13 Design of different lung CoC models. (a) 3D NSCLC spheroid model investigating lung cancer progression during EMT. (Reprinted from Ref. [106]. Copyright © 2013, Royal Society of Chemistry.) (b) Schematic diagram of alveolar and small airway-on-chip used to reconstitute lung cancer growth showing cancer cells infiltrating the endothelium layer. (Reprinted from Ref. [107]. Copyright © 2018, Elsevier.) (c) Tri-culture model using an electrospun PLGA nanofiber membrane. (Reprinted from Ref. [108]. Copyright © 2018, Royal Society of Chemistry)

investigated by either co-culturing with A549 cells or tri-co-culture with A549 and HUVECs (Fig. 4.13c). Upon the application of the EGFR anticancer drug Gefitinib in co-culture conditions, A549 cells displayed a significant drug resistance. More interestingly, in the case of tri-culture condition, A549 cells were found to be able to induce endothelial cells to undergo apoptosis and commence tumor invasion [108].

5.3 Integration of CoC Systems with Advanced Technologies

CoC platforms simulate closely the *in vivo* cancer microenvironments and thus can provide unprecedented accuracy than traditional static cell culture models. The choice of building material and design of microfluidic system can be easily modified (e.g., to incorporate electrodes). Therefore, numerous technologies such as advanced quantitative optical imaging, biosensing, and precise manipulation techniques can be readily integrated into CoC systems. The wealth of information that can be obtained from these highly predictive CoC models could help advance the basic understanding, prevention, and management of cancer. This section will review the recent examples of these advanced technologies and how they are incorporated into the microfluidic systems to address different aspects of cancer characterizations.

5.3.1 Integration of Super-Resolution Microscopies

PDMS is a popular material for building microfluidic system due to its ease of fabrication, biocompatibility, and gas permeability [27]. Not only is PDMS suitable for long-term cell culture, it is optically transparent, making it suitable for various microscopy techniques. The substrate for microfluidic device can range from standard microscope slide, Petri dish to thin glass cover slips which are compatible with most microscope objectives including high magnification objectives. By integrating advanced optical microscopy technologies, CoC systems can be imaged with high accuracy, helping researchers to elucidate various biochemical processes and pathways involved in cancer.

Wide-field imaging techniques such as phase tomography and epi-fluorescence are popularly used due to the simple microscopy setup and the ease to acquire images. Although such wide-field technique can provide fast imaging speed (due to full-frame acquisition), they ultimately suffer reduced contrast and poor axial resolution [111]. On the other hand, confocal fluorescence microscope, which implements a pinhole in front of the detector and uses laser as the excitation light source, can provide optical sectioning capability and drastically increase the imaging resolution. For example, a confocal microscope was used for a microfluidic system composed of different microchannel widths to study cancer cell motility within a confined space [112]. As reported by Tong and coworkers, human osteosarcoma (HOS) and breast cancer (MDA-MB-231) cell lines were imaged under confocal microscopy and the cellular cytoskeleton was clearly visualized (Fig. 4.14a). Not only can the fixed cells be imaged, some microscopes have incorporated a live cell chamber unit that has temperature, CO₂, and humidity controls. More compact ones

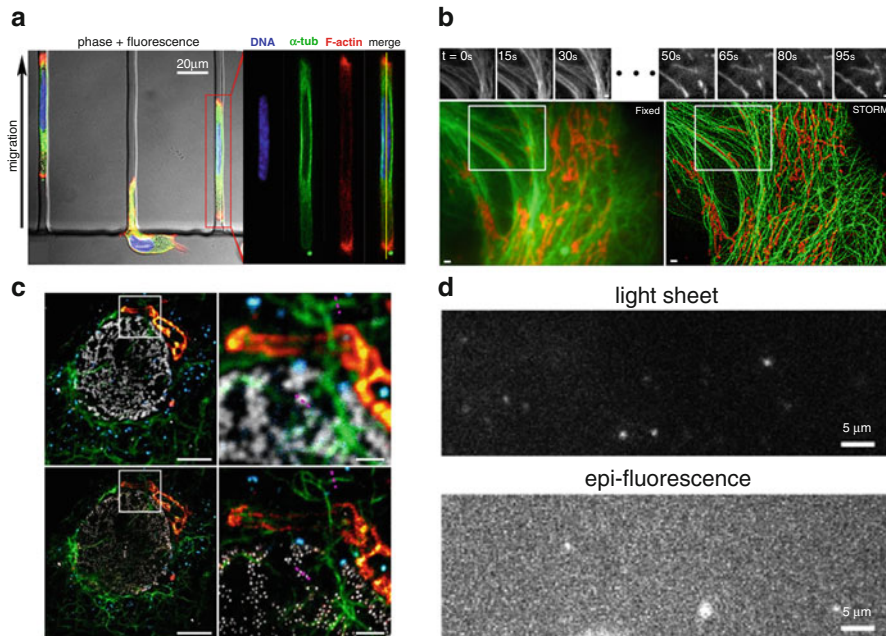


Fig. 4.14 Integration of advanced microscopies with microfluidic systems. **(a)** Confocal image of HOS cells migrating into 3 μm-wide channels. (Adapted from Ref. [112]. Copyright © 2012, PLOS.) **(b)** Mammalian cell microtubules and mitochondria were imaged using epifluorescence microscopy and STORM super-imaging technique. Scale bars, 1 μm. (Reprinted with permission from Ref. [113]. Copyright © 2015, PLOS.) **(c)** Four-color hyperSTED data in a fixed Vero cell comparing the conventional confocal overlay with super resolution STED overlay with enlarged views of two regions. Blue: peroxisomes, green: vimentin, red hot: giantin, grey: nuclear pores. Scale bars, 5 μm left panels and 1 μm right panels. (Adapted from Ref. [115]. Copyright © 2017, Springer Nature.) **(d)** Comparison of light sheet high resolution microscopy technique with epi-fluorescence imaging of MCF-7 breast cancer cell-derived membrane vesicles in cell culture medium. (Reprinted with permission from Ref. [118]. Copyright © 2014, Royal Society of Chemistry)

are those with stage-top incubators which are suitable for lab-on-chip systems in terms of long-term cell culture and imaging.

Conventional optical imaging techniques are restrained by the diffraction limit making it difficult to image biomolecular and subcellular processes. Super-resolution microscopy is capable of imaging subcellular events and biomolecules at an unprecedented accuracy (in nanometer dimension) and to help understand various biochemical processes and pathways. Some important key parameters need to be considered when choosing a specific type of microscopy are: lateral and temporal resolution, imaging depth, fluorophore photobleaching, and phototoxicity [111].

Super-resolution microscopy methods, such as stochastic optical reconstruction microscopy (STORM), have enabled visualization of subcellular structures below the optical resolution limit. Tam et al. reported to use STORM imaging

technique in conjunction with a microfluidic system to visualize mitochondrial dynamics, morphology, and nanoscale protein distribution in live cells in high resolution [113]. The incorporation of fluid-injection devices can deliver predetermined amount of reagent to the selected imaging chamber for automated immunoassays. A high temporal resolution (up to 50 ms) and spatial resolution (of 24 nm) were achieved and only a low laser power density ($\sim 0.2 \text{ W/cm}^2$) was used which significantly minimized the potential phototoxic effect to live cells. Microtubules and mitochondria were imaged using the STORM technique and were well resolved (Fig. 4.14b). Furthermore, multicolor STORM imaging has also been shown to image axon structures provided improved accuracy in neuron tracing with resolutions of 44 nm laterally and 116 nm axially [114].

The alternative method, stimulated emission depletion microscopy (STED), creates super-resolution images by selective deactivation of fluorophores, minimizing the area of illumination at the focal point, and can outperform traditional confocal microscopy (Fig. 4.14c) [115]. Live cell imaging using STED has been demonstrated with lateral resolutions of 60–150 nm at 28 frames per second [111]. However, photobleaching of fluorophores with the use of a high laser power is considered as a potential limitation of STED microscopy [116].

Structured illumination microscopy (SIM) is also another widely used super-resolution microscopy where a patterned light in different orientations and interference patterns was used to illuminate a specimen, allowing a lateral resolution of 100 nm and an axial resolution of 200 nm with subsecond acquisition rate for live-cell imaging [117]. On chip imaging using this technique could also be quite possible as this super-resolution microscopy relies on a laser-based wide-field microscopy set up.

Light sheet fluorescence microscopy (LSFM) uses a plane of laser light instead of a point (as in traditional confocal microscopy) and can acquire images two- to threefolds faster than point scanning methods [111]. LSFM have reduced phototoxicity, improved signal-to-noise ratio and penetration depth profile. Thus, visualization of highly dynamic processes within cells, such as vesicle trafficking, is possible. LSFM technique has recently been integrated with a microfluidic system to image the membrane vesicles released by cells [118]. Cell-derived membrane vesicles, such as exosomes, are highly correlated with cancer disease progression, e.g., tumor growth and metastasis [119]. Deschout et al. reported a microfluidic chip integrated with LSFM for accurate fluorescent single particle tracking, where size and concentration of membrane vesicles were analyzed [118]. The vesicles were isolated from MCF-7 breast cancer cell and measurements were conducted in both cell culture medium and in interstitial fluid collected from primary human breast tumors. Particles of 200 nm were accurately imaged with much improved background in comparison to traditional fluorescence microscopy (Fig. 4.14d).

5.3.2 Integration of Biosensors

The tumor microenvironment is distinctively different from that of normal healthy tissue. Differences such as pH and O_2 concentration (e.g., hypoxia) often form part

of the niche favoring tumor progression. Using microfluidic systems to model different aspects in cancer microenvironments have been shown with great success (Sessions 3.1 & 3.2), and the integration of different biosensing techniques into microfluidic systems adding capability of monitoring cell growth, metabolism in responses to stimulations (e.g., drugs) further enhances this technology. Being able to analyze cell metabolism in real time is important to monitor tumor growth and to screen effects of added pharmaceuticals. Important parameters that regulate cellular metabolism, include pH (acidification), oxygen (respiration), glucose and lactate (energy metabolism), and short-lived reactive oxygen/nitrogen species (ROS/RNS) [120]. For example, in a healthy tissue, the oxygen concentrations are between 20 to 150 μM . Pathological condition such as in hypoxia, the oxygen is reduced to below 25 μM [120]. The normal pH value of typical cell culture medium is 7.4. However, due to cell metabolism over time, cell acidification will occur. Glucose is the major energy source in cell culture and in high concentrations (10 mM) and decreases over time. Short-lived reactive species also play important roles in certain biological processes [120].

Advances in miniaturized biosensors incorporated with microfluidic systems have been shown as a powerful tool for the measurement of metabolic parameters of cancer cells with high sensitivity and selectivity. Recent efforts have been looking into integrating biosensing microelectrodes for the real-time monitoring and analysis of stimulation of biological samples. Grist et al. reported a gas-permeable three-layered microfluidic device to integrate ratiometric optical oxygen sensors (Fig. 4.15a) [121]. This system has been shown to be able to achieve spatial and temporal oxygen control. Ratiometric sensors, which incorporated a reference luminescent dye (oxygen-insensitive) offered enhanced robustness and stability and only a simple fluorescence microscope was needed for the readouts. The lower limit of detection for oxygen levels was 0.06% which was below the oxygen range for physiological conditions for hypoxia: modest (2.5%), moderate (0.5%), and severe (0.1%) hypoxia [121].

Similarly, Misun et al. have recently reported an integration of enzyme-based multi-analyte biosensors into a microfluidic culture platform to monitor the metabolism of human colon cancer microtissues (HCT116) [122]. The sensor modules consisted of four platinum working electrodes, a platinum counter electrode, and an Ag/AgCl reference electrode (Fig. 4.15b). Oxidase enzymes were conjugated on electrodes to realize a real-time monitoring of the concentrations of lactate and glucose based on amperometry. The detection limit was found to be below 10 μM . Moreover, in 3D microtissues (diameter 300–500 μm) size-dependent lactate secretion rates in the range of nmol h^{-1} could be measured on chip.

Some microfluidic systems can integrate multiple sensors capable of simultaneous measurement of several parameters. For example, Weltin et al. have reported a multisensor microfluidic device to monitor the metabolism of T98G human brain cancer cells [123]. This platform included a cell culture chamber with integrated pH and O_2 chemo-sensors for the continuous measurement as well as for monitoring of lactate production and glucose consumption (Fig. 4.15c). The pH sensors were based on thin-film iridium oxide electrodes while the oxygen sensors were based on the

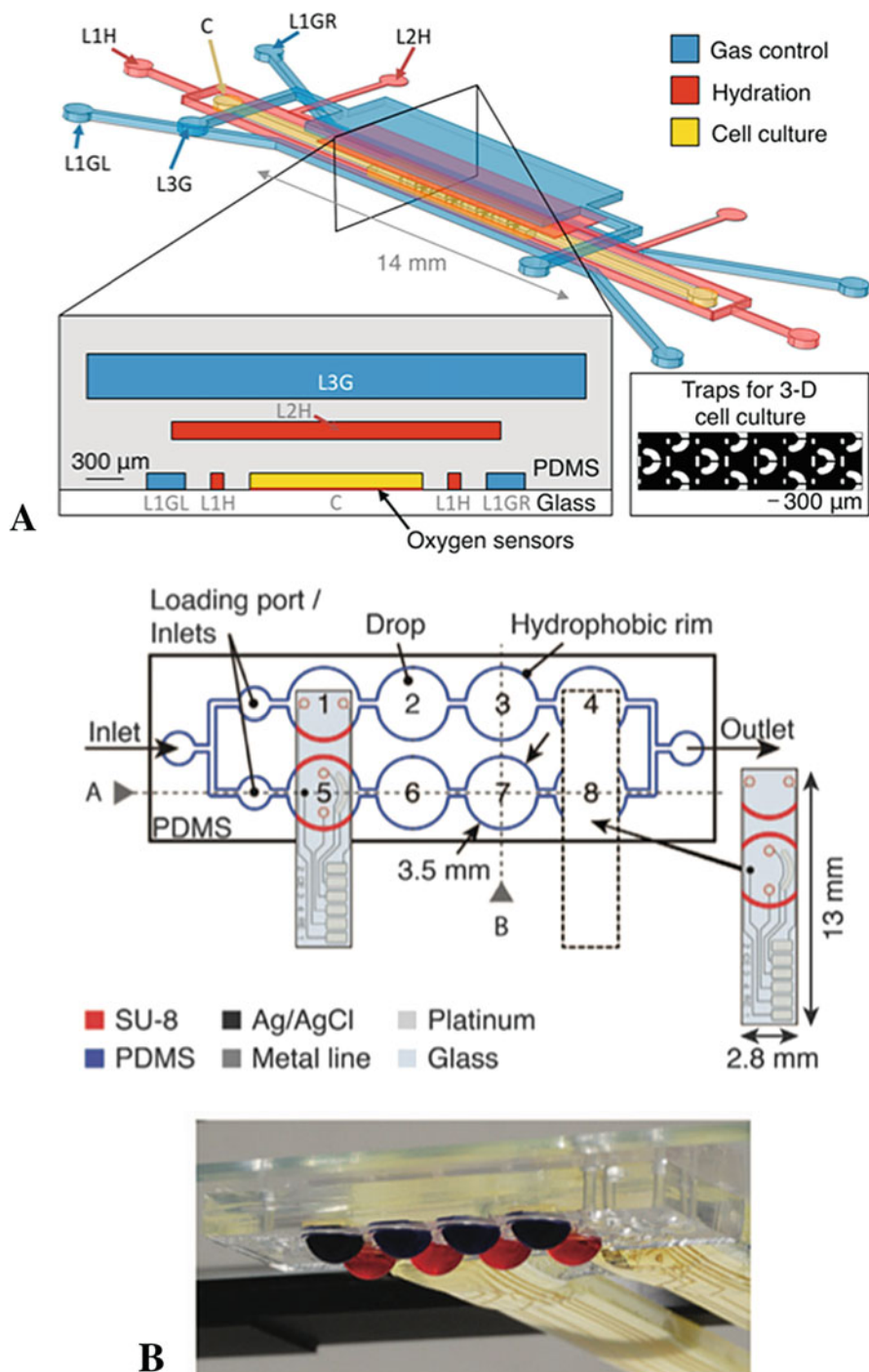


Fig. 4.15 (continued)

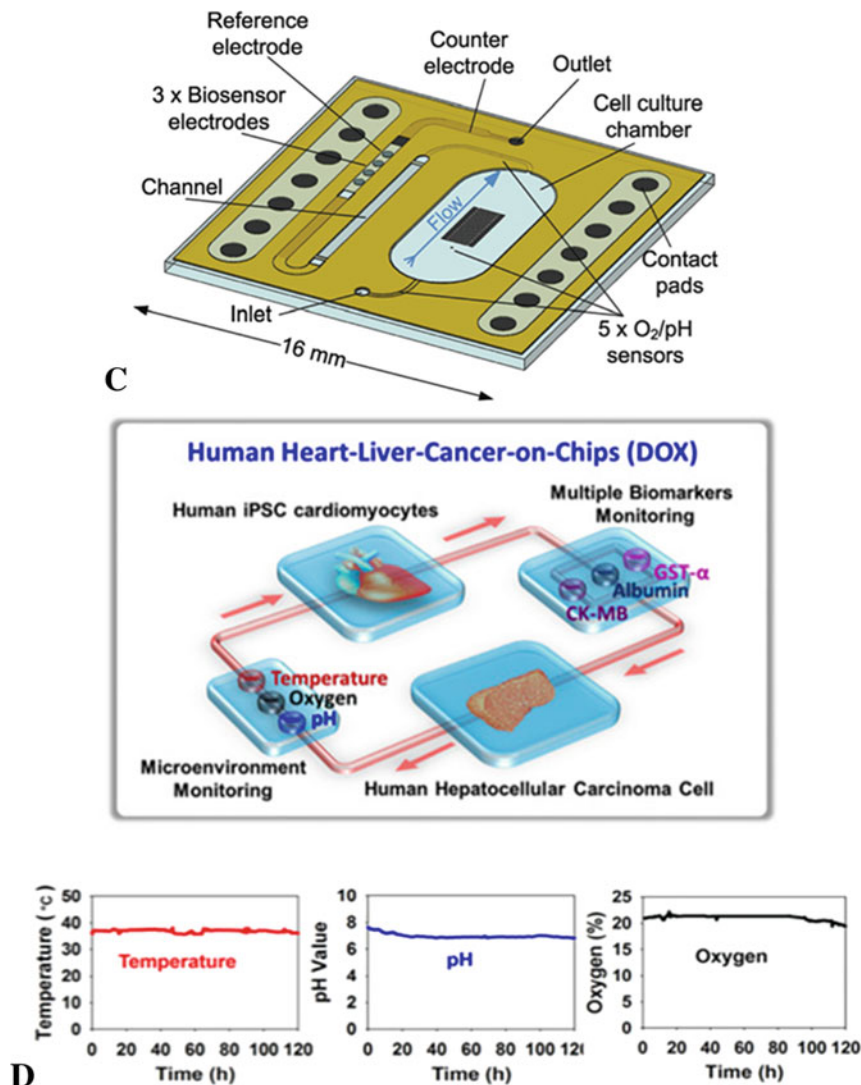


Fig. 4.15 Integration of CoC systems with microsensors. (a) A multilayered microfluidic device with integrated oxygen control. The schematic shows 3D and cross-sectional views of the device. (Reprinted from Ref. [121]. Copyright © 2015, MDPI.) (b) A microfluidic hanging-drop network and sensor glass plug-ins was used for monitoring the metabolism of rate of colon carcinoma cell, HCT116. (Reprinted from Ref. [122]. Copyright © 2016, Springer Nature.) (c) Illustration of a chip layout with embedded biosensors for pH and O₂ monitoring. (Reprinted from Ref. [123]. Copyright © 2014, Royal Society of Chemistry.) (d) Human heart-liver-CoC platform to monitor temperature, pH, and oxygen level over time. (Adapted from Ref. [124]. Copyright © 2017, Proceedings of the National Academy of Sciences)

amperometric reduction of dissolved oxygen at the platinum electrodes. At the biosensor electrodes, glucose or lactate was converted by the glucose oxidase or lactate oxidase, which was embedded inside a membrane. All parameters were successfully measured outside the cell culture chamber, and in a functional test of adding cytochalasin B drug to cancer cells changes of pH and lactate level were detected.

Furthermore, only until recently an interconnected liver-heart CoC has been successfully combined with optical pH and oxygen sensors together with electrochemical immunobiosensors [104]. The optical pH sensor detected the absorption of cell culture medium supplemented with phenol red that indicated pH value while the oxygen sensor was based on an oxygen-sensitive fluorescent dye (Fig. 4.15d). Label-free electrochemical-based immunobiosensors that could monitor soluble biomarkers were also incorporated into the microfluidic culture system.

5.3.3 Integration of Dielectrophoretic Manipulation

Aside from sensing applications, microelectrodes embedded within microfluidic devices can also be used for physical manipulation of cells. Dielectrophoresis (DEP) is the electrokinetic phenomenon which occurs when a dielectric particle (e.g., cell) is placed in an electric field gradient. Most biological cells have dielectric properties in an electric field and can be controlled by a DEP force. DEP has been routinely used with cell-based microfluidic systems to spatially isolate, position, pattern, and separate target cells [26].

Various metallic microelectrodes with different geometries have been reported to induce DEP. For example, Beer et al. reported to use gold electrodes to induce DEP and with the combination of a microfluidic chip to culture different pancreatic ductal adenocarcinoma cells (PANC1) [124]. This microfluidic system, fabricated in cyclic olefin polymer, comprised of eight identical cell chambers, containing three cell culture units in each chamber, resulting in a total of 24 cell culture units per chip (Fig. 4.16a). Electrodes were integrated on the side walls of each cell chamber to generate an inhomogeneous high frequency electrical field. When the cells were perfused into the chamber, only the viable cells were selectively assembled on the culture area as those cells with intact cell membranes could be selectively guided by the DEP field. Moreover, such devices have been used for 3D PANC1 cell culture for testing against the anticancer drug, Cisplatin, where PANC1 cell vitality was decreased to 30% after 72 h incubation with 100 μM Cisplatin [124].

In a similar report by Gupta and coworkers, a DEP field was used to isolate cancer cells from blood cells [125]. It was demonstrated that a continuous-flow DEP microfluidic device where an AC electric field was applied to a spiked sample mixture consisting of cancer cells (ovarian cancer cell line, SKOV3 or breast cancer cell, MDA-MB-231) and blood cells. The base of the microfluidic chamber consisted of a polyimide film sheet electroplated with copper and gold electrodes. An acrylic sheet covered the chamber ceiling and a gasket formed the side walls.

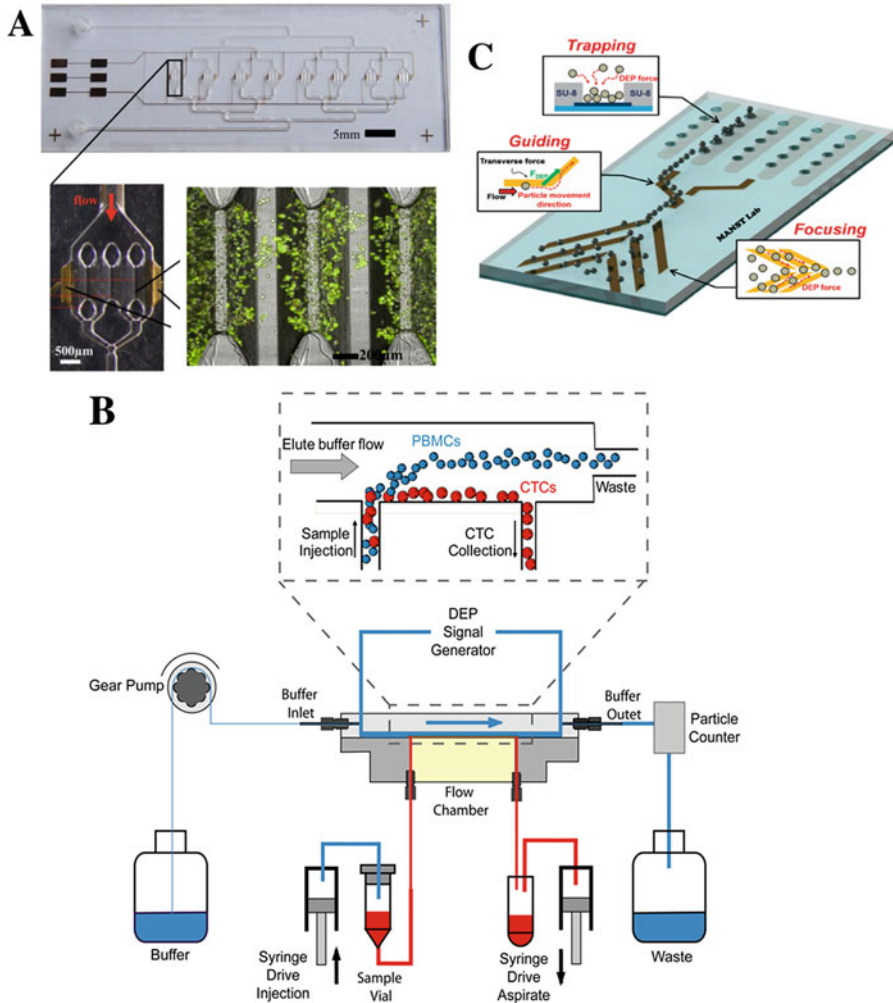


Fig. 4.16 Integration of CoC systems with DEP technology. (a) Full view of a microfluidic chip with eight culture chambers. Each chamber consisted two electrodes and three assembly ridges coated with collagen. PANC1 cells were clustered on assembly ridges when the DEP field was turned on. ([Beer] Reprinted from Ref. [124]. Copyright © 2017, Springer Nature.) (b) Schematic diagram of the separation device where CTCs were attracted to the CTC collection port while the PBMCs were deflected to the waste exit. (Reprinted with permission from Ref. [125]. Copyright © 2012, American Institute of Physics.) (c) Schematic diagram of fish-bone-structured design for three step DEP manipulations for focusing, guiding, and trapping of nanoprobes. (Reprinted with permission from Ref. [128]. Copyright © 2015, Royal Society of Chemistry)

When cells were perfused into the DEP field, the positive DEP forces were able to attract cancer cells towards the chamber floor and the blood cells were repelled towards the opposite exit (Fig. 4.16b). The average recovery of cancer cells spiked into blood samples was reported to be around 70% and the viability of cancer cells

captured was retained at 97% and above. Furthermore, the captured cells were later recultured and no difference was observed for the cell growth compared to the control, demonstrating that such DEP separation technique does not impact on cell viability.

Isolating cancer cells from blood cells is not too challenging since the physical properties of those cell types are distinctively different [125]. However, separation of two types of cancer cells from each other can be quite challenging as they share same surface biomarkers (such as EpCAM). DEP, on the other hand, has been shown to be able to differentiate two cancer types based on a subtle difference in induced electrical property, even though they have exhibit similar morphology and biomarkers. Yang and colleagues have shown to isolate prostate cancer cells (LNCaP) from colorectal cancer cells (HCT116) using DEP field under continuous flow in a microfluidic platform [126]. This separation platform consisted of a transparent acrylic plastic substrate as a top layer with one inlet and two outlet wells (one for the main channel, and the other for side channel). A pair of thin-film electrodes based on indium tin oxide were incorporated into the chip to induce the DEP field. When an AC electric field was supplied at 2.5 MHz, the prostate cancer cells experienced a negative DEP force, while the LNCaP cells experienced a positive DEP force. This charge difference consequently led to the separation of those two cell lines inside the microfluidic chip under flow. Furthermore, when the flow rates of sample mixture were kept at less than 0.4 $\mu\text{L}/\text{min}$, the separation efficiency reached up to 96%.

The integrated electrodes not only facilitate separation and detection of cancer cells, they can also be applied for capture and detection of other cancer biomarkers, such as exosomes and other protein cancer biomarkers that are secreted by cancer cells. In fact, those cancer biomarkers (e.g., exosomes or circulating DNA) are much more abundant than CTCs in circulation [13]. For example, a multiplexed microfluidic device was used for immuno-capture of exosomes secreted by breast cancer cells via electrohydrodynamic flow [127]. A fivefold increase in the exosome capture rate was observed in comparison to pressure-induced flow and with an improved limit of exosome detection (2760 exosomes per μl of sample). Similarly, Chuang et al. used a multiplexed immunosensing microfluidic chip for the detection of specific cancer biomarkers, Galectin-1 and Lactate Dehydrogenase B which are present in different grades of bladder cancer cell lysates [128]. This chip consisted of a patterned indium tin oxide electrode for sensing and central fish-bone-shaped gold electrodes for focusing and guiding of biomolecules (Fig. 4.16c). The authors were able to distinguish different grades of bladder cancer cells based on the detected biomarker concentration.

5.3.4 Integration of Magnetic Field Manipulation

Another important technique that can be readily incorporated into a CoC system for biological sample handling is the implementation of a magnetic field. Different to the fluorescence activated cell separation (FACS) technique, magnetic-activated cell sorting (MACS) uses magnetic particles instead of fluorophores and usually only a single cell type can be isolated [129]. More recently, magnetic-based techniques have been widely used in combination with microfluidic systems and offer new

capabilities. The magnetic field is generated via electromagnetics or permanent magnets which can be positioned either inside or outside the microfluidic chips. Magnetic beads provide anchoring surfaces for antibodies or other capturing molecules. Target cells such as CTCs or other sample components such as exosomes can then be specifically isolated.

For example, a combined microfluidic-micromagnetic cell separation device was reported by Kang and colleagues to isolate and detect CTCs from whole blood samples [130]. The microfluidic device consisted of a main channel and rows of dead-end side chambers for CTCs collection (Fig. 4.17a). EpCAM antibody-coated magnetic microbeads (2.8 μm in diameter) were used for selective binding to CTCs. A permanent magnet was placed on the bottom of the microfluidic channel to trap magnetic beads. M6C breast cancer cell line was used as a test case and yielded close to 90% isolation efficiency when only 2–80 breast cancer cells were spiked into 1 mL of blood. This isolation efficiency is comparable to the abundance of CTCs in cancer patients ranging from a few to hundreds of cells per ml [21]. Furthermore, 4 T1 mouse mammary tumor cells were injected into mice and were later successfully isolated using such microfluidic system after 2–4 weeks. Those isolated CTCs were viable and could later be expanded in cell culture.

Another interesting report by Earhart and co-workers utilized a “magnetic sifter” device, a structure that contained a large number of magnetic pores ($40 \times 40 \mu\text{m}^2$), to isolate CTCs, and subsequently performed gene mutational analysis [131]. This “magnetic sifter” platform consisted of a miniature microfluidic chip with an array of 3800 magnetic pores (Fig. 4.17b). Lung tumor cells, H-1650, were labeled with magnetic nanoparticles (150 nm in diameter). The labeled CTCs were then mixed with blood sample and the mixture was filtered through the magnetic sifter. Flow rates were tested from 5 to 25 ml/h and yielded from 75% to 96% CTC capture efficiency. These CTCs were then lysed and the mutational status was assessed using mutation specific anti-EGFR antibodies. Furthermore, this magnetic sifter was applied in CTC enumeration for blood samples from both healthy donors and patients with lung cancers. CTCs were detected for all six patients with titers ranging 31–96 CTCs/ml.

By arranging permanent magnets in a specific orientation, a sharp magnetic field gradient can be generated to facilitate cell manipulation [132]. Hoshino et al. developed a microfluidic device combined with three permanent magnets with alternating polarities for effective capture and enrichment of CTCs (Fig. 4.17c). Blood samples were first mixed with magnetic particles (~ 100 nm) which were pre-conjugated with anti-EpCAM antibodies. Colorectal (COLO205) and breast (SKBR3) cancer cells were used to test this microfluidic system and a CTC capture efficiency of 90% and 86%, respectively, was determined. Compared to other microchannel-based assay, fewer (25%) magnetic particles were required to obtain similar capture efficiency, while the screening speed was significantly faster (range from 2.5 to 10 ml/h).

While most magnetic manipulations were focused on the capture and isolation of CTCs [130–132], very few were focused on using such technique for capturing tumor-derived exosomes. He et al. developed a microfluidic system for both the

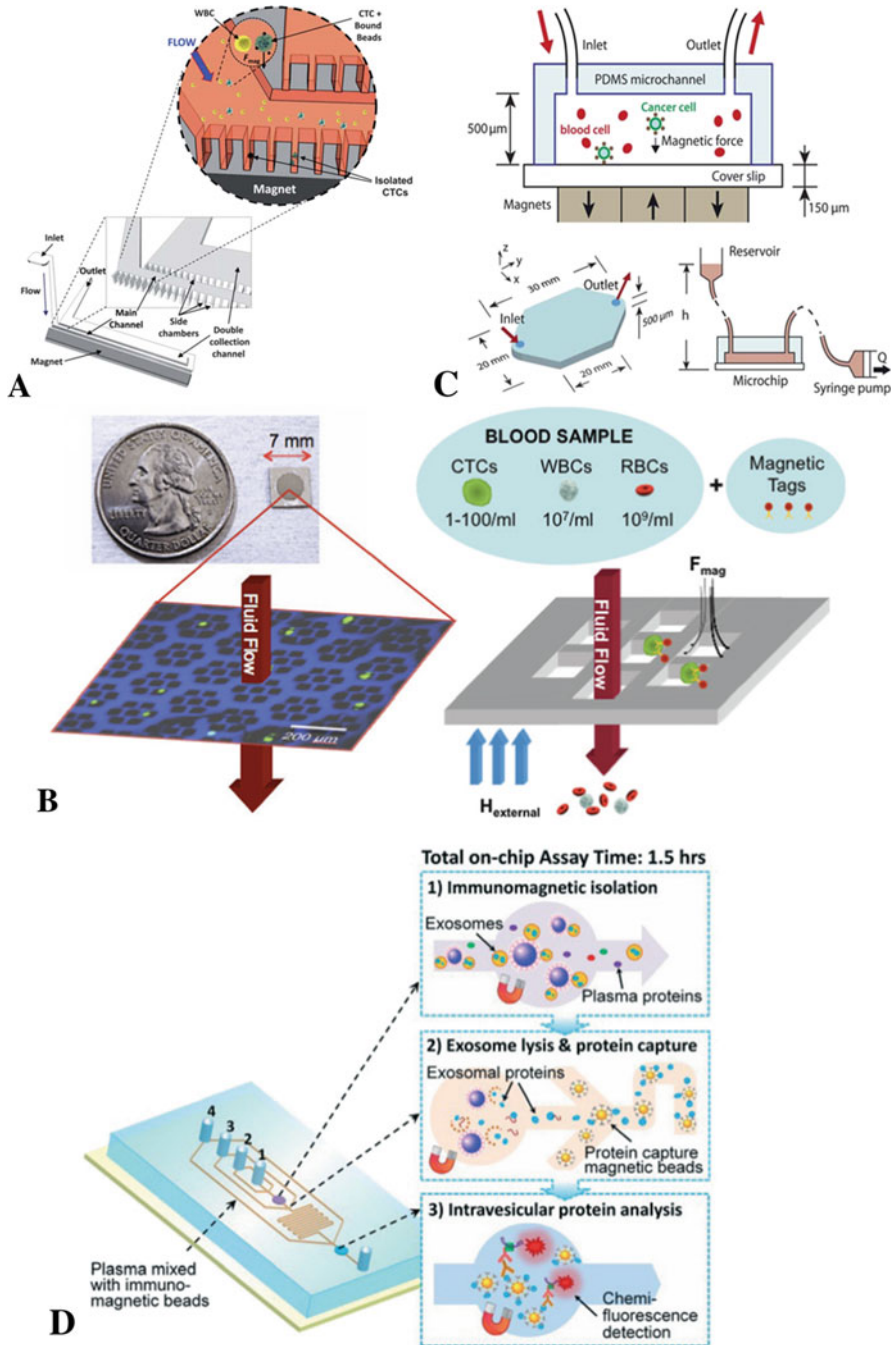


Fig. 4.17 Integration CoC system with magnetic field. (a) CTC isolation microfluidic device containing a main channel and double collection channels which are lined by rows of dead-end side

immunomagnetic capture of various exosome subpopulations and the fluorescence analysis of the exosomal surface proteins [133]. This PDMS-based chip system enabled a multi-step immunomagnetic capture method (Fig. 4.17d). The exosomes were pulled onto the bottom of the chamber after binding to the antibody-labeled magnetic beads (with >99.9% bead recovery). A lysis buffer was then perfused into the microchannel to release the intravesicular proteins. Lastly, antibody-labeled magnetic beads were once again used to capture these released proteins and were retained in the chamber by using the magnets. A sandwich immunoassay could then be performed directly on chip for further analysis.

5.3.5 Incorporation of Nanoparticles as Nanomedicines

There has been a rapid growth of interest in applying nanomaterials to cancer research due to the unique properties of certain nanomaterials for drug delivery, diagnosis, imaging, and therapeutic nature [134]. In fact, some nanoparticle (NP) carriers have been already approved by FDA to be used for cancer treatments, including polymeric micelles, liposomes, and albumin NPs. Countless novel NPs with different material, surface property, and size are being reported on a daily basis. Therefore, an accurate testing platform that can fast-track the screening of nano-carrier toxicity and drug delivery efficacy is urgently needed. Various CoC models have been developed to screen NP toxicity or the anticancer efficiency of drug-bearing NPs.

For instance, we have designed a crossed flow configuration microfluidic system as a platform to test NP toxicity in a high throughput manner [135, 136]. The aim was to immobilize a number of different cell lines inside the chip for screening against a panel of different NPs (Fig. 4.18a). We have shown to utilize lymphoma cell line (HR1K) on chip and tested against silver nanoparticles (10 nm) in different concentrations at a prescribed flow rate. We found a dose-dependent toxicity effect of the silver NPs on HR1K cell line. Furthermore, we have also demonstrated under same particle concentrations, HR1K cells experienced more cytotoxic effect in flow condition than in a static situation [135]. This crossed flow microfluidic platform can be used to immobilize other cell lines, such as adherent cell line, U87 [136]. Similarly, Grafton et al. reported to test the cytotoxicity of superparamagnetic submicron particles (SMPs, 0.86 μm). SMPs are clinical contrast agents used for MRI. In a



Fig. 4.17 (continued) chambers. A permanent magnet was placed directly beneath the side chambers to collect the magnetic bead-bound cells. (Reprinted from Ref. [130]. Copyright © 2012, Royal Society of Chemistry.) (b) A magnetic sifter device contained patterned pore arrays and enabled capture of H-1650 lung tumor cells. Pores are $40 \times 40 \mu\text{m}^2$ squares. (Reprinted from Ref. [131]. Copyright © 2014, Royal Society of Chemistry.) (c) Microchip design for capturing CTCs using EpCAM functionalized Fe_3O_4 magnetic nanoparticles with three permanent magnets of alternate polarities. (Reprinted from Ref. [132]. Copyright © 2011, Royal Society of Chemistry.) (d) A PDMS chip containing a cascading network of microchannels for multi-stage exosome analysis. (Reprinted from Ref. [133]. Copyright © 2014, Royal Society of Chemistry)

microfluidic system containing hierarchical branches emulating the structure of mammary ducts dose-dependent cytotoxicity of these SMPs on the mammary ducts was reported [137].

Testing of anticancer efficacy of drug infused NPs has also been explored in the context of CoC systems. For example, a 3D breast CoC was reported by Chen et al. consisting of a microvessel channel, an ECM containing channel, and a tumor spheroids housing compartment (Fig. 4.18b) [138]. A drug delivery system based on carbon dots was used for real-time monitoring of drug transport across the

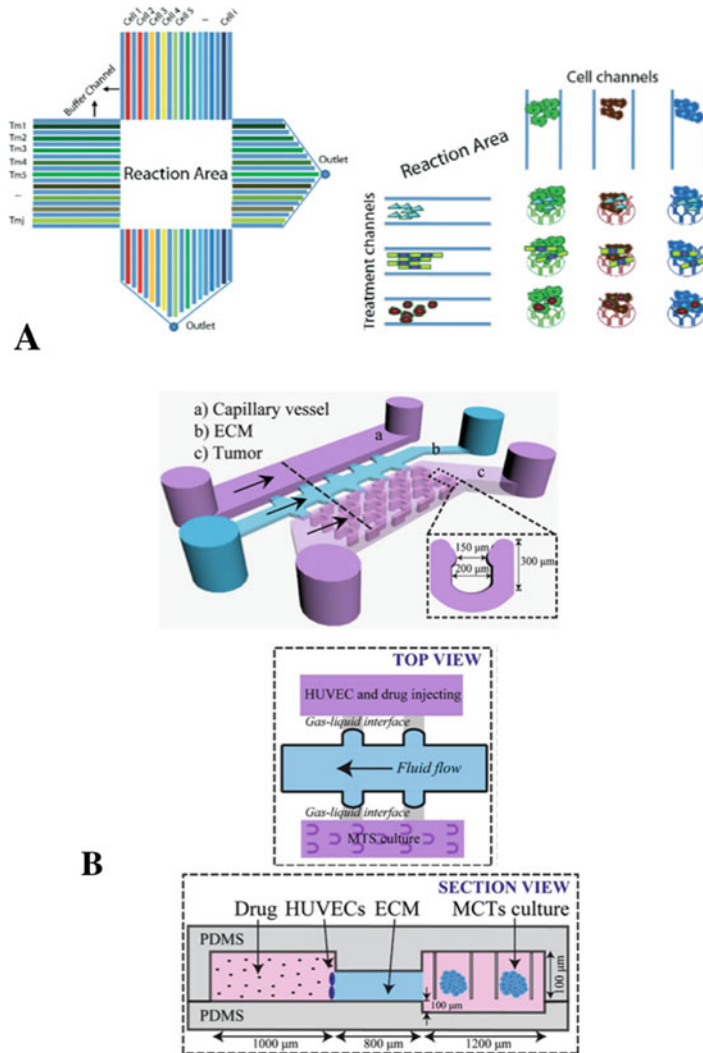


Fig. 4.18 (continued)

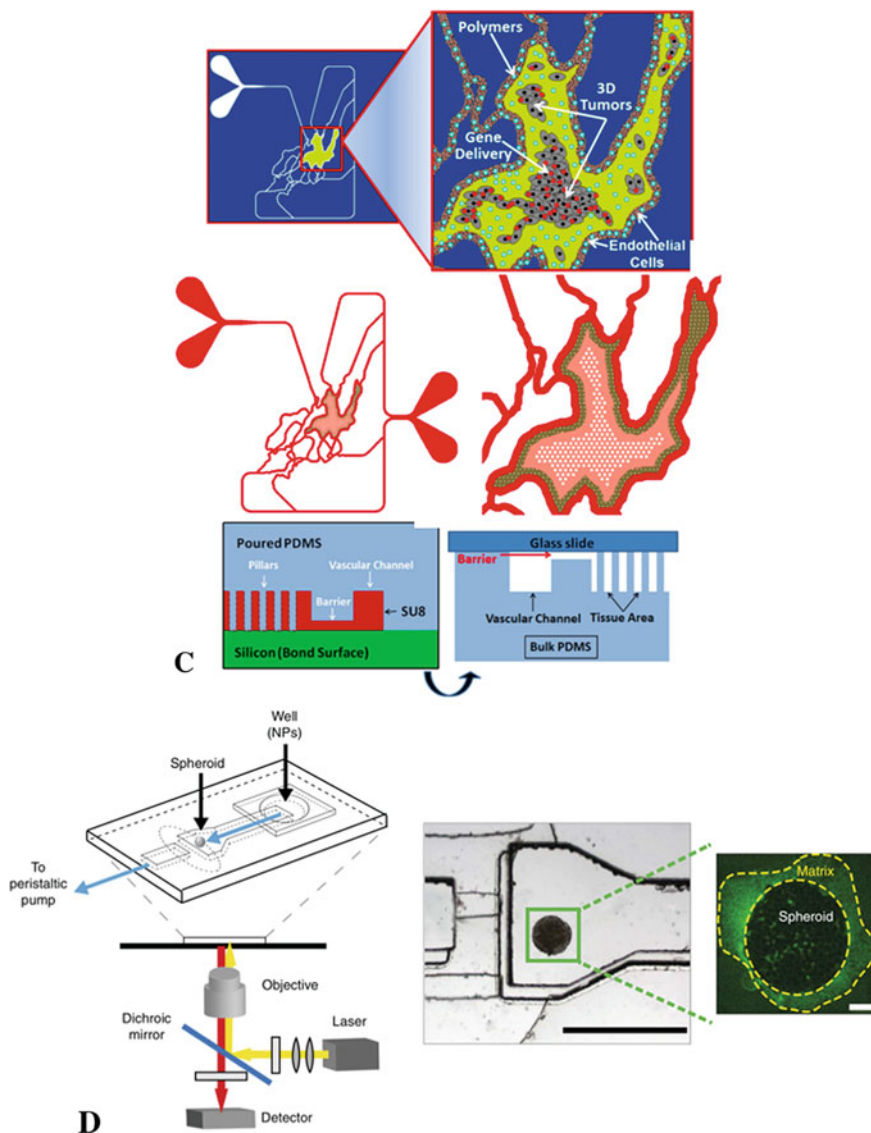


Fig. 4.18 Testing NPs in CoC systems. (a) Crossed-flow configuration of microfluidic systems used for high throughput screening of NP cytotoxicity. (Reprinted from Ref. [136]. Copyright © 2017, Royal Society of Chemistry.) (b) Schematic illustration of a microfluidic chip containing three microchannels (representing a capillary vessel, the ECM, and tumor cells) was used to test the drug delivery efficacy using DOX loaded carbon dots. (Reprinted from Ref. [138]. Copyright © 2018, Elsevier.) (c) A schematic diagram demonstrating the vascular compartments for endothelial cells and another compartment for culturing tumor cells. (Reprinted from Ref. [140]. Copyright © 2015, Elsevier.) (d) Schematic of a CoC system to study NP delivery into 3D tumor micro-tissues which were found to be dependent on NP size and interstitial flow rates. (Reprinted from Ref. [141]. Copyright © 2013, Springer Nature)

endothelial cell layer and to penetrate into cancer spheroids. Within 3 h, the synthesized drug delivery system could be effectively transported across the endothelial cell layer. Delivery of anticancer drug DOX and efficacy was assessed on chip using two breast cancer spheroid models (i.e., BT549 and T47D). A similar model by Kwak and coworkers using a microfluidic model consisting of breast cancer microenvironment surrounded by lymphatic and capillary microvessels used MCF-7 cells embedded in collagen matrix [139]. The transport of NPs into breast cancer spheroids was influenced by particle diameter, cut-off ECM pore size, collagen concentrations, and interstitial fluid pressure.

Prabhakarandian et al. recreated a 3D cervical cancer microenvironment in a CoC system with a physiologically and morphologically relevant microvasculature, mimicking leaky capillary vessels based on engineered perforations between the vascular side and the tumor cells of around 2 μm in size (Fig. 4.18c) [140]. Two types of nanopolymer-based gene delivery systems for green fluorescence protein (GFP) encoding DNA were studied to predict in vivo drug-delivery efficiencies. These results were in accordance with those from a rodent model, highlighting the predictive ability of the microfluidic device-based assay [140].

Albanese et al. reported a CoC-containing melanoma spheroid for real-time analysis of NP accumulation under physiological flow conditions [141]. Their CoC consisted of a multi-cellular spheroid immobilized in the channel of a dual-layer PDMS chip. Melanoma cell spheroids, MDA-MB-435 (280 μm), were pre-cultured outside the chip and then introduced into the CoC system using gravity-driven flow (Fig. 4.18d). The authors demonstrated that NP tissue accumulation was restricted to hydrodynamic particle diameters of less than 110 nm, with 40 nm showing the highest accumulation rate. They also demonstrated that the interstitial flow rate could affect the accumulation of NPs at the spheroid-fluid interface. Faster flow rates resulted in a higher accumulation of NPs on the spheroid's outer layer able to diffuse into the tissue over time. These findings were further confirmed with a murine xenograft model [141].

5.3.6 Incorporation of Other Technologies

Indeed, microfluidic systems have shown their great versatility to be combined with various advanced techniques, such as optical microscopy, sensors, electrical, and magnetic forces; other emerging exciting technologies are also compatible with such system for potential applications in cancer research and diagnostics. For instance, fluorescence in situ hybridization (FISH) is a well-known gene-based method to microscopically image genetic defects [70]. Combining FISH with microfluidic platform can offer the possibility of automation and with significant time and cost reduction. FISH technique has also been recently reported to be combined with CoCs for detection of cancer gene mutation [142, 143].

Furthermore, real-time quantitative PCR is a powerful technique for the quantification and rare mutation detection of nucleic acid. Digital PCR (dPCR) method has recently been integrated into a microfluidic platform. For example, a serial dilution of genomic DNA from lung cancer cell line was used to evaluate the quantitation capability of a dPCR chip and showed improved measurement accuracy compared to

real-time quantitative PCR [144]. This platform contained 10,000 reaction compartments with 0.785 nL volume each. In a similar report, single-cell RT-PCR has been demonstrated using a nanowell platform which showed superior performance of analyzing 25,600 nanowells with less than 20 picoliter volume of samples [145].

Ultrasound, an acoustic method widely used in medical imaging, has been proven to be extremely safe and also some reports have integrated this technique for on chip cell manipulations. Li et al. demonstrated an acoustic-based microfluidic device that is capable of high-throughput separation of CTCs from patient peripheral blood [117]. This platform used tilted-angle standing surface acoustic waves and was capable of separating different cancer cells from blood cells with a recovery rate better than 83%. Similarly, a novel acoustofluidic platform has also been developed by integrating focused ultrasound (FUS) with a physiologically relevant 3D microfluidic device [146]. FUS could induced local heating that triggered the release of DOX from a liposomal carrier at a localized region and higher cellular drug uptake was observed in the FUS focal region.

6 Conclusions and Future Perspectives

Despite still being at an early developmental stage, microfluidic systems, especially organ-on-chip technology, is poised to make major contributions towards the effort of drug discovery and to reduce the high cost associated with drug development [147]. This technology provides an innovative platform with high predictive power due to its mimicry of basic tissue function and architecture and is therefore an ideal platform for HTS of potential drug candidates [141]. There is a strong potential that this technology can contribute to the clinical translation of innovative therapeutics, including nanomedicine and gene therapy [21, 141].

As illustrated in this chapter, while conventional *in vitro* platforms rather poorly capture the complexity of cell-cell interactions in the human body, organ-on-chip systems have opened a new frontier in representing key-functional units of human organs. These micro-engineered systems allow studying single cells under different mechanical stimuli and gradients of signaling molecules including drugs, and have therefore already found extensive applications in cancer biology, clinical oncology, drug screening, and target identification [148].

CoC technology promises to significantly contribute in advancing our understanding of cancer and of the different players involved in generating the complex tumor microenvironment, thus fostering a new pathway to conduct mechanistic cancer studies. CoC systems can be further enhanced by integration of technologies such as super-resolution imaging, biosensing, and electrical or magnetic fields for cell manipulation. Moreover, CoC technology can potentially be applied towards personalized medicines, as patients-derived (cancer) cells could be used to reproduce the complex tumor microenvironment and to test personalized drug treatments (monitoring efficacy and unwanted side effects of different cancer therapies) [147].

Indeed, with the emergence of CoC technology, many aspects that are important to cancer progression, such as in metastasis, can now be dissected and studied in

detail. For example, as demonstrated in Session 3.1, micropores embedded in CoCs with various dimensions were fabricated to assess cancer cell migration ability through choke points mimicking intravasation events [67]. Chemical (cytokine or growth factor) and cellular (co-culture with different types of cancer cells) cues were investigated via CoCs to tease out the critical mechanism of tumor cell-induced angiogenesis [55, 56]. Moreover, anti-cancers drugs were tested in CoCs that represent different cancerous organs, such as in brain, breast, liver, and lung, in a more efficient and accurate manner (Session 3.2). In contrast, in animal models, it usually takes weeks to months to see the results of administered drugs and those findings are often not translatable to humans. Furthermore, CoCs are also very useful in cancer cell characterization and as a diagnosis tool as shown in Session 3.3. For example, CoCs can be used effectively to isolate (e.g., via magnetic or DEP filed) and characterize CTCs (e.g., super-resolution imaging) from patient liquid biopsy samples. Biosensors can also be incorporated into the CoCs for real-time and accurate measurement of cancer cell diseased state (detection of cancer biomarkers) and upon infusion of anti-cancer drugs (organic compounds or incorporated as nanomedicine composites).

Nevertheless, some challenges still need to be resolved before we can harness the full potential of CoC technology, such as recreating a tumor microenvironment that faithfully recapitulates the effects of angiogenesis, stiffness, hypoxia, and tumor-stromal interactions [22]. Moreover, building materials such as PDMS or PMMA are not always conducive to this building complex *in vivo* tissue architecture and can absorb small organic compounds, including pharmaceutical drugs [20]. In addition, cellular monitoring techniques need to be carefully chosen, for example, super-resolution on chip imaging should not induce photo-toxicity effect to live cells. From an engineering perspective, achieving a finely controlled laminar flow in microfluidic devices that mimics *in vivo* hydrodynamic, shear flow is challenging in the context of scale up for HTS. The development of advanced materials suitable for long-term “organ” culture in microfluidic device is also an unmet need. Indeed, it is essential to develop both ECM to support the intricate 3D architecture of the *in vitro* tissue and a universal media for co-culture of different cell lines [82].

Acknowledgment This work was financially supported by the Australian Research Council Discovery Grant (DP150101774), John Stocker Postdoctoral Fellowship, and the CSIRO Probing Biosystems Future Science Platform.

References

1. Fitzmaurice C, Allen C, Barber RM, Barregard L, Bhutta ZA, Brenner H, Dicker DJ, Chimed-Orchir O, Dandona R, Dandona L (2017) Global, regional, and national cancer incidence, mortality, years of life lost, years lived with disability, and disability-adjusted life-years for 32 cancer groups, 1990 to 2015: a systematic analysis for the global burden of disease study. *JAMA Oncol* 3(4):524–548
2. Stewart BW, Wild CW (2014) World cancer report. Lyon CEDEX, France: IARC Press
3. Siegel RL, Miller KD, Jemal A (2017) Cancer statistics, 2017. *CA Cancer J Clin* 67(1):7–30

4. Culligan K, Sehgal R, Mulligan D, Dunne C, Walsh S, Quondamatteo F, Dockery P, Coffey JC (2014) A detailed appraisal of mesocolic lymphangiology – an immunohistochemical and stereological analysis. *J Anat* 225(4):463–472
5. Coons SJ, Craig BM (2014) Assessing human and economic benefits of cancer prevention. In: *Fundamentals of cancer prevention*. Springer-Verlag Berlin Heidelberg: Springer, pp 15–34
6. Hanahan D, Weinberg RA (2000) The hallmarks of cancer. *Cell* 100(1):57–70
7. Wai LK (2004) Telomeres, telomerase, and tumorigenesis – a review. *Medscape Gen Med* 6(3):19
8. Seyfried TN, Huysentruyt LC (2013) On the origin of cancer metastasis. *Crit Rev Oncog* 18(1–2):43–73
9. Fidler IJ (2003) The pathogenesis of cancer metastasis: the seed and soil hypothesis revisited. *Nat Rev Cancer* 3(6):453
10. Tlsty TD, Coussens LM (2006) Tumor stroma and regulation of cancer development. *Annu Rev Pathol Mech Dis* 1:119–150
11. Young EW (2013) Cells, tissues, and organs on chips: challenges and opportunities for the cancer tumor microenvironment. *Integr Biol* 5(9):1096–1109
12. Quandt D, Zucht HD, Amann A, Wulf-Goldenberg A, Borrebaeck C, Cannarile M, Lambrechts D, Oberacher H, Garrett J, Nayak T (2017) Implementing liquid biopsies into clinical decision making for cancer immunotherapy. *Oncotarget* 8(29):48507
13. Tadimety A, Closson A, Li C, Yi S, Shen T, Zhang JX (2018) Advances in liquid biopsy on-chip for cancer management: technologies, biomarkers, and clinical analysis. *Crit Rev Clin Lab Sci* 55(3):140–162
14. Liu Z, Zhang W, Huang F, Feng H, Shu W, Xu X, Chen Y (2013) High throughput capture of circulating tumor cells using an integrated microfluidic system. *Biosens Bioelectron* 47:113–119
15. Klein CA (2009) Parallel progression of primary tumours and metastases. *Nat Rev Cancer* 9(4):302
16. Whitesides GM (2006) The origins and the future of microfluidics. *Nature* 442(7101):368–373
17. Mahto SK, Charwat V, Ertl P, Rothen-Rutishauser B, Rhee SW, Sznitman J (2015) Microfluidic platforms for advanced risk assessments of nanomaterials. *Nanotoxicology* 9(3):381–395
18. Neuzil P, Giselbrecht S, Länge K, Huang TJ, Manz A (2012) Revisiting lab-on-a-chip technology for drug discovery. *Nat Rev Drug Discov* 11(8):620
19. Balijepalli A, Sivaramakrishnan V (2017) Organs-on-chips: research and commercial perspectives. *Drug Discov Today* 22(2):397–403
20. Bhatia SN, Ingber DE (2014) Microfluidic organs-on-chips. *Nat Biotechnol* 32(8):760–772
21. Zhang YS, Zhang YN, Zhang W (2017) Cancer-on-a-chip systems at the frontier of nanomedicine. *Drug Discov Today* 22(9):1392–1399
22. Wlodkovic D, Cooper JM (2010) Tumors on chips: oncology meets microfluidics. *Curr Opin Chem Biol* 14(5):556–567
23. Sung KE, Beebe DJ (2014) Microfluidic 3D models of cancer. *Adv Drug Deliv Rev* 79:68–78
24. Choi JH, Lee J, Shin W, Choi JW, Kim HJ (2016) Priming nanoparticle-guided diagnostics and therapeutics towards human organs-on-chips microphysiological system. *Nano Convergence* 3(1):24
25. Tanner K, Gottesman MM (2015) Beyond 3D culture models of cancer. *Sci Transl Med* 7(283):283ps289–283ps289
26. Caballero D, Kaushik S, Correló VM, Oliveira JM, Reis RL, Kundu SC (2017) Organ-on-chip models of cancer metastasis for future personalized medicine: from chip to the patient. *Bio-materials* 149:98–115
27. Tsao CW, Hromada L, Liu J, Kumar P, DeVoe DL (2007) Low temperature bonding of PMMA and COC microfluidic substrates using UV/ozone surface treatment. *Lab Chip* 7(4):499–505
28. Faustino V, Catarino SO, Lima R, Minas G (2016) Biomedical microfluidic devices by using low-cost fabrication techniques: a review. *J Biomech* 49(11):2280–2292

29. Iliescu C, Taylor H, Avram M, Miao J, Franssila S (2012) A practical guide for the fabrication of microfluidic devices using glass and silicon. *Biomicrofluidics* 6(1):16505–1650516
30. Tuomikoski S, Franssila S (2005) Free-standing SU-8 microfluidic chips by adhesive bonding and release etching. *Sensors Actuators A Phys* 120(2):408–415
31. Betancourt T, Brannon-Peppas L (2006) Micro- and nanofabrication methods in nanotechnological medical and pharmaceutical devices. *Int J Nanomedicine* 1(4):483–495
32. Ghosh M, Alves C, Tong Z, Tettey K, Konstantopoulos K, Stebe KJ (2008) Multifunctional surfaces with discrete functionalized regions for biological applications. *Langmuir* 24(15):8134–8142
33. Duffy DC, McDonald JC, Schueller OJ, Whitesides GM (1998) Rapid prototyping of microfluidic systems in poly(dimethylsiloxane). *Anal Chem* 70(23):4974–4984
34. Herland A, van der Meer AD, FitzGerald EA, Park TE, Sleeboom JJ, Ingber DE (2016) Distinct contributions of astrocytes and pericytes to neuroinflammation identified in a 3D human blood-brain barrier on a chip. *PLoS One* 11(3):e0150360
35. Eger A, Mikulits W (2005) Models of epithelial–mesenchymal transition. *Drug Discov Today Dis Model* 2(1):57–63
36. Viger L, Denis F, Rosalie M, Letellier C (2014) A cancer model for the angiogenic switch. *J Theor Biol* 360:21–33
37. Heerboth S, Housman G, Leary M, Longacre M, Byler S, Lapinska K, Willbanks A, Sarkar S (2015) EMT and tumor metastasis. *Clin Transl Med* 4:6
38. Gheldof A, Bex G (2013) Cadherins and epithelial-to-mesenchymal transition. *Prog Mol Biol Transl Sci* 116:317–336
39. Yeung KT, Yang J (2017) Epithelial-mesenchymal transition in tumor metastasis. *Mol Oncol* 11(1):28–39
40. Cui W, Fowles DJ, Bryson S, Duffie E, Ireland H, Balmain A, Akhurst RJ (1996) TGF β 1 inhibits the formation of benign skin tumors, but enhances progression to invasive spindle carcinomas in transgenic mice. *Cell* 86(4):531–542
41. Kim YS, Yi BR, Kim NH, Choi KC (2014) Role of the epithelial-mesenchymal transition and its effects on embryonic stem cells. *Exp Mol Med* 46:e108
42. Kim SH, Hwang SM, Lee JM, Kang JH, Chung IY, Chung BG (2013) Epithelial-to-mesenchymal transition of human lung alveolar epithelial cells in a microfluidic gradient device. *Electrophoresis* 34(3):441–447
43. Li Y, Gao A, Yu L (2016) Monitoring of TGF- β 1-induced human lung adenocarcinoma A549 cells epithelial-mesenchymal transformation process by measuring cell adhesion force with a microfluidic device. *Appl Biochem Biotechnol* 178(1):114–125
44. Rizvi I, Gurkan UA, Tasoglu S, Alagic N, Celli JP, Mensah LB, Mai Z, Demirci U, Hasan T (2013) Flow induces epithelial-mesenchymal transition, cellular heterogeneity and biomarker modulation in 3D ovarian cancer nodules. *Proc Natl Acad Sci* 110(22):E1974
45. Ma D, Wang R, Chen S, Luo T, Chow Y-T, Sun D (2018) Microfluidic platform for probing cancer cells migration property under periodic mechanical confinement. *Biomicrofluidics* 12(2):024118
46. Malboubi M, Jayo A, Parsons M, Charras G (2015) An open access microfluidic device for the study of the physical limits of cancer cell deformation during migration in confined environments. *Microelectron Eng* 144:42–45
47. Karakas HE, Kim J, Park J, Oh JM, Choi Y, Gozuacik D, Cho YK (2017) A microfluidic chip for screening individual cancer cells via eavesdropping on autophagy-inducing crosstalk in the stroma niche. *Sci Rep* 7(1):2050
48. Zhang Y, Wen J, Zhou L, Qin L (2015) Utilizing a high-throughput microfluidic platform to study hypoxia-driven mesenchymal-mode cell migration. *Integr Biol* 7(6):672–680
49. Yamazaki D, Kurisu S, Takenawa T (2005) Regulation of cancer cell motility through actin reorganization. *Cancer Sci* 96(7):379–386
50. Toh Y-C, Raja A, Yu H, van Noort D (2018) A 3D microfluidic model to recapitulate cancer cell migration and invasion. *Bioengineering* 5(2):29

51. Nguyen TA, Yin TI, Reyes D, Urban GA (2013) Microfluidic chip with integrated electrical cell-impedance sensing for monitoring single cancer cell migration in three-dimensional matrixes. *Anal Chem* 85(22):11068–11076
52. Liu Z, Han X, Zhou Q, Chen R, Fruge S, Jo Myeong C, Ma Y, Li Z, Yokoi K, Qin L (2017) Integrated microfluidic system for gene silencing and cell migration. *Adv Biosyst* 1(6):1700054
53. Watnick RS (2012) The role of the tumor microenvironment in regulating angiogenesis. *Cold Spring Harb Perspect Med* 2(12):a006676
54. Chung S, Sudo R, Mack PJ, Wan C-R, Vickerman V, Kamm RD (2009) Cell migration into scaffolds under co-culture conditions in a microfluidic platform. *Lab Chip* 9(2):269–275
55. Hsu Y, Chang K, Chen T, Lee K, Liu C (2014) An integrated microfluidic chip for the study of metastasis and angiogenesis. In: *The 9th IEEE international conference on nano/micro engineered and molecular systems (NEMS)*, Singapore 13–16 April 2014, pp 426–429
56. Lee H, Park W, Ryu H, Jeon NL (2014) A microfluidic platform for quantitative analysis of cancer angiogenesis and intravasation. *Biomicrofluidics* 8(5):054102
57. Deryugina EI, Kiosses WB (2017) Intratumoral cancer cell intravasation can occur independent of invasion into the adjacent stroma. *Cell Rep* 19(3):601–616
58. Wyckoff JB, Jones JG, Condeelis JS, Segall JE (2000) A critical step in metastasis: analysis of intravasation at the primary tumor. *Cancer Res* 60(9):2504
59. Harney AS, Arwert EN, Entenberg D, Wang Y, Guo P, Qian B-Z, Oktay MH, Pollard JW, Jones JG, Condeelis JS (2015) Real-time imaging reveals local, transient vascular permeability, and tumor cell intravasation stimulated by TIE2hi macrophage-derived VEGFA. *Cancer Discov* 5(9):932
60. Stoletov K, Kato H, Zardoujian E, Kelber J, Yang J, Shatill S, Klemke R (2010) Visualizing extravasation dynamics of metastatic tumor cells. *J Cell Sci* 123(13):2332
61. Zervantonakis IK, Hughes-Alford SK, Charest JL, Condeelis JS, Gertler FB, Kamm RD (2012) Three-dimensional microfluidic model for tumor cell intravasation and endothelial barrier function. *Proc Natl Acad Sci* 109(34):13515
62. Agliari E, Biselli E, De Ninno A, Schiavoni G, Gabriele L, Gerardino A, Mattei F, Barra A, Businaro L (2014) Cancer-driven dynamics of immune cells in a microfluidic environment. *Sci Rep* 4:6639
63. Nagaraju S, Truong D, Mouneimne G, Nikkhah M (2018) Microfluidic tumor–vascular model to study breast cancer cell invasion and intravasation. *Adv Healthc Mater* 7(9):1701257
64. Watson EC, Koenig MN, Grant ZL, Whitehead L, Trounson E, Dewson G, Coultas LA-O (2016) Apoptosis regulates endothelial cell number and capillary vessel diameter but not vessel regression during retinal angiogenesis. *Development* 143(16):2973–2982
65. Pereira ER, Jones D, Jung K, Padera TP (2015) The lymph node microenvironment and its role in the progression of metastatic cancer. *Semin Cell Dev Biol* 38:98–105
66. Lee E, Pandey NB, Popel AS (2015) Crosstalk between cancer cells and blood endothelial and lymphatic endothelial cells in tumour and organ microenvironment. *Expert Rev Mol Med* 17:e3–e3
67. Chen YC, Allen SG, Ingram PN, Buckanovich R, Merajver SD, Yoon E (2015) Single-cell migration chip for chemotaxis-based microfluidic selection of heterogeneous cell populations. *Sci Rep* 5:9980
68. Rosenthal DT, Iyer H, Escudero S, Bao L, Wu Z, Ventura AC, Kleer CG, Arruda EM, Garikipati K, Merajver SD (2011) p38 γ promotes breast cancer cell motility and metastasis through regulation of RhoC GTPase, cytoskeletal architecture, and a novel leading edge behavior. *Cancer Res* 71(20):6338
69. Pisano M, Triacca V, Barbee KA, Swartz MA (2015) An in vitro model of the tumor-lymphatic microenvironment with simultaneous transendothelial and luminal flows reveals mechanisms of flow enhanced invasion. *Integr Biol* 7(5):525–533
70. Sato M, Sasaki N, Ato M, Hirakawa S, Sato K, Sato K (2015) Microcirculation-on-a-chip: a microfluidic platform for assaying blood- and lymphatic-vessel permeability. *PLoS One* 10(9):e0137301

71. Wirtz D, Konstantopoulos K, Searson PC (2011) The physics of cancer: the role of physical interactions and mechanical forces in metastasis. *Nat Rev Cancer* 11(7):512–522
72. Leong Hon S, Robertson Amy E, Stoletov K, Leith Sean J, Chin Curtis A, Chien Andrew E, Hague MN, Ablack A, Carmine-Simmen K, McPherson Victor A et al (2014) Invadopodia are required for cancer cell extravasation and are a therapeutic target for metastasis. *Cell Rep* 8(5):1558–1570
73. Kim Y, Williams KC, Gavin CT, Jardine E, Chambers AF, Leong HS (2016) Quantification of cancer cell extravasation in vivo. *Nat Protoc* 11:937
74. Song JW, Cavnar SP, Walker AC, Luker KE, Gupta M, Tung YC, Luker GD, Takayama S (2009) Microfluidic endothelium for studying the intravascular adhesion of metastatic breast cancer cells. *PLoS One* 4(6):e5756
75. Cardones AR, Murakami T, Hwang ST (2003) CXCR4 enhances adhesion of B16 tumor cells to endothelial cells in vitro and in vivo via beta(1) integrin. *Cancer Res* 63(20):6751
76. Riahi R, Yang YL, Kim H, Jiang L, Wong PK, Zohar Y (2014) A microfluidic model for organ-specific extravasation of circulating tumor cells. *Biomicrofluidics* 8(2):024103
77. Turley EA, Wood DK, McCarthy JB (2016) Carcinoma cell hyaluronan as a “portable” cancerized prometastatic microenvironment. *Cancer Res* 76(9):2507
78. Brett M-E, Bomberger HE, Doak GR, Price MA, McCarthy JB, Wood DK (2018) In vitro elucidation of the role of pericellular matrix in metastatic extravasation and invasion of breast carcinoma cells. *Integr Biol* 10(4):242–252
79. Boussommier-Calleja A, Atiyas Y, Haase K, Headley M, Lewis C, Kamm RD (2018) The effects of monocytes on tumor cell extravasation in a 3D vascularized microfluidic model. *Biomaterials* 198:180–193
80. Jeon JS, Zervantonakis IK, Chung S, Kamm RD, Charest JL (2013) In vitro model of tumor cell extravasation. *PLoS One* 8(2):e56910
81. Marturano-Kruik A, Nava MM, Yeager K, Chramiec A, Hao L, Robinson S, Guo E, Raimondi MT, Vunjak-Novakovic G (2018) Human bone perivascular niche-on-a-chip for studying metastatic colonization. *Proc Natl Acad Sci U S A* 115(6):1256–1261
82. Polini A, Prodanov L, Bhise NS, Manoharan V, Dokmeci MR, Khademhosseini A (2014) Organs-on-a-chip: a new tool for drug discovery. *Expert Opin Drug Discov* 9(4):335–352
83. Logun M, Zhao W, Mao L, Karumbaiah L (2018) Microfluidics in malignant glioma research and precision medicine. *Adv Biosyst* 2(5):1700221
84. Huang Y, Agrawal B, Clark PA, Williams JC, Kuo JS (2011) Evaluation of cancer stem cell migration using compartmentalizing microfluidic devices and live cell imaging. *J Vis Exp* 58:e3297
85. Han J, Jun Y, Kim SH, Hoang HH, Jung Y, Kim S, Kim J, Austin RH, Lee S, Park S (2016) Rapid emergence and mechanisms of resistance by U87 glioblastoma cells to doxorubicin in an in vitro tumor microfluidic ecology. *Proc Natl Acad Sci U S A* 113(50):14283–14288
86. Fan Y, Nguyen DT, Akay Y, Xu F, Akay M (2016) Engineering a brain cancer chip for high-throughput drug screening. *Sci Rep* 6:25062
87. Abbott NJ, Patabendige AA, Dolman DE, Yusof SR, Begley DJ (2010) Structure and function of the blood-brain barrier. *Neurobiol Dis* 37(1):13–25
88. Xu H, Li Z, Yu Y, Sizdahkhani S, Ho WS, Yin F, Wang L, Zhu G, Zhang M, Jiang L et al (2016) A dynamic in vivo-like organotypic blood-brain barrier model to probe metastatic brain tumors. *Sci Rep* 6:36670
89. Marino A, Tricinci O, Battaglini M, Filippeschi C, Mattoli V, Sinibaldi E, Ciofani G (2018) A 3D real-scale, biomimetic, and biohybrid model of the blood-brain barrier fabricated through two-photon lithography. *Small* 14(6):1702959
90. Place AE, Jin Huh S, Polyak K (2011) The microenvironment in breast cancer progression: biology and implications for treatment. *Breast Cancer Res* 13(6):227
91. Espina V, Liotta LA (2011) What is the malignant nature of human ductal carcinoma in situ? *Nat Rev Cancer* 11(1):68–75
92. Choi Y, Hyun E, Seo J, Blundell C, Kim HC, Lee E, Lee SH, Moon A, Moon WK, Huh D (2015) A microengineered pathophysiological model of early-stage breast cancer. *Lab Chip* 15(16):3350–3357

93. Gioiella F, Urciuolo F, Imparato G, Brancato V, Netti PA (2016) An engineered breast cancer model on a chip to replicate ECM-activation in vitro during tumor progression. *Adv Healthc Mater* 5(23):3074–3084
94. Heldin CH, Rubin K, Pietras K, Ostman A (2004) High interstitial fluid pressure - an obstacle in cancer therapy. *Nat Rev Cancer* 4(10):806–813
95. Walsh CL, Babin BM, Kasinskas RW, Foster JA, McGarry MJ, Forbes NS (2009) A multi-purpose microfluidic device designed to mimic microenvironment gradients and develop targeted cancer therapeutics. *Lab Chip* 9(4):545–554
96. Ozcelikkale A, Shin K, Noe-Kim V, Elzey BD, Dong Z, Zhang JT, Kim K, Kwon IC, Park K, Han B (2017) Differential response to doxorubicin in breast cancer subtypes simulated by a microfluidic tumor model. *J Control Release* 266:129–139
97. Yuan F (1998) Transvascular drug delivery in solid tumors. *Semin Radiat Oncol* 8(3):164–175
98. Goel S, Duda DG, Xu L, Munn LL, Boucher Y, Fukumura D, Jain RK (2011) Normalization of the vasculature for treatment of cancer and other diseases. *Physiol Rev* 91(3):1071–1121
99. McGuire S (2016) World cancer report 2014. Geneva, Switzerland: World Health Organization, International Agency for Research on Cancer, WHO press, 2015. *Adv Nutr* 7(2):418–419
100. Ong JP, Younossi ZM, Speer C, Olano A, Gramlich T, Boparai N (2001) Chronic hepatitis C and superimposed nonalcoholic fatty liver disease. *Liver* 21(4):266–271
101. Khazali AS, Clark AM, Wells A (2017) A pathway to personalizing therapy for metastases using liver-on-a-chip platforms. *Stem Cell Rev* 13(3):364–380
102. Patra B, Peng CC, Liao WH, Lee CH, Tung YC (2016) Drug testing and flow cytometry analysis on a large number of uniform sized tumor spheroids using a microfluidic device. *Sci Rep* 6:21061
103. Zuchowska A, Kwapiszewska K, Chudy M, Dybko A, Brzozka Z (2017) Studies of anticancer drug cytotoxicity based on long-term HepG2 spheroid culture in a microfluidic system. *Electrophoresis* 38(8):1206–1216
104. Zhang YS, Aleman J, Shin SR, Kilic T, Kim D, Mousavi Shaegh SA, Massa S, Riahi R, Chae S, Hu N et al (2017) Multisensor-integrated organs-on-chips platform for automated and continual in situ monitoring of organoid behaviors. *Proc Natl Acad Sci* 114(12):E2293–E2302
105. Pao W, Chmielecki J (2010) Rational, biologically based treatment of EGFR-mutant non-small-cell lung cancer. *Nat Rev Cancer* 10(11):760–774
106. Aref AR, Huang RY, Yu W, Chua KN, Sun W, Tu TY, Bai J, Sim WJ, Zervantonakis IK, Thiery JP et al (2013) Screening therapeutic EMT blocking agents in a three-dimensional microenvironment. *Integr Biol* 5(2):381–389
107. Hassell BA, Goyal G, Lee E, Sontheimer-Phelps A, Levy O, Chen CS, Ingber DE (2018) Human organ chip models recapitulate orthotopic lung cancer growth, therapeutic responses, and tumor dormancy in vitro. *Cell Rep* 23(12):3698
108. Yang X, Li K, Zhang X, Liu C, Guo B, Wen W, Gao X (2018) Nanofiber membrane supported lung-on-a-chip microdevice for anti-cancer drug testing. *Lab Chip* 18(3):486–495
109. Huang L, Fu L (2015) Mechanisms of resistance to EGFR tyrosine kinase inhibitors. *Acta Pharm Sin B* 5(5):390–401
110. Chabon JJ, Simmons AD, Lovejoy AF, Esfahani MS, Newman AM, Haringsma HJ, Kurtz DM, Stehr H, Scherer F, Karlovich CA et al (2016) Corrigendum: circulating tumour DNA profiling reveals heterogeneity of EGFR inhibitor resistance mechanisms in lung cancer patients. *Nat Commun* 7:13513
111. Chin LK, Lee C-H, Chen B-C (2016) Imaging live cells at high spatiotemporal resolution for lab-on-a-chip applications. *Lab Chip* 16(11):2014–2024
112. Tong Z, Balzer EM, Dallas MR, Hung W-C, Stebe KJ, Konstantopoulos K (2012) Chemotaxis of cell populations through confined spaces at single-cell resolution. *PLoS One* 7(1):e29211
113. Tam J, Cordier GA, Bálint Š, Sandoval Álvarez Á, Borbely JS, Lakadamyali M (2015) A microfluidic platform for correlative live-cell and super-resolution microscopy. *PLoS One* 9(12):e115512

114. Lakadamyali M, Babcock H, Bates M, Zhuang X, Lichtman J (2012) 3D multicolor super-resolution imaging offers improved accuracy in neuron tracing. *PLoS One* 7(1):e30826
115. Winter FR, Loidolt M, Westphal V, Butkevich AN, Gregor C, Sahl SJ, Hell SW (2017) Multicolour nanoscopy of fixed and living cells with a single STED beam and hyperspectral detection. *Sci Rep* 7:46492
116. Vicidomini G, Bianchini P, Diaspro A (2018) STED super-resolved microscopy. *Nat Methods* 15:173
117. Li D, Shao L, Chen B-C, Zhang X, Zhang M, Moses B, Milkie DE, Beach JR, Hammer JA, Pasham M et al (2015) Extended-resolution structured illumination imaging of endocytic and cytoskeletal dynamics. *Science* 349(6251):aab3500
118. Deschout H, Raemdonck K, Stremersch S, Maoddi P, Memier G, Renaud P, Jiguet S, Hendrix A, Bracke M, Van den Broecke R et al (2014) On-chip light sheet illumination enables diagnostic size and concentration measurements of membrane vesicles in biofluids. *Nanoscale* 6(3):1741–1747
119. Fleissner F, Goerzig Y, Haverich A, Thum T (2012) Microvesicles as novel biomarkers and therapeutic targets in transplantation medicine. *Am J Transplant* 12(2):289–297
120. Kieninger J, Weltin A, Flamm H, Urban GA (2018) Microsensor systems for cell metabolism – from 2D culture to organ-on-chip. *Lab Chip* 18(9):1274–1291
121. Grist SM, Schmok JC, Liu MC, Chrostowski L, Cheung KC (2015) Designing a microfluidic device with integrated ratiometric oxygen sensors for the long-term control and monitoring of chronic and cyclic hypoxia. *Sensors* 15(8):20030–20052
122. Misun PM, Rothe J, Schmid YRF, Hierlemann A, Frey O (2016) Multi-analyte biosensor interface for real-time monitoring of 3D microtissue spheroids in hanging-drop networks. *Microsyst Nanoeng* 2:16022
123. Weltin A, Slotwinski K, Kieninger J, Moser I, Jobst G, Wego M, Ehret R, Urban GA (2014) Cell culture monitoring for drug screening and cancer research: a transparent, microfluidic, multi-sensor microsystem. *Lab Chip* 14(1):138–146
124. Beer M, Kuppalu N, Stefanini M, Becker H, Schulz I, Manoli S, Schuette J, Schmees C, Casazza A, Stelzle M et al (2017) A novel microfluidic 3D platform for culturing pancreatic ductal adenocarcinoma cells: comparison with in vitro cultures and in vivo xenografts. *Sci Rep* 7(1):1325
125. Gupta V, Jafferji I, Garza M, Melnikova VO, Hasegawa DK, Pethig R, Davis DW (2012) ApoStream™, a new dielectrophoretic device for antibody independent isolation and recovery of viable cancer cells from blood. *Biomicrofluidics* 6(2):024133
126. Yang F, Yang X, Jiang H, Butler WM, Wang G (2013) Dielectrophoretic separation of prostate cancer cells. *Technol Cancer Res Treat* 12(1):61–70
127. Vaidyanathan R, Naghibosadat M, Rauf S, Korbie D, Carrascosa LG, Shiddiky MJA, Trau M (2014) Detecting exosomes specifically: a multiplexed device based on alternating current electrohydrodynamic induced nanoshearing. *Anal Chem* 86(22):11125–11132
128. Chuang C-H, Wu T-F, Chen C-H, Chang K-C, Ju J-W, Huang Y-W, Van Nhan V (2015) Lab on a chip for multiplexed immunoassays to detect bladder cancer using multifunctional dielectrophoretic manipulations. *Lab Chip* 15(14):3056–3064
129. Hoyoung Y, Kisoo K, Won Gu L (2013) Cell manipulation in microfluidics. *Biofabrication* 5(2):022001
130. Kang JH, Krause S, Tobin H, Mammoto A, Kanapathipillai M, Ingber DE (2012) A combined micromagnetic-microfluidic device for rapid capture and culture of rare circulating tumor cells. *Lab Chip* 12(12):2175–2181
131. Earhart CM, Hughes CE, Gaster RS, Ooi CC, Wilson RJ, Zhou LY, Humke EW, Xu L, Wong DJ, Willingham SB et al (2014) Isolation and mutational analysis of circulating tumor cells from lung cancer patients with magnetic sifters and biochips. *Lab Chip* 14(1):78–88
132. Hoshino K, Huang Y-Y, Lane N, Huebschman M, Uhr JW, Frenkel EP, Zhang X (2011) Microchip-based immunomagnetic detection of circulating tumor cells. *Lab Chip* 11(20):3449–3457

133. He M, Crow J, Roth M, Zeng Y, Godwin AK (2014) Integrated immunoisolation and protein analysis of circulating exosomes using microfluidic technology. *Lab Chip* 14(19):3773–3780
134. Shi J, Kantoff PW, Wooster R, Farokhzad OC (2016) Cancer nanomedicine: progress, challenges and opportunities. *Nat Rev Cancer* 17:20
135. Tong Z, Rajeev G, Guo K, Ivask A, McCormick S, Lombi E, Priest C, Voelcker NH (2018) Microfluidic cell microarray platform for high throughput analysis of particle-cell interactions. *Anal Chem* 90(7):4338–4347
136. Tong Z, Ivask A, Guo K, McCormick S, Lombi E, Priest C, Voelcker NH (2017) Crossed flow microfluidics for high throughput screening of bioactive chemical-cell interactions. *Lab Chip* 17(3):501–510
137. Grafton MMG, Wang L, Vidi P-A, Leary J, Lelievre SA (2011) Breast on-a-chip: mimicry of the channeling system of the breast for development of theranostics. *Integr Biol* 3(4):451–459
138. Chen Y, Gao D, Wang Y, Lin S, Jiang Y (2018) A novel 3D breast-cancer-on-chip platform for therapeutic evaluation of drug delivery systems. *Anal Chim Acta* 1036:97–106
139. Kwak B, Ozcelikkale A, Shin CS, Park K, Han B (2014) Simulation of complex transport of nanoparticles around a tumor using tumor-microenvironment-on-chip. *J Control Release* 194:157–167
140. Prabhakarandian B, Shen M-C, Nichols JB, Garson CJ, Mills IR, Matar MM, Fewell JG, Pant K (2015) Synthetic tumor networks for screening drug delivery systems. *J Control Release* 201:49–55
141. Albanese A, Lam AK, Sykes EA, Rocheleau JV, Chan WCW (2013) Tumour-on-a-chip provides an optical window into nanoparticle tissue transport. *Nat Commun* 4:2718
142. Perez-Toralla K, Mottet G, Guneri ET, Champ J, Bidard F-C, Pierga J-Y, Kljanienco J, Draskovic I, Malaquin L, Viovy J-L et al (2015) FISH in chips: turning microfluidic fluorescence in situ hybridization into a quantitative and clinically reliable molecular diagnosis tool. *Lab Chip* 15(3):811–822
143. Khoo BL, Warkiani ME, Tan DS-W, Bhagat AAS, Irwin D, Lau DP, Lim AST, Lim KH, Krisna SS, Lim W-T et al (2014) Clinical validation of an ultra high-throughput spiral microfluidics for the detection and enrichment of viable circulating tumor cells. *PLoS One* 9(7):e99409
144. Fu Y, Zhou H, Jia C, Jing F, Jin Q, Zhao J, Li G (2017) A microfluidic chip based on surfactant-doped polydimethylsiloxane (PDMS) in a sandwich configuration for low-cost and robust digital PCR. *Sensors Actuators B Chem* 245:414–422
145. Park SM, Wong DJ, Ooi CC, Kurtz DM, Vermesh O, Aalipour A, Suh S, Pian KL, Chabon JJ, Lee SH et al (2016) Molecular profiling of single circulating tumor cells from lung cancer patients. *Proc Natl Acad Sci U S A* 113(52):E8379–e8386
146. Zervantonakis IK, Arvanitis CD (2016) Controlled drug release and chemotherapy response in a novel acoustofluidic 3D tumor platform. *Small* 12(19):2616–2626
147. Esch EW, Bahinski A, Huh D (2015) Organs-on-chips at the frontiers of drug discovery. *Nat Rev Drug Discov* 14(4):248–260
148. Edington CD, Cirit M, Chen WLK, Clark AM, Wells A, Trumper DL, Griffith LG (2017) Integration of systems biology with organs-on-chips to humanize therapeutic development. *Proc. SPIE 10061, Microfluidics, BioMEMS, and Medical Microsystems XV*, 1006113



Design of Nanoparticles for Focused Ultrasound Drug Delivery

5

Paul Cressey, Weiqi Zhang, Mihnea Turcanu, Sandy Cochran, and Maya Thanou

Contents

1	Definition of the Topic	206
2	Overview	206
3	Introduction	206
3.1	Nanoparticles in Cancer Therapy	206
3.2	Fundamentals of Ultrasound	208
3.3	Focused Ultrasound in Tissues	210
4	Methods Used in the Development of FUS Tumor Treatments	211
4.1	High-Intensity Focused Ultrasound Systems	211
4.2	Image-Guided Focused Ultrasound	212
4.3	Cavitation Effects on Tissues	212
5	Experimental Methodology Used in Ultrasound Drug Delivery	214
5.1	Methodology for Liposome Formulation (Thin-Film Hydration)	214
5.2	Methodologies Used in the Formulation of Polymer Nanoparticles	215
5.3	Microbubble Preparation Techniques	215
5.4	Instrumental Sizing Methodology (Dynamic Light Scattering (DLS))	216
5.5	Instrumental Techniques to Determine Phase Transition Temperatures (Differential Scanning Calorimetry (DSC))	216
5.6	Instrumentation and Experimental Methodology to Carry Out Ultrasound Measurements	216
6	Nanoparticles Used in Conjunction with Ultrasound	217
6.1	Thermosensitive Liposomal Drug Carriers	217
6.2	Lysolipid-Containing Thermosensitive Liposomes	219

P. Cressey

Department of Chemistry, King's College London, London, UK

W. Zhang · M. Thanou (✉)

School of Cancer and Pharmaceutical Sciences, King's College London, London, UK

e-mail: maya.thanou@kcl.ac.uk

M. Turcanu · S. Cochran

School of Engineering, University of Glasgow, Glasgow, UK

6.3	Polymer Modified Thermosensitive Liposomes	221
6.4	Theranostic Liposomes	223
6.5	Micro- and Nano-Bubbles as Cavitation Sources	225
6.6	Polymeric Nanoparticles for Ultrasound Mediated Drug Delivery	230
7	Conclusions and Future Perspective	232
	References	232

1 Definition of the Topic

As a well-established method for clinical imaging, ultrasound can also be used as source of focused waves to selectively affect tissues by activating drug carriers and/or improving drug uptake in tumors providing a novel strategy for targeted treatment [1]. In this chapter we describe the design of nanoparticles that can respond to effects induced by focused ultrasound that can be used in cancer therapy.

2 Overview

The development of nanomaterials for therapeutic applications was first described in the 1970s. Since then, the emerged field of nanomedicine has been gaining more attention as an effective cancer treatment [2]. A more recent trend has been the development of stimuli responsive particles, many of these have been formulated to be responsive to: pH, enzymes, redox, temperature, and pressure [3, 4]. In particular, the development and application of temperature and pressure sensitive particles activated by focused ultrasound is an emerging field for nanoparticle drug delivery. Therefore, within this chapter we will give a unique focus on how to develop nanoparticles that can be used in conjunction with ultrasound for drug delivery, on the methodology used within the field to characterize the particles, and finally we will discuss the different ways ultrasound can be used to trigger drug release efficiently. We will also go over the wide range of different ultrasound activatable nanoparticles including (1) thermosensitive liposomes, (2) lysolipid containing thermosensitive liposomes, (3) polymer modified thermosensitive liposomes, (4) theragnostic liposomes, (5) microbubbles, and (6) polymer nanoparticles. The aim of this chapter is to establish a broader understanding of how ultrasound can be used for drug delivery and on the rational design of suitable nanomaterials and nanoparticles for ultrasound-mediated drug delivery in cancer therapy.

3 Introduction

3.1 Nanoparticles in Cancer Therapy

Solid tumors result from the unregulated growth of malignant cells, invading the surrounding tissues. The treatment of solid tumors in the clinic with chemotherapy or radiotherapy is challenging due to dose limiting and life limiting side effects [5]. To

Table 5.1 Examples of nanomedicines for cancer therapy which are FDA approved (a) or currently undergoing late phase clinical trials

Product	Therapeutically active component	Disease treated
^a Doxil [10]	Pegylated liposomal doxorubicin	Ovarian/breast cancer
^a Abraxane [11]	Albumin-bound paclitaxel	Pancreatic cancer
^a DaunoXome [12]	Liposomal Daunorubicin	HIV-related Kaposi sarcoma
^a Oncaspar [13]	PEGasparaginase	Acute lymphocytic leukaemia
Onco-TCS [14]	Liposomal vincristine	Non-Hodgkin lymphoma
LEP-ETU [15]	Liposomal paclitaxel	Ovarian/breast/lung cancers
Aroplatin [16]	Liposomal NDDP (cisplatin analogue)	Colorectal cancer
^a Marqibo [17]	Liposomal vincristine	Leukaemia
Lipoplatin [18]	Liposomal cisplatin	Pancreatic/breast/head and neck cancer
Paclical [9]	Paclitaxel micelles	Ovarian Cancer
^a Eligard [19]	PLGH/leuprolide polymer construct	Prostate cancer
^a Onivyde [20]	Liposomal irinotecan	Pancreatic cancer
ThermoDox [21, 22]	Thermosensitive liposomal doxorubicin	Hepatocellular carcinoma

alleviate the severity of the side effects associated with chemotherapy, researchers have encapsulated various chemotherapeutic drugs into nanoparticles [6]. By encapsulating the drugs within nanoparticles, the associated side effects are reduced and the circulation time of the drug is improved [7]. Nanomedicines have had some clinical successes with examples of both FDA-approved therapies and those undergoing clinical trials outlined in Table 5.1 [8, 9].

While all the above nanomedicines are used in the treatment of cancer in the clinic their formulation and mechanisms of action vary drastically, for example: Doxil[®] is a pegylated liposomal formulation with doxorubicin as the payload [23]. This liposome has a long blood half-life due to the incorporation of polyethylene glycol 2000 (PEG₂₀₀₀) lipids into the formulation. Doxil[®] shows an improvement over free doxorubicin, as it reduces the cardiotoxicity of free doxorubicin and increases tumor dosing [23]. The increase in uptake is due to the ability of nanoparticles (20–500 nm) to accumulate into tumors through gaps in the endothelial lining. This process is called the enhanced permeability and retention (EPR) effect [24]. Onivyde[®] is another approved pegylated liposomal formulation but contains irinotecan, which is used to treat pancreatic cancer [20]. The liposomes accumulate in the tumor passively via the EPR effect and slowly release irinotecan. Irinotecan blocks the function of topoisomerase I, causing DNA strand break leading to cell death [25]. Abraxane[®] is delivery vector with a size of 130 nm; it consists of paclitaxel bound to albumin and it is used in the treatment of breast cancer [26]. Abraxane dramatically improves the poor solubility of paclitaxel improving the amount of drug in circulation and again passively targets the tumor via the EPR effect.

Another nanoparticle that found application in oncology is Eligard[®]; however not through the above EPR effect but through the mechanism of slow release. Eligard[®] is a slow release nanomedicine formed of PLGA (poly (DL-lactide-co-Glycolide) and leuprolide acetate and is used to treat prostate cancer [19]. Eligard[®] is injected subcutaneously where it slowly releases the leuprolide acetate into the blood stream over the course of months [27]. Leuprolide acetate is a gonadotropin-releasing hormone (GnRH), which decreases testosterone and estradiol levels [28].

The above success stories for nanomedicines in the clinic show that the field has promise as a future staple in cancer therapy. However, the promise of a cure-all nanomaterial for cancer therapy is yet to materialize. This is partially due to nanoparticles' ability to get the drug to the tumor site, but the rate of drug release into the surroundings is low [29]. To address this shortfall, researchers have turned to developing nanoparticles to rapidly release the entire payload encapsulated when stimulated [3, 29]. These particles are referred to as stimuli-responsive nanoparticles. Researchers have developed particles that respond to a variety of stimuli including; pH, enzymes, light, magnetism, redox, heat, and pressure (sound) [3]. The most well-known stimuli responsive nanoparticle is ThermoDox[®]. ThermoDox[®] is a thermosensitive liposomal formulation developed by Celsion [21]. It is currently undergoing a global phase III clinical trial in combination with radiofrequency ablation against primary hepatocellular carcinoma [30].

In this chapter, we will focus on the design and applications of nanoparticles that respond to heat or pressure. Specifically, those using focused ultrasound to activate drug release from the nanoparticles (heat) and/or using focused ultrasound increasing drug uptake through difficult biological barriers (pressure) will be discussed.

3.2 Fundamentals of Ultrasound

Sound vibrations can be defined as longitudinal mechanical waves propagating through a medium. Sound waves which propagate at frequencies greater than 20 kHz are inaudible to the human ear and are termed ultrasound waves [31]. Ultrasound is produced by devices called ultrasound transducers, which convert electrical energy into mechanical energy (ultrasound waves).

Ultrasound can be used for both diagnosis (ultrasound imaging) and/or therapeutic purposes (tumor ablation and/or hyperthermia induced drug release) [32, 33]. In the diagnostic clinic, ultrasound-based technologies are widely used, as they are cheap, safe, and compact in size making them one of the few imaging techniques transportable to the patient.

In therapy, the effect of ultrasound on tissues can be modulated by changing multiple parameters, i.e., duty cycle, frequency, acoustic pressure, wave shape, and intensity.

The duty cycle is the ratio of pulse duration against pulse period. A low duty cycle can be used to maintain set temperatures in tissues, which is important for

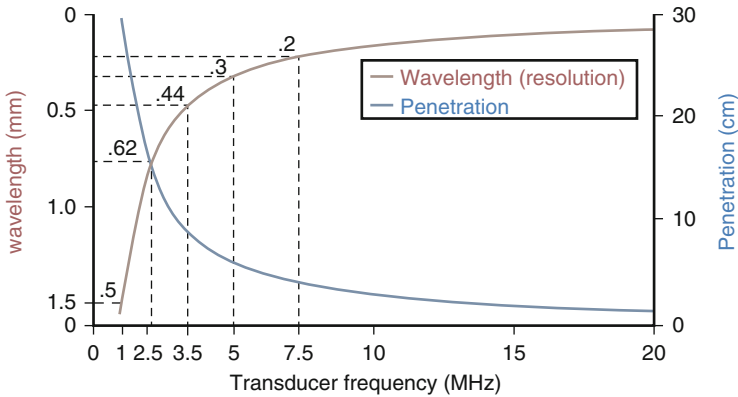


Fig. 5.1 Relationship between frequency and tissue penetration/spatial resolution. (Figure adapted from [36])

maintaining hyperthermia below ablative temperatures. Tu et al. showed that a 1.17 MHz focusing transducer at a duty cycle of 100% can rapidly increase the temperature above 70 °C, whereas at a duty cycle of 6.9% can maintain a temperature of 44 °C [34].

Frequency alters the penetration depth of the ultrasound beam. For medical application, ultrasound can be divided up into three frequency ranges: low frequency (20–200 kHz), medium frequency (0.3–3 MHz), and high frequency (>3 MHz) [31]. Low frequency ultrasound has excellent tissue penetration, but very poor spatial resolution (>10 mm). This is due to tissue penetration being inversely proportional to frequency (Fig. 5.1) [35].

High frequency ultrasound (>10 MHz) is not widely used. Although it has excellent spatial resolution (<1 mm), tissue penetration is superficial (<1 cm), limiting clinical relevance [37]. Therefore, to have reasonable tissue penetration and spatial resolution, ultrasound of around 1 MHz is used. A 1 MHz ultrasound transducer achieves tissue penetration of around 3 cm and resolution of approximately 1.5 mm [35]. The frequency also controls the likelihood and type of cavitation which will be discussed later.

When an ultrasound wave propagates through a medium, it causes a change in pressure through a series of compression and decompression events. This change in pressure is referred to as the acoustic pressure. The acoustic pressure exerted by an ultrasound wave is directly correlated to the amount of energy deposited into the target. Acoustic pressure is measured using a hydrophone. The hydrophone is used to determine the maximum (peak positive) pressure and the minimum (peak negative) pressure at the location during a full pulse [38–40]. The acoustic pressure is often in the order of MPa.

Ultrasound Intensity, also referred to as acoustic intensity, is the amount of power carried by the ultrasound wave, divided by the surface area in which it is applied. Acoustic intensity is measured in W/cm². For acoustic plane waves, ultrasound

intensity (I) is proportional to the acoustic pressure (P), and inversely proportional to the density of the media (ρ) and the propagation velocity of the wave (c) as outlined in the following equation:

$$I = \frac{P^2}{\rho c}$$

This means that as the wave penetrates tissue, the intensity of the wave decreases. This attenuated energy causes tissue heating through the transformation of scattered beams into heat [41]. One megahertz ultrasound beam is attenuated by approximately 50% after passing through 7 cm of soft tissue.

3.3 Focused Ultrasound in Tissues

A major advantage of ultrasound energy deposition is that can be used without requiring invasive surgical procedures. In therapy ultrasound transducers are often designed to focus the ultrasound waves into a small focal area. As shown in Fig. 5.2, the typical size of the focus point used is $1 \times 1 \times 9$ mm (grain of rice shaped) [42]. This focal area experiences ultrasound intensity hundreds of times higher than the surrounding tissue. This leads to selective heating at the focal point without damaging other tissues within the beam as ultrasound intensity drops exponentially away from the focus point (Fig. 5.2) [43, 44].

By focusing the ultrasound beams, tissue attenuation is decreased. However, care must be taken when focusing ultrasound waves in close proximity to bone tissue; beam attenuation through bone tissue is ~ 15 times higher than through soft tissue, leading to rapid heating of the bone tissue [46].

The confined focal area of the ultrasound is key to the design of treatments using smart nanoparticles which respond to an increase in temperature and/or to pressure changes exerted by the ultrasound waves. The increase in temperature (hyperthermia) can be used to trigger a phase transition in smart materials, thus inducing the

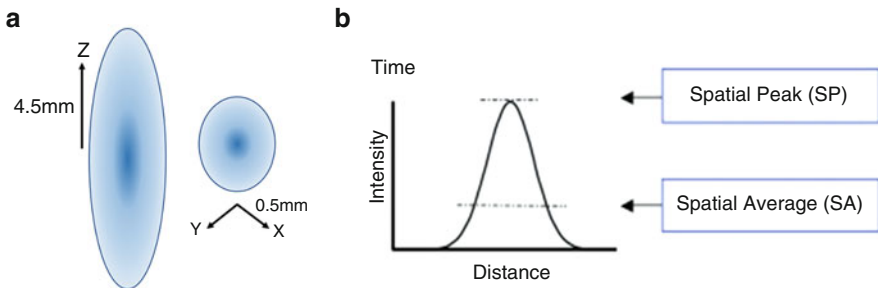


Fig. 5.2 (a) Ultrasound intensity of vertical and horizontal cross-sections of a focused ultrasound focal point. (b) Graphical representation of ultrasound intensity versus distance. (Adapted from [45])

release of a therapeutic payload only at the heated focal point. Additionally, ultrasound can be used to induce cavitation of micro/nanobubbles which can be used to increase the uptake of drugs into tumors via sonoporation.

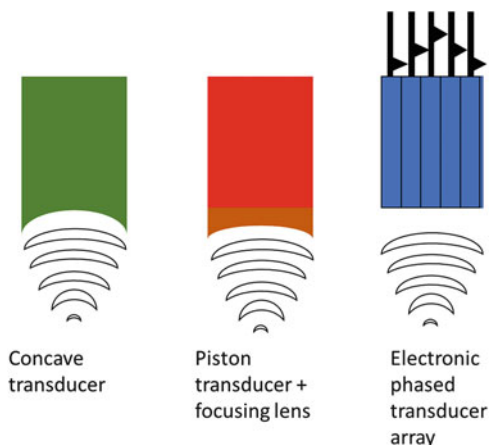
4 Methods Used in the Development of FUS Tumor Treatments

4.1 High-Intensity Focused Ultrasound Systems

High-intensity focused ultrasound is a method which enables the deposition of energy within a tumor without damaging the surrounding healthy tissue. High-intensity focused ultrasound devices used in the clinic fall into three main types: extracorporeal, transrectal, and interstitial [43]. Extracorporeal transducer systems are the most commonly used systems and are used for targeting areas readily accessible. Readily accessible areas are targets no deeper than 10 cm from the skin and which the ultrasound beam can reach without passing through obstructing media such as bone tissue or gas. This area is referred to as the acoustic window. Transrectal systems are used exclusively for prostate treatments, as extracorporeal devices will not work due to the highly attenuating properties of gas that is present in the bowel. Finally, interstitial devices are being developed for biliary duct and esophageal tumors, which are difficult to treat extracorporeally.

Focusing of ultrasound beams can be achieved through various methods. The most common is using a concave self-focusing transducer. Other ways include modifying a piston transducer with an acoustic lens or using electronically phased transducer arrays (Fig. 5.3) [47–49]. While concave transducers were the first to be used in therapy, they were required from extremely long treatment times. This is due to having to manually “scan” the entire tumor volume, which can be in the order of cm^3 , with an average focal point of only $1 \times 1 \times 9$ mm on average.

Fig. 5.3 Graphical representation of a focused concave transducer, a piston transducer using a focusing acoustic lens, and a transducer array with electronic focusing



With the development of transducer arrays, treatment time can be shortened. This is accomplished by varying the phase of the transducers. The position of the focal spot can be controlled electronically without needing to manually move the system [50]. This allows for the focal point to be rapidly scanned over the tumor. It is even possible for a phased array to have multiple foci further decreasing treatment time. Phased transducers also account for the distortions made due to the beam passing through bone or fibrous tissues; they can correct and maintain the tight focal point required for focused ultrasound treatments [51].

4.2 Image-Guided Focused Ultrasound

Recent advances in nanotechnology involve modifying drug carriers to also contain an imaging modality for the formulation of (nano-)theranostic systems. Nanotheranostic systems passively accumulate into tumors using the EPR effect, allowing for high accumulation of both the therapeutic and imaging contrast within the tumor [52]. Theranostic nanoparticles can be used in conjunction with focused ultrasound as nanoparticle uptake can be monitored using the imaging modality, and the drug release can be triggered only when uptake is sufficient. For use as an image-guided focused ultrasound delivery agent, the particle needs to have the following properties: (1) the payload is released under ultrasound irradiation, (2) the payload release can be monitored using the imaging technique, and (3) the imaging modality is clinically available. The most commonly used imaging technique for image-guided focused ultrasound is MRI or ultrasound [53]. While ultrasound imaging is cheaper, it does not allow precise monitoring of the temperature in the tumor and has poorer spatial resolution than MRI. MRI is used as it can monitor the temperature increases, via MR thermometry [54]. Being able to monitor the temperature is essential for ablation therapies [55]. This led to the development of magnetic resonance-guided focused ultrasound (MRgFUS). The technique uses MR images to generate precise anatomical images of the tumor that can then be used as a guide for the ablation treatment [56, 57]. The development of smart nanoparticles that can act as both MRI contrast agents, which help generate for better images of the tumor site, and thermosensitive drug delivery vehicles, releasing chemotherapy directly into the tumor site. These nanoparticles when used in synergy with MRgFUS could further increase its clinical efficacy.

4.3 Cavitation Effects on Tissues

The application of focused ultrasound in therapy is not limited to thermal effects; it can also be used to initiate the cavitation of gas bubbles. When gas bubbles are subjected to an ultrasound wave, they undergo rapid expansion at the peak negative pressure, followed by compression at the peak positive pressure, this causing the particles to oscillate rapidly. This phenomenon is referred to as cavitation [58].

There are two different types of cavitation: stable and inertial (Fig. 5.5). Stable cavitation occurs when the bubble grows until it reaches its resonant size, after which it oscillates around this diameter. Stable cavitation only occurs when the bubble is subjected to its resonant frequency. The resonant frequency is dependent on the size of the bubble (Fig. 5.4). To initiate stable cavitation with a 1.5 MHz transducer, the radius of the bubble needs to be approximately 2–3 μm [59].

Stable cavitation can reversibly permeabilize biological barriers, such as the blood-brain barrier and tumor cell membranes, allowing an increase in drug uptake to these areas [60]. Inertial cavitation occurs at higher peak negative pressures, leading to asymmetrical bubble oscillations and eventually, to bubble collapse (Fig. 5.5). Inertial cavitation can be used for the same application as stable cavitation. However, the effects it induces are harsher due to larger shear forces exerted by the explosive collapse.

Fig. 5.4 Microbubble resonance frequency as a function of radius. (Figure used with permission from [59])

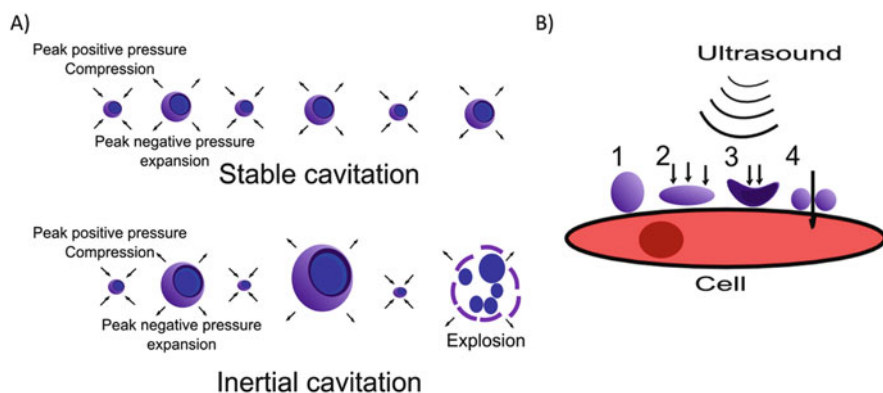
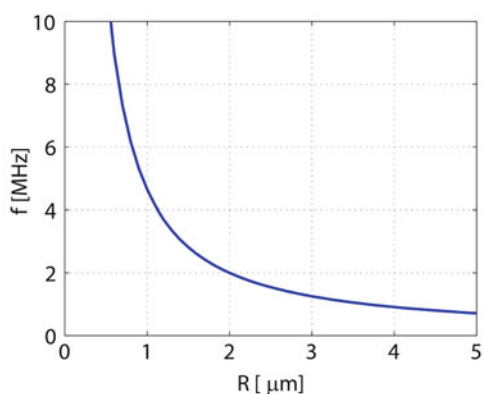


Fig. 5.5 (a) The effect of ultrasound on bubble cavitation: (top) stable cavitation, (bottom) inertial cavitation. (b) Inertial cavitation creates an asymmetric microjet directed only towards the cell. (Adapted from [61])

5 Experimental Methodology Used in Ultrasound Drug Delivery

5.1 Methodology for Liposome Formulation (Thin-Film Hydration)

A common and simple technique for the preparation of liposomes is the thin-film hydration method. This method involves mixing the lipids dissolved in organic solvents (chloroform and/or methanol) at the required mol% before removing the organic solvents (under steady stream of $N_{2(g)}$ or in vacuo) forming a thin lipid film. The second step is to hydrate the film in an aqueous medium followed by multiple freeze-thaw cycles to break up the lipid film forming a suspension. To form liposomes from the resulting suspension, two methods are employed; sonication to reduce the particles to roughly the right size followed by extrusion through a polycarbonate membrane of the correct size, or by using only extrusion but multiple cycles using progressively smaller membranes each time until the correct size is achieved (Fig. 5.6) [62–64].

However, the thin-film hydration method has one drawback in that the lipids will be distributed across both sides of the membrane. This can be addressed by using an additional formulation method called the “post-insertion method”; this is used to add lipids only into the outer layer of the membrane post formulation. The post-insertion method has been used in the literature to add targeting functionality to preformed-drug loaded liposomes [65]. The loading of drug molecules into liposomes has been performed mainly by two overarching methods: passive loading (during formulation) or active loading (post formulation). Passive loading is used extensively with hydrophobic drugs (i.e., amphotericin B taxol, annamycin, etc.) with encapsulation efficiencies approaching 100%. Alternatively, passive loading can also be used for highly water-soluble drugs which can encapsulate up to 30% of the dissolved drug. This type of passive loading is highly dependent on liposome concentration and size [64]. Active loading is performed on water-soluble drugs that have protonatable functionalities and can be encapsulated using a pH gradient. The pH gradient causes precipitation of the drug within the liposome, thus greatly increasing the encapsulation efficiency which can approach 100% [66].

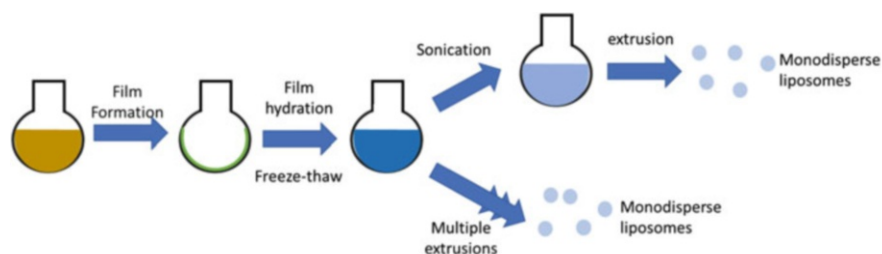


Fig. 5.6 Graphical representation of the steps involved in the thin-film hydration method for liposome formulation

5.2 Methodologies Used in the Formulation of Polymer Nanoparticles

To formulate drug loaded polymer micelles, there are five widely used methods used in the literature [67, 68]. The most extensively used method is using dialysis. In this technique, the block copolymer and the drug are dissolved in a common water miscible organic solvent (DMF/DMSO) followed by dialysis against water. The slow replacement of the organic solvent with the water through the semipermeable membrane triggers the self-assembly of the hydrophobic polymer blocks, which results in the encapsulation of the drug [67]. The second method is termed the oil-in-water emulsion method and entails dissolving the block copolymer and the drug into either water or a volatile water immiscible organic solvent (chloroform/DCM). The organic phase is then added slowly to the water phase under vigorous stirring and the organic solvent is removed by evaporation, resulting in drug loaded micelle formation [69]. The third method called the solvent evaporation method is very similar to the thin film method used to make liposomes. The polymer and drug are dissolved into a volatile organic solvent; the solvent is then removed to form a film of polymer impregnated with the drug. The aqueous phase is then added to the film and the polymer micelles are formed by vigorously shaking the solution [70]. The co-solvent evaporation method is almost identical to the oil-to-water method, except in this case the polymer and drug are dissolved into a water miscible organic solvent and mixed with the aqueous phase. The organic solvent is then evaporated from the solution forming the drug-loaded polymer micelles [71]. The final method employed in making drug loaded polymer micelles is referred to as the freeze dry method. In this method, the polymer and drug are dissolved into a freeze-dryable organic solvent, for example, tert-butanol. The organic solvent and water are mixed, freeze-dried, and reconstituted in water forming the polymer micelles [72]. Typical loading efficacies of these techniques is up to 20%; however, the choice of loading method is highly dependent on the polymer and drug molecule used [67].

5.3 Microbubble Preparation Techniques

Microbubbles are clinically used as ultrasound contrast agents because of this most research is carried out using the commercially available formulations. The first commercially available and FDA approved microbubble formulation was Albunex[®], a albumin shelled microbubble formulation with sizes ranging between 1 and 15 μm [73]. More recently, lipid-coated microbubbles formulations have also become commercially available with the most common being SonoVue[®] and Definity[®] [73]. These formulations are made by hydrating lyophilized lipids and stabilizing agents under an atmosphere of sulfur hexafluoride (SonoVue[®]) or octafluoropropane (Definity[®]). For more information on the formulation of microbubbles, please refer to an excellent review by Stride and Edirisinghe [74]. Nanobubbles on the other hand are not commercially available and have to be formulated in the lab. This is accomplished by first formulating liposomes (using

the thin-film method), followed by replacing the headspace with an ultrasound contrast gas (perfluorocarbon or sulphur hexafluoride) followed by rapid shaking to encapsulate the gas within the liposomes [75].

5.4 Instrumental Sizing Methodology (Dynamic Light Scattering (DLS))

Dynamic light scattering (DLS), also known as quasi-elastic light scattering (QELS) or photon correlation spectroscopy (PCS), is a nondestructive method routinely used to determine the hydrodynamic size of nano/micron-sized particles in solution [76]. DLS works by measuring the scattering intensity of nanoparticles in Brownian motion when irradiated by a monochromatic beam of light. As the scattering fluctuates on a micro-second timescale, the fluctuations are measured using an autocorrelation function and fitted to an exponential. The decay of the correlation function is used to determine the rate of diffusion. By using the standard assumptions of spherical size, known viscosity of the suspending medium, low concentration as well as the measured diffusion, it is used to calculate the particle size. While DLS has gained popularity due to rapid analysis and minimal calibration requirements, it is faced with some shortcomings including: degradation of signal-to-noise at low concentrations or inter-particle interaction at high concentrations [77]. This method is used in both academia and industry to measure the size of particles. It is also used to determine both long- and short-term stability of nanoparticles with instability being correlated to changes in the hydrodynamic radius of the particles. This makes DLS one of the most useful techniques for measuring both particles sizes and stability.

5.5 Instrumental Techniques to Determine Phase Transition Temperatures (Differential Scanning Calorimetry (DSC))

Differential scanning calorimetry (DSC), a well-known versatile technique in nano-particle research, can be used to determine: the glass transition of polymers, the phase transition of liposomes, as well as the effect that loaded drugs have on the transition temperatures [78]. This technique is invaluable in the development of thermal responsive liposomes and thermally responsive polymer systems due to being able to quickly and efficiently determine transition temperature of nanoparticles, which is crucial for drug release under focused ultrasound-induced hyperthermia.

5.6 Instrumentation and Experimental Methodology to Carry Out Ultrasound Measurements

Ultrasound transducer characterization involves output acoustic power and pressure measurements. Acoustic power measurements enable assessment of the ability of a

transducer to affect the behavior of contrast agents. A useful instrument in this regard is a radiation force balance which quantifies the displacement of a balance from an equilibrium position caused by energy incident in an US wave. This displacement is directly correlated to radiation power readout. Additionally, acoustic pressure measurements or pressure mapping show the spatial distribution of the US field. This requires a hydrophone, amplifier, and data acquisition instrument for recording pressure values at different locations in the field [79].

The instrumentation required to conduct US measurements includes a signal generator for producing repeating electronic signals and a power amplifier, in case the power input requirements are not met by the signal generator. When transducers are used to monitor US activity in a system, a preamplifier and oscilloscope enables the readout of the voltage. Different therapeutic ultrasound applications require different system configurations. Ultrasound can be delivered extra- or intracorporeally. Extracorporeal applications require transducer-skin coupling typically with US coupling gel [80]. A stereotactic frame is sometimes necessary to ensure subject immobility throughout the procedure. An intracorporeal transducer, integrated into an ingestible capsule or a catheter, can be placed in close proximity to a target zone, but satisfactory US operation can sometimes require sophisticated approaches, potentially including robotics [81].

Treatment monitoring often requires the procedure to be conducted in an MRI scanner; this requires highly specialized US transducers [82]. Further options may include near infrared fluorescence imaging, microultrasound, or quantitative ultrasound imaging [81, 83].

6 Nanoparticles Used in Conjunction with Ultrasound

Nanomaterials used in ultrasound drug delivery include: liposomes, micro/nano-bubbles, and polymers. In this section, we will discuss the utilization of these nanomaterials for ultrasound-mediated drug delivery.

6.1 Thermosensitive Liposomal Drug Carriers

When designing a thermosensitive formulation using the correct lipid composition is important? Thermosensitive liposomes have to undergo a gel to liquid crystalline phase transition (T_m) around 39–42 °C (mild hyperthermia) [84, 85]. Below the T_m , the bilayer is in the gel phase. In the gel phase, the bilayer is impermeable as the hydrocarbon chains are fully extended and the head group is anchored in one place (Fig. 5.7). Above the T_m , the bilayer transitions into the liquid-crystalline phase. In the liquid crystalline phase, the head group becomes more mobile and the hydrocarbon chains lose their rigidity permeating the bilayer (Fig. 5.7) [86].

The T_m of liposomes is primarily influenced by the base lipids. The base lipids used in thermosensitive formulations are: 1,2-dipalmitoyl-sn-glycero-3-phosphocholine (DPPC, T_m 41 °C), 1,2-distearoyl-sn-glycero-3-phosphocholine (DSPC, T_m 55 °C),

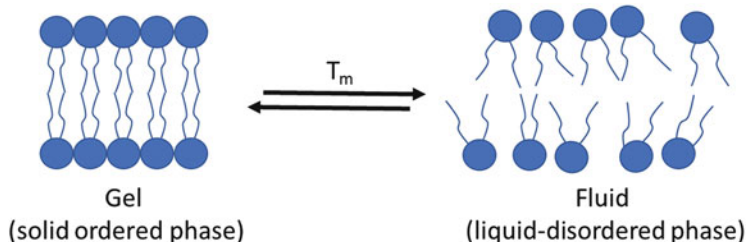


Fig. 5.7 Bilayer packing before and after the temperature dependent phase transition of the membrane. The change from gel phase to liquid phase is associated with drug release

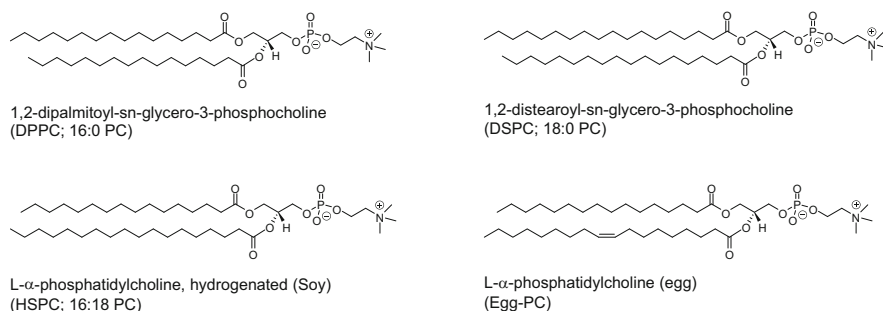


Fig. 5.8 Chemical structures of commonly used base lipids: DPPC, DSPC, HSPC, Egg-PC

hydrogenated soy L- α - phosphatidylcholine (HSPC, T_m 52 °C), or Egg L- α -phosphatidylcholine (Egg-PC, T_m -5 °C to -15 °C) (Fig. 5.8) [87]. HSPC and Egg-PC are not commonly used as they are lipid extractions from natural sources (soy beans/egg yolks). They are mixtures of lipids making reproducibility between batches difficult. For this reason, synthetic phospholipids such as DPPC and DSPC are more commonly used.

The effect of lipid mol% in the formulation was reported in one of the first thermosensitive liposome publications by Yatvin et al. The liposomes used in this study were based on mixtures of DPPC/DPSC encapsulating carboxyfluorescein (CF) and the rate of release was monitored. The rate of release was shown to be at a maximum at 38 °C for the liposomes of just DPPC, whereas liposomes of DPPC/DSPC (3:1) the release rate peaked at 43.5 °C [88]. The addition of DSPC while increasing the T_m also increased the permeability of the bilayer due to the formation of grain boundaries. Grain boundaries are caused by inhomogeneous packing in the bilayer [89]. The major limitation to the application of the original liposomes was a short in vivo lifetime, due to uptake by the reticuloendothelial system and premature release of the payload [90].

One method to increase the stability of thermosensitive liposomes in vitro and in vivo is to incorporate cholesterol into the formulation. Cholesterol rich membranes have been shown to be less sensitive to opsonization, the process responsible for nanoparticle clearance [91]. Cholesterol is a naturally occurring steroid used to

stabilize membranes towards a liquid-ordered phase [92]. Therefore, by tuning the amount of cholesterol in the formulation, the T_m of the liposome can be tuned, which in turn determines release properties [93, 94]. Merlin and co-workers reported a number of DPPC/DSPC/Chol liposomes with varying cholesterol content. Liposomes containing 18% cholesterol showed an increase in stability compared to DPPC/DPSC at 37 °C limiting unwanted drug release, while retaining drug release at 43 °C. Increasing the mol% of cholesterol above 20% caused the membrane to become liquid-ordered and lose the desired thermal transition properties [95]. This study showed that cholesterol plays an important role in stabilizing membranes, but the amount incorporated needs to be tightly controlled to maintain thermally triggered drug-release properties.

The *in vivo* lifetime (plasma half-life) can also be increased by incorporating PEGylated lipids into the formulation [96]. The stabilizing effect of PEG lipids was studied by Kenworthy et al. who used different DPSE-PEG lipids with varying molecular weight PEG chains (350/750/200/500) and the required mol% in the formulation to protect against opsonization. In this study 5% DSPE-PEG₂₀₀₀ was found to adequately cover the bilayer [97]. The addition of 4% DPSE-PEG₂₀₀₀ was shown by Needham et al. to have little effect on the T_m of the liposome formulation with shift of ~1 °C [98]. However, any further increase in the concentration of the PEG lipid had opposite effects and caused destabilization of the bilayer [99].

Traditional thermosensitive liposomes incorporate both the stabilizing effects of cholesterol and PEG surface modifications. However, this type of liposome has relatively high T_m 's around 42–45 °C and full drug release requires over 30 min. This can lead to extensive tissue damage in the clinical setting when applying temperatures close to that required to initiate coagulative necrosis [100, 101].

6.2 Lysolipid-Containing Thermosensitive Liposomes

While traditional liposomes released their payload under hyperthermia, the rate of release was slow and relatively high hyperthermic temperatures were needed to initiate the release. To address this, Dewhirst and Needham pioneered a new field by incorporating lysolipids into PEGylated thermosensitive liposomes [102, 103]. The first lysolipids incorporated by Needham were 1-palmitoyl-2-hydroxy-sn-glycero-3-phosphocholine (MPPC) and 1-stearoyl-2-hydroxy-sn-glycero-3-phosphocholine (MSPC) (Fig. 5.10). They showed that incorporating lysolipid into the formulation dramatically increased the release rate of encapsulated doxorubicin at the gel-liquid phase transition temperature (Fig. 5.9).

At 15% MPPC, the liposomes released their payload within 20 s when heated to 43 °C. This increase in release rate was explained by stabilization of the grain boundaries in the liposome membrane. Grain boundaries are defects in the crystalline packing of the membrane. When heated to the liquid phase, the lysolipids stabilize grain boundary structures. This leads to pore formation within the membrane facilitating drug release (Fig. 5.10). DSPE-PEG lipids also help in the stabilization of the membrane pores [98, 105].

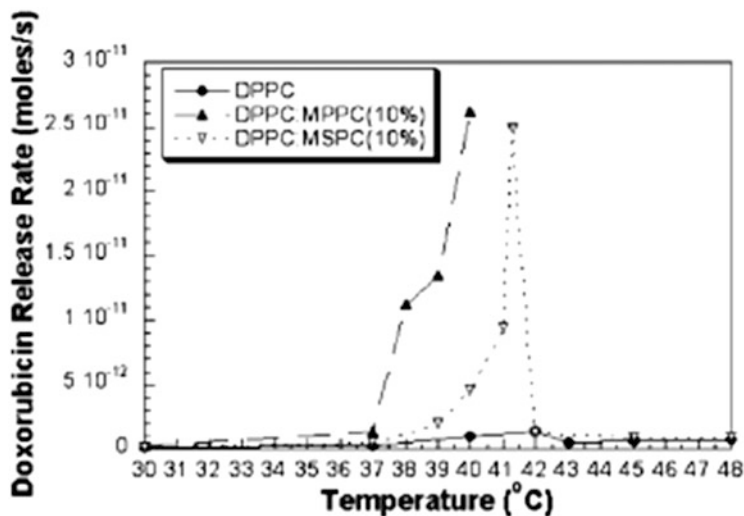


Fig. 5.9 Doxorubicin release rates (Mol/s) for DPPC: DSPE.PEG₂₀₀₀ (96:4), DPPC: DSPE.PEG₂₀₀₀:MPPC (86:4:10), and DPPC: DSPE.PEG₂₀₀₀:MSPC (86:4:10) against temperature (°C). (Figure used with permission from [104])

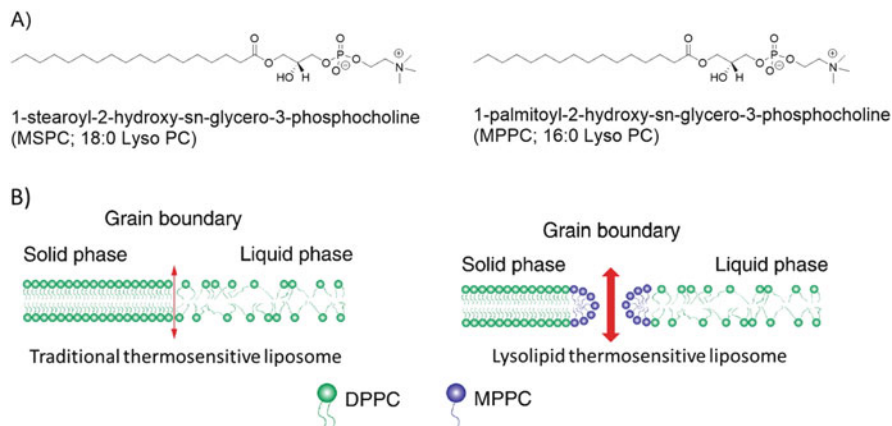


Fig. 5.10 (a) Chemical structures of common lysolipids (left) MSPC, (right) MPPC. (b) Proposed mechanism of grain boundary formation in traditional liposomes (left) and grain boundary pore stabilization by lysolipid containing liposomes (right). (Adapted from [106])

The membranes of lysolipid containing liposomes are less stable than traditional liposome formulation; this instability leads to greatly enhanced release rates for doxorubicin [104]. The Needham group took this formulation further by reducing the release temperature from 43 °C down to between 40 °C and 42 °C, this was done to reduce hyperthermia-related side effects [102, 107]. The formulation was

comprised of DPPC, MPPC, and DSPE.PEG₂₀₀₀ in the following ratio 90:10:4. Celsion took these observations and used them to develop ThermoDox[®] which is comprised of DPPC (86.5 mol%), MSPC (9.7 mol%), and DSPE.PEG₂₀₀₀ (3.8 mol %). ThermoDox[®] coupled with radiofrequency ablation (RFA) is currently undergoing phase III clinical trials against hepatocellular carcinoma [108]. The phase I trials indicated that doses of 50 mg/m² were tolerated and results of Phase III indicated an improvement of overall survival for a group treated with RFA of >45 min.

However, the plasma *half-life* of lysolipid formulations is inherently less stable than traditional liposomes, due to the dissociation of the lysolipid from the membrane. Banno et al. reported that around 70% of the lysolipids are lost from the formulation after 1 h post injection [109]. This was hypothesized to be due to dilution of the liposomes and interactions of the liposome with other lipid membranes in vivo causes the lysolipid to leach from the membrane [109, 110]. An alternative lysolipid formulation was developed by Tagami et al. who incorporated both the lysolipid and the PEG chain into a single moiety by using Brij surfactants [111]. Brij surfactants are commercially available PEGylated surfactants. This study compared surfactants with C16 and C18 carbon chains and varying PEG lengths. Brij78 at 4 mol% was found to be the optimal lipid conditions for thermosensitive properties with a transition temperature of 41 °C and doxorubicin loading of 95%. The Brij78-containing liposomes released doxorubicin faster than ThermoDox-like liposomes (DPPC: MPSC: DSPE.PEG₂₀₀₀ (86:10:4)) with 100% release within 2 min at 40 °C. Interestingly, the sharper release at 40 °C did not affect the stability of the formulation at 37 °C in serum with 10–20% release over 30 min. Tagami et al. went on to test their optimized formulation which comprised of DPPC and Brij78 (96:4) in vivo in mice bearing mammary carcinoma tumors (EMT-6). The in vivo studies resulted in a 1.4-fold increase in doxorubicin uptake into the heated tumor over ThermoDox-like liposomes and a 5.2-fold increase over free doxorubicin. The concentration of doxorubicin found within the heart was also reduced by a factor of 15 when compared to the free drug. ¹H-NMR experiments showed that incubation of the Brij78-containing liposomes with other vesicles caused leaching of the Brij78 from the membrane; this extraction could cause significant loss in the in vivo stability of the particles due to loss of the PEG coating [112].

While we can design formulations with excellent drug-release profiles, improvement over the base lipids is required to develop the next generation. This is due to then present modifications increasing the drug release but simultaneously decreasing the stability of the particles at physiological temperatures, usually resulting in short blood clearance times.

6.3 Polymer Modified Thermosensitive Liposomes

Another method to increase the release rate of the drugs from traditional thermosensitive liposomes is to include synthetic polymers that disrupt the membrane upon heating [106]. There are two main types of thermoresponsive polymers; low critical

solution temperature (LCST) and upper critical solution temperature (UCST). LCST and UCST are polymers with critical temperature points below (LCST) or above (UCST) in which they are completely miscible with the solvent [113]. For a polymer solution below its LCST, the polymer and solvent are miscible; however, upon heating, the polymer becomes insoluble. This transition is referred to as coil-to-globule transition and is entropically driven (Fig. 5.11) [106]. Polymers incorporated into liposome formulations are predominantly LCST, the most common being poly(*N*-isopropylacrylamide) (poly(NIPAM)) [114–116].

This field was pioneered by Kono and co-workers who used coupled poly-NIPAM which has a LCST of 32 °C with octadecyl acrylate to anchor the polymer into the bilayer [118]. The incorporation of the copolymer into liposomes of DPPC or egg-PC resulted in an improvement in calcein or carboxyfluorescein release at 41 °C [118, 119]. However, significant drug release was also observed in these systems around the LCST temperatures, compounding the evidence that it was the polymer destabilizing the membrane. This issue was later solved by Kono et al. by incorporating an additional polymer unit with a higher LCST, for example, acryloyl-pyrrolidine which has a LCST of 52 °C [119]. This modification to the polymer lead to a polymer construct with a LCST of 40 °C, increasing the stability of the liposomes. Ta et al. incorporated poly(*N*-isopropylacrylamide-co-propylacrylic acid) copolymer into the membrane of doxorubicin-loaded liposomes [117]. This formulation was both responsive to pH and temperature; the particles released 60% of the payload within 1 min after heating at 42 °C at pH 5 in vitro. In vivo studies were carried out on Fischer rats bearing rat adenocarcinoma (13,762 MAT B III) tumors. Hyperthermia was produced using a FUS, 1.15-MHz 8 element transducer, with an average tumor temperature of 42.9 ± 0.9 °C. The in vivo results suggested that the dual responsive system releases a greater quantity of drug into the tumors compared to conventional thermosensitive liposomes. This increase in tumor drug concentration could be due to synergistic activation of the formulation in the acidic tumor microenvironment; however, this was not confirmed [117]. One major issue with this system is the lack of biodegradability of the copolymer incorporated into

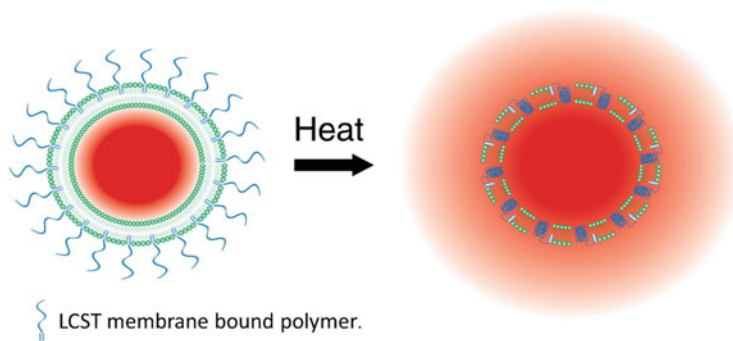


Fig. 5.11 LCST phase transition of a polymer modified liposome. (Figure reused with permission from [117])

the liposomes, which could be problematic if the polymer dissociates from the formulation *in vivo*. Park et al. took this idea forward by substituting the polymer with a fatty acid conjugated biodegradable elastin like polypeptide (ELP) in a liposomal formulation of DPPC, DSPE-PEG₂₀₀₀, cholesterol, and ELP (55:2:15:0.4125) [120]. ELP acts as a LCST polymer in which below the transition temperature, it is water soluble, when the temperature increases the peptide aggregates into the membrane causing membrane instability [121, 122]. Incorporation of ELP increased the stability of the formulation in serum with less than 20% doxorubicin leakage over 30 min, while a lysolipid-containing formulation displayed over 50% drug release under the same conditions. This observation was mirrored *in vivo* with the particle having a higher circulation time with 41% of the injected dose of doxorubicin still in circulation after 5 h, compared to 14% for the lysolipid-containing formulation. This increase in circulation time leads to an increase in therapeutic efficacy in a murine squamous cell carcinoma model.

To conclude, polymer-modified thermosensitive liposomes have promise as ultrasound activatable nanoparticles, with tunable release properties using copolymerization methods with a wide variety of monomers. However, the particles show broad release profiles and the synthesis of the polymers are not controlled well due to the use of radical polymerization methods. Newer living polymerization techniques could help solve these issues with *in vivo* and *in vitro* studies still being carried out.

6.4 Theranostic Liposomes

Multifunctional nanomedicines have been developed over the past 15 years, which preferentially accumulate in tumors. These particles have been designed to both treat and image the tumor simultaneously. These nanoparticles are referred to as nano-theranostics [123–125]. Nano-theranostic technologies can be engineered to selectively bind to biomarkers on specific cells or lesions, potentially allowing for the development of personalized medicines. The increase in tumor uptake due to the EPR effect, along with the imaging modality of nano-theranostic particles can allow for detection and treatment of metastases [126]. The ability to treat and visualize metastases could offer significant advantages to nano-theranostic treatments, as metastases are the leading cause of cancer-related death [127–129].

Originally imaged-guided systems were developed to aid in ablation therapies. Initial studies were carried out using ultrasound-guided focused ultrasound platforms [130]. However, this technique provided limited anatomical detail and no information on the tumor temperature during ablation [131]. Therefore, a major shift towards the development of MRI-guided systems was observed. MRI-guided systems are superior in the anatomical detail acquired and allow monitoring of the tumor temperature during ablation [132, 133].

Initial studies were carried out on liposomes co-encapsulating gadolinium-based contrast agents alongside the drug payload. De Smet and co-workers used two thermosensitive liposomes loaded with both doxorubicin and ProHance[®] (FDA approved small molecule MRI contrast agent ([Gd].HP.DO3A)). The formulations

investigated in this study were, one traditional temperature sensitive liposome (TTSL; DPPC: HSPC: Cholesterol:DPPE.PEG₂₀₀₀; 50:25:15:3) and a low temperature sensitive liposome (LTSL; DPPC:MPPC:DPPE-PEG₂₀₀₀; 86:10:4). The stability and release profiles at 37 °C and 42 °C were determined using phantoms. The low temperature sensitive liposome formulation displayed a faster release at 42 °C and a higher leakage of doxorubicin at 37 °C when compared to the traditional thermosensitive formulation [134]. Due to the increased stability of the traditional thermosensitive formulation, the authors took this formulation into *in vivo* studies in rats bearing 9 L gliosarcoma tumors. An MRI-guided focused ultrasound system was used to induce hyperthermia within the tumor burden for 30 min. During the treatment, the local release of ProHance was monitored using T₁ mapping of the tumor. A good relationship between the increase in T₁ relaxation and intratumor doxorubicin concentration was found, indicating that release of encapsulated drug can be monitored *in situ* via T₁ relaxation changes of the co-encapsulated MRI contrast agent [135]. This change in T₁ relaxation agrees with the previous reports that have shown that encapsulation of gadolinium contrast agents reduce relaxivity due to water exchange between the bulk water and the encapsulated contrast agent is retarded by the bilayer [136]. Rizzitelli et al. carried out a similar study using Doxil-like liposomes (DPPC:DSPC:Chol:DSPE.PEG200- (10:5:4:1)) again loaded with doxorubicin and ProHance. Within this study, sequential application of low-intensity pulsed ultrasound was used to release the drug and MRI contrast agent from the liposome while also increasing tumor uptake via a sonoporation mechanism. This proposed mechanism was tested *in vivo* on BALB/c mice bearing mammary adenocarcinoma tumors. The release of the payload was tracked by T₁ relaxivity enhancement with clear correlations between ultrasound application and overall doxorubicin uptake. In this study, however, the combination of the liposomes and the pulsed ultrasound caused complete regression of the tumor burden after 20 days [137]. Other drugs have also been co-encapsulated with MRI contrast agents. Affram and co-workers encapsulated gemcitabine alongside Magnevist[®] for the treatment of pancreatic cancer. Within this study, mice bearing pancreatic carcinoma (MiaPaCa-2) were used. The encapsulation of gemcitabine reduced the blood clearance by a factor of 17, while also reducing the effective dose amount by half compared to free gemcitabine. However, within this study, no significant increase in relaxivity was observed, in *ex-vivo* tumor images. While this formulation shows promise for pancreatic treatment, the MRI contrast of the particle will need further optimization before this can be realized [138].

The research carried out in our group is aimed at developing multimodal thermosensitive theranostic liposomes. These thermosensitive liposomes incorporate (MRI contrast and near-infrared fluorophore) labelled lipids directly into the bilayer to allow imaging of tumor uptake, while also releasing a therapeutic payload upon mild hyperthermia. We prepared topotecan-loaded liposomes, incorporating a near infrared fluorophore lipid conjugate (XL750) which was detectable by near infrared fluorescence (NIR; 750–950 nm). The topotecan-loaded liposomes were administered into SHO mice bearing ovarian adenocarcinoma tumors (IGROV-1). The near infrared label allowed real time monitoring of the particle biodistribution. Drug

release was measured by the fluorescent microscopy measuring the intrinsic fluorescent properties of topotecan. An increase in topotecan uptake was measured in the tumors subjected to hyperthermia (42 °C). Hyperthermia was induced using a heating block [139]. This trial study provided a proof of principle for real-time biodistribution tracking of nanoparticle anticancer therapies using near infrared imaging. After the successful trial study, the formulation was taken forward into additional investigations this time using high-intensity focused ultrasound to induce localized hyperthermia. A dual tumor mouse model using SHO mice with IGROV-1 tumors was used in the study. A dual tumor model was used to determine the effect of ultrasound on nanoparticle uptake within the same animal. High-intensity focused ultrasound application of 3 min at 42 °C 30 min post *i.v* injection greatly enhanced the uptake of the liposomes into the heated tumors. The high-intensity focused ultrasound induced increase in liposome uptake amplified by adding a second treatment of 5 min at 42 °C, 90 min post injection (Fig. 5.12). Hyperthermia temperatures were maintained and monitored using subcutaneously implanted fine-wire thermocouples. Accumulation was determined by near infrared fluorescence and hyperthermia-triggered drug release was detected by an enhancement in topotecan fluorescence emission [83].

Both studies show the benefits of tracking the biodistribution and drug release *in vivo* can lead to stark changes in relative tumor uptake of nanoparticles.

Another facet of our work is the incorporation of MRI labels into liposomal nanoparticles. This can be done by incorporating a DOTA (1,4,7,10-tetraazacyclododecane-1,4,7,10-tetraacetic acid) headgroup onto a lipid tail [140]. By adding MRI contrast into the bilayer, this allows for clear monitoring of the particles pharmacokinetics, especially particle accumulation into tumors. Additional benefits for MRI visibility are the use of clinically available magnetic resonance-guided focus ultrasound platforms, as well as direct monitoring of hyperthermia in real time via thermometry [141, 142].

Overall theranostic and/or stimuli responsive nanoparticles are becoming increasingly more valuable tools for targeted drug release to specific tissues. The clinical efficacy of theranostic particles will be shown in the near future, but they are an important step into the realms of personalized medicine.

6.5 Micro- and Nano-Bubbles as Cavitation Sources

Ultrasound can also be used to increase the uptake of molecules or other particles using cavitation. Blood is a degassed liquid, meaning that cavitation will not occur unless it is subjected to very high-pressure ultrasound. A way around this is to use cavitation nuclei which reduce the pressure threshold required to initiate cavitation. Cavitation nuclei can be formed from nanoparticles encapsulating a heavy gas core. Gases commonly used are fluorinated, i.e., octafluoropropane, decafluorobutane, and sulfur hexafluoride. These gases are used because they are biocompatible and inert, making them applicable for *in vivo* applications [143]. Microbubbles can be either lipid or polymer particles loaded with a heavy gas with sizes varying between 1 and

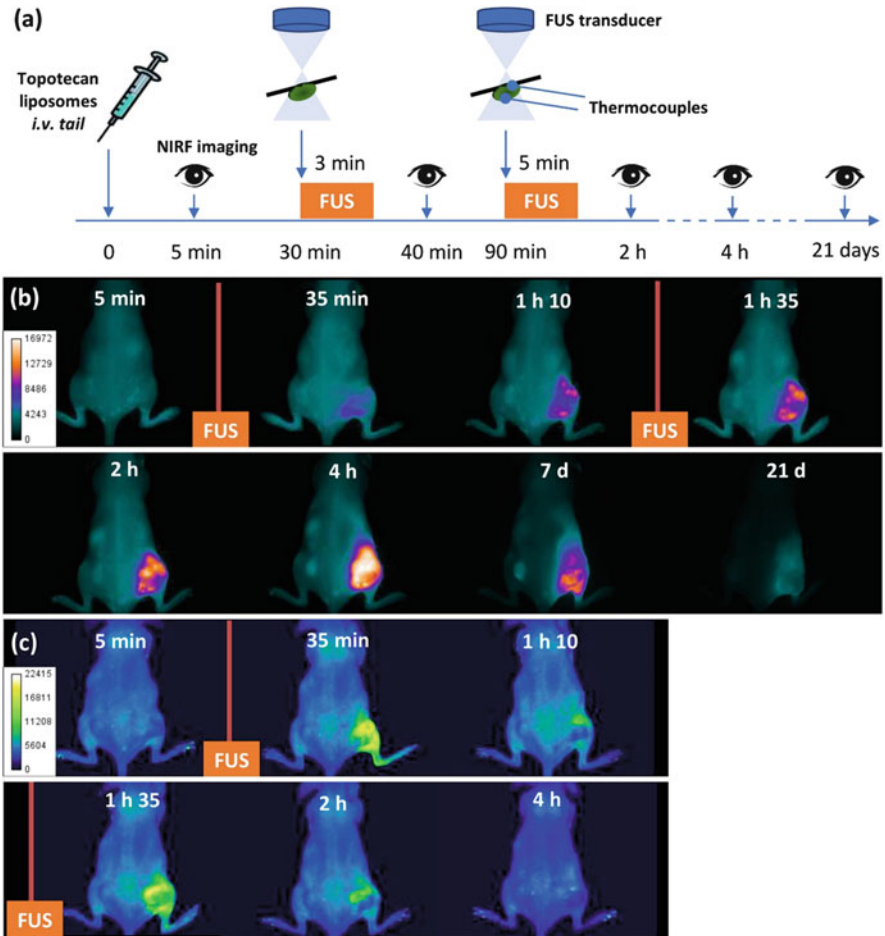


Fig. 5.12 (a) Schematic of hyperthermia treatment regime. (b) Near infrared fluorescence images of tumor uptake after treatment. (c) Intrinsic topotecan fluorescence images indicating drug release from the liposomes. (Figure reused with permission from [83])

10 μm . Nanobubbles have the same general structure as microbubbles but are $<1 \mu\text{m}$ in size. Lipid-based bubbles are referred to as soft shelled and allow the encapsulated gases to oscillate at low pressures. Polymer systems, on the other hand, are hard shelled and the gas can only oscillate after destruction of the particle.

Microbubbles can be used to enhance drug delivery through multiple mechanisms. They can initiate endocytosis, transcytosis, create pores in cell membranes (sonoporation), and permeabilize cell to cell junctions. All these mechanisms are believed to be primarily the result of inertial cavitation events causing damage to cell membranes. The likelihood of cavitation events depends on the magnitude of energy delivered and is calculated using the Mechanical Index (MI) formula. The MI is the unitless ratio between the beam's peak negative pressure and the square root of the

frequency. Intracellular delivery of propidium iodide to epithelial cells has been successfully achieved at an MI between 0.2 and 0.4 [144].

To observe microbubble and cell membrane interactions, an elegant study was carried out by Nico and co-workers using high speed photography and fluorescent microscopy. The microbubbles were subjected to ultrasound at 1 MHz with a 0.4 MPa peak negative pressure. The oscillating microbubbles were visualized using an ultrafast transmission microscope pushing and pulling on the membrane exerting mechanical stress. This stress leads to rapid membrane deformation and perforation after 5 s [145]. Kudo et al. measured the uptake of the membrane impermeable fluorophore propidium iodide. The uptake of propidium iodide was synchronous with the inertial cavitation and subsequent microjet formation following a 3 μ s burst with a 1.1 MPa peak negative pressure. Interestingly, sonoporation caused large micron-sized holes within the membranes. In some cells, fluorescent signals were measured but no obvious pores were observable. This suggested that the membranes re-seal rapidly after sonoporation [146]. Mehier-Humbert and co-workers conducted a study to determine the size of the membrane pores formed during stable cavitation. This *in vitro* work employed phospholipid lipid-based microbubbles encapsulating perfluorocarbon as the cavitation nuclei against MAT B III cells. The cells were exposed to 402 kPa peak negative pressure for 10 s using a 1.15 MHz transducer. The pores formed were approximately 100 nm in size and allowed the delivery of FITC modified dextran (Fig. 5.13) [147]. These studies show that sonoporation is an effective way to permeate cell membranes; this was taken forward as a method for increasing drug delivery to selective areas [147–150].

As previously mentioned microbubbles can be used to permeabilize cell junctions, one cell junction in the body that is exceptionally difficult to bypass is the blood-brain barrier (BBB) [151, 152]. Mesiwala and co-workers showed that high-intensity focused ultrasound could reversibly open the BBB at the focal point, with normal function returning within 72 h. Microscopy enabled the observation of two possible mechanisms by which high intensity focused ultrasound operated: either by opening of the BBB while preserving brain architecture, or by opening it by damaging the tissue exposed to ultrasound. Both mechanisms of opening were attributed to widening and damaging the integrity of the capillary endothelial cell tight junctions [153–155]. The opening of the BBB using microbubbles and MRI-guided focused ultrasound was recently achieved by Black and collaborators in humans during a phase I clinical trial (Fig. 5.14). This study was carried out using a 1024 transducer array operated at a frequency of 220 kHz. In all five patients, the BBB was successfully opened in the selected area reversibly and repeatedly, with no clinically significant adverse effects [156].

This method of BBB opening could allow the delivery of large therapeutic molecules normally unable to accumulate into the brain [157]. Hynynen's group proved this to be feasible by using microbubbles alongside MRI-guided focused ultrasound to successfully deliver a dopamine D₄ receptor-targeting antibody into Swiss-webster mice brains [158]. This study was quickly followed by another study again by the Hynynen group, where they delivered the FDA-approved anti-human

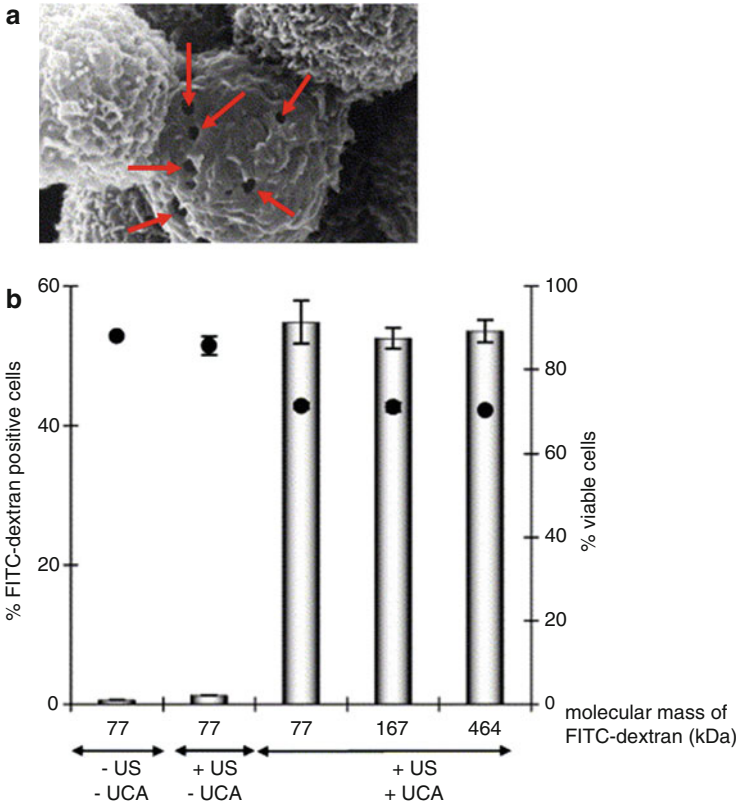


Fig. 5.13 (a) Images of sonoporation in MAT B III cells insonified with a focused transducer (2.25 MHz, peak negative pressure 570 kpa). Pores sizes were in the order of 100 nm. Cells were fixed immediately after sonication with glutaraldehyde and observed with SEM after gold sputtering at a magnification of $\times 10,000$. (b) Uptake of various FITC-dextrans into MAT B III cell after sonication with or without microbubbles (UCA). (Adapted from [147])

epidermal growth factor receptor 2 monoclonal antibody Herceptin (trastuzumab). The amount of Herceptin delivered was determined by measuring the amount of human IgG in sonicated versus control sections. Additionally, this was correlated to the extent of MRI-monitored BBB opening. This allows for a future noninvasive method of determining drug delivery location [159]. Small molecules normally unable to cross the BBB have also been delivered using focused ultrasound; i.e., doxorubicin, 1,3-bis(2-chloroethyl)-1-nitrosourea and epirubicin [160–162]. The delivery of drugs by combining both the microbubble and the drugs into one moiety was also achieved by Wheatley et al. who developed a poly(lactic acid) shelled microbubble loaded with doxorubicin. The particles were around $2\ \mu\text{m}$ in size with a doxorubicin concentration of 6.2 mg/g. A dramatic improvement of doxorubicin concentration within VX2-implanted rabbits was observed after injection of bubbles + ultrasound exposure [163].

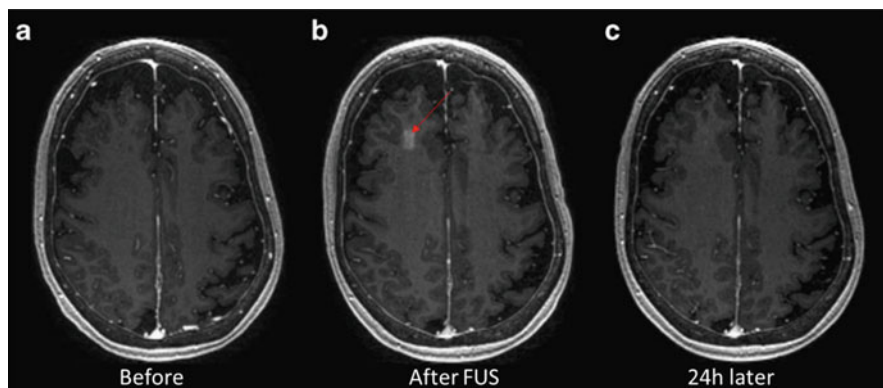


Fig. 5.14 Axial T₁ weighted gadolinium MR images, (a) baseline, (b) immediately after sonication, and (c) 24 h after the procedure. Red arrow used to indicate area of enhance contrast. (Figure reused with permission from [156])

However, a major drawback in the use of microbubbles is their very short in vivo half-life between 5 and 10 min. Due to the short lifetime, microbubbles only act on endothelial cells. Ultrasound exposures for microbubble compositions are usually between 5 and 20 min and the ultrasound is usually applied just after or even during microbubble injection. By changing the size of the bubbles to submicron, a much longer half-life is observed [75]. However, the small size makes the growth step during cavitation more difficult due to the increased surface tension.

Due to their smaller size, nanobubbles have been shown to be able to extravasate into tumors. This was proven by Yang et al. who clearly showed that near-infrared fluorescence-labelled nanobubbles accumulated into breast cancer (MDA-MB-231) tumors [164]. This gives nanobubbles a clear advantage over microbubbles which are limited to the vasculature. Fan and co-workers showed that nanobubbles can also be used to enhance the delivery of doxorubicin into mice bearing (PC3) prostate tumors. Nanobubbles (5×10^7) with an average size of 485 ± 33 nm was injected and then subjected to ultrasound at a frequency of 1 MHz and intensity of 1 W/cm^2 . Under these conditions, the nanobubbles were all destroyed within 15 min. The tumors subjected to nanobubbles, doxorubicin, and ultrasound showed significant reduction in size compared to the control groups [165]. Zhang et al. constructed a pH-sensitive polymeric nanodroplet loaded with doxorubicin and perfluorocarbon [166]. The nanodroplets were constructed from pH-sensitive polymers: *N, N'*-diethylenediamine (DEA), histamine (His), and 2-(diisopropylamino)ethylamine (DIP) grafted to polyethylene glycol (mPEG) and poly (_L-aspartic acid) (PAsp) copolymer. The pH sensitivity was tested with a dramatic size increase in size from 161 ± 9 nm at pH 7.4 to 400 ± 11 nm at pH 6.8. The sharp increase in size in acidic environments lowers the vaporization threshold for the encapsulated perfluorocarbon, allowing for more efficient conversion of the nanodroplets into nanobubbles upon low frequency ultrasound application. The system was tested in vivo on nude mice

bearing C6 glioma xenograft tumors. Mice were treated with the formulation on day 1, 4, 7, and 11 in conjunction with low-frequency focused ultrasound. The animals treated exhibited significantly slower tumor growth with 87.5% of animal surviving the duration of the study (40 days) compared to the control group (PBS) in which all animals died within 33 days [166]. The Hartley group carried out an interesting study by encapsulating nanoemulsions inside liposomes to form pseudo nanobubbles [167]. A range of lipids including: 1,2-Dimyristoyl-sn-glycero-3-phosphocholine (DMPC), 1,2-dihexadecanoyl-sn-glycero-3-phosphocholine (DPPC), 1,2-Dipalmitoyl-sn-glycero-3-phosphate (DPPA), and DSPE-PEG-₂₀₀₀-NH.folate were used in this study. The nanoemulsions were made by hydrating DPPA, DPPC, or DMPC with perfluorohexane/perfluoropentane (600/1000 mg), the resulting mixture was sonicated and extruded to achieve sizes of ~ 100 nm. The liposomes were formed separately from DMPC or DPPC and DSPE-PEG-₂₀₀₀-NH.folate (98.8:1.2) using a thin-film hydration method, followed by extrusion through a 200 nm membrane, this lead to liposomes of sizes varying from 200 to 500 nm. The liposomes and nanoemulsions were formed separately and mixed via sonication (20 kHz, 1.5 W/cm^2) on ice to encapsulate the nanoemulsions within the liposomes. To evaluate if the encapsulated nanoemulsions could vaporize under ultrasound application, and liposome membrane rupture would occur *in vitro* studies were carried out on HeLa cells. Liposomes encapsulating both calcein (fluorescent small molecule) and the nanoemulsion were incubated with HeLa cells for 2 h at 37°C followed by a short burst of ultrasound (20 kHz, 1 W/cm^2 , 2 s). After ultrasound exposure, the cells were washed and the calcein in the cytosol was assessed using fluorescent confocal microscopy. These confocal images show that both folate and the encapsulated nanoemulsions are required for calcein release into the cytosol. This study shows that drug release from liposomes can be activated by low frequency ultrasound by vaporization of a co-encapsulated nanoemulsions causing membrane rupture [167]. The initial studies on nanobubbles show promise due to their increased lifetimes and ability to cross the vasculature. With additional development they could prove to be a valuable tool for drug delivery in cancer therapy.

6.6 Polymeric Nanoparticles for Ultrasound Mediated Drug Delivery

Kost et al. was first to use polymer systems for ultrasound-mediated delivery. They showed that biodegradable polymers, such as polyanhydrides, polyglycolide, and polylactides, increased the release rate of incorporated molecules by 20-fold and increased the polymer degradation rate by fivefold when combined with ultrasound. This effect was also investigated with nonbiodegradable copolymers ethylene/vinyl acetate but only a tenfold increase in release rate was observed. The release rate was proportional to the intensity of the ultrasound applied. For *in vivo* rat studies, the group sonicated with a 20 kHz transducer for 20 min, delivering 5 W/cm^2 at a duty cycle of 50%. Drug concentrations *in vivo* were increased following ultrasound

application, suggesting an increase in degradation of the implanted polymer. The degradation was believed to be cavitation-dependent, not temperature dependent [168]. After this pioneering publication, additional studies on polymer systems in conjunction with focused ultrasound have been carried out [67, 169].

For example, the Rapoport group have made multiple types of polymeric micelles using Pluronic P-105 block copolymer (poly(-ethylene oxide)-co-poly(propylene oxide)-co-poly(ethylene oxide)). In one study, a fluorescently labelled Pluronic P-105 with C-368 (labelled on the hydroxyl groups) was added to the formulation and the effect of continuous wave and pulsed ultrasound on doxorubicin uptake in HL-60 cells was studied in both PBS and the micellar P-105 solutions. Continuous wave and pulsed ultrasound at 20 kHz augmented DOX uptake in both PBS and Pluronic micelles. Ultrasound intensity enhanced uptake with increasing power up to 33 mW/cm² where significant sonolysis was observed. The uptake of the micelles was also tested using an ultrasound pulse sequence over a continual beam. Pulse durations of up to 2 s long and continuous ultrasound facilitated comparable drug uptake. Ultrasound pulse duration had no effect on drug uptake in the PBS sample. This suggested that over the 2 s duration, the drug release and uptake were similar. This resulted from two mechanisms controlling the ultrasound activation of the micelles. These mechanisms work in synergy with the ultrasound releasing the drug from the micelles while simultaneously increasing the uptake of the micelles by permeating the cell membranes [170]. The authors further develop a second generation of ultrasound activated polymeric micelles. The second generation formulation is a mixture of: Pluronic P-105 block, PEG-PBLA (poly(ethylene glycol)-poly(β -benzyl-L-aspartate)), and DSPE-PEG₂₀₀₀ (1,2-distearoyl-sn-glycero-3-phosphoethanolamine-*N*-[methoxyl(polyethylene glycol)-2000]). The incorporation of PEG into the formulation reduces particle recognition by the reticulo-endothelial system [171]. Doxorubicin was encapsulated in the micelles. The micelles and free doxorubicin were tested in vivo with and without sonication using an ovarian carcinoma (A2780) tumor model in nu/nu mice. A 30 s ultrasound treatment using a 1 MHz transducer increased doxorubicin accumulation in the tumor by a factor of 1.7. The effect of the ultrasound treatment increased with increasing time between injection and irradiation. This was attributed to releasing the payload after the micelles had accumulated into the tumor interstitium via the EPR effect. Tumor volumes decreased to 70% for free doxorubicin; however, the same dose of doxorubicin (3 mg/kg) loaded into micelles reduced the tumor volume to 36% [172]. Polymeric nanoparticles have also been formulated that were imageable and activatable by ultrasound application. This study was carried out by Ma et al. who used a porous agent made from mPEG-PLGA to act as the imaging/delivery vehicle. The surface of the particle was further modified with two antibodies; anti-carcinoembryonic antigen and anti-carbohydrate antigen 19-9 to convey a targeting modality. In vitro uptake was compared between ultrasound (1 MHz, 20% duty cycle, 1 W/cm², 60 s exposure time) and ultrasound-mediated microbubble destruction (SonoVue, 2:5 ratio). Ultrasound alone showed an uptake efficiency of 30%, whereas ultrasound-mediated microbubble destruction increased the uptake by 10% due to sonoporation of the cell membranes. Ultrasound contrast

images were investigated *in vitro* and *in vivo*. The compounds had similar contrast to SonoVue microbubbles [173]. A combination of both ultrasound imaging and ultrasound drug release could have clinical usefulness; however, to the best of my knowledge, no polymer-based ultrasound activated polymer systems are in clinical trials.

7 Conclusions and Future Perspective

Focused ultrasound is a powerful technique that enables drug delivery from nanoparticles into tumors, as well as permeation of biological barriers previously an incredibly difficult challenge to circumvent. While nanoparticles have been shown to play an important role in focused ultrasound treatments, the development of purpose-made nanoparticles for focused ultrasound applications is still required to maximize their effects on tissues and on therapeutic drug delivery. The first steps in this development have been described above, and by using the factors described, we can design nanoparticles that respond to ultrasound application. However, further optimization of the formulations is needed to fully realize their clinical effectiveness in conjunction with focused ultrasound. That being said, it is expected that near-future studies in MRI-guided focused ultrasound will soon show the efficacy of this technique in the clinic for deep-tissue drug delivery applications.

References

1. Al-Bataineh O, Jenne J, Huber P (2012) Clinical and future applications of high intensity focused ultrasound in cancer. *Cancer Treat Rev* 38:346–353
2. Rodalleg A, Fanciullino R, Lacarelle B, Ciccolini J (2018) Seek and destroy: improving PK/PD profiles of anticancer agents with nanoparticles. *Expert Rev Clin Pharmacol* 11:599–610
3. Lee Y, Thompson DH (2017) Stimuli-responsive liposomes for drug delivery. *Wiley Interdiscip Rev Nanomed Nanobiotechnol* 9:e1450
4. Hu X, Li F, Wang S, Xia F, Ling D (2018) Biological stimulus-driven assembly/disassembly of functional nanoparticles for targeted delivery, controlled activation, and bioelimination. *Adv Healthc Mater* 1800359:1–19
5. Murray JC, Carmichael J (1995) Targeting solid tumours: challenges, disappointments, and opportunities. *Adv Drug Deliv Rev* 17:117–127
6. Sriraman SK, Aryasomayajula B, Torchilin VP (1994) Barriers to drug delivery in solid tumors. *Tissue Barriers* 271:58–65
7. Tran S, DeGiovanni P-J, Piel B, Rai P (2017) Cancer nanomedicine: a review of recent success in drug delivery. *Clin Transl Med* 6:44
8. Bobo D, Robinson KJ, Islam J, Thurecht KJ, Corrie SR (2016) Nanoparticle-based medicines: a review of FDA-approved materials and clinical trials to date. *Pharm Res* 33:2373–2387
9. Pillai G (2014) Nanomedicines for cancer therapy: an update of FDA approved and those under various stages of development. *SOJ Pharm Pharm Sci* 1:1–13
10. Patel J (1996) Liposomal doxorubicin: Dox. *J Oncol Pharm Pract* 2:201–210
11. De Luca R, Blasi L, Alù M, Gristina V, Cicero G (2018) Clinical efficacy of nab-paclitaxel in patients with metastatic pancreatic cancer. *Drug Des Devel Ther* 12:1769–1775

12. Petre CE, Dittmer DP (2007) Liposomal daunorubicin as treatment for Kaposi's sarcoma. *Int J Nanomedicine* 2:277–288
13. Masetti R, Pession A (2009) First-line treatment of acute lymphoblastic leukemia with pegasparginase. *Biologics* 3:359–368
14. Sarris AH et al (2000) Liposomal vincristine in relapsed non-Hodgkin's lymphomas: early results of an ongoing phase II trial. *Ann Oncol* 11:69–72
15. Chang H, Yeh M (2012) Clinical development of liposome-based drugs: formulation, characterization, and therapeutic efficacy. *Int J Nanomedicine* 7:49–60
16. Dragovich T et al (2006) A phase 2 trial of the liposomal DACH platinum L-NDDP in patients with therapy-refractory advanced colorectal cancer. *Cancer Chemother Pharmacol* 58:759–764
17. Bao P et al (2016) Vincristine sulfate liposomes injection (VSLI, Marqibo): results from a phase I study in children, adolescents, and young adults with refractory solid tumors or leukemias. *Pediatr Blood Cancer* 63:997–1005
18. Boulikas T (2009) Clinical overview on Lipoplatin™: a successful liposomal formulation of cisplatin. *Expert Opin Investig Drugs* 18:1197–1218
19. Sartor O (2006) Eligard®6: a new form of treatment for prostate Cancer. *Eur Urol Suppl* 5:905–910
20. Zhang H (2016) Onivyde for the therapy of multiple solid tumors. *Onco Targets Ther* 9:3001–3007
21. Lyon PC et al (2017) Clinical trial protocol for TARDOX: a phase I study to investigate the feasibility of targeted release of lyso-thermosensitive liposomal doxorubicin (ThermoDox®) using focused ultrasound in patients with liver tumours. *J Ther Ultrasound* 5:1–8
22. Hong CW, Libutti SK, Wood BJ (2013) Liposomal doxorubicin plus radiofrequency ablation for complete necrosis of a hepatocellular carcinoma. *Curr Oncol* 20:274–277
23. Solomon R, Gabizon AA (2008) Clinical pharmacology of liposomal anthracyclines: focus on pegylated liposomal doxorubicin. *Clin Lymphoma Myeloma* 8:21–32
24. Kobayashi H, Watanabe R, Choyke PL (2014) Improving conventional enhanced permeability and retention (EPR) effects; what is the appropriate target? *Theranostics* 4:81–89
25. Kline CLB, El-Deiry WS (2013) Personalizing colon cancer therapeutics: targeting old and new mechanisms of action. *Pharmaceuticals* 6:988–1038
26. Miele E, Spinelli GP, Miele E, Tomao F, Tomao S (2009) Albumin-bound formulation of paclitaxel (Abraxane® ABI-007) in the treatment of breast cancer. *Int J Nanomedicine* 4:99–105
27. Sartor O (2003) Eligard: leuprolide acetate in a novel sustained-release delivery system. *Urology* 61:25–31
28. Wilson AC, Vadakkadath Meethal S, Bowen RL, Atwood CS (2007) Leuprolide acetate: a drug of diverse clinical applications. *Expert Opin Investig Drugs* 16:1851–1863
29. Bulbake U, Doppalapudi S, Kommineni N, Khan W (2017) Liposomal formulations in clinical use: an updated review. *Pharmaceutics* 9:1–33
30. Celsion (2018). Available at: <https://celsion.com/thermodox/>
31. Mitragotri S (2005) Healing sound: the use of ultrasound in drug delivery and other therapeutic applications. *Nat Rev Drug Discov* 4:255–260
32. Kim Y, Rhim H, Choi MJ, Lim HK, Choi D (2008) High-intensity focused ultrasound therapy: an overview for radiologists. *Korean J Radiol* 9:291
33. Carovac A, Smajlovic F, Junuzovic D (2011) Application of ultrasound in medicine. *Acta Inform Medica* 19:168
34. Tu J et al (2012) Controllable in vivo hyperthermia effect induced by pulsed high intensity focused ultrasound with low duty cycles. *Appl Phys Lett* 101:1–5
35. Edler I, Lindström K (2004) The history of echocardiography. *Ultrasound Med Biol* 30:1565–1644
36. Otto C (2000) Principles of echocardiographic image acquisition and Doppler analysis. *Textbook Clin Echocardiogr*
37. Toosonix. Available at: <https://www.toosonix.com/technology/>. Accessed Oct 2018

38. Karaböce B, Şahin A, Ince AT, Skarlatos Y (2015) Characterization of pressure fields of focused transducers at TÜBTAK UME. *Phys Procedia* 70:1241–1245
39. Zhou Y, Zhai L, Simmons R, Zhong P (2006) Measurement of high intensity focused ultrasound fields by a fiber optic probe hydrophone. *J Acoust Soc Am* 120:676–685
40. Haller J, Jenderka K-V, Durando G, Shaw A (2012) A comparative evaluation of three hydrophones and a numerical model in high intensity focused ultrasound fields. *J Acoust Soc Am* 131:1121–1130
41. O'Brien WD (2007) Ultrasound-biophysics mechanisms. *Prog Biophys Mol Biol* 93:212–255
42. Hijnen N, Langereis S, Grill H (2014) Magnetic resonance guided high-intensity focused ultrasound for image-guided temperature-induced drug delivery. *Adv Drug Deliv Rev* 72:65–81
43. Zhou Y-F (2011) High intensity focused ultrasound in clinical tumor ablation. *World J Clin Oncol* 2:8–27
44. Canney MS, Bailey MR, Crum LA, Khokhlova VA, Sapozhnikov OA (2008) Acoustic characterization of high intensity focused ultrasound fields: a combined measurement and modeling approach. *J Acoust Soc Am* 124:2406–2420
45. Nelson TR, Fowlkes JB (2009) Ultrasound biosafety considerations for the practicing sonographer and sonologist. *J Ultrasound Med* 28:139–150
46. Smith NB, Temkin JM, Shapiro F, Hynynen K (2001) Thermal effects of focused ultrasound energy on bone tissue. *Ultrasound Med Biol* 27:1427–1433
47. Szabo TL, Lewin PA (2013) Ultrasound transducer selection in clinical imaging practice. *J Ultrasound Med* 32:573–582
48. Spadoni A, Daraio C (2010) Generation and control of sound bullets with a nonlinear acoustic lens. *Proc Natl Acad Sci* 107:7230–7234
49. Hynynen K et al (2006) Pre-clinical testing of a phased array ultrasound system for MRI-guided noninvasive surgery of the brain-A primate study. *Eur J Radiol* 59:149–156
50. Hutchinson EB, Hynynen K (1998) Intracavitary ultrasound phased arrays for prostate thermal therapies: MRI compatibility and in vivo testing. *Med Phys* 25:2392–2399
51. Pernot M, Aubry JF, Tanter M, Thomas JL, Fink M (2003) High power transcranial beam steering for ultrasonic brain therapy. *Phys Med Biol* 48:2577–2589
52. Muthu MS, Leong DT, Mei L, Feng SS (2014) Nanotheranostics – application and further development of nanomedicine strategies for advanced theranostics. *Theranostics* 4:660–677
53. Rosenberg C et al (2013) PRFS-based MR thermometry versus an alternative T1 magnitude method – comparative performance predicting thermally induced necrosis in hepatic tumor ablation. *PLoS One* 8:1–11
54. Lewis MA, Staruch RM, Chopra R (2015) Thermometry and ablation monitoring with ultrasound. *Int J Hyperth* 31:163–181
55. Zhi-Yu H et al (2017) A clinical study of thermal monitoring techniques of ultrasound-guided microwave ablation for hepatocellular carcinoma in high-risk locations. *Sci Rep* 7:1–8
56. Roberts A (2008) Magnetic resonance-guided focused ultrasound for uterine fibroids. *Semin Intervent Radiol* 25:394–405
57. Lindner U et al (2012) Focal magnetic resonance guided focused ultrasound for prostate cancer: initial north American experience. *Can Urol Assoc J* 6:E283–E286
58. Sun T et al (2015) Acoustic cavitation-based monitoring of the reversibility and permeability of ultrasound-induced blood-brain barrier opening. *Phys Med Biol* 60:9079–9094
59. Kooiman K, Vos HJ, Versluis M, De Jong N (2014) Acoustic behavior of microbubbles and implications for drug delivery. *Adv Drug Deliv Rev* 72:28–48
60. Aw MS, Paniwnyk L, Losic D (2016) The progressive role of acoustic cavitation for non-invasive therapies, contrast imaging and blood-tumor permeability enhancement. *Expert Opin Drug Deliv* 13:1383–1396
61. Boissenot T, Bordat A, Fattal E, Tsapis N (2016) Ultrasound-triggered drug delivery for cancer treatment using drug delivery systems: from theoretical considerations to practical applications. *J Control Release* 241:144–163

62. Moghimipour E, Handali S (2012) Utilization of thin film method for preparation of celecoxib loaded liposomes. *Adv Pharm Bull* 2:93–98
63. Zhang H (2016) Thin-film hydration followed by extrusion method for liposome preparation. *Liposomes*:17–22
64. Akbarzadeh A et al (2013) Liposome: classification, preparation, and applications. *Nanoscale Res Lett* 8:1–8
65. Allen TM, Sapra P, Moase E (2002) Use of the post-insertion method for the formation of ligand-coupled liposomes. *Cell Mol Biol Lett* 7:889–894
66. Gubernator J (2011) Active methods of drug loading into liposomes: recent strategies for stable drug entrapment and increased in vivo activity. *Expert Opin Drug Deliv* 8:567–582
67. Rapoport N (2007) Physical stimuli-responsive polymeric micelles for anti-cancer drug delivery. *Prog Polym Sci* 32:962–990
68. Miller T et al (2013) Drug loading of polymeric micelles. *Pharm Res* 30:584–595
69. Kataoka K, Matsumoto T, Yokoyama M, Okano T (2000) Doxorubicin-loaded poly(ethylene glycol)-poly(benzyl-L-aspartate) copolymer micelles: their pharmaceutical characteristics and biological significance. *J Control Release* 64:143–153
70. Zhang X et al (1997) An investigation of the antitumour activity and biodistribution of polymeric micellar paclitaxel. *Cancer Chemother Pharmacol* 40:81–86
71. Jette KK, Law D, Schmitt EA, Kwon GS (2016) Preparation and drug loading of poly(ethylene glycol)-block-poly(epsilon-caprolactone) micelles through the evaporation of a cosolvent azeotrope. *Pharm Res* 21:1184–1191
72. Fournier E, Dufresne MH, Smith DC, Ranger M, Leroux JC (2004) A novel one-step drug-loading procedure for water-soluble amphiphilic nanocarriers. *Pharm Res* 21:962–968
73. Sirsi S, Borden M (2009) Microbubble compositions, properties and biomedical applications. *Bubble Sci Eng Technol* 1:3–17
74. Stride E, Edirisinghe M (2008) Novel microbubble preparation technologies. *Soft Matter* 4:2350–2359
75. Wu H et al (2013) Acoustic characterization and pharmacokinetic analyses of new nanobubble ultrasound contrast agents. *Ultrasound Med Biol* 39:2137–2146
76. Stetefeld J, McKenna SA, Patel TR (2016) Dynamic light scattering: a practical guide and applications in biomedical sciences. *Biophys Rev* 8:409–427
77. Patravale V, Dandekar P, Jain R (2012) Characterization techniques for nanoparticulate carriers. In: *Nanoparticulate drug delivery*. Woodhead Publishing, Oxford, pp 87–121
78. Demetzos C (2008) Differential scanning calorimetry (DSC): a tool to study the thermal behavior of lipid bilayers and liposomal stability. *J Liposome Res* 18:159–173
79. Stewart F et al (2018) A prototype therapeutic capsule endoscope for ultrasound-mediated targeted drug delivery. *J Med Robot Res* 03:1840001
80. Chen H, Hwang JH (2013) Ultrasound-targeted microbubble destruction for chemotherapeutic drug delivery to solid tumors. *J Ther Ultrasound* 1:1
81. Stewart FR et al (2017) Acoustic sensing and ultrasonic drug delivery in multimodal theranostic capsule endoscopy. *Sensors (Switzerland)* 17, 1553, 1–24
82. Thanou M, Gedroyc W (2013) MRI-guided focused ultrasound as a new method of drug delivery. *J Drug Deliv* 2013:616197
83. Centelles MN et al (2018) Image guided thermosensitive liposomes for focused ultrasound drug delivery: using NIRF labelled lipids and topotecan to visualise the effects of hyperthermia in tumours. *J Control Release* 280:87–98
84. Lokerse WJM, Kneidl A, Petrini M, Lindner LH (2018) Liposomes for hyperthermia triggered drug release. In: *Theranostics and image guided drug delivery*. Royal Society of Chemistry, Cambridge, UK, pp 137–164
85. Needham D, Park JY, Wright AM, Tong J (2012) Materials characterization of the low temperature sensitive liposome (LTSL): effects of the lipid composition (lysolipid and DSPE-PEG2000) on the thermal transition and release of doxorubicin. *Faraday Discuss* 161:515–534

86. Kneidl B, Peller M, Winter G, Lindner LH, Hossann M (2014) Thermosensitive liposomal drug delivery systems: state of the art review. *Int J Nanomedicine* 9:4387–4398
87. Li J et al (2014) A review on phospholipids and their main applications in drug delivery systems. *Asian J Pharm Sci* 10:81–98
88. Yatvin MB, Weinstein JN, Dennis WH, Blumenthal R (1978) Design of liposomes for enhanced local release of drugs by hyperthermia. *Science* 202:1290–1293
89. Lu T, ten Hagen TLM (2017) Inhomogeneous crystal grain formation in DPPC-DSPC based thermosensitive liposomes determines content release kinetics. *J Control Release* 247:64–72
90. Kao YJ, Juliano RL (1981) Interactions of liposomes with the reticuloendothelial system. Effects of reticuloendothelial blockade on the clearance of large unilamellar vesicles. *Biochim Biophys Acta* 677:453–461
91. Semple SC, Chonn A, Cullis PR (1996) Influence of cholesterol on the association of plasma proteins with liposomes. *Biochemistry* 35:2521–2525
92. McMullen TPW, McElhaney RN (1996) Physical studies of cholesterol-phospholipid interactions. *Curr Opin Colloid Interface Sci* 1:83–90
93. Novell A et al (2015) Focused ultrasound influence on calcein-loaded thermosensitive stealth liposomes. *Int J Hypertherm* 31:349–358
94. Demel RA, De Kruyff B (1976) The function of sterols in membranes. *BBA Rev Biomembr* 457:109–132
95. Merlin JL (1991) Encapsulation of doxorubicin in thermosensitive small unilamellar vesicle liposomes. *Eur J Cancer Clin Oncol* 27:1026–1030
96. Dos Santos N et al (2007) Influence of poly(ethylene glycol) grafting density and polymer length on liposomes: relating plasma circulation lifetimes to protein binding. *Biochim Biophys Acta Biomembr* 1768:1367–1377
97. Kenworthy AK, Hristova K, Needham D, McIntosh TJ (1995) Range and magnitude of the steric pressure between bilayers containing phospholipids with covalently attached poly(ethylene glycol). *Biophys J* 68:1921–1936
98. Needham D, Park J, Wright M (2013) Materials characterization of the low temperature sensitive liposome (LTSL): effects of the lipid composition (lysolipid and DSPE – PEG2000) on the thermal transition and release of doxorubicin. *Faraday Discuss* 161:563–589
99. Li L et al (2010) Triggered content release from optimized stealth thermosensitive liposomes using mild hyperthermia. *J Control Release* 143:274–279
100. Lin JC, Song CW (1993) Influence of vascular thermotolerance on the heat-induced changes in blood flow, pO₂ and cell survival in tumors. *Cancer Res* 53:2076–2080
101. Storm FK, Harrison WH, Elliott RS, Morton DL (1979) Normal tissue and solid tumor effects of hyperthermia in animal models and clinical trials normal tissue and solid tumor effects of hyperthermia in animal models and clinical trials. *Cancer Res* 39:2245
102. Needham D, Anyarambhatla G, Kong G, Dewhirst MW (2000) A new temperature-sensitive liposome for use with mild hyperthermia: characterization and testing in a human tumor xenograft model. *Cancer Res* 60:1197–1201
103. Anyarambhatla GR, Needham D (1999) Enhancement of the phase transition permeability of DPPC liposomes by incorporation of MPPC: a new temperature-sensitive liposome for use with mild hyperthermia. *J Liposome Res* 9:491–506
104. Mills JK, Needham D (2005) Lysolipid incorporation in dipalmitoylphosphatidylcholine bilayer membranes enhances the ion permeability and drug release rates at the membrane phase transition. *Biochim Biophys Acta Biomembr* 1716:77–96
105. Ickenstein LM, Arfvidsson MC, Needham D, Mayer LD, Edwards K (2003) Disc formation in cholesterol-free liposomes during phase transition. *Biochim Biophys Acta Biomembr* 1614:135–138
106. Ta T, Porter TM (2013) Thermosensitive liposomes for localized delivery and triggered release of chemotherapy. *J Control Release* 169:112–125
107. Kong G et al (2000) Efficacy of liposomes and hyperthermia in a human tumor xenograft model: importance of triggered drug release. *Cancer Res* 60:6950–6957

108. Tak WY et al (2018) Phase III HEAT study adding lyso-thermosensitive liposomal doxorubicin to radiofrequency ablation in patients with unresectable hepatocellular carcinoma lesions. *Clin Cancer Res* 24:73–83
109. Banno B et al (2010) The functional roles of poly(ethylene glycol)-lipid and lysolipid in the drug retention and release from lysolipid-containing thermosensitive liposomes in vitro and in vivo. *J Pharm Sci* 99:2295–2308
110. Sandström MC, Ickenstein LM, Mayer LD, Edwards K (2005) Effects of lipid segregation and lysolipid dissociation on drug release from thermosensitive liposomes. *J Control Release* 107:131–142
111. Tagami T, Ernsting MJ, Li SD (2011) Optimization of a novel and improved thermosensitive liposome formulated with DPPC and a Brij surfactant using a robust in vitro system. *J Control Release* 154:290–297
112. Tagami T, Ernsting MJ, Li SD (2011) Efficient tumor regression by a single and low dose treatment with a novel and enhanced formulation of thermosensitive liposomal doxorubicin. *J Control Release* 152:303–309
113. Ward MA, Georgiou TK (2011) Thermoresponsive polymers for biomedical applications. *Polymers (Basel)*:1215–1242
114. Wei H, Cheng S, Zhang X, Zhuo R (2009) Thermo-sensitive polymeric micelles based on poly (*N*-isopropylacrylamide) as drug carriers. *Prog Polym Sci* 34:893–910
115. Twaites BR, De C, Alarco H, Go DC, Alexander C (2005) Thermoresponsive polymers as gene delivery vectors: cell viability, DNA transport and transfection studies. *J Control Release* 108:472–483
116. Vihola H, Laukkanen A, Valtola L, Tenhu H, Hirvonen J (2005) Cytotoxicity of thermo-sensitive polymers poly (*N*-isopropylacrylamide), poly (*N*-vinylcaprolactam) and amphiphilically modified poly (*N*-vinylcaprolactam). *Biomaterials* 26:3055–3064
117. Ta T et al (2014) Localized delivery of doxorubicin in vivo from polymer-modified thermosensitive liposomes with MR-guided focused ultrasound-mediated heating. *J Control Release* 194:71–81
118. Kono K, Hayashi H (1994) Temperature-sensitive liposomes: liposomes bearing poly (*N*-isopropylacrylamide). *J Control Release* 30:69–75
119. Hayashi H, Kono K, Takagishi T (1996) Temperature-controlled release property of phospholipid vesicles bearing a thermo-sensitive polymer. *Biochim Biophys Acta* 1280: 127–134
120. Park SM et al (2013) Novel temperature-triggered liposome with high stability: formulation, in vitro evaluation, and in vivo study combined with high-intensity focused ultrasound (HIFU). *J Control Release* 170:373–379
121. Urry D, Physical W (1997) Chemistry of biological free energy transduction as demonstrated by elastic. *J Phys Chem* 5647:11007–11028
122. Meyer DE, Chilkoti A (2004) Quantification of the effects of chain length and concentration on the thermal behavior of elastin-like polypeptides. *Biomacromolecules*:846–851
123. Roy Chowdhury M, Schumann C, Bhakta-Guha D, Guha G (2016) Cancer nanotheranostics: strategies, promises and impediments. *Biomed Pharmacother* 84:291–304
124. Jo SD, Ku SH, Won YY, Kim SH, Kwon IC (2016) Targeted nanotheranostics for future personalized medicine: recent progress in cancer therapy. *Theranostics* 6:1362–1377
125. Wright M, Centelles M, Gedroyc W, Thanou M (2018) Image guided focused ultrasound as a new method of targeted drug delivery. In: *Theranostics and image guided drug delivery*. Royal Society of Chemistry, Cambridge, UK, pp 1–39
126. Liang C, Xu L, Song G, Liu Z (2016) Emerging nanomedicine approaches fighting tumor metastasis: animal models, metastasis-targeted drug delivery, phototherapy, and immunotherapy. *Chem Soc Rev* 45:6250–6269
127. Mehlen P, Puisieux A (2006) Metastasis: a question of life or death. *Nat Rev Cancer* 6:449–458
128. Guan X (2015) Cancer metastases: challenges and opportunities. *Acta Pharm Sin B* 5:402–418

129. Seyfried TN, Huysentruyt LC (2013) On the origin of cancer metastasis. *Crit Rev Oncol* 18:43–73
130. Kovatcheva R et al (2015) Ultrasound-guided high-intensity focused ultrasound treatment of breast fibroadenoma – a multicenter experience. *J Ther Ultrasound* 3:1
131. Li S, Wu P-H (2013) Magnetic resonance image-guided versus ultrasound-guided high-intensity focused ultrasound in the treatment of breast cancer. *Chin J Cancer* 32:441–452
132. Kim YS (2015) Advances in MR image-guided high-intensity focused ultrasound therapy. *Int J Hyperth* 31:225–232
133. Quesson B, De Zwart JA, Moonen CTW (2000) Magnetic resonance temperature imaging for guidance of thermotherapy. *J Magn Reson Imaging* 12:525–533
134. De Smet M, Langereis S, van den Bosch S, Grüll H (2010) Temperature-sensitive liposomes for doxorubicin delivery under MRI guidance. *J Control Release* 143:120–127
135. De Smet M, Heijman E, Langereis S, Hijnen NM, Grüll H (2011) Magnetic resonance imaging of high intensity focused ultrasound mediated drug delivery from temperature-sensitive liposomes: an in vivo proof-of-concept study. *J Control Release* 150:102–110
136. Unger E, Shen DK, Wu GL, Fritz T (1991) Liposomes as MR contrast agents: pros and cons. *Magn Reson Med* 22:304–308; discussion 313
137. Rizzitelli S et al (2016) The release of Doxorubicin from liposomes monitored by MRI and triggered by a combination of US stimuli led to a complete tumor regression in a breast cancer mouse model. *J Control Release* 230:57–63
138. Affram K et al (2017) Smart thermosensitive liposomes for effective solid tumor therapy and in vivo imaging. *PLoS One* 12:1–22
139. Rosca EV et al (2015) Thermosensitive, near-infrared-labeled nanoparticles for topotecan delivery to tumors. *Mol Pharm* 12:1335–1346
140. Kamaly N et al (2008) Bimodal paramagnetic and fluorescent liposomes for cellular and tumor magnetic resonance imaging. *Bioconjug Chem* 19:118–129
141. Senneville BD et al (2007) MR thermometry for monitoring tumor ablation. *Eur Radiol* 17:2401–2410
142. Rieke V, Pauly K (2008) MR thermometry. *J Magn Reson Imaging* 27:376–390
143. Sboros V (2008) Response of contrast agents to ultrasound. *Adv Drug Deliv Rev* 60:1117–1136
144. Wang M et al (2018) Sonoporation-induced cell membrane permeabilization and cytoskeleton disassembly at varied acoustic and microbubble-cell parameters. *Sci Rep* 8:1–12
145. van Wamel A et al (2006) Vibrating microbubbles poking individual cells: drug transfer into cells via sonoporation. *J Control Release* 112:149–155
146. Kudo N, Okada K, Yamamoto K (2009) Sonoporation by single-shot pulsed ultrasound with microbubbles adjacent to cells. *Biophys J* 96:4866–4876
147. Mehier-Humbert S, Bettinger T, Yan F, Guy RH (2005) Plasma membrane poration induced by ultrasound exposure: implication for drug delivery. *J Control Release* 104:213–222
148. Fan Z, Kumon RE, Deng CX (2014) Mechanisms of microbubble-facilitated sonoporation for drug and gene delivery. *Ther Deliv* 5:467–486
149. Lentacker I, De Cock I, Deckers R, De Smedt SC, Moonen CTW (2014) Understanding ultrasound induced sonoporation: definitions and underlying mechanisms. *Adv Drug Deliv Rev* 72:49–64
150. Qin P, Han T, Yu ACH, Xu L (2018) Mechanistic understanding the bioeffects of ultrasound-driven microbubbles to enhance macromolecule delivery. *J Control Release* 272:169–181
151. Abbott NJ (2013) Blood-brain barrier structure and function and the challenges for CNS drug delivery. *J Inher Metab Dis* 36:437–449
152. Kumar Pandey P, Kumar Sharma A, Gupta U (2016) Blood brain barrier: an overview on strategies in drug delivery, realistic in vitro modeling and in vivo live tracking. *Tissue Barriers* 4:1–14
153. Mesiwala AH et al (2002) High-intensity focused ultrasound selectively disrupts the blood-brain barrier in vivo. *Ultrasound Med Biol* 28:389–400

154. Sheikov N, McDannold N, Sharma S, Hynynen K (2008) Effect of focused ultrasound applied with an ultrasound contrast agent on the tight junctional integrity of the brain microvascular endothelium. *Ultrasound Med Biol* 34:1093–1104
155. Deng J et al (2012) The role of caveolin-1 in blood-brain barrier disruption induced by focused ultrasound combined with microbubbles. *J Mol Neurosci* 46:677–687
156. Lipsman N et al (2018) Blood-brain barrier opening in Alzheimer's disease using MR-guided focused ultrasound. *Nat Commun* 9:1–8
157. Burgess A, Shah K, Hough O, Hynynen K (2015) Focused ultrasound-mediated drug delivery through the blood- brain barrier. *Expert Rev Neurother* 15:477–491
158. Kinoshita M, McDannold N, Jolesz FA, Hynynen K (2006) Targeted delivery of antibodies through the blood-brain barrier by MRI-guided focused ultrasound. *Biochem Biophys Res Commun* 340:1085–1090
159. Kinoshita M, McDannold N, Jolesz FA, Hynynen K (2006) Noninvasive localized delivery of Herceptin to the mouse brain by MRI-guided focused ultrasound-induced blood-brain barrier disruption. *Proc Natl Acad Sci* 103:11719–11723
160. Liu H-L et al (2010) Blood-brain barrier disruption with focused ultrasound enhances delivery of chemotherapeutic drugs for glioblastoma treatment. *Radiology* 255:415–425
161. Liu H-L et al (2010) Magnetic resonance monitoring of focused ultrasound/magnetic nanoparticle targeting delivery of therapeutic agents to the brain. *Proc Natl Acad Sci* 107:15205–15210
162. Treat LH et al (2007) Targeted delivery of doxorubicin to the rat brain at therapeutic levels using MRI-guided focused ultrasound. *Int J Cancer* 121:901–907
163. Eisenbrey JR et al (2010) Development and optimization of a doxorubicin loaded poly(lactic acid) contrast agent for ultrasound directed drug delivery. *J Control Release* 143:38–44
164. Yang H et al (2016) Novel dual-mode nanobubbles as potential targeted contrast agents for female tumors exploration. *Tumor Biol* 37:14153–14163
165. Fan X et al (2016) Inhibition of prostate cancer growth using doxorubicin assisted by ultrasound-targeted nanobubble destruction. *Int J Nanomedicine* 11:3585–3596
166. Zhang L et al (2018) Size-modulable nanoprobe for high-performance ultrasound imaging and drug delivery against cancer. *ACS Nano* 12:3449–3460
167. Javadi M, Pitt WG, Belnap DM, Tsosie NH, Hartley JM (2012) Encapsulating nanoemulsions inside eliposomes for ultrasonic drug delivery. *Langmuir* 28:14720–14729
168. Kost J, Leong K, Langer R (1989) Ultrasound-enhanced polymer degradation and release of incorporated substances. *Proc Natl Acad Sci U S A* 86:7663–7666
169. Quader S, Kataoka K (2017) Nanomaterial-enabled cancer therapy. *Mol Ther* 25:1501–1513
170. Marin A, Muniruzzaman M, Rapoport N (2001) Acoustic activation of drug delivery from polymeric micelles: effect of pulsed ultrasound. *J Control Release* 71:239–249
171. Tan JS, Butterfield DE, Voycheck CL, Caldwell KD, Li JT (1993) Surface modification of nanoparticles by PEO/PPO block copolymers to minimize interactions with blood components and prolong blood circulation in rats. *Biomaterials* 14:823–833
172. Gao ZG, Fain HD, Rapoport N (2005) Controlled and targeted tumor chemotherapy by micellar-encapsulated drug and ultrasound. *J Control Release* 102:203–222
173. Ma J et al (2016) Biodegradable double-targeted PTX-mPEG-PLGA nanoparticles for ultrasound contrast enhanced imaging and antitumor therapy in vitro. *Oncotarget* 7:80008–80018



Magneto-Responsive Nanomaterials for Medical Therapy in Preclinical and Clinical Settings

Kheireddine El-Boubbou

Contents

1	Definition of Topic	241
2	Overview	242
3	Introduction	242
3.1	MNP-Based Nanotechnology in Cancer Treatment	244
4	Experimental Methodology	249
4.1	Preparation of MNPs for Biomedical Applications	249
5	Key Research Findings	255
5.1	MNPs for Diagnosis, Multimodal Imaging, and Tissue Engineering	255
5.2	MNPs for Therapeutics and Drug Delivery Applications	264
5.3	Nanomedicines in the Clinic	281
6	Conclusion and Future Perspective	283
	References	285

1 Definition of Topic

Magneto-responsive nanomaterials proved to be extremely beneficial in a whole bunch of industrial and commercial applications, ranging from catalytic systems, magnetic storage, photonic and electronic devices to biological and biomedical theranostics. In particular, the preparation of magnetic nanoparticles (MNPs), mainly made of iron oxides, for both diagnostics (detection, imaging, biosensing) and therapeutics (hyperthermia, magnetic targeting, and drug delivery) has occupied a privileged position among other nanocomposites. Due to their nanoscale

K. El-Boubbou (✉)

Department of Basic Sciences, College of Science & Health Professions (COSHP), King Saud bin Abdulaziz University for Health Sciences (KSAU-HS), King Abdulaziz Medical City, National Guard Health Affairs, Riyadh, Saudi Arabia

King Abdullah International Medical Research Center (KAIMRC), King Abdulaziz Medical City, National Guard Health Affairs, Riyadh, Saudi Arabia

e-mail: elboubboukh@ngha.med.sa; boubbouk@ksau-hs.edu.sa

dimensions, unique physiochemical properties, intrinsic magnetic characteristics, biocompatibilities, and abilities to function on the biomolecular and cellular levels, MNPs have been thoroughly investigated in medicine as magnetic imaging contrast-enhancing probes, hyperthermia agents, and magnetic-guided drug delivery carriers for disease theranostics. By avoiding healthy tissues, enabling reduced toxicities, and controlling the delivery of chemotherapeutics to specific locations, MNPs has indeed great potentials to increase drug therapeutic efficacies and minimize their adverse side effects giving promise for next-generation clinical nanomedicines for cancer treatment.

2 Overview

The rationale of this chapter is to focus on the recent developments and advancements of MNPs and drug-conjugated MNPs for cancer theranostics in preclinical and clinical settings. First, a brief overview on the use of MNPs as magneto-responsive drug targeting agents, hyperthermia vehicles, and drug delivery carriers in cancer theranostics is presented. Next, the most prevalent synthetic and characterization techniques for biocompatible MNPs used for biomedical endpoints are outlined. Then, notable examples demonstrating the progress of MNPs in multimodal diagnostic imaging, tissue engineering, and medical therapeutics are described. Special focus is set on the use of drug-conjugated MNPs for therapeutic applications in cancer treatments with discussion on the challenges and limitations of targeted drug delivery. Finally, the potential of nanomedicines in influencing clinical care is highlighted, presenting magnetic nanoformulations approved or yet to be approved in the clinic.

3 Introduction

“*Nanotechnology*” refers simply to the chemistry of the “*small*” – very small where novel and exciting phenomena occur. The manufacturing and syntheses of certain biomolecules at the atomic and molecular resolution, in a controlled precise manner, is a perfect example of what is today known as nanotechnology [1, 2]. This has continuously inspired scientists to seek innovative methodologies to produce nanostructures with tailored features, novel physical and chemical (physicochemical) properties, and specific optical, electronic, and magnetic characteristics [3, 4]. At the nanoscale, most of the material is surface and very little is volume (i.e., materials have large surface-to-volume ratio). Things this small have much more outside (surface) than they have inside (volume), leading to substantial space for biomolecular and multivalent ligand conjugation. Consequently, extensive research between functionalized nanoconstructs and natural biological living systems has lately drawn a lot of attention, with continuous development of innovative approaches and novel instrumentations to fully explore, understand, and predict the nano-bio interface.

In the last decades, many investigations have been devoted to study nanomaterials (NMs) or more specifically nanoparticles (NPs), a topic far too broad to be reviewed here. A search for the terms “NMs or NPs” and “magnetic” narrows the field considerably, but it is interesting to find the wide spectrum of successful applications they have been used in, particularly for biological purposes [5–7]. Research on preparation of various hybrid nanocomposites (i.e., gold NPs, carbon nanotubes, quantum dots, silica NPs, MNPs, liposomal and polymeric formulations, etc.) and their respective theranostic applications is quite robust and continues to grow rapidly [8–10]. Particularly, MNPs made of iron oxides (i.e., magnetite (Fe_3O_4)/maghemite ($\gamma\text{-Fe}_2\text{O}_3$)) proved to be extremely beneficial in a wide spectrum of industrial and research areas ranging from catalytic systems, magnetic storage, photonic and electronic devices to biological, biomedical, and drug delivery applications [11–14]. The use of colloidal and biocompatible MNPs for both diagnostics [15–18] and therapeutics [19–23] has occupied a unique position among other nanocomposites. The main reason for such immense biomedical utilization is their low toxicities and excellent superparamagnetic properties allowing them to be utilized as contrast-enhancing probes for magnetic resonance imaging (MRI). Besides, MNPs hold great promise as hyperthermia agents and chemotherapeutic carriers for controlled and magneto-responsive targeted drug delivery, enabling minimized side effects and reduced drug resistance of the conventional chemo-drugs. Many previous reviews in this field focus chiefly on the use of MNPs as MRI contrast agents and their use in biomedical applications, particularly diagnostic applications [24–28]. The uniqueness about this chapter is to rather give an overview on the use of MNPs in advanced cancer theranostics, particularly the potential utilization of drug-conjugated MNPs in magnetic drug targeting, drug delivery, and magnetic hyperthermia. Special emphasis is set on important and notable examples employing MNPs for multimodal imaging, tissue engineering, and targeted drug delivery therapeutics in preclinical studies. Possibilities, challenges, and postulated barriers for effective translation of the developed magnetic cancer nanomedicines into the clinic is also conferred, providing an overview on past and present magnetic nanoformulations used currently in clinical settings or yet to be clinically approved. Understanding current limitations and learning lessons from approved cancer nanomedicines will definitely impact clinical success of drug-conjugated MNP delivery systems and their future potential in magneto-responsive anticancer clinical theranostics.

The main advantages of using MNPs for medical cancer theranostics are: (1) easy scaled-up preparation; (2) facile chemical functionalization and drug conjugation; (3) nano sizes (5–200 nm); (4) excellent biocompatibilities and stabilities; and (5) superior magnetic responsiveness (Fig. 6.1). Such unique properties allow MNPs to be utilized as imaging contrast probes, hyperthermia agents, magnetic-guided vectors, and drug delivery carriers with great potentials in clinical settings. Nevertheless, despite such unique capacities, urgent development of magnetic nanoformulations are constantly needed to overcome several current major challenges and limitations, in continuous attempts to efficiently translate delivery of therapeutics into clinical patient care. Such successful translation from “lab to clinic”

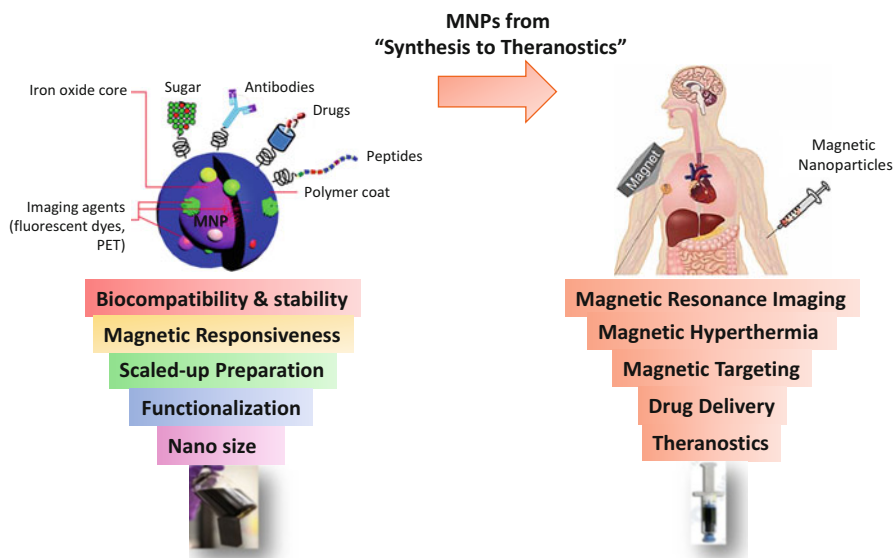


Fig. 6.1 Illustrative image showing the architecture of magnetic nanoparticles (MNPs), their functionalization, and their unique intrinsic properties. Such well-designed MNPs can be utilized in advanced medical theranostics as magnetic imaging probes, hyperthermia agents, magnetic-guided vectors, and drug delivery carriers

is dependent upon several important factors including their physicochemical properties, intrinsic toxicities, drug loading/release, scaled-up syntheses, and, hence, optimizing overall parameters for effectual medical performance. To begin with, a brief overview on the utilization of MNP-based nanotechnology in advanced cancer research, particularly their magneto-responsive use in drug targeting, hyperthermia, and drug delivery, is presented. In that regards, many names have been denoted in the literature for such MNPs ranging from monocrystalline iron oxide nanoparticles (MIONs), crosslinked iron oxides (CLIONs), superparamagnetic iron oxides (SPIONs), and ultrasmall SPIOs (USPIONs) depending on their physiochemical properties. Herein, to avoid confusion, all will be referred to as simply MNPs, unless otherwise indicated for a particular application.

3.1 MNP-Based Nanotechnology in Cancer Treatment

Although the search for enhanced cancer therapies are ongoing on a daily basis, many present chemotherapeutic drugs are not reaching the desired efficacies. With a deeper understanding and researching of how cancer progresses, innovative therapeutic approaches beyond the conventional therapies are constantly evolving. A range of cancer therapies such as targeted therapy, immunotherapy, hormonal therapy, angiogenesis inhibitors, and thermal ablation (i.e., hyperthermia) are under

extensive development and some have reached clinical trials [29]. Nevertheless, all the conventional and emerging treatments are often limited by the accessibility to the sites of metastases and the lack of selectivity/specificity towards tumor cells, especially for advanced stages of cancer. Furthermore, such approaches suffer from tremendous harsh and long-term side effects, drug resistance, high dose requirements, and low-to-moderate efficacies. Recently, the use of personalized and specific tumor molecular profiles, commonly known as personalized medicine, to determine optimum individualized therapy options is examined [30]. In this approach, treatment decisions are based on tumor molecular biomarkers (i.e., DNA, RNA, metabolic profiles), rather than tumor tissue type or anatomical site of origin. Nonetheless, doubts remain to whether cancer patients respond to such therapies [31]. Up to now, it seems multimodal therapy (combination of radio, chemo, or immuno, etc.), along with personalized cancer treatments, on case by case assessment, provides the best chances for patients' survival in clinical practice. Thus, continuously seeking alternative and complementary ways to detect, treat, and combat metastatic cancer with less side effects is an everyday necessity.

With the application of nanotechnology to the medical field (referred to as nanomedicine), novel promising approaches to treat cancers, particularly the metastatic types, have been actively established [32]. Doxil[®] (liposome-encapsulated Doxorubicin (Dox)) is widely used to treat ovarian cancer and Kaposi's sarcoma while protecting patients from the cardiotoxicity of the free drug [33]. Abraxane[®] (protein-bound Paclitaxel (PTX)) is approved to treat metastatic breast cancer [34]. Feraheme[®] (iron oxide MNPs), which is approved for the treatment of iron deficiency anaemia, has shown efficacy for the early staging of lymph node metastasis in patients with prostate and testicular cancers and are in current trials for brain tumor imaging [35]. Although very few nanomedicines have reached the clinic [10], many others have been hampered by many biological and chemical barriers, especially when it comes to injecting nanoformulations intravenously to target drugs to specific sites of tumors. With identifying the problems and pitfalls of directing drugs using nanomedicines and overcoming the many challenges encountered [36], it is anticipated that future nano-based systems will introduce new capabilities, including advances in localized drug delivery and treatment responses. Bearing in mind the long time (10–15 years) it takes to efficiently move basic science discoveries into clinical applications – often described as “*bench to bedside*” translational work, an indeed great endeavors are awaiting in our conducts to effectively treat cancer.

3.1.1 Magnetic Drug Targeting

Since MNPs are highly responsive to an external magnetic field, such unique property makes it possible to concentrate the particles in the target area by means of a magnetic field using either an internally implanted permanent magnet or an externally applied magnetic field (Fig. 6.2a). This phenomenon is known as magnetic drug targeting (MDT). In MDT, MNPs must have high magnetic susceptibility to possess higher local concentration efficiency. A high-field, high-gradient, or rare earth magnet (i.e., Neodymium Nd-Fe-B) over a targeted tumor site, in order to in situ concentrate and retain MNPs is typically used. In fact, the idea of using magnetic

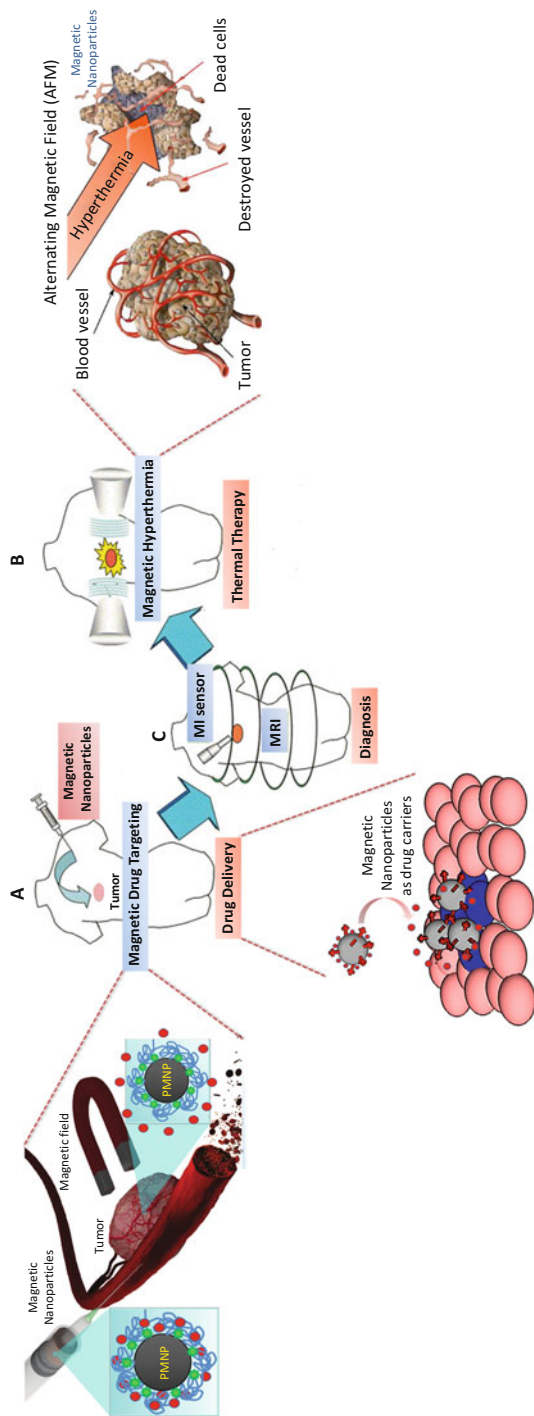


Fig. 6.2 The theranostic uses of MNPs for (a) magnetic drug targeting (MDT) and drug delivery; (b) magnetic fluid hyperthermia (MFH), and (c) magnetic resonance imaging (MRI) diagnosis. (a) Schematic representation of drug-conjugated MNPs injected intravenously and directed to the tumor by the absence (drug delivery) or the presence of an external magnet (MDT), releasing the drug selectively at the tumor site. (b) Photograph of MFH treatment comprising intratumoral injection of MNPs or drug-conjugated MNPs at the diseased site and applying an alternating magnetic field (AMF) to destroy the tumor. (Adapted with permission from Refs. [265–267])

particles for drug targeting in cancer therapy dates back to the early 1960. Relying on intentional obstruction of tumor vessels, Freeman et al. were the first to propose that magnetic microspheres could be transported through the vascular system and concentrated in a specific part of the body with the aid of an external magnetic field [37]. Thereafter, many groups described the use of various types of magnetic microparticles or NPs loaded with different chemotherapeutics for magnetically guided drug targeting in cancer tumor-bearing animal models [38–42]. Importantly, phase I–III clinical studies of drug-loaded magnetic targeted carriers in patients with hepatocellular carcinoma were reported [43, 44]. However, in such or interrelated studies [45], while preclinical results turned out in complete or partial tumor remission, phase I–III clinical trials resulted in no clinically significant efficacies compared to free drugs with insufficient tumor responses. Limited by the magnet strength and tissue penetration depth (i.e., penetration depth of ~ 0.5 cm when using a 0.6 T Nd-Fe-B permeant magnet), MDT is, thus, only suitable for diseased areas that are fairly superficial or therapy that may need a minimal invasive procedure [46–49]. In recent years, however, gradient magnetic field (e.g., 7 T MRI scanners) has been proved to be a useful tool to efficiently and better direct MNP carriers [50].

3.1.2 Magnetic Fluid Hyperthermia

With their intrinsic magnetic abilities, one of the major potentials of MNPs in clinical settings is their use as magnetic hyperthermia vehicles (Fig. 6.2b). However, to realize the importance of such approach, we need to first define hyperthermia. Hyperthermia implicates the use of “high temperature heat to damage and kill cancer cells or to make cancer cells more sensitive to the effects of radiation and/or chemotherapy” [51, 52]. In this therapy, tumors are typically heated to 41 °C and up to 47 °C, as tumor cells possess higher heat sensitivity over normal cells, resulting in damage to tumor cells only. The warming of a local (specific tumor site), regional (organ, limb, or body cavity), or whole body (metastatic cancer) is achieved using various techniques that deliver energy to heat the tumor (i.e., by electromagnetic field, microwaves, radiowaves, ultrasound, or infrared waves). Although these techniques are able to increase the intracellular temperature up to the cellular death, they can provoke harmful side effects such as ionization of the genetic material or lack of selectiveness, causing harmful secondary effects in the surrounding healthy tissues. Furthermore, each of these external triggers has certain limitations: for example, electromagnetic fields can penetrate deeply (>15 cm) into tissue, but they are difficult to focus [53, 54]. High-intensity focused ultrasound (HIFU) can penetrate into tissue to a volume of several mm³, but its capabilities are diminished when applied within bones or gas-filled organs [55]. Infrared waves, spanning ~ 750 – 1300 nm, penetrate tissue to depths of up to 1 cm, after which penetration decreases substantially [56]. Thus, the search of new mechanisms capable of efficiently increasing the temperature of damaged areas specifically, while keeping the rest of tissues healthy is immensely needed.

Magnetic hyperthermia or magnetic fluid hyperthermia (MFH) involves delivering MNPs at the tumor site and applying an alternating magnetic field (AMF) [57–59]. This thermotherapy is based on the fact that MNPs can transform

electromagnetic energy from an external high-frequency field to heat due to relaxation of their rotating magnetic moments. For clinical use of MNPs in hyperthermia, the NPs must have small sizes (to reach tumor sites), high saturation magnetizations (to guarantee efficient heating), and homogenous distributions (to reach uniform therapeutic temperature throughout tumor tissues), hence, inducing minimal damage to peritumoral tissues. Clinical studies for application of MNP hyperthermia therapy in humans were initiated in 2007 on prostate cancer [60]. The results revealed that interstitial heating using MNPs was feasible and well tolerated in patients with locally recurrent prostate cancer. More recently, MNPs were used in hyperthermia therapy to treat metastatic bone tumors, with reduced lesion and visible bone formation observed [60]. Another noteworthy development investigated the effectiveness of MFH using dextran-coated MNPs and silane-coated MNPs (denoted as BU48) on intracellular hyperthermia of human mammary carcinoma cells in vitro and intratumorally injected in a mouse model in vivo [61, 62]. Their successful studies led to preclinical and clinical testing in patients with prostate and glioblastoma tumors which led to clinical approval of NanoTherm[®] [63–65]. Recently, therapies combining MFH/MDT or MFH/MDT and chemotherapy are currently under extensive investigations, where designed thermo-responsive drug-loaded MNPs release chemotherapeutic drugs selectively by applying external magnetic field [66, 67]. The heat generated by MNPs change the structure of the thermo-sensitive materials that usually turns into swollen structures, leading to the release of loaded drugs at tumor sites, thereby increasing the effectiveness of therapy [52]. Likewise, the combination of magnetic hyperthermia and radiotherapy has been proved to be clinically effective in brain cancer and prostate cancer patients undergoing phase II trials in humans [63].

3.1.3 Magnetic Drug Carriers

Many chemotherapeutic drugs clear from the body rapidly or are expelled out of cancer cells/tumors, preventing their intracellular accumulation to cytotoxic levels [68]. Consequently, the efficiency of systematic chemotherapeutics is reduced, leading to serious off-target side effects. This challenge has been a major cause in cancer chemotherapy utilizing potent drugs that are highly toxic to both cancerous and normal cells, often leading to failure of tumor chemotherapy clinically [69]. The clinical significance of using the nanovehicle approach lies in the ability to specifically direct a drug or drug carrier to intended targets to minimize conventional drug-originated systemic toxic side effects (Fig. 6.2). In general, targeted drug delivery refers to largest drug accumulation within the target site using drug-loaded NPs. For effective delivery, the MNP system should: (1) possess large payloads of drugs per NP attached and delivered; (2) be targeted to specific diseased tumor, and (3) allow controlled-release of drugs at the intended target intracellularly and intratumorally with high efficacies. Directing MNPs to sites of metastasis in cancer is majorly based on passive and/or active approaches, which can be achieved irrespective of NPs possessing magnetic materials.

“*Passive targeting*” implies that the delivery of therapeutic NPs is primarily driven by the enhanced permeability and retention (EPR) effect [70]. Because of

the leaky endothelium and vascularate at the diseased site (i.e., tumor) that is absent in normal tissues and organs, significant and increased localization of NPs (i.e., extravasation) can be achieved. This process is further aided by the dysfunctional tumor-limited lymphatic drainage, preventing NPs to get back into the circulation. In contrast to normal tissues, most solid tumors feature rapidly developed vasculature with loose tight-junction and fenestrations ($\sim 200\text{--}2000$ nm), allowing increased tumor vascularate permeability [71]. These factors combined lead to selective NP accumulation in many tumors through EPR effect. However, this effect is limited to tumors larger than ~ 4.6 mm in diameter (~ 100 mm³ in volume), hindering its use for targeting small, unvascularized metastases [72].

“Active targeting” (also known as targeted drug delivery), on the other hand, is used to describe specific interactions between functionalized nanocarrier and the target diseased cells having over or exclusive expression of epitopes or receptors. It, thus, requires a chemical specificity that enables the NP to bind to unique moieties that are presented by the specific cancer cell. The conjugation of specific targeting ligands to the NP surfaces are typically based on two main chemistries: (1) reactive functionalities present on the nanomaterial platforms; (2) functional groups present on the targeting ligands (proteins, peptides, carbohydrates, antibodies, nucleic acids, folic acid, enzymes, genes, growth factors, imaging agents, etc.) to be conjugated [73]. Cancer cells, whether metastatic or part of the primary tumor, can upregulate certain cell-surface molecules and secreted factors, and may even express specific endogenous surface proteins that can be targeted. Thus, the binding affinity of the NP to the molecules of interest must be carefully considered, as well as binding specificity and immunological effects. Antibody conjugates (i.e., drug, polymer, or radioisotope-labeled antibodies) are currently in the clinic for targeting cancer. ¹³¹I-tositumomab (Bexxar) is a combination therapy that involves a radio-labeled CD20-specific antibody for targeting follicular B cell lymphoma [74]. Antibody-based conjugates have been also used on various nanodelivery systems [75–77]. Likewise, short peptides, including those with integrin-binding domains, can be conjugated to MNPs and can increase their binding to specific cell types within a tissue [78–80]. High-throughput methods, such as phage display, are being constantly examined to discover novel targeting ligands, ranging from antibodies and peptides to nucleic acid-based ligands (aptamers) [81]. Small-molecule-binding domains, such as the folate receptor which is overexpressed in human oral carcinoma, metastatic breast, colorectal, and other cancers, are also under extensive investigations and demonstrate affinity to folic acid-functionalized NPs [82].

4 Experimental Methodology

4.1 Preparation of MNPs for Biomedical Applications

Achieving a series of size-controlled, narrowly dispersed, uniform, highly magnetic, stable, colloidal, and biocompatible MNPs for biomedical and clinical endpoints remain unambiguously challenging. Consequently, numerous publications

describing various synthetic routes to prepare such high-quality MNPs have appeared and are excellently reviewed elsewhere [5, 12, 14, 83–85]. In fact, particular attention should be directed to the synthetic methods of MNPs as those can significantly affect the size, shape, structure, dimensions, properties and, hence, the fate of the NPs in a certain biomedical application. The major difficulty in designing any synthetic technique remains to employ simple, practical, and cost-effective ways to produce large quantities of MNPs that are stable for months and do not precipitate from their dispersions. The other key factor is using the above approach to get uniform nanocolloids with controlled sizes and morphologies. Of the various physical, chemical, or biological methodologies utilized (i.e., laser pyrolysis, sonochemical, vaporization-condensation processes, biological extracts etc.), solution phase chemical procedures including co-precipitation, thermal decomposition, hydrothermal/solvothermal, microemulsion, and sol-gel syntheses are the most employed [83, 86–88]. Most commonly, two main synthetic techniques were popularized for the preparation of MNPs utilized for biomedical or clinical endpoints: co-precipitation and thermal decomposition. Thereafter, the as-prepared MNPs are typically characterized using different microscopy and spectroscopy techniques including transmission electron microscopy (TEM), high-resolution TEM (HR-TEM), scanning electron microscopy (SEM), dynamic light scattering (DLS), zeta-potential, thermo-gravimetric analysis (TGA), X-ray diffraction (XRD), UV-vis absorption, Fourier transform infrared (FTIR) spectroscopy, fluorescent emission spectroscopy, and high resolution-magic angle spinning (HR-MAS) NMR [89]. For magnetic characterization, magnetization curves and relaxivity measurements are routinely recorded.

4.1.1 Co-precipitation Method

Co-precipitation of iron salts in basic aqueous media prepared in the presence or absence of surfactants/polymers has been the foremost employed approach to produce hydrophilic MNPs readily soluble in water (Fig. 6.3a) [90, 91]. This protocol was first explored by Massart in 1981 and is, therefore, known as the “Massart method” [92]. This co-precipitation procedure is probably the simplest, easiest, and fastest methodology to obtain MNPs. However, the obtained NPs are commonly agglomerated due to difficulty in controlling narrow size distribution, shape, uniformity, and morphology [93]. Typically, magnetite or maghemite NPs are prepared by aging appropriate stoichiometric ratios of ferrous (Fe^{2+}) and ferric (Fe^{3+}) salts in an aqueous basic media (NH_4OH or NaOH) at $\sim 25\text{--}100$ °C temperatures. When preparing magnetite, the reaction should be done under inert atmosphere to protect the core against oxidation to other oxide forms. The MNPs produced are mostly spherical, negatively charged, and relatively homogenous. The yield, size, shape, crystallinity, surface properties, and polydispersity of the final material depend on many factors including the sequence of addition of reagents, pH, temperature, stirring or mechanical agitation, and nature/concentration of the iron salts. Changes in any of these parameters determine the composition of the nanocrystal and, consequently, the electrostatic surface charge, morphology, and biological performance of the prepared NPs [94]. A typical precipitation procedure to produce

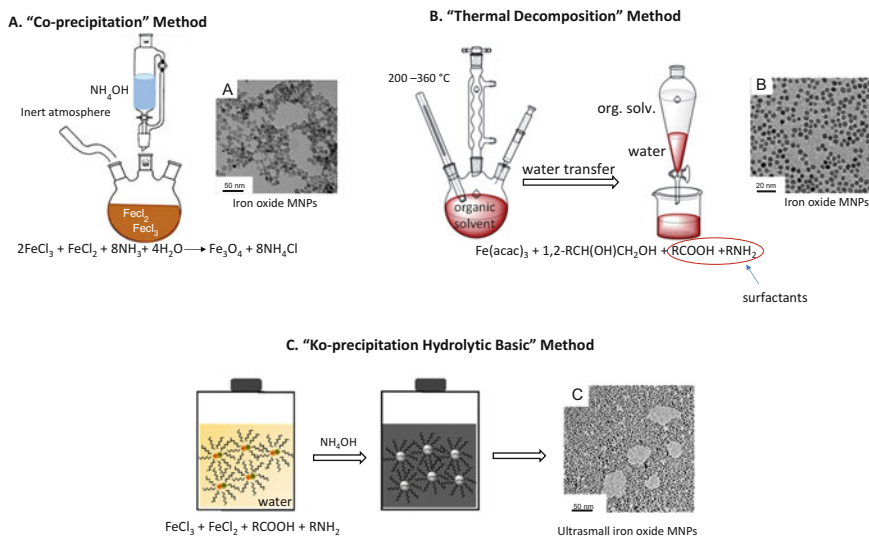


Fig. 6.3 Schematic representation for the most popular methods utilized for the synthesis of iron oxide MNPs for biomedical applications. Typical representative transmission electron microscopy (TEM) images for each approach are shown. (Adapted with permission from Refs. [91, 114, 128])

magnetite with relatively good size, shape, and uniformity consists of mixing a solution of $\text{FeCl}_3 \cdot 6\text{H}_2\text{O}$ and $\text{FeCl}_2 \cdot 4\text{H}_2\text{O}$ (2:1 molar ratio) with stirring or mechanical agitation of about 2000 rpm under inert atmosphere. The resulting solution is heated to 70–100 °C, and immediately the speed is elevated to 7500 rpm while adding quickly a solution of NH_4OH (10% by volume). A dark precipitate of Fe_3O_4 magnetite NPs is classically produced. As discussed, in an aqueous alkaline medium, polarizing or highly charged cations or anions (i.e., ammonium or alkaline) may give rise to flocculation or agglomeration. Small NPs have an extremely high surface area to volume ratio and cluster easily to minimize their surface energy. Thus, the addition of chelating organic anions (i.e., carboxylates, phosphates, and sulfates) or complexing polymers (e.g., dextran, polyethylene glycol (PEG), polyvinylpyrrolidone (PVP), polyglutamic acid (PGA), polyvinyl alcohol (PVA), polyacrylic acid (PAA), polylactic acid (PLA), poly(lactic-co-glycolic acid) (PLGA), polyethyleneimine (PEI), etc.) during the formation of iron oxides prevents the agglomeration to certain extent, and imparts protection and stabilization to the NPs, preventing the core material from degradation or oxidation [5]. According to the nature of the organic coat, and the molar ratio between the coat and the iron salts, the chelation of these organic ions/complexing polymers on the iron oxide surface can either prevent nucleation and then lead to larger particles or inhibit the growth of the crystal nuclei, leading to small NPs. Importantly, the coat renders the NPs biocompatible, which is significant for biomedical applications. In many cases, the protecting coat can be used for further functionalization, i.e., with other NPs or targeting ligands (i.e., carbohydrates, antibodies, cell penetrating peptides, small

peptides, aptamers, folic acid) [73]. For instance, dextran-coated iron oxide-based magnetic materials (i.e., CLIONs, SPIONs, USPIONs, and related systems) have been clinically approved for imaging of liver lesions and lymph nodes (i.e., Feridex[®], Resovist[®], Sinerem[®]) [95, 96]. On the other hand, silica-coated magnetic materials are also extensively utilized and has been used in clinical imaging (GastroMARK[®]), due to their reactive silanol surface groups [97, 98]. A clear advantage of this latter approach is the easy, versatile, and well-established chemistry used for further modification of the surface with the different commercially available siloxanes [99–101]. It is to be noted that recent progress on the precipitation of stabilized NPs using different capping agents (i.e., small organic molecules/anions [102–104] or polymers/block copolymers [105–107]) has been exploited to improve on size distributions, stabilities, and dispersibilities. Nevertheless, majority of the resulting materials formed using the above-modified hydrolytic routes were practically agglomerated and uncontrolled.

4.1.2 High-Temperature Thermal Decomposition Method

High-temperature thermal decomposition of organometallic precursors (Fe(Cup)₃, Fe(CO)₅, Fe(acac)₃, Fe-oleate, Fe-carboxylate or mixed M²⁺Fe₂³⁺-oleate) in high-boiling nonpolar organic solvents at elevated temperatures (~200–360 °C) has been elegantly demonstrated to yield hydrophobically coated MNPs with noticeable improvements in size control, monodispersity, and uniformity [108–114]. Ligand-exchange approaches are then typically employed to replace the hydrophobic chains on the particle surface by hydrophilic biomolecules rendering them water soluble (Fig. 6.3b) [115–118]. The synthesis of nanocrystals using such organic-based thermolysis procedures have popularized two major approaches: “hot-injection” by rapid introduction of reagents into the hot solution (≥ 300 °C) containing surfactants or “heating-up” a premixed solution of precursors, surfactants, and solvent to a certain temperature (up to 360 °C) to achieve the burst of nucleation and initiate the particle growth [119]. This latter procedure has been successfully utilized to synthesize monodisperse nanocrystals of a wide range of materials [120]. Among the many examples, thermal decomposition of organometallic compounds (i.e., iron-oleate complex) in high-boiling-point nonpolar organic solvents (i.e., benzyl ether) has proven to be an attractive route for the synthesis of highly monodisperse, uniform, and crystalline MNPs. Hyeon et al. synthesized superparamagnetic maghemite γ -Fe₂O₃ nanocrystals via a high-temperature aging of iron-oleic metal complex using iron pentacarbonyl (Fe(CO)₅) in the presence of oleic acid in dioctyl ether at 100 °C and heating up to 300 °C to produce uniform MNPs [110]. In 2004, instead of using the toxic and expensive Fe(CO)₅, the same group reported the elegant ultralarge-scale synthesis of monodispersed nanocrystals via the slow heating of metal-oleate complex and oleic acid in high boiling solvents [108]. Cheon et al. prepared well-defined single-crystalline γ -Fe₂O₃ nanocrystals with different shapes ranging from diamonds, triangles, to spheres were also synthesized using the thermolysis of Fe(CO)₅ in the presence of dodecylamine as the capping ligand [121]. Various metal NPs were also synthesized using the

heat-up thermal decomposition method. Sun and his colleagues prepared highly uniform monodisperse FePt nanoparticles by heating a reaction mixture containing platinum acetylacetonate, $\text{Fe}(\text{CO})_5$, 1,2-hexadecanediol, oleic acid, and oleyl amine [113]. Based on this method, the Sun group enclosed the most cited and widely followed synthesis of highly monodispersed controlled-sized magnetite Fe_3O_4 nanoparticles (4 nm) from a high-temperature (200–300 °C) 1,2-hexadecanediol solution of iron(III) acetylacetonate ($\text{Fe}(\text{acac})_3$) in the presence of oleic acid and oleylamine [112]. Larger size NPs (8, 12, 16 nm) can be formed via seed-mediated growth of the smaller nanocrystals. By controlling the quantity of the NP seeds, different sizes of nanoparticles can be synthesized. Furthermore, different sizes of metal ferrites (MFe_2O_4 , where $\text{M} = \text{Co}, \text{Fe}, \text{Mn}$, etc.) were also prepared in the form of monodisperse nanoparticles by the seed-mediated growth process using $\text{Fe}(\text{acac})_3$ and $\text{M}(\text{acac})_2$ as reactants [114]. In another noteworthy report, the synthesis of size- and shape-controlled magnetic (Fe, Cr, Mn, Co and Ni) oxide nanocrystals, based on high-temperature pyrolysis of metal fatty acid salts as the precursors and alkylamines as the activation reagents in noncoordinating solvents (octadecene) heated at 300 °C, was also reported [122]. Extensive mechanistic studies and observations have shown that enhanced uniformity with better and narrower size distributions can occur at high temperatures in organic solvents but is more difficult to control in aqueous media at low temperatures [119, 120]. Despite the evident improvements in size control and monodispersity using the above-mentioned procedures, such thermolysis method has major limitations. First, it is necessary to heat the reaction mixture to very high temperatures up to 360 °C which needs highly trained personnel and, in practice, is dangerous and tedious. Second, the polyalcohol components used as the iron-reducing agent are not only expensive, but also cause many side reactions of polyaldehydes and polyorganic acids making the process of separating the byproducts extremely complex. Besides, difficult multistep processes of synthesizing and purifying the intermediate precursors are applied reducing the reaction efficiencies [123]. All this often leads to inconveniency for industrial scale-up. Finally, there is a limit to the choice of the NP capping agents which should be only long hydrophobic alkyl chains. This is a chief and major disadvantage of the thermolysis approaches, as no polymers can be directly used and the final product is, thus, only dispersible in organic nonpolar solvents (i.e., hexanes). In short, these high-temperature thermolysis methods are complicated, costly, toxic, industrially limited, and usually lead to NPs with poor solubility in water greatly limiting their bio-clinical fates. Examples to improve on the thermal decomposition in organic solvents to fabricate one-step water-soluble monodisperse magnetite nanoparticles have been reported. For instance, Li and coworkers reported one-pot thermal decomposition of $\text{Fe}(\text{acac})_3$ using strong polar 2-pyrrolidone as a coordinating solvent to produce water-soluble magnetite nanocrystals [124]. They also have succeeded in preparing water-soluble magnetite nanocrystals simply by refluxing inexpensive hydrated ferric salts in 2-pyrrolidone [125]. Ge et al. synthesized water-soluble magnetite nanocrystals by rapidly injecting a preheated NaOH /diethylene glycol solution into a mixture

of PAA/FeCl₃/diethylene glycol heated at ~ 245 °C [126, 127]. Nevertheless, those thermolysis procedures are not very popular due to their coating limitation and, thus, followed to lesser extent by researchers.

4.1.3 Ko-precipitation Hydrolytic Basic (KHB) Method

As discussed above, using the conventional water-phase co-precipitation protocols, there tends to be difficulties in achieving high well-defined narrow nanocrystalline size, monodispersity, and uniformity. On the other hand, using the thermal decomposition procedures requires heating to very high temperatures, which in practice is dangerous, tedious, and need well-trained personnel and the resulting material is not water soluble. Consequently, there is still no notable universal practical process to produce MNPs with good monodispersity, required size distribution, and tailor-made versatility. A simple, fast, and safe strategy to efficiently produce biocompatible, colloidal, well-dispersed and stable MNPs, avoiding the complex high-temperature thermal chemistry is, thus, highly desirable. In a recent work, we sought to design a method of producing well-controlled highly-magnetic narrowly-dispersed metal oxide nanocolloids [128]. Our methodology offers the simplicity of the conventional co-precipitation procedures, with the high-quality dispersibility usually obtained by the thermolysis processes. This methodology offers simpler, faster, nontedious, and tailor-made strategy to effectively produce various acid-stabilized colloidal and stable MNPs dispersed in hydrophilic or hydrophobic solvents, on demand. The approach relies on sequential basic hydrolytic in situ precipitation (*Ko-precipitation*) of inexpensive and nontoxic metal salts compartmentalized by stabilizing organic acids (hydrophobic acids, polymeric acids, amino acids or polyamino acids) and amines, without the use of high-boiling point solvents and elevated temperatures (Fig. 6.3c). The so-called “*Ko-precipitation Hydrolytic Basic (KHB)*” method consists of the following components: inexpensive metallic ions dissolved in aqueous media (i.e., Fe³⁺ and M²⁺ salts, where M = Ti, Cr, Mn, Fe, Co, Ni, Cu and Zn), organic carboxylic acid surfactants including saturated or unsaturated hydrophobic acids (C_nCOOH, C_n: hydrocarbon, 6 < n < 30) polymeric acids (i.e., hyaluronic acid, carboxymethyl dextran, and their acid-based derivatives, acrylic-based polymers (PAA, PLA, PLGA), or amino acids (i.e., arginine, lysine, glutamic acid) and their polyamino acids, in addition to co-surfactants (alkylamines C_nNH₂, C_n: hydrocarbon, 6 < n < 30), and a base (NH₄OH or NaOH) [129]. In a specific example, iron oxide nanocolloids were prepared by sequentially mixing Fe³⁺ salts, with different concentrations of oleic acid for 20 min. Subsequently, hexylamine and aqueous Fe²⁺ salts were then added into the mixture. Addition of the base allowed the formation of ultrasmall, ultrastable, and well-dispersed nanocolloids of iron oxide MNPs. The color of the solution changes gradually from reddish emulsion to black solution upon MNP precipitation. The particle size can be tuned from 2 to 6 nm by controlling the acid to iron precursor molar ratios. Depending on the organic acid used, the obtained MNPs can be readily dispersed in various solvents for months with remarkable stabilities. It is worth mentioning that monosized MNPs synthesized below a critical particle size <15 nm typically consist of a single magnetic domain with superparamagnetism and high saturation magnetization

properties. This is an important feature as superparamagnetic NPs respond rapidly to an applied magnetic field, but exhibit negligible residual magnetism away from the magnetic field, rendering such prepared particles especially attractive for *in vitro* and *in vivo* biomedical applications.

5 Key Research Findings

5.1 MNPs for Diagnosis, Multimodal Imaging, and Tissue Engineering

The effective treatment of metastatic cancerous disease chiefly depends on early imaging and appropriate diagnosis. Molecular imaging with high-relaxivity contrast MRI probes is one of the most promising diagnostic approaches in this regards, offering resolution of anatomy and early detection of specific associated disease biomarkers [130, 131]. To date, several MNPs based on iron oxide have been approved for clinical use as MRI contrast agents. One of the first MRI agents approved by FDA was an oral contrast based on large iron oxide particles for MR imaging of bowel/gastrointestinal tract (i.e., GastroMark[®]/Lumirem[™], hydrodynamic radius (D_H) = 300 nm) [97]. Another oral iron-based negative MRI contrast is known as Abdoscan[®] (Ferristene), which is 50 nm iron oxide MNPs in 3.5 μm spheres of polystyrene resin [132]. Nonetheless, production of both contrasts was discontinued because of low commercial and medical interest. The second type of negative contrasts that has passed through the preclinical and clinical stages is imaging agents for intravenous, intratumoral, intrathecal, or intramuscular administration. These are mainly used to image liver/spleen/lymph nodes in patients with pelvic, prostate, bladder, or breast cancer, and are briefly summarized here. Relatively large iron oxide MNPs are used for liver/spleen imaging such as Feridex[®]/Endorem[™] with D_H = 80–200 nm, and Resovist[®]/Cliavist[™] with D_H = 60 nm [98, 133]. Smaller iron oxide particles are selected for lymph node/bone marrow/carotid atherosclerotic plaques imaging (i.e., Sinerem[®]/Combidx[™], D_H = 20–40 nm) [134, 135], and perfusion and liver lesion imaging (i.e., Clariscan[®]/Feruglose, D_H = 20 nm) [136]. Further details on the use of MNPs as MRI contrast agents can be found in the following references [28, 96, 137–139].

Though FDA cleared the use of the above-mentioned MNPs, the two main clinically used commercial agents (i.e., Feridex I.V.[®] and Gastromark[®]) have been discontinued by their manufacturers and, hence, withdrawn from the market mainly because of unsatisfactory statistical evidence of efficacy. Moreover, the approved Resovist[®], Clariscan[®], and Sinerem[®] showed either insufficient efficacy or proved to be commercially uncompetitive with the gadolinium(Gd)-based positive contrasts (i.e., Primovist/Eovist – which is preferred by medical doctors with high specificity for liver targeting). In brief, these FDA-approved MNP products were discontinued despite their excellent biocompatibility and safety profiles. Only Resovist[®] is currently available in only a few countries (i.e., Japan) and Sienna+[®] is in use in Europe

for sentinel lymph node biopsies imaging [140–142]. These carboxydextran-coated MNPs are subcutaneously injected into the interstitial tissue of patients with breast cancer and detected with a specific detection system known as SentiMag[®] magnetometer, and not by MRI. *Unfortunately, as of now, there is no commercially available MNP-based imaging contrast agent for intravenous administration used in the clinic.*

5.1.1 MNPs for Multimodal Imaging

An important and powerful means in biomolecular imaging for patients with metastatic cancer is MNP-based multimodal imaging (Fig. 6.4) [143, 144]. MRI, X-ray computed tomography (CT), positron emission tomography (PET), single photon emission computed tomography (SPECT), and fluorescence imaging display complementary strengths in terms of spatial and temporal resolution, with the possibility to generate contrast, sensitivity, and multiplex imaging [145]. Thus, dual- or multimodal labeled MNPs, which combine two or more imaging modalities into a single vehicle, have been pursued for such purposes. Such all-in-one designed agents can combine the advantages of different techniques, such as the important anatomical

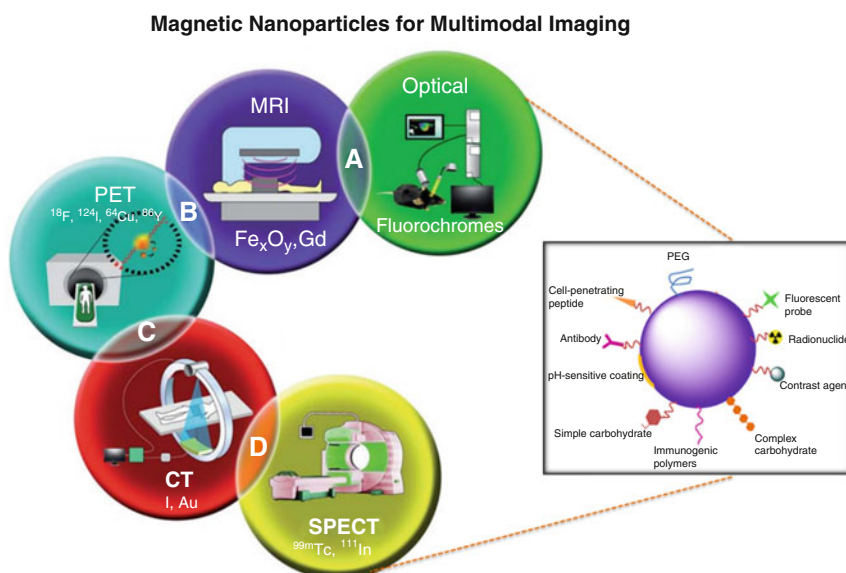


Fig. 6.4 Schematic for the use of functionalized and labeled MNPs for multimodal diagnostic imaging including optical, MRI, positron emission tomography (PET), X-ray computed tomography (CT), and single photon emission computed tomography (SPECT). These imaging techniques display complementary strengths in terms of spatial and temporal resolution, with the possibility to generate contrast, sensitivity, and multiplex imaging, offering a powerful means in increasing the specificity and signal strength of diagnosis for patients with metastatic cancer. (Reproduced with permission from Ref. [268])

information gained from the soft-tissue contrast of MRI with the high sensitivity of PET, increasing the specificity and signal strength of diagnosis [146, 147]. Besides, when fluorochromes are coupled to MNPs, optical imaging including fluorescence reflectance imaging, fluorescence-mediated tomography (FMT), confocal microscopy, flow cytometry, and near-infrared (NIR) fluorescence imaging is feasible. In particular, fluorochromes that emit in the NIR spectral window (preferably VT680, AF680 or Cy5.5) penetrate tissue for several centimeters, thereby rendering fluorescence imaging techniques clinically practical. The target biomolecules can be also specifically labeled with fluorescent probes, dyes, tags, crosslinking reagents or imaging agents before being attached to MNPs. Josephson et al. conjugated arginyl peptides to CLIO, followed by the attachment of the indocyanine dye Cy5.5, allowing lymph nodes detection by MRI and NIR fluorescence simultaneously [148]. In another work, Pittet et al. described the preparation of magneto-fluorescent NPs having membrane-translocating properties for immune T-cell labeling in vitro and multimodal imaging of administered cells in vivo [149]. In an elegant report, Moore et al. prepared cancer-targeted multimodal imaging probes consisting of Cy5.5-CLIO attached to FITC-labeled EPPT peptides to target the underglycosylated mucin-1 (uMUC-1) antigen in vitro and in a tumor-bearing animal model (Fig. 6.5a) [150]. In their work, in vivo MRI and NIR imaging experiments showed specific accumulation of the probe in uMUC-1-positive tumors, but no signal in control tumors. Such multimodal imaging probe has a potential to greatly aid in screening prospective patients for early cancer detection as well as staging and imaging of the recurrence of tumors and monitoring of therapeutic efficacy. In another study, Nahrendorf et al. demonstrated the usefulness of trimodal imaging probes where they labeled a dextranated and DTPA-modified magneto-fluorescent NP (20 nm) with the PET tracer ^{64}Cu to yield a PET, MRI, and optically detectable probe allowing imaging of macrophages in inflammatory atherosclerotic plaques (Fig. 6.5b) [151]. Following this study, the same group embarked on the fabrication of hybrid PET-CT/FMT imaging CLIO probes containing the clinical PET ^{18}F -isotope and a far-red fluorochrome (VT680) for FMT, fluorescence histology, and flow cytometry (Fig. 6.5c) [152]. Using a mouse model of cancer, they demonstrated the distinct tumoral locations in multiple channels in vivo by measuring tumoral proteases, macrophage content, and integrin expression simultaneously. The combined PET-CT/FMT multichannel imaging offers parallel interrogation of up to five molecular targets. Recently, Kirschbaum et al. illustrated imaging of innate immune cells in a model of multiple sclerosis where they used high-field MRI to map inflammatory infiltrates and fluorescently-labeled CLIO NPs for cellular tracking. In their work, NPs showed good cellular specificity for innate immune cells in vivo, whereas there was only sparse uptake by adaptive immune cells. Those results show that noninvasive molecular imaging of innate immune responses can serve as an imaging biomarker of disease activity with potential clinical applications in a wide range of inflammatory diseases [153]. All these promising results and multimodal NP capabilities enhance the simultaneous examination of disease biomarkers, and ultimately improve our understanding of the underlying biological mechanisms enabling early disease detection and diagnosis.

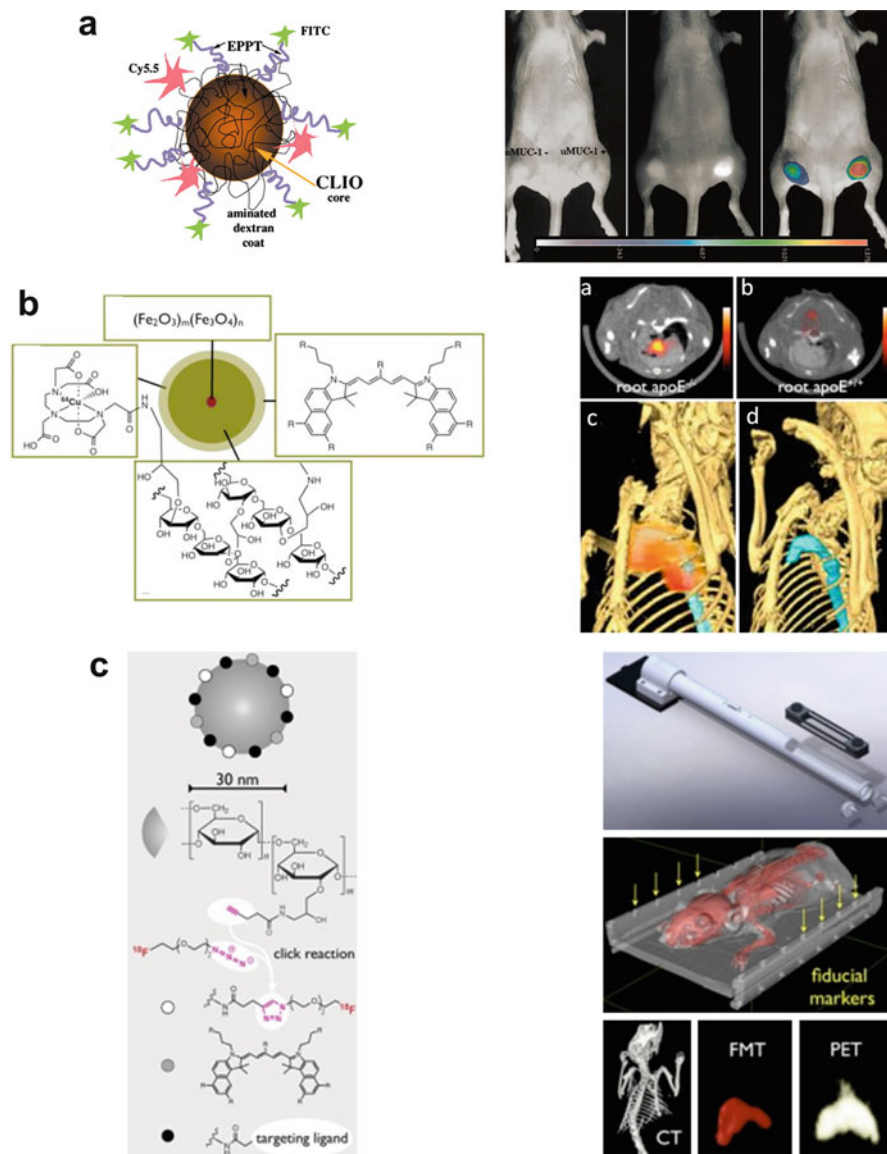


Fig. 6.5 Examples of multimodal PET/CT/fluorescence-labeled MNPs. (A) Schematic image of Cy5.5-CLIO NP probes attached to FITC-labeled EPPT (YCAREPPTRTTFAYWG) peptides. White light (left), NIR (middle) images, and a color-coded map (right) of mice bearing bilateral underglycosylated mucin-1 antigen (uMUC-1)-negative (U87) and uMUC-1-positive (LS174T) tumors showing specific accumulation of the probe in uMUC-1-positive tumors, but not in control tumors. (B) Image of the tri-modality probe ^{64}Cu -TNP containing a radiotracer ^{64}Cu attached to DTPA, iron oxide core with crosslinked aminated dextran coating for MRI, and the fluorochrome VT680 for fluorescence imaging. PET-CT imaging of inflammatory atherosclerosis in apoE^{-/-} mice facilitated by ^{64}Cu -TNP. Fused PET-CT images of the aortic root (a) of aged apoE^{-/-} mice

Not only fluorochromes can be conjugated to MNPs, but also gadolinium ion (Gd^{3+})-based imaging probes were investigated. Gd-complexes generally have short circulating times due to rapid excretion through urine [154]. For clinical diagnostics, various Gd(III) complexes and chelates conjugated to different inorganic, biological, or polymeric platforms have been developed, in an effort to better enhance MR bright imaging of targeted organs and tissues [155, 156]. Several reports have shown that Gd-bound nanoformulations offer several times higher T_1 relaxivities, and hence brighter contrast, than those corresponding to nonbound Gd chelates. Thus, for significant improvement of diagnosis accuracy, it is imperative to develop MNP-based dual contrasts comprising two different modes of imaging (T_1 - and T_2 -weighted MR images). In one notable example, Bae et al. prepared Gd-labeled biocompatible magnetite NPs (GMNPs) and demonstrated their use as dual contrast agents for T_1 - and T_2 -weighted MR images by conducting in vitro and in vivo imaging (Fig. 6.6a) [157]. In their work, oleic acid-coated MNPs were surface-exchanged with a mixed layer of 3,4-dihydroxy-L-phenylalanine (DOPA)-conjugated PEG and dopamine via strong coordination bonds of their catechol groups with the surface of iron oxide [158]. The amine-terminated dopamine allows subsequent modification with Gd-DTPA through the formation of an isothiurea bond with DTPA. Their results showed that the designed GMNPs exhibited both positive and negative contrast enhancement on T_1 - and T_2 -weighted MR images. Such dual contrast approach may help to overcome the limitations of traditional iron oxide-based or Gd-based contrast agents, thereby expanding opportunities of MRI for diverse theranostic applications. Shen et al. prepared Gd-labeled superparamagnetic Fe_3O_4 NPs and fluorescent CuInS_2 (CIS) quantum dots conjugated with RGD peptides (Fig. 6.6b) for tri-mode targeted T_1 -, T_2 -weighted MR and fluorescence imaging of pancreatic cancer [159]. Their MRI results showed significant brightened and darkened enhancement effects after NP injection through tail vein in tumor-bearing mice, demonstrating that the designed NPs exhibit both positive T_1 and negative T_2 contrast effects at the same time. The simultaneous positive and negative enhancement significantly improves the diagnosis accuracy in MRI, while the presence of quantum dots can assist in fluorescence imaging of tumor



Fig. 6.5 (continued) showing strong PET signal in these vascular territories with high plaque burden, whereas no activity is observed in the same vasculature of wild-type mice (*b*). The 3D-maximum intensity reconstruction of the fused dataset (*c*) demonstrates focal PET signal (red) in the proximal thoracic aorta (blue) of an apoE $^{-/-}$ mouse, but not in wild type (*d*). (C) ^{18}F -CLIO-VT680 NPs made of iron oxide core and a dextran shell attached to the clinical PET isotope ^{18}F with click chemistry. An NIR fluorochrome was conjugated for FMT, fluorescence histology, and flow cytometry. This probe can be derivatized with targeting ligands, such as peptides or small molecules on demand. An imaging cassette and an adapter specifically developed for use in the Inveon PET-CT platform (top). Surface-rendered CT image of a mouse inside the imaging cassette (middle); the lid of the cassette was segmented out to show the fiducial wells that are used for FMT/PET-CT fusion (yellow arrows). A 3D reconstruction of a CT, FMT, and PET dataset after injection of ^{18}F -CLIO-VT680 into a mouse model of cancer (bottom). (Reproduced with permission from Ref. [150–152])

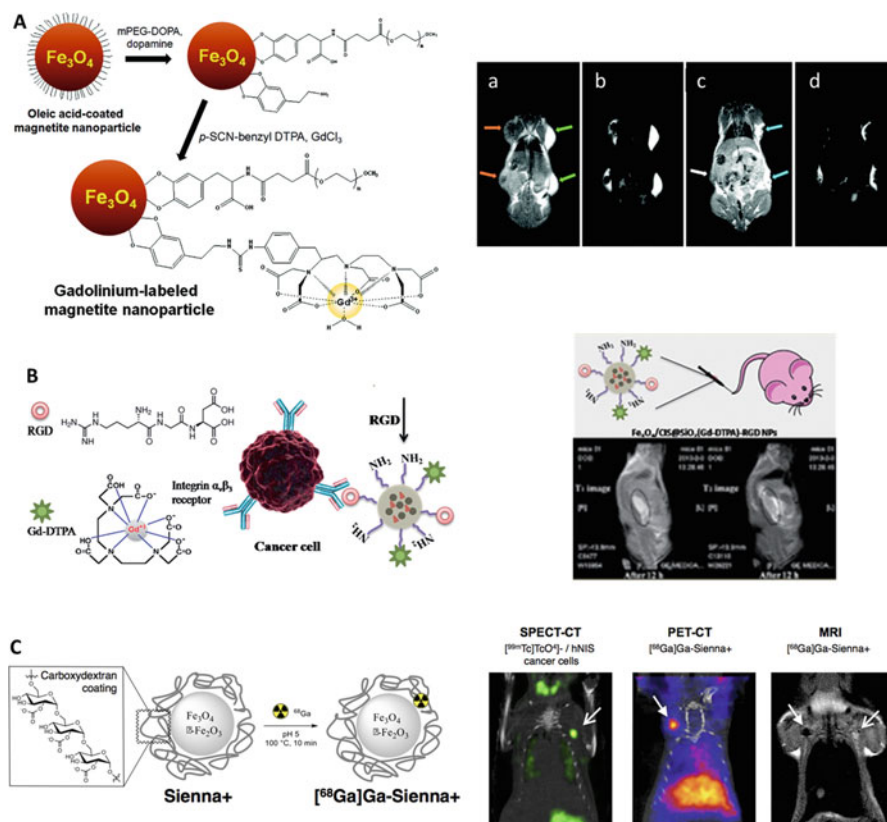


Fig. 6.6 Schematic illustrations of multifunctional gadolinium (Gd)-labeled MNPs. (A) Synthesis of Gd-labeled magnetite NPs (GMNPs) as dual contrast agents for T_1 - and T_2 -weighted MRI. (a) T_1 -weighted and (b) T_2 -weighted MR images of a mouse injected with Magnevist and Feridex (the orange arrows indicate the injection sites of Feridex, and the green arrows indicate the injection sites of Magnevist); (c) T_1 -weighted and (d) T_2 -weighted magnetic resonance images of a mouse injected with GMNPs. While Magnevist appears as a bright area in the T_1 -weighted MRI and Feridex shows a dark signal void in T_2 -weighted images, GMNPs displayed a bright signal enhancement and a marked signal drop at the injection site on the T_1 - and T_2 -weighted MR images, respectively. The above results showed that GMNPs exhibit both positive and negative contrast enhancement on T_1 - and T_2 -weighted MR images. (B) Scheme for the formation of Fe_3O_4 /(CIS)@SiO₂(Gd-DTPA)-RGD NPs containing Gd-labeled Fe_3O_4 NPs and fluorescent CuInS₂ (CIS) quantum dots conjugated with arginine-glycine-aspartic acid (RGD) peptides. (Left) T_1 - and (right) T_2 -weighted MR images of the entire abdomen of pancreatic adenocarcinoma mice model injected with the designed NPs through the tail vein after 12 hrs. T_1 and T_2 MR images of the tumor show significant brightened (left) and darkened (right) enhancement effect after NP injection, demonstrating that the designed multifunctional NPs exhibit both positive T1 and negative T2 contrast effects at the same time significantly improving the diagnosis accuracy in MRI. (C) Chelator-free ^{68}Ga -radiolabeling of Sienna+ with examples of SPECT-CT, PET-CT, and MR images showing its successful use to detect sentinel lymph node location and metastatic status in a metastatic breast cancer mouse model. Such multimodal [^{68}Ga]Ga-Sienna+ MNP probes could, thus, be a useful preoperative imaging tool to guide sentinel lymph node biopsy in clinical practice. (Reproduced with permission from Ref. [157, 159, 160])

tissue in clinical surgery. Very recently, the clinically approved Sienna[®] MNPs were radiolabeled with ⁶⁸Ga without a chelator to produce [⁶⁸Ga]Ga-Sienna+, and used as PET/CT/MRI multimodal imaging tool to detect sentinel lymph node location and metastatic status in a metastatic breast cancer mouse model (Fig. 6.6c) [160]. SPECT-CT imaging confirmed metastasis in the left axillary lymph nodes and lungs. In PET-CT, significantly higher [⁶⁸Ga]Ga-Sienna+ uptake was seen in the healthy axillary lymph nodes than in the metastatic one. In MRI, [⁶⁸Ga]Ga-Sienna+ uptake in healthy lymph nodes was observed by decreased MR signal in T2/T2* weighted sequence, whereas metastatic lymph node appeared unchanged. Thus, using multimodal [⁶⁸Ga]Ga-Sienna+ MNP probes assisted multimodal imaging, healthy sentinel lymph nodes can be distinguished from the metastatic ones and could, thus, be a useful preoperative imaging tool to guide sentinel lymph node biopsy in clinical practice.

With the preparation of novel well-engineered magnetic hybrid nanomaterials with superior fluorescent capabilities, uniform and tunable sizes, high magnetic content loading, and maximized stable fluorophore coverage, this field is continuously advancing. In particular, the controlled combined synthesis of gold or quantum dots with MNPs can be used for multiplexed molecular diagnosis and in vivo imaging applications, including NIR absorption, MRI responses, photon scattering, and magneto-motive photo-acoustic imaging [161]. Gold nanoparticles (GNPs) have been widely acknowledged to possess unique optical properties, particularly for surface plasmon resonance (SPR) [162, 163]. When the NPs are irradiated by laser, the SPR absorption of GNPs is followed by rapid conversion of light into heat, allowing it to be used for biomedical photo-thermal ablation. Besides, extensive research has been currently focused on the use of GNPs as contrast agents for CT, replacing the ionic iodine-based contrast typically causing harmful effects, especially for patients with renal problems [164, 165]. Thus, hybridization of MNPs with gold results in a novel platform which benefits from the unique properties of both materials [166, 167]. The obtained hybrid NPs can be potentially used as dual-contrast agents to provide synergistic effects in both CT and MR imaging, and can be exploited for therapeutic applications such as photo-thermal ablation, hyperthermia, and thermo-sensitive drug delivery. For such purposes, Mahmoudi and Shokrgozar reported compact uniform gold-coated MNPs by trapping fluorescent polymeric dyes between the iron core and the gold shell (Fig. 6.7a) [168]. Such approach not only produces a magnetically sensitive material with NIR and MRI properties, but also offers new modality with permanent fluorescence capabilities (no decay, bleaching, or dilution), allowing the use of such probes for molecular imaging and long-term in vitro and in vivo tracking purposes. Quantum dots, on the other hand, have emerged as superior fluorescent nanoprobe for dynamic molecular imaging and for multiplexed biomedical diagnostics at ultrahigh sensitivity [169]. In one report, co-assembling MNPs with fluorescent quantum dots to form colloidal magneto-fluorescent supernanoparticles (SPs) was conferred (Fig. 6.7b) [170]. These colloidal SPs are made of MNP “core” fully surrounded by a “shell” of fluorescent quantum dots and overcoated with thin silica layer. After surface PEGylation, these silica-coated magneto-fluorescent SPs were shown to be

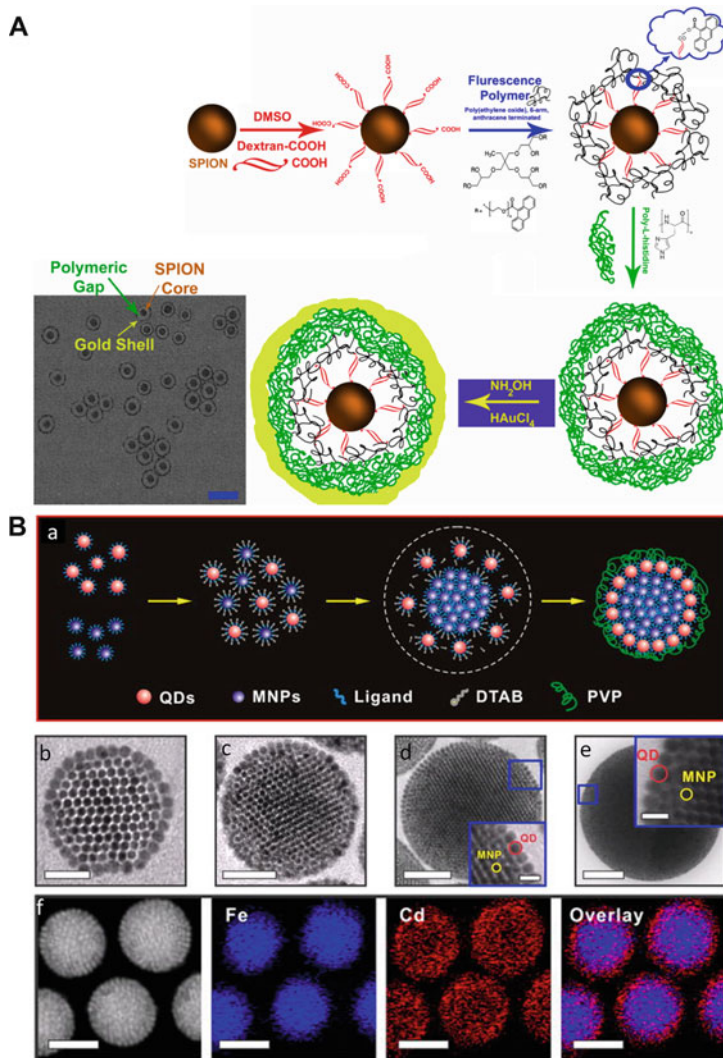


Fig. 6.7 Schematic representations for the preparation of magnetic gold/quantum dots hybrid nanomaterials. (A) Scheme for the preparation of gold-coated MNPs possessing a fluorescent polymeric gap with respective TEM images (scale bar is 40 nm). (B) (a) Scheme for the formation of core-shell magneto-fluorescent supermanoparticles (SPs) with respective high magnification TEM images of SPs with average diameters of (b) 80 ± 9 nm, (c) 120 ± 13 nm, (d) 235 ± 30 nm, and (e) 360 ± 60 nm (scale bars are 30 nm, 50 nm, 70 nm, and 100 nm, respectively). (f) Representative images of dark-field scanning TEM and EDS elemental mapping of as-prepared SPs (scale bars are 80 nm). Such examples present well engineered and controlled combined synthesis of gold or quantum dots with MNPs to be used for in vivo multiplexed molecular diagnosis and imaging applications including NIR absorption, MRI responses, photon scattering, and magneto-motive photo-acoustic imaging. (Reproduced with permission from Ref. [168, 170])

magnetically manipulated inside living cells while being optically tracked. Importantly, these SPs can also serve as *in vivo* multiphoton and magnetic resonance dual-modal imaging probes. All these notable examples suggest great potential use of multifunctional hybrid MNP as a promising platform for multimodal imaging to aid the early detection of cancer and to improve patient prognosis.

5.1.2 MNPs for Tissue Engineering

In a relatively new research area, many progresses have been made in the use of magneto-responsive NPs to control biological live cells, cell functions, cellular patterning, cell sheet assembly, and tissue engineering by applying magnetic fields [171–175]. One of the goals of tissue engineering is to accomplish controlled delivery of cells to develop functional substitutes of lost or damaged tissue constructs. Typically, tissue engineering is based on *in vitro* culturing of cells onto 3D biocompatible and biodegradable scaffolds to mimic their native function, followed by introduction of the colonized scaffold into the donor. These scaffold materials should be designed with specific biochemical, physical, and mechanical cues such as tissue-matching stiffness to result in improved repair and regeneration. Advances in cellular patterning, including cell sheet, hydrogels, 3D printing, inkjet printing, and laser-assisted bioprinting methods have been thoroughly investigated for organized tissue engineering [176]. However, despite recent improvements, tissue engineering still faces a number of challenges such as poor cell seeding and invasion due to the tortuosity and depth of the scaffold, or the implanted material degrading and releasing byproducts that may trigger certain inflammatory responses. A novel promising strategy, known as magnetic force-based tissue engineering (Mag-TE), has been successfully utilized for a number of applications including stem cell guidance, retention, and differentiation, preparation of small diameter artificial blood vessels, skeletal muscles preparation, urinary tissue, vascular tissue, and bone tissue formation [177–179]. In Mag-TE, cells are labeled with functional MNPs enabling the manipulation of cells as well as the control of cell functions by applying an external magnetic field. This approach has been used to circumvent many of the current limitations of tissue engineering, such as better cell seeding efficacies and invasion into 3D scaffolds [180–182], or as part of a scaffold-free strategy to build portions of transplantable tissues from mesenchymal stem cells (MSCs), adipose-derived regenerative (ADR) cells, or induced pluripotent stem (iPS) cells [183–185]. Moreover, it is possible to build scaffold-free portions of skin, liver, or muscle tissue in a variety of shapes. As a proof-of-concept, oriented dense muscle sheets, strings, and rings from mouse myoblasts were produced by Mag-TE [178]. In addition to such proof-of-concept studies, Mag-TE has also been assessed *in vivo* in a bone regeneration model where human multilayered MSC sheets were produced and implanted in the cranial defect of a nude rat with histological findings showing significant bone growth 14 days post implantation [179]. In another report, the same group created multilayered MSC sheets with ~300 μm thickness. The transplanted MSC sheet was successfully engrafted into ischemic tissues of mice and stimulated neovascularization in response to limb

ischemia [183]. This technique has been also used in pro-angiogenic therapy, where multilayered ADR and iPS cell sheets were generated and engrafted successfully in ischemic mouse models to promote vascularization of the hypoxic tissue. For instance, Kito et al. examined the therapeutic potential of iPS cell sheets created by Mag-TE technology for reparative angiogenesis [185]. Here, cells were labeled with magnetite nanoparticle-containing liposomes (MCLs), mixed with extracellular matrix (ECM) precursor embedding system, where the magnetized cells formed 3D multilayered cell sheets. In vivo implantation of iPS cell sheets into ischemic tissues of nude mice promoted revascularization and increased expressions of VEGF and bFGF in ischemic tissue. Thus, transplantation of such or analogous cell sheets may have great future potentials in regenerative medicine for ischemic limbs as well as cardiac diseases.

As mentioned earlier, enhanced cell seeding efficacies and invasion into 3D porous scaffolds can be achieved using MNPs. In this respect, a variation of Mag-TE known as magnetic-assisted cell seeding (Mag-seeding) specifically facilitates the seeding of cells into the deep internal space of the 3D scaffolds, resulting in higher scaffold-seeding efficiencies. In this technique, cells are labeled with MNPs, placed on top of the scaffold, and then driven to invade the scaffold by magnetic forces from below. Mag-seeding has proven effective in promoting infiltration and distribution of magnetically labeled fibroblasts in PLGA, collagen, and polystyrene materials. Furthermore, incorporation of MNPs in biomaterials in combination with magnetic force permits the construction of magnetically actuated scaffolds with potentials in bone tissue regeneration [186–188]. Magnetically actuated scaffolds also provide a platform for cell and drug delivery on demand [189]. Typically, this is performed with ferromagnetic hydrogels (ferrogels), consisting of hydrogels incorporating MNPs and further enriched with growth factors and/or cells. Upon the application of a magnetic field, the hydrogel contracts, expelling the biomolecules and/or cells contained within it. If the ferrogel is placed at an injury site, it can act as a potent delivery vehicle. Alternatively to release on-demand, growth factors can be covalently conjugated to the ferromagnetic particles to be delivered in a sustained manner. For example, thrombin- and bFGF-conjugated MNPs embedded in fibrin hydrogels were found to encourage the proliferation and differentiation of cells to be used in the regeneration of spinal cord injuries [190].

In summary, the magnetic manipulation of cellular functions and structures through MNP-based actuation is a relatively new strategy, and it has shown considerable potential in tissue engineering. Making populations of MNP-labeled cells cluster by magnetically induced system is a desirable way of constructing cell sheets, complex 3D tissue-like structures, and magnetically responsive composite scaffolds with promising potentials in regenerative medicine.

5.2 MNPs for Therapeutics and Drug Delivery Applications

From liposomes and polymeric formulations to iron oxide MNPs, various nanomaterials and methods have been finding their niche in targeting cancer. Some

important examples of such drug delivery systems have already been described, with the most prominent illustrations focused on the FDA approved liposomal formulations entrapping drugs noncovalently (Doxil[®], DaunoXome[®], Myocet[®], etc.). Moreover, several polymeric nanoconstructs include core-shell particles, which often involve a material that noncovalently entrap the drug molecules. A noteworthy example is PLGA-based biodegradable NPs, which are FDA-approved materials that incorporate hydrophobic drugs [191]. Hydrogel NPs, also known as nanogels, are crosslinked hydrophilic polymer networks engineered to bind drugs [192]. They can also swell or shrink in response to factors such as pH or temperature. Gold NPs (shells, spheres and rods) have been used for thermoablative photo-thermal therapies, where the interaction between tissue-transparent NIR light and gold NPs results in the rapid heating of the NP, killing the tumor cells in their vicinity [193, 194]. However, from all the above vehicles, MNPs are uniquely special as they exhibit great promise in magneto-responsive theranostic applications including MDT, MFH, and/or drug delivery. The first step towards tapping this potential has been recently taken when MNP-based formulations for the treatment of iron deficiency (Feraheme[®]) and solid tumors using MFH (NanoTherm[®]) entered the clinic.

While different start-up companies (Geurbet, Magforce, Chemicell GmbH etc.) manufacture MNPs for numerous magneto-responsive diagnostic purposes, very few companies succeeded in commercializing MNPs for therapeutics and clinical endpoints. FeRx Inc. produced Dox-MTC, however, because of the insufficient efficacy in phase II/III clinical trials, the company ceased its production in 2008. Magnetic NP hydrogel (MagNaGel[®]) from Alnis Biosciences Inc. also commercialized a material comprising chemotherapeutic agents, Fe oxide colloids, and targeting ligands, but went out of business as well. Chemicell Inc. currently commercializes fluidMAG[®], nano-ferrofluids consisting of an aqueous dispersions of coated magnetic iron oxides with diameters of 50–200 nm for potential use for MRI-diagnostics, cell separation, and MDT applications. A novel noteworthy MNP-based agent, Feraheme[®] (also known as Ferumoxytol – AMAG Pharmaceuticals), has received significant attention due to its FDA-cleared status for use in humans [195, 196]. Feraheme[®] ($D_H = \sim 30$ nm; 30 mg Fe/mL), a SPION coated with a low-molecular weight semisynthetic polyglucose sorbitol carboxymethylether designed to minimize immunological sensitivity, is particularly indicated for the treatment of iron deficiency anemia in adult patients with chronic kidney disease (CKD) [197, 198]. Currently, and due to its proven advantageous characteristic, the use of Feraheme[®] as contrast agent for MR angiography and brain tumor imaging is being examined [199]. New clinical trials involving its use to measure inflamed regions in patients with brain cancer (clinicaltrials.gov, NCT02452216 [200]) and lymph nodes in patients with prostate cancer (clinicaltrials.gov, NCT01296139 [201]) are under current investigation. Furthermore, NanoTherm[®] (15 nm aminosilane-coated MNPs; BU48) is commercialized by Magforce, Inc. for MFH treatment mainly in patients with solid tumors, where the MNPs are intratumorally introduced and then heated under AMF Nanoactivator[®] (thermoablation typically at temperatures $\sim 44.6^\circ$). The resulting magnetic field oscillates the iron oxide MNPs in the NanoTherm[®] magnetic fluid, creating therapeutic treatment temperatures within

the tumor. Another example Magnablate I (clinicaltrials.gov; NCT02033447 [202]), designed to thermally ablate solid tumors using AMF, is in a current clinical trial as a site-selective therapy for treatment of prostate tumors. As these therapies attack cancer cells via a physical mechanism, it is likely that they will benefit from synergistic combinations with other forms of therapies (i.e., radiotherapy) or potentially drug-coated MNPs. Nevertheless, to date, “*no drug-conjugated MNPs used as MDT, MFH or drug delivery carriers have entered the clinic yet.*” Thus, it is imperative to devote a section for the recent advancements for the use of drug-conjugated MNPs for cancer therapeutics and represent most notable examples in this regards. But beforehand, to achieve effective nanotherapeutics, the challenges and hurdles encountered to efficiently direct the delivery of MNP-based drug vehicle to target diseased sites are briefly discussed.

5.2.1 Challenges of Delivering MNPs to Cancer

One of the biggest challenges in drug delivery systems is to target the delivery of MNPs to specific tumor sites, without being cleared by our immune system. It was shown in most of the published reports that the majority of intravenously administered NPs are uptaken by leukocytes and macrophages and accumulate in the reticuloendothelial system (RES), particularly the liver, spleen, bone marrow and lymph nodes (depending on the NPs' properties) [203]. This is an indirect passive process, as receptors on the surface of leukocytes bind NPs as part of a normal immune response. Because of the short circulation times and the low concentration of NPs penetrating the tumor tissues (despite the EPR effect), low therapeutic levels are achieved. Even when active targeting with specific ligand-receptor interaction is sought, only marginal intracellular drug accumulation is achieved, since “*active targeting occurs only after blood circulation and extravasation.*” Thus, the main limitation concerns the residence time of NPs in the bloodstream. Consequently, researchers actively explore strategies to enhance the blood half-life of intravenously injected NPs to achieve accumulation of drug-loaded nanocarriers at the intended sites, with reduction of their concentrations at the nontarget sites. As mentioned earlier, many polymers have been used to coat MNP surfaces including but not limited to polysaccharides (hyaluronan, dextran, chitosan, etc.), PVP, PVA, PGA, PAA, PLA, PLGA, PEI, and the mostly used PEG along with a variety of their derivatives and copolymers [84]. Coating with such polymers was found not only to provide good stabilization and protection to the formulation, but also minimize protein binding to the surface of NPs (i.e., opsonization), and, hence, prolong blood circulation times. For instance, coating MNPs with carbohydrates, such as dextran, results in the increased accumulation in lymph nodes and liver [96]. On the contrary, “stealth” polymers, such as PEG coatings, have shown to inhibit uptake by leukocytes and, thus, longer blood circulation times are achieved [204, 205]. The increased systemic circulation times appears to be dependent upon the molecular weight (MW) of PEG used (higher MWs > 50,000 exhibit better circulation half-lives) [206]. Furthermore, charge of MNPs also plays an important role, where a slightly negative or positive surface charge of MNPs is considered to be best for longer blood circulation time and enhanced tumor targeting [69, 207]. Nonetheless,

although coating with specific polymers and charge optimization have proven to be advantageous, majority of administrated NPs still end up in unintended organs, and thus require further optimization and careful assessment. Serious efforts to further enhance barrier breaching and tissue penetration of NPs should be considered, as it is widely accepted that NP payloads are more efficacious when distributed through pathological tissues.

Another chief aspect for effective targeted drug delivery systems is achievement of three key points: “enter, release, and exit.” Thus, to create pronounced therapeutic efficacy, the drug must be loaded with high efficiency onto the NP, must be intracellularly delivered to the target site where it must be released with high selectivity, and finally must clear from the body with no side-toxicities [208]. Consequently, the nanoformulations should have sufficient residence in the circulation, retention by specific characteristics within intended sites (i.e., targeting), and controlled drug release at the diseased site within a time that allows for effective functionality of the drug. All those mentioned criteria should be carefully reviewed as they tend to cause misunderstandings in defining specific drug targeting vehicles. Quite frequently drug-loaded NPs show higher tumor accumulation relative to free control drugs, but this does not translate to improved tangible efficacies. Furthermore, several complexities including identifying an effective ligand-receptor interaction, as well as the extent and distribution of target cell receptor expression, may help explain observations such as the lack of improved uptake of ligand-targeted vehicles relative to nontargeted ones by tumor cells [209, 210]. Our studies, and others, also showed that the presence of the targeting ligands does not always result in increased drug accumulation in tumors, suggesting that “active targeting” does not automatically translate into “effective drug delivery.” On the other hand, the issues of intratumoral distribution, tumor heterogeneity, and temporal receptor over-expression are not easily addressed problems and require more attention when designing drug delivery systems. Finally, promising outcomes from *in vitro* cellular studies may be quite different from outcomes for *in vivo* xenograft animal models, and, in turn, the translation of the *in vivo* outcomes into humans [211]. This necessitates standardization of efficacy and toxicity assessment along with development of improved *in vitro* animal models that can provide better correlations and predictions of nanomedicine efficacies in humans.

5.2.2 Drug-Conjugated MNPs for Cancer Therapeutics

As mentioned, the key in effective drug delivery therapeutic systems is to create optimal drug-NP interactions that prevent premature release while enabling time-controlled physiologically responsive delivery to diseased sites. For such purposes, a wide variety of drugs are conjugated to MNPs by chemical (i.e., covalent) or physical functionalization (i.e., noncovalent adsorption, encapsulation, electrostatic, hydrophobic-hydrophobic interactions). From the FDA approved formulations, the noncovalent drug conjugation (i.e., electrostatic, dipole-dipole interactions (hydrogen bonding), van der Waals forces (hydrophobic), coordination, or encapsulation) seem to be the desired choice. Besides its simplicity, a clear advantage compared to covalent linkages is that the drugs do not undergo any covalent modification and are

therefore subject to less scrutiny from our bodies [212]. Intracellular internally activated drug release can then take place by simple diffusion and/or through different endocytic mechanisms requiring chemical and biochemical stimuli (i.e., pH, hydrolysis, enzymatic activities) [213]. On the other hand, externally activated release is based on external factors, such as magnet, light, temperature, and ultrasound [214]. Such stimuli-responsive nanocarriers [215] have demonstrated, albeit at different degrees, improved in vitro and/or in vivo drug release profiles. In addition, dual and multistimuli responsive NPs that respond to a combination of two or more signals with precision site-specific drug delivery have been also examined [216].

From the many chemotherapeutic anticancer drugs, Dox and its related anthracycline family (epirubicin, daunorubicin) are the most widely used in clinical practice for the treatment of a wide range of solid tumors and cancers including leukemia, lymphoma, breast, lung, and ovarian. However, the side toxicity effects of these drugs limit their direct administration and cumulative dosage. For instance, free Dox may lead to myocardial damage and congestive heart failure and may occur as the total cumulative dose of Dox approaches 550 mg/m^2 [33]. Hence, there is a huge incentive to develop effective chemotherapeutic cargos to selectively deliver this family of chemotherapeutic drugs. Importantly, due to its free amino and hydroxyl groups and extensive π -electron network and carbon rings, interaction with various organic polymers and block copolymers coated on the NP surface is feasible, rendering its formulation of particular interest to researchers. Recently, our group developed a chemotherapeutic nanoformulation based on PVP-stabilized MNPs (PMNPs) [129], and studied its selective delivery towards different types of human breast and leukemic cancer cells, primary tumors, and solid tumors. The general observation was that while metastatic cancer cells showed enhanced nanoparticulate uptake and higher killing efficacies, their normal nontumorigenic counterparts showed less uptake and, hence, reduced potencies (Fig. 6.8A). When tested on breast cancer in vitro, Dox-loaded fluorescein-labeled PVP-MNPs (Dox@FI-PMNPs) were found to be 8 times more effective in killing the metastatic breast cancer cells (two- to threefold enhanced cytotoxicities for MDA-MB-231 compared to MCF-7), compared to the normal nontumorigenic breast cells MCF-10A, suggesting huge potentials as selective anti-cancer agents for breast cancer therapy [217]. Importantly, Dox@FI-PMNPs were also able to effectively penetrate and deliver drugs to 3D forming primary tumor cells and patient tumor biopsies (Fig. 6.8B). This delivery vehicle was based on passively targeting the anticancer drug without a specific-receptor targeting approach. Thus, even with nonreceptor targeted but rather tailored delivery system enhanced toxic responses can be achieved. Besides, selective drug delivery to different types of human leukemia cells using related chemotherapeutic MNP formulation was also tested. Our results revealed that Dox@PMNPs showed significant toxicities, effectively killing the different leukemia cells, albeit at different inhibitory concentrations (IC_{50} ranging from ~ 0.5 to $5 \mu\text{M}$ Dox). In the first report, nanoparticulate uptake and cell death were evaluated in four different types of human Acute Myeloid Leukemia (AML) target cells: ML-2, HL-60, Mono-Mac-1, and TF1-vRaf, as well as on normal human

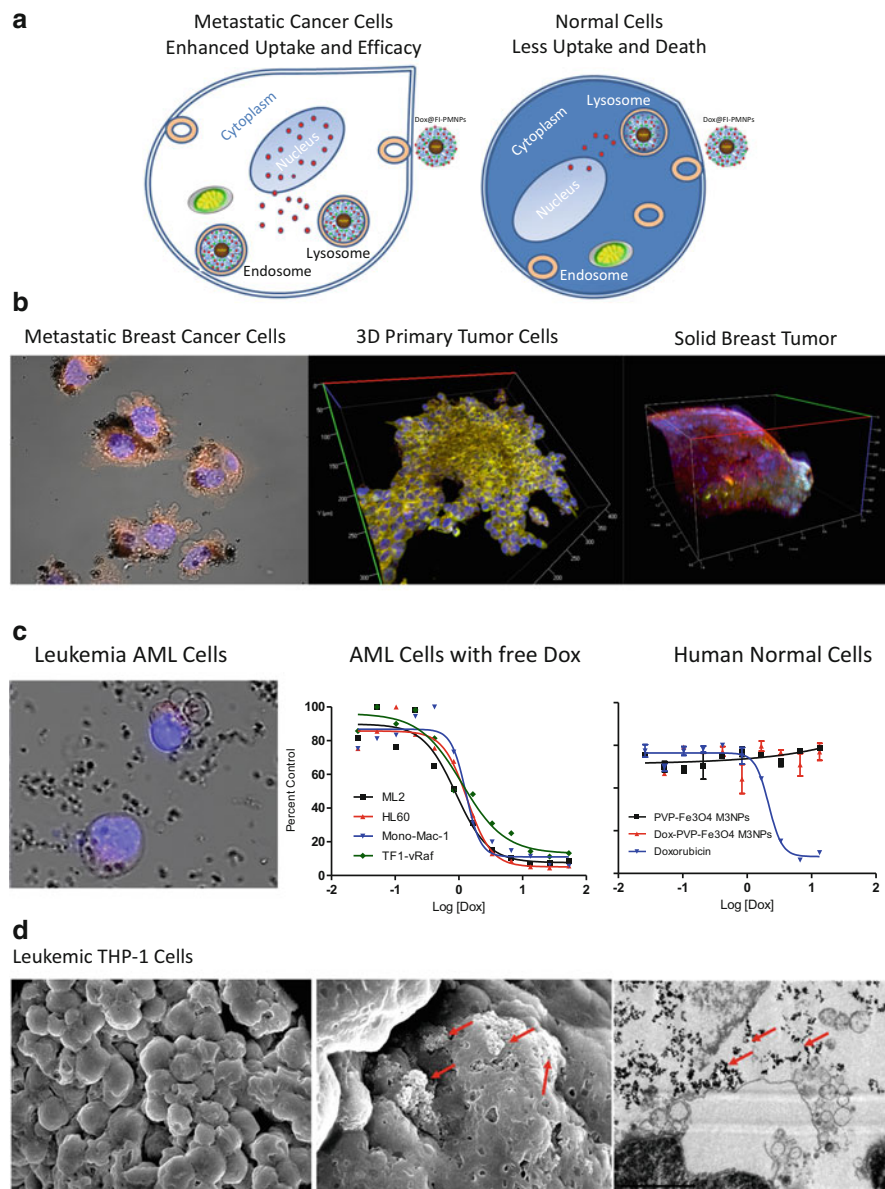


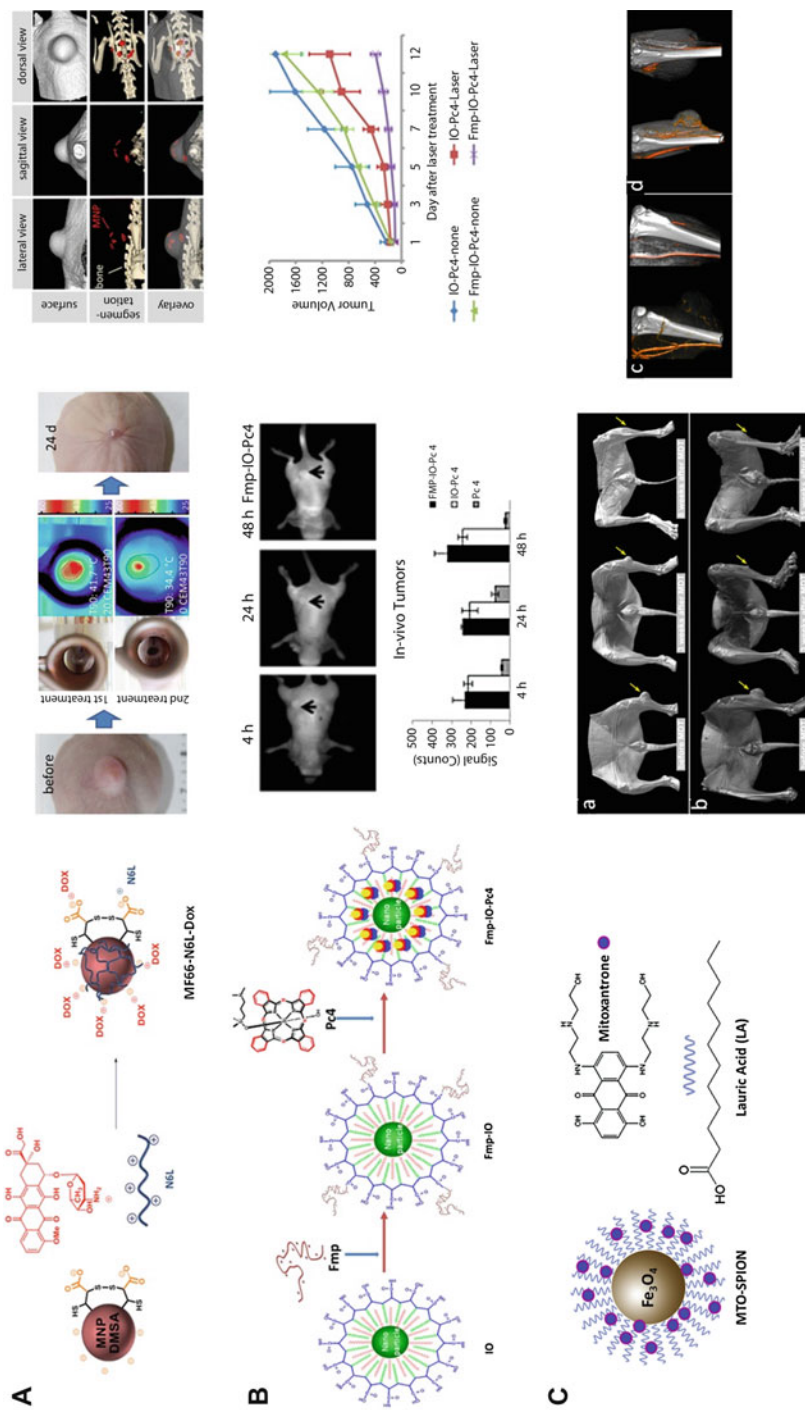
Fig. 6.8 (A) Illustrative image for the use of Dox-loaded PVP-stabilized MNPs (Dox@PMNPs) as selective drug carriers to different types of breast and leukemia cancer cells. (B) Confocal images of metastatic breast cancer cells (left), primary breast tumor cells (middle), and 3D reconstruction CLSM images of patient biopsy tumor treated with Dox@FI-PMNPs, respectively (Dox-red, FI-green, Hoechst-blue, and overlay of 3 channels-yellowish). The drug-loaded NPs attack metastatic breast cancer cells, causing apoptotic cell death, as well as penetrated 3D primary tumor cells and breast patient solid tumor biopsies (~150 μm deep into the tumor) delivering the anticancer drug intratumorally. (C) Live confocal microscopy images of representative Dox@PMNPs treated AML cell line, showing the

SVG-p12 cells [218]. Interestingly, and superior to free Dox, Dox@PMNPs were found to be more effective in killing the AML cells compared to the human normal cells ($\sim 40\times$ fold; $IC_{50} > 200 \mu\text{M}$ Dox), suggesting huge potentials as selective AML anticancer agents (Fig. 6.8C). Free Dox was found to be concurrently toxic to all the cell lines tested whether cancerous or normal. In another report, Dox@PMNPs showed enhanced and significant inhibition towards the human monocytic THP-1 cells compared to human promyelocytic leukemia cells HL-60 (two-fold enhanced cytotoxicities), with the least potency towards the normal peripheral blood mononuclear cell (PBMC) cells (up to six-fold) [219]. From live confocal imaging and electron microscopy studies (Fig. 6.8D), it was found that the observed enhanced cytotoxic effects of Dox@PMNPs is mostly dependent upon the selective and differential endocytic uptake of Dox@PMNPs, with subsequent release of Dox intracellularly to the cytoplasm, which then translocates to the nucleus after 24 h, causing apoptotic cell death. Importantly, the magnetic chemotherapeutic nanoformulation described here reduces the unwanted diffusive side effects of the free drug and allows selective drug delivery to cancerous cells. This selective payload may potentially enhance the efficacy of drugs in cancer patients and may further allow physicians to image cancerous cells exposed to Dox@PMNPs, opening new opportunities for *in vivo* image-guided cancer theranostics.

Another group prepared Dox-loaded PEGylated SPION (DLPS) and evaluated its *in vivo* potential as drug carrier system for the reduction of xenograft breast tumors induced in nude mice [220]. When magnetic targeting was applied, the toxicity of the treatment was reduced substantially, although there was no change in the therapeutic outcome, probably due to the low magnetization of the as-synthesized constructs. Kossatz et al. prepared negatively charged dimercaptosuccinic acid (DMSA)-coated MNPs (denoted as MF66) electrostatically functionalized with either Nucant pseudopeptide (N6L), Dox, or both (MF66-N6L-Dox) (Fig. 6.9A) [221]. MF66-Dox and MF66-N6L-Dox in combination with hyperthermia were more cytotoxic to breast cancer cells than the respective free drugs. A substantial tumor growth inhibition (40% of the initial tumor volume, complete tumor regression in many cases) after intratumoral injection of the NPs in tumor-bearing female athymic nude mice *in vivo* was observed. Those results represent a promising



Fig. 6.8 (continued) successful uptake of NPs by the cells causing their apoptotic cell death. Dose-dependent nonlinear regression curves of the cytotoxicity assays on human ML-2, HL-60, Mono-Mac-1, and TF1-vRaf (AML cancerous cells) as well as on SVG-p12 normal human cells as determined by XTT cell proliferation assay. Results clearly show that while free Dox was potent to all AML cell lines concurrently, Dox@PMNPs were found to be potent to the different AML cells but not to the human normal cells ($\sim 40\times$ fold), suggesting huge potentials as selective AML anticancer agents. Unloaded PMNPs were not toxic to any of the AML cell lines tested. x-axis: Dox concentration expressed in M; y-axis: absorbance at 450 nm. **(D)** SEM images of representative leukemic cell line after treatment with Dox@PMNPs for 24 h. (left) THP-1 cells without NPs, (middle) NP-treated THP-1 cells, and (right) TEM image of NP-treated THP-1 cells clearly showing the apoptotic features and potency towards the cancerous cells. (Reproduced with permission from Ref. [217–219])



strategy for translation into clinical practice when injecting the NPs intratumorally. The utilization of DMSA-coated MNPs functionalized with the positively charged anti-tumorigenic cytokine, interferon- γ (IFN- γ) with high rates of cancer inhibition and anti-angiogenic effects in pancreatic adenocarcinoma models were also reported. Thus, the simplicity of the developed DMSA-coated NPs (no covalent derivatization is involved in its synthesis) together with its magnetic core responses (i.e., MFH or MDT-assisted chemotherapy) make this system attractive for potential clinical use [222]. In another elegant study, Wang et al. generated an NP platform that combines a photodynamic therapeutic drug (Pc 4), with integrin β 1-specific cancer targeting fibronectin-mimetic peptide (Fmp) (Fig. 6.9B) [223]. Their results indicated that both nontargeted IONP-Pc 4 and targeted Fmp-IONP-Pc 4 accumulated in head and neck squamous cell carcinoma xenograft tumors with higher concentrations than the nonformulated Pc 4, even when lower doses were used, reducing the size of tumors more effectively than free Pc 4. Tietze et al. prepared MNPs coated with intercalated lauric acid bilayers and loaded it with the anticancer drug Mitoxantrone (MTO) (Fig. 6.9C) [224]. The drug appeared to be entrapped in the hydrophobic environment of the bilayer and spaces created by the soft clustering of the particles. After intra-arterial administration of MTO-SPIO NPs into rabbits, drug accumulations mainly in the tumor regions (57.2%) and to less extent in liver (14.4%) and kidneys (15.2%) were observed. The therapeutic outcome was demonstrated by complete tumor remissions and a survival probability of 26.7%. The authors noted that these outstanding outcomes are on the road towards clinical testing. The preparation of



Fig. 6.9 (continued) monitored by microcomputed tomography (μ CT). Figure is showing an example of a treatment sequence within the alternating magnetic field (AMF), the corresponding temperature distribution over the tumor surface and the effect on tumor volume. After tumor implantation, MNPs were applied intratumorally 24 h prior to the first magnetic hyperthermia treatment. Seven days later, a second hyperthermia treatment was performed. After the experimental period of 24 days, the animals were sacrificed. (Right) Intratumoral distribution of MF66-N6L-Dox as determined using μ CT 24 h prior to the first hyperthermia treatment. (B) Schematic illustration for the construction of Fmp-IO-Pc 4 NPs using Ocean's carboxyl functionalized MNPs. (Left) Levels of Pc 4 delivered as free Pc 4, IO-Pc 4, and Fmp-IO-Pc 4 in tumors at different time points by whole-body imaging. As shown, the targeted NPs Fmp-IO-Pc 4 has a more prolonged retention in tumors than either free Pc 4 or the nontargeted NP IO-Pc 4. (Right) Tumor growth curves showing tumors in the Fmp-IO-Pc 4 (targeted) group grew significantly slower than those in the IO-Pc 4 group (nontargeted). (C) Construction of MNPs coated with intercalated lauric acid bilayers and loaded it with the anticancer drug MTO. (Left) Magnetic drug targeting (MDT) in vivo therapy outcomes of the treatment of VX-2 tumors implanted in the hind limb of rabbits; panels (a) and (b) show a 3D-surface view of two rabbits. The images show the rear view of the rabbit positioned with its back down. Yellow arrows point to the tumor region on the hind limb. After 3 weeks, a clear reduction in tumor size can be observed and after 8 and 11 weeks, the tumors were no longer visible or palpable. A reduction in muscle volume in the treated region can also be observed. (c) and (d) 3D-angiographic images of the tumor region of the respective animals. Angiographic imaging demonstrates that not only the tumors but also the supporting vessel structures disappeared after the treatment, while the main vessels supporting the distal part of the limb remained unaffected. (Reproduced with permission from Refs. [221, 223, 224])

such nanoconstructs is relatively simple and inexpensive, increasing the viability of large-scale manufacturing for clinical settings. The family of FDA-approved or noncommercially prepared dextran-stabilized SPIONs were also extensively studied as drug delivery systems because many drugs can be retained noncovalently onto the organic dextran/carboxydextran coatings [58, 211, 212]. Therapeutic studies in animal models showed that these drug-loaded SPIONs caused greater tumor volume shrinkage and significantly greater efficacies than treatment with respective free drugs. Further treatment by MFH or MDT demonstrated enhanced antitumor efficacies in some cases [46, 48].

An alternative way of creating magnetic drug delivery systems is to coat the iron oxide core with a porous material, typically silica (i.e., core-shell MNPs), in which one or multiple drugs can be encapsulated [225]. One notable example of this sort was prepared by coating ultrasmall SPIONs with porous silica shell and an outer layer of hydroxypropyl cellulose (HPC) to form temperature sensitive magnetic drug carriers (Fig. 6.10) [226]. Gemcitabine (Gem) was then loaded into the silica pores, and the resulting material was tested *in vivo* against PANC-1 pancreatic tumor xenografts. Chemohyperthermia with intratumoral injections of GEM-magnetic carriers (followed by heating) resulted in significant increases in apoptotic tumor cell death compared to tumors treated with GEM-magnetic carriers' injections or hyperthermia alone. It is proposed that in the presence of the oscillating field, the local heating in the magnetic drug carriers facilitated the release of GEM from the silica pores, inducing higher cell growth inhibitory effects than chemotherapy or hyperthermia alone, thus offering great potentials to significantly improve the therapeutic efficacy of drugs for the treatment of pancreatic cancer. In another report, Kong et al. produced radiofrequency-activated hollow silica coated magnetic nanocapsules (SiMNPs) where the drugs were allowed to get sucked into their hollow capsules (80–150 nm). These SiMNPs can penetrate into the interior of tumors and allow a controlled on–off switchable release of the drug cargo via remote RF field [227]. The *in vitro* treatment of MT2 breast cancer cells and B16/BL6 mouse melanoma cells with nanocapsules containing either Camptothecin or Dox resulted in significant suppression of cancer and/or tumor growth both *in vitro* and *in vivo* breast cancer models. More approaches are also employed, in this regard, including the use of thermo-responsive smart polymeric shells (i.e., by swelling and de-swelling) or polymeric vesicles made of heterofunctional triblock polymer or any other dual or multistimuli responsive polymeric nanocarriers [216, 228, 229]. Another modules such as magneto-liposomes or magneto-dendrimers can also accommodate both hydrophilic and hydrophobic drugs and are well suited for cellular tracking using MRI, multimodal imaging, and magnetic-guided therapeutics [230–232]. Those specific systems are excellently reviewed elsewhere [233].

When the drug to be delivered is covalently bound to the MNP surface, the covalent bond should be biocompatible (stable in the bloodstream) and intracellularly biodegradable or cleavable on demand to allow controlled or environment-responsive drug release. Generally, MNPs in which drug molecules are covalently conjugated to the MNP surface exhibit low drug entrapment

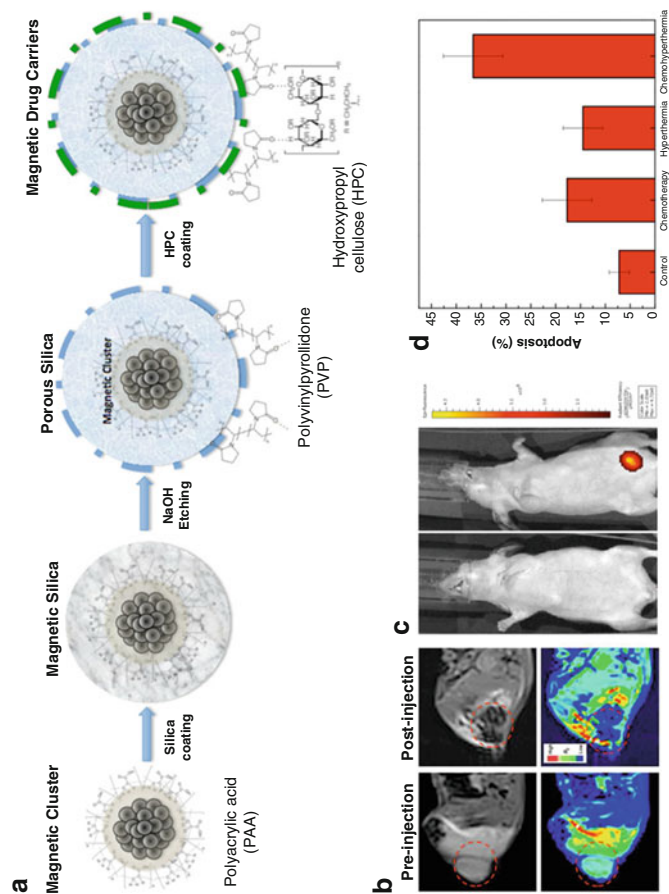


Fig. 6.10 (A) Schematic illustration describing the synthesis of GEM-loaded hydroxypropyl cellulose (HPC)-coated magnetic drug carriers. (B) In vivo multimodal imaging of intratumoral injected GEM-magnetic drug carriers; (upper) in vivo T2-weighted axial cross section MR images and (lower) color maps of pre-injection and post-injection. (C) In vivo fluorescence image of (left) control and (right) cyto780 labeled GEM-magnetic drug carriers injected mouse. (D) Incidence of apoptosis in PANC-1 pancreatic tumor xenografts after each treatment in vivo. Apoptotic index was determined by counting the percentage of apoptotic cells out of total tumor cells from five fields in each section. From the results, it is clear that combined chemohyperthermia using GEM-magnetic carriers resulted in significant increases in apoptotic tumor cell death compared to tumors treated with GEM-magnetic carriers' injections or hyperthermia alone. (Reproduced with permission from Ref. [226])

efficiency and more difficulty to release the drugs compared to noncovalent counter-conjugates conferred above. Importantly, the drug's structure and orientation should not be altered during covalent attachment; otherwise, its biological activity might be changed [234]. Bonding motifs used for this purpose are most commonly either amide linkages, pH-degradable (i.e., acid-cleavable) or enzymatically cleavable bonds, and to less extent, thermo- or redox-responsive bonds. Herein, some pronounced examples of drugs covalently attached to MNPs are presented. In one study, Methotrexate (MTX) was covalently conjugated to amine-functionalized NPs via amide bonds, demonstrating higher cytotoxicities in human breast MCF-7, human cervical HeLa cells, brain tumor cells, and 9 L glioma cells as compared to free MTX or negative control cells [67, 235, 236]. Amide bonds are chosen as they are not generally prone to hydrolysis at low pH and are typically resistant to degradation by proteases inside the cells. Another excellent report in this regards presented the development of a cooperative dual-targeted delivery platform for PTX that has promise for prostate cancer magnetically targeted treatment of tumor-bearing mice (Fig. 6.11A) [237]. The designed nanomedicine was prepared by first conjugating PTX to the high magnetic nanocarriers (HMNC), followed by functionalization with carboxylated *o*-(2-aminoethyl)polyethyleneglycol (NH₂-EPEG-COOH). Antiprostata-specific membrane antigen antibodies (AP SMA) were then conjugated onto the NPs targeting the extracellular domain of the prostate-cancer specific membrane antigen (PSMA). PTX-HMNC-EPEG-AP SMA with magnetic field achieved complete tumor regression where significant enhancement of PTX concentration at the tumor site by nearly 20-fold was observed with significantly prolonging the half-life of PTX in the circulatory system. This work demonstrates an efficient, nontoxic, and promising system for MNP-based chemotherapy with significant potential for human prostate cancer chemotherapy. Acid-cleavable (i.e., pH-degradable) bonds are another widely used linkers in covalent drug conjugation. Those bonds include, but are not limited to, hydrazones, Schiff bases (imines), acetals/ketals, oximes, and esters [238–240]. Of those various choices, many studies use hydrazone bonds because such systems tend to yield very reproducible results, are easy to prepare, and have performed comparatively well as pH-responsive nanocarriers [241–245]. In one noteworthy report, magnetic nanocubes covered with poly(methylmethacrylate) (PMMA) and covalently conjugated to Dox via a hydrazone linker, inhibited tumor growth in mice bearing HeLa xenografts which was found to be further enhanced by placing a magnet above the tumor (Fig. 6.11B) [242]. The designed pH-responsive drug delivery system based on hydrazide-decorating PMMA-coated magnetic nanocubes demonstrated great potential for controlled antitumor drug release in vitro and remotely targeted cancer therapy in vivo.

Another important class is based on enzymatically cleavable bonds which occur in cellular compartments such as endosomes/lysosomes. The enzymes that catalyze these hydrolytic processes are typically phosphatases (for linkers with cleavable phosphate groups), esterases for the degradation of ester bonds, glycosidases, and proteases that cleave specific oligopeptides. One example in this regard is reported

by Ansari et al. using lysosomally degradable peptides as drug–NP linkers [246]. In their work, the chemotherapeutic drug azademethylcolchicine was tethered to FDA-approved ferumoxylol NPs via a specific oligopeptide linker (AlaCysArgSerCitGly-HPheTyrLeuTyr) that is cleaved by membrane metalloproteinases expressed in breast cancer cells, generating a nanotherapeutic activated by tumor specific MMP-14 for tumor vascular targeting. In addition to being enzyme cleavable, the linker served as a selective vascular targeting moiety to enable active targeting of the nanosystems to tumor regions. The nanosystem exhibited enhanced accumulation in tumor regions, which was visualized and monitored by MRI, and effectively reduced tumor growth in mice. Overall, similar examples of enzymatically cleavable linkers have demonstrated great potentials for improving targeted theranostics of cancer. A less commonly employed linkers are the redox-cleavable

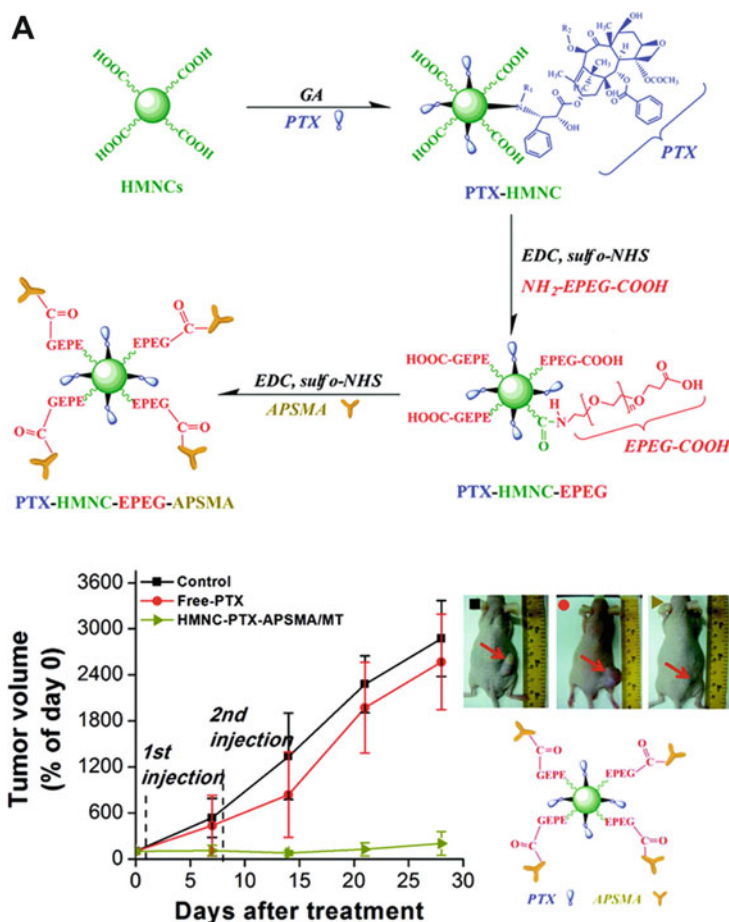


Fig. 6.11 (continued)

bonds degraded under oxidizing or reducing conditions such as thioketal or disulfide bonds [247]. Such systems have primarily been used in RNA therapies by delivering small interfering RNA (siRNA) [248–251] with promising potential in clinical outcomes. In one elegant work, Stephen et al. developed targeted convection-enhanced delivery [251] of O(6)-benzylguanine (BG) to glioblastoma multiforme (GBM) using redox-responsive, crosslinked, and biocompatible chitosan-PEG copolymer shell coated MNPs (NPCP), modified through covalent attachment of BG and tumor-targeting peptide chlorotoxin (CTX) (Fig. 6.11C) [247]. Inhibition of O(6)-methylguanine-DNA methyltransferase (MGMT) using BG has shown promise in patients; however, its clinical use is hindered by poor pharmacokinetics that leads to intolerable toxicity, thus, demanding improvements in BG biodistribution and efficacy. NPCP-BG-CTX demonstrated controlled and localized BG release under reductive intracellular conditions and proper trafficking

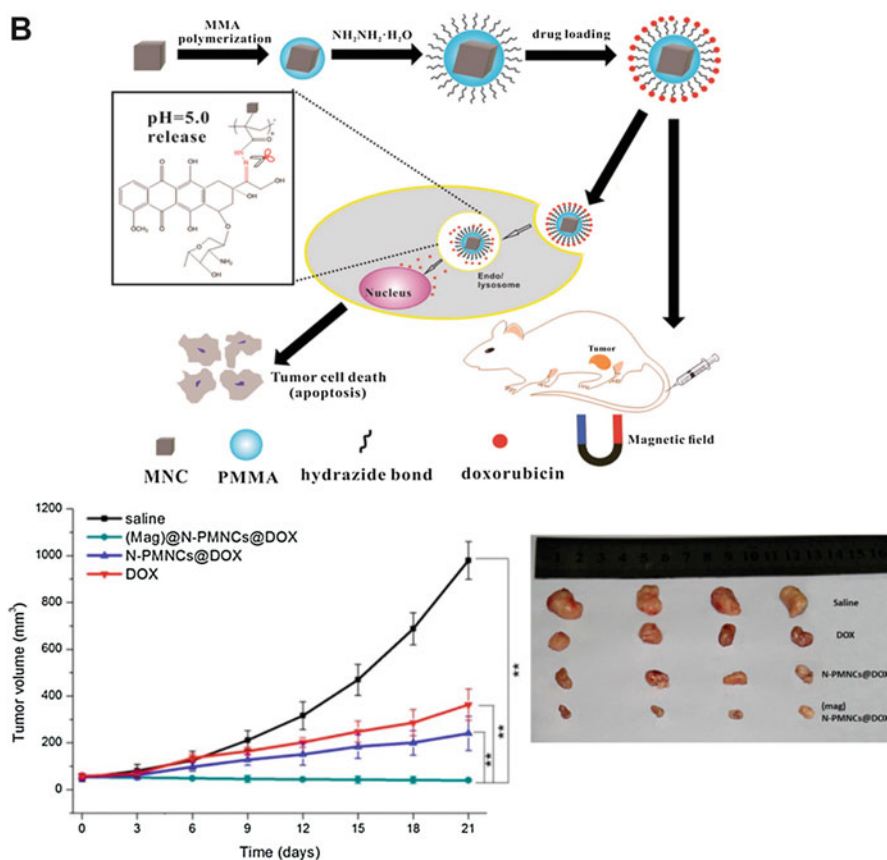


Fig. 6.11 (continued)

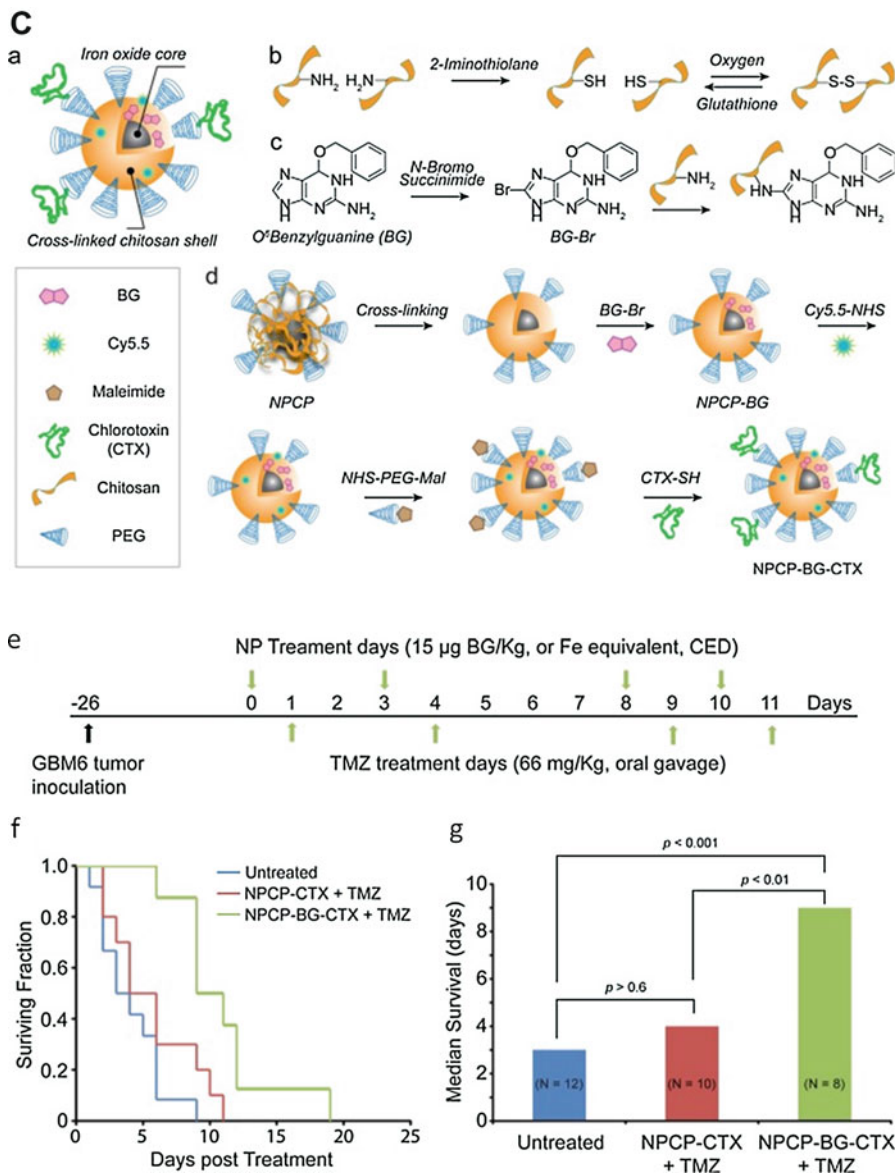


Fig. 6.11 (A) Stepwise synthesis of the dual-targeted nanomedicine, paclitaxel-conjugated PEGylated antiprostata-specific membrane antigen antibodies-immobilized high magnetic nano-carrier (PTX-HMNC-EPEG-APSMA); (right) quantitative analysis of the effects of various treatments on tumor size along with images of representative mice at 28 days after treatment for control, free PTX, and PTX-HMNC-EPEG combined with magnetic treatment (MT). PTX-HMNC-EPEG-APSMA/MT provided the most significant suppression of tumor progression and increase in animal survival relative to the other groups. Values are represented as means \pm SD ($n = 8$). Red arrows

of BG in human GBM cells *in vitro* was achieved. *In vivo*, convection-enhanced delivery of NPCP-BG-CTX produced an excellent volume of distribution (V_d) within the brain of mice bearing orthotopic human primary GBM xenografts. Significantly, concurrent treatment with NPCP-BG-CTX and the typically used chemotherapeutic drug temozolomide (TMZ) showed a threefold increase in median overall survival in comparison to NPCP-CTX/TMZ treated and untreated animals. The combination of tumor cell-specific BG controlled delivery along with the enhanced *in vivo* efficacy observed demonstrates the great potential of these NPs to improve clinical outcomes in GBM patients.

Finally, smart hybrid magnetic drug delivery nanosystems that comprise combination therapies for stimulus-controlled drug release are also reported. As an example, Hayashi et al. described the remarked *in vivo* therapeutic efficacy of multiple myeloma by combing magnetic hyperthermia and chemotherapy using smart NPs made of $\text{Fe}_3\text{O}_4/\text{Dox}/\text{polypyrrole-PEG-FA}$ NPs that generate heat in response to AMF sequentially releasing Dox (Fig. 6.12) [252]. The smart NPs are composed of a polymer with a glass-transition temperature (T_g) of 44 °C, which produce heat when the AMF is applied softening the polymer phase and leading to Dox release. In such system, the combination of MFH and chemotherapy using the designed smart NPs have proven effective to completely cure the tumor and achieve treatment without recurrence of malignancy and with no significant toxicity observed. The authors concluded that they will assess the therapeutic efficacy of the designed smart NPs by intravenous injection in tumor-bearing animal models.



Fig. 6.11 (continued) indicate the position of the implanted tumor. **(B)** Schematic illustration of the fabrication of an intracellular pH-responsive drug delivery system based on hydrazide decorating PMMA coated magnetic nanocubes (N-PMNCs). N-PMNCs@DOX was intravenously injected into nude mice without applying magnetic field or in the presence of magnetic field (Mag) N-PMNCs@DOX. Notable antitumor efficacy could be observed in the tumor tissue treated with (mag) N-PMNCs@DOX after treatments for 21 days along with optical photos of tumors collected from all mice. The results clearly indicate that (mag) N-PMNCs@DOX could efficiently targeted to tumor tissue by magnetic field for local drug delivery and subsequently inhibit the growth of tumor. **(C)** (a) Illustration of chitosan-PEG (CP) coated NPs (NPCP) crosslinked and functionalized with O6-benzylguanine (BG) and tumor-targeting peptide chlorotoxin (CTX), symbolized as NPCP-BG-CTX. (b) Crosslinking of NPCP coating through intracellular reducible disulfide linkages. (c) Activation of BG by bromination and subsequent reaction with amines on the chitosan backbone. (d) Modification of NPCP with BG and CTX to produce NPCP-BG-CTX. (e-g) Increased survival by convection-enhanced delivery (CED) of NPCP-BG-CTX in combination with the chemotherapeutic drug temozolomide (TMZ) in an orthotopic GBM6 xenograft model. (e) Tumor inoculation and treatment timeline. NPs were administered 24 h prior to TMZ treatment. Treatments were performed twice weekly for 2 weeks. (f) Kaplan–Meier survival curve. (g) Median survival and log rank statistical comparison of the three treatment groups. The results indicate that the prolonged time of survival for NPCP-BG-CTX/TMZ treated animals was caused by the therapeutic effect of NPCP-BG-CTX NPs and that the NPs administered by CED achieve excellent tumor coverage and increase median survival in an orthotopic primary GBM xenograft model. (Reproduced with permission from Ref. [237, 242, 247])

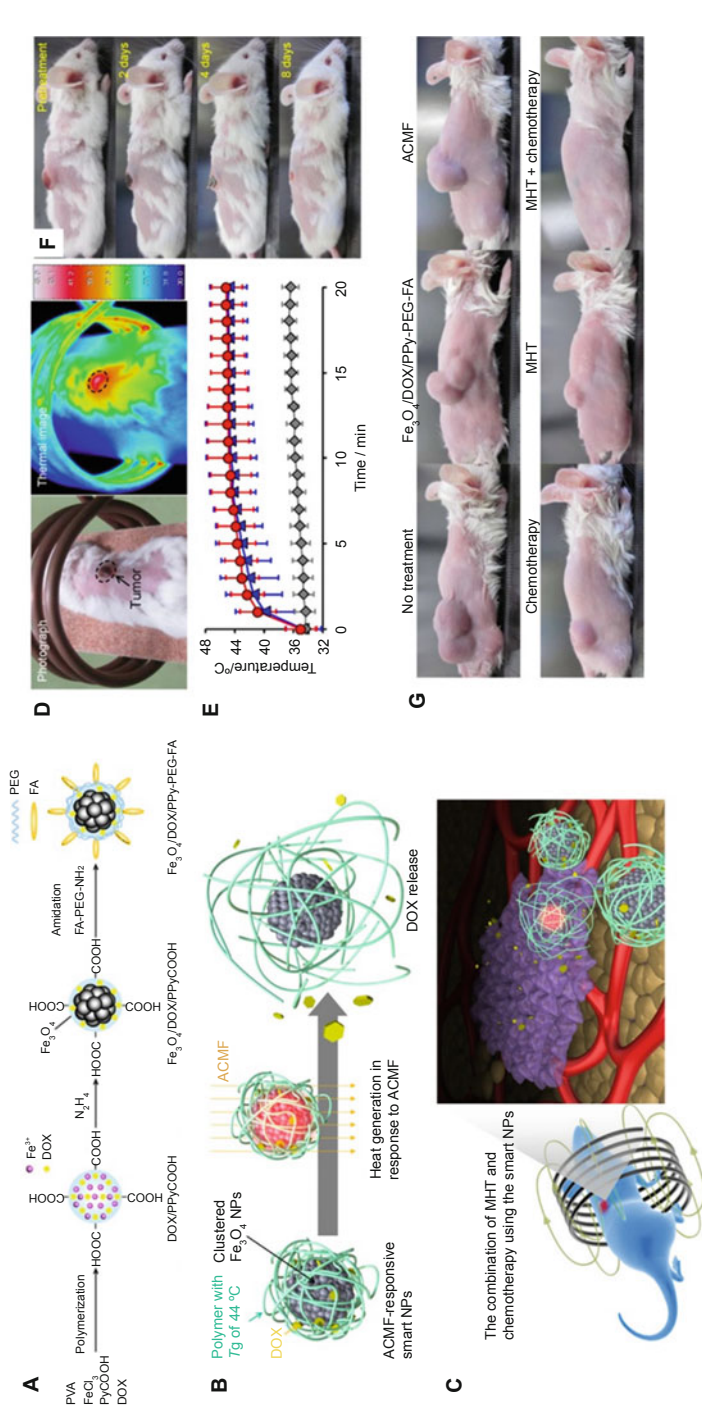


Fig. 6.12 (A) Synthesis of DOX-containing carboxylic polypyrrole functionalized Fe_3O_4 NPs ($\text{DOX}/\text{PPy}/\text{COOH}$) coated with polyethylene glycol (PEG) and folic acid (FA) (denoted as $\text{Fe}_3\text{O}_4/\text{DOX}/\text{PPy}/\text{PEG}/\text{FA}$ NPs or smart NPs). (B) Schematic illustration of the smart NPs that produce heat in response to alternating current magnetic field (ACMF) sequentially releasing DOX. (C) Illustration of cancer treatment with the combination of magnetic hyperthermia (MHT) and chemotherapy using the smart NPs. (D) Photograph and thermal image of a mouse exposed to ACMF for 20 min after injection with the smart NPs. (E) Average change of the tumor temperature of the mice injected with $\text{Fe}_3\text{O}_4/\text{DOX}/\text{PPy}/\text{PEG}/\text{FA}$ NPs, $\text{Fe}_3\text{O}_4/\text{PPy}/\text{PEG}/\text{FA}$ NPs, and no NPs with respect to ACMF exposure time ($n = 5$). (F) Follow-up photographs of mouse exposed to ACMF for 20 min after injection with $\text{Fe}_3\text{O}_4/\text{DOX}/\text{PPy}/\text{PEG}/\text{FA}$ NPs. (G) Photographs

5.3 Nanomedicines in the Clinic

The successful translation of nanomedicines into the clinic is broadly dependent upon different types of materials exhibiting varying biodistribution, pharmacokinetics, compatibility, degradation, and circulation properties [253, 254]. No single parameter can be denoted as the most important prerequisite for effective clinical cancer therapy. Equally important, are the chemical barriers such as optimizing nanomaterials' physicochemical properties, intrinsic toxicities, drug loading/release, and scaled-up syntheses. The nanomedicines should be composed of biodegradable nontoxic materials that may be cleared by the liver and kidneys. They should have biologically inert, amphiphilic, and appropriate surface coatings to increase the in vivo circulation times, and decrease off-target site accumulation. Moreover, the nanomedicines should have high drug loading capacity, releasing the drugs in a controlled manner. Most currently approved and clinically investigated NMs are chiefly based on coatings with PEG, hydrophilic sugars (i.e., dextran), or serum proteins (i.e., human serum albumin) [255].

Clinical trials focusing on delivering chemotherapeutics in nanoformulations are abundant; however, the clinically approved formulations are mainly of liposomal, polymeric, or micellar nature [9, 256]. Those formulations are excellently reviewed in details by Anselmo and Mitragotri [10]. Such formulations contain drugs enclosed in inorganic vehicles that allow the drugs to stay in the bloodstream longer so that more of the drug can reach the target sites. Doxil[®] or CAELYX[®] (PEGylated liposomal Dox, 1995), Daunoxome/DaunoXome[®] (Liposome-encapsulated Daunorubicin, 1996), DepoCyt[®] (liposomal Cytarabine), Myocet[®] (non-pegylated liposomal Dox citrate, 2000), Oncaspar[®] (PEG-asparaginase, 2006), Abraxane[®] (albumin-bound PTX, 2013), and Genexol-PM[®] (PTX-loaded polymeric micelles, 2013) are current approved formulations used to treat various types of cancers, mainly metastatic ovarian, breast, lymphomatous meningitis, myeloid leukemia, acute lymphoblastic leukemia, AIDS-related Kaposi's sarcoma, and pancreatic cancer [257]. The main reason for their approval was the equivalent/improved efficacies and reduced side-toxicities or improved safety profiles as compared with free drug chemotherapies. Quite frequently, those formulations – especially Doxil[®] and Abraxane[®] – have been used as examples of nano-based drug delivery systems, mainly because their sizes are in the nanometer size range. It is to be noted, however, that the synthesis of these formulations was not inspired by any means of today's nanotechnology [208]. Interestingly, while NPs and targeting antibodies (i.e., antibody drug-conjugates) are both approved for clinical use, systems combining these two technologies are lacking in approved products [258, 259]. Nevertheless, few







Fig. 6.12 (continued) of nontreated mice, mice injected with Fe₃O₄/DOX/PPy-PEG-FA NPs, mice exposed to ACMF, mice treated with chemotherapy, mice treated with MHT, and mice treated with combination of MHT and chemotherapy 45 days after treatment. Mice bearing subcutaneous xenograft tumors derived from the RPMI8226 multiple myeloma cell line were intratumorally injected with NPs (5 mg/kg) and then exposed to ACMF. (Reproduced with permission from Ref. [252])

technologies are being investigated in the clinic. Of those, particular attention should be placed on HER-2 targeted PEGylated liposomal Dox (MM-302) for treatment of breast cancer [260]. Currently, the most investigated attempts to modulate biodistribution in nonapproved targeted particles introduce antibody targeting (e.g., HER2, EGFR, or transferrin receptor targeting) [77, 261]. If successful, these systems will represent the first clinically approved examples of targeted NPs, which will likely facilitate the clinical investigation of additional targeted systems.

With respect to MNPs, while many iron oxide MNP formulations have been approved by the FDA, very few MNP formulations are employed in human clinical settings (Table 6.1). While NanoTherm[®] and Sienna+[®] are intratumorally or subcutaneously injected, Feraheme[®] and Resovist[®] (approved in limited countries) are the only two formulations intravenously injected. For treatment purposes, and as discussed earlier, the only two MNP-based formulations presently used in clinical setting are Feraheme[®] for the treatment of iron deficiency anemia and NanoTherm[®]

Table 6.1 MNPs used in human clinical settings

Iron oxide magnetic formulation	Hydrodynamic size (nm)	Coating	Application	Clinical relevance
Resovist [®] , Cliavist [™] (Ferucarbotran) 	60	Carboxydextran	Liver/ hepatocellular carcinoma imaging (Diagnosis)	In use in only a few countries (i.e., Japan)
Sienna+ [®] 	60	Carboxydextran	Sentinel lymph node localization (diagnosis)	Approved and in use in Europe
Feraheme [®] , Rienso [®] (Ferumoxytol) 	30	Polyglucose sorbitol carboxymethylether	Anemia deficiency in adult patients with CKD/brain tumor imaging (therapeutics/ diagnosis)	Approved and in use in the United States and Europe/ Clinical Trials
NanoTherm [®] 	15	Aminosilane	Magnetic hyperthermia on solid tumors (therapeutics)	Approved and in use in Europe

therapy for the local treatment of solid tumors. Even the most recent approved Feraheme[®] does not have an intended use for cancer therapeutics with ongoing clinical trials in progress. Thus, up to now, *no drug-conjugated MNPs are currently employed in the clinic*. In that sense, many studies concerning drug-conjugated MNP safety concerns with respect to their use in medicine such as biodistribution, cytotoxicities, and inflammation responses are continuously carried out [262, 263]. The general consensus seems to indicate that iron oxide MNPs exhibit very little or no cytotoxic activity when administered at concentrations up to 100 $\mu\text{g Fe/mL}$ [234], and even up to 8 mg Fe/mL in formulations such as Feraheme[®] [264]. Typically, clinical doses of such MNPs in humans are determined between 0.56 and 8 mg Fe/kg patient body weight, which is much less than the normal blood iron concentration (≈ 33 mg Fe/kg body weight) and relatively low compared with total body iron (~ 3500 mg) [19]. However, even when concerned potential toxicities such as some side effects and allergic reactions do occur, it is believed that the toxicity of those NPs are not caused by the magnetite cores, but rather by the particle sizes, the surface coatings and instability in biological media/serum [263]. Given that even subtle changes in MNP formulation can lead to significant changes in cytotoxicity behavior, it seems that the best is to evaluate the toxicity of each unique MNP configuration separately prior to clinical trials.

6 Conclusion and Future Perspective

The utilization of MNPs in magneto-responsive imaging and drug-targeted delivery is expected to play a chief and promising role in theranostics of cancer and other diseases. Besides magnetic hyperthermia (with some formulations already in the clinic or in clinical trials), the greatest therapeutic potential is probably associated with drug-conjugated stimuli-responsive MNP systems that can be targeted to specific tumor sites releasing the drug selectively. Our increasing research capabilities to fine engineer MNPs and to conjugate drugs to these systems in effective controllable ways make it possible to create drug-loaded MNPs with tunable drug release profiles in responses to specific internal or external stimuli. In brief, important features should be met for successful and selective drug delivery system: (1) controlled design of the NPs, (2) increased blood circulation times and reduced RES accumulation, (3) enhanced uptake by targeted tumor cells, (4) effective and selective drug delivery in target sites, and (5) appropriate clearance from the body. However, due to limitations and challenges facing the nanodrug delivery systems, only marginal advances in effective drug delivery technologies result. Overcoming the many challenges of identifying a successful active drug delivery system requires an understanding of events involving transport of drug or drug carrier to the tumor site after administration as well as the body's immuno-response. Nanoparticulate approaches can have real impact in improving drug delivery by focusing on the major problems, such as enhancing drug loading capacity, uptake by the target cells versus nontarget cells, and control of drug release at the target site. Likewise, increasing blood circulation times is expected to enhance delivery to the tumor

sites as specific biomarker receptor targeting occurs only after optimizing blood circulation times (i.e., by appropriated polymeric coatings). All this will allow effective targeting to specific locations and more drug accumulation near the tumor site, optimizing both the delivery and efficacy of chemotherapeutic drugs.

Importantly, there are some critical issues to be addressed before effective nanomedicine translation to clinic. Considering the substantial preclinical research efforts put into targeted drug delivery, it is somewhat surprising that very few formulations has been approved in clinical practice for medical therapy. A large number of NP cancer therapeutics has been claimed to exhibit excellent effective results when used in animal models, but not in humans. In most cases, the approved drugs reformulated in nanomedicines provide only a small increase in performance that large pharmaceutical companies do not consider it worth investment and development. Thus, the clinical translation of effective nanoformulation seems challenging and not as easy as anticipated. Consequently, there are urgent needs to turn the MNP drug delivery potentials into tangible outcomes (i.e., formulations that can benefit patients) by carefully addressing several key issues: (1) simple and large scaled-up NP fabrications; (2) standardization of NP with quantitative systematic assessments of their efficacies; (3) establishment of clear and detailed toxicity, immunogenicity, clearance, and safety profiles for the specific formulation in use. The systematical investigation on the interface between the engineered NPs and biological environments at various physiochemical conditions, anatomic locations and different tissue environments are necessary when designing effective MNP-based drug delivery system for clinical use. Moreover, the drug delivery systems with good potential to clinical translation should not be very complex, because of the high possibility of failure during transition from lab production to large-scale synthetic production. The practical translation into commercial human nanomedicines could be facilitated by an increased focus among researchers on the requirements of effective therapeutic development, preclinical evaluations, and more data and regulatory requirements for clinical patient care.

Finally, the highly heterogeneous tumor microenvironment demands advanced drug delivery approaches and noninvasive imaging methods to assess drug delivery efficiencies and tumor responses to therapy in individual patients. MNP-based drug carriers offer great potentials to deliver precision oncology with assistance of imaging capabilities, giving noninvasive imaging evaluation of targeted NP drug delivery and intratumoral distribution of the drug carrier. Advancements in drug-conjugated drug systems have enabled the development and exploration of novel nanotherapeutic concepts for cancer treatment including combination therapies and delivering multiple drugs/targeting agents in one vehicle tailored to a patient's specific condition. As of the moment, *"no MNPs are used in humans in clinical settings whether as imaging or drug delivery carriers."* However, despite this current absence, the excellent safety profile of these magnetic nanocarriers means that they hold substantial potential for future theranostic human clinical use, as demonstrated by the planned clinical trials of Feraheme[®]. Hopefully, this MNP formulation and many other related ones presented here will produce magneto-responsive drug therapeutic systems having commercial competitiveness and satisfactory efficacies.

Acknowledgment The author would like to thank the continuous support by KSAU-HS, KAIMRC, and Ministry of National Guard Health Affairs. This work was funded by KAIMRC under grant RC13/204/R.

Financial and Competing Interests The author declares no competing financial interests. No writing assistance was utilized in the production of this book chapter.

References

1. Mann S (2009) Self-assembly and transformation of hybrid nano-objects and nanostructures under equilibrium and non-equilibrium conditions. *Nat Mater* 8:781–792
2. Fan H, Yang K, Boye DM, Sigmon T, Malloy KJ, Xu H et al (2004) Self-assembly of ordered, robust, three-dimensional gold nanocrystal/silica arrays. *Science* 304:567–571
3. Wu W, Jiang CZ, Roy VAL (2016) Designed synthesis and surface engineering strategies of magnetic iron oxide nanoparticles for biomedical applications. *Nanoscale* 8:19421–19474
4. Xie J, Lee S, Chen X (2010) Nanoparticle-based theranostic agents. *Adv Drug Deliv Rev* 62:1064–1079
5. Gupta AK, Gupta M (2005) Synthesis and surface engineering of iron oxide nanoparticles for biomedical applications. *Biomaterials* 26:3995–4021
6. Estelrich J, Escribano E, Queralto J, Busquets MA (2015) Iron oxide nanoparticles for magnetically-guided and magnetically-responsive drug delivery. *Int J Mol Sci* 16:8070–8101
7. Huang J, Li Y, Orza A, Lu Q, Guo P, Wang L et al (2016) Magnetic nanoparticle facilitated drug delivery for Cancer therapy with targeted and image-guided approaches. *Adv Funct Mater* 26:3818–3836
8. Duncan R (2003) The dawning era of polymer therapeutics. *Nat Rev Drug Discov* 2:347–360
9. Duncan R (2011) Polymer therapeutics as nanomedicines: new perspectives. *Curr Opin Biotechnol* 22:492–501
10. Anselmo AC, Mitragotri S (2016) Nanoparticles in the clinic. *Bioeng Transl Med* 1:10–29
11. Kievit FM, Zhang M (2011) Surface engineering of iron oxide nanoparticles for targeted cancer therapy. *Acc Chem Res* 44:853–862
12. Ling D, Lee N, Hyeon T (2015) Chemical synthesis and assembly of uniformly sized Iron oxide nanoparticles for medical applications. *Acc Chem Res* 48:1276–1285
13. Jin R (2008) Super robust nanoparticles for biology and biomedicine. *Angew Chem Int Ed* 47:6750–6753
14. Gao J, Gu H, Xu B (2009) Multifunctional magnetic nanoparticles: design, synthesis, and biomedical applications. *Acc Chem Res* 42:1097–1107
15. El-Boubbou K, Zhu David C, Vasileiou C, Borhan B, Prosperi D, Li W et al (2010) Magnetic glyco-nanoparticles: a tool to detect, differentiate, and unlock the glyco-codes of cancer via magnetic resonance imaging. *J Am Chem Soc* 132:4490–4499
16. El-Boubbou K, Huang X (2011) Glyco-nanomaterials: translating insights from the sugar-code to biomedical applications. *Curr Med Chem* 18:2060–2078
17. Jun YW, Huh YM, Choi JS, Lee JH, Song HT, Kim S et al (2005) Nanoscale size effect of magnetic Nanocrystals and their utilization for Cancer diagnosis via magnetic resonance imaging. *J Am Chem Soc* 127:5732–5733
18. Gao BJ, Li L, Ho PL, Mak GC, Gu H, Xu B (2006) Combining fluorescent probes and biofunctional magnetic nanoparticles for rapid detection of Bacteria in human blood. *Adv Mater* 18:3145–3148
19. Yoo D, Jeong H, Noh S-H, Lee J-H, Cheon J (2013) Magnetically triggered dual functional nanoparticles for resistance-free apoptotic hyperthermia. *Angew Chem Int Ed* 52:13047–13051

20. Hathaway HJ, Butler KS, Adolphi NL, Lovato DM, Belfon R, Fegan D et al (2011) Detection of breast cancer cells using targeted magnetic nanoparticles and ultra-sensitive magnetic field sensors. *Breast Cancer Res* 13:R108
21. Sun C, Lee JSH, Zhang M (2008) Magnetic nanoparticles in MR imaging and drug delivery. *Adv Drug Deliv Rev* 60:1252–1265
22. De Crozals G, Bonnet R, Farre C, Chaix C (2016) Nanoparticles with multiple properties for biomedical applications: a strategic guide. *Nano Today* 11:435–463
23. Wahajuddin AS (2012) Superparamagnetic iron oxide nanoparticles: magnetic nanoplateforms as drug carriers. *Int J Nanomedicine* 7:3445
24. Lee N, Hyeon T (2012) Designed synthesis of uniformly sized iron oxide nanoparticles for efficient magnetic resonance imaging contrast agents. *Chem Soc Rev* 41:2575–2589
25. Peng E, Wang F, Xue JM (2015) Nanostructured magnetic nanocomposites as MRI contrast agents. *J Mater Chem B* 3:2241–2276
26. Jun Y-w, Lee J-H, Cheon J (2008) Chemical design of nanoparticle probes for high-performance magnetic resonance imaging. *Angew Chem Int Ed* 47:5122–5135
27. Shen Z, Wu A, Chen X (2016) Iron oxide nanoparticle based contrast agents for magnetic resonance imaging. *Mol Pharm* 14:1352, ASAP
28. Xie J, Liu G, Eden HS, Ai H, Chen X (2011) Surface-engineered magnetic nanoparticle platforms for Cancer imaging and therapy. *Acc Chem Res* 44:883–892
29. National Cancer Institute (2015) Types of treatment. <https://www.cancer.gov/>
30. Jackson SE, Chester JD (2015) Personalised cancer medicine. *Int J Cancer* 137:262–266
31. Schork NJ (2015) Personalized medicine: time for one-person trials. *Nature* 520:609–611
32. Sengupta S (2017) Cancer Nanomedicine: lessons for Immuno-oncology. *Trends Cancer* 3:551–560
33. Barenholz Y (2012) Doxil[®] – the first FDA-approved nano-drug: lessons learned. *J Control Release* 160:117–134
34. Miele E, Spinelli GP, Miele E, Tomao F, Tomao S (2009) Albumin-bound formulation of paclitaxel (Abraxane[®]) ABI-007 in the treatment of breast cancer. *Int J Nanomedicine* 4:99–105
35. Harisinghani MG, Saksena M, Ross RW, Tabatabaei S, Dahl D, McDougal S et al (2005) A pilot study of lymphotropic nanoparticle-enhanced magnetic resonance imaging technique in early stage testicular cancer: a new method for noninvasive lymph node evaluation. *Urology* 66:1066–1071
36. Min Y, Caster JM, Eblan MJ, Wang AZ (2015) Clinical translation of nanomedicine. *Chem Rev* 115:11147–11190
37. Freeman MW, Arrot A, Watson HHL (1960) Magnetism in medicine. *J Appl Phys* 31:S404
38. Widder KJ, Morris RM, Poore GA, Howard DP, Senyei AE (1983) Selective targeting of magnetic albumin microspheres containing low-dose doxorubicin: total remission in Yoshida sarcoma-bearing rats. *Eur J Cancer Clin Oncol* 19:135–139
39. Alexiou C, Arnold W, Klein RJ, Parak FG, Hulin P, Bergemann C et al (2000) Locoregional cancer treatment with magnetic drug targeting. *Cancer Res* 60:6641–6648
40. Alexiou C, Schmid RJ, Jurgons R, Kremer M, Wanner G, Bergemann C et al (2006) Targeting cancer cells: magnetic nanoparticles as drug carriers. *Eur Biophys J* 35:446–450
41. Goodwin SC, Bittner CA, Peterson CL, Wong G (2001) Single-dose toxicity study of hepatic intra-arterial infusion of doxorubicin coupled to a novel magnetically targeted drug carrier. *Toxicol Sci* 60:177–183
42. Lübke AS, Bergemann C, Huhnt W, Fricke T, Riess H, Brock JW et al (1996) Preclinical experiences with magnetic drug targeting: tolerance and efficacy. *Cancer Res* 56:4694–4701
43. Koda J, Venook A, Walser E (2002) A multicenter, phase I/II trial of hepatic intra-arterial delivery of doxorubicin hydrochloride adsorbed to magnetic targeted carriers in patients with hepatocellular carcinoma. *Eur J Cancer* 38:S18
44. Wilson MW, Kerlan RK, Fidelman NA, Venook AP, LaBerge JM, Koda J et al (2004) Hepatocellular carcinoma: regional therapy with a magnetic targeted carrier bound to doxorubicin in a dual MR imaging/ conventional angiography suite – initial experience with four patients. *Radiology* 230:287–293

45. Lübke AS, Bergemann C, Riess H, Schriever F, Reichardt P, Possinger K et al (1996) Clinical experiences with magnetic drug targeting: a phase I study with 4'-Epidoxorubicin in 14 patients with advanced solid tumors. *Cancer Res* 56:4686–4693
46. Krukemeyer MG, Krenn V, Jakobs M, Wagner W (2012) Magnetic drug targeting in a rhabdomyosarcoma rat model using magnetite-dextran composite nanoparticle-bound mitoxantrone and 0.6 tesla extracorporeal magnets – sarcoma treatment in progress. *J Drug Target* 20:185–193
47. Kumar M, Yigit M, Dai G, Moore A, Medarova Z (2010) Image-guided breast tumor therapy using a small interfering RNA nanodrug. *Cancer Res* 70:7553–7561
48. Krukemeyer MG, Krenn V, Jakobs M, Wagner W (2012) Mitoxantrone-iron oxide biodistribution in blood, tumor, spleen, and liver-magnetic nanoparticles in cancer treatment. *J Surg Res* 175:35–43
49. Li Z, Dong K, Huang S, Ju E, Liu Z, Yin M et al (2014) A smart Nanoassembly for multistage targeted drug delivery and magnetic resonance imaging. *Adv Funct Mater* 24:3612–3620
50. Muthana M, Kennerley AJ, Hughes R, Fagnano E, Richardson J, Paul M et al (2015) Directing cell therapy to anatomic target sites in vivo with magnetic resonance targeting. *Nat Commun* 6:8009
51. Bañobre-López M, Teijeiro A, Rivas J (2013) Magnetic nanoparticle-based hyperthermia for cancer treatment. *Rep Pract Oncol Radiother* 18:397–400
52. Kumar CSSR, Mohammad F (2011) Magnetic nanomaterials for hyperthermia-based therapy and controlled drug delivery. *Adv Drug Deliv Rev* 63:789–808
53. Derfus AM, von Maltzahn G, Harris TJ, Duza T, Vecchio KS, Ruoslahti E et al (2007) Remotely triggered release from magnetic nanoparticles. *Adv Mater* 19:3932–3936
54. Young JH, Wang M, Brezovich IA (1980) Frequency/depth-penetration considerations in hyperthermia by magnetically induced currents. *Electron Lett* 16:358–359
55. Kennedy JE (2005) High-intensity focused ultrasound in the treatment of solid tumours. *Nat Rev Cancer* 5:321
56. Ziegelberger G (2006) ICNIRP statement on far infrared radiation exposure. *Health Phys* 91:630–645
57. Salunkhe AB, Khot VM, Pawar SH (2014) Magnetic hyperthermia with magnetic nanoparticles: a status review. *Curr Top Med Chem* 14:572–594
58. Jeon MJ, Ahn C-H, Kim H, Chung IJ, Jung S, Kim Y-H et al (2014) The intratumoral administration of ferucarbotran conjugated with doxorubicin improved therapeutic effect by magnetic hyperthermia combined with pharmacotherapy in a hepatocellular carcinoma model. *J Exp Clin Cancer Res* 33:57
59. Giustini AJ, Petryk AA, Cassim SM, Tate JA, Baker I, Hoopes PJ (2010) Magnetic nanoparticle hyperthermia in cancer treatment. *Nano Life* 1:10
60. Revia RA, Zhang M (2016) Magnetite nanoparticles for cancer diagnosis, treatment, and treatment monitoring: recent advances. *Mater Today* 19:157–168
61. Jordan A, Scholz R, Wust P, Föhling H, Krause J, Wlodarczyk W et al (1997) Effects of magnetic fluid hyperthermia (MFH) on C3H mammary carcinoma in vivo. *Int J Hyperth* 13:587–605
62. Jordan A, Scholz R, Wust P, Schirra H, Schiestel T, Schmidt H et al (1999) Endocytosis of dextran and silan-coated magnetite nanoparticles and the effect of intracellular hyperthermia on human mammary carcinoma cells in vitro. *J Magn Magn Mater* 194:185–196
63. Maier-Hauff K, Ulrich F, Nestler D, Niehoff H, Wust P, Thiesen B et al (2011) Efficacy and safety of intratumoral thermotherapy using magnetic iron-oxide nanoparticles combined with external beam radiotherapy on patients with recurrent glioblastoma multiforme. *J Neuro-Oncol* 103:317–324
64. Johannsen M, Gneveckow U, Taymoorian K, Thiesen B, Waldöfner N, Scholz R et al (2007) Morbidity and quality of life during thermotherapy using magnetic nanoparticles in locally recurrent prostate cancer: results of a prospective phase I trial. *Int J Hyperth* 23:315–323
65. Johannsen M, Thiesen B, Wust P, Jordan A (2010) Magnetic nanoparticle hyperthermia for prostate cancer. *Int J Hyperth* 26:790–795

66. Sanson C, Diou O, Thévenot J, Ibarboure E, Soum A, Brûlet A et al (2011) Doxorubicin loaded magnetic polymersomes: theranostic nanocarriers for MR imaging and magneto-chemotherapy. *ACS Nano* 5:1122–1140
67. Chang P, Purushotham S, Rumpel H, Kee I, Ng R, Chow P et al (2014) Novel dual magnetic drug targeting and hyperthermia therapy in hepatocellular carcinoma with thermosensitive polymer-coated nanoparticles. *J Gastrointest Dig Syst* 4:198
68. Gewirtz DA, Bristol ML, Yalowich JC (2010) Toxicity issues in Cancer drug development. *Curr Opin Investig Drugs* 11:612–614
69. Li S-D, Huang L (2008) Pharmacokinetics and biodistribution of nanoparticles. *Mol Pharm* 5:496–504
70. Maeda H, Wu J, Sawa T, Matsumura Y, Hori K (2000) Tumor vascular permeability and the EPR effect in macromolecular therapeutics: a review. *J Control Release* 65:271–284
71. Hobbs SK (1998) Regulation of transport pathways in tumor vessels: role of tumor type and microenvironment. *Proc Natl Acad Sci USA* 95:4607–4612
72. Adisheshaiah PP, Hall JB, McNeil SE (2009) Nanomaterial standards for efficacy and toxicity assessment. *Wiley Interdiscip Rev Nanomed Nanobiotechnol* 2:99–112
73. Cortajarena AL, Ortega D, Ocampo SM, Gonzalezgarcía A, Couleaud P, Miranda R et al (2014) Engineering iron oxide nanoparticles for clinical settings. *Nanobiomedicine* 1:58841
74. Kaminski MS, Tuck M, Estes J, Kolstad A, Ross CW, Zasadny K et al (2005) 131I-Tositumomab therapy as initial treatment for follicular lymphoma. *N Engl J Med* 352:441–449
75. Torchilin VP, Lukyanov AN, Gao Z, Papahadjopoulos-Sternberg B (2003) Immunomicelles: targeted pharmaceutical carriers for poorly soluble drugs. *Proc Natl Acad Sci USA* 100:6039
76. Cheever MA, Allison JP, Ferris AS, Finn OJ, Hastings BM, Hecht TT et al (2009) The prioritization of Cancer antigens: a National Cancer Institute pilot project for the acceleration of translational research. *Clin Cancer Res* 15:5323–5337
77. Ross JS, Slodkowska EA, Symmans WF, Pusztai L, Ravdin PM, Hortobagyi GN (2009) The HER-2 receptor and breast cancer: ten years of targeted anti-HER-2 therapy and personalized medicine. *Oncologist* 14:320–368
78. Sugahara KN (2010) Coadministration of a tumor-penetrating peptide enhances the efficacy of cancer drugs. *Science* 328:1031–1035
79. Yang W, Luo D, Wang S, Wang R, Chen R, Liu Y et al (2008) TMTPI, a novel tumor-homing peptide specifically targeting metastasis. *Clin Cancer Res* 14:5494
80. Zhang C, Jugold M, Woenen EC, Lammers T, Morgenstern B, Mueller MM et al (2007) Specific targeting of tumor angiogenesis by RGD-conjugated ultrasmall superparamagnetic iron oxide particles using a clinical 1.5-T magnetic resonance scanner. *Cancer Res* 67:1555–1562
81. Farokhzad OC, Jon S, Khademhosseini A, Tran T-NT, LaVan DA, Langer R (2004) Nanoparticle-Aptamer Bioconjugates. *Cancer Res* 64:7668
82. Wang Z, Zhou C, Xia J, Via B, Xia Y, Zhang F et al (2013) Fabrication and characterization of a triple functionalization of graphene oxide with Fe₃O₄, folic acid and doxorubicin as dual-targeted drug nanocarrier. *Colloids Surf B: Biointerfaces* 106:60–65
83. Lu AH, Salabas EL, Schuth F (2007) Magnetic nanoparticles: synthesis, protection, functionalization, and application. *Angew Chem Int Ed* 46:1222–1244
84. Laurent S, Forge D, Port M, Roch A, Robic C, Vander Elst L et al (2008) Magnetic iron oxide nanoparticles: synthesis, stabilization, Vectorization, physicochemical characterizations, and biological applications. *Chem Rev* 108:2064–2110
85. Sun J, Zhou S, Hou P, Yang Y, Weng J, Li X et al (2007) Synthesis and characterization of biocompatible Fe₃O₄ nanoparticles. *J Biomed Mater Res A* 80:333–341
86. Qiao R, Yang C, Gao M (2009) Superparamagnetic iron oxide nanoparticles: from preparations to in vivo MRI applications. *J Mater Chem* 19:6274–6293
87. Li J, He Y, Sun W, Luo Y, Cai H, Pan Y et al (2014) Hyaluronic acid-modified hydrothermally synthesized iron oxide nanoparticles for targeted tumor MR imaging. *Biomaterials* 35:3666–3677

88. Aubery C, Solans C, Prevost S, Gradzielski M, Sanchez-Dominguez M (2013) Microemulsions as reaction media for the synthesis of mixed oxide nanoparticles: relationships between microemulsion structure, reactivity, and nanoparticle characteristics. *Langmuir* 29:1779–1789
89. El-Boubbou K, Zhu DC, Vasileiou C, Borhan B, Prosperi D, Li W et al (2010) Magnetic glyconanoparticles: a tool to detect, differentiate, and unlock the glyco-codes of cancer via magnetic resonance imaging. *J Am Chem Soc* 132:4490–4499
90. El-Boubbou K, El-Dakdouki MH, Kamat M, Huang R, Abela GS, Kiupel M et al (2014) CD44 targeting magnetic glyconanoparticles for atherosclerotic plaque imaging. *Pharm Res* 31:1426–1437
91. Calero M, Gutiérrez L, Salas G, Luengo Y, Lázaro A, Acedo P et al (2014) Efficient and safe internalization of magnetic iron oxide nanoparticles: two fundamental requirements for biomedical applications. *Nanomedicine* 10:733–743
92. Massart R (1981) Preparation of aqueous magnetic liquids in alkaline and acidic media. *IEEE Trans Magn* 17:1247–1248
93. Cheng FY, Su CH, Yang YS, Yeh CS, Tsai CY, Wu CL et al (2005) Characterization of aqueous dispersions of Fe₃O₄ nanoparticles and their biomedical applications. *Biomaterials* 26:729–738
94. Itoh H, Sugimoto T (2003) Systematic control of size, shape, structure, and magnetic properties of uniform magnetite and maghemite particles. *J Colloid Interface Sci* 265:283–295
95. Weissleder R, Elizondo G, Wittenberg J, Rabito CA, Bengele HH, Josephson L (1990) Ultrasmall superparamagnetic iron oxide: characterization of a new class of contrast agents for MR imaging. *Radiology* 175:489–493
96. Tassa C, Shaw SY, Weissleder R (2011) Dextran-coated iron oxide nanoparticles: a versatile platform for targeted molecular imaging, molecular diagnostics, and therapy. *Acc Chem Res* 44:842–852
97. Hahn PF, Stark DD, Lewis JM, Saini S, Elizondo G, Weissleder R et al (1990) First clinical trial of a new superparamagnetic iron oxide for use as an oral gastrointestinal contrast agent in MR imaging. *Radiology* 175:695–700
98. Wang YX, Hussain SM, Krestin GP (2001) Superparamagnetic iron oxide contrast agents: physicochemical characteristics and applications in MR imaging. *Eur Radiol* 11:2319–2331
99. Smith EA, Chen W (2008) How to prevent the loss of surface functionality derived from aminosilanes. *Langmuir* 24:12405–12409
100. Yamaura M, Camilo RL, Sampaio LC, Macêdo MA, Nakamura M, Toma HE (2004) Preparation and characterization of (3-aminopropyl)triethoxysilane-coated magnetite nanoparticles. *J Magn Mater* 279:210–217
101. Bruce IJ, Sen T (2005) Surface modification of magnetic nanoparticles with alkoxy silanes and their application in magnetic bioseparations. *Langmuir* 21:7029–7035
102. Mahdavi M, Ahmad M, Haron M, Namvar F, Nadi B, Rahman M et al (2013) Synthesis, surface modification and characterisation of biocompatible magnetic iron oxide nanoparticles for biomedical applications. *Molecules* 18:7533–7548
103. Yee C, Kataby G, Ulman A, Prozorov T, White H, King A et al (1999) Self-assembled monolayers of alkanesulfonic and -phosphonic acids on amorphous iron oxide nanoparticles. *Langmuir* 15:7111–7115
104. Sahoo Y, Pizem H, Fried T, Golodnitsky D, Burstein L, Sukenik CN et al (2001) Alkyl phosphonate/phosphate coating on magnetite nanoparticles: a comparison with fatty acids. *Langmuir* 17:7907–7911
105. Basuki JS, Jacquemin A, Esser L, Li Y, Boyer C, Davis TP (2014) A block copolymer-stabilized co-precipitation approach to magnetic iron oxide nanoparticles for potential use as MRI contrast agents. *Polym Chem* 5:2611–2620
106. Lu X, Niu M, Qiao R, Gao M (2008) Superdispersible PVP-coated Fe₃O₄ Nanocrystals prepared by a “One-Pot” reaction. *J Phys Chem B* 112:14390–14394

107. Lee H-Y, Lee S-H, Xu C, Xie J, Lee J-H, Wu B et al (2008) Synthesis and characterization of PVP-coated large core iron oxide nanoparticles as an MRI contrast agent. *Nanotechnology* 19:165101–165106
108. Park J, An K, Hwang Y, Park J-G, Noh H-J, Kim J-Y et al (2004) Ultra-large-scale syntheses of monodisperse nanocrystals. *Nat Mater* 3:891–895
109. Park J, Lee E, Hwang N-M, Kang M, Kim SC, Hwang Y et al (2005) One-nanometer-scale size-controlled synthesis of monodisperse magnetic Iron oxide nanoparticles. *Angew Chem Int Ed* 44:2872–2877
110. Hyeon T, Lee SS, Park J, Chung Y, Na HB (2001) Synthesis of highly crystalline and Monodisperse Maghemite Nanocrystallites without a size-selection process. *J Am Chem Soc* 123:12798–12801
111. Kim BH, Lee N, Kim H, An K, Park YI, Choi Y et al (2011) Large-scale synthesis of uniform and extremely small-sized iron oxide nanoparticles for high-resolution T1 magnetic resonance imaging contrast agents. *J Am Chem Soc* 133:12624–12631
112. Sun S, Zeng H (2002) Size-controlled synthesis of magnetite nanoparticles. *J Am Chem Soc* 124:8204–8205
113. Sun S, Murray CB, Weller D, Folks L, Moser A (2000) Monodisperse FePt nanoparticles and ferromagnetic FePt nanocrystal superlattices. *Science* 287:1989–1992
114. Sun S, Zeng H, Robinson DB, Raoux S, Rice PM, Wang SX et al (2004) Monodisperse MFe₂O₄ (M = Fe, Co, Mn) nanoparticles. *J Am Chem Soc* 126:273–279
115. Dong A, Ye X, Chen J, Kang Y, Gordon T, Kikkawa JM et al (2011) A generalized ligand-exchange strategy enabling sequential surface functionalization of colloidal nanocrystals. *J Am Chem Soc* 133:998–1006
116. Zhang T, Ge J, Hu Y, Yin Y (2007) A general approach for transferring hydrophobic nanocrystals into water. *Nano Lett* 7:3203–3207
117. El-Dakdouki MH, El-Boubbou K, Zhu DC, Huang X (2011) A simple method for the synthesis of hyaluronic acid coated magnetic nanoparticles for highly efficient cell labelling and in vivo imaging. *RSC Adv* 1:1449–1452
118. De Palma R, Peeters S, Van Bael MJ, Van den Rul H, Bonroy K, Laureyn W et al (2007) Silane ligand exchange to make hydrophobic superparamagnetic nanoparticles water-dispersible. *Chem Mater* 19:1821–1831
119. Kwon SG, Hyeon T (2011) Formation mechanisms of uniform nanocrystals via hot-injection and heat-up methods. *Small* 7:2685–2702
120. Park J, Joo J, Kwon SG, Jang Y, Hyeon T (2007) Synthesis of monodisperse spherical nanocrystals. *Angew Chem Int Ed* 46:4630–4660
121. Cheon J, Kang N-J, Lee S-M, Lee J-H, Yoon J-H, Oh SJ (2004) Shape evolution of single-crystalline iron oxide nanocrystals. *J Am Chem Soc* 126:1950–1951
122. Jana NR, Chen Y, Peng X (2004) Size- and shape-controlled magnetic (Cr, Mn, Fe, Co, Ni) oxide nanocrystals via a simple and general approach. *Chem Mater* 16:3931–3935
123. Lee Y, Lee J, Bae CJ, Park J-G, Noh H-J, Park J-H et al (2005) Large-scale synthesis of uniform and crystalline magnetite nanoparticles using reverse micelles as nanoreactors under reflux conditions. *Adv Funct Mater* 15:503–509
124. Li Z, Chen H, Bao H, Gao M (2004) One-pot reaction to synthesize water-soluble magnetite nanocrystals. *Chem Mater* 16:1391–1393
125. Li Z, Sun Q, Gao M (2005) Preparation of water-soluble magnetite nanocrystals from hydrated ferric salts in 2-pyrrolidone: mechanism leading to Fe₃O₄. *Angew Chem Int Ed* 44:123–126
126. Ge J, Hu Y, Biasini M, Beyermann WP, Yin Y (2007) Superparamagnetic magnetite colloidal nanocrystal clusters. *Angew Chem Int Ed* 46:4342–4345
127. Ge J, Hu Y, Biasini M, Dong C, Guo J, Beyermann WP et al (2007) One-step synthesis of highly water-soluble magnetite colloidal nanocrystals. *Chem Eur J* 13:7153–7161
128. El-Boubbou K, Al-Kaysi RO, Al-Muhanna MK, Bahhari HM, Al-Romaeh AI, Darwish N et al (2015) Ultra-small fatty acid-stabilized magnetite nanocolloids synthesized by in situ hydrolytic precipitation. *J Nanomater* 2015:620672. 11 pages

129. El-Boubbou K (2017) Usacid-stabilized iron-based metal oxide colloidal nanoparticles, and methods thereof. US Patent 20170110228 A1
130. Jaffer Farouc A, Nahrendorf M, Sosnovik D, Kelly Kimberly A, Aikawa E, Weissleder R (2006) Cellular imaging of inflammation in atherosclerosis using magnetofluorescent nanomaterials. *Mol Imaging* 5:85–92
131. Thorek Daniel LJ, Chen Antony K, Czupryna J, Tsourkas A (2006) Superparamagnetic iron oxide nanoparticle probes for molecular imaging. *Ann Biomed Eng* 34:23–38
132. Oksendal AN, Bach-Gansmo T, Jacobsen TF, Eide H, Andrew E (1993) Oral magnetic particles: results from clinical phase II trials in 216 patients. *Acta Radiol* 34:187–193
133. Reimer P, Balzer T (2003) Ferucarbotran (Resovist): a new clinically approved RES-specific contrast agent for contrast-enhanced MRI of the liver: properties, clinical development, and applications. *Eur Radiol* 13:1266
134. Michel SCA, Keller TM, Fröhlich JM, Fink D, Caduff R, Seifert B et al (2002) Preoperative breast cancer staging: MR imaging of the axilla with ultrasmall superparamagnetic iron oxide enhancement. *Radiology* 225:527–536
135. Trivedi RA, Mallawarachi C, U-King-Im J-M, Graves MJ, Horsley J, Goddard MJ et al (2006) Identifying inflamed carotid plaques using in vivo USPIO-enhanced MR imaging to label plaque macrophages. *Arterioscler Thromb Vasc Biol* 26:1601
136. Bachmann R, Conrad R, Kreft B, Luzar O, Block W, Flacke S et al (2002) Evaluation of a new ultrasmall superparamagnetic iron oxide contrast agent Clariscan[®], (NC100150) for MRI of renal perfusion: experimental study in an animal model. *J Magn Reson Imaging* 16:190–195
137. Jung CW, Jacobs P (1995) Physical and chemical properties of superparamagnetic iron oxide MR contrast agents: ferumoxides, ferumoxtran, ferumoxsil. *Magn Reson Imaging* 13:661–674
138. Jung CW (1995) Surface properties of superparamagnetic iron oxide MR contrast agents: ferumoxides, ferumoxtran, ferumoxsil. *Magn Reson Imaging* 13:675–691
139. Wang Y-XJ (2011) Superparamagnetic iron oxide based MRI contrast agents: current status of clinical application. *Quant Imaging Med Surg* 1:35–40
140. Thill M, Kurylcio A, Welter R, van Haasteren V, Grosse B, Berclaz G et al (2014) The central-European SentiMag study: sentinel lymph node biopsy with superparamagnetic iron oxide (SPIO) vs. radioisotope. *Breast* 23:175–179
141. Winter A, Woenkhaus J, Wawroschek F (2014) A novel method for intraoperative sentinel lymph node detection in prostate cancer patients using superparamagnetic iron oxide nanoparticles and a handheld magnetometer: the initial clinical experience. *Ann Surg Oncol* 21:4390–4396
142. Wáng YXJ, Idée J-M (2017) A comprehensive literatures update of clinical researches of superparamagnetic resonance iron oxide nanoparticles for magnetic resonance imaging. *Quant Imaging Med Surg* 7:88–122
143. Lee J-H, Huh Y-M, Jun Y-w, Seo J-w, Jang J-t, Song H-T et al (2007) Artificially engineered magnetic nanoparticles for ultra-sensitive molecular imaging. *Nat Med* 13:95–99
144. Kim J, Piao Y, Hyeon T (2009) Multifunctional nanostructured materials for multimodal imaging, and simultaneous imaging and therapy. *Chem Soc Rev* 38:372–390
145. Jarzyna PA, Gianella A, Skajaa T, Knudsen G, Deddens LH, Cormode DP et al (2010) Multifunctional imaging nanoprobe. *Wiley Interdiscip Rev Nanomed Nanobiotechnol* 2:138–150
146. Lewin M, Carlesso N, Tung C-H, Tang X-W, Cory D, Scadden DT et al (2000) Tat peptide-derivatized magnetic nanoparticles allow in vivo tracking and recovery of progenitor cells. *Nat Biotechnol* 18:410–414
147. Lee H-Y, Li Z, Chen K, Hsu AR, Xu C, Xie J et al (2008) PET/MRI dual-modality tumor imaging using arginine-glycine-aspartic (RGD)-conjugated radiolabeled Iron oxide nanoparticles. *J Nucl Med* 49:1371
148. Josephson L, Kircher MF, Mahmood U, Tang Y, Weissleder R (2002) Near-infrared fluorescent nanoparticles as combined MR/optical imaging probes. *Bioconjug Chem* 13:554–560

149. Pittet MJ, Swirski FK, Reynolds F, Josephson L, Weissleder R (2006) Labeling of immune cells for in vivo imaging using magnetofluorescent nanoparticles. *Nat Protoc* 1:73–79
150. Moore A, Medarova Z, Potthast A, Dai G (2004) In vivo targeting of underglycosylated MUC-1 tumor antigen using a multimodal imaging probe. *Cancer Res* 64:1821–1827
151. Nahrendorf M, Zhang H, Hembrador S, Panizzi P, Sosnovik DE, Aikawa E et al (2008) Nanoparticle PET-CT imaging of macrophages in inflammatory atherosclerosis. *Circulation* 117:379–387
152. Nahrendorf M, Keliher E, Marinelli B, Waterman P, Feruglio PF, Fexon L et al (2010) Hybrid PET-optical imaging using targeted probes. *Proc Natl Acad Sci USA* 107:7910–7915
153. Kirschbaum K, Sonner JK, Zeller MW, Deumelandt K, Bode J, Sharma R et al (2016) In vivo nanoparticle imaging of innate immune cells can serve as a marker of disease severity in a model of multiple sclerosis. *Proc Natl Acad Sci USA* 113:13227–13232
154. Raymond KN, Pierre VC (2005) Next generation, high Relaxivity gadolinium MRI agents. *Bioconjug Chem* 16:3–8
155. Datta A, Raymond KN (2009) Gd-hydroxypyridinone (HOPO)-based high-relaxivity magnetic resonance imaging (MRI) contrast agents. *Acc Chem Res* 42:938–947
156. Yang H, Zhuang Y, Sun Y, Dai A, Shi X, Wu D et al (2011) Targeted dual-contrast T1- and T2-weighted magnetic resonance imaging of tumors using multifunctional gadolinium-labeled superparamagnetic iron oxide nanoparticles. *Biomaterials* 32:4584–4593
157. Bae KH, Kim YB, Lee Y, Hwang J, Park H, Park TG (2010) Bioinspired synthesis and characterization of gadolinium-labeled magnetite nanoparticles for dual contrast T1- and T2-weighted magnetic resonance imaging. *Bioconjug Chem* 21:505–512
158. Amstad E, Gillich T, Bilecka I, Textor M, Reimhult E (2009) Ultrastable iron oxide nanoparticle colloidal suspensions using dispersants with catechol-derived anchor groups. *Nano Lett* 9:4042–4048
159. Shen J, Li Y, Zhu Y, Yang X, Yao X, Li J et al (2015) Multifunctional gadolinium-labeled silica-coated Fe₃O₄ and CuInS₂ nanoparticles as a platform for in vivo tri-modality magnetic resonance and fluorescence imaging. *J Mater Chem B* 3:2873–2882
160. Savolainen H, Volpe A, Phinikaridou A, Douek M, Fruhwirth GO, de Rosales RTM (2018) [⁶⁸Ga]Ga-sienna+ PET-MRI as a preoperative imaging tool for sentinel lymph node biopsy: synthesis and preclinical evaluation in a metastatic breast Cancer model. In: 13th European molecular imaging meeting – EMIM
161. Jin Y, Jia C, Huang S-W, O'Donnell M, Gao X (2010) Multifunctional nanoparticles as coupled contrast agents. *Nat Commun* 1:41
162. Pissuwan D, Valenzuela SM, Cortie MB (2006) Therapeutic possibilities of plasmonically heated gold nanoparticles. *Trends Biotechnol* 24:62–67
163. Hoskins C, Min Y, Gueorguieva M, McDougall C, Volovick A, Prentice P et al (2012) Hybrid gold-iron oxide nanoparticles as a multifunctional platform for biomedical application. *J Nanobiotechnol* 10:27
164. Thomas R, Park I-K, Jeong YY (2013) Magnetic Iron oxide nanoparticles for multimodal imaging and therapy of Cancer. *Int J Mol Sci* 14:15910–15930
165. Giljohann DA, Seferos DS, Daniel WL, Massich MD, Patel PC, Mirkin CA (2010) Gold nanoparticles for biology and medicine. *Angew Chem Int Ed* 49:3280–3294
166. Lee N, Yoo D, Ling D, Cho MH, Hyeon T, Cheon J (2015) Iron oxide based nanoparticles for multimodal imaging and Magnetoresponse therapy. *Chem Rev* 115:10637–10689
167. Reguera J, Jimenez de Aberasturi D, Henriksen-Lacey M, Langer J, Espinosa A, Szczupak B et al (2017) Janus plasmonic-magnetic gold-iron oxide nanoparticles as contrast agents for multimodal imaging. *Nanoscale* 9:9467–9480
168. Mahmoudi M, Shokrgozar MA (2012) Multifunctional stable fluorescent magnetic nanoparticles. *Chem Commun* 48:3957–3959
169. Kairdolf BA, Smith AM, Stokes TH, Wang MD, Young AN, Nie S (2013) Semiconductor quantum dots for bioimaging and biodiagnostic applications. *Annu Rev Anal Chem* 6:143–162
170. Chen O, Riedemann L, Etoc F, Herrmann H, Coppey M, Barch M et al (2014) Magneto-fluorescent core-shell supernanoparticles. *Nat Commun* 5:5093

171. Lee EA, Yim H, Heo J, Kim H, Jung G, Hwang NS (2014) Application of magnetic nanoparticle for controlled tissue assembly and tissue engineering. *Arch Pharm Res* 37:120–128
172. Corchero JL, Villaverde A (2009) Biomedical applications of distally controlled magnetic nanoparticles. *Trends Biotechnol* 27:468–476
173. Sensenig R, Sapir Y, MacDonald C, Cohen S, Polyak B (2012) Magnetic nanoparticle-based approaches to locally target therapy and enhance tissue regeneration in vivo. *Nanomedicine (Lond)* 7:1425–1442
174. Santos LJ, Reis RL, Gomes ME (2015) Harnessing magnetic-mechano actuation in regenerative medicine and tissue engineering. *Trends Biotechnol* 33:471–479
175. Betal S, Saha AK, Ortega E, Dutta M, Ramasubramanian AK, Bhalla AS et al (2018) Core-shell magnetoelectric nanorobot – a remotely controlled probe for targeted cell manipulation. *Sci Rep* 8:1755
176. Guillotin B, Guillemot F (2011) Cell patterning technologies for organotypic tissue fabrication. *Trends Biotechnol* 29:183–190
177. Perea H, Aigner J, Heverhagen JT, Hopfner U, Wintermantel E (2007) Vascular tissue engineering with magnetic nanoparticles: seeing deeper. *J Tissue Eng Regen Med* 1:318–321
178. Yamamoto Y, Ito A, Kato M, Kawabe Y, Shimizu K, Fujita H et al (2009) Preparation of artificial skeletal muscle tissues by a magnetic force-based tissue engineering technique. *J Biosci Bioeng* 108:538–543
179. Shimizu K, Ito A, Yoshida T, Yamada Y, Ueda M, Honda H (2007) Bone tissue engineering with human mesenchymal stem cell sheets constructed using magnetite nanoparticles and magnetic force. *J Biomed Mater Res B Appl Biomater* 82B:471–480
180. Sasaki T, Iwasaki N, Kohno K, Kishimoto M, Majima T, Nishimura S-I et al (2007) Magnetic nanoparticles for improving cell invasion in tissue engineering. *J Biomed Mater Res A* 86A:969–978
181. Thevenot P, Sohaebuddin S, Poudyal N, Liu JP, Tang L (2008) Magnetic nanoparticles to enhance cell seeding and distribution in tissue engineering scaffolds. *Proc IEEE Conf Nanotechnol* 2008:646–649
182. Shimizu K, Ito A, Honda H (2006) Enhanced cell-seeding into 3D porous scaffolds by use of magnetite nanoparticles. *J Biomed Mater Res B Appl Biomater* 77B:265–272
183. Ishii M, Shibata R, Numaguchi Y, Kito T, Suzuki H, Shimizu K et al (2011) Enhanced angiogenesis by transplantation of mesenchymal stem cell sheet created by a novel magnetic tissue engineering method. *Arterioscler Thromb Vasc Biol* 31:2210–2215
184. Ishii M, Shibata R, Shimizu Y, Yamamoto T, Kondo K, Inoue Y et al (2014) Multilayered adipose-derived regenerative cell sheets created by a novel magnetite tissue engineering method for myocardial infarction. *Int J Cardiol* 175:545–553
185. Kito T, Shibata R, Ishii M, Suzuki H, Himeno T, Kataoka Y et al (2013) iPS cell sheets created by a novel magnetite tissue engineering method for reparative angiogenesis. *Sci Rep* 3:1418
186. Meng J, Xiao B, Zhang Y, Liu J, Xue H, Lei J et al (2013) Super-paramagnetic responsive nanofibrous scaffolds under static magnetic field enhance osteogenesis for bone repair in vivo. *Sci Rep* 3:2655
187. Sapir Y, Cohen S, Friedman G, Polyak B (2012) The promotion of in vitro vessel-like organization of endothelial cells in magnetically responsive alginate scaffolds. *Biomaterials* 33:4100–4109
188. Singh RK, Patel KD, Lee JH, Lee E-J, Kim J-H, Kim T-H et al (2014) Potential of magnetic Nanofiber scaffolds with mechanical and biological properties applicable for bone regeneration. *PLoS One* 9:e91584
189. Cezar CA, Kennedy SM, Mehta M, Weaver JC, Gu L, Vandenburgh H et al (2014) Biphasic ferrogels for triggered drug and cell delivery. *Adv Healthc Mater* 3:1869–1876
190. Ziv-Polat O, Skaat H, Shahar A, Margel S (2012) Novel magnetic fibrin hydrogel scaffolds containing thrombin and growth factors conjugated iron oxide nanoparticles for tissue engineering. *Int J Nanomedicine* 7:1259–1274

191. Lü J-M, Wang X, Marin-Muller C, Wang H, Lin PH, Yao Q et al (2009) Current advances in research and clinical applications of PLGA-based nanotechnology. *Expert Rev Mol Diagn* 9:325–341
192. Eckmann DM, Composto RJ, Tsourkas A, Muzykantov VR (2014) Nanogel carrier design for targeted drug delivery. *J Mater Chem B Mater Biol Med* 2:8085–8097
193. Lal S, Clare SE, Halas NJ (2008) Nanoshell-enabled photothermal cancer therapy: impending clinical impact. *Acc Chem Res* 41:1842–1851
194. Park J-H, von Maltzahn G, Xu MJ, Fogal V, Kotamraju VR, Ruoslahti E et al (2010) Cooperative nanomaterial system to sensitize, target, and treat tumors. *Proc Natl Acad Sci USA* 107:981–986
195. Bullivant JP, Zhao S, Willenberg BJ, Kozissnik B, Batich CD, Dobson J (2013) Materials characterization of feraheme/ferumoxytol and preliminary evaluation of its potential for magnetic fluid hyperthermia. *Int J Mol Sci* 14:17501–17510
196. Balakrishnan VS, Rao M, Kausz AT, Brenner L, Pereira BJJ, Frigo TB et al (2009) Physico-chemical properties of ferumoxytol, a new intravenous iron preparation. *Eur J Clin Investig* 39:489–496
197. Helenek MJ, Tokars ML, Lawrence RP (2006) Methods and compositions for administration of iron. US Patent, 7754702B2
198. Pai AB, Garba AO (2012) Ferumoxytol: a silver lining in the treatment of anemia of chronic kidney disease or another dark cloud? *J Blood Med* 3:77–85
199. Bashir MR, Bhatti L, Marin D, Nelson RC (2015) Emerging applications for ferumoxytol as a contrast agent in MRI. *J Magn Reson Imaging* 41:884–898
200. ClinicalTrialsgov (2016) Using ferumoxytol-enhanced MRI to measure inflammation in patients with brain tumors or other conditions of the CNS. clinicaltrials.gov/ct2/show/NCT02452216
201. ClinicalTrialsgov (2015) Ferumoxytol enhanced MRI for the detection of lymph node involvement in prostate cancer. clinicaltrials.gov/ct2/show/NCT01296139
202. ClinicalTrialsgov (2014) Magnetic nanoparticle thermoablation-retention and maintenance in the prostate: a phase 0 study in men (MAGNABLATE I). clinicaltrials.gov/ct2/show/NCT02033447
203. Moore A, Weissleder R, Bogdanov A Jr (1997) Uptake of dextran-coated monocrystalline iron oxides in tumor cells and macrophages. *J Magn Reson Imaging* 7:1140–1145
204. Gref R, Minamitake Y, Peracchia MT, Trubetskoy V, Torchilin V, Langer R (1994) Biodegradable long-circulating polymeric nanospheres. *Science* 263:1600
205. Suk JS, Xu Q, Kim N, Hanes J, Ensign LM (2016) PEGylation as a strategy for improving nanoparticle-based drug and gene delivery. *Adv Drug Deliv Rev* 99:28–51
206. Yamaoka T, Tabata Y, Ikada Y (1994) Distribution and tissue uptake of poly(ethylene glycol) with different molecular weights after intravenous administration to mice. *J Pharm Sci* 83:601–606
207. Peng XH, Qian X, Mao H, Wang AY, Chen Z, Nie S et al (2008) Targeted magnetic iron oxide nanoparticles for tumor imaging and therapy. *Int J Nanomedicine* 3:311–321
208. Park K (2013) Facing the truth about nanotechnology in drug delivery. *ACS Nano* 7:7442–7447
209. Bae YH, Park K (2011) Targeted drug delivery to tumors: myths, reality and possibility. *J Control Release* 153:198–205
210. Leamon CP, Cooper SR, Hardee GE (2003) Folate-liposome-mediated antisense oligodeoxynucleotide targeting to cancer cells: evaluation in vitro and in vivo. *Bioconjug Chem* 14:738–747
211. Peng M, Li H, Luo Z, Kong J, Wan Y, Zheng L et al (2015) Dextran-coated superparamagnetic nanoparticles as potential cancer drug carriers in vivo. *Nanoscale* 7:11155–11162
212. Kaittanis C, Shaffer TM, Ogirala A, Santra S, Perez JM, Chiosis G et al (2014) Environment-responsive nanophores for therapy and treatment monitoring via molecular MRI quenching. *Nat Commun* 5:3384

213. Rejman J, Oberle V, Zuhorn IS, Hoekstra D (2004) Size-dependent internalization of particles via the pathways of clathrin- and caveolae-mediated endocytosis. *Biochem J* 377:159–169
214. Bennet D, Kim S (2014) Polymer nanoparticles for smart drug delivery in nanotechnology and nanomaterials. In: Sezer AD (ed) *Application of nanotechnology in drug delivery*, IntechOpen, London. <https://doi.org/10.5772/58422>
215. Mura S, Nicolas J, Couvreur P (2013) Stimuli-responsive nanocarriers for drug delivery. *Nat Mater* 12:991–1003
216. Cheng R, Meng F, Deng C, Klok H-A, Zhong Z (2013) Dual and multi-stimuli responsive polymeric nanoparticles for programmed site-specific drug delivery. *Biomaterials* 34:3647–3657
217. El-Boubbou K, Ali R, Bahhari HM, AlSaad KO, Nehdi A, Boudjelal M et al (2016) Magnetic fluorescent Nanoformulation for intracellular drug delivery to human breast cancer, primary tumors, and tumor biopsies: beyond targeting expectations. *Bioconjug Chem* 27:1471–1483
218. El-Boubbou K, Azar D, Bekdash A, Abi-Habib RJ (2017) Doxironide magnetic nanoparticles for selective drug delivery to human acute myeloid leukemia. *J Biomed Nanotechnol* 13:500–512
219. El-Boubbou K, Ali R, Bahhari HM, Boudjelal M (2017) Magnetic nanocarriers enhance drug delivery selectively to human leukemic cells. *J Nanomed Nanotechnol* 8(441):1–7
220. Gautier J, Allard-Vannier E, Burlaud-Gaillard J, Domenech J, Chourpa I (2015) Efficacy and hemotoxicity of stealth doxorubicin-loaded magnetic nanovectors on breast cancer xenografts. *J Biomed Nanotechnol* 11:177–189
221. Kossatz S, Grandke J, Couleaud P, Latorre A, Aires A, Crosbie-Staunton K et al (2015) Efficient treatment of breast cancer xenografts with multifunctionalized iron oxide nanoparticles combining magnetic hyperthermia and anti-cancer drug delivery. *Breast Cancer Res* 17:66
222. Mejías R, Pérez-Yagüe S, Gutiérrez L, Cabrera LI, Spada R, Acedo P et al (2011) Dimercaptosuccinic acid-coated magnetite nanoparticles for magnetically guided in vivo delivery of interferon gamma for cancer immunotherapy. *Biomaterials* 32:2938–2952
223. Wang D, Fei B, Halig LV, Qin X, Hu Z, Xu H et al (2014) Targeted iron-oxide nanoparticle for photodynamic therapy and imaging of head and neck cancer. *ACS Nano* 8:6620–6632
224. Tietze R, Lyer S, Dürr S, Struffert T, Engelhorn T, Schwarz M et al (2013) Efficient drug-delivery using magnetic nanoparticles – biodistribution and therapeutic effects in tumour bearing rabbits. *Nanomedicine* 9:961–971
225. Hu S-H, Liao B-J, Chiang C-S, Chen P-J, Chen IW, Chen S-Y (2012) Core-shell nanocapsules stabilized by single-component polymer and nanoparticles for magneto-chemotherapy/hyperthermia with multiple drugs. *Adv Mater* 24:3627–3632
226. Kim D-H, Guo Y, Zhang Z, Prociassi D, Nicolai J, Omary RA et al (2014) Temperature sensitive magnetic drug carriers for concurrent gemcitabine chemohyperthermia. *Adv Healthc Mater* 3:714–724
227. Kong SD, Zhang W, Lee JH, Brammer K, Lal R, Karin M et al (2010) Magnetically vectored nanocapsules for tumor penetration and remotely switchable on-demand drug release. *Nano Lett* 10:5088–5092
228. Yang J, Lee C-H, Ko H-J, Suh J-S, Yoon H-G, Lee K et al (2007) Multifunctional magneto-polymeric nanohybrids for targeted detection and synergistic therapeutic effects on breast cancer. *Angew Chem Int Ed* 46:8836–8839
229. Lim E-K, Huh Y-M, Yang J, Lee K, Suh J-S, Haam S (2011) pH-triggered drug-releasing magnetic nanoparticles for cancer therapy guided by molecular imaging by MRI. *Adv Mater* 23:2436–2442
230. Ketkar-Atre A, Struys T, Dresselaers T, Hodenius M, Mannaerts I, Ni Y et al (2014) In vivo hepatocyte MR imaging using lactose functionalized magnetoliposomes. *Biomaterials* 35:1015–1024

231. Bulte JWM, Douglas T, Witwer B, Zhang S-C, Strable E, Lewis BK et al (2001) Magnetodendrimers allow endosomal magnetic labeling and in vivo tracking of stem cells. *Nat Biotechnol* 19:1141–1147
232. Lamanna G, Kueny-Stotz M, Mamlouk-Chaouachi H, Ghobril C, Basly B, Bertin A et al (2011) Dendronized iron oxide nanoparticles for multimodal imaging. *Biomaterials* 32:8562–8573
233. Monnier CA, Burnand D, Rothen-Rutishauser B, Lattuada M, Petri-Fink A (2014) Magnetoliposomes: opportunities and challenges. *Eur J Nanomed* 6:201–2015
234. Laurent S, Saei AA, Behzadi S, Panahifar A, Mahmoudi M (2014) Superparamagnetic iron oxide nanoparticles for delivery of therapeutic agents: opportunities and challenges. *Expert Opin Drug Deliv* 11:1449–1470
235. Kohler N, Sun C, Wang J, Zhang M (2005) Methotrexate-modified superparamagnetic nanoparticles and their intracellular uptake into human cancer cells. *Langmuir* 21:8858–8864
236. Sun C, Fang C, Stephen Z, Veiseh O, Hansen S, Lee D et al (2008) Tumor-targeted drug delivery and MRI contrast enhancement by chlorotoxin-conjugated iron oxide nanoparticles. *Nanomedicine (Lond)* 3:495–505
237. Yang H-W, Hua M-Y, Liu H-L, Tsai R-Y, Chuang C-K, Chu P-C et al (2012) Cooperative dual-activity targeted nanomedicine for specific and effective prostate cancer therapy. *ACS Nano* 6:1795–1805
238. Tong R, Tang L, Ma L, Tu C, Baumgartner R, Cheng J (2014) Smart chemistry in polymeric nanomedicine. *Chem Soc Rev* 43:6982–7012
239. Wang H-C, Zhang Y, Possanza CM, Zimmerman SC, Cheng J, Moore JS et al (2015) Trigger chemistries for better industrial formulations. *ACS Appl Mater Interfaces* 7:6369–6382
240. Yu J, Chu X, Hou Y (2014) Stimuli-responsive cancer therapy based on nanoparticles. *Chem Commun* 50:11614–11630
241. El-Dakdouki MH, Zhu DC, El-Boubbou K, Kamat M, Chen J, Li W et al (2012) Development of multifunctional hyaluronan-coated nanoparticles for imaging and drug delivery to cancer cells. *Biomacromolecules* 13:1144–1151
242. Ding X, Liu Y, Li J, Luo Z, Hu Y, Zhang B et al (2014) Hydrazone-bearing PMMA-functionalized magnetic Nanocubes as pH-responsive drug carriers for remotely targeted Cancer therapy in vitro and in vivo. *ACS Appl Mater Interfaces* 6:7395–7407
243. Banerjee SS, Chen D-H (2008) Multifunctional pH-sensitive magnetic nanoparticles for simultaneous imaging, sensing and targeted intracellular anticancer drug delivery. *Nanotechnology* 19:505104
244. Zhu L, Wang D, Wei X, Zhu X, Li J, Tu C et al (2013) Multifunctional pH-sensitive superparamagnetic iron-oxide nanocomposites for targeted drug delivery and MR imaging. *J Control Release* 169:228–238
245. Wang Y, Jia H-Z, Han K, Zhuo R-X, Zhang X-Z (2013) Theranostic magnetic nanoparticles for efficient capture and in situ chemotherapy of circulating tumor cells. *J Mater Chem B* 1:3344–3352
246. Ansari C, Tikhomirov GA, Hong SH, Falconer RA, Loadman PM, Gill JH et al (2014) Development of novel tumor-targeted theranostic nanoparticles activated by membrane-type matrix metalloproteinases for combined cancer magnetic resonance imaging and therapy. *Small* 10:566–417
247. Stephen ZR, Kievit FM, Veiseh O, Chiarelli PA, Fang C, Wang K et al (2014) Redox-responsive magnetic nanoparticle for targeted convection-enhanced delivery of O6-benzylguanine to brain tumors. *ACS Nano* 8:10383–10395
248. Medarova Z, Pham W, Farrar C, Petkova V, Moore A (2007) In vivo imaging of siRNA delivery and silencing in tumors. *Nat Med* 13:372–377
249. Wilson DS, Dalmasso G, Wang L, Sitaraman SV, Merlin D, Murthy N (2010) Orally delivered thioketal-nanoparticles loaded with TNF α -siRNA target inflammation and inhibit gene expression in the intestines. *Nat Mater* 9:923–928

250. Lee J-H, Lee K, Moon SH, Lee Y, Park TG, Cheon J (2009) All-in-one target-cell-specific magnetic nanoparticles for simultaneous molecular imaging and siRNA delivery. *Angew Chem Int Ed* 48:4174–4179
251. Juratli TA, Schackert G, Krex D (2013) Current status of local therapy in malignant gliomas – a clinical review of three selected approaches. *Pharmacol Ther* 139:341–358
252. Hayashi K, Nakamura M, Miki H, Ozaki S, Abe M, Matsumoto T et al (2014) Magnetically responsive smart nanoparticles for cancer treatment with a combination of magnetic hyperthermia and remote-control drug release. *Theranostics* 4:834–844
253. Mitragotri S, Burke PA, Langer R (2014) Overcoming the challenges in administering biopharmaceuticals: formulation and delivery strategies. *Nat Rev Drug Discov* 13:655–672
254. Mitragotri S, Anderson DG, Chen X, Chow EK, Ho D, Kabanov AV et al (2015) Accelerating the translation of nanomaterials in biomedicine. *ACS Nano* 9:6644–6654
255. Jin-Wook Y, Elizabeth C, Samir M (2010) Factors that control the circulation time of nanoparticles in blood: challenges, solutions and future prospects. *Curr Pharm Des* 16:2298–2307
256. Bregoli L, Movia D, Gavigan-Imedio JD, Lysaght J, Reynolds J, Prina-Mello A (2016) Nanomedicine applied to translational oncology: a future perspective on cancer treatment. *Nanomedicine* 12:81–103
257. Pillai G (2014) Nanomedicines for cancer therapy: an update of FDA approved and those under various stages of development. *Pharm Pharm Sci* 1:13
258. Sievers EL, Senter PD (2013) Antibody-drug conjugates in cancer therapy. *Annu Rev Med* 64:15–29
259. Kamaly N, Xiao Z, Valencia PM, Radovic-Moreno AF, Farokhzad OC (2012) Targeted polymeric therapeutic nanoparticles: design, development and clinical translation. *Chem Soc Rev* 41:2971–3010
260. Wickham T, Futch K (2012) A phase I study of MM-302, a HER2-targeted liposomal doxorubicin, in patients with advanced, HER2-positive breast cancer. *Cancer Res* 72(Suppl. 24):P5-18-09
261. Verma S, Miles D, Gianni L, Krop IE, Welslau M, Baselga J et al (2012) Trastuzumab emtansine for HER2-positive advanced breast cancer. *N Engl J Med* 367:1783–1791
262. Singha N, Jenkins GJS, Asadi R, Doak SH (2010) Potential toxicity of superparamagnetic iron oxide nanoparticles (SPION). *Nano Rev* 1:5358
263. Mahmoudi M, Hofmann H, Rothen-Rutishauser B, Petri-Fink A (2012) Assessing the in vitro and in vivo toxicity of superparamagnetic iron oxide nanoparticles. *Chem Rev* 112:2323–2338
264. AMAG Pharmaceuticals Inc (2010) Feraheme™ (ferumoxytol) injection prescribing information
265. Monnier Christophe A, Burnand D, Rothen-Rutishauser B, Lattuada M, Petri-Fink A (2014) Magnetoliposomes: opportunities and challenges. *Eur J Nanomed* 6:201
266. Ito A, Shinkai M, Honda H, Kobayashi T (2005) Medical application of functionalized magnetic nanoparticles. *J Biosci Bioeng* 100:1–11
267. Kudr J, Haddad Y, Richtera L, Heger Z, Cernak M, Adam V et al (2017) Magnetic nanoparticles: from design and synthesis to real world applications. *Nanomaterials* 7:243
268. Mahmoudi M, Serpooshan V, Laurent S (2011) Engineered nanoparticles for biomolecular imaging. *Nanoscale* 3:3007–3026



Superparamagnetic Nanoparticles for Cancer Hyperthermia Treatment

7

Dipak Maity and Ganeshlenin Kandasamy

Contents

1	Definition of the Topic	300
2	Overview	300
3	Introduction	301
3.1	Basic Principles	301
4	Experimental and Instrumental Methodology	305
4.1	Size/Shape and Crystallinity	305
4.2	Structure/Surface Coatings	307
4.3	Magnetic Properties and Dispersibility	308
4.4	Calorimetric Magnetic Fluid Hyperthermia	310
4.5	In Vitro and in Vivo Magnetic Fluid Hyperthermia	311
5	Key Research Findings	313
5.1	Influence of Size/Size Distribution/Shape of SPM Nanoparticles	313
5.2	Influence of Surface Coatings and Composition of SPM Nanoparticles	315
5.3	Influence of Applied AMFs and Dispersion Media of SPM Nanoparticles	319
5.4	Biological Magnetic Fluid Hyperthermia of SPM Nanoparticles	321
6	Conclusions and Future Perspectives	324
	References	325

D. Maity (✉)

Department of Chemical Engineering, Institute of Chemical Technology Mumbai, IOC Campus,
Bhubaneswar, Odisha, India

e-mail: dipakmaity@gmail.com

G. Kandasamy

Department of Biomedical Engineering, Vel Tech Rangarajan Dr. Sagunthala R&D Institute of
Science and Technology, Chennai, Tamil Nadu, India

1 Definition of the Topic

Magnetic nanoparticles (MNPs) – especially single-domain-based superparamagnetic (SPM) nanoparticles in ferrofluid form – are primarily utilized in magnetic fluid hyperthermia (MFH)-based thermotherapy for cancer treatment applications due to their following advantages: (i) unique magnetic properties, (ii) better chemical stability, and (iii) high cytocompatibility. In MFH therapy, the cancer cells are quickly heated to the therapeutic temperatures of $\sim 42\text{--}45\text{ }^{\circ}\text{C}$ using the MNPs on exposure to externally applied alternating magnetic fields (AMFs), where the induced heat might damage the consequent proliferation of cancer cells by promoting apoptosis/mitotic death and thus preventing the tumor growth.

2 Overview

Cancer is one of the major life threatening diseases for human beings in modern world. However, recent advancements in nanoscience and nanotechnology have created new therapeutic pathways for the treatment of cancers by overcoming the major limitations associated with the conventional treatment methods – including organ damage, infertility, etc. Among different nanotherapies (applied in cancer treatment by the use of definite nanomaterials/nanoparticles), MFH-based thermotherapy via biocompatible MNPs has evolved as the most efficient therapeutic pathway for treating cancers without any significant side effects/minimal damage to the normal cells (that surround the tumors). This has been feasible mainly due to (i) high sensitivity of the cancer cells towards the elevated temperatures as compared to the normal cells, and also (ii) the size-dependent magnetic behavior of the MNPs and their inherent heat generating capability because of Brownian and Néel relaxation losses under the externally applied alternating magnetic fields (AMFs). But, the induced heat might vary with their physicochemical (size/shape/crystallinity), magnetic, and/or water dispersibility properties that depend upon the type of synthesis process or reaction conditions including their nonmagnetic surface coatings.

Herein, we have started with a brief introduction about (i) the magnetic behaviors of the materials, and basic principles of MFH including different MNPs, and (ii) the major characterization techniques required determining the physicochemical/magnetic/dispersibility properties of the MNPs. Then, we have discussed in detail about the heating performance of the MNPs with respect to their type, size, shape, and/or surface coatings. Finally, we have discussed about the current developments in the cancer treatment via MNPs-based MFH in *in vitro/in vivo* scenarios.

3 Introduction

3.1 Basic Principles

3.1.1 Superparamagnetic Behavior

It is primarily needed to understand the superparamagnetic behavior of the magnetic nanoparticles for their effective involvement in MFH applications [1–3]. In general, bulk size magnetic materials are mainly classified into the following five categories – dia-/para-/ferro-/ferri-/anti-ferro- magnetic – depending upon the magnetic dipole-dipole interactions, chemical ordering of the atoms, and electronic configuration (i.e., unpaired electrons in the outermost orbitals) [4]. However, magnetic (especially ferro-/ferri-magnetic) nanoparticles possessing superparamagnetic (SPM) behavior are effectively used in MFH applications, which means that these nanoparticles immediately get magnetized on exposure to a low applied magnetic field and demagnetized completely (i.e., zero coercivity and remanence for reversal of the magnetization) on the removal of the applied magnetic field. The SPM behavior is a size-dependent phenomenon and occurs in single-domain ferro-/ferri-magnetic nanoparticles [5].

Usually, large (i.e., bulk size) magnetic particles possess multidomain structure, where regions of uniform magnetization (i.e., magnetic domains) are separated by domain walls. This results in hysteresis loops with high coercivity (H_c) and remnant magnetization (M_r) due to distinct orientations of the spin/orbital magnetic moments in all the domains under an applied magnetic field [6, 7]. However, the transition from multidomain to single-domain structure occurs when the size (volume) of the magnetic materials is lowered below a certain point, where larger (maximum) coercivities and uniaxial anisotropy are obtained [8]. Then, the particles having size below the critical size (D_s , single domain size) is considered as single domain particles [9]. So, as the size of these single domain particles decreases, the coercive force decreases.

But, the SPM domain can be attained in these nanoparticles only when their size (or volume) is further reduced below the single-domain size [10]. Initially, the concept of SPM is developed by Neel to define the thermal fluctuations in the single-domain ferromagnetic structures [11]. Generally, the magnetic anisotropy energy (E_A) is directly proportional to the volume (V) of a particle and is given by $E_A = KV \sin^2\theta$, where V is the particle volume, K is the anisotropy energy constant, and θ is the angle between the magnetization vector and easy axis of magnetization [12]. The energy barrier KV separates the two energetically equivalent easy directions of magnetization. With decreasing particle size (i.e., volume of the single-domain nanoparticles), the thermal energy, $k_B T$, exceeds the energy barrier KV ($KV < 25k_B T$) and the magnetization is easily flipped, i.e., there is no more preferential orientation of the moment in the particle [13]. Therefore, the magnetic moments of the nanoparticles can be easily aligned in the direction of an applied magnetic field which might lead to high magnetic susceptibility (χ)/saturation

magnetization (Ms) and consequently, the zero coercivity/magnetic remanence can be observed in the hysteresis curves of the SPM nanoparticles [14, 15]. Besides, the ferri-magnetic (particularly iron oxide) nanoparticles change from single-domain state to SPM state at sizes usually less than 20 nm. For instance, the single-domain (Ds) and SPM-domain sizes of the magnetite (Fe_3O_4) nanoparticles are estimated to be around ~ 128 nm and ~ 10 nm, respectively [16].

3.1.2 Magnetic Fluid Hyperthermia (MFH)

Outline

In general, hyperthermia is a process of artificially increasing the body temperature for therapeutic purposes, where hot water-baths, radiofrequency, ultrasound, or microwaves are the commonly used sources for heat generation [17, 18]. But, the heat generated via above-mentioned modes is not localized and diffused with nonuniform temperature distribution. However recently, magnetic nanoparticles (MNPs, especially SPM nanoparticles) are used to produce localized heat (ranging between $42\text{--}45$ °C) for the cancer treatment applications on exposure to an externally applied alternating magnetic field (AMF), which is known as magnetic fluid hyperthermia (MFH) therapy [19–23]. The first attempt of MFH cancer therapy via magnetic particles is made by Gilchrist et al. in 1957 [24]. At present, the MFH therapeutic modality has reached the stages of clinical trials after numerous optimizations in the physicochemical/magnetic and heat generation properties of the SPM nanoparticles [25–27].

SPM Nanoparticles

Superparamagnetic Iron Oxide Nanoparticles

Iron oxides are one of the most commonly available and abundant compounds in nature and they can also be easily synthesized in the laboratory. Generally, iron oxides are found to have 16 different phases, which are either in the form of hydroxides (iron (II)/(III) hydroxides), oxyhydroxides (akaganeite, ferroxhyte, lepidocrocite, ferrihydrite, and goethite), or oxides/mixed oxides (magnetite, maghemite, hematite, and beta/epsilon phase iron oxides) [28–30]. Among these phases, magnetite (Fe_3O_4) and maghemite ($\gamma\text{-Fe}_2\text{O}_3$)-based iron oxides (having inverse spinel structure) are more stable and exhibit ferrimagnetism at room temperature with high magnetization, biocompatibility, and biodegradability as compared to others [31–34]. Therefore, $\text{Fe}_3\text{O}_4/\gamma\text{-Fe}_2\text{O}_3$ -based superparamagnetic iron oxide nanoparticles (SPIONs) are widely utilized in MFH applications [35–37]. Moreover, these SPIONs with controlled physicochemical/magnetic properties can be synthesized via either one of the methods including chemical coprecipitation, thermal decomposition, hydrothermal/solvothermal, sonochemical, microemulsion, microwave, or microbial methods [1, 28, 38], where the aggregation of the SPIONs during the synthesis process can be controlled by using appropriate surfactants/capping agents [39, 40].

Superparamagnetic Spinel-Ferrite Nanoparticles

Spinel-ferrites are typically comprised of iron oxides and a metal cation in their chemical ordering with formula of $M(\text{Fe}_x\text{O}_y)$, where M indicates metal cations, e.g., cobalt ion (Co^{2+}), manganese ion (Mn^{2+}), etc. [41, 42]. Usually, ferrites-based MNPs are extensively deployed in numerous applications such as catalysis, electromagnetic/optical devices, and sensing instruments [31, 43] due to their enhanced magnetic properties including saturation magnetization. However, ferrite nanoparticles with SPM behavior are also involved in MFH applications, and these nanoparticles are mainly synthesized through sol-gel, coprecipitation, ball-milling, hydrothermal, or microemulsion process [44, 45]. Nevertheless, the toxicity issue (i.e., restricted biocompatibility due to toxic metal cations) of the SPM ferrite nanoparticles is one of the major limitations in using them for direct MFH-based cancer treatments as compared to the SPIONs.

Heat Generation Mechanisms

Magnetic materials generate heat on exposure to an alternating magnetic field (AMF). Herein, the magnetic energy of the materials is dissipated as thermal energy due to different loss mechanisms including eddy current loss, hysteresis loss, susceptibility/relaxation losses, and/or their combinations [46–48]. Besides, the heat generation using the single-domain-based SPM nanoparticles is mainly due to their alignment in the direction of the applied AMF [49, 50]. Moreover, the electromagnetic to thermal energy conversion takes place when the applied AMF could overcome the energy barriers which are present in the SPM nanoparticles due to their magnetic anisotropy energy or the viscosity of the dispersive/carrier fluid and thus resulting in the realignment of their magnetic moments [51]. Hence, either Neel or Brown relaxation mechanism is responsible for heat generation in these SPM nanoparticles (e.g., SPIONs in ferrofluid form).

Moreover, the heating ability of these nanoparticles is mainly evaluated via a calorimetric approach [52]. Herein, the increase in temperature of the SPIONs-based ferrofluids is noted via fiber-optic temperature probe in correspondence to the exposure of the AMF (at a specific amplitude/frequency) that is generated by a magnetic field induction system with water-cooled turn (e.g., 9 or 17) coil(s) linked to a radiofrequency generator – as shown in Fig. 7.1.

Generally, heating efficacy of the nanoparticles is evaluated in terms of specific absorption rate (SAR in W/g_{Fe}) – based on the initial slope of the time-dependent temperature (TDT) curve – which can be determined using the following equation – Eq. (7.1) [53, 54].

$$\text{SAR} = \frac{C \Delta T}{m \Delta t} \quad (7.1)$$

Where, C is the specific heat capacity (in $\text{J kg}^{-1} \text{K}^{-1}$) of the dispersion medium (i.e., water), m is the mass fraction of Fe (in grams), and $\Delta T/\Delta t$ is the initial slope of time-dependent temperature (TDT) curves. Moreover, intrinsic loss power (ILP in $\text{nHm}^2 \text{kg}^{-1}$) is also measured by normalizing SAR with

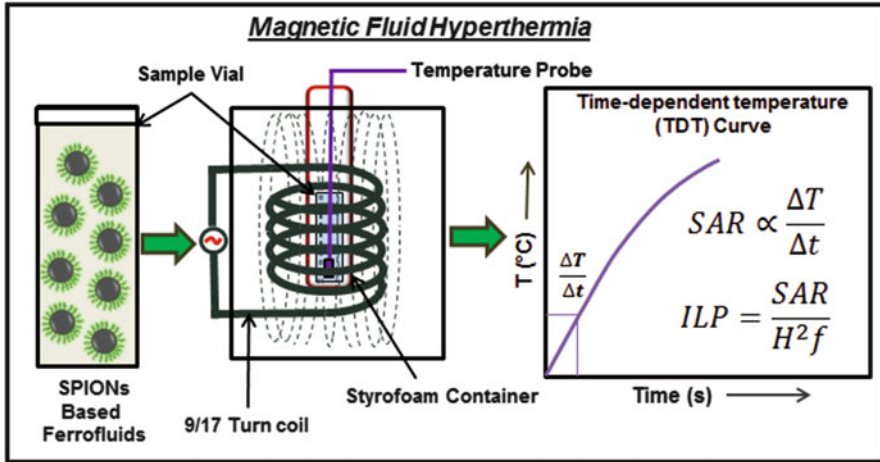


Fig. 7.1 Schematic diagram of the calorimetric method used to evaluate the heating efficiency of magnetic nanoparticles in magnetic fluid hyperthermia (MFH), wherein the change in the temperature of the SPIONs-based ferrofluids is recorded upon exposure to AMF

respect to the applied AMF using the following equation (i.e., Eq. 7.2). ILP is a newly introduced parameter to make direct comparison (of the heating efficacies of SPM nanoparticles) among the diverse MFH experiments which are performed under various AMF (field strengths/frequency) conditions by different researchers [55].

$$ILP = \frac{SAR}{H^2 f} \quad (7.2)$$

Various review articles, books, and/or book chapters have already discussed about the synthesis procedures of the SPM nanoparticles and their different biomedical applications such as magnetic resonance imaging, magnetofection, magnetic targeting, and also magnetic fluid hyperthermia (MFH) [14, 18, 29, 31, 32, 56–60]. However, there is a severe lack of comprehensive articles (i) to explain the essential characterization techniques and (ii) to exclusively discuss the heating ability of SPM nanoparticles with the emphasis on all important parameters in calorimetric/in vitro/in vivo conditions. Therefore, in this chapter we have (i) reviewed about all of the significant characterization techniques – along with their experimental methodologies – required to investigate the most vital properties of the SPM nanoparticles, and (ii) systematically discussed about the heat generation capacities (including the heating efficacies) of the recently developed SPM nanoparticles with main focus towards all the significant heat-influencing parameters including size, size distribution, shape, surface coatings, composition, applied AMFs, and dispersion media in calorimetric scenario along with in vitro and in vivo MFH therapeutic effects.

4 Experimental and Instrumental Methodology

SPM nanoparticles – particularly SPIONs (used majorly in MFH applications) – are synthesized via different chemical methods and subsequently characterized by using different instruments/techniques to investigate their inherent physicochemical/magnetic properties [61].

For this purpose, the as-prepared SPIONs are used in the form of powder (via drying) and ferrofluids suspension (via dispersing them in a suitable carrier liquid). At first, the morphology (sizes/shapes) and crystallinity/phase purity of the SPIONs are usually characterized by using transmission electron microscopy (TEM)/scanning electron microscopy (SEM) and X-ray diffraction, respectively [62–64]. Then, the surface structure of the SPIONs (i.e., type and amount of surface coating molecules) is characterized via Fourier transform infrared spectroscopy (FTIR) and thermogravimetric analysis (TGA) [65–67]. Moreover, magnetic properties (saturation magnetization, M_s) and dispersibility (including size distribution and surface charge) of the SPIONs are determined via vibration sample magnetometer (VSM) and dynamic light scattering (DLS) techniques, respectively [68–70]. In this section, we have discussed about the basic principles of the characterization techniques (TEM/SEM/XRD/FTIR/TGA/VSM/DLS) along with the sample preparation process.

4.1 Size/Shape and Crystallinity

4.1.1 Transmission Electron Microscopy (TEM)

Transmission electron microscopy (TEM) is a particle image-based characterization tool, where the accelerated electrons having high energies (in vacuum) are exploited to obtain the information about (i) the morphology (size & distribution/shape) and/or (ii) the crystallography of the nanoparticles. In TEM, an electron beam which is generated from an electron gun, and subsequently focused by the electromagnetic condensers, is transmitted through a thin sample specimen positioned in a holder. The incident electron beam interacts with the atoms in the specimen and results in inelastic/elastic-scattering/diffraction of the electrons to form different contrast images (e.g., bright-/dark-field or diffraction images). Moreover, the voltages that are used to accelerate the electron beam are ranging from 80–300 kV to obtain normal or high resolution TEM (HRTEM) images.

Bright-Field Images

In bright-field images, the samples are appeared to be darker with a brighter background, due to the strong scattering/deflection of the incident electrons ascribed to the high density/thickness of the sample specimens. This technique is useful for determining the morphological characteristics of biological, crystalline/amorphous, or metal-based samples.

Dark-Field Images

In dark-field images, the samples are seemed to be brighter with a darker background. This reverse phenomenon can be attained by tilting the primary electron beam so that the chosen diffracted beam travels along the optical axis and pass through the centered aperture. This technique is useful for detecting the crystalline grains/defects, which is not observable in bright-field images.

Diffraction Images

A diffraction pattern of the samples is obtained based on the diffracted electrons observed via back focal plane of the objective lens. Herein, a selected small area (enclosed by the aperture) of the sample is contributed to the diffraction pattern, which results in selected area electron diffraction (SAED) pattern. Moreover, the SAED patterns are obtained with (i) a regular array of spots (where several sets of planes are parallel to the beam) for a single crystal-based sample and (ii) a ring pattern (which is sum of random orientations of the individual patterns) for a polycrystalline-based sample.

Usually in TEM imaging, 5–10 μl of ethanol/water-dispersed SPIONs is dropped onto a TEM copper-grid, which is subsequently dried overnight at room temperature (RT)/40 $^{\circ}\text{C}$ to evaporate the dispersing solvent (i.e., water/ethanol) [71]. Finally, the TEM grid is placed inside the sample holder for obtaining TEM images.

4.1.2 Scanning Electron Microscopy (SEM)

Scanning electron microscopy (SEM) is another image-based characterization technique – as similar to TEM – used to investigate the morphological characteristics and/or surface topography of the particles. Normally, SEM is operated under 0.5–30 kV voltage range to obtain better images. Herein, a beam of accelerated electrons is used to scan the specimen sample, which results in the emission of a series of radiations – that are exploited to form images. The emitted radiations include:

- Secondary electrons (having energy less than 50 eV) – ejected from the outer-orbital of the atoms of the sample ascribed to multiple inelastic scattering effects.
- Back-scattered electrons (having energy greater than 50 eV) – reflected/back-scattered out of the interaction volume of the specimen attributed to the elastic scattering effects.
- Characteristic X-rays – arise from the energy difference between two electrons during their ejection from/refilling in the orbitals of the atoms.

In SEM imaging, a small amount of powdered samples of the SPIONs is spread across the surface of a double-sided carbon tape, which is further mounted on a stub and then sputter-coated with gold for better imaging purposes [72]. Then, the coated stub is placed inside the sample holder and loaded into the SEM instrument for further imaging.

4.1.3 X-Ray Diffraction (XRD)

X-ray diffraction (XRD) is a crystallographic characterization technique – utilized for investigating the crystalline phases/sizes and crystal structures/orientations of the particles. In XRD, the monochromatic X-rays – generated in an X-ray tube based on the anodic bombardment of high-energy electrons and filtered via monochromator – are elastically scattered by the sample particles (due to interactions). Subsequently, constructive interference pattern is formed to give diffraction peaks by satisfying the Bragg's Law ($n\lambda = 2d \sin \theta$) [20]. Here, n is the order of reflection (i.e., an integer corresponding to the order of diffraction plane), λ is the wavelength of X-ray, d is the inter-planar spacing (i.e., the distance between two diffraction planes), and θ is the angle of diffraction (i.e., angle between the diffraction plane and the incident X-ray).

Typically, the powdered samples of the as-prepared SPIONs are used for XRD analysis with a working scan range (i.e., 2θ) of 20° – 80° . Moreover, the crystalline nature (e.g., phases) of the SPIONs is identified from their unique d -spacing/diffraction peaks by a comparison with the standards gathered by Jointed Committee of Powder Diffraction Standards (JCPDS) or International Centre for Diffraction Data (ICDD). Furthermore, the crystallite sizes of the SPIONs are determined by using Scherrer formula – i.e., $D = (k\lambda/\beta \cos \theta)$, where D is the average crystalline size (in nm), k is the particle shape factor (i.e., k is 0.9 for spherical shapes), λ is the wavelength of X-rays (in Å), β is the peak width measured at half intensity (in radians), and θ is the diffraction angle (in degrees).

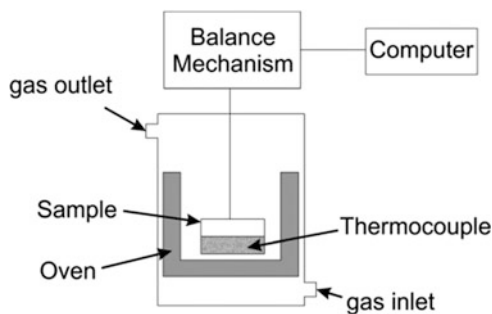
4.2 Structure/Surface Coatings

4.2.1 Fourier Transform Infrared (FTIR)

Fourier transform infrared (FTIR) spectroscopy is a surface characterization tool that is useful in determining the characteristic chemical bonds in the molecules (along with the functional groups) of the particles (e.g., SPIONs). These chemical bonds are identified based on their absorption/transmission behaviors (given in terms of intensities) in reference to the frequency of the incident IR radiation (given in terms of specific wavenumbers/wavelength). Usually, the molecules gain energies while absorbing the photons from the irradiated IR spectra, and these energies move from the lower/ground state to the higher/excited state. This results in either one of the following vibrational states (among the bonds between atoms in molecules) including stretching (symmetric/asymmetric) and bending vibrations that are characteristic to the applied IR frequency. Finally, the IR spectrum is provided in terms of absorption/transmission intensity vs. wavenumber.

Herein, a small amount of powdered SPIONs is directly placed inside a specimen holder, and scanned in the FTIR range of 550 – 4000 cm^{-1} [73]. The absorption peaks in the range of 550 – 600 cm^{-1} are typically corresponded to the Fe–O stretching vibrations of iron oxide cores, and the peaks above 600 cm^{-1} are ascribed to the different vibrations of the coating molecules that are chemically adsorbed to the surface of the SPIONs [74].

Fig. 7.2 A simplified scheme of the thermo–microgram-balance used in thermogravimetric analysis (TGA) apparatus. (Reproduced from Ref. [68])



4.2.2 Thermogravimetric Analysis (TGA)

Thermogravimetric analysis (TGA) is a thermal characterization tool which can be employed to quantitatively determine the weight change of the particles under gradual increase of their temperature in a controlled environment. In general, the weight change experienced by the particles is mainly due to their decomposition, dehydration, evaporation, oxidation, or reduction/absorption, which is mainly useful in defining the (i) chemical composition and/or (ii) thermal stability of the particles.

A thermo–microgram-balance (as shown in Fig. 7.2) in TGA apparatus is used to observe the changes in the weight of the material while heating the sample via an in-built oven, where a thermocouple is used to monitor the temperature. Herein, dried powder samples of the SPIONs is weighed in an alumina pan and placed inside the TGA apparatus, which is consequently heated from RT to 800 °C at a specific heating rate under an inert atmosphere [68]. Finally, the temperature vs. percentage of weight loss of the SPIONs shall be plotted to determine the amount of coating molecules and iron oxide core.

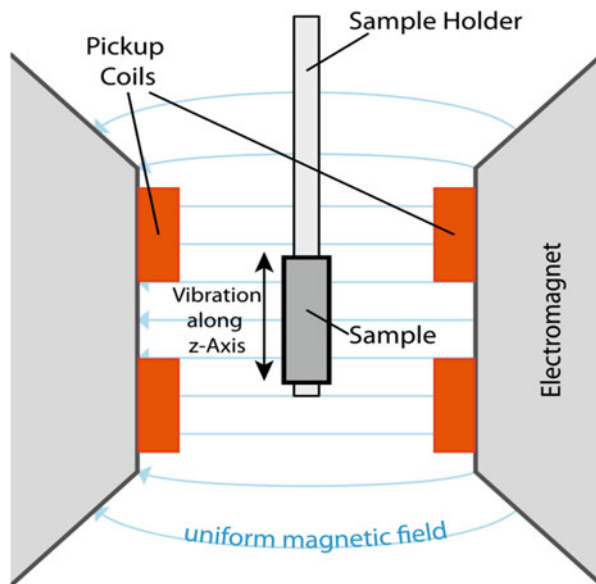
4.3 Magnetic Properties and Dispersibility

4.3.1 Vibrating Sample Magnetometry (VSM)

Vibrating sample magnetometry (VSM) is a magnetic characterization technique applied to measure the magnetic properties (such as magnetization/hysteresis loop) of the particles at RT. VSM works on the basic principle of “Faraday’s Law of Induction” which notifies that the varying magnetic field might generate an electric field which can be measured to accumulate information about the corresponding magnetic field. The sample particles is initially placed between two electromagnets (via a sample holder) – as shown in Fig. 7.3, magnetized by applying a constant magnetic field (H , via electromagnets), and then vibrated in a sinusoidal fashion (in Z -axis).

Due to the change in magnetic flux of the particles (ascribed to its sinusoidal oscillation), a voltage is induced. Then, the induced voltage signal is quantified by the nearby detection/pick-up coils, and moreover, the amplitude of this signal is

Fig. 7.3 Schematic diagram of detection set-up of vibration sample magnetometer (VSM). (Reproduced from commons.wikimedia.org/VSM)



directly proportional to the magnetic moments (M) of the sample particles. Besides, a hysteresis (M - H) loop for the particles is acquired by ramping the applied field initially to a maximum positive field, then cycled to a maximum negative field (via zero) and again increased to the maximum positive field. Finally, the data including the applied magnetic field and the corresponding magnetization are acquired.

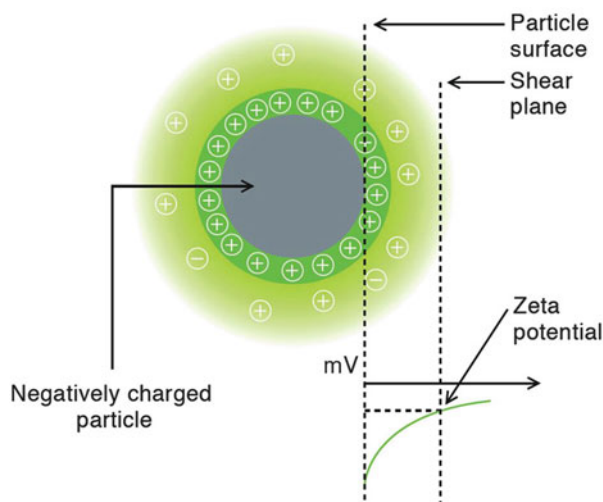
Herein, dried powder samples of SPIONs are placed in the sample holder of VSM, and consequently, a magnetic field (in a particular range) is applied to measure the magnetic properties of the SPIONs (in the form of a hysteresis curve) at RT.

4.3.2 Dynamic Light Scattering (DLS)

Dynamic light scattering (DLS) is primarily used to measure the hydrodynamic size/distribution of the particles (e.g., SPIONs) suspended in a medium (e.g., water) to determine their dispersibility/solubility. In DLS, a beam of light from a laser, which is passed through the dispersed sample particles, is scattered by the particles in the medium and subsequently observed through a photon detector. The intensities of the scattered light (measured at a known angle (i.e., θ)) might fluctuate with time as the particles diffuse in the dispersion medium due to (i) the Brownian motions and (ii) also because of the variations in the sizes (i.e., hydrodynamic diameter) of the diffusing particles. The correlation between the diffusion co-efficient of the particles and their size can be obtained (via correlator) through the Stokes-Einstein equation – Eq. (7.3) [75].

$$D_h = (k_B T)/(3\pi\eta D_t) \quad (7.3)$$

Fig. 7.4 Zeta potential as function of the surface charge of a nanoparticle at the shear plane. (Reproduced from <http://www.horiba.com>)



Where, D_h is the hydrodynamic diameter of the particles, k_B is the Boltzmann's constant, T is the measurement temperature, η is the medium viscosity, and D_t is the diffusion coefficient of the particles. Commonly, D_h is measured in the range of 0.3 nm to 10 μm via DLS.

In addition to D_h , DLS is also utilized to determine the zeta (ζ) potential of the particles to evaluate their suspension (colloidal) stability in the dispersing media. Generally, the particles possess surface charge when they are suspended in a medium. ζ potential is measured based on the scattering of light while the charged particles (in the medium) diffuse in response to an applied electric field, where this phenomenon is known as electrophoretic light scattering [76]. Normally, the velocity of the diffusing particles is determined via the Doppler shifts in the scattered light and is proportional to the electric (i.e., ζ) potential of the particles at the shear/slipping plane – as shown in Fig. 7.4. Moreover, the direction and the velocity of the diffusing particles can be utilized to determine (i) their surface charges as either positive (+) or negative (-), and (ii) the magnitude of the charges (in mV), respectively. Usually, the particles having high ζ potentials – i.e., < -30 mV and $> +30$ mV are considered to be stable since the particles do not agglomerate or flocculate beyond these ranges [77].

In general, the SPIONs based ferrofluid (FF) suspensions are prepared with appropriate dilutions, poured into the cuvettes, and finally analyzed for D_h/ζ potential via DLS at a standard temperature of 25 $^\circ\text{C}$. Usually, an average of three measurements is taken to maintain the consistency in the DLS data.

4.4 Calorimetric Magnetic Fluid Hyperthermia

Generally, calorimetric magnetic fluid hyperthermia (CMFH) studies are performed to investigate the heat induction properties of the SPM nanoparticles by exposing



Fig. 7.5 A typical hyperthermia instrument – magneTherm from nanoTherics

them to alternating magnetic fields (AMFs) using a hyperthermia instrument – for example, magneTherm from nanoTherics, as shown in Fig. 7.5.

Herein, the hyperthermia instrument (magneTherm) mainly consists of 9/17 turn coils that are used to produce the AMFs having definite amplitudes (H) and frequencies (f), which can be varied in the range of 7.1 kA/m to 15.3 kA/m, and 175.2 kHz to 1001.1 kHz, respectively. The corresponding $H \cdot f$ product values are calculated in the range of $2.4 \times 10^9 \text{ Am}^{-1} \text{ s}^{-1}$ or ($2.4 \text{ G Am}^{-1} \text{ s}^{-1}$) to $9.9 \text{ G Am}^{-1} \text{ s}^{-1}$ [78]. Usually, the required AMFs are generated by initially fixing the frequency via a function generator, and then by modifying the suitable electric voltage/current through a laboratory power supply machine. Moreover, a chiller is connected to the turn coil to maintain a specific coil temperature (i.e., $\sim 37^\circ \text{C}$) by recirculating the water while preventing the over-heating of the coil (due to constant electric voltage/current supply).

In a typical CMFH study, about 1 milliliter (ml) of the aqueous suspensions of SPM nanoparticles (aqueous ferrofluids) is poured in a clean vial and a temperature probe is inserted into the suspension through its lid. The vial (along with the probe) is affixed in a Styrofoam container and subsequently inserted into the space between the coils. The initial temperature of the aqueous ferrofluids is monitored for about ~ 2 mins with the help of the temperature probe (coupled to a data acquisition software, DAS) to check for any heat induction from the coil. Then, the AMFs (with specific $H \cdot f$ values) are applied and the time-dependent temperature (TDT) rise of the aqueous ferrofluids is consequently observed through the temperature probe. Finally, the TDT plots are made and the heating efficacies of the aqueous ferrofluids are calculated – i.e., SAR in W/g_{Fe} and ILP in $\text{nHm}^2 \text{ kg}^{-1}$ as per Eqs. (7.1 and 7.2).

4.5 In Vitro and in Vivo Magnetic Fluid Hyperthermia

In a typical in vitro MFH study, ~ 7 to 8 million cancer cells are grown in a 75 cm^2 culture-flask (at 37°C , and 5% CO_2 in an incubator) by using growth media with fetal bovine serum (FBS). After the growth, these cancer cells are trypsinized and

centrifuged (at ~800 to 1000 rpm) to acquire them in a pellet form which is then redispersed in specific amount of media to form the cancer cell stock. Then, ~1 million cancer cells (counted through hemocytometer) are taken (from the stock) and resuspended in media containing the SPM nanoparticles at specific concentrations. Then, these cancer cells along with the nanoparticles are subjected to AMF to reach the therapeutic temperature (42–45 °C), which is then maintained for the next 30–60 mins by attuning the AMF [78]. In addition, the equal number (i.e., ~1 million) of cancer cells is (i) treated under same AMF (without nanoparticles) and (ii) incubated with only nanoparticles (without AMF) at predefined concentrations.

After the MFH treatment, ~40 to 120 μ l of cell suspension is mixed with appropriate media and plated in triplicates followed by 24–72 h of incubation at 37 °C under 5% CO₂. Similar procedure is followed for the cells treated with only AMF and only nanoparticles at definite concentration. Finally, the viability (i.e., proliferation capacity) of the cancer cells (from all wells) is determined via an assay – for example MTT assay by measuring the absorbance of live cancer cells after the sequential addition of MTT (with 4–5 h incubation) and stopping solution. The formula for determining the viability of cancer cells (with/without MFH therapy) is given by the following equation – Eq. (7.4) [79].

$$\text{Cell viability} = \frac{100 * \text{Absorbance of well treated with SPIONs or AMF or both}}{\text{Absorbance of control well} - \text{without any SPIONs or AMF}} \quad (7.4)$$

In a typical *in vivo* MFH study, mice are usually grown with tumors (having specific cancer cell type – for example: human multiple myeloma cells) to reach a diameter of ~50 mm³, and divided into four different groups (with n = 5 per cohort): (i) no treatment; (ii) application of only magnetic field; (iii) only intravenous administration of SPM nanoparticles at specific concentration; and (iv) intravenous administration of SPM nanoparticles at same concentration and subsequent application of AMF (to reach the therapeutic temperature (42 or 45 °C)) for specific time after 24 h of administration [80]. An optical fiber probe is inserted into the tumor site or thermal imaging is used to monitor temperature rise during MFH treatments. After MFH, the mice are observed for specific time (~1 month) to notice any reduction in the size of the tumor. Based on this observation, 1–2 rounds of treatment are given to improve the efficacy of MFH treatments.

However, mice are euthanized if the size of tumor reaches a diameter of 1500–3500 mm³. After euthanizing, tissue samples from the mice are obtained and immediately immersed in 4% paraformaldehyde solution for 24 h for histology analysis. Then, Prussian blue staining method is used to qualitatively determine the intracellular Fe ions. Moreover, in biodistribution studies, the mice are sacrificed, and their tissues are taken out, washed, and then weighed. The tissue sample (~10 mg) is dissolved with 1 mL of aqua regia in a Teflon vial and then diluted with ultrapure water. Then, the iron concentration in the tissue solution is measured by using an iron calorimetric assay kit. Thus, the histology and biodistribution studies are performed via *in vivo* MFH studies.

5 Key Research Findings

Magnetic fluid hyperthermia (MFH) studies are performed to investigate the heat induction properties of the MNPs – i.e., mainly SPM nanoparticles (e.g., SPIONs)-based ferrofluids under an applied alternating magnetic field (AMF) produced by a hyperthermia instrument [35, 81–87]. The heat induced by the ferrofluids (via Néel and/or Brownian relaxation) and the corresponding heating efficiencies (in terms of SAR/ILP) are generally examined with respect to the physicochemical properties (i.e., size/size distribution/shape), surface coatings, composition, applied AMFs and dispersion media, which are discussed as follows.

5.1 Influence of Size/Size Distribution/Shape of SPM Nanoparticles

The sizes and the size distributions (i.e., monodispersed (narrow distribution) / polydispersed (broad distribution)) of the SPM nanoparticles considerably influence their heat generation properties.

For instance, Gonzales-Weimuller et al. have studied the heating effects of iron oxide nanoparticles in MFH by tailoring their size, where a highest SAR of 447 W/g is obtained for 14 nm particles (as compared to SAR values of 180, 130, and 200 W/g for nanoparticles with sizes of 5, 10, and 12.8 nm) on exposure to AMF with $H = 24.5$ kA/m and $f = 400$ kHz [88]. In a similar fashion, Presa et al. have observed increment in SAR values (from 4 to 58 W/g) by increasing the size of the SPIONs from 6 to 14 nm after exposing them to the AMF with $H = 7.5$ kA/m and $f = 522$ kHz [89]. In another similar study, Bakoglidis et al. have investigated the heating effects of the SPIONs with their sizes ranging from 5–18 nm by exposing them to high-frequency alternating current (ac) magnetic field with $H = 20$ kA/m and $f = 765$ kHz [90]. Herein, the SAR value has gradually incremented as the size of the nanoparticles is increased from 5 to 10 nm (in superparamagnetic region), but the SAR value has (i) decremented as the nanoparticle size changes from 10 to 13 nm (in superparamagnetic-ferromagnetic transition region) and (ii) again increased once their size has reached 18 nm (in ferromagnetic region). In another latest study, Tong et al. have synthesized magnetic iron oxide nanoparticles (MIONs) with different sizes ranging from superparamagnetic (i.e., with sizes of 6, 8, 11, and 15 nm) to ferromagnetic (with sizes of 19, 25, 33, and 40 nm) regimes, and subsequently studied their heating effects under the AMF with $H = 20.7$ kA/m, and $f = 325$ kHz [91]. The SAR values of the MIONs have dramatically increased for their sizes between 11 and 33 nm, and reached a plateau around 33–40 nm by exhibiting the maximum SAR value of 2560 W/g_{Fe} for 40-nm-sized nanoparticles. Thus, the change in sizes have significant influence on the heating effects of the nanoparticles, but the superparamagnetic size limit for the nanoparticles (~ 10 nm) should be retained for their effective application in biological conditions.

Iacovita et al. showed very high SAR value of ~1400 W/g for small monocrystalline iron oxide nanoparticles as compared to SAR value of 400 W/g for the large

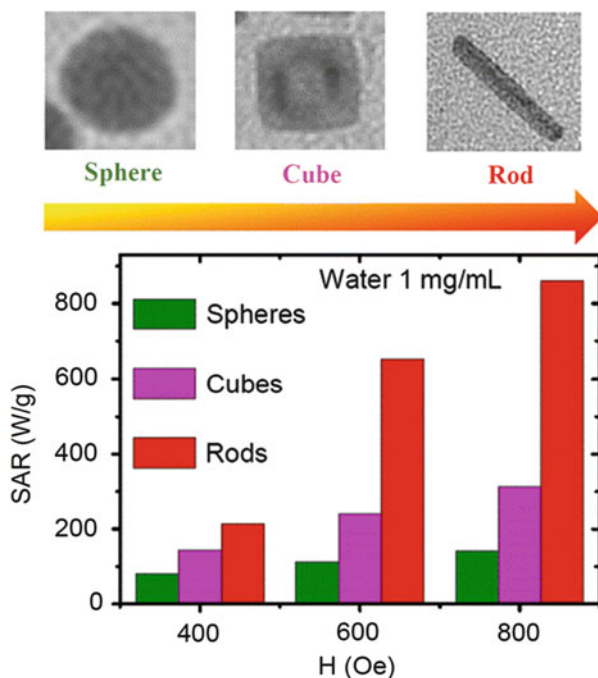
polycrystalline nanoparticles under the external AMF with $H = 65$ kA/m and $f = 355$ kHz [92]. Similarly, in another investigation, Khandhar et al. have displayed that the 16 nm spherical-shaped Fe_3O_4 nanoparticles with broader average-size distribution ($\sigma_{\text{avg}} = 0.266$) have shown reduced SAR value (i.e., 100 W/g) as compared to the value (i.e., 144 W/g) of nanoparticles with the same size and narrower size distribution ($\sigma_{\text{avg}} = 0.175$) at an applied AMF with $H = 13.4$ kA/m and $f = 376$ kHz [93]. In contradiction to the above-mentioned studies, Patsula et al. have showed high SAR value (i.e., 142 W/g) for 14-nm-sized polydispersed nanoparticles (with PDI = 1.21) as compared to the value (i.e., 22 W/g) of its monodispersed counterpart (with PDI = 1.02) at an applied AMF with $H = 24$ kA/m and $f = 400$ kHz [94]. Hence, the particle size distribution controls the heating efficacies of the MNP, but narrow size distribution is essential for uniform heat induction for in vitro MFH applications.

Magnetic nanoparticles with diverse shapes are proven to show enhanced heating effects as compared to its spherical-shaped counterparts. For example, Maity et al. have presented enhanced SAR value (i.e., 500 W/g) for nanoflower-shaped particles as compared to the value (135 W/g) for spherical-shaped SPIONs on exposure to AMF with $H = 89$ kA/m and $f = 240$ kHz [79]. Analogous result is reported by Hugounenq et al., where a high SAR value of 1992 W/g for nanoflower-shaped particles by applying a field with $H = 21.5$ kA/m and $f = 700$ kHz [95]. Similarly, Lartigue et al. have reported a SAR value of 1500 W/g for multi-core nanoparticles by exposing them to AMF with $H = 25$ kA/m and $f = 520$ kHz [96].

In another study, Guardia et al. have demonstrated SAR values up to 2452 W/g for cube-shaped iron oxide nanocrystals at an applied AMF with $H = 29$ kA/m and $f = 520$ kHz [97]. Similarly, Martinez-Boubeta et al. showed superior magnetic heating efficiency (SAR ~ 500 W/g) using the ferrimagnetic iron oxide nanocubes with an edge length about 20 nm at an applied AMF with $H = 30$ mT and $f = 765$ kHz [98]. In a similar investigation, Lv et al. have synthesized octahedral-shaped Fe_3O_4 nanoparticles and investigated their magnetic hyperthermia performances in a gel suspension, where the results indicated high SAR values up to 2629 W/g by exposing to the AMF with $H = 800$ Oe and $f = 358$ kHz [99]. Likewise, Mohapatra et al. have shown improved SAR values (up to 275 W/g) for octahedral-shaped nanoparticles at an applied field with $H = 310$ Oe and $f = 247$ kHz [100]. In another investigation, Nemati et al. have revealed high SAR value (i.e., 240 W/g) for the octopod-shaped nanoparticles as compared to the value (i.e., 140 W/g) of spherical nanoparticles with the similar size at applied AMF with $H = 800$ Oe and $f = 310$ kHz [101].

In another recent investigation, Das et al. have performed calorimetric MFH experiments using the Fe_3O_4 nanorods that also represented for a large SAR value (i.e., 862 W/g at AMF with $H = 400$ to 800 Oe and $f = 310$ kHz), which are superior to spherical and cubic nanoparticles (~ 140 and ~ 314 W/g, respectively) – as shown in Fig. 7.6 [102]. Similarly, Nemati et al. presented high heating efficacies (i.e., SAR = 125 W/g) for the nanodiscs as compared to the spherical-shaped nanoparticles (i.e., SAR = 90 W/g) for an applied field with $H = 800$ Oe and $f = 300$ kHz [103]. Moreover, the same group has reported a high SAR value of 800 W/g for the

Fig. 7.6 SAR vs. field plot for the Fe_3O_4 -based nanospheres, cubes, and nanorods. (Reproduced from Ref. [102])



iron oxide nanocubes with the similar applied magnetic field conditions [104]. Thus, the diverse shapes of the magnetic nanoparticles significantly affect their heating efficacies in MFH applications. Nevertheless, the shape-dependent toxicity should be considered for biological scenarios.

5.2 Influence of Surface Coatings and Composition of SPM Nanoparticles

Similar to the effect of size, size distribution, and shape, the surface coating of the SPM nanoparticles (attached during or after the synthesis process to make them dispersed/non-agglomerated) have considerable influences on their heat-generation behaviors and subsequent effect on the heating efficacies in MFH. For example, Regmi et al. have reported different heating efficacies (i.e., SAR values of 37, 46, and 64 W/g) for SPIONs coated with fatty acids with different chain lengths (i.e., C12, C14, and C18) [105]. In another similar study, different heating efficacies with SAR values of 140, 220, and 350 W/g are reported for the nanoparticles coated with diverse surfactants such as cetyl trimethylammonium bromide (cationic), poly(vinylpyrrolidone) (non-ionic), and sodium cholate (anionic), respectively, on exposure to AMF with $H = 25$ kA/m and $f = 765$ kHz [106]. Likewise, SAR values of 20 W/g and 60 W/g are presented for the nanoparticles coated with oleic acid and

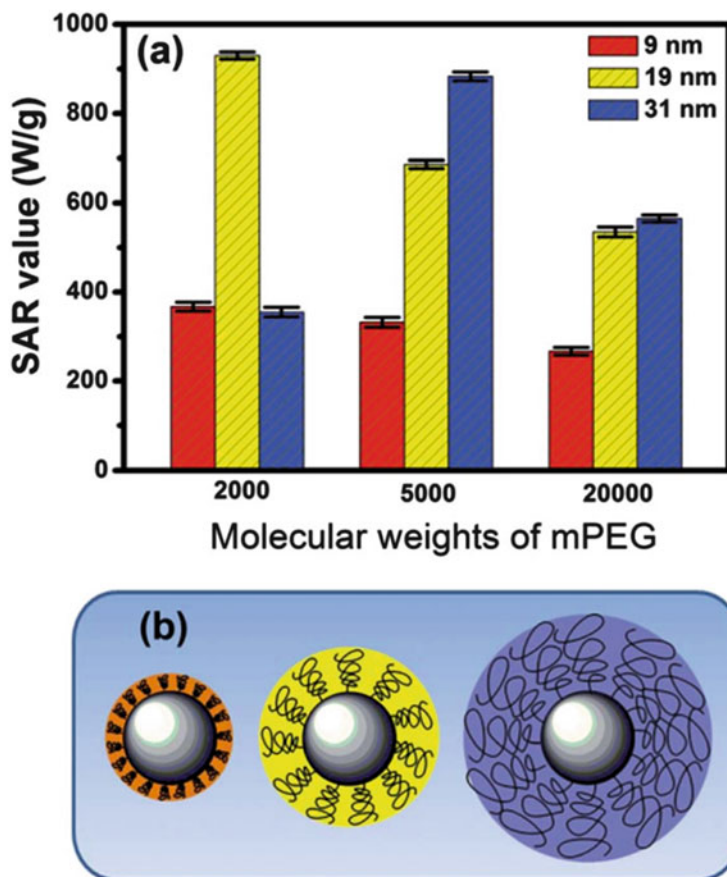


Fig. 7.7 (a) The SAR values of the different-sized Fe₃O₄ nanoparticles for different mPEG: 9 nm (orange), 19 nm (yellow), 31 nm (blue). (b) A schematic diagram of magnetic nanoparticle-based hyperthermia agents with iron oxide core and increasing mPEG coatings (2000, 5000 and 20,000). (Reproduced from Ref. [108])

trisodium citrate, respectively, while exposing them to AMF with $H = 24$ kA/m and $f = 418.5$ kHz [107].

Analogously, Liu et al. have elaborately optimized the surface coatings (i.e., methoxy poly (ethylene glycol) (mPEG) with different molecular weights of 2000, 5000, and 20,000) for Fe₃O₄ nanoparticles, where a high SAR value of 930 W/g is attained for 19-nm-sized nanoparticles coated with mPEG 2000 on exposure to AMF with $H = 27$ kA/m and $f = 400$ kHz as compared to their counterparts with different sizes (9 and 31 nm) and/or coated with mPEG 5000 or 20,000 – as shown in Fig. 7.7 [108]. Similarly, Mohammad et al. have studied the effect of gold shell on the heat-release process and the corresponding heating efficacies of the SPIONs, where the gold-coated SPIONs have exhibited a higher SAR value of 463.9 W/g as compared

to the value of 313.5 W/g for free-SPIONs for the applied AMF with $H = 123$ V at a current of 11 A, and $f = 430$ Hz [109].

Moreover, SPIONs are synthesized with different σ -conjugated small-molecule surfactants such as glycine [110], citric acid/albumin [111], sodium oleate [112], pentenoic acid [113], and glycyrrhizic acid [114] that have exhibited corresponding SAR values of 77.6 W/g (at $H = 0.385$ kOe and $f = 250$ kHz), 16.72/10.66 W/g (at $H = 3$ kA/m and $f = 215$ kHz), 14 W/g (at $H = 15.9$ kA/m and $f = 62$ kHz), 110.56 W/g (at $H = 0.1$ kW power and $f = 142$ kHz), and 17.92 W/g (at $H = 8.8$ kA/m and $f = 300$ kHz).

Furthermore, Kandasamy et al. have systematically synthesized the SPIONs with π -conjugated short-chained surfactants (having different carboxyl- or/and amine-functional groups) such as terephthalic acid (TA), aminoterephthalic acid (ATA), trimesic acid (TMA), pyromellitic acid (PMA), 1,4-diaminobenzene (14DAB), 4-aminobenzoic acid (4ABA), and 3,4-diaminobenzoic acid (34DABA), which correspondingly resulted in heating efficacies of 140, 158, 60, 72, 302, 219, and 330 W/g under the exposure to AMF with $H = 10.9$ kA/m and $f = 751.5$ kHz [78, 115–117]. Herein, 34DABA-coated SPIONs have exhibited the highest heating efficacies, which could be mainly due to (i) enhanced $\pi - \pi$ conjugation paths of surface-attached 34DABA coating molecules because of intra-functional group attractions and (ii) improved anisotropy from the formation of clusters/linear chains of the SPIONs in aqueous ferrofluid suspensions, owing to intra-/inter-functional group attractions and/or inter-particle interactions due to increasing concentrations (as shown in Fig. 7.8). Hence, the surface coatings have substantial role in altering the heating efficacies of the magnetic nanoparticles in MFH applications.

In addition, the variation in the composition of the magnetic nanoparticles – i.e., doping with different metal cations (e.g., $M = \text{Mn}$ or Co in MFe_2O_4) which results in superparamagnetic spinel-ferrite nanostructures (MnFe_2O_4 and/or CoFe_2O_4) – has also the key impact on their heating abilities. For instance, Cruz et al. have reported SAR values of 168 W/g and 29 W/g, respectively, for the MnFe_2O_4 and CoFe_2O_4 nanoparticles on exposure to the applied AMF with $H = 13.9$ kA/m and $f = 274$ kHz [118]. Recently, Phong et al. have studied the heating efficacies of the CoFe_2O_4 nanoparticles (having sizes in the range of 13–24 nm), where the SAR values are found to be decreased with the increase of their particle size, and the smallest CoFe_2O_4 nanoparticles (with 13.5 nm) exhibited the highest SAR value of 142 W/g under a low AMF with $H = 100$ Oe and $f = 240$ kHz [119]. In another recent study, Psimadas et al. showed higher SAR value of 122 W/g for the Fe_3O_4 nanoparticles in comparison to the value of 41 W/g for the CoFe_2O_4 nanoparticles under the applied AMF with $H = 19.9$ kA/m and $f = 95$ kHz [120]. In contrast to the abovementioned studies, Lee et al. have reported higher heating efficacies for the single-component MnFe_2O_4 (15 nm) and CoFe_2O_4 (9 nm) nanoparticles (SAR values of 411 W/g and 443 W/g, respectively) as compared to the single-component Fe_3O_4 (12 nm) nanoparticles (SAR value of 349 W/g) for the applied AMF with $H = 37.3$ kA/m and $f = 500$ kHz [121]. In addition, they have tuned the SAR values with the formation of core-shell (or exchange-coupled) nanoparticles by varying the

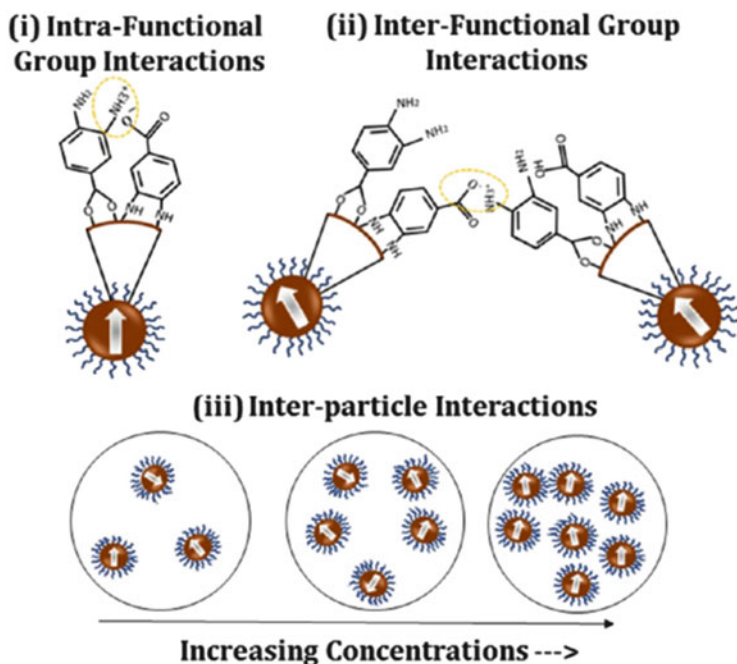


Fig. 7.8 Different types of interactions in 34DABA-coated SPION-based ferrofluid suspensions – (i) intrafunctional group interactions, (ii) interfunctional group interactions, and (iii) interparticle interactions. (Reproduced from Ref. [78])

combination of the core and shell components – i.e., $\text{CoFe}_2\text{O}_4@\text{MnFe}_2\text{O}_4 = 2280$ W/g, $\text{CoFe}_2\text{O}_4@\text{Fe}_3\text{O}_4 = 1120$ W/g, $\text{MnFe}_2\text{O}_4@\text{CoFe}_2\text{O}_4 = 3034$ W/g, $\text{Fe}_3\text{O}_4@\text{CoFe}_2\text{O}_4 = 2795$ W/g, and $\text{Zn}_{0.4}\text{Co}_{0.6}\text{Fe}_2\text{O}_4@\text{Zn}_{0.4}\text{Mn}_{0.6}\text{Fe}_2\text{O}_4 = 4000$ W/g – as shown in Fig. 7.9. Moreover in another study, Noh et al. have achieved a significantly larger SAR value of 10,600 W/g for cube-shaped core-shell $\text{Zn}_{0.4}\text{Fe}_{2.6}\text{O}_4@\text{CoFe}_2\text{O}_4$ nanoparticles on exposure to AMF with $H = 37.3$ kA/m and $f = 500$ kHz [122].

Similarly, Robles et al. have demonstrated a large increase in SAR value for the spherical-shaped core-shell $\text{Fe}_3\text{O}_4/\text{CoFe}_2\text{O}_4$ nanoparticles (199 W/g) as compared to SAR value of similar sized Fe_3O_4 nanoparticles (i.e., 8 W/g). Moreover, they have also reported that the SAR value of the $\text{Fe}_3\text{O}_4/\text{CoFe}_2\text{O}_4$ nanoparticles is increased from 199 to 461 W/g (for applied AMF with $H = 800$ Oe and $f = 310$ kHz) as the thickness of the CoFe_2O_4 shell is increased from 0.9 ± 0.5 to 2.1 ± 0.1 nm [123]. In a similar fashion, Angelakeris et al. have presented core-shell $\text{MnFe}_2\text{O}_4@\text{CoFe}_2\text{O}_4$ and $\text{CoFe}_2\text{O}_4@\text{MnFe}_2\text{O}_4$ nanoparticles with SAR values of 73 W/g and 160 W/g, respectively, for the applied AMF with $H = 28$ kA/m and $f = 765$ kHz [124]. Thus, the composition (including core-shell structure) of the nanoparticles has major influence on their heating capacities; however, the toxicity of the metal cations should be monitored for better biological results.

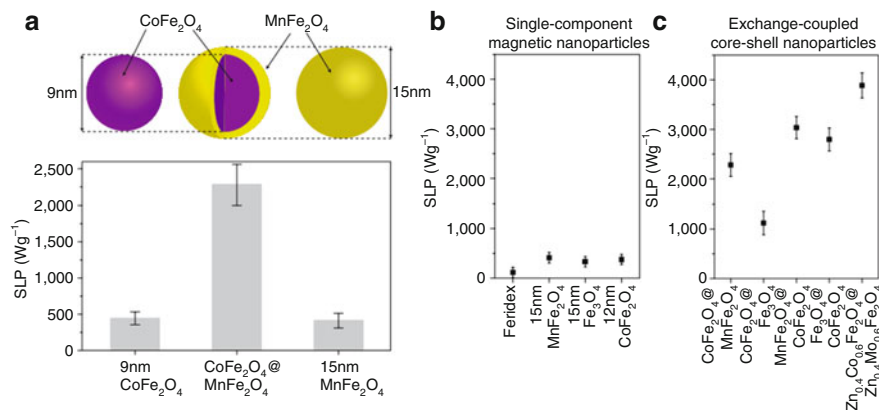


Fig. 7.9 SAR comparison of magnetic nanoparticles. **(a)** Schematic of 15 nm CoFe₂O₄@MnFe₂O₄ nanoparticle and its SAR value in comparison with the values for its components (9 nm CoFe₂O₄ and 15 nm MnFe₂O₄) for the applied AMF with $H = 37.3$ kA/m and $f = 500$ kHz. **(b)** and **(c)** SAR values of single-component magnetic nanoparticles (Feridex and MnFe₂O₄; M = Mn, Fe and Co) and various combinations of core-shell nanoparticles. Error bars indicate standard deviation ($n = 5$). (Reproduced from Ref. [121])

5.3 Influence of Applied AMFs and Dispersion Media of SPM Nanoparticles

Apart from size, size distribution, shape, surface coatings, and composition of the SPM nanoparticles, the applied AMFs (with increasing amplitudes/frequencies) have enormous influence to alter their heat-generating ability. For example, Bekovic et al. have studied the heating effects of magnetic nanoparticles at low AMF with H and f ranging from 0.5–3.5 kA/m to 50–185 kHz, where the SAR values have correspondingly increased from 0 to 0.5 W/g [125].

Similarly, Orsini et al. have determined the heating ability of 12 nm-sized iron oxide nanoparticles under AMF with H or $H_0 = 3.98$ –23.87 kA/m, and $f = 229.3$ –828 kHz, which resulted an increase in SAR values (i.e., from 0 to ~120 W/g or 200 W/g) in quadratic manner (i.e., $SAR = AH_0^2$ or Bf^2) upon the increment in the amplitudes or frequencies of the applied field – as shown in Fig. 7.10 [126]. In similar fashion, Kandasamy et al. have exposed the SPIONs to AMFs with H and f in the respective ranges of 7.1–15.39 kA/m and 175.2–1001.1 kHz, where a linearly increasing trend for the SAR values (i.e., from 48.6 to 432.1 W/g) is obtained with the increment in the magnetic fields [78]. Likewise, Hemery et al. have performed similar MFH investigations for multicore iron oxide nanoparticles by varying the applied magnetic fields (including H (0–30 kA/m) and f (149–1023 kHz)), where a significant increase of SAR values from 0 to ~2000 W/g is noted [127]. Analogous investigations are performed by other researchers and similar results are obtained [128–130]. Thus, the increase in SAR values can be attained by incrementing the amplitudes (H)/frequencies (f) of the applied magnetic fields; however, the $H \times f$

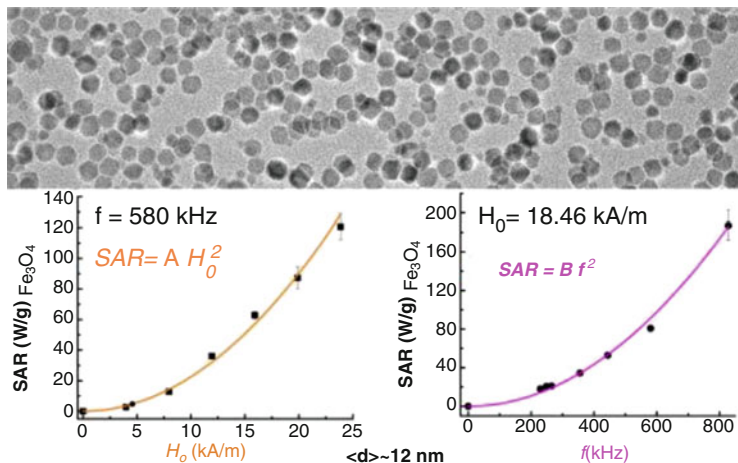


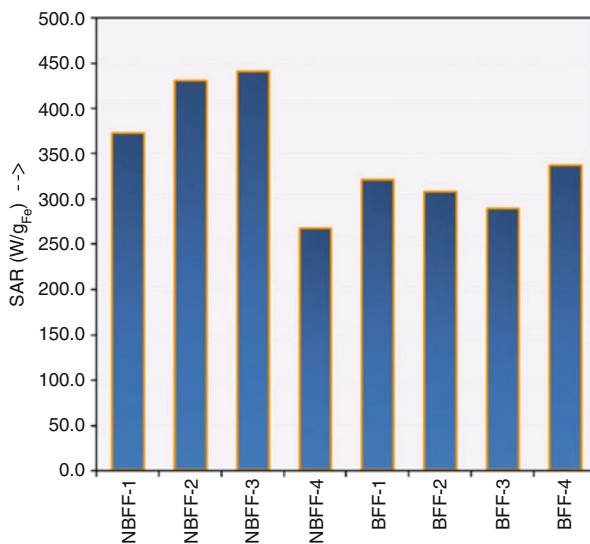
Fig. 7.10 Top figure indicates the TEM image of 12-nm-sized iron oxide nanoparticles. Lower left figure indicates the SAR of the nanoparticles versus amplitude (H_0) of AMF, measured at the fixed frequency of $f = 580.5$ kHz. Lower right figure indicates the SAR of the nanoparticles versus frequency, f , measured at the fixed field amplitude of $H_0 = 18.46$ kA/m. (Reproduced from Ref. [126])

product in AMF should not exceed $5 \times 10^9 \text{ A} \cdot \text{m}^{-1} \cdot \text{s}^{-1}$, since it is the maximum recommended product value for use in human MFH treatment.

Moreover, dispersion medium directly affects the heat generation capability of the SPM nanoparticles. For instance, Andreu et al. have studied the heating capacities of the as-synthesized spherical-shaped nanoparticles by dispersing them in different medium such as n-hexane (C_6H_{14}), n-dodecane ($\text{C}_{12}\text{H}_{26}$), n-hexadecane ($\text{C}_{16}\text{H}_{34}$), tetracosane ($\text{C}_{24}\text{H}_{50}$), and epoxy resin under the AMF with $H = 3$ kA/m and $f = 111$ kHz, which resulted in corresponding SAR values of 4.6, 2.7, 3.0, 7.3, and 0.8 W/g [131]. In another study, Piñeiro-Redondo et al. have investigated the heating capacities of the nanoparticles by dispersing them in different solvents – with increasing viscosities (η) – such as water ($\eta = 1$ mP s), ethylene glycol ($\eta = 17$ mP s), 1–2-propanediol ($\eta = 40.1$ mP s), and polyethylene glycol (PEG with $\eta = 90$ mP s), where an increase in viscosity of the solvents (i.e., from 1 to 90 mP s) resulted in a significant decrement of the SAR values (i.e., from 36.5 to 21 W/g) [132]. In a similar investigation by Kandasamy et al., the diamminobenzoic acid-coated SPIONs are magnetically separated and dispersed in a definite volume of (i) nonbiological media such as ethylene glycol (EG), diethylene glycol (DEG), triethylene glycol (TEG), and glycerol (GC) and (ii) biological media such as phosphate buffer saline (PBS), Dulbecco's modified eagle medium (DMEM), DMEM +5% fetal bovine serum (FBS), and FBS, via vigorous vortexing process to determine the heating abilities of nonbiological ferrofluids (NBFFs – 1 to 4) and biological ferrofluids (BFFs – 1 to 4), respectively, under the AMF with $H = 10.9$ kA/m and $f = 751.5$ kHz [78].

The results (as shown in Fig. 7.11) indicated that the SAR value of (i) NBFFs is gradually increased from 372.6 W/g to a maximum value of 440.4 W/g (for

Fig. 7.11 SAR values of NBFF-1, NBFF-2, NBFF-3, NBFF-4, BFF-1, BFF-2, BFF-3, and BFF-4 with corresponding dispersion media of EG, DEG, TEG, GC, PBS, DMEM, DMEM +5% FBS, and FBS for 34DABA-coated SPIONs under AMF with $H = 10.9$ kA/m and $f = 751.5$ kHz. (Reproduced from Ref. [78])



corresponding ferrofluids of NBFF-1 to NBFF-3) and then decreased to 266.9 W/g (for NBFF-4), and (ii) BFFs is gradually decreased from 321 W/g (BFF-1) to 307 W/g (BFF-2), reached to a minimum value of 288.9 W/g (BFF-3), and then increased to 336.9 W/g (BFF-4). The decrement in the SAR values from BFF-1 to BFF-3 could be due to the large aggregation of the SPIONs in the respective biological media, as apparent from the large increment in their hydrodynamic sizes, attributed to the complex interactions between the surface-functional groups of the SPIONs and the carrier liquids. However, the BFF-4 exhibited the highest SAR value among all of the BFFs, which could be due to its lowest hydrodynamic size.

In another investigation, Ludwig et al. have immobilized the magnetic nanoparticles in tissues simulated with 1% agarose gels and 10% polyvinyl alcohol (PVA) hydrogels, where a strong reduction of the SAR value (i.e., from 585 to 314 W/g) is found after the immobilization of nanoparticles in PVA as compared to agarose gel [133]. Similar results are obtained by other investigations that have been focused on the influence of solvent/dispersion medium towards the heating efficacies of the nanoparticles [93, 107, 134–136]. Thus, the size/size distribution, shape, surface coatings, composition, applied AMFs, and dispersion media have significant impact in modifying the heat generating abilities of the SPM nanoparticles.

5.4 Biological Magnetic Fluid Hyperthermia of SPM Nanoparticles

MFH-based thermotherapy has attracted major attention as one of the capable cancer treatment modalities since the heating of the cancer cells in the range of 42–45 °C

might cause crucial damages in these cells to induce apoptotic cell death [30]. For this purpose, the SPM nanoparticles are significantly involved in *in vitro* and *in vivo* cancer treatments, which are discussed as follows.

5.4.1 In Vitro Studies

Saeedi et al. have performed an *in vitro* MFH study where the viability of L929 cells has drastically reduced by induced heat using the glycyrrhizic acid coated iron oxide nanoparticles under AMF (with $H = 11.7$ kA/m and $f = 300$ kHz), while the AMF itself has no lethal effect on the control cells as indicated by their high viability [114]. In another investigation, Maity et al. have attained $\sim 74\%$ cytotoxicity in MCF-7 cancer cells by exposing them to the heat induced by magnetic nanoclusters under AMF with $H = 89$ kA/m, and $f = 240$ kHz [79]. In another recent investigation, Jadhav et al. have demonstrated 80% hyperthermic killing ability for iron oxide nanoparticles in fibrosarcoma cells on exposure to AMF with $H = 26$ kA/m and $f = 265$ kHz [137].

Similarly, Hemery et al. have investigated *in vitro* MFH efficiency of multicore (nanoflowers) vs. monocore (nanospheres) nanoparticles in glioblastoma cells as shown in Fig. 7.12 [138]. A higher cytotoxicity of $\sim 80\text{--}90\%$ is achieved for multicore nanoparticles (as compared with 40% cytotoxicity for monocore counterparts) after 30 min treatment under the AMF with $H = 12$ kA/m and $f = 473$ kHz, which is mainly due to (i) higher SAR value and internalized concentration of 265 W/g and 800 pg/cell for multicore nanoparticles (in comparison to 134 W/g and 300 pg/cell for monocore nanoparticles), respectively, and (ii) a mechanical

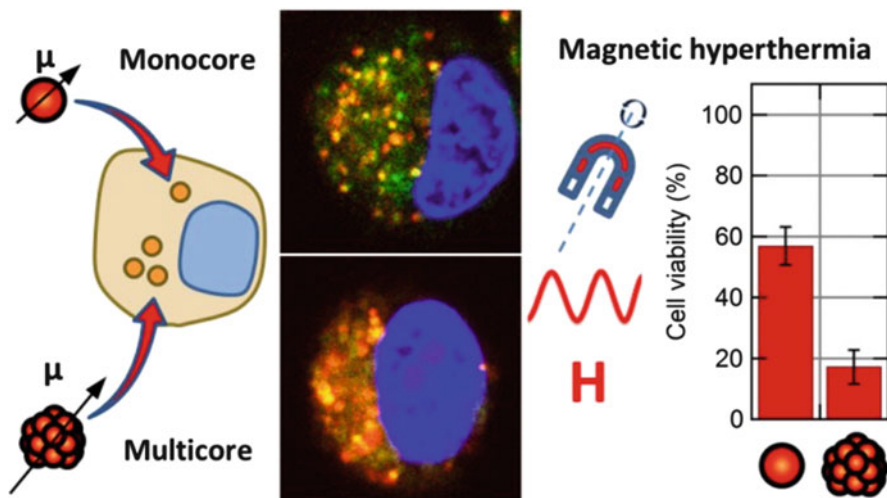


Fig. 7.12 Cellular internalization (via DY700/Hoechst 33342/Lysotracker™ green staining) and *in vitro* magnetic hyperthermia (under AMF with $H = 12$ kA/m and $f = 473$ kHz)-based cell viability studies of the monocore (nanospheres) vs. multicore (nanoflowers) nanoparticles. (Reproduced from Ref. [138])

disruption of the plasma and lysosomal membranes induced by the increased surface roughness of multicore nanoparticles.

In a similar fashion, Kandasamy et al. showed ~90% killing efficiency in MCF-7 cancer cells after treating them with terephthalic/aminoterephthalic acid coated SPIONs under the AMF with $H = 10.9$ kA/m and $f = 751.5$ kHz [116]. Likewise, they have also demonstrated a hyperthermic killing efficiency of 61–88% (via MFH) in HepG2 cancer cells by using the heat induced via diaminobenzoic acid-coated SPIONs under similar AMF conditions [78]. In another study, Zhang et al. have showed significant apoptosis in SK-BR-3 cells by using the heat induced via herceptin-directed magnetic nanoparticles under the AMF with $H = \sim 35$ kA/m and $f = 150$ kHz [139]. In another similar investigation, Majeed et al. have demonstrated decreased viability (~55%) in HeLa cells that are treated with iron oxide nanoparticles along with induction heating (i.e., MFH with AMF having $H = 400$ A and $f = 250$ kHz) as compared to those cells with only induction heating (i.e., without nanoparticles) and control (i.e., without nanoparticles and AMF) [140]. Likewise, in a study performed by Attar et al., above 90% cytotoxicity is observed in different cancer cell lines after consequent incubation with nanoparticles and application of AMF with $H = 8$ kA/m and $f = 80$ kHz. Similarly, Aljarrah et al. have significantly increased doxorubicin-induced cytotoxicity by pre-incubation of MCF-7 cells with iron oxide nanoparticles followed by a magnetic field exposure [141].

5.4.2 In Vivo Studies

Gilchrist et al. have initially performed in vivo cancer treatment (through MFH) using the heat induced by the magnetic particles under AMF with $H = 16$ – 19.2 kA/m and $f = 1.2$ MHz [142]. Recently, Zhao et al. have used magnetic iron oxide nanoparticle induced hyperthermia for the treatment of human head and neck cancer (Tu212 cell line) developed in a mouse xenograft model by using AMF with $H = 7$ kA/m and $f = 130$ kHz, where the pathological results demonstrated high epithelial tumor cell destruction associated with the hyperthermia treatment [143]. In another investigation, Hayashi et al. have reported a strong reduction in the volume of myeloma tumor in mice (i.e., one-tenth that of the control mice) after 35 days of MFH treatment (as shown in Fig. 7.13) by using folic acid (FA) and polyethylene glycol (PEG) modified SPION nanoclusters (FA-PEG-SPION NCs) under AMF with $H = 8$ kA/m and $f = 230$ kHz [80].

In addition, the MFH treated mice are found to be alive even after 12 weeks, whereas the control mice are found to be dead only at 8 weeks after the tumor induction. In a similar fashion, Yi et al. have demonstrated a significant decrease in the sizes of C6 glioma tumor in rats via MFH therapy (at the AMF with $H = 10$ kA/m and $f = 200$ kHz) by using optimized nanoparticle dosage [144]. In another investigation, Araya et al. have reported a reduction of A549 lung adenocarcinoma in mice models by using the heat inducted via ferucarbotran-based nanoparticles under AMF with $H = 24$ kA/m and $f = 142$ kHz [145]. Moreover, based on the previous in vitro and in vivo works, Spirou et al. have outlined the

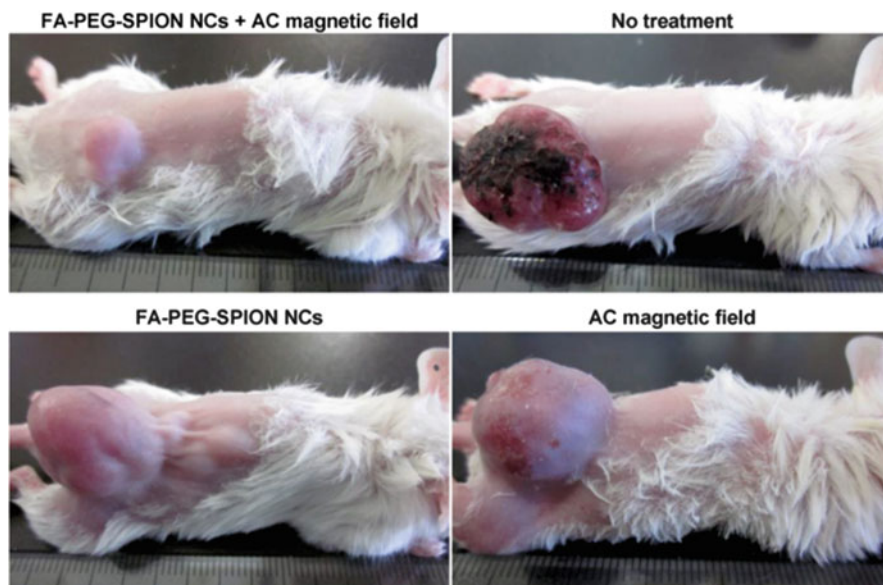


Fig. 7.13 Photographs of mice 35 days after MFH treatment with folic acid (FA)- and polyethylene glycol (PEG)-modified SPION nanoclusters (FA-PEG-SPION NCs) under AC magnetic field with $H = 8 \text{ kA/m}$ and $f = 230 \text{ kHz}$. (Reproduced from Ref. [80])

necessary considerations (after the synthesis and characterization of the MNPs – i.e., SPM nanoparticles) that a researcher must address in order to perform preclinical MFH testing for effective cancer treatments [146].

6 Conclusions and Future Perspectives

In summary, this chapter initially described a brief introduction about different types of magnetic materials, unique behavior of the SPM nanoparticles, basic principles of heat generation in MFH, and also several techniques for characterizations of the physicochemical/magnetic/dispersibility properties of the MNPs/SPM nanoparticles (i.e., SPIONs) – crucial for further MFH analysis. Then, we have discussed the influences of different key parameters including the physicochemical properties (i.e., size/size distribution/shape), surface coatings, composition, applied AMFs, and dispersion media on the heating performance of the SPM nanoparticles (as presented by different worldwide studies). Finally, we have highlighted the recent MFH investigations of the SPM nanoparticles in *in vitro* and *in vivo* scenarios. From the above discussed works, it can be concluded that (i) the key parameters should be carefully optimized for attaining better heating efficacies in calorimetric MFH studies, and (ii) the MFH-based thermotherapy can be efficiently used as individual therapy for effective cancer treatments, which could be useful in further clinical investigations.

References

1. Lin MM, Kim H-H, Kim H et al (2010) Iron oxide-based nanomagnets in nanomedicine: fabrication and applications. *Nano Rev* 1
2. Ali A, Zafar H, Zia M et al (2016) Synthesis, characterization, applications, and challenges of iron oxide nanoparticles. *Nanotechnol Sci Appl* 9:49–67. <https://doi.org/10.2147/NSA.S99986>
3. Pankhurst QA, Connolly J, Jones SK, Dobson J (2003) Applications of magnetic nanoparticles in biomedicine. *J Phys D Appl Phys* 36:R167–R181. <https://doi.org/10.1088/0022-3727/36/13/201>
4. Huber DL (2005) Synthesis, properties, and applications of iron nanoparticles. *Small* 1:482–501. <https://doi.org/10.1002/sml.200500006>
5. Bedanta S, Kleemann W (2009) Supermagnetism. *J Phys D Appl Phys* 42:013001. <https://doi.org/10.1088/0022-3727/42/1/013001>
6. Klostergaard J, Seeney CE (2012) Magnetic nanovectors for drug delivery. *Nanomedicine* 8: S37–S50
7. Sheng-nan S, Chao W, Zan-zan Z (2014) Magnetic iron oxide nanoparticles: synthesis and surface coating techniques for biomedical applications. *Chinese Phys B* 23:1–19. <https://doi.org/10.1088/1674-1056/23/3/037503>
8. Tapeinos C (2018) Magnetic nanoparticles and their bioapplications. In: Parinov IA, Chang S-H, Topolov VY (eds) *Smart nanoparticles for biomedicine*. Elsevier, Cham, pp 131–142
9. Akbarzadeh A, Samiei M, Davaran S (2012) Magnetic nanoparticles: preparation, physical properties, and applications in biomedicine. *Nanoscale Res Lett* 7:144. <https://doi.org/10.1186/1556-276X-7-144>
10. Mody VV, Singh A, Wesley B (2013) Basics of magnetic nanoparticles for their application in the field of magnetic fluid hyperthermia. *Eur J Nanomedicine* 5:11–21. <https://doi.org/10.1515/ejnm-2012-0008>
11. Cullity BD, Graham CD (2011) *Introduction to magnetic materials*, 2nd edn. Wiley, Hoboken
12. Carlos L, Jafelicci M, Beck W (2011) Magnetic and multifunctional magnetic nanoparticles in nanomedicine: challenges and trends in synthesis and surface engineering for diagnostic and therapy applications. In: *Biomedical engineering, trends in materials science*. InTech, pp 397–424
13. Lee N, Hyeon T (2012) Designed synthesis of uniformly sized iron oxide nanoparticles for efficient magnetic resonance imaging contrast agents. *Chem Soc Rev* 41:2575. <https://doi.org/10.1039/c1cs15248c>
14. Corot C, Robert P, Idée JM, Port M (2006) Recent advances in iron oxide nanocrystal technology for medical imaging. *Adv Drug Deliv Rev* 58:1471–1504. <https://doi.org/10.1016/j.addr.2006.09.013>
15. Wang Y-XJ, Hussain SM, Krestin GP (2001) Superparamagnetic iron oxide contrast agents: physicochemical characteristics and applications in MR imaging. *Eur Radiol* 11:2319–2331. <https://doi.org/10.1007/s003300100908>
16. Laurent S, Dutz S, Häfeli UO, Mahmoudi M (2011) Magnetic fluid hyperthermia: focus on superparamagnetic iron oxide nanoparticles. *Adv Colloid Interf Sci* 166:8–23. <https://doi.org/10.1016/j.cis.2011.04.003>
17. Pennacchioli E, Fiore M, Gronchi A (2009) Hyperthermia as an adjunctive treatment for soft-tissue sarcoma. *Expert Rev Anticancer Ther* 9:199–210. <https://doi.org/10.1586/14737140.9.2.199>
18. Chen H, Zhang W, Zhu G et al (2017) Rethinking cancer nanotheranostics. *Nat Rev Mater* 2:17024. <https://doi.org/10.1038/natrevmats.2017.24>
19. Kandasamy G, Maity D (2015) Recent advances in superparamagnetic iron oxide nanoparticles (SPIONs) for in vitro and in vivo cancer nanotheranostics. *Int J Pharm* 496:191–218. <https://doi.org/10.1016/j.ijpharm.2015.10.058>
20. Kitture R, Ghosh S, Kulkarni P et al (2012) Fe₃O₄-citrate-curcumin: promising conjugates for superoxide scavenging, tumor suppression and cancer hyperthermia. *J Appl Phys* 111:064702. <https://doi.org/10.1063/1.3696001>
21. Ahmed M, Douek M (2013) The role of magnetic nanoparticles in the localization and treatment of breast cancer. *Biomed Res Int* 2013:281230. <https://doi.org/10.1155/2013/281230>

22. Cheng Y, Morshed RA, Auffinger B et al (2014) Multifunctional nanoparticles for brain tumor imaging and therapy. *Adv Drug Deliv Rev* 66:42–57. <https://doi.org/10.1016/j.addr.2013.09.006>
23. Torchilin VP (2014) Multifunctional, stimuli-sensitive nanoparticulate systems for drug delivery. *Nat Rev Drug Discov* 13:813–827. <https://doi.org/10.1038/nrd4333>
24. Deatsch AE, Evans BA (2014) Heating efficiency in magnetic nanoparticle hyperthermia. *J Magn Magn Mater* 354:163–172. <https://doi.org/10.1016/j.jmmm.2013.11.006>
25. Kumar CSSR, Mohammad F (2011) Magnetic nanomaterials for hyperthermia-based therapy and controlled drug delivery. *Adv Drug Deliv Rev* 63:789–808. <https://doi.org/10.1016/j.addr.2011.03.008>
26. McCarthy JR, Weissleder R (2008) Multifunctional magnetic nanoparticles for targeted imaging and therapy. *Adv Drug Deliv Rev* 60:1241–1251. <https://doi.org/10.1016/j.addr.2008.03.014>
27. Verma J, Lal S, Van Noorden CJF (2014) Nanoparticles for hyperthermic therapy: synthesis strategies and applications in glioblastoma. *Int J Nanomedicine* 9:2863–2877
28. Laurent S, Forge D, Port M et al (2008) Magnetic iron oxide nanoparticles: synthesis, stabilization, vectorization, physicochemical characterizations and biological applications. *Chem Rev* 108:2064–2110. <https://doi.org/10.1021/cr068445e>
29. Hasany SF, Abdurahman NH, Sunarti AR, Jose R (2013) Magnetic Iron oxide nanoparticles: chemical synthesis and applications review. *Curr Nanosci* 9:561–575. <https://doi.org/10.2174/15734137113099990085>
30. Wu W, Wu Z, Yu T et al (2015) Recent progress on magnetic iron oxide nanoparticles: synthesis, surface functional strategies and biomedical applications. *Sci Technol Adv Mater* 16:023501. <https://doi.org/10.1088/1468-6996/16/2/023501>
31. Hedayatnasab Z, Abnisa F, Daud WMAW (2017) Review on magnetic nanoparticles for magnetic nanofluid hyperthermia application. *Mater Des* 123:174–196. <https://doi.org/10.1016/j.matdes.2017.03.036>
32. Hasany SF, Ahmed I, Rajan J, Rehman A (2013) Systematic review of the preparation techniques of Iron oxide magnetic nanoparticles. *Nanosci Nanotechnol* 2:148–158. <https://doi.org/10.5923/j.nn.20120206.01>
33. Veisheh O, Gunn JW, Zhang M (2010) Design and fabrication of magnetic nanoparticles for targeted drug delivery and imaging. *Adv Drug Deliv Rev* 62:284–304. <https://doi.org/10.1016/j.addr.2009.11.002>
34. Patil U, Adireddy S, Jaiswal A et al (2015) In vitro/in vivo toxicity evaluation and quantification of Iron oxide nanoparticles. *Int J Mol Sci* 16:24417–24450. <https://doi.org/10.3390/ijms161024417>
35. Périgo EA, Hemery G, Sandre O et al (2015) Fundamentals and advances in magnetic hyperthermia. *Appl Phys Rev* 2:041302. <https://doi.org/10.1063/1.4935688>
36. Maity D, Kandasamy G, Sudame A (2017) Superparamagnetic Iron Oxide Nanoparticles (SPIONs) based magnetic hyperthermia: a promising therapy in cancer treatment. In: Berhardt LV (ed) *Advances in medicine and biology*, 117th edn. Nova Science Publishers, pp 99–160
37. Praetorius NP, Mandal TK (2007) Engineered nanoparticles in cancer therapy. *Recent Pat Drug Deliv Formul* 1:37–51. <https://doi.org/10.2174/18722110779814104>
38. Thanh NTK, Maclean N, Mahiddine S (2014) Mechanisms of nucleation and growth of nanoparticles in solution. *Chem Rev* 114:7610–7630. <https://doi.org/10.1021/cr400544s>
39. Reddy LH, Arias JL, Nicolas J, Couvreur P (2012) Magnetic nanoparticles: design and characterization, toxicity and biocompatibility, pharmaceutical and biomedical applications. *Chem Rev* 112:5818–5878. <https://doi.org/10.1021/cr300068p>
40. Amstad E, Textor M, Reimhult E (2011) Stabilization and functionalization of iron oxide nanoparticles for biomedical applications. *Nanoscale* 3:2819. <https://doi.org/10.1039/c1nr10173k>
41. Mahmoudi M, Sant S, Wang B et al (2011) Superparamagnetic iron oxide nanoparticles (SPIONs): development, surface modification and applications in chemotherapy. *Adv Drug Deliv Rev* 63:24–46. <https://doi.org/10.1016/j.addr.2010.05.006>

42. Liu C, Zou B, Rondinone AJ, Zhang ZJ (2000) Chemical control of superparamagnetic properties of magnesium and cobalt spinel ferrite nanoparticles through atomic level magnetic couplings. *J Am Chem Soc* 122:6263–6267. <https://doi.org/10.1021/ja000784g>
43. Kharisov BI, Dias HVR, Kharissova OV (2014) Mini-review: ferrite nanoparticles in the catalysis. *Arab J Chem*. <https://doi.org/10.1016/j.arabjc.2014.10.049>
44. Tatarchuk T, Bououdina M, Judith Vijaya J, John Kennedy L (2017) Spinel ferrite nanoparticles: synthesis, crystal structure, properties, and perspective applications. In: Springer Proceedings in Physics. pp 305–325
45. Kefeni KK, Msagati TAM, Mamba BB (2017) Ferrite nanoparticles: synthesis, characterisation and applications in electronic device. *Mater Sci Eng B Solid-State Mater Adv Technol* 215:37–55. <https://doi.org/10.1016/j.mseb.2016.11.002>
46. Moroz P, Jones SK, Gray BN (2002) Magnetically mediated hyperthermia: current status and future directions. *Int J Hyperth* 18:267–284. <https://doi.org/10.1080/02656730110108785>
47. Maureen L, Awalpreet S, Kaur P et al (2016) Hyperthermia using nanoparticles – promises and pitfalls. *Int J Hyperth* 00:1–13. <https://doi.org/10.3109/02656736.2015.1120889>
48. Krishnan KM (2010) Biomedical nanomagnetism: a spin through possibilities in imaging, diagnostics, and therapy. *IEEE Trans Magn* 46:2523–2558. <https://doi.org/10.1109/TMAG.2010.2046907>
49. Kita E, Oda T, Kayano T et al (2010) Ferromagnetic nanoparticles for magnetic hyperthermia and thermoablation therapy. *J Phys D Appl Phys* 43:474011. <https://doi.org/10.1088/0022-3727/43/47/474011>
50. Obaidat I, Issa B, Haik Y (2015) Magnetic properties of magnetic nanoparticles for efficient hyperthermia. *Nano* 5:63–89. <https://doi.org/10.3390/nano5010063>
51. Shaterabadi Z, Nabiyouni G, Soleymani M (2018) Physics responsible for heating efficiency and self-controlled temperature rise of magnetic nanoparticles in magnetic hyperthermia therapy. *Prog Biophys Mol Biol* 133:9–19. <https://doi.org/10.1016/j.pbiomolbio.2017.10.001>
52. Abenojar EC, Wickramasinghe S, Bas-Concepcion J, Samia ACS (2016) Structural effects on the magnetic hyperthermia properties of iron oxide nanoparticles. *Prog Nat Sci Mater Int* 26:440–448. <https://doi.org/10.1016/j.pnsc.2016.09.004>
53. Shah RR, Davis TP, Glover AL et al (2015) Impact of magnetic field parameters and iron oxide nanoparticle properties on heat generation for use in magnetic hyperthermia. *J Magn Magn Mater* 387:96–106. <https://doi.org/10.1016/j.jmmm.2015.03.085>
54. Kozissnik B, Bohorquez AC, Dobson J, Rinaldi C (2013) Magnetic fluid hyperthermia: advances, challenges, and opportunity. *Int J Hyperth* 29:706–714. <https://doi.org/10.3109/02656736.2013.837200>
55. Kallumadil M, Tada M, Nakagawa T et al (2009) Suitability of commercial colloids for magnetic hyperthermia. *J Magn Magn Mater* 321:1509–1513. <https://doi.org/10.1016/j.jmmm.2009.02.075>
56. Hong-Ying S, Chang-Qiang W, Dan-Yang L, Hua A (2015) Self-assembled superparamagnetic nanoparticles as MRI contrast agents – a review. *Chinese Phys B* 24:127506. <https://doi.org/10.1088/1674-1056/24/12/127506>
57. Kim J, Piao Y, Hyeon T (2009) Multifunctional nanostructured materials for multimodal imaging, and simultaneous imaging and therapy. *Chem Soc Rev* 38:372–390. <https://doi.org/10.1039/b709883a>
58. Zhang W, Wu C, Silva SRP (2018) Proposed use of self-regulating temperature nanoparticles for cancer therapy. *Expert Rev Anticancer Ther* 18:723–725. <https://doi.org/10.1080/14737140.2018.1483242>
59. Jones CF, Grainger DW (2009) In vitro assessments of nanomaterial toxicity. *Adv Drug Deliv Rev* 61:438–456. <https://doi.org/10.1016/j.addr.2009.03.005>
60. Blanco-Andujar C, Teran FJ, Ortega D (2018) Current outlook and perspectives on nanoparticle-mediated magnetic hyperthermia. In: *Iron Oxide nanoparticles for biomedical applications*. Elsevier, pp 197–245

61. Faraji M, Yamini Y, Rezaee M (2010) Magnetic nanoparticles: synthesis, stabilization, functionalization, characterization, and applications. *J Iran Chem Soc* 7:1–37
62. Maity D, Ding J, Xue J-M (2008) Synthesis of magnetite nanoparticles by thermal decomposition: time, temperature, surfactant and solvent effects. *Funct Mater Lett* 01:189–193. <https://doi.org/10.1142/S1793604708000381>
63. Maity D, Choo SG, Yi J et al (2009) Synthesis of magnetite nanoparticles via a solvent-free thermal decomposition route. *J Magn Magn Mater* 321:1256–1259. <https://doi.org/10.1016/j.jmmm.2008.11.013>
64. Chandrasekharan P, Maity D, Yong CX et al (2011) Vitamin E (d-alpha-tocopheryl-co-poly (ethylene glycol) 1000 succinate) micelles-superparamagnetic iron oxide nanoparticles for enhanced radiotherapy and MRI. *Biomaterials* 32:5663–5672. <https://doi.org/10.1016/j.biomaterials.2011.04.037>
65. Maity D, Pradhan P, Chandrasekharan P et al (2011) Synthesis of hydrophilic superparamagnetic magnetite nanoparticles via thermal decomposition of Fe(acac)₃ in 80 Vol% TREG + 20 Vol% TREM. *J Nanosci Nanotechnol* 11:2730–2734. <https://doi.org/10.1166/jnn.2011.2693>
66. Maity D, Ding J, Xue J-M (2009) One-pot synthesis of hydrophilic and hydrophobic Ferrofluid. *Int J Nanosci* 08:65–69. <https://doi.org/10.1142/S0219581X09005748>
67. Maity D, Chandrasekharan P, Si-Shen F et al (2010) Polyol-based synthesis of hydrophilic magnetite nanoparticles. *J Appl Phys* 107:09B310. <https://doi.org/10.1063/1.3355898>
68. Tenório-Neto ET, Jamshaid T, Eissa M et al (2015) TGA and magnetization measurements for determination of composition and polymer conversion of magnetic hybrid particles. *Polym Adv Technol* 26:1199–1208. <https://doi.org/10.1002/pat.3562>
69. Maity D, Ding J (2011) Single step synthesis of hydrophobic and hydrophilic nanoparticles via thermal decomposition. *Int J Nanosci* 10:943–947. <https://doi.org/10.1142/S0219581X11008745>
70. Maity D, Zoppellaro G, Sedenkova V et al (2012) Surface design of core-shell superparamagnetic iron oxide nanoparticles drives record relaxivity values in functional MRI contrast agents. *Chem Commun* 48:11398. <https://doi.org/10.1039/c2cc35515a>
71. Tan YF, Chandrasekharan P, Maity D et al (2011) Multimodal tumor imaging by iron oxides and quantum dots formulated in poly (lactic acid)-d-alpha-tocopheryl polyethylene glycol 1000 succinate nanoparticles. *Biomaterials* 32:2969–2978. <https://doi.org/10.1016/j.biomaterials.2010.12.055>
72. Mi Y, Liu X, Zhao J et al (2012) Multimodality treatment of cancer with herceptin conjugated, thermomagnetic iron oxides and docetaxel loaded nanoparticles of biodegradable polymers. *Biomaterials* 33:7519–7529. <https://doi.org/10.1016/j.biomaterials.2012.06.100>
73. Prashant C, Dipak M, Yang CT et al (2010) Superparamagnetic iron oxide – loaded poly (lactic acid)-d-alpha-tocopherol polyethylene glycol 1000 succinate copolymer nanoparticles as MRI contrast agent. *Biomaterials* 31:5588–5597. <https://doi.org/10.1016/j.biomaterials.2010.03.070>
74. Maity D, Kale SN, Kaul-Ghanekar R et al (2009) Studies of magnetite nanoparticles synthesized by thermal decomposition of iron (III) acetylacetonate in tri(ethylene glycol). *J Magn Magn Mater* 321:3093–3098. <https://doi.org/10.1016/j.jmmm.2009.05.020>
75. Muthukumar T, Gnanaprakash G, Philip J (2012) Synthesis of stable magnetic Nanofluids of different particle sizes. *J Nanofluids* 1:85–92. <https://doi.org/10.1166/jon.2012.1006>
76. Kedar U, Phutane P, Shidhaye S, Kadam V (2010) Advances in polymeric micelles for drug delivery and tumor targeting. *Nanomed Nanotechnol Biol Med* 6:714–729. <https://doi.org/10.1016/j.nano.2010.05.005>
77. Maity D, Chandrasekharan P, Yang C-T et al (2010) Facile synthesis of water-stable magnetite nanoparticles for clinical MRI and magnetic hyperthermia applications. *Nanomedicine* 5:1571–1584. <https://doi.org/10.2217/nmm.10.77>
78. Kandasamy G, Sudame A, Luthra T et al (2018) Functionalized hydrophilic superparamagnetic Iron oxide nanoparticles for magnetic fluid hyperthermia application in liver Cancer treatment. *ACS Omega* 3:3991–4005. <https://doi.org/10.1021/acsomega.8b00207>

79. Maity D, Chandrasekharan P, Pradhan P et al (2011) Novel synthesis of superparamagnetic magnetite nanoclusters for biomedical applications. *J Mater Chem* 21:14717. <https://doi.org/10.1039/c1jm11982f>
80. Hayashi K, Nakamura M, Sakamoto W et al (2013) Superparamagnetic nanoparticle clusters for cancer theranostics combining magnetic resonance imaging and hyperthermia treatment. *Theranostics* 3:366–376. <https://doi.org/10.7150/thno.5860>
81. Thomas R, Park I-K, Jeong YY (2013) Magnetic iron oxide nanoparticles for multimodal imaging and therapy of cancer. *Int J Mol Sci* 14:15910–15930. <https://doi.org/10.3390/ijms140815910>
82. Baskar G, Ravi M, Panda JJ et al (2017) Efficacy of dipeptide-coated magnetic nanoparticles in lung Cancer models under pulsed electromagnetic field. *Cancer Investig* 0:1–12. <https://doi.org/10.1080/07357907.2017.1318894>
83. Lahiri BB, Muthukumaran T, Philip J (2016) Magnetic hyperthermia in phosphate coated iron oxide nanofluids. *J Magn Magn Mater* 407:101–113. <https://doi.org/10.1016/j.jmmm.2016.01.044>
84. Rodríguez-Luccioni HL, Latorre-Estevés M, Méndez-Vega J et al (2011) Enhanced reduction in cell viability by hyperthermia induced by magnetic nanoparticles. *Int J Nanomedicine* 6:373–380
85. Lemal P, Geers C, Rothen-Rutishauser B et al (2017) Measuring the heating power of magnetic nanoparticles: an overview of currently used methods. *Mater Today Proc* 4: S107–S117. <https://doi.org/10.1016/j.matpr.2017.09.175>
86. Blanco-Andujar C, Ortega D, Southern P et al (2015) High performance multi-core iron oxide nanoparticles for magnetic hyperthermia: microwave synthesis, and the role of core-to-core interactions. *Nanoscale* 7:1768–1775. <https://doi.org/10.1039/C4NR06239F>
87. Cervadoro A, Giverso C, Pande R et al (2013) Design maps for the Hyperthermic treatment of tumors with superparamagnetic nanoparticles. *PLoS One* 8:e57332. <https://doi.org/10.1371/journal.pone.0057332>
88. Gonzales-Weimuller M, Zeisberger M, Krishnan KM (2009) Size-dependant heating rates of iron oxide nanoparticles for magnetic fluid hyperthermia. *J Magn Magn Mater* 321:1947–1950. <https://doi.org/10.1016/j.jmmm.2008.12.017>
89. de la Presa P, Luengo Y, Multigner M et al (2012) Study of heating efficiency as a function of concentration, size, and applied field in γ -Fe₂O₃ nanoparticles. *J Phys Chem C* 116:25602–25610. <https://doi.org/10.1021/jp310771p>
90. Bakoglidis KD, Simeonidis K, Sakellari D et al (2012) Size-dependent mechanisms in AC magnetic hyperthermia response of iron-oxide nanoparticles. *IEEE Trans Magn* 48:1320–1323. <https://doi.org/10.1109/TMAG.2011.2173474>
91. Tong S, Quinto CA, Zhang L et al (2017) Size-dependent heating of magnetic Iron oxide nanoparticles. *ACS Nano* 11:6808–6816. <https://doi.org/10.1021/acsnano.7b01762>
92. Iacovita C, Florea A, Dudric R et al (2016) Small versus large iron oxidemagnetic nanoparticles: hyperthermia and cell uptake properties. *Molecules* 21:1–21. <https://doi.org/10.3390/molecules21101357>
93. Khandhar AP, Ferguson RM, Krishnan KM (2011) Monodispersed magnetite nanoparticles optimized for magnetic fluid hyperthermia: implications in biological systems. *J Appl Phys* 109:173–175. <https://doi.org/10.1063/1.3556948>
94. Patsula V, Moskvina M, Dutz S, Horák D (2016) Size-dependent magnetic properties of iron oxide nanoparticles. *J Phys Chem Solids* 88:24–30. <https://doi.org/10.1016/j.jpcs.2015.09.008>
95. Hugounenq P, Levy M, Alloyeau D et al (2012) Iron oxide monocrystalline Nanoflowers for highly efficient magnetic hyperthermia. *J Phys Chem C* 116:15702–15712. <https://doi.org/10.1021/jp3025478>
96. Lartigue L, Hugounenq P, Alloyeau D et al (2012) Cooperative organization in iron oxide multi-core nanoparticles potentiates their efficiency as heating mediators and MRI contrast agents. *ACS Nano* 6:10935–10949. <https://doi.org/10.1021/nn304477s>
97. Guardia P, Di Corato R, Lartigue L et al (2012) Water-soluble iron oxide nanocubes with high values of specific absorption rate for cancer cell hyperthermia treatment. *ACS Nano* 6:3080–3091. <https://doi.org/10.1021/nn2048137>

98. Martinez-Boubeta C, Simeonidis K, Makridis A et al (2013) Learning from nature to improve the heat generation of iron-oxide nanoparticles for magnetic hyperthermia applications. *Sci Rep* 3:1652
99. Lv Y, Yang Y, Fang J et al (2015) Size dependent magnetic hyperthermia of octahedral Fe₃O₄ nanoparticles. *RSC Adv* 5:76764–76771. <https://doi.org/10.1039/C5RA12558H>
100. Mohapatra J, Mitra A, Aslam M, Bahadur D (2015) Octahedral-shaped Fe₃O₄ nanoparticles with enhanced specific absorption rate and R2 Relaxivity. *IEEE Trans Magn* 51:3–6. <https://doi.org/10.1109/TMAG.2015.2439213>
101. Nemati Z, Alonso J, Martinez LM et al (2016) Enhanced magnetic hyperthermia in Iron oxide Nano-octopods: size and anisotropy effects. *J Phys Chem C* 120:8370–8379. <https://doi.org/10.1021/acs.jpcc.6b01426>
102. Das R, Alonso J, Nemati Porshokouh Z et al (2016) Tunable high aspect ratio Iron oxide Nanorods for enhanced hyperthermia. *J Phys Chem C* 120:10086–10093. <https://doi.org/10.1021/acs.jpcc.6b02006>
103. Nemati Z, Salili SM, Alonso J et al (2017) Superparamagnetic iron oxide nanodisks for hyperthermia therapy: does size matter? *J Alloys Compd* 714:709–714. <https://doi.org/10.1016/j.jallcom.2017.04.211>
104. Nemati Z, Alonso J, Rodrigo I et al (2018) Improving the heating efficiency of Iron oxide nanoparticles by tuning their shape and size. *J Phys Chem C* 122:2367–2381. <https://doi.org/10.1021/acs.jpcc.7b10528>
105. Regmi R, Black C, Sudakar C et al (2009) Effects of fatty acid surfactants on the magnetic and magnetohydrodynamic properties of ferrofluids. *J Appl Phys* 106:113902. <https://doi.org/10.1063/1.3259382>
106. Filippousi M, Angelakeris M, Katsikini M et al (2014) Surfactant effects on the structural and magnetic properties of Iron oxide nanoparticles. *J Phys Chem C* 118:16209–16217. <https://doi.org/10.1021/jp5037266>
107. Soares IP, Lochte F, Echeverria C et al (2015) Thermal and magnetic properties of iron oxide colloids: influence of surfactants. *Nanotechnology* 26:425704. <https://doi.org/10.1088/0957-4484/26/42/425704>
108. Liu XL, Fan HM, Yi JB et al (2012) Optimization of surface coating on Fe₃O₄ nanoparticles for high performance magnetic hyperthermia agents. *J Mater Chem* 22:8235. <https://doi.org/10.1039/c2jm30472d>
109. Mohammad F, Balaji G, Weber A et al (2010) Influence of gold Nanoshell on hyperthermia of super paramagnetic Iron oxide nanoparticles (SPIONs). *J Phys Chem C Nanomater Interfaces* 114:19194–19201. <https://doi.org/10.1021/jp105807r>
110. Barick KC, Hassan PA (2012) Glycine passivated Fe₃O₄ nanoparticles for thermal therapy. *J Colloid Interface Sci* 369:96–102. <https://doi.org/10.1016/j.jcis.2011.12.008>
111. Cheraghipour E, Javadpour S (2013) Cationic albumin-conjugated magnetite nanoparticles, novel candidate for hyperthermia cancer therapy. *Int J Hyperth* 29:511–519. <https://doi.org/10.3109/02656736.2013.803605>
112. Araújo-Neto RP, Silva-Freitas EL, Carvalho JF et al (2014) Monodisperse sodium oleate coated magnetite high susceptibility nanoparticles for hyperthermia applications. *J Magn Mater* 364:72–79. <https://doi.org/10.1016/j.jmmm.2014.04.001>
113. Darwish MSA, Stibor I (2016) Pentenoic acid-stabilized magnetic nanoparticles for nano-medicine applications. *J Dispers Sci Technol* 37:1793–1798. <https://doi.org/10.1080/01932691.2016.1140584>
114. Saeedi M, Vahidi O, Bonakdar S (2017) Synthesis and characterization of glycyrrhizic acid coated iron oxide nanoparticles for hyperthermia applications. *Mater Sci Eng C* 77:1060–1067. <https://doi.org/10.1016/j.msec.2017.04.015>
115. Kandasamy G, Sudame A, Bhati P et al (2018) Systematic magnetic fluid hyperthermia studies of carboxyl functionalized hydrophilic superparamagnetic iron oxide nanoparticles based ferrofluids. *J Colloid Interface Sci* 514:534–543. <https://doi.org/10.1016/j.jcis.2017.12.064>

116. Kandasamy G, Sudame A, Bhati P et al (2018) Systematic investigations on heating effects of carboxyl-amine functionalized superparamagnetic iron oxide nanoparticles (SPIONs) based ferrofluids for in vitro cancer hyperthermia therapy. *J Mol Liq* 256:224–237. <https://doi.org/10.1016/j.molliq.2018.02.029>
117. Kandasamy G, Sudame A, Maity D (2017) ATA and TA coated superparamagnetic iron oxide nanoparticles: promising candidates for magnetic hyperthermia therapy. *Adv Mater Lett* 8:873–877. <https://doi.org/10.5185/amlett.2017.1730>
118. Cruz MM, Ferreira LP, Ramos J et al (2017) Enhanced magnetic hyperthermia of CoFe_2O_4 and MnFe_2O_4 nanoparticles. *J Alloys Compd* 703:370–380. <https://doi.org/10.1016/j.jallcom.2017.01.297>
119. Phong PT, Phuc NX, Nam PH et al (2018) Size-controlled heating ability of CoFe_2O_4 nanoparticles for hyperthermia applications. *Phys B Condens Matter* 531:30–34. <https://doi.org/10.1016/j.physb.2017.12.010>
120. Psimadas D, Baldi G, Ravagli C et al (2014) Comparison of the magnetic, radiolabeling, hyperthermic and biodistribution properties of hybrid nanoparticles bearing CoFe_2O_4 and Fe_3O_4 metal cores. *Nanotechnology* 25:025101. <https://doi.org/10.1088/0957-4484/25/2/025101>
121. Lee J-H, Jang J-T, Choi J-S et al (2011) Exchange-coupled magnetic nanoparticles for efficient heat induction. *Nat Nanotechnol* 6:418–422. <https://doi.org/10.1038/nnano.2011.95>
122. Noh SH, Na W, Jang JT et al (2012) Nanoscale magnetism control via surface and exchange anisotropy for optimized ferrimagnetic hysteresis. *Nano Lett* 12:3716–3721. <https://doi.org/10.1021/nl301499u>
123. Robles J, Das R, Glassell M et al (2018) Exchange-coupled $\text{Fe}_3\text{O}_4/\text{CoFe}_2\text{O}_4$ nanoparticles for advanced magnetic hyperthermia. *AIP Adv* 8:056719. <https://doi.org/10.1063/1.5007249>
124. Angelakeris M, Li ZA, Hilgendorff M et al (2015) Enhanced biomedical heat-triggered carriers via nanomagnetism tuning in ferrite-based nanoparticles. *J Magn Magn Mater* 381:179–187. <https://doi.org/10.1016/j.jmmm.2014.12.069>
125. Bekovic M, Hamler A (2010) Determination of the heating effect of magnetic fluid in alternating magnetic field. *IEEE Trans Magn* 46:552–555. <https://doi.org/10.1109/TMAG.2009.2033944>
126. Jović Orsini N, Babić-Stojić B, Spasojević V et al (2018) Magnetic and power absorption measurements on iron oxide nanoparticles synthesized by thermal decomposition of $\text{Fe}(\text{acac})_3$. *J Magn Magn Mater* 449:286–296. <https://doi.org/10.1016/j.jmmm.2017.10.053>
127. Hemery G, Keyes AC, Garaio E et al (2017) Tuning sizes, morphologies, and magnetic properties of Monocore versus multicore Iron oxide nanoparticles through the controlled addition of water in the polyol synthesis. *Inorg Chem* 56:8232–8243. <https://doi.org/10.1021/acs.inorgchem.7b00956>
128. Cobianchi M, Guerrini A, Avolio M et al (2017) Experimental determination of the frequency and field dependence of specific loss power in magnetic fluid hyperthermia. *J Magn Magn Mater* 444:154–160. <https://doi.org/10.1016/j.jmmm.2017.08.014>
129. Verde EL, Landi GT, Carrião MS et al (2012) Field dependent transition to the non-linear regime in magnetic hyperthermia experiments: comparison between maghemite, copper, zinc, nickel and cobalt ferrite nanoparticles of similar sizes. *AIP Adv* 2. <https://doi.org/10.1063/1.4739533>
130. Kuraica MM, Iskrenović P, Perić M et al (2018) External magnetic field influence on magnetite and cobalt-ferrite nano-particles in ferrofluid. *Chem Pap* 72:1535–1542. <https://doi.org/10.1007/s11696-017-0380-8>
131. Andreu I, Natividad E, Solozábal L, Roubeau O (2015) Same magnetic nanoparticles, different heating behavior: influence of the arrangement and dispersive medium. *J Magn Magn Mater* 380:341–346. <https://doi.org/10.1016/j.jmmm.2014.10.114>
132. Piñeiro-Redondo Y, Bañobre-López M, Pardiñas-Blanco I et al (2011) The influence of colloidal parameters on the specific power absorption of PAA-coated magnetite nanoparticles. *Nanoscale Res Lett* 6:383. <https://doi.org/10.1186/1556-276X-6-383>

133. Ludwig R, Stapf M, Dutz S et al (2014) Structural properties of magnetic nanoparticles determine their heating behavior – an estimation of the in vivo heating potential. *Nanoscale Res Lett* 9:602. <https://doi.org/10.1186/1556-276X-9-602>
134. Cabrera D, Camarero J, Ortega D, Teran FJ (2015) Influence of the aggregation, concentration, and viscosity on the nanomagnetism of iron oxide nanoparticle colloids for magnetic hyperthermia. *J Nanopart Res* 17. <https://doi.org/10.1007/s11051-015-2921-9>
135. Etheridge ML, Hurlley KR, Zhang J et al (2014) Accounting for biological aggregation in heating and imaging of magnetic nanoparticles. *Technology* 02:214–228. <https://doi.org/10.1142/S2339547814500198>
136. Spizzo F, Sgarbossa P, Sieni E et al (2017) Synthesis of Ferrofluids made of Iron oxide Nanoflowers: interplay between carrier fluid and magnetic properties. *Nano* 7:373. <https://doi.org/10.3390/nano7110373>
137. Jadhav NV, Prasad AI, Kumar A et al (2013) Synthesis of oleic acid functionalized Fe₃O₄ magnetic nanoparticles and studying their interaction with tumor cells for potential hyperthermia applications. *Colloids Surf B Biointerfaces* 108:158–168. <https://doi.org/10.1016/j.colsurfb.2013.02.035>
138. Hemery G, Genevois C, Couillaud F et al (2017) Monocore vs. multicore magnetic iron oxide nanoparticles: uptake by glioblastoma cells and efficiency for magnetic hyperthermia. *Mol Syst Des Eng* 2:629–639. <https://doi.org/10.1039/C7ME00061H>
139. Zhang J, Dewilde AH, Chinn P et al (2011) Herceptin-directed nanoparticles activated by an alternating magnetic field selectively kill HER-2 positive human breast cells in vitro via hyperthermia. *Int J Hyperth* 27:682–697. <https://doi.org/10.3109/02656736.2011.609863>
140. Majeed J, Pradhan L, Ningthoujam RS et al (2014) Enhanced specific absorption rate in silanol functionalized Fe₃O₄ core-shell nanoparticles: study of Fe leaching in Fe₃O₄ and hyperthermia in L929 and HeLa cells. *Colloids Surf B Biointerfaces* 122:396–403. <https://doi.org/10.1016/j.colsurfb.2014.07.019>
141. Aljarrah K, Mhaidat NM, Al-Akhras M-AH et al (2012) Magnetic nanoparticles sensitize MCF-7 breast cancer cells to doxorubicin-induced apoptosis. *World J Surg Oncol* 10:62
142. Gilchrist RK, Medal R, Shorey WD et al (1957) Selective inductive heating of lymph nodes. *Ann Surg* 146:596–606. <https://doi.org/10.1097/00000658-195710000-00007>
143. Zhao Q, Wang L, Cheng R et al (2012) Magnetic nanoparticle-based hyperthermia for head & neck cancer in mouse models. *Theranostics* 2:113–121. <https://doi.org/10.7150/thno.3854>
144. Yi GQ, Gu B, Chen LK (2014) The safety and efficacy of magnetic nano-iron hyperthermia therapy on rat brain glioma. *Tumor Biol* 35:2445–2449. <https://doi.org/10.1007/s13277-013-1324-8>
145. Araya T, Kasahara N et al (2013) Antitumor effects of inductive hyperthermia using magnetic ferucarbotran nanoparticles on human lung cancer xenografts in nude mice. *Onco Targets Ther* 6:237. <https://doi.org/10.2147/OTT.S42815>
146. Spirou S, Costa Lima S, Bouziotis P et al (2018) Recommendations for in vitro and in vivo testing of magnetic nanoparticle hyperthermia combined with radiation therapy



Quantitative Methods for Investigating Dissociation of Fluorescently Labeled Lipids from Drug Delivery Liposomes

8

Rasmus Münter, Kasper Kristensen, Dennis Pedersbæk,
Thomas L. Andresen, Jens B. Simonsen, and Jannik B. Larsen

Contents

1	Definition of the Topic	334
2	Overview	334
3	Introduction	334
3.1	Liposomes as a Drug Delivery System	334
3.2	Tracking Liposomal Drug Delivery Systems	336
4	Experimental and Instrumentation Methodology	337
4.1	Liposome Preparation	337
4.2	Size Exclusion Chromatography Dissociation Assay	341
4.3	Single Liposome Dissociation Assay	347
4.4	Comparison Between the SEC and SLiD Methods	351
5	Review and Analysis of Key Research Findings	352
5.1	Lipid Exchange Is a Well-Known Phenomenon	352
5.2	Dissociation of Fluorescently Labeled Lipids	352
5.3	Dissociation of Polymer-Conjugated Lipids	353
5.4	Dissociation of Drug-Conjugated Lipids	354
5.5	Dissociation of Targeting-Ligand-Conjugated Lipids	354
5.6	Dissociation Trends: How to Predict Lipid Dissociation	354
6	Conclusions and Future Perspective	355
	References	356

R. Münter · K. Kristensen · D. Pedersbæk · T. L. Andresen · J. B. Simonsen · J. B. Larsen (✉)
Center for Nanomedicine and Theranostics, Technical University of Denmark, Lyngby, Denmark
Department of Health Technology (DTU Healthtech), Technical University of Denmark, Lyngby,
Denmark
e-mail: jannla@dtu.dk

1 Definition of the Topic

A key prerequisite for image-based research on nanocarriers for drug delivery is that the recorded fluorescence can be accurately assigned to originate from the nanocarrier in question. For liposomal nanocarriers, fluorescent labeling is typically achieved by labeling a minority of the lipid species making up the liposome. Early work determined that lipid species can transfer between membrane components within a solution, nevertheless the fluorescently labeled lipids (FLLs) of drug delivery liposomes are intrinsically assumed to stay associated with the liposome, even when placed in a biological environment. To efficiently test this assumption, routine methods capable of investigating the dissociation of FLLs from liposomes should be implemented. Here we present two experimental methodologies able to quantitatively characterize the degree of FLL dissociation from liposomes when subjected to human blood plasma, mimicking the biological environment experienced by the carrier when travelling in the human body. Routine implementation of such methodologies could facilitate the appropriate selection of FLLs displaying low liposome dissociation, hereby generating more reliable liposomal uptake and trafficking studies.

2 Overview

Liposomes are synthetic lipid vesicles, which hold great potential for use in drug delivery, with some formulations already in clinical use and many more being developed. It has long been known that lipids are able to exchange between liposomes and other circulating plasma components such as extracellular vesicles, lipoprotein particles, and proteins. For liposomes with special, low-abundance components, e.g., lipids conjugated to fluorophores, polymers, drugs, or tumor-targeting ligands, the dissociation could lead to severe alterations in liposome function. For fluorescently labeled lipids, a significant dissociation of these would hamper the ability of researchers to follow the trafficking and uptake of liposomes in tissues and cells, potentially leading to misinterpretation of the targeting abilities of liposomes. Despite these major implications of lipid dissociation, it is not routinely tested when new liposome formulations are developed. Here, we present two methods for studying dissociation of FLLs, based on either size exclusion chromatography or single liposome microscopy. While offering different degrees of detail and complexity, both can in a quantitative manner address whether FLLs incorporated into drug delivery liposomes dissociate from the liposomes during circulation.

3 Introduction

3.1 Liposomes as a Drug Delivery System

Synthetic lipid vesicles, also known as liposomes, are the most common nanoscale carrier used for medical applications [1]. Liposomal systems are primarily used for cancer therapy, but clinically approved liposome-based products are also used as

analgesics, viral vaccines, and for treating fungal diseases [2–5]. Liposomes consist of a phospholipid bilayer surrounding an aqueous lumen. Thus they can deliver both hydrophilic drugs, encapsulated into the lumen, and hydrophobic drugs, incorporated into the lipid bilayer [3, 5]. The major advantages of liposomal systems are their high degree of biocompatibility and the ability for delivery of encapsulated drug to target sites while minimizing the systemic drug exposure [1, 5, 6]. Also, liposomes offer a flexible delivery platform where the biochemical and physical properties can be easily modified by varying the individual components making up the liposome. Despite these attractive features, after 50 years of immense research in developing new and improved liposomal drug delivery systems, the amount that has made it to the clinic remains small [1, 7]. This highlights the need for rethinking all aspects of liposome drug delivery research [8, 9], including the routine implementation of methodologies like the ones presented here, facilitating fundamental characterization of liposome properties.

In many treatment applications, liposomes are not actively directed towards the disease site [10]. In cancer therapy, the accumulation of liposomes in the tumor tissue is often discussed in the context of a phenomenon known as the Enhanced Permeability and Retention (EPR) effect [11]. This effect occurs as the vasculature around tumors is more leaky than regular blood vessels, which results in the liposomes extravasating from the blood vessels into the interstitium and into the tumor. Furthermore, tumors usually lack effective lymphatic drainage, meaning that the liposomes are retained in the tumor. The EPR effect is potentially experienced for macromolecules larger than 40 kDa as these are not subject to renal clearance, and it has been found that nanoparticles in a size range from 20 to 150 nm are optimal for exploiting the EPR effect [12]. Encapsulation of small-molecule drugs into long-circulating liposomes can thus potentially enhance the tumor delivery significantly compared to free drugs, which are typically nonspecifically distributed throughout the body, causing both side effects and reduced efficiency [5, 13]. To exploit the EPR effect, liposomes need to avoid the body's natural clearance machinery and for this purpose, liposomes are often coated with the hydrophilic polymer Polyethylene Glycol (PEG) [14]. Doing this, researchers achieve what is known as “stealth” liposomes, such as the benchmark formulation Doxil, representing the first FDA approved liposome formulation used in cancer treatment [15, 16].

Compared to the nonspecific targeting, potentially facilitated by the EPR effect, attempts to design liposomes that are actively targeting tumors have been a focus in the field of nanomedicine for more than 50 years [5]. This includes coating the liposomes with ligands or antibodies that will recognize the tumor target cell population [17, 18]. For example, solid tumors in breast, colorectal, ovary, and prostate cancers often overexpress epidermal growth factor receptors (EGFR), and stealth liposomes can be targeted to these tumors by conjugating antibody fragments against these receptors to the end of the PEG chains [19]. Small non-peptide ligands such as folate, a vitamin critical for DNA synthesis, have also been used to deliver paclitaxel-loaded liposomes into tumor cells, as the folate receptor is often overexpressed in tumors, but only weakly expressed in healthy tissue [20]. Despite these efforts, no liposomal system actively targeting cancer cells has yet reached the clinic.

3.2 Tracking Liposomal Drug Delivery Systems

Studies on the ability of liposomes to cross biological barriers, traffic to their target cell destination, and reach intracellular compartments are often based on microscopy or flow cytometry, where the liposomes are tracked using fluorescent labels [21]. These fluorescent labels, which are commercially available from several well-established manufacturers, are typically based on fluorophores linked to a lipid anchor. These constructs are then incorporated into the membrane of the liposomes. Liposomal carriers in general, and “stealth” liposomes containing PEG coating in particular, are considered very stable and assumed to stay intact during circulation [15, 16]. This has led to the intrinsic assumption that the FLLs used to label liposomes stay associated to the liposomes throughout the duration of an uptake or localization experiment. However, several studies have indicated that lipids can exchange between liposomes and plasma components [22, 23] even when the liposomes are PEGylated [24–26]. Such potential FLL dissociation could lead to both false negatives and false positives in uptake experiments [27]. Thus, as recently demonstrated [28], it is of great importance to address the dissociation of FLLs incorporated into liposomes in order to facilitate better and more reliable development of liposomal drug delivery systems.

In this chapter, we first describe the currently used methods for preparing FLL containing liposomes and the methodology employed for evaluating their basic physicochemical properties. Next we present two methods that allow for direct quantification of FLL dissociation from liposomes in blood plasma, thus mimicking the potential FLL dissociation in a drug delivery scenario. Using these methods to study the stability of a formulation before initiating *in vivo* studies on liposomal distribution and targeting, will allow researchers to determine if they can trust the results from their biological uptake and localization experiments.

The first method is a Size Exclusion Chromatography (SEC) assay, which is relative simple, requires a minimal amount of specialized equipment and offers a very direct quantification. The second method is a Single Liposome Dissociation (SLiD) Assay, based on quantitative microscopy. Compared to the SEC method, it allows for a more in-depth and sensitive evaluation of the dissociation process, addressing whether the dissociation happens uniformly from the whole population of liposomes or only from a minority. The main drawback of the SLiD method is the required access to advanced microscopes.

It must be stressed that both methods can in principle be used to study any lipid labeled with a fluorescent tracer, thus making them applicable to study dissociation of many types of lipid constructs, e.g., conjugated to polymers, drugs, proteins, etc. Several lipid constructs often used in liposomes for drug delivery, e.g., PEGylated lipids, are commercially available with fluorescent labels. Alternatively, many constructs can be acquired biotinylated, which can then be labeled indirectly using streptavidin-linked fluorophores. Finally, if working with peptides or proteins (such as targeting antibodies), the dissociation of the protein construct can be studied by labeling the protein directly using one of the many kits on the market for covalent fluorophore labeling.

4 Experimental and Instrumentation Methodology

4.1 Liposome Preparation

4.1.1 Background

There are several key factors to take into account during the design of the liposome formulation. First, choosing lipids with different characteristics will influence the transition temperature of the formed lipid bilayer [29]. The transition temperature is a collective property of the membrane, below which the bilayer will be in solid ordered or gel phase and above which the bilayer will be in a more disordered liquid phase. This fluidity of the bilayer is determined by the length and saturation of the fatty acid lipid tails as well as the structure of their head group. Long, saturated fatty acid tails promote high transition temperatures, while short, unsaturated tails promote low transition temperatures. Figuratively, the lipid bilayer of the liposomes in a gel phase will have a solid morphology similar to butter, while the disordered liquid phase will have morphology similar to oil. It is well known that membrane fluidity is strongly modulating how leaky the liposomes are with respect to encapsulated compounds [30]. Accordingly, tuning membrane fluidity to ensure stable encapsulation while still facilitating efficient drug release on cue is a topic of immense research.

Liposomes usually consist of a combination of two, three, or more different lipids. A typical constituent of drug delivery liposomes is 20–40% cholesterol, shown to modify membrane rigidity and lower the interaction between the liposome and serum components, leading to prolonged circulation [15]. While the head group of many phospholipids are zwitterions, lipids with anionic or cationic head groups are often included in liposome formulations. These charged lipids can endow liposomes with certain functions, e.g., cationic lipids can enhance delivery into cells [31]. Finally, liposomes for drug delivery are often functionalized with synthetic lipids, where a lipid anchor is chemically conjugated to, e.g., a polymer, peptide, fluorophore, or targeting ligand.

4.1.2 Materials and Instrumentation Needed

- Freeze dryer
- Tert-butanol
- Lipids, e.g., HSPC, Cholesterol and DSPE-PEG2000 in powder forms.
- Fluorescently labeled lipids, e.g., Carbocyanine dyes (DiO, DiI, DiD, etc.), Rhodamine-labeled lipids, Atto-labeled lipids.
- Mini extrusion kit (Avanti Polar Lipids)
- Polycarbonate filters and support filters (Whatman)
- Buffer, e.g., 10 mM HEPES, 137 mM NaCl, pH 7.4.

4.1.3 Procedure

For preparing liposomes, we typically use a standard protocol relying on lyophilized lipid mixtures. First we discuss this protocol in detail, before we introduce other preparations methods that are also routinely used [32]. The lyophilization methodology suggested is most applicable to lab-scale production of liposome suspensions, that is, either for *in vitro* experiments (where 1 mL or less will usually be enough) or

in vivo studies in mice (where 5–10 mL will be sufficient for a study). For large-scale production of liposomes, which is often based on modified versions of ethanol injection and requires specialized equipment, excellent reviews exist [32, 33].

Preparing Lipid Powder Mixtures

1. Lipids are acquired in powder forms and stored at $-20\text{ }^{\circ}\text{C}$.
2. Bring the lipids to room temperature.
3. Mix tert-butanol (tBut) with MilliQ (MQ) or distilled water to a final ratio of tBut:MQ 9:1. Pure tBut has a freezing point at $25.5\text{ }^{\circ}\text{C}$ and is thus a solid at room temperature, but upon adding the water, it will become liquid. It may be beneficial to heat the tBut container, in order to speed up the melting process upon addition of MQ.
4. Weigh lipids and dilute them in the tBut:MQ mixture to a final concentration of 10–50 mM. The exact concentration should be adjusted for the purpose. For preparing very small volumes or very dilute formulations of liposomes, lipid stocks should be more dilute for making pipetting easier and more accurate. Likewise, lipids that only make out a small proportion of the total lipid composition, e.g., FLLs, should be more dilute.
5. Make sure lipids are completely dissolved by heating, magnet stirring and if necessary sonication. Saturated lipids and cholesterol may be heated for complete solvation.
6. Mix the lipid stocks in glass vials to the final lipid ratio required for the formulation.
7. An important parameter when formulating FLL-containing liposomes is choosing the appropriate amount of FLL, since a too high or too low FLL content can severely affect liposome performance. At a molar ratio of 0.1%, a 100 nm liposome can be estimated to contain ~ 100 labels per liposome, depending on the exact lipid types used. Going lower than this might mean that the liposomes are not sufficiently bright for doing, e.g., flow cytometry. Also, if the amount of labeled lipids becomes too low, the inhomogeneity between individual liposomes in the amount of incorporated labeled lipids can lead to significant liposome to liposome variations in their fluorescence output, adding unwanted noise to the read-out [34]. On the other hand, if the FLL concentration is high, liposome properties might get compromised, e.g., if using an FLL with a charged fluorophore, or with a lipid anchor with a structure different from the remaining lipids. Furthermore, at high concentrations where fluorophores are packed closely together, the fluorophores might self-quench in the membrane. We thus recommend to keep the labeling between 0.5% and 0.05% molar ratio.
8. Make sure that the lipids are properly mixed, e.g., by heating and vortexing.
9. Snap-freeze the glass vial in liquid nitrogen until the solvent is completely frozen.
10. Put lid on the vial, but do not tighten completely to allow the solvent to escape from the vial during freeze drying.
11. Transfer the vials to a freeze dryer for overnight treatment. We have successfully used an Epsilon 2–4 LSCplus Freeze dryer (Martin Christ) running at 0.5 mBar and $-20\text{ }^{\circ}\text{C}$.

Hydrating Lipid Powder Mixtures

1. Remove the vials with the dried lipid samples from the freeze-dryer and equilibrate to room temperature.
2. Add buffer of choice reaching the desired lipid concentration. In general, lipid concentrations above 50 mM will be problematic to handle in the downstream procedures.
3. Heat the above phase transition temperature of the lipids and stir with magnet for 1–2 h. Avoid longer incubations, as the heating will accelerate hydrolysis of the lipids [35].
4. Excessive vortexing of PEGylated formulations are discouraged, as they according to our experience tend to form a foam.

Controlling Lamellarity

Upon hydration, liposomes may often come out as multilamellar rather than unilamellar, meaning that several bilayers are stacked per liposome, resembling the layers of an onion. Unilamellar liposomes can, however, be achieved by exposing them to freeze-thaw cycles, where the vial with the liposome suspension is frozen in liquid nitrogen and thawed in a heating bath [36, 37]. Such cycles can also improve encapsulation of drugs [38, 39]. Typically, samples are exposed to around 10 of such cycles, but recent literature has suggested that an annealing step, where the liposomes are stored at $-1.4\text{ }^{\circ}\text{C}$ or $-22\text{ }^{\circ}\text{C}$ for 16 h, will allow only one such cycle to achieve maximum encapsulation [40].

Controlling Size

While liposomal structures form spontaneously when the lipid film is hydrated, it will usually result in a very polydisperse population: While sizes may vary from 25 nm up to several micrometers [41], PEGylated formulations tend to spontaneously form particles with a size around 500 nm [42]. For drug delivery purposes, a size range from 20 to 150 nm is optimal [12], so formulations are typically downsized to 100–150 nm by extrusion. Employing the mini extrusion kit from Avanti Polar Lipids, the liposome formulation is passed several times from one syringe to another, through a holder fitted with a porous polycarbonate membrane. The membranes come in sizes with pores of, e.g., 50, 100, 200 nm, etc. Since we wish an average liposome size around 100 nm, we typically pass the liposome solution 11 times through a 100 nm membrane, giving us a fairly monodisperse population of liposomes with a size around 120 nm.

Syringes for the mini extrusion kits come in 250 μL or 1 mL volumes. While larger volumes can of course be divided into several portions that are extruded separately, 3–10 mL batches of liposomes are preferably extruded using a LIPEX thermobarrel extruder from Evonik. Using a nitrogen bottle, the liposome mixture is extruded under high pressure (up to 58.6 bar) through a polycarbonate membrane similar to those used for the mini extrusion kit. While these high-pressure kits, that comes for volumes up to 800 mL, are uni-directional, the same liposome suspension can be passed several times through the same filter to improve the PDI.

An alternative to extrusion is sonication. The size of sonicated liposomes will be dependent on the time and power of the sonication, and may vary for specific liposome formulations. It has, e.g., been shown that cholesterol content affects the size of sonicated liposomes, something that is not experienced for extruded liposomes [43]. The most precise and reproducible method for producing monodisperse liposome formulations on lab scale is thus extrusion techniques [32].

Preparing Liposomes by Other Methods

If a freeze-dryer is not available, a popular lipid-mixture preparation method is based on chloroform evaporation. Instead of tert-butanol, lipids are dissolved in a chloroform:methanol (9:1) solution, which is evaporated under flow of an inert gas such as argon or nitrogen. To make sure that all organic solvent has been evaporated, the vial with the lipid mixture is kept at vacuum overnight. While being a very simple method, this method is often sought avoided due to the potential health risks of working with chloroform.

Another method employed for preparing liposomes is ethanol injection [44]. In this method, the lipids are dissolved in ethanol and mixed, but without evaporating the organic solvent. Instead, the lipid mixture is slowly added to an aqueous buffer, e.g., using a syringe pump. After this, the ethanol is evaporated. Despite being very fast and easy to perform, the maximum lipid concentration achievable using this method is relatively low, both due to the maximum solubility of most lipids in ethanol being lower than in other organic solvents, but also because the maximum concentration of ethanol in the water/ethanol mixture needs to be very low [44].

Finally, liposomes can be produced by forming mixed micelles of detergent and phospholipids in aqueous buffers [45–48]. The detergent is removed using dialysis or BioBeads, and the phospholipids eventually form liposomes when the detergent is removed. This method is heavily used if liposomes need to incorporate biological material in the membrane, such as transmembrane proteins [47, 49], but is less used for mass producing drug delivery liposomes.

Determining the Size and Zeta Potential of Liposomes

The gold standard for determining the size of nanoparticle formulations is Dynamic Light Scattering [50]. Briefly, the sample is exposed to a monochromatic light source, typically a laser and the light scattering is measured. The temporal fluctuations of the light scattering are analyzed to calculate the size of the particles by assuming Brownian motion: large slow-moving particles will cause slow fluctuations in the scattered light, while small fast-moving particles will cause fast fluctuations.

Alternatives to DLS include Nanoparticle Tracking Analysis (NTA) and Fluorescence Correlation Spectroscopy (FCS). Also, particle size can be deduced using electron microscopy techniques such as Transmission Electron Microscopy (TEM) and Scanning Electron Microscopy (SEM), although these are hampered by lower statistics and the need for very elaborate and potential detrimental sample preparation.

The zeta potential of liposomes is the apparent surface charge [51]. It is usually measured using light scattering techniques in a setup where the particles move in an electric field. Classically, Laser Doppler Electrophoresis is used, where a red- or blue-shift in the scattered light can be used to determine the direction of the particle

movement. Higher precision, especially for particles with a zeta potential close to zero in high-salt buffer, can however be achieved with Phase Analysis Light Scattering techniques (PALS), or developments hereof.

Determining the Lipid Concentration

An important aspect of liposome preparation is to measure the final lipid concentration in the liposome suspension. Usually there will be a loss of lipids during extrusion as the lipids may adsorb to the filters, resulting in a final concentration around 20% lower than the starting concentration.

In our lab, we use Inductively Coupled Plasma Mass Spectrometry (ICP-MS) to measure the concentration of phosphorus in samples, thereby measuring the phospholipid concentration. Be aware that if dilute liposome formulations are prepared in phosphate buffers, there will be a significant background contribution to the total phosphorus signal measured. This imposes some uncertainty to the measured phospholipid concentration, so we often employ HEPES buffers for lipid rehydration rather than PBS.

Another popular method is High Performance Liquid Chromatography (HPLC) coupled to an Evaporative Light Scattering Detector (ELSD) [52–54]. The strength of the HPLC-ELSD method is that it allows the user to monitor the loss of single lipid species (e.g., in the extrusion step) by choosing an appropriate HPLC column and gradient. This may be beneficial if, e.g., charged lipids or PEGylated lipids are incorporated into the formulation.

The phospholipid concentration can also be estimated using a chemical approach followed by a colorimetric readout as this does not require any specialized equipment. In the Stewart assay, phospholipids are complexed with ammonium ferrothiocyanate, which absorbs at 485 nm. By comparing the absorbance, measured on a spectrophotometer, to that of a known standard, the phospholipid concentration can be calculated [55]. In the Bartlett assay, the phosphate groups are converted into inorganic phosphate by treatment with perchloric acid before running the colorimetric assay [56]. Researchers choosing to perform the Bartlett assay should thus be aware that this procedure, like the ICP-MS approach, could be compromised by a high background signal if the liposomes are rehydrated in phosphate buffers.

4.2 Size Exclusion Chromatography Dissociation Assay

4.2.1 Background

Size Exclusion Chromatography (SEC) separates molecules according to differences in size, as they pass through a SEC matrix packed into a column. The medium used for SEC consists of inert and chemically stable spherical porous beads. The pores, as well as the space between the beads, are filled with buffer, and the separation is usually carried out isocratically (i.e., not changing the composition of the elution buffer throughout the process).

When a sample is applied to the column, large components will run past the beads with the buffer flow directly through the column and hence elute first in what is known as the void volume. Smaller molecules enter the porous beads and thus be retarded as the

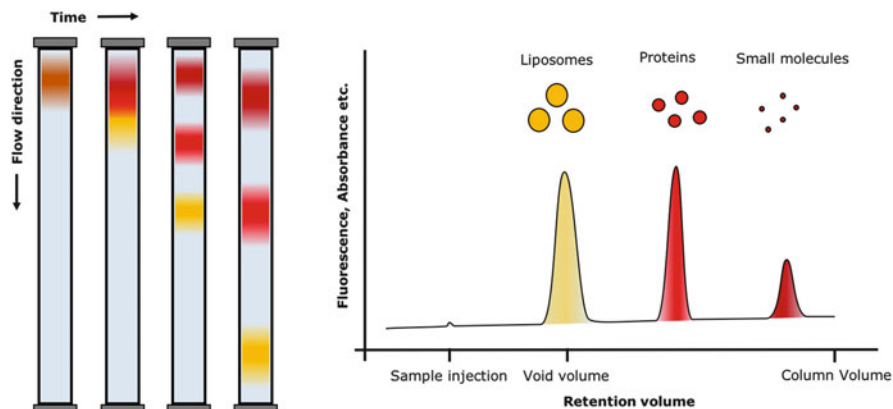


Fig. 8.1 When a sample is added to a SEC column, large particles (yellow) will run directly through the matrix and elute from the column in the void. Smaller particles (red) will be retarded as they pass through the porous material, meaning that they elute later

sample passes through the matrix. In other words, smaller molecules will have a longer path through the porous material and thus be retained in the column. Consequently, smaller molecules will elute later from the column, as displayed in Fig. 8.1.

There is a large selection of SEC matrices available on the market with different fractionation ranges; that is, the size range of the molecules they are able to separate from each other. Some matrices are optimal for separating proteins from small molecules and to perform salt exchange, while other matrices are better suited for separating large proteins from small proteins. For measuring dissociation of lipid conjugates from liposomes in biological environments, we are interested in matrices that are able to separate the liposomes from even the largest proteins as well as from naturally occurring nanoparticles such as the most abundant lipoproteins including high-density (HDL) and low-density (LDL) lipoproteins [57]. The larger, but less abundant, plasma components such as very low-density lipoproteins (VLDL), chylomicrons, and extracellular vesicles (exosomes), however, have sizes similar to typical drug delivery liposomes [58], therefore these cannot be separated from liposomes by size-dependent techniques.

4.2.2 Materials and Instrumentation

- Blood sample vials and blood sampling kit (e.g., BD Vacutainer).
- Buffer, e.g., 10 mM HEPES, 137 mM NaCl, pH 7.4.
- Black flat-bottom 96-well plates.
- Centrifuge for microcentrifuge tubes.

Additional materials needed for the protocol are discussed in detail below.

Size Exclusion Chromatography Column

- Columns can be acquired pre-packed, or the SEC matrix can be acquired as slurry or powder for packing an empty column. Columns furthermore come in several

lengths. Long columns give a better separation but also requires more time to run. We typically use 20 cm EconoColumn columns from BioRad or C10/20 columns from GE Healthcare – both packed inhouse.

- Choosing the right matrix: For separating liposomes from plasma components, we use a Sepharose CL-4B matrix. This matrix gives a neat separation of liposomes from proteins [59]. If it is of interest to investigate which plasma components the dissociated lipids associate with, a column that gives a better separation of plasma proteins and HDL particles, e.g., Superdex 200 Increase, can be recommended. Using a column with a lower fractionation range is, however, also at the expense of achieving a good separation of the liposomes from the plasma components.

System to Run the Chromatography

- A wide selection of both specialized automated systems and simpler manual setups are available on the market.
- In our group, we typically use an automated LC-20 AD setup from Shimadzu, equipped with a DGU-20A SR degassing unit and a SIL-20 AC HT autosampler.
- Alternatively, we use a Masterflex peristaltic pump from Cole-Palmer with appropriate tubing and a retort stand for holding the column.
- An essential part of the protocol is the ability to collect fractions after they have passed through the column. For our automated Shimadzu setup, we have a FRC-10A fraction collector coupled to our instrument. When using the manual setup, fractions are collected by hand in microcentrifuge tubes.

Protein LoBind Tubes

The Protein LoBind tubes have the same dimensions as the regular 1.5 or 2 mL Eppendorf microcentrifuge tubes but are designed to prevent absorption of proteins to the plastic surface, thus reducing the loss of proteins in the handling steps.

Plate Reader

A plate reader setup is employed to measure fluorescence intensity at specified wavelengths. We use a TECAN Spark microplate reader and transfer our samples into black flat-bottomed 96-well plates.

Liposomes

Liposomes prepared by any of the methods previously described containing FLLs.

4.2.3 Extraction of Plasma and Liposome Incubation

The plasma should preferably be freshly prepared from newly drawn blood samples, as described below. This also necessitates the use of blood drawing kit and blood sampling tubes (we use a Vacuette SAFETY Blood collection set and collect the blood in BD Vacutainer EDTA tubes), as well as staff trained in drawing blood samples. Alternatively, plasma and serum can be acquired from several large suppliers.

1. Collect blood in Vacutainer EDTA tubes.
2. Transfer the blood to Protein LoBind tubes.
3. Centrifuge at 3000 g for 15 min in order to separate cells from plasma.
4. Acquire the plasma supernatant carefully, transfer to fresh protein LoBind tubes, and use as quickly as possible, preferably within 24 h. Plasma can be stored at 4 °C for up to 5 days or at −18 °C for 1 year [60].
5. Add liposomes to the plasma in the amount necessary to reach the wanted final concentration.
 - (a) Concentration: To perform the FLL dissociation study in an environment close to the *in vivo* scenario one needs to consider at which concentration the liposome should be incubated in plasma. The concentration range can vary, depending on whether the researcher attempts to mimic a human or murine *in vivo* scenario. We typically perform our incubations around 2 mM.
 - (b) Sample size: In order to achieve a high resolution (good separation) from the SEC column, a small sample size is recommended by the supplier, not higher than 4% of the total column volume. For a 10 mm/20 cm column, the sample volume should thus be kept below approx. 500 µL. However, reducing the sample volume will also lead to decreased signal-to-noise ratio, when reading the sample fluorescence in step 12. Furthermore, based on supplier recommendation, the SEC resolution is not further increased when going below 0.5% of the total column volume. A sample size around 200–300 µL has proved quite successful in our lab for the 10 mm/20 cm column.
 - (c) Also prepare control samples where the same liposome concentration used in the plasma experiment is prepared in a buffer such as PBS or HEPES. The buffer should be the same as the one in which the liposomes have been prepared or as a minimum match the osmolarity of that buffer. These controls will show if FLL dissociation is happening in the buffer environment, and if the samples contain FLL micelles or unconjugated fluorophore. Furthermore, it will allow for determining the void fractions of the column, and thus help in determining which fractions contain the liposome-associated fluorophores, and which contain the dissociated fluorophores.
 - (d) Finally, include a plasma blank, where liposomes without the fluorescent label are added to the plasma. Although this contribution is typically minimal, this control will allow the adjustment for intrinsic plasma protein fluorescence background.
6. Incubate at 37 °C under shaking or rotation. This type of incubation can to some degree mimic the *in vivo* conditions, although it will not give rise to the exact same mechanical stress. In order for the experiment to be relevant, the incubation time should reflect the expected circulation half-life of the liposomes. For typical stealth liposomes, the incubation time should thus be around 24 h or more (circulation half-lives up to 65 h are reported for PEGylated liposomes) [15]. For targeted formulations, the incubation time can probably be decreased. Alternatively, a time-course study can be done, following the dissociation kinetics of the FLL.

4.2.4 Running the Column

1. Equilibrate the column in a buffer such as PBS or HEPES. Optimally, use the same elution buffer as the buffer used to prepare the samples in step 4.2.3.5.
2. Add the sample to the column. See step 4.2.3.5.b for volume considerations.
3. Collect 1 mL fractions in Protein LoBind tubes for the entire run, at least until a complete volume exchange of the SEC column.
4. Make sure that everything has eluted and that the column is properly rinsed, before adding the next sample.

4.2.5 Analysis of Fractions

1. Transfer equal volumes of each fraction to all wells in the 96-well plate, at least 75 μ L in order to cover the bottom of the well.
2. Read fluorescence intensity on a plate reader. Use emission and excitation wavelengths relevant for the fluorophore label used to track the lipid conjugate. If doing many SEC runs, resulting in the samples being divided into several microwell plates, make sure to use the same gain settings for all plates. If a plate-reader is not available, the analysis can also be done using, e.g., a cuvette-based fluorometer or instrumentation such as a NanoDrop spectrofluorometer (ThermoFisher Scientific). However, we would recommend a microplate reader for high-throughput analysis.
3. Use the fractions from SEC with unlabeled liposomes to subtract the background fluorescence from both the plasma runs and the buffer control runs.
4. Plasma proteins can be followed by measuring the tryptophan fluorescence at 280 nm excitation, 350 nm emission.

To support the findings from the fluorescence intensity measurement, it can be worthwhile to measure the optical density, as absorption is less sensitive to environmental changes than fluorescence. However, this should also include proper controls for background subtraction at the measured wavelength to compensate for the scattering from the liposomes and other plasma components, as well as light absorption by plasma proteins. A detailed description of this subtraction of background absorbance can be found in recently published work [28].

For non-fluorescent samples, other methods can be used to analyze the concentration of a given compound in a sample. Inductively Coupled Plasma Mass Spectrometry (ICP-MS) can be used to follow, e.g., elution of platinum-based drugs, High Performance Liquid Chromatography (HPLC) or Liquid Chromatography Mass Spectrometry (LC-MS) can be used to measure elution of UV active compounds, given that no other plasma components elute from the selected HPLC column simultaneously with the analyte. Moreover, leakage of nonlipid compounds, such as encapsulated drugs, can be detected using similar methodologies.

4.2.6 Calculating FLL Dissociation from Liposomes

Figure 8.2 is an example of an elution profile of fluorescently labeled liposomes after incubation in plasma.

The amount of lipid dissociation can be calculated using two different methods:

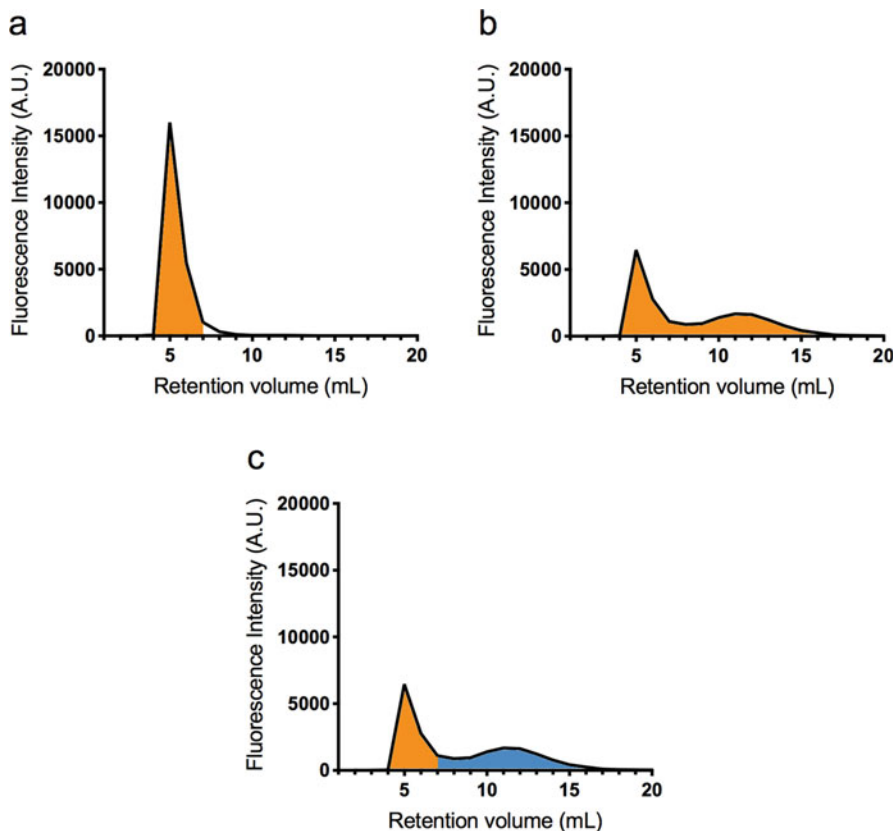


Fig. 8.2 Typical elution profiles of liposomes formulated with fluorescently labeled lipid after incubation in (a) buffer, and (b, c) plasma, determined from the fluorescence intensity of the label in each fraction collected. The area under the curve is integrated to determine the amount of fluorescent label. A_{VB} is the area of the void volume in buffer, A_{Tot} is the area of the total elution volume of the fluorescent label in plasma, A_{VP} is the area of the void volume in plasma and A_{DP} is the area of the dissociated fluorescent label in plasma

Method 1: Total Profile

The “total profile” method uses the entire profile of the single run in plasma. The area of the elution profile with FLLs co-eluting with the liposomes, that is, the area of the void peak A_{VP} , can be used to determine the percentage of FLLs still being associated to the liposomes, using the following equation:

$$D(\%) = \left(1 - \frac{A_{VP}}{A_{Tot}} \right) * 100\%$$

The areas, A_{VP} and A_{Tot} , is defined in Fig. 8.2.

Method 2: Void Method

The void method is based on comparing the fluorescence intensity of the void fractions for a liposome in buffer (A_{VB}) to the fluorescence intensity of the same fractions for a liposome incubated in plasma (A_{VP}). The extent of dissociation is calculated from the decrease in area of the void peak.

$$D(\%) = \left(1 - \frac{A_{VP}}{A_{VB}}\right) * 100\%$$

Pros and Cons of the Total Method and the Void Method

A benefit of the total profile method is that the calculations are made from one single run, minimizing uncertainty from sample variation. Furthermore, the total method doesn't only rely on the loss of fluorescence emission in the void fractions, but also on the increase of fluorescence in the fractions with leaked FLLs. Thus, compared to the void method, the total method is not as sensitive to changes in the fluorescent properties of the liposome-associated FLLs in plasma versus in buffer, e.g., due to quenching of fluorescence by plasma components.

It is important to keep in mind, though, that the fluorescence properties of the label could change when the lipid is transferred from the liposome to the plasma proteins. The fluorescence intensity could, e.g., increase due to reduced self-quenching when lipids are no longer packed closely together in the liposomal membrane. This would result in an overestimation of the dissociation. Alternatively, the altered environment experienced by the FLL when being complexed to a plasma protein could lead to either a fluorescence increase or decrease. Such environmental dependent changes in fluorescence intensity can be monitored by comparing the area of the total elution volume of the fluorescent label in both plasma and buffer. If the values are the same, it is unlikely that changes in fluorescence intensity are affecting the measurements.

For the void method, two different samples are compared, thus the calculation is more sensitive to sample variations as this could impose noise in the data. A benefit of the void method is that only the void fractions need to be analyzed. The number of samples to be examined for lipid content can hence be reduced, which is especially important if choosing another nonfluorescent and more time-consuming analysis method (e.g., ICP-MS, HPLC or LC-MS, as mentioned above).

4.3 Single Liposome Dissociation Assay

4.3.1 Background

The underlying concept of the Single Liposome Dissociation (SLiD) assay is based on previously published methodologies [34, 61] for imaging single liposomes using fluorescence microscopy and is here adopted to quantify the dissociation of FLL from liposomes. In the SLiD assay individual liposomes are immobilized on a passivated glass surface through streptavidin-biotin coupling (Fig. 8.3a). This ensures that the same liposomes can be followed over time and accurately imaged

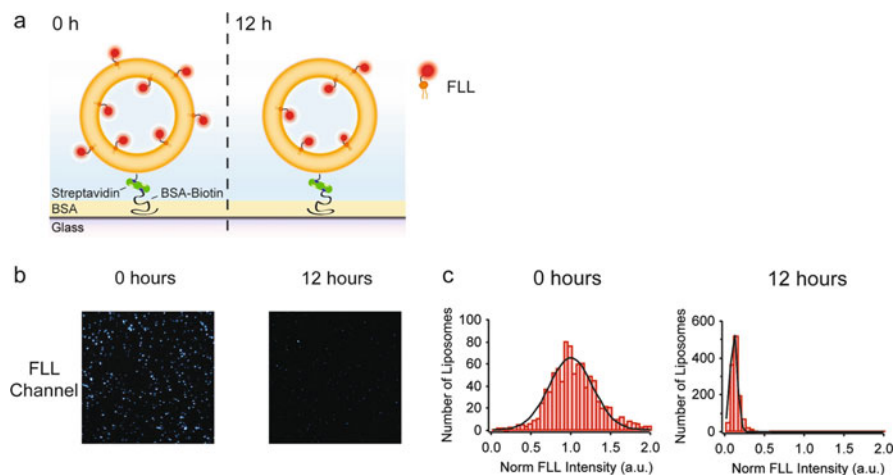


Fig. 8.3 SLiD assay for FLL liposome dissociation studies at the single liposome level **(a)** Scheme depicting the sandwich build up (BSA:BSA-Biotin and Strep) enabling immobilization of individual liposomes. Liposomes depicting FLL dissociation after 0 h (left) and 12 h (right) incubation in blood plasma. **(b)** Example of typical micrographs of the FLL channel displaying the FLL intensity on individual liposomes after 0 h (left) and 12 h (right) incubation in blood plasma. **(c)** Quantitative data analysis plotting a histogram of normalized integrated FLL intensities for individual liposomes after 0 h (left) and 12 h (right) incubation in blood plasma, revealing the overall decreased FLL intensity indicative of FLL liposome dissociation

using confocal/Total Internal Reflection Fluorescence (TIRF) microscopy. Then data analysis software is used to extract the integrated intensity of individual liposomes, allowing for a quantitative assessment of FLL dissociation.

The single liposome nature of the SLiD assay allows for direct visual inspection of the lipid dissociation process as it happens over time and can address intra-sample heterogeneities in the FLL dissociation behavior [34, 62]. Such heterogeneities are accessible because the SLiD assays measures individual liposomes meaning that the FLL dissociation process can be elucidated in more detail than with bulk techniques, which can only report a single average value [63, 64]. The SLiD assay can detect if dissociation only occurs from a subset of liposomes, e.g., if there is a difference in the FLL dissociation propensity between small and large liposomes. Also, the dissociation pathway can be studied in depth, tracking if dissociation happens in a graded or in an all-at-once scenario. Furthermore, if the microscope setup allows for it, measurement can be performed at the physiological temperature and it does not need to involve any washing of the sample. Finally, the material consumption in the SLiD assay can be extremely low, making it suitable for screening of expensive formulations and compounds.

4.3.2 Materials and Instrumentation

- Bovine Serum Albumin (BSA)
- Biotinylated BSA (BSA-Biotin)

- Streptavidin (Strep)
- Microscopy coverslips (e.g., Ibidi 8 well μ -slide)

Additional materials needed for the protocol are discussed in detail below.

Microscope

In order to perform quantitative microscopy on surface immobilized elements, it is advisable to use imaging modalities that allow for the elimination of out of focus emission such as confocal- or TIRF microscopy. This will increase the signal-to-noise ratio and detection efficiency. It is important to note that the instrumentation suggestions above merely serve as guidelines for optimal performance and that the SLiD assay can be performed on standard inverted fluorescence microscopes.

Plasma

The same requirements for plasma as for the SEC assay, see above.

Liposomes

Overall the same conditions regarding liposomes used for the SEC assay applies for the SLiD assay, with the addition that the SLiD requires the inclusion of a biotinylated lipid in order to immobilize the liposomes on the streptavidin covered surface. We typically add DSPE-PEG-Biotin in a molar ratio of 0.05%.

Microscope Chamber

The SLiD assay requires a surface suited for quantitative microscopy on which the liposomes can be attached (Fig. 8.3a). This can be achieved either by a home-build microscope holder able to fit a thoroughly cleaned glass slide or through commercially available microscope chambers as the Ibidi 8 well μ -slide with glass bottom. No matter the option, it is important that the glass surface is clean and planar before proceeding to the surface preparation step.

Preparing Surfaces

1. Prepare 1 g/L stock solutions of BSA and BSA-Biotin as well as a 0.2 g/L stock solution of Strep. All prepared in a buffer matching the one used for handling the liposomes, e.g. 10 mM Hepes, 137 mM NaCl, pH 7.4.
2. Mix BSA and BSA-biotin solutions in a 10:1 ratio, add to chamber and incubate for 20 min at room temperature. The added volume will be dependent on the chamber/slide used, but the amount need to cover the whole surface. For the Ibidi 8 well μ -slide, we typically add 300 μ L.
3. Wash surfaces with buffer by adding and removing the same volume as in step 2 eight times.
4. Add Strep to the chamber for a final concentration of 0.025 g/L and incubate for 10 min at room temperature.
5. Wash surfaces with buffer by adding and removing the same volume as in step 2 eight times.

The surfaces can be prepared one day in advance and stored at 4 °C.

4.3.3 Incubation and Imaging

Performing the SLiD assay allows for two possible experimental approaches, both of which will be described in detail below.

In-chamber Dissociation Measurement

If possible, start microscope heating and make sure it has stabilized at 37 °C.

1. Immobilize liposomes on the surface by adding a diluted amount to the chamber and wait for an adequate liposome surface density. The aim is to have a surface density where enough liposomes are in the field-of-view to ensure high-throughput measurement (typically a few hundred liposomes per frame), while avoiding that the signal from individual liposomes are overlapping. We typically dilute the liposome samples to 10 μM and add 5 μL of this to 300 μL buffer in an Ibidi 8 well μ -slide.
2. Acquire an image before adding blood plasma. Make sure that each liposome is sampled with an appropriate amount of pixels allowing for accurate data treatment (a pixel size of 25 nm works well in our lab). Also, use laser intensities allowing for good signal-to-noise levels while not leading to significant frame-to-frame bleaching. To verify that no significant bleaching occurs, a control experiment in buffer can be performed where 20–50 images are sequentially acquired using the experimental microscopy settings. By following the integrated intensity of the individual particles frame by frame, the amount of bleaching can be quantified, making sure that it is limited to a few percent over the course of the experiment.
3. Carefully exchange chamber buffer with blood plasma, making sure not to touch the sample holder or glass slide as this could lead to movement of the field of view and eliminate the possibility of tracking the same liposomes over time.
4. Acquire an image at $t = 0$ h. The intensity in this image can later be compared to the image acquired before addition of plasma to control for medium-induced changes in fluorescence intensity.
5. Acquire images over a given time period at specific time intervals, remembering to readjust the focal plane if drift occurs.

In-solution Dissociation Measurement

While the direct in-chamber measurement discussed above gives the unique possibility of following the FLL dissociation for the same liposome over time, it do require some skill and an optimal experimental setup. Also the liposome immobilization could potentially impose issues related to the strain and altered interaction kinetics due to the static position and uneven concentration of liposomes. To circumvent such issues, the liposome and plasma incubation can be performed in solution, before immobilizing liposomes to chamber and measure the FLL intensity at selected time points. Doing this, the FLL dissociation can now be tracked for individual liposomes within the population, although not for the same liposome over time.

1. Perform liposome and plasma incubation as described above in the SEC section, but with liposomes containing a biotinylated lipid to enable surface immobilization.

2. At selected time points, remove buffer from the imaging chamber and add a fraction of the liposomes-plasma incubation solution. Allow for surface immobilization and acquire image.
3. Repeat in new chamber for subsequent time points.

Optimal Image Quality

Be aware that for optimal image quality it is important that the surface is planar to secure even illumination and detection in the whole field of view. Also, if the microscope is heated, this can lead to thermal drift, something that needs to be monitored and corrected for especially when performing the in-chamber assay. For some microscopy platforms and software packages, an option exists where multiple spots on the surface can be imaged simultaneously. Doing this will greatly increase the number of liposomes that can be sampled in a single experiment; however, care needs to be taken that all images are correctly in focus.

Image Analysis

The important parameter to extract from the microscopy images is the total integrated fluorescence intensity from each particle, since this value reflects the amount of FLL in each liposome. This extraction can be done by dedicated and sophisticated home-build data routines, but free available plug-ins for this purpose also exist in software like Fiji (Image J). We have previously used the plug-in software ComDet, which is able to detect particles in an image over a certain size threshold (to filter out noise). The plugin integrates the total fluorescence intensity for all pixels covered by the single particle/liposome and gives a list of fluorescence intensities for all single particles as an output along with the coordinates of the center of the particle. If the liposomes are labeled with two FLLs, the plugin is also able to detect colocalization between the two channels, and give the ratio between the integrated intensity for each fluorophore in the particle. This allows for direct comparison of dissociation rates of two FLLs from the exact same liposome.

4.4 Comparison Between the SEC and SLiD Methods

The table below gives an overview of the advantages and limitations of the SEC and SLiD methods as well as the possibilities the methods offers for extending the proposed studies.

	SEC	SLiD
Specialized equipment needed	None (fluorescence reader required)	Confocal microscope (or similar)
Simplicity	Very simple	Microscopy and data analysis requires some training
Kinetic studies	Requires new sample for each timepoint	Same sample can be monitored over time

(continued)

	SEC	SLiD
Possible to distinguish individual liposomes: e.g., observe if all liposomes dissociate to a similar extent, or if some remain intact while other are degraded completely	No	Yes
Possible to distinguish liposomes from same sized, naturally occurring nanoparticles (VLDL, Chylomicrons)	No	Yes
Possible to analyze to which other plasma component the dissociated FLLs have associated with	Yes	No
Possible to analyze sample by other means than fluorescence	Yes	No

5 Review and Analysis of Key Research Findings

5.1 Lipid Exchange Is a Well-Known Phenomenon

It has been known for half a century that phospholipids exchange between membranes in a lipid-type-dependent manner when in a biological environment [65, 66]. Later it was demonstrated that lipid depletion from membranes did not only occur via active transport by lipid transfer proteins and lipoprotein particles [22, 23] but could also take place spontaneously [67]. Extensive investigations on the kinetics of lipid transfer between membranes are hence available in the literature [68–71]. Lipid exchange between vesicles, cells, lipoprotein particles, and proteins was thus a well-known phenomenon long before liposomes for drug delivery entered the clinic. Nevertheless, as we will elaborate on below, the dissociation of FLLs and other lipid conjugates from drug delivery liposomes is rarely discussed and not systematically studied although it could have pronounced effect on liposome function.

5.2 Dissociation of Fluorescently Labeled Lipids

A few recent studies have addressed how FLLs dissociates from lipid nanoparticles [27, 28, 72–75]. This has been shown to lead to FLL association with cells independently of the particles, thus causing false positives in cellular uptake studies. For example, Snipstad et al. demonstrated with flow cytometry that some fluorescent dyes were associating with cells, even when the nanoparticles into which the dyes were embedded were not associating with the cells [27]. Other recent studies on the subject have intended to develop *in vitro* assays that can predict lipid transfer in biological environments. As models for biological components, these studies have, e.g., investigated the transfer into acceptor emulsions [73], oil phases [74], or lipid nanocapsules of various sizes [72]. The detection method has either been based on

FRET [72, 75], SEC [72], flow cytometry [73], or fluorescence intensity of the acceptor oil phase [74]. In a very different approach, Zhu et al. used Quartz Crystal Microbalance to study transfer of lipids from a flow of anionic liposomes onto a cationic acceptor membrane [76]. The authors suggested that the slow release of liposomes from the surface was due to exchange of charged lipids causing a loss of electrostatic attraction. While none of the above studies demonstrated lipid dissociation in a true biological environment, Liu and Thayumanavan have used FRET to demonstrate FLL release from polymer nanogels in serum [77]. Recently, we have reported the dissociation of a range of commonly used FLLs from stealth liposomes incubated in biological environments using the methodologies described in detail in this chapter [28].

The recent focus on FLL dissociation is in sharp contrast to the previous two decades, where the dissociation of lipids from liposomes in biological environments often has been neglected. This is potentially due to a lack of awareness about the basic dynamics of the self-assembled systems used in drug delivery. Methods such as fluorescence microscopy and flow cytometry rely heavily on the assumption that the presence of FLLs in a cell means that the liposomes were internalized, but this is not necessarily true [28] and at least is something that should be routinely tested. FLL dissociation from liposomes is a phenomenon that researchers should strive to avoid when designing liposome formulations. FLLs that are dissociating from the liposomes could be taken up by cells independently of the liposomes, causing false positives. This would trick researchers into believing that a formulation that is not taken up by their target cells, actually has abilities to target the cell population of interest and perhaps enter a certain subcellular compartment. Alternatively, if the FLLs dissociate from the liposomes and stay in the medium, the ability of a formulation to be taken up by cells could be greatly underestimated.

5.3 Dissociation of Polymer-Conjugated Lipids

As mentioned earlier in the chapter, FLLs is not the only component of liposomal drug delivery liposomes where untimely dissociation could be detrimental for liposome function. Other lipid-conjugated moieties bestow liposomes with unique properties, the most abundantly used being the polymers used to produce “stealth” liposomes [16]. Such long-circulating “stealth” liposomes, where the surface is coated with either gangliosides [78] or PEG [79], were invented in the late 1980s and paved the way for using liposomes in the clinic for treatment of cancer. It has been suggested that the long-circulating properties of PEGylated liposomes could be due to the engrafted hydrophilic polymers creating a hydration shell around the liposomes, thus sterically hindering interactions with other components in the plasma [80, 81]. This could in turn reduce binding of the serum proteins mediating clearance by immune cells or prevent liposome aggregation – two explanations for the long-circulation properties that have been discussed extensively, but after 30 years still remain a matter of debate [82–84]. However, spontaneous lipid transfer between vesicles was quite early demonstrated not to be prevented by PEGylation,

as the PEG-conjugated lipids themselves were also dissociating, both *in vitro* and *in vivo* [24–26]. It was also demonstrated that the loss of engrafted PEG could significantly reduce the circulation time and that the retention of PEG on the liposome surface could be actively controlled by choosing the proper lipid anchor, e.g., DSPE rather than POPE, or lipids with long saturated hydrocarbon tails rather than short unsaturated ones [24, 25]. In conclusion, dissociation of polymer-conjugated lipids can result in stealth liposomes losing their long-circulating properties, compromising the function of the polymer-coating.

5.4 Dissociation of Drug-Conjugated Lipids

Besides PEG lipids, dissociation of conjugated lipids could be important if the conjugated compound was a drug in itself. Many studies have investigated the conjugation of drugs to lipid anchors [85, 86], e.g., linking chemotherapeutics such as paclitaxel [87], chlorambucil [88], or melphalan [89] to constructs that are readily loaded into the lipid bilayer of the liposomal membrane. Clinically, the immunostimulant mifamurtide is used to treat osteosarcoma in the liposomal drug formulation sold under the name Mepact [90, 91]. For lipid-conjugated drugs, dissociation from the liposome may be a problem, since the entire concept of using nanoparticles is usually to exploit them as a delivery platform. Dissociation of drug-conjugated lipids from the liposomal carrier could result in a less active liposome and thus decreased efficiency of therapy. It could also be that the dissociation of drug-conjugated lipids would result in the drug being distributed in the body, giving rise to the adverse toxic reactions.

Here we will like to highlight that the issue of drug-conjugated lipid dissociation could potentially be flipped to an advantage and lead to liposomes being used as a controlled delivery platform. This would require that the extent of drug-conjugated lipid dissociation could be properly understood and characterized, allowing for long circulating liposomes to serve as inactive carriers, which slowly and in a controlled manner release drug-conjugated lipids to the surroundings.

5.5 Dissociation of Targeting-Ligand-Conjugated Lipids

Dissociation of targeting ligands such as antibody fragments would result in a loss of targeting abilities for the liposome formulation, thus decreasing the efficiency of the delivery properties of the system. While this could explain why liposomes that have excellent uptake abilities *in vitro* show poor tumor accumulation and low efficacy *in vivo*, it will probably not impose the same safety issues as leakage of drugs could do.

5.6 Dissociation Trends: How to Predict Lipid Dissociation

To avoid untimely dissociation of FLLs and other lipid-conjugated moieties, an in-depth mechanistic understanding of the parameters that govern lipid dissociation

from liposomes is needed. A membrane model-based and fundamental characterization of the molecular trends underlying lipid transfer between vesicles was done by Silvius et al. in 1993 [92]. They found that the length of the lipid tails as well as number of double bonds was the main determining factors, with an increase in tail length and degree of saturation correlating with less dissociation. In another study, Silvius et al. demonstrated that the nature of the conjugated species also affects the transfer of lipids between vesicles remarkably [26]. It was demonstrated that for PEG with increasing polymer length, the lipid transfer between liposomes increased. However, for molecules where the conjugate tended to interact with the membrane, such as for dextrans, increasing chain length did not lead to increase in the transfer rate, indicating that the conjugated moiety plays a significant role in regulating liposome dissociation. Supporting this, they found that for small-molecule conjugates, the dissociation trends were very similar to that experienced for the lipid alone. However, as was demonstrated by Hughes et al., the most widely used fluorescent labels have very varying trends to interact with lipid bilayers, which could also affect the trend of a FLL label to stay associated to the lipid bilayer or not [93].

The vast majority of mechanistic studies of lipid transfer between membrane model systems discussed in the previous sections were performed in a buffer environment without proteins and thus not in a biologically relevant environment. This is important since dissociation of lipid conjugates from liposomes in plasma might not only depend on how strongly the lipid and its conjugate interacts with the liposome but also how strong they interact with other components in the plasma. Thus the dissociation trend in plasma can be hard to foresee, based on correlations to results obtained in buffer. The methodology presented in this chapter can however be a good stepping stone to start to address these questions and quantify the degree of dissociation of FLLs or other fluorescently labeled lipid conjugates from liposomes into plasma or serum. We have recently shown that the degree of dissociation from liposomes in human plasma varies greatly between commercially available FLLs [28]. We found that FLLs with longer (C_{18}) acyl chains dissociated less than FLLs with shorter (C_{16}) chains and that liposomes containing more saturated lipids displayed less FLL dissociation as compared to liposome predominantly prepared with unsaturated lipids. Finally, the highest dissociation was observed for a cholesterol-based FLL, indicating this to be a poor choice for FLL membrane anchoring. We also demonstrated that different fluorophores conjugated to the same lipid anchor had quite different dissociation propensities, suggesting that also the properties of the fluorescent moiety of the FLL can strongly affect the FLL dissociation. To fully elucidate the physicochemical properties of FLLs that drive their liposome dissociation, a complete systematic study needs to be conducted.

6 Conclusions and Future Perspective

Here we present two assays of varying complexity and degree of detail, but both with a capability of addressing the central dogma of FLL dissociation from drug delivery liposomes. We stress that both methods is in principle capable of detecting the

dissociation of any fluorescently labeled lipid-conjugated system. Thus a plethora of liposome components can be investigated by smartly choosing labeling site and fluorophore. We believe that the implementation of dissociation control experiments should be part of any liposomal drug delivery project that relies on fluorescent measurements and imaging.

References

1. Sercombe L et al (2015) Advances and challenges of liposome assisted drug delivery. *Front Pharmacol* 6:13
2. Anselmo AC, Mitragotri S (2016) Nanoparticles in the clinic. *Bioeng Transl Med* 1:10–29
3. Bulbake U, Doppalapudi S, Kommineni N, Khan W (2017) Liposomal formulations in clinical use: an updated review. *Pharmaceutics* 9:33
4. Allen TM, Cullis PR (2013) Liposomal drug delivery systems: from concept to clinical applications. *Adv Drug Deliv Rev* 65:36–48
5. Bozzuto G, Molinari A (2015) Liposomes as nanomedical devices. *Int J Nanomedicine* 10:975–999
6. Mouritsen OG (2011) Lipids, curvature, and nano-medicine. *Eur J Lipid Sci Technol* 113:1174–1187
7. Landesman-Milo D, Peer D (2016) Transforming Nanomedicines from lab scale production to novel clinical modality. *Bioconjug Chem* 27:855–862
8. Wilhelm S et al (2016) Analysis of nanoparticle delivery to tumours. *Nat Rev Mater* 1:12
9. Time to deliver (2014) *Nat Biotechnol* 32:961–961
10. Peer D et al (2007) Nanocarriers as an emerging platform for cancer therapy. *Nat Nanotechnol* 2:751
11. Fang J, Nakamura H, Maeda H (2011) The EPR effect: unique features of tumor blood vessels for drug delivery, factors involved, and limitations and augmentation of the effect. *Adv Drug Deliv Rev* 63:136–151
12. Blanco E, Shen H, Ferrari M (2015) Principles of nanoparticle design for overcoming biological barriers to drug delivery. *Nat Biotechnol* 33:941–951
13. Hwang JY, Li Z, Loh XJ (2016) Small molecule therapeutic-loaded liposomes as therapeutic carriers: from development to clinical applications. *RSC Adv* 6:70592–70615
14. Maeda H, Nakamura H, Fang J (2013) The EPR effect for macromolecular drug delivery to solid tumors: improvement of tumor uptake, lowering of systemic toxicity, and distinct tumor imaging in vivo. *Adv Drug Deliv Rev* 65:71–79
15. Immordino ML, Dosio F, Cattel L (2006) Stealth liposomes: review of the basic science, rationale, and clinical applications, existing and potential. *Int J Nanomedicine* 1:297–315
16. Nag OK, Awasthi V (2013) Surface engineering of liposomes for stealth behavior. *Pharmaceutics* 5:542–569
17. Deshpande PP, Biswas S, Torchilin VP (2013) Current trends in the use of liposomes for tumor targeting. *Nanomedicine* 8:1509–1528
18. Riaz MK et al (2018) Surface functionalization and targeting strategies of liposomes in solid tumor therapy: a review. *Int J Mol Sci* 19:1–27
19. Mamot C et al (2005) Epidermal growth factor receptor-targeted immunoliposomes significantly enhance the efficacy of multiple anticancer drugs in vivo. *Cancer Res* 65:11631–11638
20. Wu J, Liu Q, Lee RJ (2006) A folate receptor-targeted liposomal formulation for paclitaxel. *Int J Pharm* 316:148–153
21. Ducat E, Evrard B, Peulen O, Piel G (2011) Cellular uptake of liposomes monitored by confocal microscopy and flow cytometry. *J Drug Delivery Sci Technol* 21:469–477
22. Tall AR (1980) Studies on the transfer of phosphatidylcholine from unilamellar vesicles into plasma high density lipoproteins in the rat. *J Lipid Res* 21:354–363
23. Tall AR (1986) Plasma lipid transfer proteins. *Annu Rev Biochem* 27:361–367

24. Parr MJ, Ansell SM, Choi LS, Cullis PR (1994) Factors influencing the retention and chemical-stability of poly(ethylene glycol)-lipid conjugates incorporated into large unilamellar vesicles. *BBA-Biomembranes* 1195:21–30
25. Li WM, Xue L, Mayer LD, Bally MB (2001) Intermembrane transfer of polyethylene glycol-modified phosphatidylethanolamine as a means to reveal surface-associated binding ligands on liposomes. *Biochim Biophys Acta Biomembr* 1513:193–206
26. Silvius JR, Zuckermann MJ (1993) Interbilayer transfer of phospholipid-anchored macromolecules via monomer diffusion. *Biophys J* 64:A73–A73
27. Snipstad S et al (2017) Labeling nanoparticles: dye leakage and altered cellular uptake. *Cytometry A* 91:760–766
28. Münter R et al (2018) Dissociation of fluorescently labeled lipids from liposomes in biological environments challenges the interpretation of uptake studies. *Nanoscale* 10:22720–22724
29. Israelachvili JN (2015) *Intermolecular and surface forces*. Elsevier Science, Amsterdam
30. Kraft JC, Freeling JP, Wang Z, Ho RJY (2014) Emerging research and clinical development trends of liposome and lipid nanoparticle drug delivery systems. *J Pharm Sci* 103:29–52
31. Simões S et al (2005) Cationic liposomes for gene delivery. *Expert Opin Drug Deliv* 2:237–254
32. Wagner A, Vorauer-Uhl K (2011) Liposome technology for industrial purposes. *J Drug Delivery Sci Technol* 2011:591325
33. Charcosset C, Juban A, Valour JP, Urbaniak S, Fessi H (2015) Preparation of liposomes at large scale using the ethanol injection method: effect of scale-up and injection devices. *Chem Eng Res Des* 94:508–515
34. Larsen J, Hatzakis NS, Stamou D (2011) Observation of inhomogeneity in the lipid composition of individual nanoscale liposomes. *J Am Chem Soc* 133:10685–10687
35. Grit M, de Smidt JH, Struijke A, Crommelin DJA (1989) Hydrolysis of phosphatidylcholine in aqueous liposome dispersions. *Int J Pharm* 50:1–6
36. Mayer LD, Hope MJ, Cullis PR, Janoff AS (1985) Solute distributions and trapping efficiencies observed in freeze-thawed multilamellar vesicles. *Biochim Biophys Acta Biomembr* 817:193–196
37. Traikia M, Warschawski DE, Recouvreur M, Cartaud J, Devaux PF (2000) Formation of unilamellar vesicles by repetitive freeze-thaw cycles: characterization by electron microscopy and P-31-nuclear magnetic resonance. *Eur Biophys J Biophys Lett* 29:184–195
38. Hayakawa E, Nakakura M, Kato Y, Okubo Y, Hosokawa T (1991) Encapsulation of doxorubicin into liposomes by a freeze-thawing method using buffer solution. *Chem Pharm Bull* 39:773–776
39. Xu X, Khan MA, Burgess DJ (2012) Predicting hydrophilic drug encapsulation inside unilamellar liposomes. *Int J Pharm* 423:410–418
40. Costa AP, Xu X, Burgess DJ (2014) Freeze-anneal-thaw cycling of unilamellar liposomes: effect on encapsulation efficiency. *Pharm Res* 31:97–103
41. Akbarzadeh A et al (2013) Liposome: classification, preparation, and applications. *Nanoscale Res Lett* 8:102
42. Szleifer I, Gerasimov OV, Thompson DH (1998) Spontaneous liposome formation induced by grafted poly(ethylene oxide) layers: theoretical prediction and experimental verification. *Proc Natl Acad Sci* 95:1032
43. Lapinski MM, Castro-Forero A, Greiner AJ, Ofoli RY, Blanchard GJ (2007) Comparison of liposomes formed by sonication and extrusion: rotational and translational diffusion of an embedded chromophore. *Langmuir* 23:11677–11683
44. Pons M, Foradada M, Estelrich J (1993) Liposomes obtained by the ethanol injection method. *Int J Pharm* 95:51–56
45. Zumbuehl O, Weder HG (1981) Liposomes of controllable size in the range of 40 to 180 nm by defined dialysis of lipid/detergent mixed micelles. *Biochim Biophys Acta Biomembr* 640:252–262
46. Jiskoot W, Teerlink T, Beuvery EC, Crommelin DJA (1986) Preparation of liposomes via detergent removal from mixed micelles by dilution – the effect of bilayer composition and process parameters on liposome characteristics. *Pharm Weekbl -Scientific Edition* 8:259–265

47. Lévy D, Bluzat A, Seigneuret M, Rigaud J-L (1990) A systematic study of liposome and proteoliposome reconstitution involving Bio-Bead-mediated Triton X-100 removal. *Biochim Biophys Acta Biomembr* 1025:179–190
48. Ollivon M, Lesieur S, Grabielle-Madelmont C, Paternostre MT (2000) Vesicle reconstitution from lipid–detergent mixed micelles. *Biochim Biophys Acta Biomembr* 1508:34–50
49. Seddon AM, Curnow P, Booth PJ (2004) Membrane proteins, lipids and detergents: not just a soap opera. *Biochim Biophys Acta Biomembr* 1666:105–117
50. Bhattacharjee S (2016) DLS and zeta potential – what they are and what they are not? *J Control Release* 235:337–351
51. Smith MC, Crist RM, Clogston JD, McNeil SE (2017) Zeta potential: a case study of cationic, anionic, and neutral liposomes. *Anal Bioanal Chem* 409:5779–5787
52. Jeschek D, Lhota G, Wallner J, Vorauer-Uhl K (2016) A versatile, quantitative analytical method for pharmaceutical relevant lipids in drug delivery systems. *J Pharm Biomed Anal* 119:37–44
53. Shibata H, Yomota C, Okuda H (2013) Simultaneous determination of polyethylene glycol-conjugated liposome components by using reversed-phase high-performance liquid chromatography with UV and evaporative light scattering detection. *AAPS PharmSciTech* 14:811–817
54. Zhong Z, Ji Q, Zhang JA (2010) Analysis of cationic liposomes by reversed-phase HPLC with evaporative light-scattering detection. *J Pharm Biomed Anal* 51:947–951
55. Stewart JCM (1980) Colorimetric determination of phospholipids with ammonium ferri-thiocyanate. *Anal Biochem* 104:10–14
56. Itoh YH, Itoh T, Kaneko H (1986) Modified Bartlett assay for microscale lipid phosphorus analysis. *Anal Biochem* 154:200–204
57. Kuai R, Li D, Chen YE, Moon JJ, Schwendeman A (2016) High-density lipoproteins: nature's multifunctional nanoparticles. *ACS Nano* 10:3015–3041
58. Simonsen JB (2017) What are we looking at? Extracellular vesicles, lipoproteins, or both? *Circ Res* 121:920–922
59. Grabielle-Madelmont C, Lesieur S, Ollivon M (2003) Characterization of loaded liposomes by size exclusion chromatography. *J Biochem Biophys Methods* 56:189–217
60. Hess JR (2010) Conventional blood banking and blood component storage regulation: opportunities for improvement. *Blood Transfus* 8(Suppl 3):s9–s15
61. Larsen JB et al (2015) Membrane curvature enables N-Ras lipid anchor sorting to liquid-ordered membrane phases. *Nat Chem Biol* 11:192–U176
62. Elizondo E et al (2012) Influence of the preparation route on the supramolecular organization of lipids in a vesicular system. *J Am Chem Soc* 134:1918–1921
63. Hatzakis NS et al (2009) How curved membranes recruit amphipathic helices and protein anchoring motifs. *Nat Chem Biol* 5:835–841
64. Bhatia VK, Hatzakis NS, Stamou D (2010) A unifying mechanism accounts for sensing of membrane curvature by BAR domains, amphipathic helices and membrane-anchored proteins. *Semin Cell Dev Biol* 21:381–390
65. Reed CF (1968) Phospholipid exchange between plasma and erythrocytes in man and the dog. *J Clin Invest* 47:749–760
66. Wirtz KWA, Zilversmit DB (1968) Exchange of phospholipids between liver mitochondria and microsomes in vitro. *J Biol Chem* 243:3596–3602
67. Martin FJ, MacDonald RC (1976) Phospholipid exchange between bilayer membrane vesicles. *Biochemistry* 15:321–327
68. Jones JD, Thompson TE (1989) Spontaneous phosphatidylcholine transfer by collision between vesicles at high lipid-concentration. *Biochemistry* 28:129–134
69. Jones JD, Thompson TE (1990) Mechanism of spontaneous, concentration-dependent phospholipid transfer between bilayers. *Biochemistry* 29:1593–1600
70. Brown RE (1992) Spontaneous lipid transfer between organized lipid assemblies. *Biochim Biophys Acta* 1113:375–389

71. Pownall HJ, Bick DLM, Massey JB (1991) Spontaneous phospholipid transfer – development of a quantitative model. *Biochemistry* 30:5696–5700
72. Simonsson C et al (2016) Inter-nanocarrier and nanocarrier-to-cell transfer assays demonstrate the risk of an immediate unloading of dye from labeled lipid nanocapsules. *Eur J Pharm Biopharm* 98:47–56
73. Petersen S, Fahr A, Bunjes H (2010) Flow cytometry as a new approach to investigate drug transfer between lipid particles. *Mol Pharm* 7:350–363
74. Bastiat G et al (2013) A new tool to ensure the fluorescent dye labeling stability of nanocarriers: a real challenge for fluorescence imaging. *J Control Release* 170:334–342
75. Ambegia E et al (2005) Stabilized plasmid-lipid particles containing PEG-diacylglycerols exhibit extended circulation lifetimes and tumor selective gene expression. *BBA-Biomembranes* 1669:155–163
76. Zhu T, Jiang ZY, Ma YQ (2012) Lipid exchange between membranes: effects of membrane surface charge, composition, and curvature. *Colloids Surf B Biointerfaces* 97:155–161
77. Liu B, Thayumanavan S (2017) Importance of evaluating dynamic encapsulation stability of amphiphilic assemblies in serum. *Biomacromolecules* 18:4163–4170
78. Allen TM, Chonn A (1987) Large unilamellar liposomes with low uptake into the reticuloendothelial system. *FEBS Lett* 223:42–46
79. Klibanov AL, Maruyama K, Torchilin VP, Huang L (1990) Amphipathic polyethyleneglycols effectively prolong the circulation time of liposomes. *FEBS Lett* 268:235–237
80. Blume G, Cevc G (1993) Molecular mechanism of the lipid vesicle longevity *in vivo*. *Biochim Biophys Acta* 1146:157–168
81. Allen C et al (2002) Controlling the physical behavior and biological performance of liposome formulations through use of surface grafted poly(ethylene glycol). *Biosci Rep* 22:225–250
82. Moghimi SM, Szebeni J (2003) Stealth liposomes and long circulating nanoparticles: critical issues in pharmacokinetics, opsonization and protein-binding properties. *Prog Lipid Res* 42:463–478
83. Dos Santos N et al (2007) Influence of poly(ethylene glycol) grafting density and polymer length on liposomes: relating plasma circulation lifetimes to protein binding. *BBA-Biomembranes* 1768:1367–1377
84. Butcher NJ, Mortimer GM, Minchin RF (2016) Unravelling the stealth effect. *Nat Nanotechnol* 11:310–311
85. Adhikari P et al (2017) Nano lipid-drug conjugate: an integrated review. *Int J Pharm* 529:629–641
86. Irby D, Du CG, Li F (2017) Lipid-drug conjugate for enhancing drug delivery. *Mol Pharm* 14:1325–1338
87. Du R et al (2014) Antitumor effect of iRGD-modified liposomes containing conjugated linoleic acid-paclitaxel (CLA-PTX) on B16-F10 melanoma. *Int J Nanomedicine* 9:3091–3105
88. Pedersen PJ et al (2009) Synthesis and biophysical characterization of chlorambucil anticancer ether lipid prodrugs. *J Med Chem* 52:3408–3415
89. Kuznetsova NR et al (2014) Targeting liposomes loaded with melphalan prodrug to tumour vasculature via the Sialyl Lewis X selectin ligand. *J Drug Target* 22:242–250
90. Nardin A, Lefebvre ML, Labroquere K, Faure O, Abastado JP (2006) Liposomal muramyl tripeptide phosphatidylethanolamine: targeting and activating macrophages for adjuvant treatment of osteosarcoma. *Curr Cancer Drug Targets* 6:123–133
91. Frampton JE (2010) Mifamurtide: a review of its use in the treatment of osteosarcoma. *Paediatr Drugs* 12:141–153
92. Silvius JR, Leventis R (1993) Spontaneous interbilayer transfer of phospholipids – dependence on acyl-chain composition. *Biochemistry* 32:13318–13326
93. Hughes LD, Rawle RJ, Boxer SG (2014) Choose your label wisely: water-soluble fluorophores often interact with lipid bilayers. *PLoS One* 9:e87649



Integrated Multilayer Microfluidic Platforms with Silicon Architectures for Next-Generation Health Diagnostic Systems

Aditya Kasukurti, Hari Hara Sudhan Lakshmanan, Sarojini Tiwari, and Jeevan Maddala

Contents

1	Definition of the Topic	361
2	Overview	362
3	Introduction	362
4	Experimental Methodology	364
4.1	Sensors and Actuators	366
4.2	Fabrication	374
4.3	Multilayer Microfluidic Devices(MMD) and Integration with Silicon Layer	377
4.4	Controllers	377
5	Key Research Findings	383
5.1	Whole Blood Analysis	383
5.2	Organs on Chip	385
5.3	Microfluidic Applications in Bionanomaterials and Nanomedicine	386
5.4	Large-Scale Data Integration for Healthcare Diagnostics	387
6	Conclusions and Future Perspectives	388
	References	390

1 Definition of the Topic

Majority of research on lab-on-chip devices was on single layer devices. Stacking a combination of microfluidic layers to silicon architecture gives substantial advantage to integrate precise sensors, actuators, and control systems. Advantages of multilayer

A. Kasukurti (✉)
Intel Corp, Portland, OR, USA
e-mail: kasukurti.aditya@gmail.com

H. H. S. Lakshmanan
OHSU, Portland, OR, USA

S. Tiwari · J. Maddala (✉)
WVU, Morgantown, WV, USA
e-mail: jeevan.iit@gmail.com

stack are: (i) multiple functions can be incorporated into single chip and (ii) simultaneous analysis of both macroscopic and microscopic properties, for example, characterizing blood as a bulk fluid and at the individual component level at the same time. Such integrated systems enable the applications that lead to development of comprehensive diagnostics system. Challenges for developing such devices are integrating multiple layers – a combination of biocompatible microfluidics and silicon architectures; individual automated systems that incorporate sensors, actuators, and control systems; development of rapid data analysis and management; and development of diagnostic metrics to manipulate the actuators based on the responses (feedback control). This chapter reviews existing literature and techniques to address the above challenges through the prospect of a state-of-the-art silicon integrated lab-on-chip device with advanced automation coupled with novel data analysis tools to address critical applications in healthcare.

2 Overview

Microfluidics is a crucial part for developing next-generation in vitro diagnostic systems. Integrating these systems with silicon architecture and using emerging machine learning and data analysis techniques is rapidly changing the medical diagnostics systems. In this chapter, we discuss very large-scale integrated microfluidic systems (VLSIMS) that are changing the scenario of point of care diagnostics – real-time personalized blood analysis and organs-on-chip (OOC) systems. We review novel fabrication and integration techniques available to develop these systems. Such integrated systems need rapid data analysis techniques to infer diagnostics; for example, understanding the overall information of the blood as a bulk fluid and also studying the individual components generate massive amount of data. These systems need to swiftly analyze this data and synthesize a comprehensive diagnostic information. Recent trends in machine learning and edge computing are also reviewed in this chapter.

3 Introduction

Lab-on-chip technology is essentially a miniaturized tool handling micro- or nano-liters of fluid to accomplish numerous applications. Microfluidic lab-on-chip technology has gained popularity in fields such as diagnostics, drug delivery, cell biology, computation, and reaction engineering. The immense popularity in detection or sensing, imaging, drug delivery, diagnostics, and cell biology is owed to its many advantages over conventional methods. It instills many advantages such as rapid analysis, high throughput, portability, low space, and sample requirement in various processes [1–3]. In cell biology, spatial and temporal control has been applied to the fundamental study of cell sorting and handling [3, 4]. This field has brought up a revolution in the discovery of nanoparticles due to ease in control of size and shape distribution within microchannels [1]. In addition, low reagent

consumptions and easy fabrication make these devices cost-effective and easy to implement [5]. The following paragraphs bring together the end use of microfluidics in point-of-care diagnostics field and the role of highly integrated microfluidic platforms in optimizing healthcare.

Ultra low cost microfluidic diagnostic devices fitting “ASSURED” criteria (i.e., affordable, sensitive, specific, user-friendly, rapid and robust, equipment-free, deliver to the users who need them), set by the World Health Organization [6], could be pivotal in wellness and preventive care for the extreme point-of-care regime through self-monitoring by an untrained person. Beyond these, we propose here an advanced microfluidic lab-on-chip diagnostics companion for a trained medic at secondary point-of-care like a health center for effective and efficient treatment to increase success rate, speed up recovery, and reduce cost of treatment by preventing repeat visits.

In this data-driven era, advanced point-of-care (aPOC) diagnostics systems for personalized healthcare require rapid analysis of all biological parameters, measurable through minimally invasive techniques, to generate the datasets necessary to feed the cloud-based massive multiparameter analysis. Large-scale integrated and multiplexed microfluidic devices will address this gap [7]. Microfluidic large-scale integration includes thousands of micromechanical valves (actuators), sensors, and control systems on the same chip. Automation at this level is of designing many tiny robots that efficiently handle nanoliters of fluids and also precisely perturb these micro environments to enable simultaneous measurement of multiple parameters. Advanced semiconductor manufacturing technologies will allow for large-scale integration of such robots to a silicon architecture at the chip level for future mass produced microfluidic systems that enable challenging studies like whole blood analysis, organ-on-chip, cancer-on-chip, etc. Figure 9.1 shows the basic building blocks of such advanced systems and highlights the level of integration involved through an example case study of a hands-free rapid multifactor whole blood analysis system that can assist a physician to personalize healthcare for the patient.

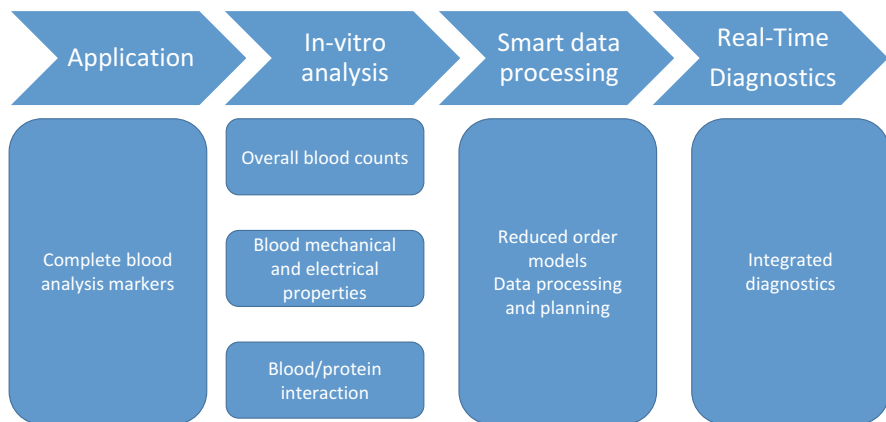


Fig. 9.1 Basic components for a complete blood analysis system

The suggested whole blood analysis application could include, in the first stage, a highly integrated microfluidic system that can simultaneously gather single cell level electrical, mechanical properties, imaging, scatter and fluorescence data for accurate cell classification and enumeration for RBCs, WBCs, platelets, rare cell statistics, etc. while simultaneously analyzing blood plasma for protein markers, free RNA and bulk properties like viscoelasticity, etc. Additional stages of analysis based on initial findings could include preemptive screening for platelet/WBC activation times [8], blood coagulation speeds, drug allergies, as well as other blood-based drug screening to feed a cloud-assisted real-time multifactor data analysis to autogenerate a powerful diagnostics report available during the current patient visit, thus enabling a personalized treatment plan.

This chapter introduces all the critical components like sensors, actuators, control systems, and data analysis tools necessary for such advanced integrated microfluidic systems. The chapter also discusses the current trends and advances in the fields of microfluidics/semiconductor fabrication and big data analysis that can be leveraged to enable large-scale integration and widespread adoption of systems like the whole blood-based diagnostic companion and organ/body-on-chips studies.

4 Experimental Methodology

Spatiotemporal (space and velocity) control of discrete nanoliter volume fluids in microchannels has promising benefits to cell biology, drug delivery, micro-reactors, and nanotechnology. Such applications of lab-on-chip technologies require easy and reliable manipulation of nanoliter volume of fluids. Sensors and actuators form an important part of an actively controlled microfluidic device. Over the recent years, several techniques are developed to simplify the fabrication and prototyping of these devices with novel kinds of sensing and actuation techniques. Innovations in the use of active control in these devices, from open loop to feedback, have widened the applications of lab-on-chip technology. Herein, we review and highlight the basic building blocks that are necessary to achieve complete automated lab-on-chip systems.

All the applications in microfluidics require the following basic components as seen in Fig. 9.2. This section summarizes the existing literature on understanding and fabricating these building blocks.

In microfluidics, controllers are used to regulate either droplet generation or droplet speed or target destination of individual cells or everything simultaneously. Controllers are microprocessing devices that can perform computation based on a predefined algorithm. Every control system has three main components: sensors, controller, and actuators. We identify the control variables (CV) and manipulated variables (MV) based on control applications. Sensors are instruments that can measure and report the CVs and MVs to the controller. The controller works either based on a predefined model that helps determine changes to MV to control the CV or an optimizer that predicts the model in real time to achieve control [9]. The

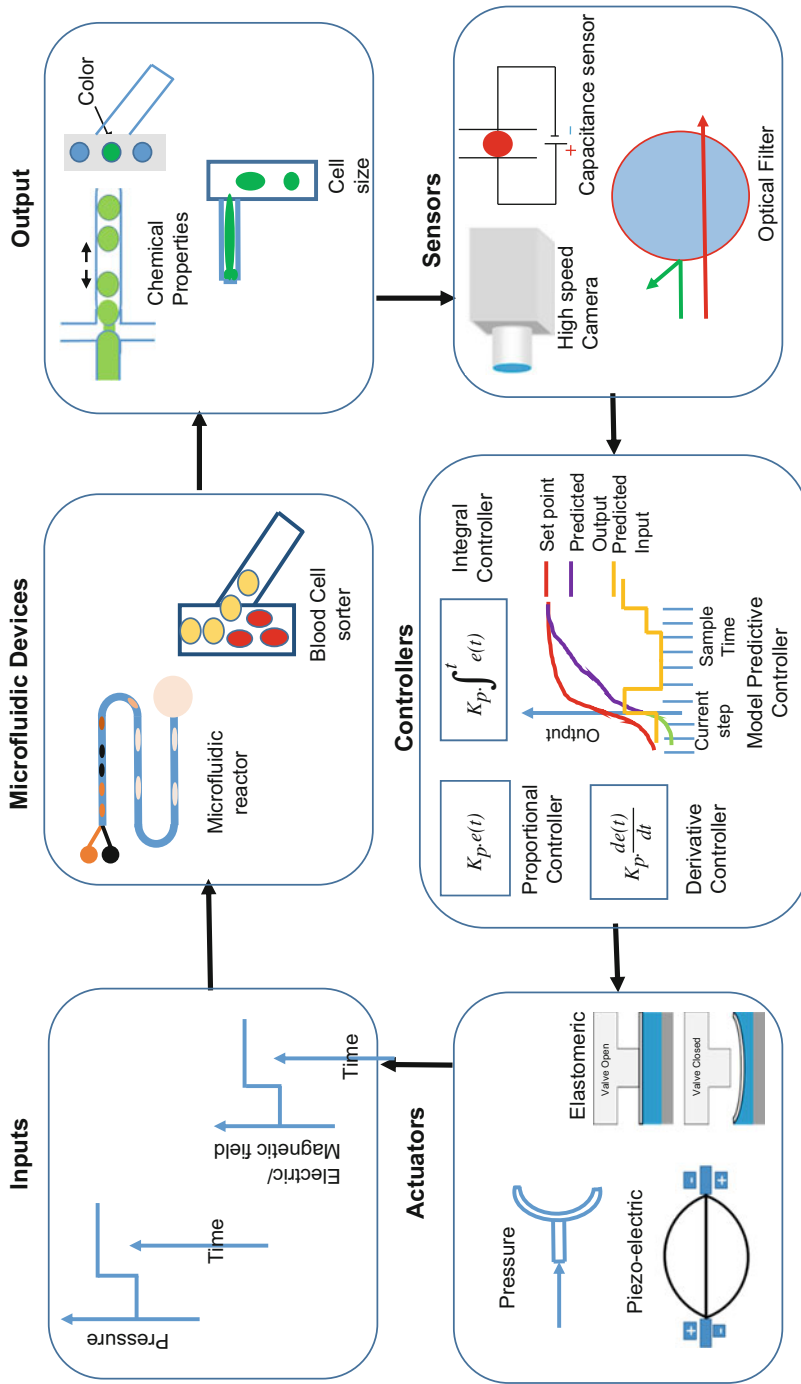


Fig. 9.2 Control system in microfluidics

controller takes inputs from the sensors and dictates the actuators to modify MVs. An actuator is the final element in control system that implements the controller's decision.

We define inputs and outputs with respect to the controller. A controller can have various inputs to communicate with a system to know if the process output is within predefined limit. Similarly, whenever a controller takes a decision to change the MV to adjust the system it communicates to the actuators through various signals, we call these signals as outputs of a controller. Typical examples of controller inputs are pressure, electric, or magnetic signals. Outputs from a controller are signals to the actuators. Typical examples of controller output are magnetic, electrical, or pressure based on the actuator. Most of the time it is electrical signal that is transduced by the actuator. Sensors are devices that communicate the real-time process output/state as an input to the controller. Sensors are of various types such as optical, electrical, and magnetic depending on the control variable. Actuator is the final piece in the controller puzzle. Actuators are mostly valves for flow control or some heat source for temperature control. Droplets can be controlled by flow control devices such as valves. Piezo-electric, pneumatic, and elastomeric valves solve most of the actuation goals in a microfluidic device.

Controllers integrated with sensors and actuators maintain the process under conditions favorable to the user. There are many choices of controllers available such as proportional, integral, derivative, and model predictive controller based on the way the controllers respond to error. We choose controllers based on the frequency of control action, limits on offset, and other constraints.

In this section, we look at the basic actuators, sensors, and controllers relevant to microfluidic systems.

4.1 Sensors and Actuators

A sensor is a physical device that measures system's parameters or variables dynamically. It can either be on-line for real-time data collection or offline for collecting data every few days. A sensor is typically selected based on its performance and reliability. A sensor will usually detect the location and/or composition of the cell/discrete fluid in the channel. In microfluidics applications, many on and off channel sensors are utilized to serve their purpose [10]. Most of the current research is directed toward optical techniques as they are easy to implement and operate in lab-scale microfluidic experiments.

Actuators, on the other hand, bring a change in a variable such that the pressure differs across a microchannel. Here, the actuator's response time after receiving a signal from a sensor plays a vital role in the overall speed and reliability of the system. These are necessary components of a control system. When designed according to system's need, they bring about the change necessary to achieve its objective. The usual approach in the recent works has been to manipulate flow either by varying hydrodynamic resistances or by a valve operated through electrical, mechanical, magnetic, or optical means. The force by which actuators are operated

in various microfluidic applications can be classified into pressure, mechanical, electrical, mechanical, and optical. Sensing in the field of spatial and temporal control of droplets is mostly carried out by optical means.

4.1.1 Electrical

Electric potential difference is widely used for actuation and detection techniques in digital microfluidics due to ease of its fabrication and operation. Actuations by electrical means are usually carried out by applying voltage from an external source. This voltage is supplied (for actuation) or captured (for detection) through various means such as integrated electrodes or wires inserted on the microchannels. The following passages summarize similar techniques in various applications of droplet microfluidics.

Flow cytometry applications such as cell sorting usually require specific reactions or cell properties leading to high preparation and reaction time. Microfluidic techniques overcome these limitations but have low throughput due to miniaturization. Hence, actuators with a high degree of control and ease in fabrication are employed.

Ahn et al. made high-speed microfluidic sorting devices separating water droplets flowing in oil streams. The first device consisted of the inverted Y-shaped channel with one leg shorter than the other and a pair of indium tin oxide electrodes (ITO) electrodes placed at the junction. The drops flow down the waste channel in the absence of electric field due to the low hydrodynamic resistance offered by its shorter length. As soon as the electrodes are activated or energized, the drops move to the collection channel with an average frequency of 1.6 kHz. This frequency was considerably improved to 4 kHz by using bidirectional manipulation. In this setup, the channel lengths were same, and an additional ITO electrode was placed to the left side of the junction. The water droplets moved to whichever side the electrodes were energized [11]. This methodology, however, was not tested on living cells. Additionally, automation using a simple on and off controller could improve the throughput considerably.

A feedback controlled highly sensitive detection and sorting system for living fluorescent cells (*E. coli* expressing R-phycoerythrin) was developed based on similar principles. The voltage supply activated electrodes placed at the separation junction as soon as the sensor detected the colored cells. The polarity thus generated separated the cells suspended in aqueous phase almost instantaneously [12]. A high throughput in cell sorting invariably increases voltage and power requirements. This limitation too was eliminated when Chen et al. achieved a high-speed automated cell sorting utilizing power as low as 0.1 mW, a voltage less than 10 V, and a throughput of 1000 particles per second. This automated sorting system was made of a fluorescence detection, real-time signal processing, and field programmable gate array (FPGA). The microfluidic input channel divides into a waste and two collection channels on the either side. As soon as a particle is detected by the optical system, a piezoelectric actuator (response time 0.1–1 ms) changes the flow dynamics by expanding and contracting and thus pushing the particles to the collection channels. *E. coli* sorting on the same device occurred at a speed of 330 cells/s with high sorting efficiency of 70% [13, 14]. All these devices can be grouped as linear systems where

the applied voltage is clearly the manipulated variable. This external voltage essentially changes the flow direction of suspended cells or droplets by either using their inherent polarity or hydrodynamics of carrier fluid. The on-off controllers employed in such systems seem to suffice, but more precise and reliable control can be achieved by using error-based controllers such as PID. This would, of course, require a thorough study on actuator's influence on flow hydrodynamics on a continuous time scale. Additionally, one would need to handle the nonlinearity hence imposed on the system.

Manifesting electrical actuators to study reaction kinetics in microchannels have been proved useful. Hans et al. used a metal electrode to measure the enzymatic kinetics of hydrogen peroxide (H_2O_2). The electrodes were strategically placed in the channel so that the microbubble creates a signal as soon as it touches both the electrodes. A calibration curve of H_2O_2 concentration vs electric signal strength was used to derive the concentration variation during the actual reaction. The data obtained were used to successfully derive Michaelis-Menten kinetics of H_2O_2 . The major highlights of this work were low sample consumption (less than 50 μL), no fluorescence tagging was required, and ease in fabricating microfluidic channel with integrated electrochemical sensor [13, 14]. The inherent electrochemical property of hydrogen peroxide simplified the study. Similar studies on neutral molecules such as protein and organic compounds would require additional techniques such as inducing conductivity or polarity into the molecules. Metal electrodes are commonly used in electrochemical detection techniques but suffer from fouling and narrow potential range. Suea-Ngam et al. used carbon paste electrodes (CPEs), first of its kind, integrated on their microfluidic chip to detect dopamine (DA) and ascorbic acid (AA) in intravenous drugs. The authors determined the optimum voltage, droplet size, and total flow rate for the detection of these components in a micro bubble using their standard solutions. The detection limit in this technique was 20 μM requiring a small working area of 0.25 mm^2 . The percentage errors in detection of DA in upamine, domine-250, and dopamax were 0.9, 1.69, and 1.46, respectively. The same for the detection of AA in ascorbic acid was 2.86 [15, 16]. The microfluidic platform resulted in a very high detection limit of the components with small errors when compared to existing batch processes. The low concentration of DA and AA (0.1 M each) in aqueous phase retained its polarity, and hence electric signals could be generated when these microbubbles came in contact with CPEs. As long as the samples are dilute, the electric detection techniques are fast and reliable. The detection technique alone is good enough to achieve the objectives of aforementioned work. These techniques can, however, be coupled with simple controllers to attain the additional purpose. For example, in reaction kinetic study a controller can extend the reaction time when hydrogen peroxide concentration is too low to be detected.

Fast and reliable electric actuation can also be achieved by electrowetting techniques. This kind of actuation uses polarizable and conductive microdroplets as an electrode to complete a circuit with a counter electrode powered by an external voltage source. In one such study, the authors first designed microchips with various configurations of electrodes and insulators. Finally, they demonstrated the

dependence of applied voltage to droplet's velocity. The average velocity of more than 10 cm/s could be achieved for a voltage range of 15–100 V. A threshold voltage has to be exceeded for droplets to start moving indicating a delay or lag in actuation time [15–17]. There are two important deductions in this work. First, the external voltage depends on the average linear velocity of the micro-droplets for different proportional scaling of electrode pitch, gap spacing, and droplet volume. The plots indicated nonlinear trends. Second, the velocity and displacement against time are also nonlinear. The inherent nonlinearity can further be complicated by implementing controllers in such devices. A suitable linear approximation can simplify the control problem where applied voltage can be used as a manipulated variable. As for the control variables, either of velocity and displacement can be chosen based on one's need.

Electrowetting can not only control droplets position but also its size at the point of generation. Link et al. [11] fabricated a microfluidic device to precisely control the droplet size at the point of its generation. The usual infusion methods use the interfacial tension between water and oil to form droplets, but the size of the drops cannot be controlled precisely. This work demonstrated that electrowetting techniques can help overcome this limitation. The external voltage applied to the electrodes fabricated within the device creates an electric field. This field capacitively charges oil and water interface and the water droplet is thus formed. This work clearly deduces the dependence of droplet size on applied voltage. At a constant water infusion rate of 20 nL/s, decreasing profiles of droplet sizes vs voltage applied were obtained for three different infusion rates of oil (80, 110, and 140 nL/s). Further, oppositely charged water droplets were fused together under similar device configurations [16, 17].

Controlling droplet size is not enough unless a uniform droplet size or volume can be obtained throughout the process. Bransky et al. created such uniform droplets (less than 3% deviation from average size) using a controllable piezoelectric actuator integrated on their microfluidic device. A cross and a T-junction with water and oil reservoirs (placed at a fixed height) were used separately to create droplets. The piezoelectric actuator was inserted into the PDMS device such that it rested a little away from the membrane. The external voltage amplitude of the actuator ranged from 30 to 120 V changing the droplet volume linearly from 260 to 950 pL [18, 19]. The linearity in applied voltage and droplet size ($R^2 = 0.993$) calls for a feedback control system for precise on-demand droplet generation of desired size or volume. The droplet size can be a controlled variable, while the voltage can be manipulated to move the actuator and hence the membrane at the oil and aqueous phase junction.

4.1.2 Optical

Optical means are popular in microfluidic manipulation and are mostly used as sensors. Since this field is still at experimentation level, an optical microscope attached to a CCD camera is an affordable and reliable sensor. Researchers integrate various techniques to improve the detection limit as summarized in the following paragraphs.

A high-end optical detection method using a confocal microscope, mirrors, and optical fibers was set up with the microfluidic channel to separate *E. coli* expressing R-phycoerythrin. The setup consisted of Ar ion laser, two dichroic mirror filters, optical fibers, band pass filters, avalanche photodiodes, and a pulse divider. The laser coupled into the microscope using dichroic filter excited the fluorescent cells. The light collected by objective was split into green and red spectral parts and directed into respective entrance slits by optical fibers. Additional band pass filters in these fibers ensured enhanced detection and suppression of background light. The signals were detected by avalanche photodiodes and split by a pulse divider for one part to reach the analyzer while the other reached the hardware processor which automatically controlled the sorting [12]. The use of filters at strategic positions ensured a high signal to noise ratio and hence a reliable detection system. However, the instrumentation is expensive and not portable from a commercial point of view. A laser-induced fluorescence detection was used by Cao et al. to sort encapsulated particles using a solenoid valve. A set of neutral density filters adjusted the intensity of laser beams focused on the channel. A dichroic beam splitter reflected them into the objective. Spectral filters improved the quality of fluorescent emission collected by the same objective. The lights collected were then converted into electrical signals using a PMT equipped with a low noise current preamplifier. A differential comparator processed the signal and fed it to a microcontroller [18, 19]. This technique uses similar working principles with more precise results but is limited to laboratory experiments.

Most optical sensing systems suffer from propagation loss within the channel. A high-intensity beam is a solution, but it is a challenge to determine an optimal intensity to excite living cells without incurred damage. Cho et al. coated the walls of their microfluidic cell sorter with amorphous Teflon. This not only created a waveguide during laser excitation of the mammalian cells, it ensured an optimum intensity to brighten the cell without any mutilation. The fluorescence thus emitted is collected by a microscope objective. The signals are then filtered consecutively by spatial and optical filters before entering a photomultiplier tube (PMT). The fluorescence signals when modulated by this spatial filter register different waveforms on PMT corresponding to different locations of the cells through the channel and thus tracking their path. The output from PMT is fed to a real-time control processor embedded with field programmable gate array (FPGA) which automates the mammalian cell sorting [20]. Microfluidic-based mammalian cell sorting imposes challenges such as high throughput, purity, and recovery of unstressed cells. HeLa, a kind of mammalian cells which express a fused histogen-green fluorescent protein, was sorted rapidly using optical switch control overcoming the above difficulties. The sorting device consists of a three-way microfluidic network (input, waste, and collection channels), a near-infrared laser for an optical switch, a visible wavelength laser for detection, and fluorescence measurement. The infrared laser deflects the detected cells to the collection channels using laser beams. The laser-on or response time of this device ranges from 2 to 4 ms with varying cell density in the input channel. The throughput ranges from 23 to 106 cells per second with purity as high as 98.5%. The total sorting time varied from 9 to 44 min [21]. Living cells are

delicate and can easily be damaged during analysis or experiments. The actuation by optical means other than being fast and reliable can be applied without distorting living cells.

Optical detection techniques are highly advantageous for monitoring microscale reactions for a simple reason that light can penetrate these devices easily. Lignos et al. manufactured lead sulfide (PbS) and lead selenide (PbSe) nanocrystals (NCs) in a droplet microfluidic system integrated with real-time detection to map the chemical reactions. The droplets exiting the channel after the reaction were optically excited using light emitting diodes (LED). The fluorescence spectra from individual droplets were then measured using a fiber-based spectrometer. The authors summarize the variations in the droplet spectra as the initial conditions such as substrate ratio, temperature, and residence time changes [22]. The inferences from these spectral emissions can be analyzed to make suitable control algorithms. The control techniques can drastically improve upon the reaction kinetics and hence the required product composition. A paper by Krishnadasan et al. formulated a control algorithm for the synthesis of nano-cadmium selenide (CdSe) QCs using microfluidic channels. The reacting particles in the channel were ignited using laser and the fluorescent spectra thus emitted were monitored using a CCD spectrometer. The data from variations in the emission spectra with a change in temperature and substrate injection rates were utilized to form a control algorithm which can drive the reaction to the desired product composition and size [23]. Maceiczky and Demello suggested an on-demand synthesis of QCs (CdSe and CdSeTe) using similar optical detection system. They used the data from emission spectra of the reacting particles to formulate a model-based algorithm using Universal Kriging [24]. All these novel algorithms are yet to be visualized through experiments. Nevertheless, these spectral data can be used to predict reaction conditions in a microchannel without the need of setting the sensor up every time a QC is manufactured.

The online detection in nanomaterial manufacturing simplifies the kinetic studies for microscale reactions occurring in microchannels. The mode of detection can be photothermal, fluorescence, or absorbance spectroscopy depending on the sensitivity requirement for a given reaction. All of these methods give a comprehensive idea on the shape, size, and chemical composition of the formed nanoparticle [25, 26].

4.1.3 Pressure

Pressure actuation in microfluidic devices is brought about by using integrated or external valves. The opening and closing of these valves are operated through a vacuum or inert gas inlets. The following paragraphs bring together works that have used pressure actuation in manipulating droplets in the microchannel.

Sorting and trapping of EGFP fractions from pNB estrange (two different expressions of *E. coli* bacteria) were accomplished using pressure controlled mechanical valves. These valves were integrated on a T-shaped microfluidic channel using multilayer soft lithography techniques. An algorithm controlled the opening and closing of a set of five valves (three peristaltic and two switches) for trapping and reverse sorting. The valves responded in 5 microseconds. The recovery rate of EGFP fraction varied from 16% to 50% consuming 2 to 3 h [26]. The relation between the

cell velocity (control variable) and pump frequency (manipulated variable) is linear. Here, the valves are operated by an on and off the controller. An advanced controller such as PID can smoothly open and close the valves to control the cell's velocity with more precision, hence improving the sorting time and rate. Integration of such complex control system into the microfluidic channel is an area if explored can unlock new paradigms.

The sorting of living cells with no damage was achieved using pressure actuation. The system consists of a fluorescence detection method, a sorting microfluidic channel and an actuation channel. The dynamics of the flow in actuation channel is controlled by a solenoid valve. As soon as the desired cell is detected, the solenoid valves open, pushing the fluid in the actuation channel toward the collection channel. The cells move toward the waste channel by default due to its shorter length. This system has a sorting frequency as high as 50 Hz with 1 ms response time of the valve. The living cells could be sorted with a throughput of 30 cells per seconds with collection percentage of 93.7% [19]. Despite following an off-chip actuation system, the response time was very high. The clear reason behind that is having a separate detection and actuation channel in the device. That way, the cells and the particles are studied and manipulated individually. This will increase the overall sorting time, but the purity in sorting is very high as demonstrated. The feedback control used here is an on and off the system. A more complex control system can give better output in terms of manipulating cell's location. This, of course, would require a thorough study on the effects of applied pressure on flow hydrodynamics in the microchannel.

Steering of droplets in microchannels using an integrated valve in the single layered device can make microfluidic applications simpler. Abate and Weitz characterized such device relating the actuation pressure to the average flow velocity of droplets. Apparently, the linear relationship between the two indicates a simplified control problem. The actuator here was a membrane valve which is essentially a T-shaped channel placed perpendicular to one of the two branches to the main inlet. This membrane expands on the application of external pressure and blocks the branch which in turn changes its hydrodynamic resistances. This makes the droplets flow into the other branch [27]. The actuator response time, although not studied, would be low enough to build a feedback control for this problem. It can be a single input single output system with actuation pressure as manipulating variable and velocity of exiting droplets as control variables. The quantification of membrane contraction or expansion with varying actuation pressure would be an essential requirement.

The usual technique to generate droplet is to use an external device to pump oil and aqueous phase through channels. The surface tension between the two phases forms droplets at the junction. A 2009 work by Zeng et al. uses an integrated valve on T-shaped microchannel to generate droplets on demand. The aqueous and the oil phase flow under negative pressure applied at the end of the channel. The valve, placed at aqueous phase inlet, when closed, the water flow cuts off and a droplet is formed immediately at the T-junction. The response time of the microvalve (50 to 500 ms) is varied to decide on the optimum droplet size and volume (1.3 to 13.3 nL). The authors successfully show the linear dependence of microvalve open/response

time to the droplet size. Further, they create and fuse multiple droplets by extending the number of channels and valves [28]. The objective of this device here is to generate droplets on-demand by solely changing the opening of the microvalve. The relation between the valve opening time and the droplet size is linear, which means the system can be approximated to a first-order linear system. The actuation time here is represented in terms of the time it is taken by a valve to open completely which is at least 50 ms. It is then varied to understand the relationship between droplet size measured as its volume. It can be considered to be a step input system with an output represented by droplet size and the manipulated variable being the actuation time or valve opening itself.

4.1.4 Magnetic

Magnetic actuation in spatiotemporal control of droplets is an area less explored when compared to other techniques. The related works, although few, are promising from automation and control perspective and are summarized below.

Di-electrophoresis (electric manipulation of biological cells) is known to denature the cells to some extent. Lee et al. hence used electronically controlled magnetic field to spatially control the movement of bovine capillary endothelial cells (BCE). Their device consists of the distribution of micro-coils over a microfluidic channel connected to an integrated circuit (IC). This IC supplies current and controls the magnetic fields by activating the micro-coils (one at a time) to move the microfluidic bubbles to the desired location. At a single magnetic peak intensity of 15G, BCE containing magnetic beads could be trapped at the force of 50pN. It moved to a different location with an average speed of 6 $\mu\text{m/s}$ by subsequent switching of alternate magnetic coils [29]. The writer demonstrated an excellent example of an integrated device which can single-handedly manipulate particle location in a micro-channel. Although the experiment was carried only for discrete movement of droplets, it can be extended for a continuous flow with real-time integrated control. It will require a detailed study on how the magnetic force (manipulated variable) affects the droplet position (controlled variable).

Manipulating cells in channels with precision and control is a sought after field for the wide range of applications it covers. Magnetic manipulation of fluids for splitting, exchange, trapping, and demulsification was achieved by Zhang et al. by using hydrophobic ferrofluid as a continuous phase in their microchannels. Magnets of size ranging from 1 to 3 mm were used to create magnetic fields. The change in effective magnetic field gradient broke the droplets in the main channel into three different ones which moved along the three branches. The ferrofluid not only acted as a hydrophobic continuous phase but also directed the droplet motion as its hydrodynamic changed with external magnetic field. Further, they demonstrated trap and release of water droplets in another device containing microwells. These wells stored the droplets when the ferrofluid repelled from the external magnetic field and released them when the external magnetic field repelled the fluid in wells [30]. This magnetic droplet merging, splitting, and trapping system can be made efficient and precise by implementing control techniques. The fluid motion actuating magnetic field can serve as a manipulative variable, while the interactive magnetic

force between the fluid and external field can be the control variable. This force plays a major role in droplet motion, thus a mathematical relation between the two would be essential to design control techniques.

4.1.5 A Comparative Study on Actuators

Optical detection methods are widely used in various application of microfluidics. The reason behind the same is a demand for high-speed detection systems of droplets of nano- and microscale sizes. The optical detection systems although following the same working principles can still be categorized based on the methodologies and excitation sources. It can either be on-chip meaning the sensor is integrated into the device or off-chip where a sensor is connected to the device. The detection technique in both on- and off-chip sensors can be classified into fluorescence, absorbance, laser-induced fluorescence (LIF), and chemiluminescence. Each of these techniques can be coupled with devices such as optical fibers, CCD cameras, or photomultiplier tubes (PMT) in an off-chip approach. On the other hand, waveguides, CMOS imager, or photodetectors are integrated on the device in an on-chip approach. Despite all the advances, these techniques have detection limits on practical time scale [10, 11]. Both on- and off-chip approaches are utilized in the spatiotemporal control of droplets. Synthesis of nanomaterials such as quantum dots is best monitored by optical means for the need of quick detection of the high-speed reactions. Algorithms to control nanomaterial manufacture in microchannels have been suggested based on the radiation emitted by the reacting particles as summarized under Sect. 4.1.1 of this chapter. However, active control using actuators is not yet studied in the literature. Actuators can be used in microchannels to precisely control reaction rates and microreactor (droplets) size to achieve desired nanomaterial structures with high accuracy.

The electric means are the most popular actuation techniques in droplet microfluidic owing to the high processing speed. Although in an application such as cell sorting that involves living bacterial or mammalian cell, pressure and magnetic actuations are a better choice over electrical to prevent cell deterioration. Electric actuation and optical detection are also favored in studying rapid kinetics over other techniques because the molecule under study exhibits polarizing property or is soluble in water. The same technique would not help kinetic study nonpolarizable or water insoluble compounds. More techniques are yet to be explored in this area.

Pressure and magnetic actuation systems are less explored when compared to electric and optical systems. Both on- and off-chip systems require external instrumentation which adds to the cost and reduces portability. Besides, the processing speed in such actuations is relatively low.

4.2 Fabrication

Since the standardization of microfluidic device fabrication [31], soft lithography has branched into many techniques to suit various applications. For instance, integrating micro sensors and actuators into devices has added new protocols to the classical

methods of fabrications. The devices designed vary in their fabrication methods. In the field of automation and control, the fabrication methods are broadly classified into the following.

4.2.1 Single Layer Soft Lithography

Soft lithography is widely used in fabricating microfluidic channels because of the ease in prototyping and handling. A transparency of the desired channel design is patterned on a spin-coated (with photoresist) silicon wafer using UV rays. This wafer (now called master) is covered with polydimethylsiloxane (PDMS) and cured in an oven at desired temperature. The mold hence formed is irreversibly bonded to a glass substrate. The microchannels are now ready for experiments. Single layered devices can be further categorized into those with or without integrated features. These additional features on the devices can be either *in situ*, meaning integrated into the channels, or *ex situ*, meaning connected to channels externally.

4.2.2 Ex Situ Features

In *ex situ* features, the channels are designed to have a simple additional channel or a reservoir to bring about actuation and detection from an external source. The dimensions of these features, although not optimized, are chosen to give the best actuation and detection speed.

The work by Dittrich and Schuille (2003) demonstrated how polarity switching can sort fluorescent cells in a T-shaped microchannel. They achieved a high sorting rate by inserting external electrodes at the junction of waste and collection channels. The additional feature on the channel was reservoirs. These reservoirs were punched before bonding to the glass slide and were used for inserting the external electrode wires. An electric controller connected to these wires changed the polarity as and when desired [12]. Another high-speed cell sorting using external solenoid valves was achieved by Cao et al. In addition to the inlets for water and oil, the device had an interrogation (23 μm wide) and actuation channels (80 μm wide and 2 mm long). The fluid flow in the actuation channel was controlled by the external valve, while the interrogation channel was used to observe the bubbles to be sorted [19]. Lignos et al. synthesized and observed semiconductor nanocrystals by adding an additional channel to their device. A three-channel inlet (for lead, sulfur, and carrier oil) was connected to an outlet. The outlet channel was continued to a heating zone where the reaction occurred, seen by a rapid color change in droplets. A channel free from oil (carrier fluid) followed the heating zone where the drops were excited by a light emitting diode (LED). The fluorescence spectra from individual droplets are measured through a fiber-based spectrometer to study the reaction kinetics.

4.2.3 In Situ (Integrated) Features

To achieve an objective, for instance, to control sorting of droplets, the additional feature in the microchannel can be integrated on the device itself in the form of valves or membranes. The actuation and detection speed gets improved. The device gets more portable eliminating the need for external devices.

The work by Zhang et al. achieved manipulation and collection of droplets using magnetic blocks of portable sizes (1 to 3 mm long). These blocks manipulated the carrier fluid containing magnetic nanoparticles and the flow hydrodynamics. The aqueous droplets under the influence of the flow could be relocated, split, trapped, and demulsified within the channel [30]. Zeng et al. used a T-shaped channel integrated with a microvalve to control droplet generation, size, composition, and their fusion. This pneumatic microvalve was constructed at the opening of the oil phase inlet. The flow of the oil and aqueous phase was controlled by regulating the pressure in evacuated bottles attached at the end reservoirs of the channels [28]. A flexible elastomeric membrane integrated on the device in a single layer adds to the many advantages of single layer soft lithography. The device consists of a main channel and a T-shaped control channel placed 13 μm apart. The fluid entering the control channel inlet compresses the main channel to change its hydrodynamic resistance and thus the velocity of the fluid in it changes [26, 27].

4.2.4 Double-Layer Soft Lithography

The devices in this technique are formed by bonding two layers of PDMS molds irreversibly first with each other and then on a glass substrate. Each layer has its own function to perform. Double-layered microfluidic channels almost always have integrated features that lead to either actuation or detection functionalities in them. Such features in spatiotemporal control of droplets are summarized below.

Fu et al. devised a control layer to integrate valves and pumps into their device. The channels meant for sorting cells were constructed on a different layer called fluidic layer. Control layer consisted of multiple lines ending with valves. The closing and opening of the valves were actuated by the flow of pressurized nitrogen and vacuum, respectively. The whole cell sorting process was automated by digitally controlling the valves through a fast Zener-diode circuit [26]. The pneumatic control setup was fabricated as previously described [32]. Guo et al. used the similar double-layered device to create a droplet on demand assay. The control layer is a set of single-layered microfluidic channels that ends with a valve at the crossing points of channels in liquid layer. The valves are actuated by compressed air with pressure around 400 kPa. This pressure is provided by electronic solenoid valves under the control of data acquisition module [33].

4.2.5 A Comparative Study on Fabrication Techniques

Integrated (in situ) features for actuation or detection are always at advantage over ex situ categories in both single- and double-layered microchannels due to their ease of handling and operation. The only advantage of a single-layered in situ feature over double layer is the less time consumed in fabrication. But as the system gets more complicated to handle more than two control functions, another layer to control the actuation device is desirable over single-layered in situ devices. As more researchers have progressed toward in situ features, there are many areas still unexplored. For example, the dimensions of these additional features are not optimized for their function. A fully automated detection-actuation-controller microfluidic system to control the position and velocity of droplets is yet to be invented.

Researchers are increasingly using droplet-based microfluidics-based systems for diagnosis (biomedical devices), reaction analysis, discovery of drugs, droplet-based display, and identification of cells. A lot of these applications require sorting or screening of droplets/cells, synchronization of droplets, and sometimes segregating and storing droplets. Though many passive techniques exist to control droplets, some applications need active control strategies using a sensor, a controller, and an actuator. In addition to the challenges involved in fabricating a droplet-based device, designing an active control system to improve the applications of droplet systems is a field on its own. Spatiotemporal dynamics of droplets in microfluidic networks can be quite complex to model and control as droplets have shown to exhibit interesting nonlinear dynamics in networks [34]. In the following sections, we describe and discuss the various controllers and their applications in digital microfluidics.

4.3 Multilayer Microfluidic Devices(MMD) and Integration with Silicon Layer

Multilayer microfluidic devices have been explored and demonstrated for applications that need more functionality than one layer can deliver, including organ on a chip [35, 36], devices needing more sophisticated structures like valves, pumps, etc. Techniques like anodic bonding, 3D printing and 3D printing with pattern transfer (printed transfer molding) [37, 38], adhesive bonding [39, 40], etc. have been employed to achieve multilayer devices of reasonable complexity. Often times these multilayer PDMS/glass/PMMA microfluidics have also been coupled with silicon layer to leverage the precision electronics (sensors, LEDs, etc.) semiconductor manufacturing can deliver [41, 42]. Silicon layers can include optical detectors, electrical/electrochemical sensors, LED and laser light sources, amplifiers, ADCs, noise filters, and signal processing elements [43, 44].

4.4 Controllers

A controller achieves an objective, usually maintaining a set point, with the help of sensors and actuators; process model present in the controller or a real-time model predictor enables a controller to adjust certain variables in order to achieve zero error situation. There are controllers that operate without any sensors or actuators such as open-loop controllers; they continue to operate autonomously without observing the state of the process. While there are controllers that compute the actions, on a limited frequency, based on the current state of the process or the predicted effect of disturbances, such as feedback and feedforward controllers.

In a microfluidic device that transports confined droplets, a feedback of the implemented controller action benefits the controller's ability to predict and correct future errors with precision. Feedback controllers such as proportional-integral-derivative (PID) and model predictive control (MPC) are powerful controllers that can take on complex tasks such as spatiotemporal control of droplets. Figure 9.2a, b,

and **c** illustrate the instances where an open-loop, on off, and MPC controllers can be used in microfluidic devices that involve droplet control. A controller operating based on changes in set-point is said to solve a servo problem, while a controller maintaining a set-point despite the process disturbances is said to solve a regulatory problem.

The first step in designing a controller is identifying the process inputs and outputs and modeling their dynamic behavior. In a feedback controller, controller input is the dynamic process output/state that is monitored to gauge the quality of the process, for example, droplet position, color, and volume. The controller inputs are usually referred to as control variables (CV). The input is compared with the set-point to compute the error. Controller output is the change in process input necessary to attain zero error in the process. The controller calculates it based on the dynamic process model and the error computed from the process; typical examples of controller output in a microfluidic device are change in inlet flow rate of oil and change in voltage to electrodes. We refer to controller inputs as control variables (CV) and outputs as manipulated variables (MV).

A mathematical model of process dynamics forms the basis of relation between controller input and output. Process models are developed based on the choice of control variables in the system. Hagen-Poiseuille law relating pressure drop and flow rate in a pipe is an example of a process model that can be used to control pressure drop in a channel by manipulating the flow rate.

Models used in droplet microfluidics involve variables (inlet flow rate, inlet pressure, inlet sequence) and parameters (length of channel, viscosity of fluid, density of fluid) that determine outputs like droplet traffic, droplet sizes, droplet positions, droplet velocity, etc.

4.4.1 Classification of Controllers

Controllers are either open loop or closed loop based on their nature of interaction with the system. An open-loop controller that is autonomous in nature does not keep track of the consequences of its control action, while a feedback controller continuously monitors the CVs for feedback on its control actions. A feed forward controller on the other hand predicts the effect of disturbances on a process before they are realized, to make control actions.

Open-Loop Controllers

Controllers that operate without feedback from a process are open-loop controllers. The decisions by an open-loop controller are completely independent of the current state of the process. These controllers are capable of solving simple and repetitive tasks. The processes involving uncertainty and complex dynamics cannot be controlled with these kinds of autonomous controllers.

In droplet microfluidics, droplet sorting based on charge does not require feedback. Link et al. [16, 17] have demonstrated the use of the electric field as an open-loop controller to sort positively charged droplets from the other droplets. This control method offers a lot of flexibility and speed as it involves switching electric field without moving parts and a very simple control logic. The large forces that can

be applied to a droplet make this technique robust for sorting of charged droplets. Neutral droplets could also be charged and controlled using this method [16]. Figure 9.3 shows sorting of positively charged droplets to one branch of a microfluidic network using the electric field.

Feedback Controllers

A controller that operates based on feedback from the process is a feedback controller. These controllers can monitor the process changes in the presence of disturbances and adjust the process inputs to maintain the CV at a set point. Feedback controller needs sensors that can continuously send data on the CV or on a state of the system that can help determine CV.

Feedback controllers are classified into proportional, integral, derivative, and model predictive controllers based on the nature of their control action. All of these controllers take action based on the process model and the control variable involved in the decision. Automation in chemical process plants has led to the development of these controllers, and through control researchers, they have found their way into digital microfluidics. We describe the nature and applications of these controllers under the coming sections.

Proportional Integral and Derivative Control (PID)

Proportional controllers increase or decrease the process input proportionally with the error in process output. Proportional controllers are easy to implement; however, they carry an unavoidable offset. For processes that require precise control, proportional integral controllers remove this offset by adding an integral time constant to the model. Most often PI controllers are enough to achieve control over processes,

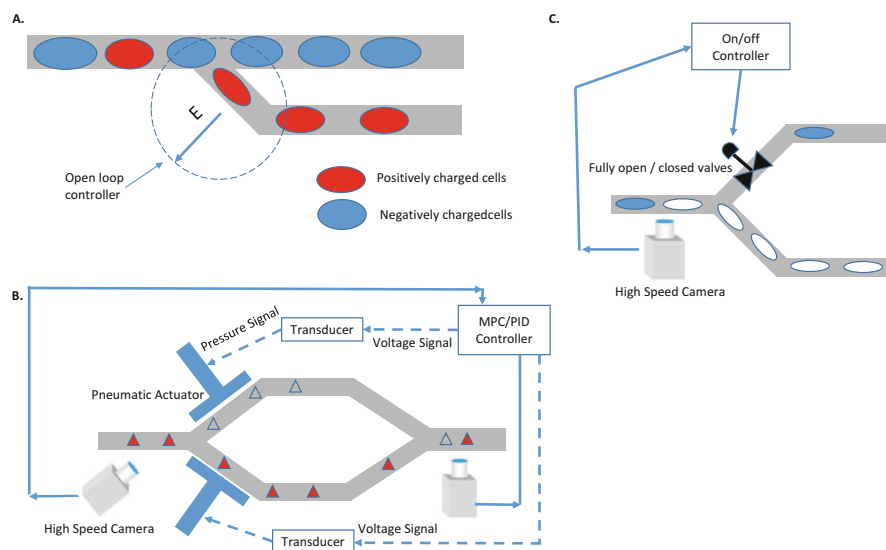


Fig. 9.3 A basic controller classification

while some processes have strict limits on oscillations in output where a derivative action is added to predict the error in advance and stabilize the process.

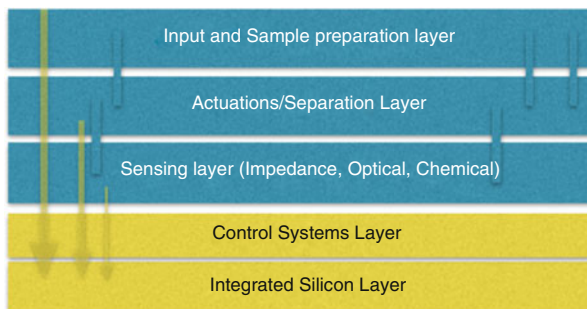
Feedback controllers have found some interesting applications in microfluidics. They are employed for precise droplet generation, fusion, and splitting. The dynamics of droplet transport in microfluidic networks presents a challenge in the selection and design of the controller.

All electronic droplet generation without moving parts uses feedback control to produce droplets of various sizes synchronously without a syringe. All electronic droplets generation performed using electrowetting on dielectric (EWOD) was demonstrated by Jian et al. in the year 2008 [45].

The droplet volume was continuously measured through capacitance, a technique established by Fair et al. The feedback of droplet volume is used to control the voltage across two sites. The error between the target capacitance and the real-time capacitance is minimized using a proportional-integral-derivative (PID) controller to achieve the generation of a droplet of the desired volume in the creation site. Figure 9.4a is a representation of the feedback process that was used in their work to generate small daughter droplets from a mother droplet in a reservoir. In this work, the hardware was designed to update the voltage outputs and measure droplet volume as fast as 1 ms in order to achieve actuation and sensing criteria for less than 1% volume control precision for a 225 nl droplet. A proportional controller could solve the problem very well but the oscillations in droplet volume, once the droplet is generated, is better controlled through the derivative action and the error accumulation due to capillary forces are dealt with the integral action of the PID controller. An error of less than 4% in the final droplet volume has been reported in the literature for this technique [46].

PI controllers are also used to control droplet lengths to produce droplets of various volumes in a T-junction. Flow rate ratio of continuous and dispersed phase is linearly related to the length of the droplet formed in the T-junction at a low capillary number ($C_a \leq 0.1$). PI controller implemented with this model that predicts the droplet size from the flow ratio achieved precisely controlled droplet generation; however, the control speed was limited by the speed of image processing [47], a classic example of sensors limiting the efficiency of the control system.

Fig. 9.4 Integrated microfluidic platform layers



Another example of PID controllers in droplet microfluidics is the spatiotemporal control of droplets with feedback. Improved stability and precision control are some of the benefits offered through these controllers. Yoko Abe et al. have demonstrated the use of feedback-based spatial control of droplets in a device filled with electro-conjugate fluid (ECF). ECF generates a powerful flow (ECF flow) when a high voltage is applied across a pair of electrodes in the device. The position of the droplet is sensed through image processing technique, and the controller decides the next voltage signal to drive the droplet closer to the target position. Closer the droplet to the target position, lesser the voltage applied to ECF. The block diagram in Fig. 9.4b captures the essence of control algorithms used in the device. The position is measured as a function of a pixel in the “x” coordinate (x_c) and compared along with the target coordinate (x_t). The error (ϵ) decides the voltage to be applied between the electrode pairs to move the droplets [48]. Image processing speed/optical detection limits the speed of the applied control technique. On-chip integration makes control easier with just the sensor as an external device.

Model Predictive Control (MPC)

Mathematical models describing the dynamic behavior of processes are nonlinear in nature. Yet, for the design of PID controllers, they are linearized around their target value introducing errors in control action. Though these errors are tolerable in most of the processes, some operations like spatiotemporal control of droplets require the use of nonlinear models to achieve precise control.

Model predictive controller also works on nonlinear models, optimizing the input values needed to achieve minimum error taking into account all practical constraints. Most of the practical constraints such as sampling time and actuator limitations are accounted as constraints in an optimization algorithm to find the best actuation/control moves that can minimize the process error. MPC can handle multiple PIDs, processes with MIMO type models, and multiple disturbances. It is the complexity of the optimization problem that determines the efficiency of MPC.

Controllers based on MPC use the process model along with constraints to calculate an optimized set of actuations that will minimize the error in process output when implemented. Synchronization of droplets is an example of a nonlinear problem in digital microfluidics. Droplet synchronization calls for feedback and continuous actuation of the valves or other actuators. Maddala et al. [47] have simulated the use of MPC-based control algorithm for sort-synchronization of droplets in a microfluidic loop. Droplet positions are sensed through a high-speed camera, and optimal valve actuations are determined that will synchronize droplets at the outlet of the channel. Each time when an input is received, a new set of optimal actuations are determined and the first of them is implemented.

There are not enough applications of MPC in digital microfluidics. This type of controller in digital microfluidics can tackle the highly nonlinear and complex models observed in this field and can be seen as an opportunity for control researchers.

Fuzzy Logic Control

Fuzzy controllers are unique in the way they process the inputs received from the process. Unlike the other feedback controllers they do not have a process model that they use to determine the best manipulated variable. Instead they work very similar to the human operators in an industry. Fuzzy logic needs a well-defined table of outputs and inputs and some classification into different sets based on process need. They have fuzzification, processing, and defuzzification stages before they decide on the precise action to be implemented. In fuzzification, the input values are converted to linguistic terms such as high, low, cool, hot, etc., based on predefined sets in those names. Then they are processed to identify the corresponding fuzzy output such as increase the speed or decrease the flow rate, etc., to be applied to the process. In the end the output is defuzzified to a crisp output value that is applied to the process. They are very popular in the field of robotics where the encountered models are highly nonlinear. Fuzzy control logic works based on experience and heuristics. An unknown process cannot be handled with a fuzzy logic. Fuzzy controllers are referred to as intelligent controllers because of the way they process the inputs.

Fuzzy control has been used to control a pneumatic pump to manipulate positions of droplets in a biochip. Yung Chiang Chung et al. [49] have demonstrated the use of fuzzy logic-based controller in improving the extraction efficiency of DNA. The sample and buffer were moved at a necessary rate to achieve improved collision and better reaction efficiency through fuzzy logic-based controller. Jie Gao's [49, 50, 51] work on multi-droplet manipulation, moving, merging, and chasing using electro-wetting and fuzzy logic-based feedback controller is another example of how fuzzy logic could be exploited to improve the applications of lab-on-chip technologies in the future.

4.4.2 Optimization

Optimization is the process of minimizing or maximizing an objective function within the defined constraints and few variables to manipulate. The variables that are allowed to change are decision variables whose choices will determine the best value of the objective function. In synchronizing droplets, exit time difference is the objective function, actuator speed the constraint, and the actuator positions as the decision variables. Optimization is also used in designing complex microfluidic networks to achieve a predefined objective such as combinatorial chemistry [52–54].

Complex nonlinear models like spatiotemporal dynamics of droplets need fast and reliable optimization techniques and call for the use of powerful controllers like MPC. Each droplet makes discrete decisions in a continuous flow system. Synchronizing droplets to form patterns then becomes a mixed integer nonlinear programming (MINLP) problem. Optimization of MINLP systems within a small period (time) available before a droplet makes the decision forms a key challenge in the application of MPC in real time. Maddala et al. [47] have shown that an optimization technique coupled with MPC could theoretically alter the spatiotemporal dynamics of droplets in a microfluidic device.

5 Key Research Findings

5.1 Whole Blood Analysis

Blood is a complex biological fluid comprising cellular components suspended in protein-rich plasma. These components including WBCs, RBCs, platelets, cell-free nucleic acids, exosomes, proteins, lactase, glucose, antibodies, other biomarkers [55, 56], and rare cells like circulating tumor cells (CTCs) [57], circulating mesenchymal cells (CMCs), circulating endothelial cells (CECs), and putative circulating stem cells (CSCs) perform distinct functions *in vivo*, and their enumeration and enrichment have been of enormous significance to clinical diagnosis and biological research as they are known to reflect the physiological state of the person, disease progression, and development of resistance to therapy [58]. Due to this and its 2 h *in vitro* half-life as a fluid, innumerable microfluidic studies have been published on blood with focus on study of one or more of these components as biomarkers for a particular use case. Microfluidic platforms have been used on blood samples for real-time cell enumeration and differentiation using optical sensors (imaging, scatter, FACS-style [59], spectroscopic, SERS [60], SPR) [10, 61] and electromagnetic sensors (resistive, capacitive, magnetic, electrochemical, piezoelectric, micromechanical, faradic) [62–70]. This classification information is also used to initiate cell separation/enrichment within the microfluidic devices using a variety of approaches including flow shaping [71, 72], pressure driven [73, 74], dielectric [71, 75], magnetic [76, 77], optical trapping [78–83], etc. Beyond these real-time cell level analysis technologies, many microfluidic technologies have been developed to perform blood-based analysis that need short incubation/processing times needed for applications like signal amplification and detection methods, including PCR, immunoassays [69, 84], biosensors, and cell/platelet activation/drug response [85–89] studies which provide further insights.

Here we envision a multilayer microfluidic device coupled with a silicon sensing layer with integrated real-time computation for simultaneous tracking of the largest feasible set of biomarkers/sensors with the hypothesis that multiparameter parallel data collection could lead to novel insights that are otherwise masked. The hypothesis draws strength from advanced semiconductor manufacturing technology that could deliver a single system-on-a-chip with integrated components including arrays of image sensors, solid state LED/photodetectors, precise electromagnetic components for measurement, amplification, noise-filtering, ADC, and signal processing, as well as direct integration into onboard CPU/GPU/FPGA/VPU for lossless real-time analysis coupled with the versatility of microfluidic platforms that can prepare and deliver the sample of interest to the sensors at the sensing layer.

In the use case of blood analysis, this would allow for simultaneous measurement of glucose, cell counts, and cell/platelet differentiation based on optical imaging [59], differentiation based on autofluorescence and fluorescence [69, 90–92], differentiation based on light scatter, light absorbance, electrical impedance [69], capacitance, blood plasma and cell lysate analysis for proteins [88], antibody and cell-free nucleic acids characterization through electrochemical analysis, surface plasmon resonance (SPR) [93, 94], surface-enhanced Raman scattering (SERS), on-chip spectroscopy [95, 96],

magnetic susceptibility, dielectrophoretic susceptibility, faradic catalytic amplification, and biosensors. Most of the external components not integrated into the microfluidic devices used in these analyses have been already implemented in silicon-based semiconductor devices for other commercial applications [61, 63, 85, 97–101]. With all the individual blocks already available and commercially implemented, it would merely be an engineering exercise of systems integration to package them for near-simultaneous measurement of multiple parameters on the same blood sample. We argue that the decision making often tends to be more accurate if we can increase the number of sensors/variables supplied to a system.

The multilayered device proposed would have a fluidic input layer, an actuation/separation layer, an optical sensing layer, an electrical sensing layer, and coupling layer on top of silicon layer [42, 92] with integrated sensors, electronics, optoelectronics, and compute elements. The layers are connected where necessary by: “Via’s” that transport liquids/air from one layer to the other to move the analyte as well as the air necessary for valving [38]; electrical connectors for actuation/pumping and carrying back any additional sensors located outside the silicon layer; and optical waveguides [102] for tunneling light from the LED/laser sources on the silicon layer to the optical sensing layer as well as piping the light from the sample to the optical sensor arrays, photodetectors in the silicon layer. There could also be optical fibers linking layers where integrated waveguides are not adequate/feasible.

The fluidic input layer is the interface for all reagents/analytes [103] necessary for the device to function. It may also include modules for sample preparation [104], amplification, tagging/incubating, partitioning sample components, and waste collection/neutralization. The actuation/separation layer includes the actuators for the valves in the rest of the device as well as additional bulk separation modules to partition blood based on passive or field-based enrichment modules including filters, sieves, micropillars, electric/magnetic fields, etc. [105–108]. The optical sensing layer can include optics and modules to enable imaging flow cytometry and associated cell sorting [82, 109–115]/flow shaping [59, 116, 117], fluorescence activated cell sorting (FACS) [59], surface plasmon resonance (SPR) [93, 94], surface-enhanced Raman scattering (SERS) [118], on-chip spectroscopy [95, 96] that are coupled with the optical sensors in the silicon layer through waveguides and optical fibers. The electrical sensing layer contains modules setup for electromagnetic sensing (resistive, capacitive, magnetic, electrochemical, piezoelectric, micromechanical, faradic) [62–69]. This layer is designed to be closest to the silicon layer for the shortest possible interconnects before reaching the integrated electronics that perform signal amplification, noise filtering, and analog-to-digital conversion completed with minimum latency, losses, and noise associated with traditional setups that rely on off-chip signal processing. The compute layer includes the integrated microprocessors, graphics processors/vision processing units, network interface, and signal processing units that perform data analysis for flow control and classification analysis to generate a comprehensive diagnostic companion analysis for the medic. The compute layer provides real-time decisions to adjust sample preparation, process optimization, enrichment strategy, drug screening plan, and waste neutralization based on results at each

level of analysis. This could provide a customized report for each patient while also doing a multicomponent analysis to identify patterns leading to higher accuracy in diagnosis and medication.

5.2 Organs on Chip

Organs on chip (OOC) is a device that mimics organ level cell behavior in an *in vitro* environment [119, 120]. These devices are fabricated using microfluidic techniques and tissue cells are cultured in them thus mimicking the micro environments of *in vivo* conditions *in vitro*. The process is to grow tissue cells from different parts of the human body, for example, heart, liver, lung, muscle [121], on a PDMS chip to replicate human tissue barriers. The advantage of such systems is the ability to create precise micro environments of human tissue interactions. These micro environments can be exploited to understand the impact of specific chemicals/drugs. Such systems are crucial for personalized medicine and drug discovery. The next paragraphs give a high-level summary of various organs-on-chip platforms [121].

Blood vessel on chip is designed by coating the PDMS-based microfluidic channels with fibronectin [122] and flushed with endothelial growth media. The endothelial cells are pipetted into these channels and are incubated. The surface thus gets coated with endothelial cells. To make a cylindrical channel for blood flow, a capillary tube is inserted into the microfluidic channel, and after the endothelization, the capillary tube is removed leaving a circular channel to study the blood and endothelial interaction. Understanding blood vessel physiology has broad applications in predicting blood vessel bio-mechanics, fluid shear and stretch [123], wound healing [122], vascular injury [124], drug discovery, and hemostasis/thrombosis [122, 125].

Lung on chip [126] was built with soft lithography techniques that created an *in vitro* alveolar capillary interface of the human lung. This device was used to study the alveolar response to bacteria and nanoparticles. Fluorescent microscopy was used to quantify alveolar-capillary interface. Heart on chip [127, 128] muscular thin films are designed with flexible elastomeric polymers and anisotropic cardiac cells and tissues. The contraction and expansion of heart muscles is quantified by these deformations of the elastomeric polymer designed using microfluidics.

Designing these organs on chip with multilayer integration is challenging but gives unprecedented advantage in looking at all barriers holistically. The current challenges for the organs on chip systems are: (i) interfacing multiple organs on single chip; (ii) measuring simultaneously optical, electrical, and chemical information; and (iii) measuring both the local and the global parameters simultaneously. Current chips are mostly limited to measuring optical properties. Measuring other mechanical properties of these systems such as electrical and mechanical properties gives better understanding of these systems. *In situ* continuous monitoring of the OOC is critical to use these chips to full potential.

These devices should not only have continuously monitoring sensors but also have feedback based actuators to precisely perturb the micro environments. The literature in developing such integrated OOC devices is very limited. Yu Shrike Zhang et al. [129] developed a modular OOC device that integrated sensors for monitoring micro environmental properties such as pH, O₂, and temperature; soluble biomarkers were monitored using electrochemical immuno-biosensors. Similar OOC optical properties are measured using fluorescent microscopes. The automation and integration of the sensors to the OOC gave uninterrupted continuous monitoring of a combined liver and heart on chip platforms.

5.3 Microfluidic Applications in Bionanomaterials and Nanomedicine

5.3.1 Bio-nanomaterials

Nanomaterials (size range of 1–100 nm) that are either entirely composed of biomolecules or partially built into them qualify as bionanomaterials. Bionanomaterials are being used for targeted drug therapy in cancer treatment research, for diagnostics, and in cosmetics [130]. Worapol et al. delivered siRNA to cancer cells in mice using biologically modified silica nanoparticles [130–132], and Inmaculada et al. developed magneto-plasmonic nanoparticles with potential applications in magnetic resonance imaging [133]. The above examples highlight the ongoing research in the development and application of bionanomaterials in clinical medicine. One of the biggest challenges in bionanomaterials research is the consistency in production from batch to batch. Microfluidic systems offer the advantage of tuning the size and quality for nanoparticle production without losing high rate of production. Due to the inherent small channels, microfluidic devices offer improved control over reaction conditions. Moreover, microfluidic systems have also enabled real-time characterization of nanoparticles during production [130]. These kinds of integrated systems will greatly reduce the time and money needed for clinical translation of nanoparticles. Jong-min et al. used 3D flow focusing in parallel microfluidic systems to synthesize poly(lactide-co-glycolide)-b-polyethyleneglycol (PLGA-PEG) nanoparticle that are currently in phase I clinical trials for prostate cancer treatment [134]. They reported a maximum production rate of 84 mg h⁻¹ with eight parallel systems and tested their nanoparticles in mice for fluorescence. Increasing sophistication in the manufacture of bionanomaterials will enhance their success in biomedical applications. Highly integrated microfluidic devices with advanced process control and real-time optimization systems proposed in this chapter are poised perfectly to resolve challenges in production and characterization of bionanomaterials.

5.3.2 Nanomedicine

Nanomedicine primarily involves the use of nanoparticles to assist disease treatment. Major progress in nanomedicine has come in the form of targeted drug delivery through nanoparticles as carriers [130–132]. Highly unstable drugs and

biomolecules can also be delivered to target organs safely through nanocarriers. The progress in clinical translation of nanomedicine has not been keeping up with the pace of laboratory research due to problems associated with production, characterization, and *in vivo* testing of nanoparticles. Microfluidic technology is becoming common in the development of lipid-based nanocarriers that are highly valued for their versatility in encapsulating both hydrophilic and hydrophobic loads. Alex Leung et al. [135] used microfluidic mixing to synthesize lipid nanoparticles with siRNA and identified a nanostructured core formed as a result of rapid microfluidic mixing. Organs-on-chip platforms enable *ex vivo* testing of nanoparticles for their organ selectivity [127, 128] and allow integration to mimic pharmacokinetics of human body. Cancer on chip models are also being developed to test cancer drugs and allow personalized medicine possibilities in future. Balabhaskar et al. developed a microfluidic platform to test the efficacy of two different nanopolymer-based drug delivery systems [136]. Advanced microfluidic systems with multiparameter analysis like the ones proposed here when developed to analyze cancer cells from patients could potentially enable personalized drug testing system.

5.4 Large-Scale Data Integration for Healthcare Diagnostics

With the advent of the Internet of Things (driven by low cost easily deployable sensing and connectivity) and associated advances in biosensors integration owing to an increasing number of use cases for disease diagnosis and drug screening, healthcare providers have access to mountains of data at their disposal to analyze and optimize healthcare at the individual level. Advanced multilayered microfluidic devices as proposed in Sect. 5.2 with multiplexed sensing also generate huge amounts of data that often need to be processed near-real-time to be able to complete all the many sequential analysis within the few hours of *in vitro* stability of biological fluids outside the body. For example, imaging flow cytometry techniques rely on ultrafast image processing (>100 fps) to extract cell properties like size, shape, color, and response to forces for cell classification in real time to feedback decisions necessary for downstream flow shaping or single-cell manipulation of the cells of interest for isolation and enrichment. Similar data processing speeds are needed for other sensing strategies including on-chip FACS, electrical impedance spectroscopy, absorbance/scatter, etc. to allow for high-speed classification needed for decision-making on the strategy downstream of each of these sensing locations in the process flow. However, these big data image/signal processing workloads have historically been very compute intensive leading to longer than optimal processing times (often hours) often ending up as offline analysis for post-mortem analysis. Adding to this challenge and as proposed in the multiplexed sensing strategy in Sect. 5.2, due to the inherent heterogeneity within human beings, genetic or otherwise, in their physiology and how they respond to stressants like disease, drugs, and other stimuli, as well as heterogeneity at the cell level due to age, disease, mutation etc., individual cell properties like size, shape, density, appearance, specific fluorescent markers, or susceptibility to magnetic, electrical, or light fields, and drug response in

isolation are not always adequate to classify with confidence and there is a need for multiparameter cross-correlation analysis. Recently, developments in the field of big data analysis, often driven by e-commerce firms for user data analysis, have started trickling into the field of healthcare to address a similar requirement: find trends/commonalities in extremely large, often incomplete, unstructured, and seemingly unrelated data piles with a large number of variables. Novel data processing approaches, enabled by huge advances in computational hardware capabilities, have pushed these data analyses to close to real time using machine learning and deep learning architectures where either the cell classification or cell identification or both is handled by pretrained models that can dole out classification at real time [115, 137–142]. This is not uncommon to the face detection algorithms widely deployed on smartphones or Movidius VPU chip-powered Intel compute stick/Google clip [143–145]. Recently this has also been demonstrated on an ultraportable raspberry Pi platform paving the path for compact, low power on-chip integration of the detection and the classification systems. In these systems, the training of the models is often performed in the cloud with crowd sourced data, and the on-chip compute systems are fed the trained models to perform inference and classify real time. Trained models are available for a variety of biological analysis including machine learning models for disease detection in liquid biopsies [146], cell counting [147], cancer screening [148, 149], cell feature extraction [115, 117], and flow shaping [115], while there is an increasing amount of literature/training/toolsets to retrain existing popular models for new systems with small datasets and achieve reasonable accuracies in classification [138, 140, 142, 150–152]

6 Conclusions and Future Perspectives

The exercise here was to conceptualize a one-stop advanced microfluidic analysis system and push to see how much we can do with one sample – with a goal of leveraging advances in computation and create an able virtual assistant to a doctor at point of care for customized, guess-free medical care that could optimize care and reduce cost and treatment time while increasing survival rate as well as patient comfort. We envision an advanced POC microfluidic device through systems integration and packaging via VLSI technology coupled to advances in sensor technology and computational technology to power a multiparameter co-analysis that could deliver valuable insights to dramatically improve decision making at the doctors office. In here, technologies developed in microfluidics systems are adapted to integrate with an extremely capable sensing and computation silicon layer (SOC). This can also cater to other applications like environmental sensing, food quality monitoring, and biosecurity applications. Inspiration is drawn from the IOT boom, advances in computational tools, both hardware (capable low power edge compute, extremely powerful cloud) and software (machine learning and DNN). A clear analogy would be quality-of-life improvement delivered by modern day smartphones that offer unreal artificial intelligence at the edge in the form of technologies that were recently science fiction and suggestions/interactions that are close to human like. Current day smartphones rely on up to 20 sensors to identify

context information of the user and provide very tailor-made and accurate suggestions and interactions/responses, often freaky. These include camera-based face recognition/image processing, speech recognition, fingerprint sensor, GPS, ultrasonic range finder, battery sensor, temperature sensor, humidity sensor, multi-axis accelerometer, light sensor, proximity sensor, etc. In this, the Google Assistant relies on a combination of sensors to recognize user spoken request and respond appropriately with human-like interpretation and relevance. While the speech recognition engine itself is a marvel with offline inference for some set of actions with an onboard neural network inference chip, Google relies on cloud-based neural networks to generate a highly relevant response by relying on a multitude of other variables that provide context to the conversation that allows it to make a meaningful and highly accurate interpretation of a much wide range of phrases with varying noise/accents. This context could be data from the many other sensors like the users' location, local weather, time of day, and recent searches. We also see a similar tactic applied improvement of face recognition where camera-based image detection is being assisted by additional sensors that provide depth information as well as deeper colors to allow for a better 3D representation as well as low light performance. This additional data coupled with a dedicated RAM and VPU for offline neural network inference is able to deliver real-time face/object/text recognition and better autofocus. Sometimes they leverage Phase-Detection AutoFocus (PDAF) coupled with some AI neural network wizardry to extract depth. DNNs these days can look at 200000 labels for classification with adequately trained models (Microsoft's Watson or other cloud sources training models). This is the age of "Internet of Things" where we are able to collect huge amounts of data needed to train neural network models to find patterns not imagined by humans. A smart diagnostics companion in Figs. 9.5

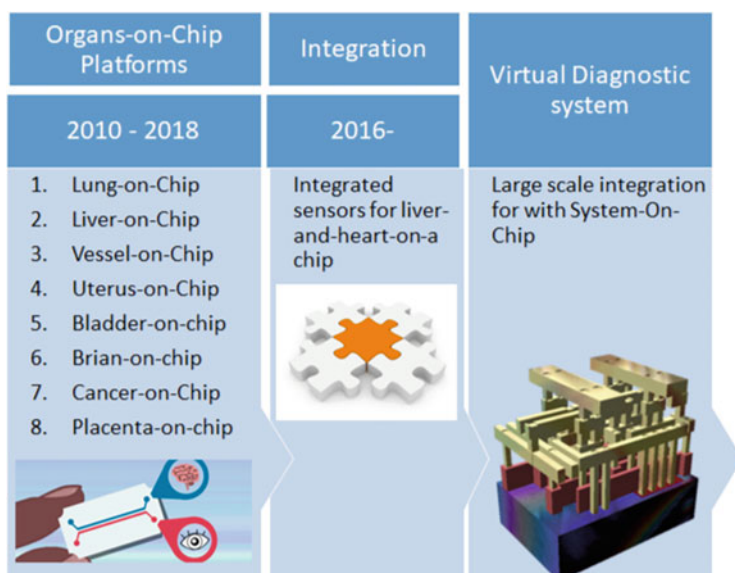


Fig. 9.5 Evolution and future of organs-on-chip platforms

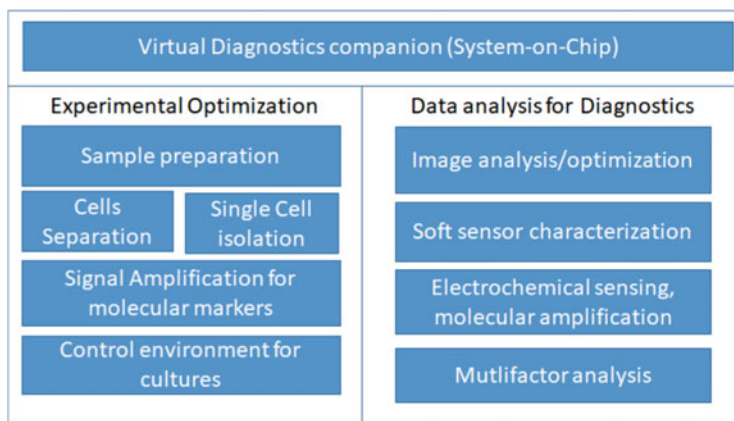


Fig. 9.6 Virtual diagnostics companion through and SOC integrated into a microfluidic VLSI platform

and 9.6 above provides a superior disease diagnosis by gathering all the evidence available to improve the context of a symptom, also preemptively screens/simulates all the alternate treatment paths before identifying the best possible path to speed up final diagnosis, optimizes reagent usage/cost while also preemptively screens appropriate drugs such as anticoagulants, antibiotics, and chemotherapy.

Acknowledgments This work was supported by West Virginia University startup funds awarded to J. Maddala.

References

1. Casadevall i Solvas X, deMello A (2011) Droplet microfluidics: recent developments and future applications. *Chem Commun* 47:1936–1942
2. Chou W-L, Lee P-Y, Yang C-L et al (2015) Recent advances in applications of droplet microfluidics. *Micromachines* 6:1249–1271
3. Teh S-Y, Lin R, Hung L-H, Lee AP (2008) Droplet microfluidics. *Lab Chip* 8:198
4. Paguirigan AL, Beebe DJ (2008) Microfluidics meet cell biology: bridging the gap by validation and application of microscale techniques for cell biological assays. *BioEssays* 30:811–821
5. Song H, Chen DL, Ismagilov RF (2006) Reactions in droplets in microfluidic channels. *Angew Chem Int Ed Engl* 45:7336–7356
6. Jamal S, Agrawal YK (2013) Advances in microfluidics: lab-on-a-chip to point of care diagnostic devices. *Adv Sci, Eng Med* 5:385–394
7. Zilberman-Rudenko J, Sylman JL, Lakshmanan HHS et al (2016) Dynamics of blood flow and thrombus formation in a multi-bypass microfluidic ladder network. *Cell Mol Bioeng* 10:16–29
8. Zilberman-Rudenko J, White RM, Zilberman DA et al (2018) Design and utility of a point-of-care microfluidic platform to assess hematocrit and blood coagulation. *Cell Mol Bioeng* 11:519–529
9. Maddala J, Rengaswamy R (2013) Droplet digital signal generation in microfluidic networks using model predictive control. *J Process Control* 23:132–139

10. Kuswandi B, Nuriman, Huskens J, Verboom W (2007) Optical sensing systems for microfluidic devices: a review. *Anal Chim Acta* 601:141–155
11. Ahn K, Kerbage C, Hunt TP et al (2006) Dielectrophoretic manipulation of drops for high-speed microfluidic sorting devices. *Appl Phys Lett* 88:024104
12. Dittrich PS, Schuille P (2003) An integrated microfluidic system for reaction, high-sensitivity detection, and sorting of fluorescent cells and particles. *Anal Chem* 75:5767–5774
13. Chen CH, Cho SH, Tsai F et al (2009) Microfluidic cell sorter with integrated piezoelectric actuator. *Biomed Microdevices* 11:1223–1231
14. Han Z, Li W, Huang Y, Zheng B (2009) Measuring rapid enzymatic kinetics by electrochemical method in droplet-based microfluidic devices with pneumatic valves. *Anal Chem* 81:5840–5845
15. Suea-Ngam A, Rattanasart P, Chailapakul O, Srisa-Art M (2015) Electrochemical droplet-based microfluidics using chip-based carbon paste electrodes for high-throughput analysis in pharmaceutical applications. *Anal Chim Acta* 883:45–54
16. Pollack MG, Shenderov AD, Fair RB (2002) Electrowetting-based actuation of droplets for integrated microfluidics. *Lab Chip* 2:96–101
17. Link DR, Grasland-Mongrain E, Duri A et al (2006) Electric control of droplets in microfluidic devices. *Angew Chem Int Ed Engl* 45:2556–2560
18. Bransky A, Korin N, Khoury M, Levenberg S (2009) A microfluidic droplet generator based on a piezoelectric actuator. *Lab Chip* 9:516–520
19. Cao Z, Chen F, Bao N et al (2013) Droplet sorting based on the number of encapsulated particles using a solenoid valve. *Lab Chip* 13:171–178
20. Cho SH, Chen CH, Tsai FS et al (2010) Human mammalian cell sorting using a highly integrated micro-fabricated fluorescence-activated cell sorter (μ FACS). *Lab Chip* 10:1567
21. Wang MM, Tu E, Raymond DE et al (2005) Microfluidic sorting of mammalian cells by optical force switching. *Nat Biotechnol* 23:83–87
22. Lignos I, Protesescu L, Stavrakis S et al (2014) Facile droplet-based microfluidic synthesis of monodisperse IV–VI semiconductor nanocrystals with coupled in-line NIR fluorescence detection. *Chem Mater* 26:2975–2982
23. Krishnadasan S, Brown RJC, deMello AJ, deMello JC (2007) Intelligent routes to the controlled synthesis of nanoparticles. *Lab Chip* 7:1434–1441
24. Maceiczkyk RM, deMello AJ (2014) Fast and reliable metamodeling of complex reaction spaces using universal kriging. *J Phys Chem C* 118:20026–20033
25. Maceiczkyk RM, Lignos IG, deMello AJ (2015) Online detection and automation methods in microfluidic nanomaterial synthesis. *Curr Opin Chem Eng* 8:29–35
26. Fu AY, Chou H-P, Spence C et al (2002) An integrated microfabricated cell sorter. *Anal Chem* 74:2451–2457
27. Abate AR, Weitz DA (2008) Single-layer membrane valves for elastomeric microfluidic devices. *Appl Phys Lett* 92:243509
28. Zeng S, Li B, X'ou S et al (2009) Microvalve-actuated precise control of individual droplets in microfluidic devices. *Lab Chip* 9:1340–1343
29. Lee H, Lee H, Liu Y et al (2005) An IC/microfluidic hybrid microsystem for 2D magnetic manipulation of individual biological cells. In: ISSCC. 2005 IEEE international digest of technical papers. Solid-state circuits conference
30. Zhang K, Liang Q, Ai X et al (2011) On-demand microfluidic droplet manipulation using hydrophobic ferrofluid as a continuous-phase. *Lab Chip* 11:1271–1275
31. Duffy DC, McDonald JC, Schueller OJ, Whitesides GM (1998) Rapid prototyping of microfluidic systems in poly(dimethylsiloxane). *Anal Chem* 70:4974–4984
32. Unger MA, Chou HP, Thorsen T et al (2000) Monolithic microfabricated valves and pumps by multilayer soft lithography. *Science* 288:113–116
33. Guo Z-X, Zeng Q, Zhang M et al (2011) Valve-based microfluidic droplet micromixer and mercury (II) ion detection. *Sens Actuators A Phys* 172:546–551
34. Schindler M, Ajdari A (2008) Droplet traffic in microfluidic networks: a simple model for understanding and designing. *Phys Rev Lett* 100:044501

35. An F, Qu Y, Liu X et al (2015) Organ-on-a-chip: new platform for biological analysis. *Anal Chem Insights* 10:39–45
36. Stieger B (2016) Faculty of 1000 evaluation for organ-on-a-chip: new platform for biological analysis. F1000 – Post-publication peer review of the biomedical literature
37. Glick C, Schwartz A, Srimongkol M et al (2018) Rapid assembly of multilayer microfluidic structures. In: 2018 IEEE micro electro mechanical systems (MEMS)
38. Glick CC, Srimongkol MT, Schwartz AJ et al (2016) Rapid assembly of multilayer microfluidic structures via 3D-printed transfer molding and bonding. *Microsyst Nanoeng* 2:16063. <https://doi.org/10.1038/micronano.2016.63>
39. Saharil F, Carlborg CF, Haraldsson T, van der Wijngaart W (2012) Biocompatible “click” wafer bonding for microfluidic devices. *Lab Chip* 12:3032
40. Chen X, Zhang L, Li H et al (2013) Development of a multilayer microfluidic device integrated with a PDMS-cellulose composite film for sample pre-treatment and immunoassay. *Sens Actuators A Phys* 193:54–58
41. Tsai L-F (2011) Bonding of polydimethylsiloxane microfluidics to silicon-based sensors. *J Micro/Nanolithogr MEMS MOEMS* 10:043009
42. Iliescu C, Taylor H, Avram M et al (2012) A practical guide for the fabrication of microfluidic devices using glass and silicon. *Biomicrofluidics* 6:016505
43. Tsybeskov L, Hirschman KD, Duttagupta SP, Fauchet PM. An LED for silicon-based integrated optoelectronics. In: 1996 54th annual device research conference digest
44. Su Y (2012) All-optical signal processing using integrated silicon photonic devices. In: 2012 11th international conference on information science, signal processing and their applications (ISSPA)
45. Gong J, Kim C-JCJ (2008) All-electronic droplet generation on-chip with real-time feedback control for EWOD digital microfluidics. *Lab Chip* 8:898–906
46. Fair RB, Pollack MG, Woo R et al. A micro-watt metal-insulator-solution-transport (MIST) device for scalable digital bio-microfluidic systems. In: International electron devices meeting. Technical digest (Cat. No.01CH37224)
47. Maddala J, Vanapalli SA, Rengaswamy R (2011) Sort-synchronization control in microfluidic loop devices with experimental uncertainties using a model predictive control (MPC) framework. *IFAC Proc Vol* 44:4886–4891
48. Abe Y, Takemura K, Sato K et al (2013) Droplet μ TAS using electro-conjugate fluid – feedback position control of multiple droplets in flow channel matrix. *Sens Actuators A Phys* 198:1–7
49. Chung Y-C, Wen B-J, Lin Y-C (2007) Optimal fuzzy sliding-mode control for bio-microfluidic manipulation. *Control Eng Pract* 15:1093–1105
50. Lin C-J, Lin C-J, Chen Y-Y, Hang F-R. Fuzzy processing on GPS data to improve the position accuracy. In: Soft computing in intelligent systems and information processing. Proceedings of the 1996 Asian fuzzy systems symposium
51. Zhang G, Lu J, Gao Y (2015) Fuzzy bi-level decision making. In: Multi-Level Decision Making. Intelligent systems reference library, vol 82. Springer, Berlin, Heidelberg, pp 175–205
52. Maddala J, Rengaswamy R (2014) Design of multi-functional microfluidic ladder networks to passively control droplet spacing using genetic algorithms. *Comput Chem Eng* 60:413–425
53. Maddala J, Wang WS, Vanapalli SA, Rengaswamy R (2012) Traffic of pairs of drops in microfluidic ladder networks with fore-aft structural asymmetry. *Microfluid Nanofluidics* 14:337–344
54. Kasule JS, Maddala J, Mobed P, Rengaswamy R (2016) Very large scale droplet microfluidic integration (VLDMI) using genetic algorithm. *Comput Chem Eng* 85:94–104
55. Mohammed M-I, Desmulliez MPY (2011) Lab-on-a-chip based immunosensor principles and technologies for the detection of cardiac biomarkers: a review. *Lab Chip* 11:569–595
56. Alix-Panabières C, Pantel K (2014) Technologies for detection of circulating tumor cells: facts and vision. *Lab Chip* 14:57–62

57. Uttley L, Whiteman BL, Woods HB et al (2016) Building the evidence base of blood-based biomarkers for early detection of cancer: a rapid systematic mapping review. *EBioMedicine* 10:164–173
58. Mazumder R (2015) Blood-based companion diagnostics. *The journal of precision medicine*
59. Kasukurti A, Eggleton CD, Desai SA, Marr DWM (2015) FACS-style detection for real-time cell viscoelastic cytometry. *RSC Adv* 5:105636–105642
60. Yaghobian F, Weimann T, Güttler B, Stosch R (2011) On-chip approach for traceable quantification of biomarkers based on isotope-dilution surface-enhanced Raman scattering (IDSERS). *Lab Chip* 11:2955
61. Wu J, Gu M (2011) Microfluidic sensing: state of the art fabrication and detection techniques. *J Biomed Opt* 16:080901
62. Zhu Y, Fang Q (2013) Analytical detection techniques for droplet microfluidics – a review. *Anal Chim Acta* 787:24–35
63. Cole MC, Kenis PJA (2009) Multiplexed electrical sensor arrays in microfluidic networks. *Sens Actuators B Chem* 136:350–358
64. Petchakup C, Li K, Hou H (2017) Advances in single cell impedance cytometry for biomedical applications. *Micromachines* 8:87
65. Holmes D, Morgan H (2010) Single cell impedance cytometry for identification and counting of CD4 T-cells in human blood using impedance labels. *Anal Chem* 82:1455–1461
66. Claudel J, Nadi M, El Mazria O, Kourtiche D (2017) High reliability microfluidic biosensor for single cell impedance cytometry. In: 2017 eleventh international conference on sensing technology (ICST)
67. Morgan H, Spencer D (2015) Microfluidic impedance cytometry for blood cell analysis. *RSC Nanoscience and Nanotechnology*. pp 213–241
68. Simini F, Bertemes-Filho P (2018) Bioimpedance in biomedical applications and research. Springer, Cham
69. Chen J, Xue C, Zhao Y et al (2015) Microfluidic impedance flow cytometry enabling high-throughput single-cell electrical property characterization. *Int J Mol Sci* 16:9804–9830
70. Iacovacci V, Lucarini G, Ricotti L, Mencias A (2016) Magnetic field-based technologies for lab-on-a-chip applications. In: Lab-on-a-chip fabrication and application, IntechOpen. <https://doi.org/10.5772/62865>
71. Yang S, Ündar A, Zahn J (2005) Biological fluid separation in microfluidic channels using flow rate control. American society of mechanical engineers, fluids engineering division (Publication) FED. 261. <https://doi.org/10.1115/IMECE2005-80501>
72. Stoecklein D, Wu C-Y, Owsley K et al (2014) Micropillar sequence designs for fundamental inertial flow transformations. *Lab Chip* 14:4197–4204
73. Dutta D (2013) Enhanced microfluidic separation by pressure-driven flow. *Encyclopedia of microfluidics and nanofluidics*, pp 1–13. https://doi.org/10.1007/978-3-642-27758-0_1747-1
74. Raj A, Suthanthiraraj PPA, Sen AK (2018) Pressure-driven flow through PDMS-based flexible microchannels and their applications in microfluidics. *Microfluid Nanofluidics* 22. <https://doi.org/10.1007/s10404-018-2150-5>
75. Lewpiriyawong N, Yang C (2014) Dielectrophoresis field-flow fractionation for continuous-flow separation of particles and cells in microfluidic devices. In: Wang L. (ed) *Advances in transport phenomena 2011*. *Advances in transport phenomena*, vol 3. Springer, Cham. pp 29–62
76. Modak N, Datta A, Ganguly R (2008) Cell separation in a microfluidic channel using magnetic microspheres. *Microfluid Nanofluidics* 6:647–660
77. Shields CW 4th, Ohiri KA, Szott LM, López GP (2017) Translating microfluidics: cell separation technologies and their barriers to commercialization. *Cytometry B Clin Cytom* 92:115–125
78. Buican TN (1991) Automated cell separation techniques based on optical trapping. In: ACS symposium series. pp 59–72

79. Grover SC, Skirtach AG, Gauthier RC, Grover CP (2001) Automated single-cell sorting system based on optical trapping. *J Biomed Opt* 6:14–22
80. Applegate RW Jr, Squier J, Vestad T et al (2006) Microfluidic sorting system based on optical waveguide integration and diode laser bar trapping. *Lab Chip* 6:422–426
81. Applegate R Jr, Squier J, Vestad T et al (2004) Optical trapping, manipulation, and sorting of cells and colloids in microfluidic systems with diode laser bars. *Opt Express* 12:4390–4398
82. Kasukurti A, Potcoava M, Desai SA et al (2011) Single-cell isolation using a DVD optical pickup. *Opt Express* 19:10377
83. Dholakia K, MacDonald MP, Zemánek P, Cizmár T (2007) Cellular and colloidal separation using optical forces. *Methods Cell Biol* 82:467–495
84. Sun Y, Haglund TA, Rogers AJ et al (2018) Review: microfluidics technologies for blood-based cancer liquid biopsies. *Anal Chim Acta* 1012:10–29
85. Bogue R (2016) Lab-on-a-chip and other miniaturised analytical instruments. *Sens Rev* 36:109–114
86. Chen L, Bode AM, Dong Z (2017) Circulating tumor cells: moving biological insights into detection. *Theranostics* 7:2606–2619
87. Liu J, Qiang Y, Alvarez O, Du E (2018) Electrical impedance microflow cytometry with oxygen control for detection of sickle cells. *Sens Actuators B Chem* 255:2392–2398
88. Swensen JS, Xiao Y, Ferguson BS et al (2009) Continuous, real-time monitoring of cocaine in undiluted blood serum via a microfluidic, electrochemical aptamer-based sensor. *J Am Chem Soc* 131:4262–4266
89. Song H, Li H-W, Munson MS et al (2006) On-chip titration of an anticoagulant argatroban and determination of the clotting time within whole blood or plasma using a plug-based microfluidic system. *Anal Chem* 78:4839–4849
90. Wolff A, Perch-Nielsen IR, Larsen UD et al (2003) Integrating advanced functionality in a microfabricated high-throughput fluorescent-activated cell sorter. *Lab Chip* 3:22
91. Chen Y, Wu T-H, Chung A et al (2014) Pulsed laser activated cell sorter (PLACS) for high-throughput fluorescent mammalian cell sorting. *Proceedings of SPIE – The international society for optical engineering*. 9164. <https://doi.org/10.1117/12.2060914>
92. Chandrasekaran A, Packirisamy M (2010) Integrated microfluidic biophotonic chip for laser induced fluorescence detection. *Biomed Microdevices* 12:923–933
93. Lee H, Xu L, Koh D et al (2014) Various on-chip sensors with microfluidics for biological applications. *Sensors* 14:17008–17036
94. Tokel O, Yildiz UH, Inci F et al (2015) Portable microfluidic integrated plasmonic platform for pathogen detection. *Sci Rep* 5:9152
95. Berchtold C, Bosilkovska M, Daali Y et al (2013) Real-time monitoring of exhaled drugs by mass spectrometry. *Mass Spectrom Rev* 33:394–413
96. Freire S, Wheeler A (2008) Interfaces between microfluidics and mass spectrometry. In: Li D (ed) *Encyclopedia of microfluidics and nanofluidics*. Springer, Boston, pp 1–9
97. Ma X, Li M, He J-J (2013) CMOS-compatible integrated spectrometer based on echelle diffraction grating and MSM photodetector array. *IEEE Photonics J* 5:6600807
98. Bates KE, Lu H (2016) Optics-integrated microfluidic platforms for biomolecular analyses. *Biophys J* 110:1684–1697
99. Kinsey JL (1977) Laser-induced fluorescence. *Annu Rev Phys Chem* 28(1):349–372
100. Peroz C, Dhuey S, Goltsov A et al (2011) Digital spectrometer-on-chip fabricated by step and repeat nanoimprint lithography on pre-spin coated films. *Microelectron Eng* 88:2092–2095
101. Liu R, Wang N, Kamili F, Fatih Sarioglu A (2016) Microfluidic CODES: a scalable multiplexed electronic sensor for orthogonal detection of particles in microfluidic channels. *Lab Chip* 16:1350–1357
102. Ashiba H, Fujimaki M, Awazu K et al (2016) Microfluidic chips for forward blood typing performed with a multichannel waveguide-mode sensor. *Sens Bio-Sens Res* 7:121–126
103. Wilhelm E, Neumann C, Duttenhofer T et al (2013) Connecting microfluidic chips using a chemically inert, reversible, multichannel chip-to-world-interface. *Lab Chip* 13:4343
104. Chen X, Cui D, Chen J (2012) Integrated microfluidic chips for whole blood pretreatment. On-chip pretreatment of whole blood by using MEMS technology. pp 110–116. <https://doi.org/10.2174/978160805147211201010110>

105. Hou HW, Bhagat AAS, Lee WC et al (2011) Microfluidic devices for blood fractionation. *Micromachines* 2:319–343
106. Alazzam A, Hilal-Alnaqbi A, Alnaimat F et al (2018) Dielectrophoresis-based microfluidic devices for field-flow fractionation. *Med Devices Sens* 1:e10007
107. Alvankarian J, Majlis B (2015) Tunable microfluidic devices for hydrodynamic fractionation of cells and beads: a review. *Sensors* 15:29685–29701
108. Sahore V, Sonker M, Nielsen AV et al (2018) Automated microfluidic devices integrating solid-phase extraction, fluorescent labeling, and microchip electrophoresis for preterm birth biomarker analysis. *Anal Bioanal Chem* 410:933–941
109. Kasukurti A, Eggleton CD, Desai SA et al (2014) A simple microfluidic dispenser for single-microparticle and cell samples. *Lab Chip* 14:4673–4679
110. Kasukurti A (2014) Combining optical and hydrodynamic forces for single cell characterization, isolation and delivery, PhD diss., Colorado School of Mines, Golden, CO. <http://hdl.handle.net/11124/16984>
111. Vaidyanathan R, Yeo T, Lim CT (2018) Microfluidics for cell sorting and single cell analysis from whole blood. *Methods Cell Biol* 147:151–173
112. Majeed B, Liu C, Van Acker L et al (2014) Fabrication of silicon based microfluidics device for cell sorting application. In: 2014 IEEE 64th electronic components and technology conference (ECTC)
113. Girault M, Kim H, Arakawa H et al (2017) An on-chip imaging droplet-sorting system: a real-time shape recognition method to screen target cells in droplets with single cell resolution. *Sci Rep* 7:40072
114. Mazutis L, Gilbert J, Lloyd Ung W et al (2013) Single-cell analysis and sorting using droplet-based microfluidics. *Nat Protocol* 8:870–891
115. Stoecklein D, Lore KG, Davies M et al (2017) Deep learning for flow sculpting: insights into efficient learning using scientific simulation data. *Sci Rep* 7:46368
116. Samsel L, Dagur PK, Raghavachari N et al (2013) Imaging flow cytometry for morphologic and phenotypic characterization of rare circulating endothelial cells. *Cytometry B Clin Cytom* 84:379–389
117. Heo YJ, Lee D, Kang J et al (2017) Real-time image processing for microscopy-based label-free imaging flow cytometry in a microfluidic chip. *Sci Rep* 7:11651. <https://doi.org/10.1038/s41598-017-11534-0>
118. Su X, Xu Y, Zhao H et al (2019) Design and preparation of centrifugal microfluidic chip integrated with SERS detection for rapid diagnostics. *Talanta* 194:903–909
119. Bhatia SN, Ingber DE (2014) Microfluidic organs-on-chips. *Nat Biotechnol* 32:760–772
120. Wang Z, Roya S, Kyo-in K, Kim K (2015) Organ-on-a-chip platforms for drug delivery and cell characterization: a review. *Sens Mater* 27(6):487–506
121. Grosberg A, Nesmith AP, Goss JA et al (2012) Muscle on a chip: in vitro contractility assays for smooth and striated muscle. *J Pharmacol Toxicol Methods* 65:126–135
122. van der Meer AD, Vermeul K, Poot AA et al (2010) A microfluidic wound-healing assay for quantifying endothelial cell migration. *Am J Physiol Heart Circ Physiol* 298:H719–H725
123. Zheng W, Jiang B, Wang D et al (2012) A microfluidic flow-stretch chip for investigating blood vessel biomechanics. *Lab Chip* 12:3441–3450
124. Neeves KB, Onasoga AA, Wufsus AR (2013) The use of microfluidics in hemostasis: clinical diagnostics and biomimetic models of vascular injury. *Curr Opin Hematol* 20:417–423
125. Jain A, van der Meer AD, Papa A-L et al (2016) Assessment of whole blood thrombosis in a microfluidic device lined by fixed human endothelium. *Biomed Microdevices* 18:73. <https://doi.org/10.1007/s10544-016-0095-6>
126. Huh D, Matthews BD, Mammoto A et al (2010) Reconstituting organ-level lung functions on a Chip. *Science* 328:1662–1668
127. Grosberg A, Alford PW, McCain ML, Parker KK (2011) Ensembles of engineered cardiac tissues for physiological and pharmacological study: heart on a chip. *Lab Chip* 11:4165–4173
128. Agarwal A, Goss JA, Cho A et al (2013) Microfluidic heart on a chip for higher throughput pharmacological studies. *Lab Chip* 13:3599

129. Zhang YS, Aleman J, Shin SR et al (2017) Multisensor-integrated organs-on-chips platform for automated and continual in situ monitoring of organoid behaviors. *Proc Natl Acad Sci U S A* 114:E2293–E2302
130. Valencia PM, Farokhzad OC, Karnik R, Langer R (2012) Microfluidic technologies for accelerating the clinical translation of nanoparticles. *Nat Nanotechnol* 7:623–629
131. Ngamcherdtrakul W, Morry J, Gu S et al (2015) Cationic polymer modified mesoporous silica nanoparticles for targeted siRNA delivery to HER2+ breast cancer. *Adv Funct Mater* 25:2646–2659
132. Ngamcherdtrakul W, Morry J, Gu S et al (2015) Cancer nanomedicine: cationic polymer modified mesoporous silica nanoparticles for targeted siRNA delivery to HER2 breast cancer. *Adv Funct Mater* 25:2629–2629
133. Urries I, Muñoz C, Gomez L et al (2014) Magneto-plasmonic nanoparticles as theranostic platforms for magnetic resonance imaging, drug delivery and NIR hyperthermia applications. *Nanoscale* 6:9230–9240
134. Lim J-M, Bertrand N, Valencia PM et al (2014) Parallel microfluidic synthesis of size-tunable polymeric nanoparticles using 3D flow focusing towards in vivo study. *Nanomedicine* 10:401–409
135. Leung AKK, Hafez IM, Baoukina S et al (2012) Lipid nanoparticles containing siRNA synthesized by microfluidic mixing exhibit an electron-dense nanostructured core. *J Phys Chem C Nanomater Interfaces* 116:18440–18450
136. Prabhakarandian B, Shen M-C, Nichols JB et al (2015) Synthetic tumor networks for screening drug delivery systems. *J Control Release* 201:49–55
137. Cao C, Liu F, Tan H et al (2018) Deep learning and its applications in biomedicine. *Genomics Proteomics Bioinformatics* 16:17–32
138. Ching T, Himmelstein DS, Beaulieu-Jones BK et al (2018) Opportunities and obstacles for deep learning in biology and medicine. *J R Soc Interface* 15:20170387. <https://doi.org/10.1098/rsif.2017.0387>
139. Van Valen DA, Kudo T, Lane KM et al (2016) Deep learning automates the quantitative analysis of individual cells in live-cell imaging experiments. *PLoS Comput Biol* 12:e1005177
140. Chen CL, Mahjoubfar A, Tai L-C et al (2016) Deep learning in label-free cell classification. *Sci Rep* 6:21471
141. Li L (2010) Machine learning methods for computational biology, Open dissertation press. ISBN-10:1360962859. ISBN-13:978-1360962856
142. Riordon J, Sovilj D, Sanner S et al (2018) Deep learning with microfluidics for biotechnology. *Trends Biotechnol* 37:310. <https://doi.org/10.1016/j.tibtech.2018.08.005>
143. Ionica MH, Gregg D (2015) The Movidius myriad architecture's potential for scientific computing. *IEEE Micro* 35:6–14
144. (2016) Google works with Movidius to deploy advanced machine intelligence on mobiles. *Biometric Technol Today* 2016:12
145. Othman NA, Aydin I (2018) A new deep learning application based on Movidius NCS for embedded object detection and recognition. In: 2018 2nd international symposium on multi-disciplinary studies and innovative technologies (ISMSIT)
146. Ko J, Baldassano SN, Loh P-L et al (2018) Machine learning to detect signatures of disease in liquid biopsies – a user's guide. *Lab Chip* 18:395–405
147. Huang X, Jiang Y, Liu X et al (2016) Machine learning based single-frame super-resolution processing for lensless blood cell counting. *Sensors* 16. <https://doi.org/10.3390/s16111836>
148. Ko J, Bhagwat N, Yee SS et al (2017) Combining machine learning and nanofluidic technology to diagnose pancreatic cancer using exosomes. *ACS Nano* 11:11182–11193
149. Singh DK, Ahrens CC, Li W, Vanapalli SA (2017) Label-free, high-throughput holographic screening and enumeration of tumor cells in blood. *Lab Chip* 17:2920–2932
150. Wang Z, Boddada A, Parker B et al (2018) A high-resolution minimicroscope system for wireless real-time monitoring. *IEEE Trans Biomed Eng* 65:1524–1531
151. Berthier J, Brakke KA, Berthier E (2016) *Open microfluidics*. Wiley, Beverly
152. Delamarche E, Kaigala GV (2018) *Open-space microfluidics: concepts, implementations, applications*. Wiley, Weinheim



Characterization of ATP Nanoliposome Treatment for Regeneration of Injured Spinal Cord

10

Girish J. Kotwal, Michael Martin, Eyas M. Hattab, and Sufan Chien

Contents

1	Definition of Topic	398
2	Overview	398
3	Introduction	399
	3.1 Nanotechnology of Intracellular ATP Delivery	399
	3.2 Macrophage Polarization and Tissue Regeneration	399
4	Experimental Material	400
	4.1 Materials for ATP Formulation Analysis	400
	4.2 HPLC-Related Materials and Specifications	400
	4.3 Cell Culture and Sample Preparation	401
	4.4 Materials for ATP Encapsulation with Liposomes	401
	4.5 Animals Required for Spinal Cord Injury and Treatment Evaluation	401
5	Methods	401
	5.1 HPLC for Measurement of ATP, ADP, and AMP in Electrolyte	401
	5.2 Cell Culture and Dosing Cells with ATP Liposomes	403
	5.3 Preparation of ATP-Laden Nanoliposomes	404

G. J. Kotwal (✉)
Noveratech LLC, Louisville, KY, USA
e-mail: GJKOTW01@gmail.com

M. Martin
Noveratech LLC, Louisville, KY, USA

Micro/Nano Technology Center, University of Louisville, Louisville, KY, USA
e-mail: Martin@louisville.edu

E. M. Hattab
Department of Pathology and Laboratory Medicine, School of Medicine Louisville, University of Louisville, Louisville, KY, USA

S. Chien
Noveratech LLC, Louisville, KY, USA

Hiram Polk Department of Surgery, School of Medicine Louisville, University of Louisville, Louisville, KY, USA

5.4	ATP Nanoliposome Used in Treatment of Injured Spinal Cord and Visualization by Transmission Electron Microscopy (TEM) and Checking for Sterility	405
5.5	Spinal Cord Injury in Rats: Histology and Immunohistochemistry	406
5.6	Notes	407
6	Key Research Findings	408
6.1	Current Status of Nanoliposomes in Medical Applications	408
6.2	Current Status of ATP Nanoliposomes	408
6.3	Current Research Findings That Advance Translation of the Application of ATP Nanoliposomes	408
7	Conclusions and Future Perspectives	411
	References	413

1 Definition of Topic

Traumatic spinal cord injury (SCI), due to automobile accidents, falls, or sport injuries, is a significant global public health concern. Following intracellular delivery of adenosine triphosphate (ATP) nanoliposomes or gamma-thio ATP nanoliposomes and immunohistochemical staining with antibodies to CD 68 and CD 163, the effects of treatment of injured rat spinal cord sections can be examined. ATP is the energy currency of the cell. A method to measure ATP and its metabolites (ADP and AMP) in cells treated with ATP-encapsulated nanoliposomes is outlined. The detection limit using HPLC and UV absorption for ATP is 0.1 micromole. The method is applicable for characterizing the amount of ATP encapsulated in the lipid bilayer, leakage and degradation of ATP-laden nanoliposomes. The potential of exclusively the ATP-laden nanoliposomes, as a potential treatment for accelerating wound healing has been extensively studied in a rabbit model of wound healing. This method is also applicable to studying the energy state of the cells in culture and how this is influenced by treatment with ATP nanoliposomes with varying lipid composition. The provision of a supplemental intracellular ATP supply is evaluated to determine the structural integrity of the spinal cord (as judged by the spinal cord histology of the white and gray matter). Immunohistochemical analysis is performed to assess whether there is greater proliferation of the regenerative M2 (CD68⁺ and CD163⁺) macrophage population compared to the M1 (CD68⁺ and CD163⁻) population. Examination of spinal cord sections could determine whether candidates like the ATP nanoliposomes either alone or in combination with an anticomplement agent could have a potential benefit in regeneration and accelerating functional recovery following injury.

2 Overview

Spinal cord injury (SCI) is a major global public health problem [1, 2] that currently has no reliable or specific medical treatment [3–5]. Primary SCI is well known to activate complement pathways and inflammation, resulting in secondary injuries that include permanent neuron death and apoptosis [6]. Inhibition of the complement pathways and inflammation can therefore alleviate the secondary injuries associated

with traumatic brain injury, spinal cord injuries, and with neurodegenerative diseases [7]. Therefore, complement pathways can be targeted for SCI treatments [8, 9].

Previous studies have shown that the vaccinia virus complement control protein (VCP) decreases the influx of neutrophils into the damaged spinal cord [10]. Treatment with VCP also improved the functional recovery of the spinal cord, as demonstrated by behavior studies [11]. However, VCP treatments have room for further improvement in functional recovery beyond administration of VCP alone. For example, damage to the endothelial lining of the spinal cord vasculature is a major factor in the pathogenesis of the spinal cord injury, and the healing process could also be accelerated by intracellular delivery of ATP nanoliposomes to enhance recovery. Investigation of this innovative hypothesis of combining these two extensively characterized agents as a synergistic treatment for SCI requires studying the exclusive effects of ATP nanoliposomes administered to the epicenter of the injured spinal cord.

3 Introduction

3.1 Nanotechnology of Intracellular ATP Delivery

ATP is the energy currency of the cell. It is a large molecule that cannot be taken up by cells, and only the ATP synthesized inside cells is available for energy required to maintain cellular functions. Nanotechnology has made it possible to study the effects of intracellular delivery of ATP in cell culture as well as in an animal model. Based on years of studies in a rabbit wound model, it has been found that the ATP nanoliposomes accelerate wound healing by causing changes in immune cell composition at the site of the wound where ATP nanoliposomes are applied [12, 13]. ATP encapsulated inside nanoliposomes is released in the cells when the cells are treated with ATP nanoliposomes. This increased intracellular ATP levels contributes to the upregulation of several mRNAs and small, noncoding RNAs, most significantly the small nuclear RNAs that form the spliceosome. The spliceosome then would contribute to greater splicing of pre-mRNA to translatable spliced RNA [14]. The quantitation of high energy phosphates and related metabolic byproducts that include ATP, adenosine diphosphate (ADP), adenosine monophosphate (AMP), and related adenine family members enables estimation of the energy state of cells. The methods for quantitation described here will be useful in the quality control of ATP nanoliposome formulations and optimization of the lipid composition process.

3.2 Macrophage Polarization and Tissue Regeneration

Several years of research on intracellular delivery of ATP by our group has demonstrated that macrophages contribute to accelerated wound healing due to elimination of the 3–5-day lag phase that occurs during normal healing [12,

13]. The pathway for this role of macrophages in a rabbit wound model of M1 to M2 macrophage polarization has been reviewed previously [15]. We recently reported a significant upregulation of U1 and U4 spliceosomal snRNAs by ATP nanoliposomes and postulated that the molecular mechanism for accelerated wound healing involves an increase in pre-mRNA processing to functional mRNA inside cells after treatment with ATP nanoliposomes [14]. Herein we describe our method for administering ATP nanoliposomes at the epicenter of an injured spinal cord and methods to evaluate its regenerative ability by staining cross sections of the spinal cord to observe the integrity of the gray and the white matter. The method for immunohistochemical characterization of the macrophages present at the epicenter 5 days after ATP nanoliposome administration is detailed. The numbers of regenerative M2 (CD68⁺, CD163⁺) macrophages, in comparison to the control spinal cord (treated with nanoliposomes containing nonmetabolizable gamma-thio-ATP) is estimated and semiquantified. Predominantly, M1 (CD68⁺, CD163⁻) macrophages are found in control treated spinal cord while M2 are found in treated spinal cord.

4 Experimental Material

4.1 Materials for ATP Formulation Analysis

Here we outline the materials used in high-performance liquid chromatography (HPLC) for detection of adenosine phosphate, culture and dosing of rabbit kidney cells, and the preparation of ATP-laden nanoliposomes. All materials utilize ultra-pure water with a resistivity 18 M Ω -cm at room temperature that has further been sterilized with ultraviolet light.

4.2 HPLC-Related Materials and Specifications

4.2.1 HPLC Hardware

Use a 0.5 μ m particulate filter, Krud Katcher from Phenomex, part number AF0-5727. Downstream of the Krud Katcher, install a reverse-phase C18 precolumn to protect the column from contamination by cellular debris. Luna Column C18 (2) (18 carbon alkanes), 5 micron, 250 mm \times 4.6 mm, volume 4.15 ml, Phenomenex part no: 00A-4252-E0, 00G-4252-e0 was used.

4.2.2 Mobile Phases

Mobile phase A is composed of potassium phosphate monobasic KH₂PO₄ (50 mmol/L) in deionized water. The resulting pH should naturally reach 4.5 without adjustment. Note that some recipes call for pH = 6.5 but the lower pH produces better separation between the ATP and ADP peaks. Mobile phase B is 100% methanol in DI. Record lot numbers for methanol and potassium phosphate.

4.3 Cell Culture and Sample Preparation

4.3.1 Cells and Culture

Rabbit kidney cells (RK-13) were the kind gift of Dr. Bernard Moss of the National Institutes of Health, Growth: Minimum Essential Medium (MEM) with 10% v/v Fetal Bovine Serum (FBS) from Gibco by Life Technologies, RPMI from Gibco, Rinse: Gibco PBS pH: 7.2, trypsin was from ATCC.

4.3.2 Preparation of Cells for Analysis

Lysis buffer was 100 mM Tris as a physiological buffer, 4 mM EDTA to chelate divalent ions and prevent ATPases from affecting the measurement, 0.1% v/v Triton as a detergent to disrupt cell and organelle membranes.

4.4 Materials for ATP Encapsulation with Liposomes

Soy phosphatidylcholine (Soy PC), N-[1-(2,3-Dioleoyloxy)propyl]-N,N,N-trimethylammonium methyl-sulfate (DOTAP) from Avanti Polar Lipids. Trehalose and Mg-ATP from Sigma Aldrich.

4.5 Animals Required for Spinal Cord Injury and Treatment Evaluation

No human subjects were involved. Rats were used for the spinal cord injury using a protocol approved by the Institutional Animal Care and Use Committee (IACUC). In this case, University of Louisville School of Medicine, Louisville, KY, and the methods followed were in accordance with institutional guidelines. All animals used to illustrate the method are to be treated humanely.

5 Methods

5.1 HPLC for Measurement of ATP, ADP, and AMP in Electrolyte

To configure an HPLC, we used an NGC Explorer from Biorad Inc., to have a loop volume of 1 ml, with a 0.5 μ m particulate filter and pre-column upstream of the reverse-phase column. Detection uses principally 255 nm UV absorbance but includes conductivity as well.

The method is adapted from Guan et al. [16] and was chosen to minimize the use of toxic solvents. Method Settings include the following parameters.

- Parameters:
 - Column: Luna C18A
 - Detector: 255 nm
 - Flow: 0.7 ml/min

- A Reagent: KH_2PO_4 50 mM in water
- B Reagent: 100% Methanol
- Equilibration step:
 - Time: 7 min
 - Segment type: Isocratic (constant concentration)
 - Reagents: 5%B + 95%A
- Sample application:
 - Load loop manually through a 0.1 μm or 0.2 μm syringe filter
 - Sample injection with system pump: Use flow rate from method settings
 - System buffers: Use same inlets as method settings
- Column wash – modified step
 - Time: 12 min
 - Segment type: Isocratic (constant concentration).
 - Reagents: 5%B + 95%A
- Column wash:
 - Segment 1:
 - Time: 12 min
 - Segment type: Isocratic (constant concentration)
 - Reagents: 20%B + 80%A
 - Segment 2:
 - Time: 12 min
 - Segment type: Isocratic (constant concentration)
 - Reagents: 5%B + 80%A

1. Calibration of HPLC for ATP, ADP, and AMP: Prepare aliquots of 1.5 ml 1 mM ATP, ADP, and AMP. Freeze at -20°C . As needed, dilute 1 mM sample to 0.1 mM, 0.01 mM, 0.001 mM, and 0.0001 mM injecting samples through a 0.1 or 0.2 μm polycarbonate filter. Rinse syringe three times in DI water and wipe needle surface after each injection as there will be noticeable carry over at or below 0.01 mM. An example of a chromatogram produced by 0.01 mM ATP is shown in Fig. 10.1. Integrate the peak area of each sample and use these data to

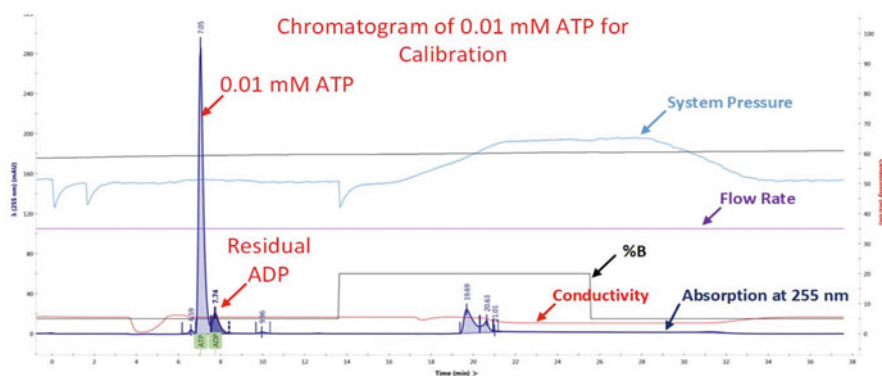


Fig. 10.1 Example chromatogram of a 0.01-mM ATP sample used to calibrate the HPLC

Fig. 10.2 Calibration curves for ATP, ADP, and AMP.

There are three data points at each of four concentrations: 0.1 mM, 0.01 mM, 0.001 mM, and 0.0001 mM

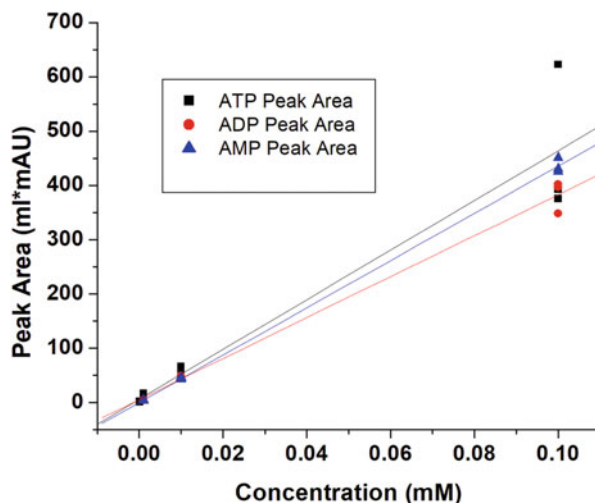


Table 10.1 Result of linear regression from calibration data, $Y = A + B \cdot X$

Analyte	A	A error	B	B error	R	Standard deviation	P
ATP	6.39	21.45	4575	427	0.959	61.9	<0.0001
ADP	5.74	6.02	3737	99	0.997	14.9	<0.0001
AMP	0.28	2.79	4354	51	0.999	6.92	<0.0001

perform a linear regression for calibration. Figure 10.2 illustrates the calibration curves for ATP, ADP, and AMP. Table 10.1 lists the results of a linear regression from the calibration data.

5.2 Cell Culture and Dosing Cells with ATP Liposomes

1. Rk-13 growth from the freezer: From a -80°C freezer, grow Rk-13 cells to confluence in a 75 cm^2 flask in 5 ml of minimal essential medium (MEM) and 10% FBS at 37°C in 5% CO_2 . Every 24 h exchange with 10 ml of the same medium until confluent, usually 3 days.
2. Cell culture in six-well plates and dosing: Seed cells grow to confluence in MEM and FBS (2.5% v/v), usually 1 to 2 days. To dose confluent cells, rinse in PBS and add 2 ml MEM + FBS (2.5%), then add 0.2 ml of ATP liposomes, shake gently, and return to incubator. After dosing with liposomes of various formulations, the time course of absorption may also be studied, e.g., by harvesting every several hours.
3. Harvesting cells from a six-well plate: Remove growth medium from wells. Then wash in 2 ml of cold (4°C) PBS, add from the side being careful not to touch cells with pipette tip. Shake gently and remove. Add 1 ml of RPMI to each well and use a cell scraper to remove cells from the bottom of the wells (see Note 4). Shake gently, tilt the wells, and perfuse from top to bottom. Remove cells with a sterile pipette and put into 1.5 ml Eppendorf tubes. Place tubes in ice while harvesting

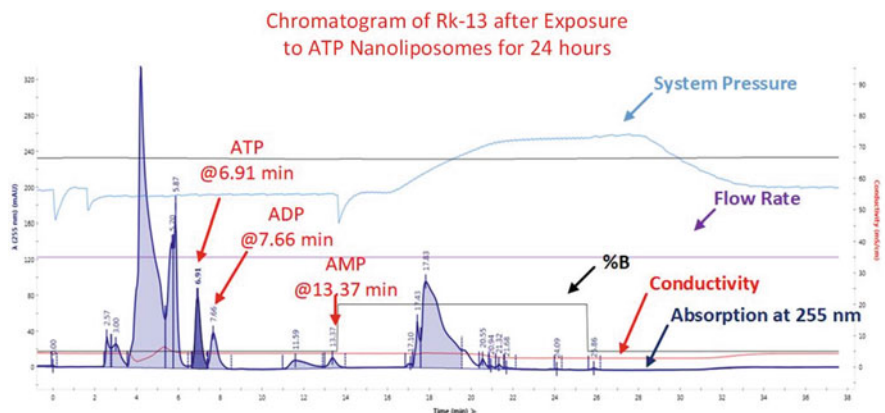


Fig. 10.3 Example chromatogram after exposing cells to ATP liposomes for 24 h. Integration of the analyte peaks gives $3.9 \mu\text{M}$ ATP and $3.0 \mu\text{M}$ ADP. AMP was not quantitated in this sample

and centrifuge for 5 min, 4°C , $10,000g$. Remove supernatant and discard, leaving a cell pellet, and store in a freezer (-80°C) until ready to analyze (see Note 5).

4. Preparing the cell pellet for analysis: Remove samples from -80°C and add 1.5 ml of room temperature lysis buffer. Vortex mix for 3 min and then centrifuge for 5 min, 4°C , $10,000g$. Withdraw supernatant with HPLC injection syringe and inject through a 0.1- μm or 0.2- μm particulate filter. Figure 10.3 illustrates a typical chromatogram showing ATP located at 6.91 min, ADP at 7.66 min, and AMP at 13.37 min. Data showing the time course of ATP absorption for the RK-13 can be found in Fig. 2 of Kotwal et al. [14]. Conveniently, the analyte peaks of interest avoid interference related to other cellular components. Before performing such measurements, it should be noted that we confirmed the location and calibration of the adenosine peaks in the lysis buffer only using standards. This was necessary as the presence of a surfactant may have an influence on the elution times through the column.

5.3 Preparation of ATP-Laden Nanoliposomes

1. Preparation of liposome contents: Dilute 10 mM Mg-ATP in 10 mM KH_2PO_4 , adjust to pH 7.4 using KOH, and store at 4°C .
2. Preparation and mixing of lipids: In a round bottom flask, prepare 98.2 mg/ml of electrolyte of soy phosphatidylcholine (Ave. MW: 783.77 g/mole), DOTAP 2 mg/ml of electrolyte, add chloroform sufficient to dissolve lipids, e.g., 0.05 g/ml to 0.025 g/ml. Note that DOTAP is a cationic lipid used widely as a transfection agent. Allow the lipids to thoroughly solvate by mixing at room temperature in a rotating round bottom flask (we use a Buchi R-100 rotary evaporator).

3. Removal of chloroform in a rotary evaporator: Place the lipid mixture in a 500 ml to 1000 ml round bottom flask and attach it to the rotary evaporator. Set the rotation speed to 4 and angle to $\sim 60^\circ$ with respect to the vertical. Set the water bath temperature to 45°C , condenser temperature to 25°C , and pressure to 500 mbar. Note that this condenser temperature is not sufficient to recover the chloroform, and it will eventually be pumped out of the system. Proper ventilation is important as chloroform is a known carcinogen. Evaporation should be performed for 12–24 h. Complete solvent removal by lyophilization for 12–24 h. Afterward, the remaining solids should appear as a yellow film on the walls of the flask.
4. Manufacture of liposomes: Rehydrate the lipid cake from in a rotary evaporator by adding the Mg-ATP/ KH_2PO_4 electrolyte to the dried lipids with a volume sufficient to reach 100 mg of lipid/ml of electrolyte. If the sample is to be lyophilized, the disaccharide and cryoprotectant trehalose may be added to the buffer in a molar ratio of 2:1 with lipids (see Note 6). Set the bath temperature to 55°C , condenser temperature to 25°C , rotation at 4, and leave the pressure at ambient for 24 h. The result should appear milky white.
5. In order to make the liposomes unilamellar and set the size, extrusion was performed at least twice through track-etched polycarbonate filters with 200 nm filters at 60°C . Then they were extruded at least twice through 100 nm polycarbonate filters at 60°C . The result will be a milky white material.

5.4 ATP Nanoliposome Used in Treatment of Injured Spinal Cord and Visualization by Transmission Electron Microscopy (TEM) and Checking for Sterility

The nanoliposome-encapsulated Mg-ATP was prepared by Avanti Polar Lipids (Alabaster, AL, USA) and received as a lyophilized powder, which is reconstituted in sterile water.

The nanoliposomes composition is HSPC/DOTAP (50:1 mol ratio), 10 mM ATP, trehalose/HSPC (2,1 molar ratio), and 10 mM KH_2PO_4 and are rehydrated to a mass concentration of 100 mg/ml in deionized water as a stock solution containing 0.1 mgs per microliter.

The average diameter of the liposomes was 120–160 nm as measured using a DynaPro Particle Size Analyzer (Proterion Corporation, NJ) [12].

The sterility of the nanoliposomes was confirmed by spreading the vesicles onto nutrient agar culture plates for detection of bacterial contaminants and onto Sabouraud dextrose agar plates for detection of fungal contamination. Contaminated batches are discarded.

Transmission electron microscopy (TEM) was carried out without staining by placing Formvar-coated nickel slot grids onto 20 μl of the nanoliposomes at a 1 mg/ml concentration and then inverting them, removing the excess fluid, and allowing the grids to dry. The grids were then examined using a Hitachi HT7700 instrument and the images are captured with a 16-megapixel AMT V700 digital camera.

5.5 Spinal Cord Injury in Rats: Histology and Immunohistochemistry

Rat models of SCI have been used previously to study pathologies, and the results have been considered for human application [17–19].

Adult Sprague-Dawley male rats were deeply anesthetized by IP injection of 50 mg/kg of pentobarbital. The back was shaved and the hair removed by vacuum.

The surface around the vertebral column was disinfected with Dermachlor™ concentrated wash followed by Dermachlor™ 105 wash.

Lubricant was added to both eyes, 10 ml saline was injected IV, and the rat was placed on a heating pad. The ATP nanoliposome test sample 1mg/ml or thio-ATP nanoliposome control sample were filled in capillaries.

An incision was made between T7 and T11 and supplementary isoflurane anesthesia was supplied. Sutures were placed and a laminectomy was performed at the T9 vertebra.

A contusion assembly consisting of a Horizon impactor was cleaned with sterile water and then adjusted to 150 kilodynes to deliver a mild to moderate injury.

The dura was opened, the rat was placed in a metal stabilizer, the T9 spinous process was removed, and the exposed spinal cord was subjected to moderate contusion injury using the impactor.

The first injection of 1 μ l of 10 mg/ml ATP nanoliposomes or 1 μ l of 10 mg/ml of gamma-thio-ATP control nanoliposomes was administered; 3 min later, a second identical 1 μ l injection was administered on the other side, 1.6 mm inside the cord.

The incision was then closed with sutures or clips. Bacitracin was applied over the sutures or clips and 0.1 ml gentamycin (50 mg/ml) in 5 ml of saline was injected.

The bladder was emptied, by squeezing the lower abdomen of the rat.

A subcutaneous injection of 0.3 mg/ml buprenorphine in sterile saline (1:4, v/v) was given at 0.45 ml/rat once on the day of the procedure and twice a day for the next 5 days.

On the 5th day after treatment, the rats were deeply anesthetized via IP injections of 50 mg/kg of pentobarbital and placed securely on a dissecting rack.

Using surgical scissors, the diaphragm was opened and the heart was exposed.

A perfusion needle was then inserted through the left atrium and ventricle, and into the ascending aorta.

A small puncture was then made in the right atrium in order to allow blood and other fluids to drain. Next, 200–250 ml of 0.01 phosphate-buffered saline (PBS) was pumped through the rat's circulatory system, followed by 400–500 ml of 4% paraformaldehyde in 0.01M PBS.

The rat is then dissected and its spinal cord pieces were removed using surgical scalpels and forceps and placed in 4% paraformaldehyde in PBS overnight.

The spinal cord sections were then cryoprotected by placing them in a solution of 25% sucrose in 0.01M PBS; all sections were maintained at 4° C until frozen.

The spinal cord sections harvested on day 5 were checked for integrity by staining sections with hematoxylin and eosin and by immunohistochemistry with antibodies

to CD68 and CD163. Spinal cord sections were frozen in OCT using the isopentane/liquid nitrogen method.

Frozen blocks were cut at 8 μm onto charged glass slides.

The tissue sections were allowed to air dry for 10 min and then fixed in alcoholic formalin for 10 min at room temperature.

The slides were rinsed in distilled water and immediately placed on a Leica Bond III instrument for automated staining.

Treatment with both antibodies followed the same protocol: heat-induced epitope retrieval using Leica epitope retrieval 2 for 20 min, peroxidase blocking for 5 min, primary antibody incubation for 15 min, post primary for 8 min, Polymer for 8 min, DAB for 10 min, and hematoxylin for 10 min.

The Leica Refine System for chromogenic light microscopy was used for the post primary, polymer, DAB, and hematoxylin steps. These, along with the epitope retrieval 2, were proprietary reagents.

5.6 Notes

1. ATP nanoliposomes could lose activity from freezing and thawing, and it is important to never freeze the ATP nanoliposome formulation more than once.
2. The best way to quality control the ATP inside the nanoliposome is to measure the ATP released when the ATP nanoliposomes are treated with 0.1% Triton X 100.
3. The best way to preserve the nanoliposomes is to refrigerate them as soon as they are prepared and never freeze them unless required for long-term use.
4. Sterility is very critical and the best way to handle is to do transfer in a sterile laminar flow cabinet.
5. Increase of back pressure, or sometimes loss of resolution, necessitates changing precolumn and Krud Katcher.
6. Might be good to modify the method to add 5% methanol to the electrolyte as this is the minimum concentration used in the method and this would prevent the growth of organisms in the KH_2PO_4 which was a problem.
7. A pH of 4.5 in the mobile phase improves separation between ATP and ADP versus physiological.
8. This step may be a significant source of error in the measurement. It is critical to remove all the cells from each well.
9. Cells can rapidly metabolize available ATP, particularly after being removed from MEM; thus, it is important to keep cell pellets at 4 $^\circ\text{C}$ until ready to be frozen. It might also be useful to use the lysis solution *before* placing the cells in low temperature storage.
10. We have found that many preparations of nanoliposomes and the ATP inside are actually quite stable for at least 6 months being stored at 4 $^\circ\text{C}$, and lyophilization may be unnecessary unless long-term (over 6 months) storage is required.

6 Key Research Findings

6.1 Current Status of Nanoliposomes in Medical Applications

From the beginning of this century, research has been ongoing to study the effects of nanoliposomes in a number of animal models for a range of human disease conditions. Examples of applications includes protection of endothelial barrier following ischemia reperfusion injury of organs for transplantation [20, 21], incorporation of therapeutic biomolecules with anti-complement properties like the vaccinia virus complement control protein (VCP) and antithrombotic proteins [22, 23], anti-vascular candidates that block metastasis in cancer therapy [24], delivery of molecules for CNS disease conditions like Alzheimer's disease and Parkinson's disease which are larger than sizes that can penetrate the blood brain barrier [25–28], adjuvants in vaccines, signal enhancers/carriers in cancer therapy [29], chronic disease treatment with nanodelivery systems [30], and antimicrobial drug delivery [31].

6.2 Current Status of ATP Nanoliposomes

ATP Nanoliposome for intracellular delivery although first reported around the turn of the century for organ preservation has not yet reached the patient bed side. The bench research on ATP nanoliposomes has been extensive with the focus being on a rabbit wound model and on understanding the complexity of the molecular and cellular mechanisms as they relate to determining how the acceleration of wound healing occurs upon treatment with ATP nanoliposomes [12, 13, 15, 33]. There is a gross change in the wound, which includes granuloma formation upon treatment with ATP nanoliposomes within 24 h [33]. Immunohistochemical studies have shown the cellular changes occur in the form of macrophage proliferation and collagen formation, which seals the wound rapidly. What happens following ATP levels increasing inside cells in terms of significant changes in RNA expression primarily driven by U1 and U4 RNAs which accelerate the formation of spliceosome which then fast tracks the mRNA processing from pre-mRNA by a well-known process of splicing [14].

6.3 Current Research Findings That Advance Translation of the Application of ATP Nanoliposomes

- The appearance of the ATP nanoliposomes was determined by TEM observation of the unstained preparation. A wide range of sizes was observed for the nanoliposomes (Fig. 10.4). While most of them having diameters of 120–160 nm, some of the particles were greater than 500 nm.
- A method was developed to quantitate adenosine phosphates using high-performance liquid chromatography with ultraviolet absorption detection. The

KBRIN TEM CORE VITASOL IMAGES WITHOUT STAINING

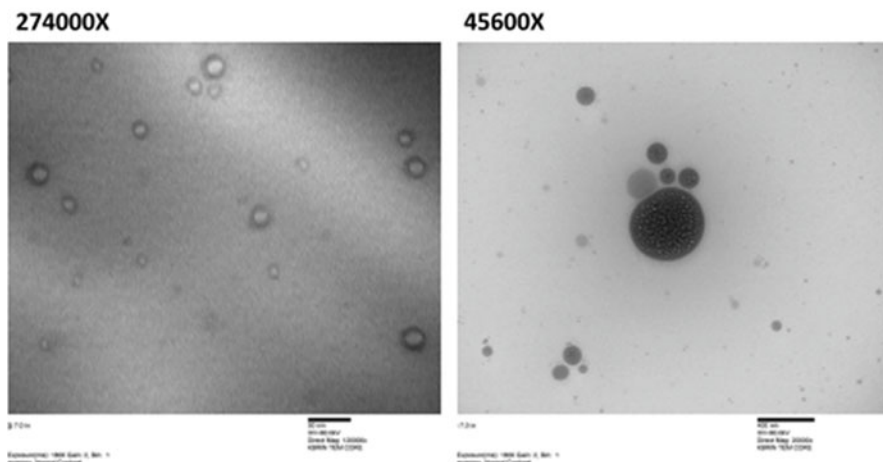


Fig. 10.4 ATP nanoliposome from the batch used in the spinal cord study was deposited on Formvar-coated nickel slot grids and allowed to dry. The grids were examined unstained in a Hitachi HT7700 TEM and the images were captured by a 16-megapixel AMT V700 digital camera. The image on the left is that of ATP nanoliposomes at 286000 \times print magnification and the one at the right is that of print magnification of 456000 \times

detection limit from calibration standards was 0.1 μM with elution times of 6.91 min for ATP, 7.66 min for ADP, and 13.37 min for AMP.

- Methods for preparing HPLC-compatible samples from cells grown in culture and treated with ATP nanoliposomes or controls indicate that treatment with ATP nanoliposome results in increasing amounts of intracellular ATP from the time of treatment to 24 h [14]. Increasing intracellular ATP results in overexpression of snRNA U4 and SnRNA U4. Both of these RNAs are central to the formation of the spliceosome that is essential for the processing of premRNA to translatable mRNA.
- All analytes were detected without interferences from lysed cells.

The cellular changes in the epicenter of the injured spinal cord were determined by immunohistochemical and histological examinations of sections of the spinal cord, as shown in Fig. 10.5. The histology results revealed by hematoxylin and eosin staining, shown in Fig. 10.5a, indicated that treatment of the injured spinal cord with ATP nanoliposomes resulted in little mononuclear cell influx (semi-quantitative +) and loss of integrity when compared to the control spinal cord shown in Fig. 10.5d. The control injured spinal cord treated with gamma-thio-ATP nanoliposomes showed a significant influx of mononuclear cells (semiquantitative ++++). Furthermore, Eriochrome[®] cyanine staining indicated that injured spinal cord sections had better integrity after treatment with ATP nanoliposomes

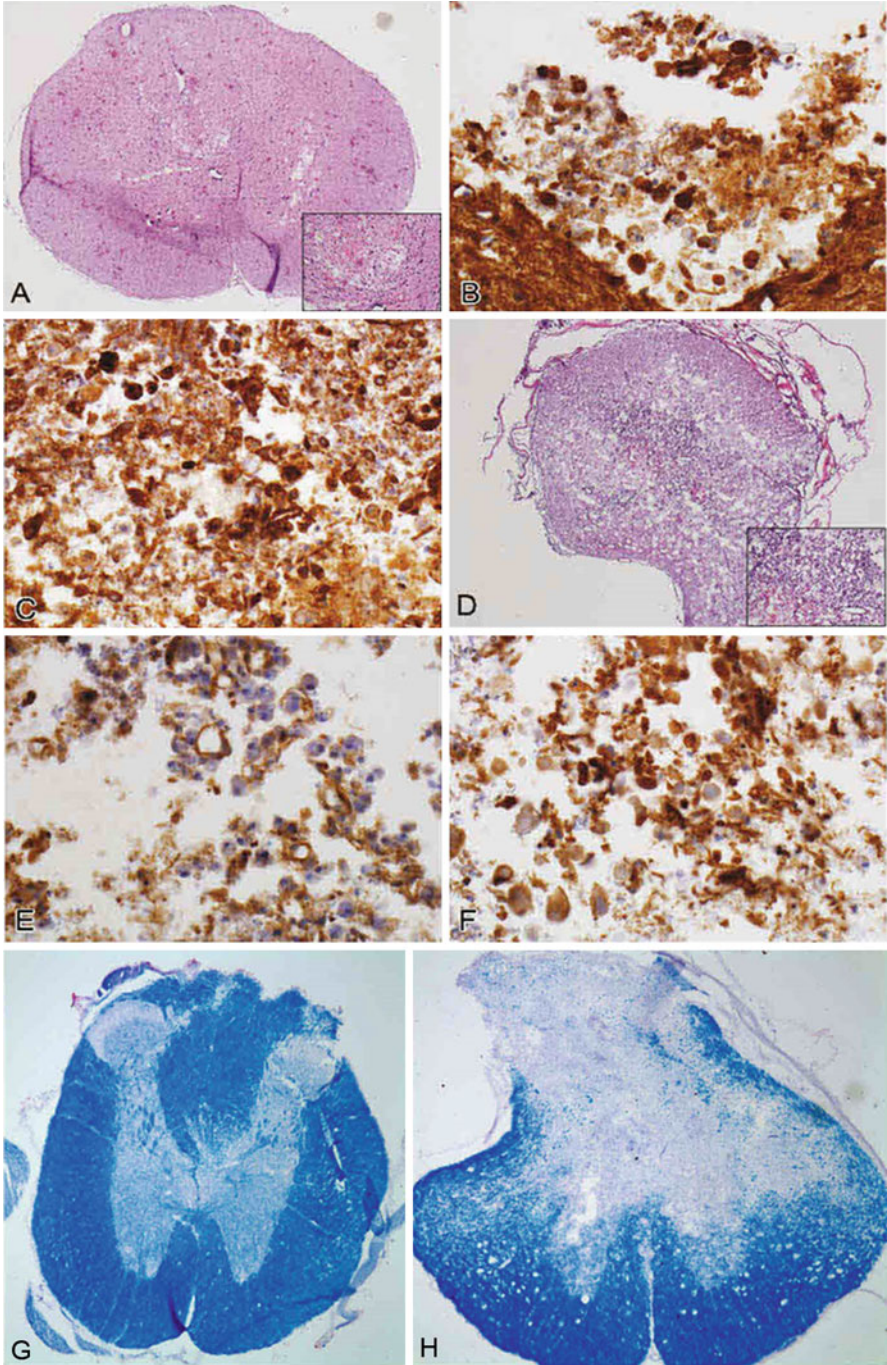


Fig. 10.5 (continued)

(Fig. 10.5g) than the control treatment with gamma-thio-ATP nanoliposomes (Fig. 10.5h).

Immunohistochemical staining with antibodies to CD68 (++) and CD163 (+++) revealed increases in the proportion of regenerative M2 macrophages (CD68+, CD163+) in the injured spinal cord following treatment with ATP nanoliposomes (Fig. 10.5b and c) when compared to the delivery of gamma-thio ATP nanoliposomes (Fig. 10.5e and f). The gamma-thio-ATP nanoliposome treatment instead increased the influx of either M1 macrophages (CD68+, CD163-) or destructive macrophages (semiquantitative +++) and decreased the number of CD68 (semi quantitative +) and CD163 (semiquantitative ++) macrophages.

7 Conclusions and Future Perspectives

Taken together, the results presented here indicate that the use of a combination of ATP nanoliposomes and VCP would be expected to inhibit the complement-mediated inflammatory neurodegenerative response as well as bring about an accelerated restoration of spinal cord integrity by mechanisms suggested in the illustration in Fig. 10.6. The ATP nanoliposomes will ensure an appropriate immune response by speeding up the physical recovery of the spinal cord. Such investigations suggest that although VCP treatment on its own can improve the structural and functional recovery from SCI in rats, treatments in combination with ATP delivery are likely to mirror the uninjured spinal cord in appearance.

Kong and Gao have concluded that macrophage polarization is a key event in SCI [32]. To our knowledge, the potential of ATP nanoliposome treatment for recovery of SCI or other agents could be tested using the method described. This method described provides the first evidence for the proliferation of regenerative M2 macrophages, as well as the maintenance and recovery of spinal cord integrity in the days following injury in response to ATP nanoliposome treatment at the SCI site. While this approach of direct ATP delivery may not be the most suitable for human intervention, it demonstrates the benefit of ATP nanoliposomes, and further

Fig. 10.5 (a) A section from an injured spinal cord treated with ATP nanoliposomes; the section was harvested 5 days after treatment and stained with H&E. (d) A section from an injured spinal cord treated with gamma-thio-ATP (negative control) nanoliposomes; the section was harvested 5 days after treatment and stained with H&E. Note the relative preservation of the spinal cord architecture in image A compared to the near-total distortion and effacement by macrophages in image d. Immunostaining for the CD68 surface marker corresponding to treatment with ATP nanoliposomes (b) and gamma-thio-ATP nanoliposomes (e). Immunostaining for the CD163 surface marker corresponding to treatment with ATP nanoliposomes (c) and gamma-thio ATP nanoliposomes (f). A section from an injured spinal cord treated with ATP nanoliposomes; the section was harvested 5 days after treatment and stained with Eriochrome[®] cyanine (g). A section from an injured spinal cord treated with gamma-thio-ATP (negative control) nanoliposomes; the section was harvested 5 days after treatment and stained with Eriochrome[®] (h). The section treated with ATP nanoliposomes shows better integrity

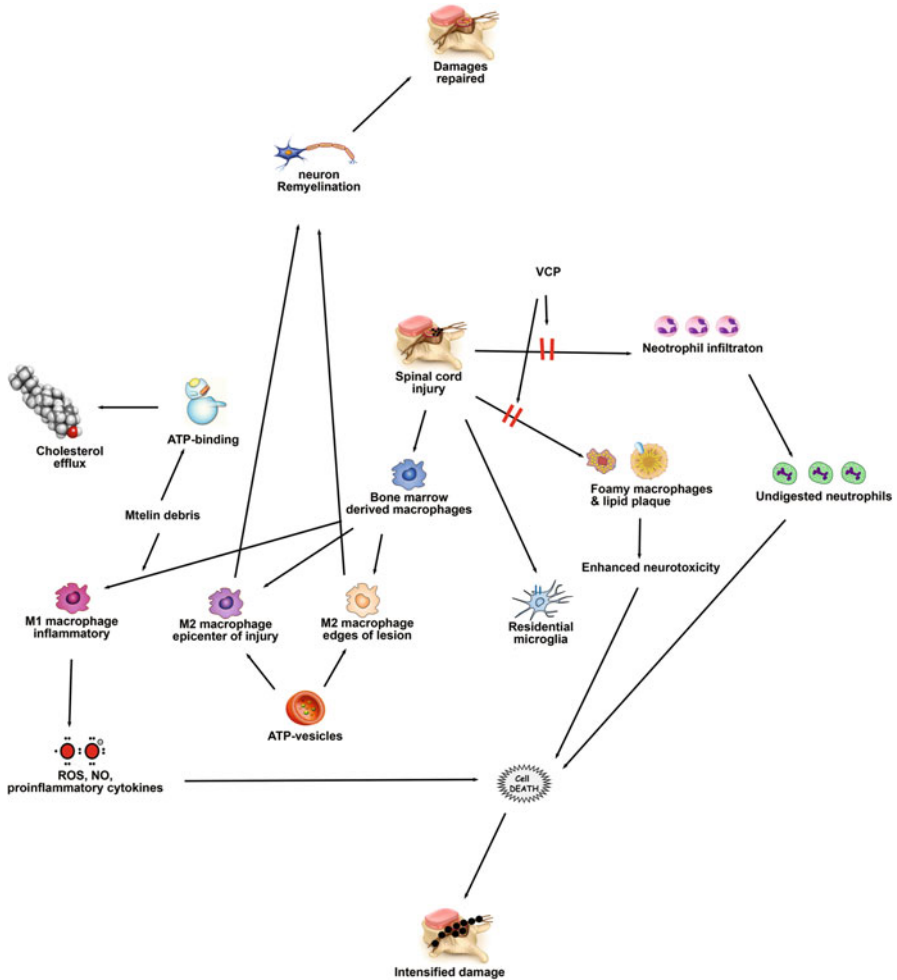


Fig. 10.6 An illustration of the events following spinal cord injury without any intervention and the proposed intervention with a combination of VCP and ATP nanoliposomes to limit the inflammatory damage and accelerate regenerative process

refinements will need to be considered to make this method of treatment more applicable for human administration following SCI. Together, VCP and delivery of ATP will not only inhibit the complement mediated inflammatory neurodegenerative response but also bring about an accelerated restoration of spinal cord integrity by ensuring the appropriate immune response by speeding functional recovery of the spinal cord corresponding to the physical recovery as illustrated in Fig. 10.6. The earlier investigations suggested that individually VCP treatment improved structural and functional recovery from SCI in rats, but feasibility studies for use as a future treatment needs to be done in combination with an ATP delivery system to mirror the uninjured SC.

The potential for spinal cord recovery following injury with ATP nanoliposome treatment had not been studied before, and therefore this is the first indication showing the proliferation of regenerative macrophage M2 as well as the maintenance and recovery of spinal cord integrity through days following injury and treatment at the site of injury. While this approach of direct delivery may not be most suitable for any human intervention, it demonstrates the benefit of ATP nanoliposomes which can be considered for further refinement to make it more applicable to human administration following spinal cord injury.

Acknowledgments The authors would like to thank Dr. Bernard Moss of the NIAID, NIH for providing us with the initial stock of RK-13 cells and Arkadiusz Slawomir Slusarczyk from the group of Dr. Martha Bickford, Department of Anatomical Sciences, University of Louisville School of Medicine for expert assistance with electronmicroscopy of the nanoliposome formulations and Dr. Harshul Pandit for his assistance in suggesting initial HPLC methods. The embedding of frozen spinal cords, sectioning and hematoxylin and eosin staining was performed in the special procedures lab of the Department of Pathology and Laboratory Medicine, University of Louisville School of Medicine by Ms. Melissa Peak. The spinal cord injury with the weight drop method and the microinjection was carried out by Ms. Christine Yarberry from the Kentucky Spinal Cord Injury Research Center (KSCIRC) at the University of Louisville School of Medicine, Louisville, KY. The staining of the spinal cord sections with Nissyl/Cresyl violet for the gray matter and Eriochrome cyanine for the white matter was carried out by Ms. Alice Shum-Siu from the laboratory of Dr. David Magnusson at the KSCIRC. This work was supported in part by grants DK74566, AR52984, HL114235, GM106639, DK104625, DK105692, and OD021317 from the National Institutes of Health and in part from the Kentucky Cabinet for Economic Development, Office of Entrepreneurship, under the Grant Agreement KSTC-184-512-12-138 and KSTC-184-512-14-174 with the Kentucky Science and Technology Corporation.

References

1. Rubiano AM, Carney N, Chesnut R, Puyana JC (2015) Global neurotrauma research challenges and opportunities. *Nature* 527:S193–S197
2. Singh A, Tetreault L, Kalsi-Ryan S, Nouri A, Fehlings MG (2014) Global prevalence and incidence of traumatic spinal cord injury. *Clin Epidemiol* 6:309–331
3. Craig A, Tran Y, Guest R et al (2016) Psychological impact of injuries sustained in motor vehicle crashes: systematic review and meta-analysis. *BMJ Open* 6:e011993
4. Sweis R, Biller J (2017) Systemic complications of spinal cord injury. *Curr Neurol Neurosci Rep* 17:8
5. Widerstrom-Noga E (2017) Neuropathic pain and spinal cord injury: phenotypes and pharmacological management. *Drugs* 77:967–984
6. Kopper TJ, Gensel JC (2018) Myelin as an inflammatory mediator: myelin interactions with complement, macrophages, and microglia in spinal cord injury. *J Neurosci Res* 96:969–977
7. Kotwal GJ, Fernando N, Zhou J, Valter K (2014) Exploring the potential benefits of vaccinia virus complement control protein in controlling complement activation in pathogenesis of the central nervous system diseases. *Mol Immunol* 61:204–209
8. Kulkarni AP, Kellaway LA, Kotwal GJ (2005) Herbal complement inhibitors in the treatment of neuroinflammation: future strategy for neuroprotection. *Ann N Y Acad Sci* 1056:413–429
9. Kulkarni AP, Kellaway LA, Lahiri DK, Kotwal GJ (2004) Neuroprotection from complement-mediated inflammatory damage. *Ann N Y Acad Sci* 1035:147–164
10. Reynolds DN, Smith SA, Zhang YP et al (2003) Vaccinia virus complement control protein modulates inflammation following spinal cord injury. *Ann N Y Acad Sci* 1010:534–539

11. Reynolds DN, Smith SA, Zhang YP et al (2004) Vaccinia virus complement control protein reduces inflammation and improves spinal cord integrity following spinal cord injury. *Ann N Y Acad Sci* 1035:165–178
12. Howard JD, Sarojini H, Wan R, Chien S (2014) Rapid granulation tissue regeneration by intracellular ATP delivery—a comparison with Regranex. *PLoS One* e91787(2014):9
13. Kotwal GJ, Sarojini H, Chien S (2015) Pivotal role of ATP in macrophages fast tracking wound repair and regeneration. *Wound Repair Regen* 23:724–727
14. Kotwal GJ, Martin MD, Chien S (2018) Significant upregulation of U1 and U4 spliceosomal snRNAs by ATP nanoliposomes explains acceleration of wound healing, due to increased pre-mRNA processing to functional mRNA. *Nanomedicine* 14(4):1289–1299. <https://doi.org/10.1016/j.nano.2018.03.003>
15. Kotwal GJ, Chien S (2017) Macrophage differentiation in normal and accelerated wound healing. *Results Probl Cell Differ* 62:353–364
16. Guan Y, Wang J, Sun J (2011) A method for determination of hexokinase activity by RP-HPLC. *Wuhan Univ J Natur Sci* 16(6):535–540
17. Dietz V, Schwab ME (2017) From the rodent spinal cord injury model to human application: promises and challenges. *J Neurotrauma* 34:1826–1830
18. Kjell J, Olson L (2016) Rat models of spinal cord injury: from pathology to potential therapies. *Dis Model Mech* 9:1125–1137
19. Nardone R, Florea C, Holler Y et al (2017) Rodent, large animal and non-human primate models of spinal cord injury. *Zoology (Jena)* 123:101–114
20. Fensterer TF, Keeling WB, Patibandla PK, Pushpakumar S, Perez-Abadia G, Bauer P, Soni CV, Anderson GL, Maldonado C (2013) Stabilizing endothelium of donor hearts with fusogenic liposomes reduces myocardial injury and dysfunction. *J Surg Res* 182(2):331–338. <https://doi.org/10.1016/j.jss.2012.10.022>
21. Pushpakumar SB, Perez-Abadia G, Soni C, Wan R, Todnem N, Patibandla PK, Fensterer T, Zhang Q, Barker JH, Maldonado C (2011) Enhancing complement control on endothelial barrier reduces renal post-ischemia dysfunction. *J Surg Res* 170(2):e263–e270. <https://doi.org/10.1016/j.jss.2011.06.010>. Epub 2011 Jul 7. PubMed PMID: 21816416; PubMed Central PMCID: PMC3175310
22. Goga L, Pushpakumar SB, Perez-Abadia G, Olson P, Anderson G, Soni CV, Barker JH, Maldonado C (2011) A novel liposome-based therapy to reduce complement-mediated injury in revascularized tissues. *J Surg Res* 165(1):e51–e57. <https://doi.org/10.1016/j.jss.2010.09.033>. Epub 2010 Oct 16. PubMed PMID: 21074780; PubMed Central PMCID: PMC3005705
23. Goga L, Perez-Abadia G, Pushpakumar SB, Cramer D, Yan J, Todnem N, Anderson G, Soni C, Barker J, Maldonado C (2010) Cell membrane modification for rapid display of bi-functional peptides: a novel approach to reduce complement activation. *Open Cardiovasc Med J* 4:157–165. <https://doi.org/10.2174/1874192401004010157>. PubMed PMID: 20922044; PubMed Central PMCID: PMC2948132
24. Nik ME, Momtazi-Borojeni AA, Zamani P, Navashenaq JG, Iranshahi M, Jaafari MR, Malaekheh-Nikouei B (2019) Targeted-nanoliposomal combretastatin A4 (CA-4) as an efficient antivascular candidate in the metastatic cancer treatment. *J Cell Physiol*. <https://doi.org/10.1002/jcp.28230>. [Epub ahead of print]. Review
25. Wong KH, Riaz MK, Xie Y, Zhang X, Liu Q, Chen H, Bian Z, Chen X, Lu A, Yang Z (2019) Review of current strategies for delivering Alzheimer’s disease drugs across the blood-brain barrier. *Int J Mol Sci* 20(2):pii:E381. <https://doi.org/10.3390/ijms20020381>. Review
26. Teleanu DM, Chircov C, Grumezescu AM, Teleanu RI (2019) Neurotoxicity of nanomaterials: an up-to-date overview. *Nanomaterials (Basel)* 9(1):pii:E96. <https://doi.org/10.3390/nano9010096>. Review
27. Costa C, Moreira JN, Amaral MH, Sousa Lobo JM, Silva AC (2019) Nose-to-brain delivery of lipid-based nanosystems for epileptic seizures and anxiety crisis. *J Control Release* 295:187–200. <https://doi.org/10.1016/j.jconrel.2018.12.049>. Epub 2019 Jan 2. Review
28. Teleanu DM, Chircov C, Grumezescu AM, Volceanov A, Teleanu RI. Blood-brain delivery methods using nanotechnology. *Pharmaceutics*. 2018;10(4):pii:E269. <https://doi.org/10.3390/>

- [pharmaceutics10040269](#). Review. PubMed PMID: 30544966; PubMed Central PMCID: PMC6321434
29. Zhai B, Zeng Y, Zeng Z, Zhang N, Li C, Zeng Y, You Y, Wang S, Chen X, Sui X, Xie T (2018) Drug delivery systems for elemene, its main active ingredient β -elemene, and its derivatives in cancer therapy. *Int J Nanomedicine* 13:6279–6296. <https://doi.org/10.2147/IJN.S174527>. eCollection 2018. Review. PubMed PMID: 30349250; PubMed Central PMCID: PMC6186893
 30. Ganesan P, Karthivashan G, Park SY, Kim J, Choi DK (2018) Microfluidization trends in the development of nanodelivery systems and applications in chronic disease treatments. *Int J Nanomedicine* 13:6109–6121. <https://doi.org/10.2147/IJN.S178077>. eCollection
 31. Moorcroft SCT, Jayne DG, Evans SD, Ong ZY (2018) Stimuli-responsive release of antimicrobials using hybrid inorganic nanoparticle-associated drug-delivery systems. *Macromol Biosci* 18(12):e1800207. <https://doi.org/10.1002/mabi.201800207>. Epub 2018 Oct 14. Review
 32. Kong X, Gao J (2017) Macrophage polarization: a key event in secondary phase of acute spinal cord injury. *J Cell Mol Med* 2195:941–954
 33. Sarojini H, Billeter AT, Eichenberger S et al (2017) Rapid tissue regeneration induced by intracellular ATP delivery—a preliminary mechanistic study. *PLoS One* 12:e0174899



An Insight into Characterizations and Applications of Nanoparticulate Targeted Drug Delivery Systems

11

Ayan Kumar Barui, Batakrishna Jana, and Ja-Hyoung Ryu

Contents

1	Definition of Topic	417
2	Overview	418
3	Introduction and Background	418
4	Experimental Methodology	419
4.1	Physicochemical Characterizations	420
4.2	Biological Characterizations	431
5	Therapeutic Applications of Drug Delivery Systems: Key Research Findings	439
5.1	Gold Nanoparticles	439
5.2	Silver Nanoparticles	440
5.3	Zinc Oxide Nanoparticles	441
5.4	Iron Oxide Nanoparticles	443
5.5	Titanium Oxide Nanoparticles	444
5.6	Carbon Nanotubes	445
5.7	Carbon Dots	446
5.8	Mesoporous Silica Nanoparticles	446
6	Conclusions: Challenges and Future Perspective	448
	References	449

1 Definition of Topic

Nanoparticle-based targeted drug delivery system (DDS) is one of the major applications of nanotechnology in modern biomedical research. Basically, it comprises of bare or functionalized biocompatible nanoparticles with or without targeting ligands

Ayan Kumar Barui and Batakrishna Jana contributed equally with all other contributors.

A. K. Barui · B. Jana · J.-H. Ryu (✉)

Department of Chemistry, Ulsan National Institute of Science and Technology (UNIST), Ulsan, Republic of Korea

e-mail: jhryu@unist.ac.kr

and one or more chemotherapeutic drugs. While the targeting efficacy of DDS without targeting ligands involves passive targeting through enhanced permeability and retention (EPR) effect, DDS containing targeting ligands (e.g., protein, antibodies, peptides, and small molecules) relies on their specificity to cell surface receptors. To achieve combination therapy, two or more chemotherapeutic drugs (exhibiting synergistic effect) are often loaded on nanoparticulate DDS. Besides site-specific delivery, the release of drugs from the DDS and stability of nanomaterials are also important factors to develop an effective nanomedicine that could overcome the disadvantages (e.g., nonspecificity, less bioavailability, and adverse side effect) associated with conventional treatment strategies of different diseases. To comprehend the drug release, stability of nanomaterials as well as ultimate therapeutic applications of DDS, it is highly essential to gradually develop and understand relevant physicochemical and biological characterization techniques. In view of the rapid growth of modern biomedical research involving drug delivery, it might be speculated that many nanomedicines based on DDS would come up in near future for practical therapeutic applications in human.

2 Overview

Nanotechnology offers an extensive shift in modern days diagnostic as well as therapeutic treatment strategies for various types of diseases. The applications of nanotechnology are generally described as nanomedicine. The huge implication of nanomedicine for several disease theranostics might be manifested to the facile interaction of nanoparticles with cell surface receptors, proteins, DNA/RNA, and other biomolecules because of their nanoscale size similarity. Almost all of the conventional drugs for the treatment of some certain diseases have some common limitations such as side effect, nonspecificity issue, and low bioavailability. In this scenario, nanomedicine could play an important role through targeted drug delivery approach, where nanoparticles act as a drug carrier for the delivery of drugs to the specific disease site with better efficacy and reduced systemic toxicity. Although nanomedicine shows several biomedical applications, nanoparticle-based targeted drug delivery has got maximum attention to the researchers. Since past decades, numerous literature report only the applications of targeted drug delivery of different nanomaterials. However, the report describing the characterizations of drug delivery system (DDS) is very scarce. In this context, this chapter describes the detailed chemical and biological characterizations of nanoparticulate targeted DDS as well as their brief therapeutic applications. Finally, we conclude with diverse challenges and future aspects of nanoparticle-based targeted DDS.

3 Introduction and Background

Nanotechnology refers to an interdisciplinary field of contemporary science and technology encompassing the field of physics, chemistry, engineering, and biology [1–3]. It deals with various types of nanoparticles, having unique physicochemical characteristics

such as mechanical, electrical, optical, and biological properties as compared to the corresponding bulk substances, which could be attributed to their high surface area to volume ratio. Due to possessing unusual and interesting properties, nanomaterials exhibit various applications in diverse fields including agriculture, [4] energy, [5] catalysis, [6] electronics, [7] and environment [8]. Although nanotechnology involves numerous applications, it especially brings revolution in modern biomedical research field in terms of developing new therapeutic and diagnostic treatment strategies of different diseases via nanomedicine approach [9, 10]. The extensive applications of nanotechnology in healthcare research could be manifested by the easier interaction of nanoparticles with cell surface receptors (~10 nm), proteins (~1–20 nm), and nucleic acids (~2 nm) owing to their size (nanoscale range) similarity factor [9, 11].

Since past decades, scientists have highly engaged in design and development of various kinds of functionalized/engineered nanomaterials often called as nanocomposites for different therapeutic and diagnostic applications including cancer therapy, tissue engineering, wound healing, antimicrobial activity, bioimaging, and biosensor [9]. However, major reports related to the biomedical applications of nanocomposite systems demonstrate their potential for designing efficient drug delivery systems (DDSs), owing to their unique physicochemical features such as large surface area, high drug loading capacity, easier functionalization, and controlled drug release. The basic criteria for effective DDSs include slow and sustained release of therapeutic drugs as well as their delivery to the specific site of body system [12]. To achieve site-specific delivery of drug, researchers have generally employed either passive targeting or active targeting approaches [13]. While passive targeting strategy relies on enhanced permeability and retention (EPR) effect, [14] active targeting involves the conjugation of nanoparticles with some active ligands (e.g., recombinant proteins, peptides, antibodies, and small molecules) which would recognize cell surface receptors more specifically [15].

The most common nanocomposites employed for targeted drug delivery applications are based on noble metals (e.g., gold nanoparticles: AuNPs and silver nanoparticles: AgNPs), transition metal oxides (e.g., ZnO nanoparticles, TiO₂ nanoparticles, super paramagnetic iron oxide nanoparticles: SPIONs), carbon materials (e.g., graphene oxide: GO, carbon nanotubes: CNTs, carbon dots: CDs, etc.), silica (silica nanoparticles: SiNPs), lanthanides (cerium nanoparticles: CeNPs, gadolinium nanoparticles: GdNPs), as well as different organic/polymeric nanomaterials. Although various literature demonstrated the applications of targeted DDS, the reports related to the characterizations of DDS are very limited. In this circumstance, this chapter offers an overview of in-depth characterizations as well as brief therapeutic applications of recently developed nanoparticulate targeted DDS, which are described in the following sections.

4 Experimental Methodology

Proper characterization of nanoparticles is highly essential prior to their applications in any field especially in biomedical science and so for targeted drug delivery application. The physicochemical characterizations of nanoparticles for targeted

DDSs are based on their morphology, hydrodynamic size, surface charge, functionalization, stability, drug loading capacity, encapsulation efficiency, and drug release profile. On the other hand, biological characterizations for efficacy and mechanism of action of different DDSs include cellular uptake, cell viability assay, apoptosis assay, western blot, immunohistochemistry, and biodistribution. The following sections elaborately discuss the physicochemical as well as biological characterizations of nanoparticles and nanoparticulate targeted DDSs.

4.1 Physicochemical Characterizations

4.1.1 Analytical Techniques

There are various analytical techniques available for characterization of bare as well as functionalized nanoparticles such as transmission electron microscopy (TEM), scanning electron microscopy (SEM), atomic force microscopy (AFM), dynamic light scattering (DLS), X-ray diffraction (XRD), ultra violet spectroscopy (UV), Fourier-transform infrared spectroscopy (FT-IR), and nuclear magnetic resonance (NMR). While the morphology of nanomaterials is characterized by TEM, SEM, and AFM, the hydrodynamic size and surface charge of nanoparticles are characterized by DLS. TEM and DLS are also employed for the stability study of nanomaterials. XRD analysis provides the crystalline characteristics of nanoparticles. The functionalization of the nanoparticles is generally confirmed by FT-IR, NMR, and UV. Fluorimeter and UV spectroscopy are often employed for measuring the drug loading capacity and the encapsulation efficiency. The next sections elaborately discuss the characterization methodologies of nanoparticles and their DDSs.

4.1.2 Particle Size and Morphology

The nanoparticles are primarily characterized by their particle size distribution and morphology. The drug release from the nanoparticles is largely dependent on the particle size of the nanoparticle. Fast drug release is observed in case of small size nanoparticles due to their large surface area [16]. In contrast, slow diffusion of drug occurs when the drug is encapsulated inside the larger particles. Moreover, during the storage and transportation of the dispersed nanoparticles solution, there is a trend of aggregation in case of small size particles [16]. Therefore, there is a mutual compromise between the small size of the particles and maximum stability [17]. Also, extent of degradation of polymeric nanoparticles depends on the particle size, e.g., with increasing the particle size, the extent of poly (lactic-co-glycolic acid) degradation increases [18]. The surface morphology of the nanoparticles plays an important role in determining their stability for biological and biotechnological application. There are various analytical tools available for measuring the nanoparticle size as well the morphology as discussed below.

Dynamic Light Scattering (DLS)

DLS is very simple and widely used techniques for determination of the particle size. The size distribution profile of small Brownian particles in colloidal suspension in

nano or submicron ranges or polymer in solution is measured by DLS technique. When shining monochromatic light (laser) is exposed to solution of spherical particles in Brownian motion, Doppler shift occurs. There is a change in the wavelength of the incoming light as a result of hitting the monochromatic light with the moving particles. The size of the particles is determined by the extent of this change in wavelength. Various types of nanoparticles including polymers, micelles, lipid, proteins, carbohydrate, and inorganic nanoparticles are characterized by DLS. This measurement depends on the particle concentration, type of the ions in the medium, size of surface structures, and size of the particle core. DLS software of commercial instruments typically displays the particle population at different diameters. There is only one population in case of monodisperse solution. Multiple particle populations are observed in polydisperse systems. In 2012, Lee et al. developed a target-specific long-acting delivery system of interferon α (IFN α) for the treatment of hepatitis C virus (HCV infection). The authors have developed a hybrid material of AuNPs and hyaluronic acid (HA) for targeted delivery of interferon α (IFN α). IFN α was attached to HA-AuNPs through physical binding. Synthesis of HA-AuNP/IFN α complex was fully characterized by various spectroscopic techniques. The change in the particle size of AuNPs after attachment of HA and IFN α was measured by DLS. The mean hydrodynamic diameter of AuNPs was increased after HA and IFN α attachment (Fig. 11.1a) [19].

Transmission Electron Microscopy (TEM)

The most common technique to analyze the morphology, shape, and size of the nanoparticles is the TEM. Moreover, the aggregation tendency and the stability of the nanoparticles are often studied by TEM. It provides direct images of the nanoparticles and also accurate estimation of nanoparticle homogeneity. TEM is a microscopy technique based on the interaction between a thin sample and a uniform current density electron beam. When the electron beam reaches the sample, part of the electrons is transmitted, while the rest are scattered [20]. The magnitude of the interaction depends on several factors such as size, elemental composition, and sample density. The final images are produced with the information gathered from the transmitted electrons. Nanoparticle solution is deposited onto support grid or films during TEM characterization. To make nanoparticles unaffected against the instrument vacuum and easy handling, they are fixed using negative staining agent such as uranyl acetate and phosphotungstic acid. Alternatively, nanoparticle sample is exposed to liquid nitrogen temperatures after embedding in vitreous ice. One of the limitations of TEM is the difficulty in quantifying a large number of particles. Lee et al. used TEM for characterization of AuNP/IFN α and HA-AuNP/IFN α complex, used for targeted delivery of interferon α (IFN α) for the treatment of hepatitis C virus (HCV infection). The monodispersed morphology was observed in TEM images of AuNP/IFN α and HA-AuNP/IFN α complex (Fig. 11.1b) [19].

Scanning Electron Microscopy (SEM)

SEM is another type of electron microscope. The size, shape, and surface morphology of the nanoparticles with direct visualization is determined by this microscope. SEM

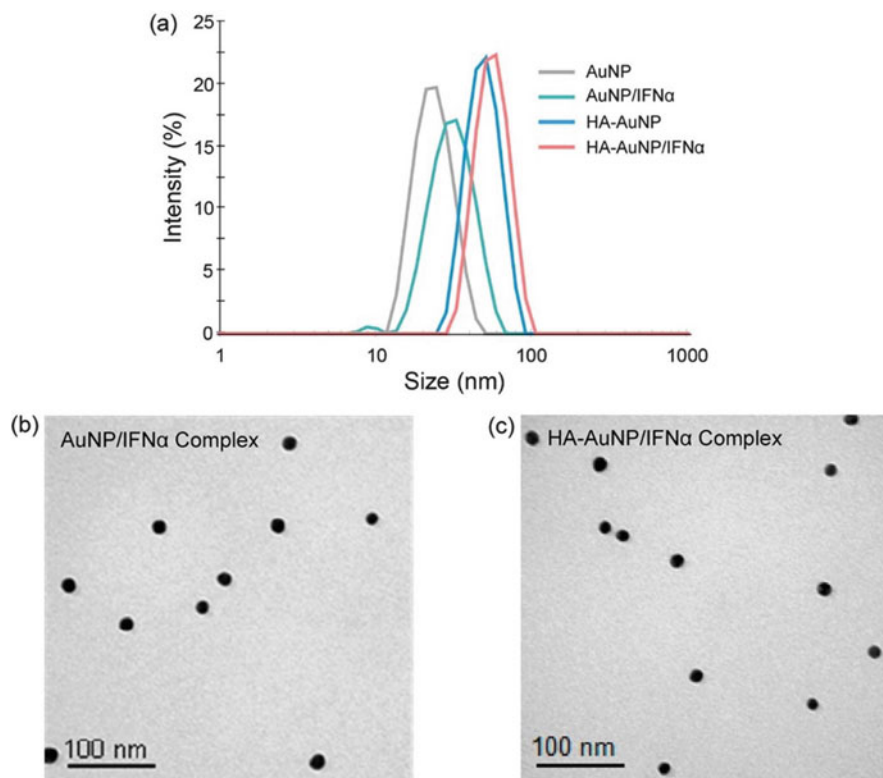


Fig. 11.1 (a) Dynamic light scattering analysis for the hydrodynamic diameter of AuNP/IFN α and HA-AuNP/IFN α complexes. Transmission electron microscopic images of (b) AuNP/IFN α and (c) HA-AuNP/IFN α complexes. (Adapted from Ref. [19]. Copyright © 2012, American Chemical Society)

constructs the images of the sample scanning its surface with a focused beam of electrons in a raster scan pattern. The surface topography and composition of the sample is obtained from the various signals, which is produced by the interaction of the electrons and the atoms in the sample. For nanoparticles characterization by SEM, the solution of nanoparticles should be converted into a dry powder. Then it will be further mounted on a sample holder and coated with conductive metal using a sputter coater. The whole sample is scanned with a focused fine beam of electrons [21]. The surface characteristics of the sample are determined by secondary electrons, emitted from the sample surface. The average mean size obtained from SEM and DLS is comparable. The disadvantages of this technique include high cost, time consuming process and frequent need of complementary information about size distribution [22]. In 2011, Sanpui et al. reported chitosan nanocarriers (NCs)-based delivery system, where the authors delivered silver nanoparticles (AgNPs) to mammalian cells. The authors observed that AgNP-nanocarriers (Ag-CS NCs) with very low concentrations of the

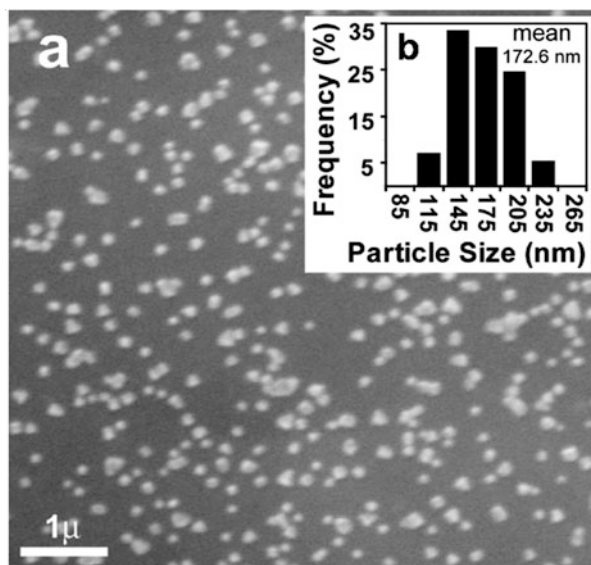


Fig. 11.2 (a) Typical SEM image of Ag-CS NCs. (b) (Inset) Particle size distribution calculated based on the SEM images and mean particle size was found to be 172.6 nm. (Adapted from Ref. [23]. Copyright © 2011, American Chemical Society)

AgNPs induces apoptosis to the mammalian cells. The average size and morphology of Ag-CS NCs was determined by SEM, which was found to be 172.6 nm (Fig. 11.2) [23].

Atomic Force Microscopy (AFM)

AFM is based on a physical scanning of samples at submicron level. A probe tip of atomic scale is required during AFM analysis. It offers ultrahigh resolution in particle size measurement [24]. This technique is also used for studying the particle size and morphology of the nanoparticles. The samples are generally scanned in contact mode or noncontact mode based on the properties of the samples. A topographical map is produced by tapping the probe on to the surface across the sample during contact mode; however, in noncontact mode, the probe drifts over the surface. The main advantage of AFM is, even nonconducting samples are imaged without any specific treatment. For that reason, delicate biological and polymeric nano- and microstructures also can be imaged [25]. The most accurate description of size, distribution of size, and real picture is obtained from AFM (without any mathematical calculation), which helps in understanding the effect of functionalization as well as various biological condition [26]. In 2010, Liu et al. developed a delivery platform based on PEGylated nanographene oxide for hydrophobic anticancer drug SN38 delivery. The authors characterized graphene oxide (GO) and PEGylated graphene oxide (NGO-PEG) by AFM. The as-made GO sheets were 50–500 nm in size, whereas NGO-PEG was ~5 to 50 nm. The researchers also checked the water and serum stability of GO and NGO-PEG. It was found that GO was aggregated in serum as well as in DMEM medium, but NGO-PEG was stable in those solutions (Fig. 11.3) [27].

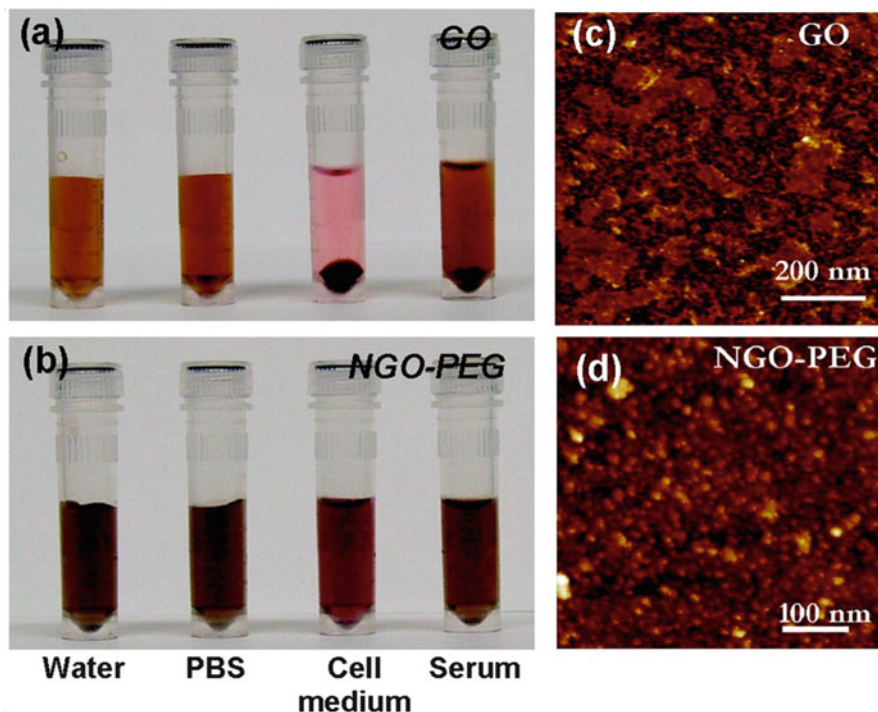


Fig. 11.3 PEGylation of graphene oxide: photos of GO (a) and NGO-PEG (b) in different solutions recorded after centrifugation at 10000g for 5 min. GO crashed out slightly in PBS and completely in cell medium and serum (top panel). NGO-PEG was stable in all solutions; AFM images of GO (c) and NGO-PEG (d). (Adapted from Ref. [27]. Copyright © 2008, American Chemical Society)

4.1.3 Surface Functionalization

Surface functionalization of the nanoparticles is very essential aiming various biomedical and biotechnological applications of inorganic, organic, and polymeric nanoparticles. The surface of the nanoparticles is functionalized with various molecules like PEGylation with polyethylene glycol for increasing the hydrophilicity and biocompatibility of the nanoparticles. The nanoparticles surface can also be functionalized with proteins, small molecules, peptides, various receptor targeting ligand, and anticancer drugs for various biomedical applications. After functionalization of nanoparticles, there is alteration in their size and surface morphology which are usually characterized by measuring the size distribution by TEM or DLS, and the surface charge by DLS. Most importantly, the functionalization of nanoparticles is generally characterized by various spectroscopic techniques such as UV-Vis spectroscopy, FT-IR, and NMR. Here we discuss the various spectroscopic techniques for characterization of functionalized nanoparticles.

UV-Vis Spectroscopy

One of the most important techniques for characterization of nanoparticles functionalization is UV-Vis spectroscopy. It is an absorption spectroscopy or reflectance spectroscopy in the ultra violet-visible spectral region. Absorption spectroscopy is complementary to fluorescence spectroscopy. Absorption measures transition from the ground state to the excited state, while fluorescence spectroscopy deals with transitions from the excited state to the ground state. Various nanoparticles have characteristic UV absorption peak, which is shifted to higher or lower wavelength or the intensity is lowered and increased after the functionalization. There is the appearance of new absorption peak or disappearance of exiting peak due to functionalization of nanoparticles in some cases. As discussed earlier, Lee et al. developed AuNPs-based DDS for targeted delivery of interferon α (IFN α) for the treatment of hepatitis C virus. The formation of AuNP/IFN α and HA-AuNP/IFN α complex was assessed by UV-Vis spectra. The surface plasmon resonance (SPR) band of AuNPs is red-shifted after attachment of IFN α , which confirms the interaction of IFN α with AuNPs. Moreover, the SPR peaks shifted from 519 to 523 and 527 nm as a result of stepwise binding of HA-SH and IFN α to AuNP (Fig. 11.4) [19].

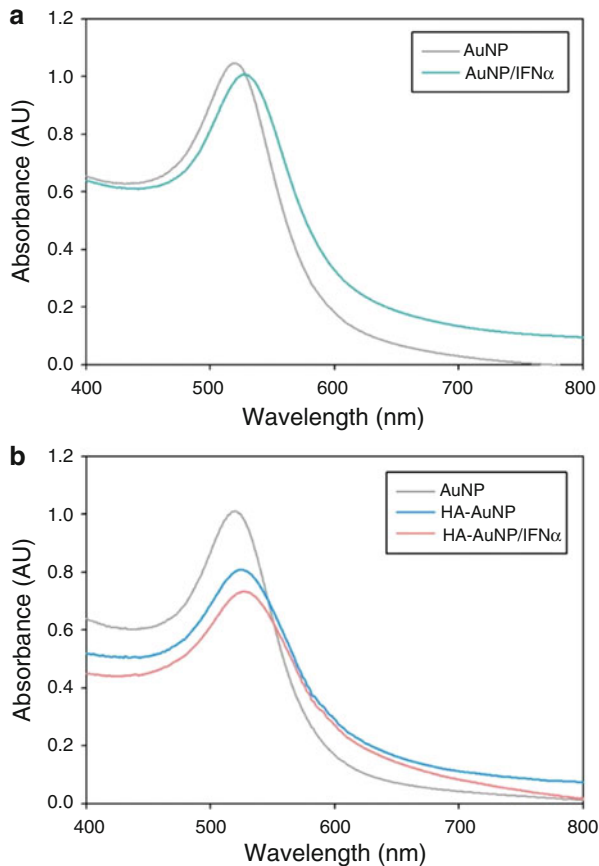
FT-IR Spectroscopy

This is the most frequently used techniques for the characterization of functionalized nanoparticles. An infrared spectrum of absorption or emission of nanoparticles is obtained using FT-IR spectroscopy. An FTIR spectrometer simultaneously collects high-spectral-resolution data over a wide spectral range. The term Fourier-transform infrared spectroscopy implies that a Fourier transform (a mathematical process) is necessary to convert the raw data into the actual spectrum. There are some nanoparticles such as graphene and CNTs, which have characteristics FT-IR absorption peaks. There is shift in the FT-IR absorption peak position as well as appearance of the new peaks in the FT-IR spectrum of functionalized nanoparticles depending on the type of functionality present in the attached functional group. FT-IR technique is the direct proof of the functionalization of nanoparticles.

NMR Spectroscopy

Since its discovery, NMR has grown to be one of the major characterization tool for scientists to obtain information about the structure and dynamics of molecules with atomic resolution. It has also important application in characterization of nanoparticles functionalization. It is a spectroscopic technique to observe local magnetic fields around atomic nuclei. An NMR signal is generated by excitation of the nuclei sample with radio waves into nuclear magnetic resonance, when the sample is placed in a magnetic field. The signal is detected with sensitive radio receivers. The intramolecular magnetic field around an atom in a molecule changes the resonance frequency. As a result, details of the electronic structure of a molecule and its individual functional groups are obtained. The synthesis of organic nanoparticles, polymeric nanoparticles, lipid nanoparticles, and micelle are usually confirmed by ^1H and ^{13}C NMR spectroscopy. NMR spectra of functionalized nanoparticles are

Fig. 11.4 UV-Vis spectra of (a) AuNP/IFN α and (b) HA-AuNP/IFN α complexes. (Adapted from Ref. [19]. Copyright © 2012, American Chemical Society)



changed due to different functionality and the interaction of the attached molecules with the nanoparticles. A novel gold conjugate (GNP-NHN = Dox-mPEG) with doxorubicin (DOX) shielded by PEGylation on the surface of GNPs is designed by Cui et al. [28] Fig. 11.5 represents the synthetic procedure of a novel lipionic acid (LA)-modified PEG derivative of Dox (LA-NHN = Dox-mPEG)-attached gold nanoparticles (GNP-NHN = Dox-mPEG) and their intracellular drug release mechanism. GNP-NHN = Dox-mPEG enters into the cancer cells through endocytosis mechanism followed by the liberation of Dox-mPEG in acidic lysosomes and then free Dox in cytoplasm, which is catalyzed by esterase.

The authors characterized the DDS GNP-NHN = Dox-mPEG through FT-IR and ^1H NMR spectroscopy (Fig. 11.6). All the data supports the successful synthesis of GNP-NHN = Dox-mPEG. A two-step stimulus-responsive drug release in response to an acidic environment in lysosomes and then esterase in the cytoplasm has been achieved with DOX-GNPs conjugate with improved solubility and stability, which allows sustained drug release to increase antitumor efficacy.

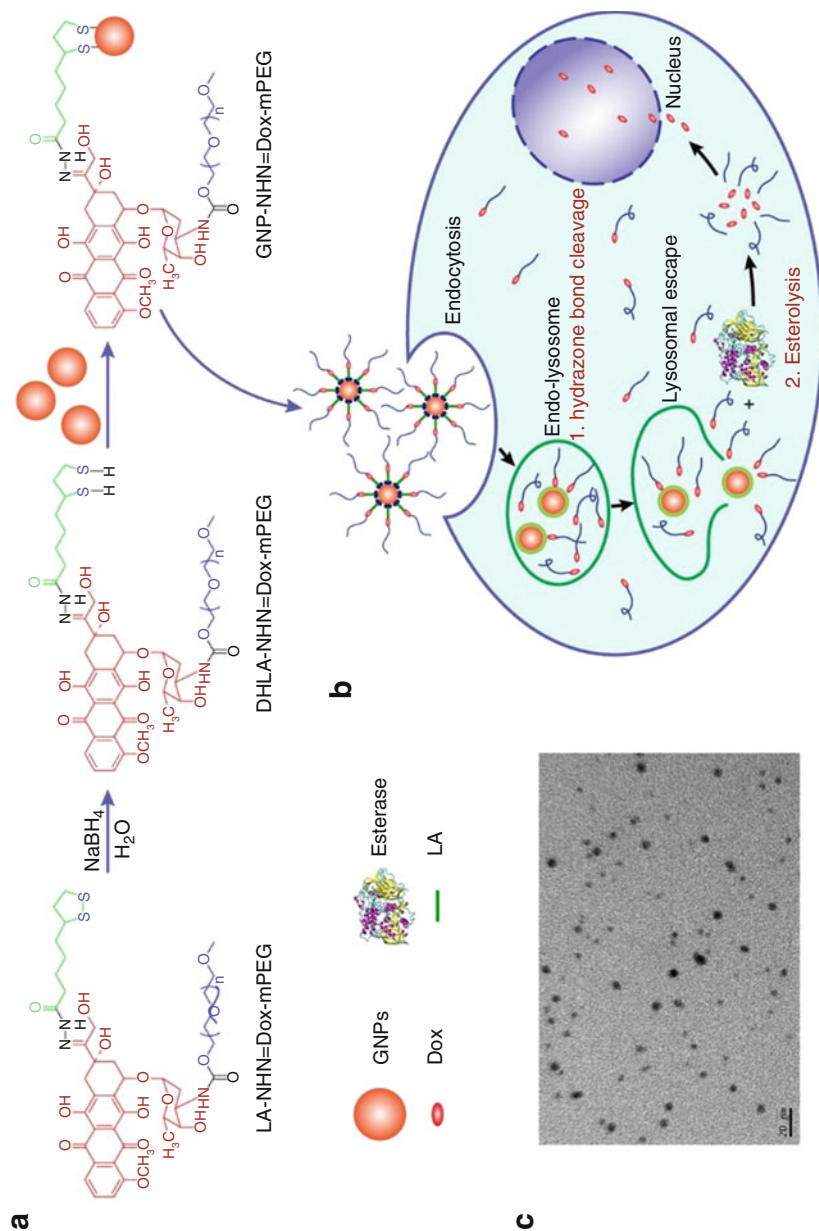


Fig. 11.5 (a) The structure of GNP-NHN = Dox-mPEG and (b) an illustration of its intracellular drug release mechanism. (c) TEM image of GNP-NHN = Dox-mPEG. The scale bar is 20 nm. (Adapted from Ref. [28]. Copyright © 2017, American Chemical Society)

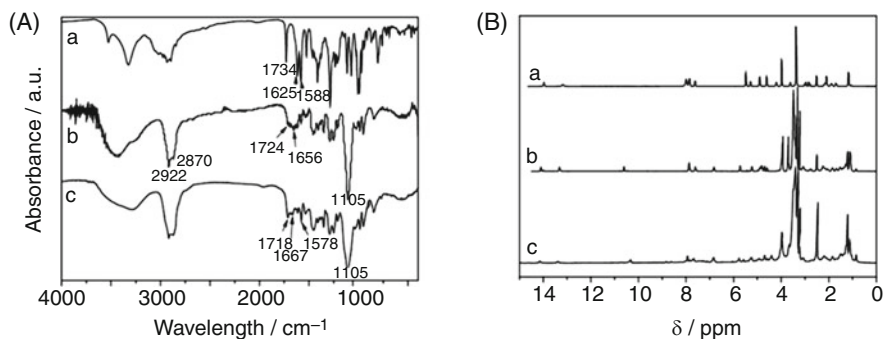


Fig. 11.6 (A) FT-IR spectra and (B) ^1H NMR spectra of (a) Dox·HCl, (b) LA-NHN=Dox-mPEG, and (c) GNP-NHN=Dox-mPEG. (Adapted from Ref. [28]. Copyright © 2017, American Chemical Society)

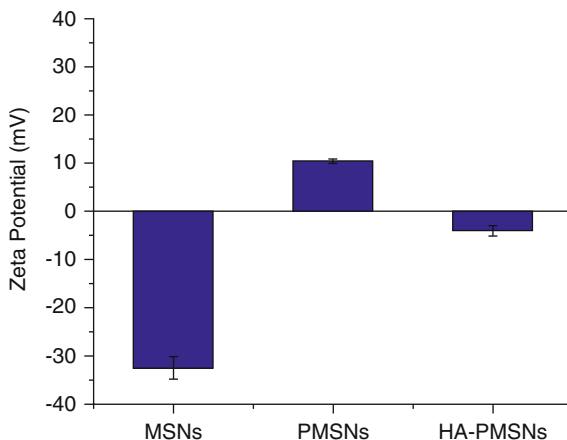
4.1.4 Surface Charge

Interaction of nanoparticles with the bioactive molecules as well as with the biological environment is determined by their surface charge and intensity. Surface charge of the nanoparticle is estimated by measuring its zeta potential. Zeta potential of the nanoparticles determines the stability of colloidal materials. High zeta potential values (either positive or negative) of nanoparticles indicate the high stability and nonaggregation tendency. Moreover, the surface hydrophobicity, nature of the materials encapsulated within the nanoparticles, and type of materials coated or functionalized on the surface are also determined by measuring the zeta potential values [29]. Recently, Palanikumar et al. introduced a degradable mesoporous silica nanoparticle (MSN) system as a simple, facile, and versatile drug delivery vehicle, decorated with HA, which augmented the targeted delivery of doxorubicin hydrochloride to CD44 over-expressed cancer cells. The successful coating of polymeric gatekeeper as well as HA on the MSN was confirmed by measuring the zeta potential (Fig. 11.7) [30].

4.1.5 Drug Loading and Encapsulation Stability and Drug Release

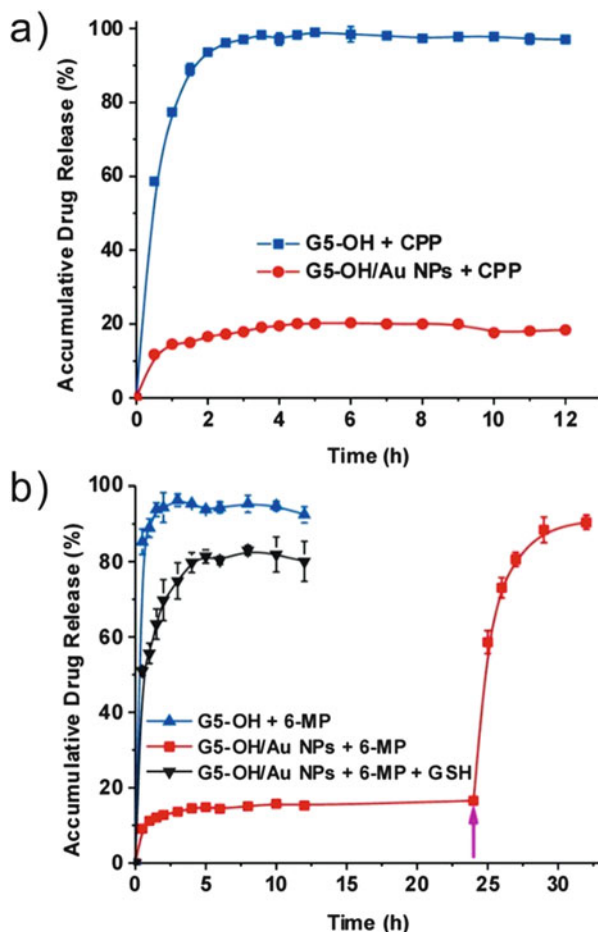
A crucial property of nanoparticle-based therapeutic systems is drug release, directly related to the drug stability and the therapeutic results. It is a process by which the drug loaded in or on the nanomaterials is released in the body through diffusion or dissolution of the nanomaterials matrix releasing the drug in solution or the release of the drug from the nanoparticles by biodegradation, a process of breakdown of the DDSs inside the body. One should consider both the drug release and biodegradation during the development of nanoparticle-based DDS. Generally, the effectiveness of drugs not only depends on its active component, but its diffusion and solubility. The effectiveness of the nanoparticle-based drug delivery is affected by the particle size and the release process, which is again affected by the biodegradation of the particle matrix. Faster rate of drug release is observed in case of smaller particles as it has large surface area to volume ratio, so most of the drug molecules will be near the

Fig. 11.7 Zeta potential measurement for MSNs, PMSNs, HA-PMSNs. (Adapted from Ref. [30]. Copyright © 2018, American Chemical Society)



particle surface. In contrast, in case of larger size particles, slower drug release is observed as its larger core allows more drugs to be encapsulated per particles. Therefore, particle size is an important factor to consider during design of nanoparticle-based DDS. There are two important parameters “drug loading capacity” and “drug entrapment efficiency,” which determine the capacity of DDS. Drug loading capacity denotes the mass of the drug encapsulated in the nanoparticles/mass of the nanoparticles, whereas drug entrapment efficiency denotes mass of the loaded drug/mass of initial drug. Various techniques such as high-performance liquid chromatography (HPLC) after ultracentrifugation, gel-filtration, ultra-filtration, and UV spectroscopy are used to measure these parameters. Similar techniques for determination of drug loading are also used for drug release analysis, which is generally assessed for a period of time to evaluate the drug release mechanism [31, 32]. In general, release rate of the drug depends on several factors such as desorption of the surface bound or adsorbed drug, drug solubility, nanomaterials matrix degradation or erosion, and drug diffusion out of the nanomaterials matrix. When the drug is loaded to the nanoparticle through covalent attachment, the drug release is affected completely by drug-nanomaterials diffusion. When the drug is encapsulated inside nanomaterials, diffusion of the drug from the nanomaterials interior controls the drug release. In an encapsulated drug where the drug is uniformly distributed inside the nanomaterials matrix, drug release occurs by diffusion and/or erosion of the matrix. The diffusion largely controls the mechanism of release, when the diffusion of the drug is faster than matrix erosion. Recently, various DDSs have been reported, where the drug release is controlled by external stimuli such as light, pH, and enzyme. In 2013, Wang et al. developed dendrimer-encapsulated gold nanoparticles (DEGNPs) as a carrier of thiolated anticancer drugs. Thiol-containing drugs such as captopril and 6-mercaptopurine loaded within DEGNPs showed an “off–on” release behavior in the presence of thiol-reducing agents such as glutathione and dithiothreitol (Fig. 11.8) [33].

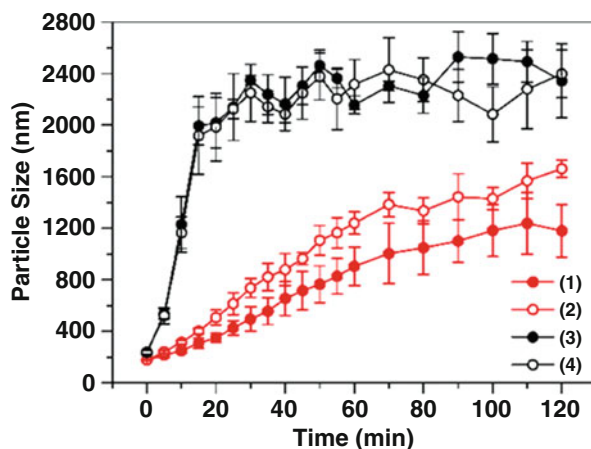
Fig. 11.8 In vitro release profiles of CPP (a) and 6-MP (b) from G5-OH and G5-OH/Au NPs. The purple arrow (b) indicates the addition of DTT into the complex solution at 24 h. (Adapted from Ref. [33]. Copyright © 2013, American Chemical Society)



4.1.6 Nanoparticle Stability

Stability of the nanoparticles is measured by the DLS. Aggregation tendency of the nanoparticles over time can be measured by measuring the size of the nanoparticles in DLS over time. If there is aggregation of the nanoparticles, there will be larger population of particles with larger radius and size of the nanoparticles will increase with time. In contrast, there will be no change in the particle size in case of the stable nanoparticles. Stability of the nanoparticle plays a critical role in determining their potential application in drug delivery. There are two terms “colloidal stability” and “serum stability” most frequently used to address the stability of the nanoparticles. When a nanoparticle is added to the biological medium such as phosphate buffer saline (PBS) and Dulbecco’s modified Eagle’s medium (DMEM), their intrinsic properties such as surface charge, size, and aggregation state could change significantly due to interaction with the physicochemical properties of the solution such as pH, components, and temperature. These properties of the nanoparticle determined

Fig. 11.9 Particle sizes of SFNPs prepared with acetone or ethanol as a function of time in serum-free DMEM or 0.01 mol/L PBS. (1) SFNPs prepared with acetone in serum-free DMEM; (2) SFNPs prepared with acetone in 0.01 mol/L PBS; (3) SFNPs prepared with ethanol in serum-free DMEM; and (4) SFNPs prepared with ethanol in 0.01 mol/L PBS. (Adapted from Ref. [34]. Copyright © 2015, American Chemical Society)



the colloidal stability of nanoparticles. Such properties of the nanoparticles do not change in case of the nanoparticle which have good colloidal stability. However, poor colloidal stability makes the nanoparticle unsuitable for drug delivery application. There is another term, i.e., serum stability, which signifies the stability of the nanoparticle in blood serum. The nanoparticle must remain unchanged and circulate in the blood for a moderately long period of time after intravenous injection to be accumulated at the target site, to be used as a potential drug delivery candidate. In 2015, Wang et al. reported the increase in colloidal stability of silk fibroin nanoparticles after coating with cationic polymer for effective drug delivery application. The authors checked the colloidal stability of their nanoparticles by measuring the change in the particle size by DLS over time (Fig. 11.9) [34].

4.2 Biological Characterizations

4.2.1 Cell Viability Assay

Cell viability assay is one of the fundamental assays to comprehend the biocompatibility of the nanoparticles, and therapeutic efficacy of these biocompatible nanoparticulate targeted DDS in vitro [35–40]. To perform cell viability assay, researchers have used various reagents including MTT (3-(4, 5-dimethylthiazol- 2-yl)-2, 5-diphenyl tetrazolium bromide), alamarBlue, and trypan blue. In MTT reagent-based cell viability assay, yellow-colored MTT is reduced by the mitochondrial dehydrogenase present in the cells, leading to the formation of purple formazan crystals, whose absorbance could reflect the viable cells [35, 36]. On the other hand, nonfluorescent alamarBlue reagent (resazurin-based blue-colored solution) is getting reduced upon entering into live cells leading to the formation of red fluorescent resorufin, whose absorbance or fluorescence can reflect the cell viability. Trypan blue dye is also used for determining the cell viability, where the principle is that living cells can exclude the trypan blue dye due to their intact membrane, while dead cells cannot.

Among all these reagents described above, MTT reagent has most frequently been used for checking the cell viability in presence of any materials and so for nano-conjugated system [35–40]. To perform cell viability assay, cells (generally, 10,000 cells/well) are seeded in all the wells of 96-well tissue culture plate and kept inside a humidified incubator system (37 °C, 5% CO₂) for 24 h. The cells are then treated with the nanoparticles and/or DDS at different concentrations for a certain period of times (generally, 24–72 h). After this, media in the wells are replaced by DMSO–MeOH (1:1; v/v) mixture to solubilize the purple formazan crystals, followed by checking the absorbance of the purple solution in each well of the plate using a multimode reader at 570 nm. The cell viability in presence of the treatment materials can be normalized by considering the viability of untreated control cells as 100%. For example, Bollu et al. developed MSU-2 as well as MCM-41-based chloro- and amine-functionalized SiNPs containing anticancer drug curcumin [35]. Cell viability study using MTT reagent (Fig. 11.10) demonstrated that the curcumin-loaded DDSs (MSU-2: V3 and MCM-41: V6) exhibited more inhibition of cancer cells (A549, MCF-7, and B16F10)

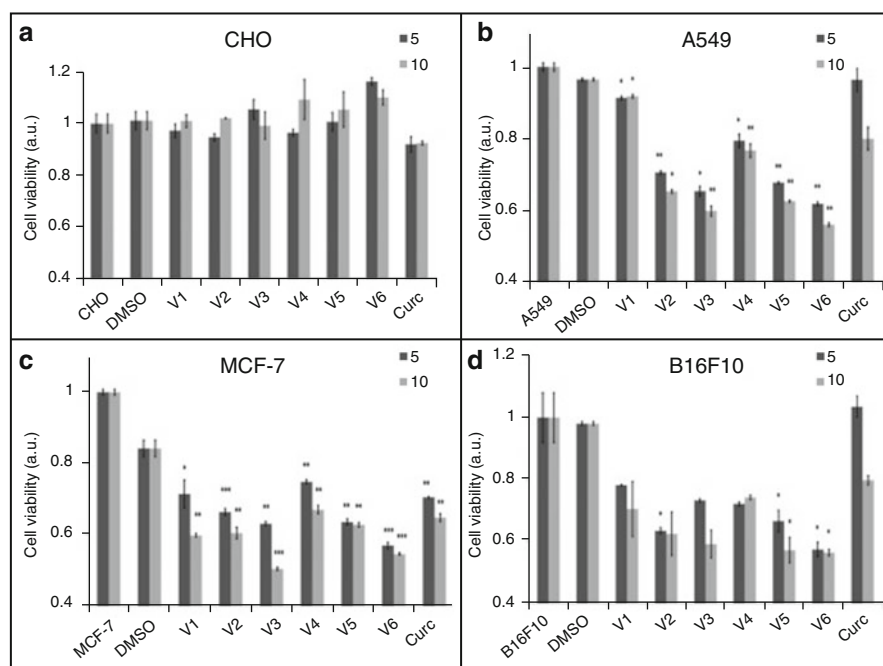


Fig. 11.10 Cell viability assay in normal (CHO) and cancerous (A549, MCF-7, B16F10) cell lines incubated with V1–V6. (a) All the materials (V1–V6), including curcumin-loaded materials, exhibit their biocompatible nature into CHO cells. (b–d) Curcumin-based nanostructured V3 and V6 materials show significant cytotoxicity in various cancer cells [A549 (b), MCF-7 (c), and B16F10 (d)] compared to pristine curcumin suggesting the materials as potent drug delivery systems. Curcumin and DMSO have been used as positive and vehicle control experiments, respectively. Numerical values 5 and 10 indicate doses in μM with respect to curcumin. *P ≤ 0.05, **P ≤ 0.005, ***P ≤ 0.0005 compared to control. (Adapted from Ref. [35]. Copyright © 2016, Royal Society of Chemistry)

proliferation in a dose-dependent manner as compared to untreated control cells, corresponding chloro- (MSU-2: **V1** and MCM-41: **V4**), and amine (MSU-2: **V2** and MCM-41: **V5**)-functionalized SiNPs as well as free curcumin. However, all the SiNPs-based materials (**V1-V6**) are found to be biocompatible in normal CHO cells. Overall, the cell viability study depicted the therapeutic potential of the SiNPs-based DDSs **V3** and **V6**.

4.2.2 Cellular Internalization

Cellular internalization of nanomaterials and corresponding DDS is another basic assay to rationalize their mode of actions. Cellular uptake of nanoparticulate DDS have often been characterized by means of several techniques including fluorescence/confocal microscopy, flow cytometry, TEM, and ICP-OES/ICP-MS [35, 36]. In case of fluorescence/confocal microscopy and flow cytometry-based cellular uptake characterizations of DDS, the nanoparticles or therapeutic drug should possess inherent fluorescence properties that could be detected by the respective instruments. For instance, Bollu et al. synthesized curcumin-loaded functionalized SiNPs-based DDSs (**V3** and **V6**) as described in earlier section and studied the kinetics of internalization of **V3** and **V6** in A549 cells through fluorescence microscopy exploiting the inherent green fluorescence of curcumin [35]. The result exhibited that **V3**- and **V6**-treated cells showed more green fluorescence as compared to untreated control cells, and the intensity of green fluorescence was enhanced with time (Fig. 11.11). The result suggested that intracellular uptake

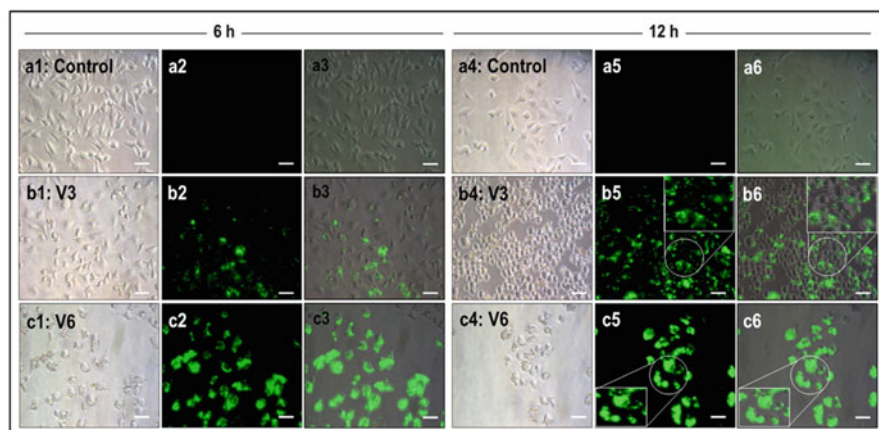


Fig. 11.11 Investigation of intracellular uptake of **V3** and **V6** in A549 cells using fluorescence microscopy. Kinetic study for cellular internalization using fluorescence microscopy shows that the cellular uptake of curcumin-loaded materials **V3** and **V6** increases in a time-dependent manner as indicated by the enhanced green fluorescence intensity with time. Row 1: control (a1–a3: 6 h; a4–a6: 12 h); Row 2: cells treated with **V3** (b1–b3: 10 μ M w.r.t. curcumin, 6 h; b4–b6: 10 μ M w.r.t. curcumin, 12 h); Row 3: cells treated with **V6** (c1–c3: 10 μ M w.r.t. curcumin, 6 h; c4–c6: 10 μ M w.r.t. curcumin, 12 h). Column 1 and Column 4: bright field images; Column 2 and Column 5: green fluorescent images; Column 3 and Column 6: merging of bright field and green fluorescent images. The inset picture shows the enlarged images of cellular fluorescence. Scale bar = 50 μ m. (Adapted from Ref. [35]. Copyright © 2016, Royal Society of Chemistry)

of **V3** and **V6** was increased with time. This cellular uptake study was further confirmed by flow cytometry as well as ICP-OES analysis.

When the nanoparticles and the drug do not have fluorescence characteristics, some dyes (e.g., DiI, FITC, Rhodamine, Cyanine, etc.) have often been conjugated with the nanoparticulate DDS so that their internalization can be monitored either through fluorescence/confocal microscopy or flow cytometry instrument. The kinetic study of internalization of the DDSs could even be performed by these techniques by incubating the cells with DDSs for different time points. It is to be mentioned here that the cells could be live or fixed using paraformaldehyde (PFA) for fluorescence/confocal microscopy experiment. However, the cells are trypsinized after treatment followed by washing with Dulbecco's phosphate-buffered saline (DPBS) and then analyzed with flow cytometry instrument. Besides microscopy and flow cytometry, TEM have often been employed to analyze treated cells for understanding the localization of nanoparticulate system inside cells, whether in cytoplasm or nucleus. ICP-OES and ICP-MS techniques are also used to determine the cellular internalization of DDSs in terms of the content of respective elements present in nanoparticles.

4.2.3 In Vitro Mechanistic Study

To understand the mechanistic pathways for therapeutic efficacy of DDSs, scientists have employed several methodologies including apoptosis assay, determination of reactive oxygen species (ROS), immunocytochemistry, and western blot, which are briefly described in this section.

Scientists have often employed apoptosis assay to understand whether a material-based toxicity to cells are induced via apoptosis pathway [35, 36, 39]. Apoptosis assay for nanoparticulate DDSs are carried out either through propidium iodide (PI)/Hoechst staining-based fluorescence microscopy or by means of flow cytometry analysis. PI (DNA binding dye) can stain more the damaged DNA of nucleus during late apoptosis process. In case of microscopy method, the cells are generally treated with DDSs for a certain time period, followed by fixation with PFA and permeabilization using triton-X. The cells are then incubated with PI/Hoechst solution for some periods, washed with DPBS, and analyzed through fluorescence/confocal microscopy. On the other hand, for flow cytometry technique, after the respective treatments with DDS, the cells are washed with DPBS and stained with Annexin V FITC and PI staining solution, followed by analysis in flow cytometry instrument.

ROS plays an important role for various cellular signaling pathways. Therefore, researchers often check whether DDSs could induce the formation of intracellular ROS such as H_2O_2 or O_2^- using fluorescence/confocal microscopy technique [35, 36]. To measure the generation of intracellular ROS, cells are first treated with nanoparticulate DDS, followed by staining with either H_2DCFDA (green fluorescence for H_2O_2) or DHE (red fluorescence for O_2^-) and then analyzed with fluorescence/confocal microscopy. The cellular esterase could cleave the acetate group of H_2DCFDA , which can get oxidized by DDS-induced intracellular H_2O_2 , leading to the formation of green fluorescent DCF (2',7'-dichlorofluorescein), that could be detected through fluorescence/confocal microscopy [38]. On the other hand, the formation of intracellular O_2^- could be

assessed by observing the red fluorescence deriving from the reaction of DDS-induced O_2^- and DHE, leading to the generation of 2-hydroxyethidium (red fluorescent). For instance, Kotcherlakota et al. developed KIT-6 (**S2**), MSU-2 (**S4**), as well as MCM-41 (**S6**) based functionalized SiNPs conjugated with anticancer drug curcumin and demonstrated the efficient antiproliferative effect of all these DDSs, especially **S4** to various cancer cells (A549, MCF-7 and SKOV3) as compared to free curcumin [36]. The authors employed fluorescence microscopy study (Fig. 11.12) using DHE reagent, which revealed that all these DDSs (**S2**, **S4**, and **S6**), especially **S4**, induced intracellular formation of O_2^- (evidenced by red fluorescence) as compared to the untreated control cells and corresponding functionalized SiNPs without drug attachment (**S1**, **S3**, and **S5**). The result indicated that formation of ROS might play a crucial role underlying therapeutic potential of the DDSs.

Immunocytochemistry has been used by various researchers to understand the expression of different proteins in cells treated with nanomedicine. These proteins are

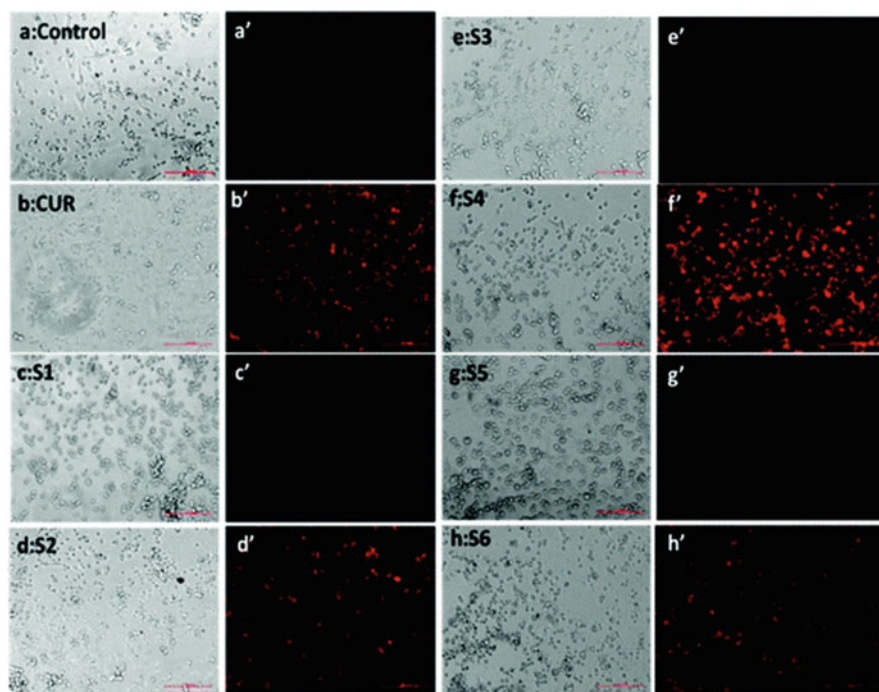
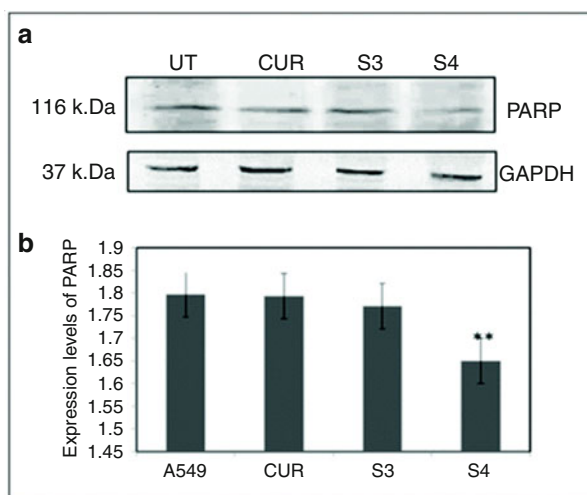


Fig. 11.12 Determination of intracellular superoxide anion radicals in A549 cells by fluorescence microscopy. The results show the formation of the superoxide ion radical in cells treated with curcumin-loaded materials. Phase images (**a–h**) and corresponding fluorescent images (**a'–h'**) of A549 cells. (**a–a'**): untreated control cells; (**b–b'**): cells treated with curcumin (10 μ M); (**c–c'**): cells treated with **S1**; (**d–d'**): cells treated with **S2**; (**e–e'**): cells treated with **S3**; (**f–f'**): cells treated with **S4**; (**g–g'**): cells treated with **S5**; (**h–h'**): cells treated with **S6**. The doses of all curcumin-loaded silica materials are 10 μ M w.r.t. curcumin. Scale bar = 200 micron. (Adapted from Ref. [36]. Copyright © 2016, Royal Society of Chemistry)

often responsible in regulating the cellular mechanism which plays important role in the therapeutic efficacy of the nanomedicine. The cells are generally seeded on coverslips, and after the treatment with nanomedicine, the cells are washed with DPBS, fixed with PFA, and permeabilized with triton-X. The cells are then subjected to blocking using BSA in TBST buffer, followed by incubation with primary antibody and fluorescence moiety conjugated secondary antibody sequentially for certain time periods. The coverslips are mounted with DAPI for nucleus staining and sealed using nail polish, followed by analyzing through fluorescence/confocal microscopy.

Similar to immunocytochemistry, expression of different proteins responsible for cell signaling cascades are often been investigated using western blot technique. To perform western blot, the cells are first incubated with nanomedicine for certain time periods. The cells are then lysed employing RIPA buffer (radioimmune precipitation assay buffer) which contains protease inhibitor cocktail [35, 36]. To get the cell lysate, the cell suspension are centrifuged, followed by estimation of protein content in lysate using Bradford assay or BCA assay. The equal amount of proteins is loaded on SDS-polyacrylamide gel and blotted on PVDF or nitrocellulose membrane after separation through electrophoresis. The proteins are blocked using BSA or nonfat dry milk and incubated with primary and secondary antibodies sequentially for some periods. The blot is then developed using colorimetric or chemiluminescence reagents to understand the expression of the target proteins. For instance, Kotcherlakota et al. developed functionalized SiNPs-based curcumin-loaded DDS (**S4**) as described in earlier section and studied the mechanism of therapeutic potential of the DDS through western blot analysis [36]. The result revealed that **S4** treatment in A549 cancer cells led to downregulation of the expression of poly ADP ribose polymerase (PARP) protein as compared to control experiment and corresponding amine-functionalized SiNPs (Fig. 11.13). The result suggested that **S3** exhibited cancer therapeutic potential by inducing apoptosis in cancer cells.

Fig. 11.13 Western blot analysis for poly ADP ribose polymerase (PARP) expression in A549 cells. (a) Immunoblotting shows the downregulation of the PARP levels in cells treated with **S4** compared to untreated control cells, indicating the induction of apoptosis by the material. (b) The quantification of PARP expression with respect to GAPDH is presented as a histogram. *P “ 0.05, **P ” 0.005 compared to control. (Adapted from Ref. [36]. Copyright © 2016, Royal Society of Chemistry)



4.2.4 In Vivo Studies

To comprehend the practical validity of *in vitro* biological characterizations and therapeutic potential of nanoparticulate targeted DDSs, their *in vivo* characterization/experiments in animal models are highly essential. The *in vivo* studies employing DDSs generally include tumor regression analysis, biodistribution, histopathology, and immunohistochemistry. For instance, Sau et al. developed different AuNPs-based nanoformulations for cancer therapeutics application [41]. These nanoformulations included (F2) AuNPs-MDA (MDA: 11-mercaptopundecanoic acid), (F3) AuNPs-Dex (Dex: Dexamethasone), (F4) AuNPs-MDA-Dex, (F5) AuNPs-Dex MDA, as well as (F1) water-Dex-MDA formulation without AuNPs. Intraperitoneal administration of these formulations to melanoma tumor containing C57BL6/J mice showed that F5 significantly inhibited the tumor growth in comparison with other formulations and untreated (UT) control experiment, as observed by tumor regression analysis (Fig. 11.14a–c). Immunohistochemistry study of tumor sections of different groups also revealed that F5 induced more apoptosis as compared to UT and other formulations, as indicated by the TUNEL-based green fluorescence in the respective tumor section (Fig. 11.14d). Additionally, the biodistribution of AuNPs in F5-administered mice through ICP-MS showed higher entrapment of AuNPs in tumor than in other vital organs such as lungs, spleen, and kidney. The overall result suggested the cancer therapeutic potential of F5 nanoformulation.

The following section briefly discusses the experimental methodology of different *in vivo* studies. In case of targeted DDS for cancers, respective doses of DDS are administered through various routes (i.p.: intraperitoneal, i.v.: intravenous, i.m.: intramuscular, intratumoral, and oral) to animals (e.g., mouse, rat, rabbit, and others) containing tumors for some certain days. The volume of the tumors are measured from starting day of experiment to sacrificing day to plot the regression of tumors that would give an overview of the therapeutic potential of the DDS [42].

Similar to cellular uptake experiment *in vitro*, nanoparticulate DDS could be characterized by *in vivo* biodistribution analysis either through ICP-OES/ICP-MS or *in vivo* imaging system. Various important organs (e.g., brain, heart, lung, liver, kidney, spleen, etc.) of animals are collected after sacrificing, followed by washing with DPBS and digested in nitric acid. The digested tissue solutions are subjected to ICP-OES/ICP-MS analysis to detect the availability of the DDSs with respect to the content of respective elements present in nanoparticles. On the other hand, sometimes DDS containing NIR dye might be administered to the animals for some time periods, and then after sacrificing the animals, the vital organs are analyzed through *in vivo* imaging system to understand the biodistribution of the DDS in different organs.

Histopathology is one of the common methods to understand the structural change of organs due to toxicity of any kind of materials [43]. Therefore, researchers often perform histopathology of different organs of animals administered with nanoparticulate DDS. In brief, after completion of experiment period, the vital organs of animals are collected, washed with DPBS, and fixed with PFA. The tissue samples are then embedded in paraffin, sectioned, and fixed on clean slides. The

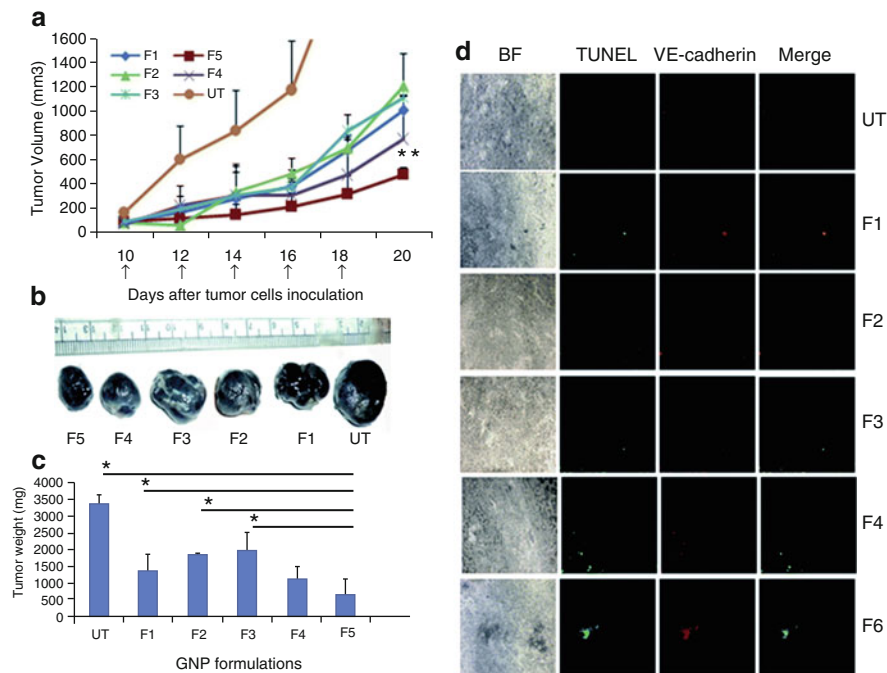


Fig. 11.14 Therapeutic study of GNP formulation: (a) tumor regression curve after subcutaneous implantation of B16F10 cells in C57BL/6J mice followed by intraperitoneal injection of F1–F5 or kept untreated (UT). Days of injection are indicated by black arrows. The dose of Dex in F1 was 10 mg kg^{-1} , whereas that in F3–F5 was 5 mg kg^{-1} . ** Denotes $p < 0.005$ for the F5 treatment with respect to the F1 treatment. (b) Representative tumors from mice of untreated group and different treated groups in the tumor model experiment (in vivo). (c) Comparison of average weight of isolated tumors from mice respectively treated with GNPs (F1–F5) or from the untreated (UT) group. * Denotes $p < 0.05$. (d) Microscopic pictures of $10 \mu\text{m}$ tumor sections from UT, and F1–F5 (upper to lower). Panels from left respectively indicate the tissue architecture in bright field (BF), apoptotic regions in TUNEL assay (green fluorescent), region with endothelial cells having VE-cadherin stained (red fluorescent) and merger (yellow) of the second and the third panels from the left. All the images are taken at $10\times$ magnification. (Adapted from Ref. [41]. Copyright © 2016, Royal Society of Chemistry)

slides are dipped in xylene, rehydrated with ethanol, rinsed with water, and placed in hematoxylin solution. After that, the tissue slides are washed with acidic water, rinsed with 70% ethanol, and dipped in eosin solution, followed by dehydration using absolute ethanol. Finally, tissue slides are rinsed in xylene and mounted using mounting media followed by analyzing under bright-field microscope.

Similar to in vitro immunocytochemistry, in vivo tissue samples of animals administered with DDS are often analyzed through immunohistochemistry experiment to check the expression of proteins of interest. Briefly, the tissue samples are washed with DPBS, fixed with PFA, and rinsed with 20% glycerol. While

processing, the tissue samples are embedded in paraffin, sectioned, and fixed on clean slides. The tissue slides are dipped in isopropanol and xylene for few minutes and warmed in sodium citrate buffer. After cooling, the tissues are subjected to block with BSA in TBST buffer, followed by incubation with primary antibody and fluorescence moiety-tagged secondary antibody for few hours sequentially. Finally, the tissue samples are washed with TBST buffer and mounted with DAPI for nucleus staining. The tissue slides are then analyzed through fluorescence/confocal microscopy to comprehend the expression of the target proteins.

5 Therapeutic Applications of Drug Delivery Systems: Key Research Findings

Since past decades, scientists have developed various active and passive targeted nanoparticulate DDSs using different biocompatible nanoparticles, including gold, silver, zinc oxide, iron oxide, titanium dioxide, CNTs, CDs, and SiNPs. The following sections briefly discuss the therapeutic applications of few recent advancement of these nanomaterial-based DDSs.

5.1 Gold Nanoparticles

Over the past decades, AuNPs have been developed for a wide variety of applications including catalysis, bioanalysis, and imaging. But the most important application of AuNPs drawing attention to the researchers is the use of AuNPs as an ideal drug delivery scaffold because they are known to be nontoxic and nonimmunogenic. Researchers can readily functionalize the AuNPs with multiple targeting molecules and have shown their excellent potential for the delivery of various potential anticancer and antibacterial drugs. Several AuNPs-based drugs are currently under clinical trials [44, 45]. In the recent years, researchers are trying to develop various drug delivery platform based on AuNPs for better antitumor efficacy. In this context, a pH-responsive DDS has been developed by Aryal et al. [46] The authors have developed hydrophilic DOX-conjugated AuNPs, which exhibit a significant pH-responsive drug release. Thiolated methoxy polyethylene glycol (MPEG-SH) and methyl thioglycolate (MTG) at an equal molar ratio have been used to stabilize the AuNPs. The anticancer drug DOX has been attached to the MTG segments of the thiol-stabilized AuNPs through hydrazine as the linker. DOX-conjugated AuNPs have the potential to deliver the anticancer drugs to their target site to simultaneously enhance CT imaging contrast and facilitate photo-thermal cancer therapy. In another study, Brown et al. have functionalized naked AuNPs with a thiolated poly(ethylene glycol) (PEG) monolayer capped with a carboxylate group to tether the active component of the anticancer drug oxaliplatin for improved drug delivery [47]. The nanoparticle-conjugated drug shows as good as, or significantly better, cytotoxicity than oxaliplatin alone in all of the cell lines. It has also unusual ability to penetrate the nucleus in the lung cancer cells. Green

synthesis of AuNPs was achieved by Kumar et al. using the extract of eggplant as a reducing agent. HA serves as a capping and targeting agent [48]. Metformin (MET) was successfully loaded on HA-capped AuNPs (H-AuNPs), and this formulation binds easily on the surface of the liver cancer cells. This formulation exhibited better targeted delivery as well as increased regression activity than free MET in HepG2 cells. Suarasan et al. further developed a new pH- and temperature-responsive nanochemotherapeutic system based on DOX non-covalently bound to biosynthesized gelatin-coated gold nanoparticles (DOX-AuNPs@gelatin) [49]. The high drug loading capacity and effective drug release under pH control combined with the advantage of multimodal visualization inside cells clearly indicate the high potential of our DOX-AuNPs@gelatin delivery system for implementation in nanomedicine.

5.2 Silver Nanoparticles

Besides AuNPs, AgNPs are also extensively used as an effective drug delivery platform. For instance, Benyettou et al. demonstrated simultaneous intracellular delivery of DOX and alendronate (Ald) by bisphosphonate Ald-coated AgNPs (Ald@AgNPs) for improving the anticancer therapeutic indices of both drugs [50]. Dox- and Ald-loaded AgNPs (Dox-Ald@AgNPs) show better anticancer activity in vitro than either Ald or Dox alone. Ald@AgNPs nanoplatform can accommodate the attachment of other drugs as well as targeting agents and can be used as a general platform for drug delivery. Figure 11.15 represents the synthesis of Ald@AgNP and dye/drug conjugation, intracellular uptake of drug-Ald@AgNPs, and subsequent drug release. Intracellular release of drug occurred within the acidic microenvironment of late endosomes and lysosomes. In another study, Li et al. functionalized the surface of AgNPs by polyethylenimine (PEI) and paclitaxel (PTX) to evaluate the cytotoxic effect of Ag@PEI@PTX on HepG2 cells and corresponding anticancer mechanism [51]. It has been shown that Ag@PEI@PTX could enhance the cytotoxic effects on HepG2 cells and triggered intracellular reactive oxygen species. Further the signaling pathways of AKT, p53, and MAPK were activated to advance cell apoptosis. The result shows that Ag@PEI@PTX can be used as an appropriate candidate for chemotherapy of cancer. Liang et al. have further developed HA modified AgNPs for targeting CD44 receptors over-expressed cancer cell lines for targeted cancer therapy [52]. HA was used as the reducing agent and stabilizer and for targeting CD44. The antitumor efficacy was significantly improved by HA modification. Moreover, multiple mechanisms including the decline of mitochondrial membrane potential, cell-cycle arrest, apoptosis, and autophagy are involved for the enhanced anticancer activities of HA-AgNP, which provided a promising solution for AgNPs-mediated cancer treatment. In another study, Wang et al. proposed one-step synthesis approach for folic acid (FA)-coated AgNPs for DOX drug delivery [53]. Paramasivam et al. also reported biopolymers of chitosan (CH) and dextran sulfate (DS)-coated silver nanorods (AgNRs) for encapsulation of water-soluble antibacterial drugs like ciprofloxacin hydrochloride (CFH)

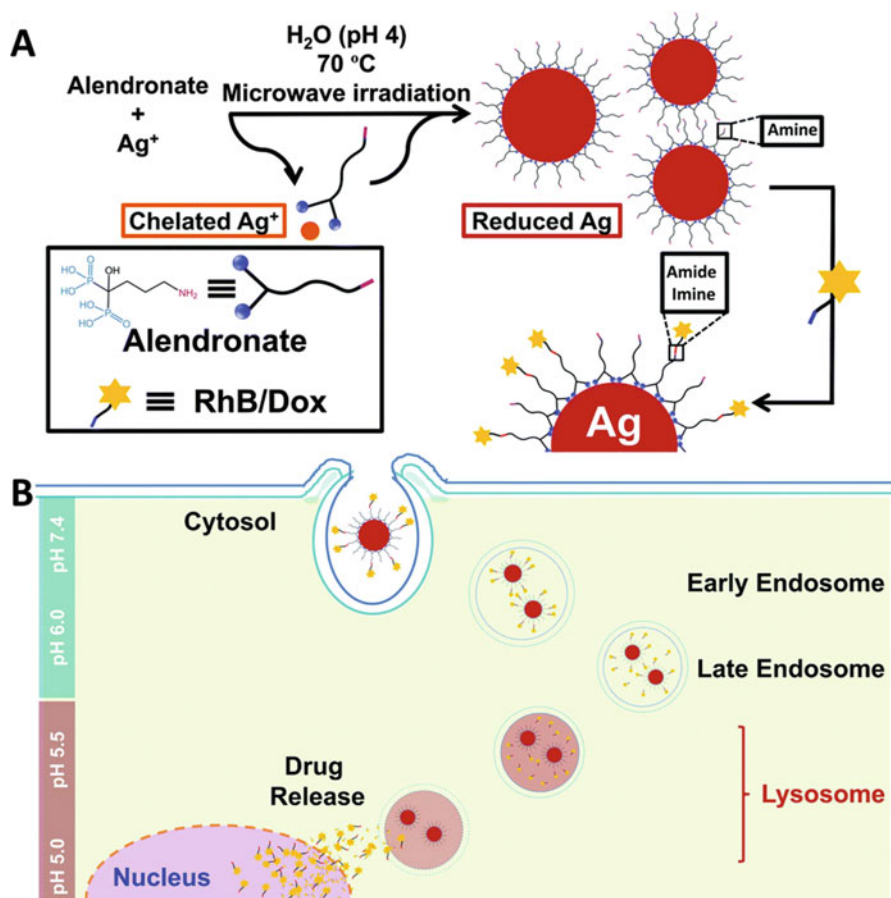


Fig. 11.15 (a) Schematic representation of Ald@AgNP formation and dye/drug conjugation. (b) Schematic representation of the uptake of drug–Ald@AgNPs into cells and drug cargo release. (Adapted from Ref. [50]. Copyright © 2015, Royal Society of Chemistry)

[54]. The authors compared the encapsulation of drugs and profiles of drug release to that of spherical AgNPs. Such system shows unique and attractive characteristics required for drug delivery.

5.3 Zinc Oxide Nanoparticles

Zinc oxide (ZnO)-based drug delivery platform has many advantages over the other DDSs as it is benign and weakly toxic. This property of ZnO nanoparticle makes it ideal for drug delivery application. In this context, Cai et al. developed a pH-responsive drug delivery platform for intracellular controlled release of drugs

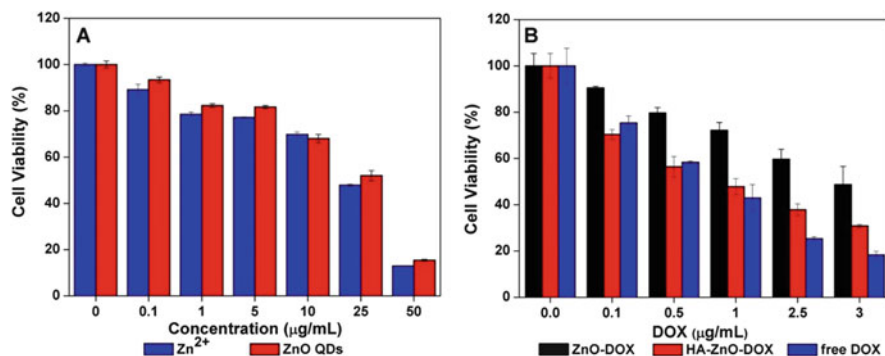


Fig. 11.16 Cytotoxicity assay of A549 cells after 48 h of incubation with (a) ZnO QDs and comparable concentrations of Zn²⁺ ions; (b) ZnO – DOX, HA – ZnO – DOX, and free DOX. (Adapted from Ref. [55]. Copyright © 2016, American Chemical Society)

based on acid-decomposable, luminescent-aminated ZnO quantum dots (QDs) [55]. NH₂-ZnO QDs are attached with dicarboxyl terminated PEG to increase their stability in physiological condition, followed by the attachment of a targeting ligand HA to target the CD44 over-expressed cancer cells. PEG-functionalized ZnO QDs are loaded with DOX via formation of metal-DOX complex and covalent interactions. Dissociation of the metal-drug complex and a controlled DOX release was occurred as pH-sensitive ZnO QDs dissolved to Zn²⁺ in acidic endosome/lysosome after cellular uptake, leading to achieve a synergistic therapy. Figure 11.16 represents the cytotoxicity of ZnO QDs and comparable concentrations of Zn²⁺ ion in human lung cancer (A549) cell line. The result showed that both displayed significant antitumor effect with the dosage surpassing 25 µg/mL. The cytotoxicity of ZnO-DOX, HA-ZnO-DOX, and free DOX was also evaluated in A549 cell line. Dose-dependent toxicity was found in all the three groups. Moreover, toxicity of HA-ZnO-DOX was higher than ZnO-DOX due to specific targeting of HA. In another study, an iron oxide–zinc oxide core-shell nanoparticle has been synthesized, which can deliver carcinoembryonic antigen into dendritic cells [56]. As a result, enhanced tumor antigen-specific T-cell responses delayed tumor growth and better survival was obtained in nanoparticle–antigen complex-treated mice, immunized with dendritic cells. In another report, Chen et al. synthesized core-shell structured NCs with ZnO QDs-conjugated AuNPs as core and amphiphilic block copolymer (containing poly l-lactide: PLA inner arm and a folate-conjugated sulfated polysaccharide outer arm) as shell for targeted anticancer drug delivery. Both NCs and CPT-loaded NCs show better antitumor efficacy in mice [57]. In another study, water-soluble curcumin was delivered by 3-mercaptopropionic acid (MPA)-functionalized ZnO-NPs. ZnO-MPA-curcumin complex shows enhance toxicity on MDA-MB-231 breast cancer cells compared to free curcumin, which suggests novel ZnO-MPA-curcumin

nanoformulation is promising and could be considered for new therapeutic application [58]. Further, Han et al. reported the targeted photocatalytic and chemotherapy in a multifunctional drug delivery platform based on aptamer-functionalized ZnO nanoparticles (NPs) [59]. Aptamer-ZnO NPs system loaded with anticancer drugs shows higher rate of death of cancer cells compared to that of single photocatalytic or chemotherapy. The results indicate the potential of aptamer-functionalized semiconductor nanoparticles for targeted photocatalytic and chemotherapy against cancer.

5.4 Iron Oxide Nanoparticles

Magnetic iron oxide (IO) nanoparticles are extensively used as a promising theranostic candidate for drug delivery. For example, Chen et al. showed the delivery of DOX by a reducible copolymer self-assembled with superparamagnetic iron oxide nanoparticles (SPIONs) [60]. rPAA@SPIONs were synthesized by the alkyl grafts of reducible copolymers made of polyamidoamine (rPAA) with PEG/dodecyl amine graft intercalated with the oleic acid layer capped on the surface of magnetite nanocrystals. rPAA@SPIONs loaded with anticancer drug DOX inhibited the tumor growth in mice with xenograft MDA-MB-231 breast tumor. In another study, Park et al. converted drug-loaded polymeric NPs into polymer iron oxide nanocomposites (PINCs) by dopamine polymerization for drug delivery application [61]. PINCs was accumulated in poorly vascularized subcutaneous SKOV3 xenografts that did not support the EPR effect by in vivo magnetophoretic delivery and showed better efficacy. Nasongkla et al. also developed iron oxide nanoparticle-based theranostic abbreviated as SPIO-DOX-cRGD micelles for targeted drug delivery. The authors loaded DOX and a cluster of magnetic iron oxide nanoparticles into the cores of PEG-PLA micelles, which was further functionalized with cRGD targeting ligand for targeting the integrin $\alpha\beta3$ of tumor or endothelial cells. SPIO-DOX-cRGD micelles exhibited enhanced uptake in $\alpha\beta3$ overexpressing endothelial cells [62]. In another study, Hwu group conjugated iron oxide nanoparticle surfaces by PTX, a mitotic inhibitor used in cancer chemotherapy, through a phosphodiester moiety to increase the efficacy of PTX [63]. Further, Quan et al. developed a human serum albumin (HSA)-coated iron oxide nanoparticles (HINPs) and loaded DOX onto the HINPs to assess the potential of the conjugate (D-HINPs) as theranostic agent [42]. D-HINPs showed a striking tumor suppression effect that was comparable to that of Doxil and greatly outperformed free Dox in a 4 T1 murine breast cancer xenograft model. Such a strategy can be readily applicable to other types of anticancer drugs, making HINPs a promising theranostic nanoplatform. Figure 11.17 represents the tumor growth inhibition study and body weight change by the treatment of D-HINPs in 4 T1 tumor model. The result shows the significant antitumor effect of D-HINPs, and it does not cause any toxicity to mice.

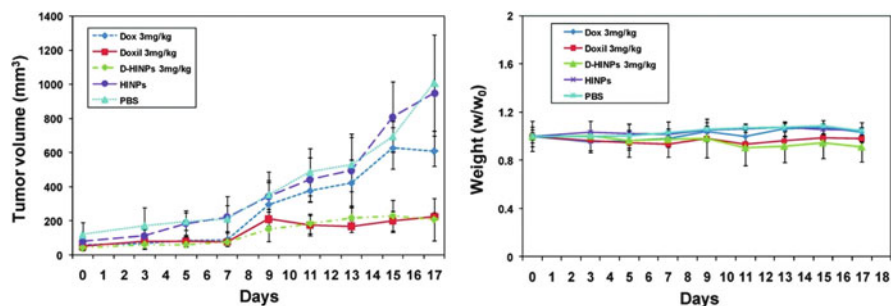


Fig. 11.17 Left: tumor growth curves for treatment with (1) D-HINPs (3 mg of Dox/kg); (2) free Dox (3 mg of Dox/kg); (3) Doxil (3 mg of Dox/kg); (4) HINPs (with same Fe concentration as in 1) and (5) PBS. D-HINPs showed similar therapeutic efficacy to Doxil and greatly outperformed free Dox. Right: change of mouse body weight during treatment ($n = 5/\text{group}$). (Adapted from Ref. [42]. Copyright © 2011, American Chemical Society)

5.5 Titanium Oxide Nanoparticles

Titanium oxide with its unique properties is found to be a potential candidate in drug delivery. For instance, Li et al. designed biocompatible one-dimensional titanium dioxide whiskers (TiO_2 Ws) loaded with daunorubicin (DNR) and explored it for drug delivery application and anti-tumor function [64]. Intracellular concentration and potential anti-tumor efficiency of DNR is greatly increased in presence of TiO_2 Ws in human hepatocarcinoma cells (SMMC-7721 cells), indicating TiO_2 Ws could produce an efficient drug delivery carrier effect importing DNR into target cells. This study reveals that TiO_2 Ws-based delivery of anticancer drugs represents a promising approach in cancer therapy. Further, Kamari et al. prepared insulin conjugated montmorillonite nanocomposites, which were further coated with TiO_2 to modulate the slow release of insulin from the DDS [65]. The results showed that incorporation of TiO_2 coating significantly enhanced the drug loading, while reducing the amount of drug release, so that the nanocomposites without and with TiO_2 coating could release insulin after 60 min and 22 h at pH 7.4, respectively. The authors suggest that these findings could be used for converting the administration of insulin from injection to oral. In another study, graphene oxide/ TiO_2 /DOX (GO/ TiO_2 /DOX) composites was loaded into the chitosan/PLA solutions to synthesize the electrospun chitosan/PLA/GO/ TiO_2 /DOX nanofibrous scaffolds via electrospinning process for increasing the efficacy of DOX [66]. The higher sustained release rate of DOX following the small burst release was achieved from nanofibrous scaffolds having 30 and 50 m thicknesses within 2 weeks incubation time. It was also found that the DOX release rate is faster in pH 5.3 compared to pH 7.4. Higher proliferation inhibition effect of nanofibers on target lung cancer cells was observed in the presence of magnetic field. Wang et al. also introduced PEI-modified novel multifunctional porous titanium dioxide (TiO_2) nanoparticles to achieve ultraviolet (UV) light-triggered drug release [67]. Additionally, FA was chemically attached to the surface of the functionalized multifunctional porous TiO_2 nanoparticles through

amide linkage with free amine groups of PEI to effectively promote cancer-cell-specific uptake through receptor-mediated endocytosis. A typical poorly water-soluble anticancer drug PTX was incorporated in multifunctional porous TiO₂ nanoparticles and its drug delivery efficiency was studied. The anticancer effect was controlled by the amount of drug released from multifunctional porous TiO₂ nanoparticles regulating the UV-light radiation time. This multifunctional porous TiO₂ nanoparticle shows a combination of stimuli-triggered drug release and cancer cell targeting. Further, Leon et al. prepared a novel targeting DDS for 2-methoxyestradiol (2ME) for improving the clinical application of this antitumor drug [68]. For this purpose, TiO₂-PEG-2ME composite was formed, where 2ME was encapsulated in titanium dioxide (TiO₂) nanoparticle coated with PEG. Modifying TiO₂ NPs with PEG loaded with the 2ME drug showed that the titanium dioxide nanocarrier has potential application as a system of drug delivery.

5.6 Carbon Nanotubes

Among various nanomaterials, CNTs have drawn particular attention as carriers of biologically relevant molecules due to their unique physical, chemical, and physiological properties. For example, Chen et al. developed a novel single-walled carbon nanotube (SWNT)-based tumor-targeted DDS, consisting of a functionalized SWNT attached to tumor-targeting modules biotin and a spacer as well as prodrug, taxoid with a cleavable linker that is activated to its cytotoxic form inside the tumor cells upon internalization and in situ drug release [69]. It has been observed that this tumor-targeting DDS shows high potency toward specific cancer cell lines, thereby forming a solid platform for further development. In another study, Li et al. synthesized antibody of P-gp (anti-P-gp)-functionalized water-soluble single-walled carbon nanotubes (Ap-SWNTs) loaded with Dox, Dox/Ap-SWNTs, for overcoming the multidrug resistance (MDR) of K562 human leukemia cells [70]. The resulting Ap-SWNTs specifically recognize the multidrug-resistant human leukemia cells (K562R) and demonstrate controllable release performance for Dox toward the target K562R cells by near-infrared radiation (NIR) exposure. Dox/Ap-SWNTs showed 2.4-fold higher cytotoxicity and significant cell proliferation suppression toward K562R leukemia cells ($p < 0.05$) as compared with free Dox. Further, a dual-targeting DDS has been developed for treatment of brain glioma by Ren et al., based on PEGylated oxidized multiwalled carbon nanotubes (O-MWNTs) modified with angiopep-2 (O-MWNTs-PEG-ANG) [71]. O-MWNTs can distribute in brains, accumulate in tumors, and have ultrahigh surface area with remarkably high loading of anticancer drug DOX. Angiopep-2 can specifically combine to the low-density lipoprotein receptor-related protein (LRP) receptor overexpressed on the blood-brain barrier (BBB) and glioma cells, which was selected as targeting ligand. The antiglioma effect of DOX-loaded O-MWNTs-PEG-ANG (DOX-OMWNTs-PEG-ANG) was determined by C6 cytotoxicity and median survival time of glioma bearing mice, which revealed a better antiglioma effect than DOX, which suggests that O-MWNTs-PEG-ANG is a promising

dual-targeting carrier for brain tumor treatment. Further, Zhang et al. reported a pH-responsive targeted DDS based on single-wall carbon nanotubes (SWCNTs), functionalized with carboxylate groups and coated with a polysaccharide material [72]. Functionalized SWCNTs was loaded with the anticancer drug DOX at physiological pH (pH 7.4) and is only released in lysosomal pH and the pH characteristic of certain tumor environments. SWCNTs was also attached to FA, a targeting agent for many tumors for selective delivery DOX into the lysosomes of HeLa cells with much higher efficiency than free DOX. Meng et al. also reviewed the design and synthesis of SWNT-based DDSs and their pharmacokinetic, cancer targeting, and therapeutic properties both *in vitro* and *in vivo* [73].

5.7 Carbon Dots

CDs are exceptional nanocarriers due to their potential optical properties and biocompatibility. For instance, Feng et al. have reported a cisplatin (IV) prodrug conjugated CDs based extracellular micro-environment responsive DDS (CDs-Pt (IV)@PEG-(PAH/DMMA)) for imaging guided drug delivery [74]. High tumor inhibition efficacy and low side effects of cisplatin(IV) was observed in the presence of CDs nanocarrier, proving its capability as a smart drug nanocarrier with enhanced therapeutic effects. In another study, a smart stimuli-responsive DDS has been reported by Majumder et al. [75] Carbon-dot-coated novel alginate beads (CA-CD) was used as a drug delivery vehicle, in which garlic extract (GE), a model drug containing allicin, was loaded to form the DDS CA-CD-GE. The DDS exhibits pH-dependent controlled drug release which results in increased therapeutic efficiency. CA-CDGE is both stimuli responsive and a controlled drug release system as it releases drug according to the pathogen concentration (MRSA).

5.8 Mesoporous Silica Nanoparticles

In recent past, several research groups including ours have developed different MSN-based DDSs. For instance, Chen et al. developed dextrin-coated, DOX-conjugated MSNs-based DDS which could release DOX at a faster rate at mild acidic pH (pH 6.0) as compared to physiological (pH 7.4) [76]. The faster release of DOX at acidic pH might be due to the hydrolysis of Schiff's base (pH sensitive) present in the said DDS. Additionally, the *in vivo* studies in tumor (H22 cells)-bearing mice model illustrated the enhanced retention time and more entrapment of the DDS in tumor in comparison with pristine DOX, indicating the therapeutic efficacy of the DDS. In another report, M. B. Cardoso and group synthesized FA-modified SiNPs-based DDS containing anticancer drug curcumin [77]. The DDS exhibited efficient delivery of curcumin to prostate cancer cells (PC3). The authors further showed that the DDS was more cytotoxic to PC3 cells as compared to the prostate epithelial cell (PrEC), indicating the targeting efficacy of the DDS. Further, Palanikumar et al. reported a simple as well as robust procedure for the synthesis of

polymer (containing pyridine disulfide hydrochloride: PDS and PEG)-functionalized, targeting ligand (cyclic (Arg-Gly-Asp-D-Phe-Cys: cRGDfC)-decorated MSN-based DDSs containing hydrophilic anticancer drugs doxorubicin hydrochloride or cisplatin [78]. Here, PEG on MSN surface facilitated the water solubility and could prevent the nonspecific interaction with different biomacromolecules. On the other hand, PDS augmented the functionalization of the targeting ligand on MSN surface. The DDS exhibited high drug loading capability with 44 wt% for doxorubicin hydrochloride and 33 wt% for cisplatin. The results depicted that doxorubicin hydrochloride-conjugated polymer-wrapped MSNs (PMSNs) containing cRGDfC ligand (RGD-PMSNs) exhibited better cytotoxicity in KB cells (human nasopharyngeal carcinoma cells) as compared to the nonligand-wrapped PMSNs, indicating targeting efficacy of the DDS. Additionally, while both cisplatin- and Dox-loaded PMSNs were administered to KB cells, their synergistic effect showed better cytotoxic potential as compared to the treatment with single drug-loaded DDS, suggesting the potential applications of PMSNs for combination therapy. In another study, MSNs were used as a drug carrier for various hydrophobic anticancer drug (DOX, PTX, camptothecin: CPT, tamoxifen: TMX, Cur: curcumin), having high drug loading capability and colloidal stability [79]. The results illustrated that the combination of DOX-CPT-PTX and DOX-CPT-Cur with polymer-coated MSNs (PMSNs) showed better cytotoxicity to KB cells as compared to the DDS with single drug loading. Moreover, targeting ligand (RGD peptide: KB cells; SP94 peptide: HepG2 hepatocellular carcinoma cells) containing CPT-loaded PMSNs exhibited better cytotoxic potential and cellular uptake as compared to the nonligand-decorated PMSNs, suggesting the targeting efficacy of DDSs. Very recently, Oh et al. have developed GSH-modified anticancer drug (DOX and CPT)-loaded MSNs, decorated with HER2-binding affibody combined with glutathione-S-transferase (GST), to form a protein corona shielding nanoparticle (PCSN)-based targeted DDSs [80]. The affibody served as the targeting moiety as well as it could prevent the protein corona formation around the nanoplatform. Confocal microscopy study in Raw264.7 cells showed that the protein corona shield minimized the cellular uptake of PCSN in macrophages as compared to the PEGylated MSN (PEG-MSN). Further, confocal microscopy revealed that CPT-conjugated PCSN exhibited significant cytotoxicity to HER2 receptor over-expressing SKBR3 breast cancer cells as compared to HER2 receptor negative cells HEK293T, suggesting the targeting efficacy and potential application of the DDS for breast cancer therapy. To assess the *in vivo* biodistribution, the authors administered DiD-loaded PCSN and PEG-MSN to SKBR3 tumor-bearing nude mice intravenously. Post 48 h of injection, the mice were sacrificed and the vital organs were collected, followed by analysis through *in vivo* imaging system. The result exhibited that fluorescence intensity for PCSN group was significantly higher in tumor as compared to PEG-MSN group (Fig. 11.18a–b). Moreover, for PEG-MSN group, no such difference in fluorescence intensity between tumor and reticuloendothelial systems (liver and spleen) was observed. However, PCSN group exhibited almost seven times higher fluorescence signal in tumor than that in reticuloendothelial systems. The result suggested that the protein corona shielding could facilitate the

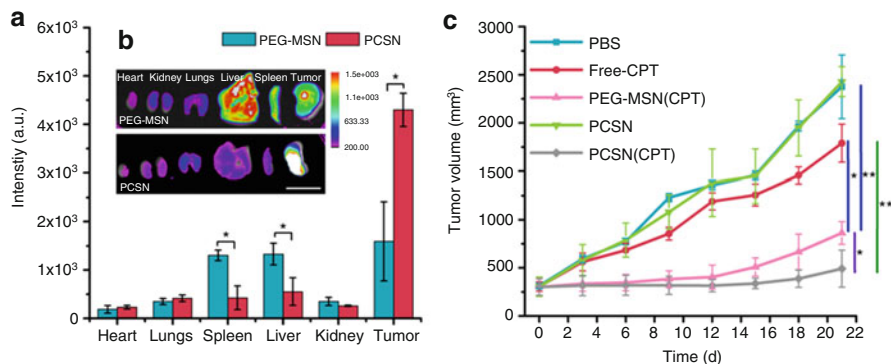


Fig. 11.18 Ex vivo and in vivo efficiency of PCSN. (a, b) Fluorescence images of organs and tumors 48 h after intravenous injection and biodistribution of injected formulations in animals with SK-BR3 tumor xenograft from fluorescence intensity analysis. In vivo antitumor effects in different treatment groups loaded with camptothecin (CPT) (1.5 mg/kg of mice) (scale bar is 2 cm). (c) Growth curve of tumor volume after intravenous injection with various groups of carriers until day 21 ($n = 6$ mice per group, mean \pm 1 day [$n = 6$ mice per group, mean \pm SD, statistical significance was calculated by one-way analysis of variance, * $P < 0.05$, ** $P < 0.01$]). (Adapted from Ref. [80]. Open Access Journal)

nanoparticles to avoid immune system, thereby enhanced entrapment in target tumor site. Additionally, CPT-loaded PCSN (PCSN-CPT) exhibited better in vivo therapeutic efficacy as compared to CPT-loaded PEG-MSN and free CPT in terms of more tumor volume regression in SKBR3 tumor-containing mice (Fig. 11.18c). The overall experimental data demonstrated that binding of GST-HER2 affibody with MSNs leads to the formation of protein corona shield, which could minimize the interaction of PCSN with serum protein as well as improved its tumor targeting efficacy and therapeutic potential.

6 Conclusions: Challenges and Future Perspective

Since past decades, nanoparticulate targeted DDSs have been emerged as one of the revolutionizing nanomedicine approaches that could serve as an alternative to the conventional therapeutic treatment strategies for different diseases. Although, the study related to nanoparticulate targeted DDS have gradually been growing, the systematic investigation of nano-toxicity to humans is in early stage [81]. The physicochemical properties of nanomaterials such as size, morphology, surface charge, and stability often play a vital role behind their toxicological profile. To evaluate the nanotoxicity, the interaction of nanoparticles with cells, tissue, blood, proteins, and nucleic acids are to be thoroughly studied [82]. Additionally, number of doses of nanoparticulate system, administration route (i.p., i.v., i.m., intramuscular, intratumoral, and oral), and immunological response are also to be assessed during the evaluation of toxicity profile of any nanomaterials. It is well known that

in vitro toxicity data of nanosystem might or might not be the similar in case of in vivo conditions. Therefore, in-depth evaluation of toxicological profile of nanoparticulate system is immensely important for the safety of our lives. Another challenge for nanomaterial-based system is that there is no precise uniform protocol for the assessment of toxicity of nanomaterials. It imposes the necessity for the development of standard protocols that would be followed globally, to get more reliable toxicity data for particular nanomedicine, which would be beneficial for practical biomedical applications of nanomaterials for human. Besides nanotoxicity, the fate of the nanomaterials for prolonged periods inside body system has to be considered for checking their adverse side effects. In this context, it is highly essential to investigate the pharmacokinetics, pharmacodynamics, and excretion of nanoparticulate systems. It is to be mentioned here that after investigating the thorough toxicological as well as pharmacokinetic profiles of therapeutic nanomaterials, the nanoformulations should be subjected to clinical trials, so that we could avail the practical benefits from the nanomedicines for different diseases. Although, there is not so much nanoparticulate targeted DDS available in market, considering the growth of present research in drug delivery field, we could expect many more nanomedicines would arise for practical biomedical applications for human in near future.

Acknowledgment This work was supported by the National Research Foundation of Korea (NRF) grant funded by the Korean Government (MSIP) (2016R1A5A1009405, 2017R1A2B4003617, and 2016R1E1A2A01954001).

References

1. Schaefer HE (2010) Nanoscience. The science of the small in physics, engineering, chemistry, biology and medicine. Springer Science+Business Media, Berlin
2. Teli MK, Mutalik S, Rajanikant GK (2010) Nanotechnology and nanomedicine: going small means aiming big. *Curr Pharm Des* 16:1882–1892
3. Dai L (2006) Carbon nanotechnology recent developments in chemistry, physics, materials science and device applications. Elsevier, Amsterdam
4. Khot LR, Sankaran S, Maja JM, Ehsani R, Schuster EW (2012) Applications of nanomaterials in agricultural production and crop protection: a review. *Crop Prot* 35:64–70
5. Lohse SE, Murphy CJ (2012) Applications of colloidal inorganic nanoparticles: from medicine to energy. *J Am Chem Soc* 134(38):15607–15620
6. Enterkin JA, Poepfelmeier KR, Marks LD (2011) Oriented catalytic platinum nanoparticles on high surface area strontium titanate nanocuboids. *Nano Lett* 11(3):993–997
7. Shipway AN, Katz E, Willner I (2000) Nanoparticle arrays on surfaces for electronic, optical, and sensor applications. *ChemPhysChem* 1(1):18–52
8. Han C, Andersen J, Pillai SC, Fagan R, Falaras P, Byrne JA, Dunlop PSM, Choi H, Jiang W, O'Shea K, Dionysiou DD (2013) Chapter green nanotechnology: development of nanomaterials for environmental and energy applications. In: Shamim N, Sharma VK (eds) Sustainable nanotechnology and the environment: advances and achievements, ACS symposium series, pp 201–229
9. Barui AK, Kotcherlakota R, Bollu VS, Nethi SK, Patra CR (2017) Biomedical and drug delivery applications of functionalized inorganic nanomaterials. In: Biopolymer-based

- composites: drug delivery and biomedical applications. Woodhead Publishing, Copyright holder: Elsevier, Cambridge
10. Barui AK, Kotcherlakota R, Patra CR (2018) Medicinal applications of metal nanoparticles. In: *Metal nanoparticles: synthesis and Applications in Pharmaceutical Sciences*. Wiley-VCH Verlag GmbH & Co. KGaA, Weinheim
 11. Winter JO (2007) Nanoparticles and nanowires for cellular engineering. In: *Nanotechnologies for the Life Sciences*. Wiley-VCH Verlag GmbH & Co. KGaA
 12. Cho KJ, Wang X, Nie SM, Chen Z, Shin DM (2008) Therapeutic nanoparticles for drug delivery in cancer. *Clin Cancer Res* 14(5):1310–1316
 13. Torchilin VP (2010) Passive and active drug targeting: drug delivery to tumors as an example. *Handb Exp Pharmacol* 197:3–53
 14. Bae YH, Park K (2011) Targeted drug delivery to tumors: myths, reality and possibility. *J Control Release* 153(3):198–205
 15. Danhier F, Feron O, Preat V (2010) To exploit the tumor microenvironment: passive and active tumor targeting of nanocarriers for anti-cancer drug delivery. *J Control Release* 148(2):135–146
 16. Bhatia S (2016) Nanoparticles types, classification, characterization, fabrication methods and drug delivery applications. In: *Natural polymer drug delivery systems*. Springer International Publishing, Cham
 17. Redhead HM, Davis SS, Illum L (2001) Drug delivery in poly(lactide-co-glycolide) nanoparticles surface modified with poloxamer 407 and poloxamine 908: in vitro characterisation and in vivo evaluation. *J Control Release* 70(3):353–363
 18. Betancor L, Luckarift HR (2008) Bioinspired enzyme encapsulation for biocatalysis. *Trends Biotechnol* 26(10):566–572
 19. Lee MY, Yang JA, Jung HS, Beack S, Choi JE, Hur W, Koo H, Kim K, Yoon SK, Hahn SK (2012) Hyaluronic acid-gold nanoparticle/Interferon α complex for targeted treatment of hepatitis c virus infection. *ACS Nano* 6(11):9522–9531
 20. Reimer L, Kohl H (2009) *Transmission electron microscopy physics of image formation*, vol 51. Springer, New York, pp 1–15
 21. Jores K, Mehnert W, Drecusler M, Bunyes H, Johan CKM (2004) Investigation on the stricter of solid lipid nanoparticles and oil-loaded solid nanoparticles by photon correlation spectroscopy, field flow fractionation and transmission electron microscopy. *J Control Release* 17:217–227
 22. Molpeceres J, Aberturas MR, Guzman M (2000) Biodegradable nanoparticles as a delivery system for cyclosporine: preparation and characterization. *J Microencapsul* 17(5):599–614
 23. Sanpui P, Chattopadhyay A, Ghosh SS (2011) Induction of apoptosis in cancer cells at low silver nanoparticle concentrations using chitosan nanocarrier. *ACS Appl Mater Inter* 3(2):218–228
 24. zurMuhlen Z, zurMuhlen E, Niehus H, Mehnert W (1996) Atomic force microscopy studies of solid lipid nanoparticles. *Pharm Res* 13(9):1411–1416
 25. Shi HQG, Farber L, Michaels JN, Dickey A, Thompson KC, Shelukar SD, Hurter PN, Reynolds SD, Kaufman MJ (2003) Characterization of crystalline drug nanoparticles using atomic force microscopy and complementary techniques. *Pharm Res* 20(3):479–484
 26. Polakovic M, Gorner T, Gref R, Dellacherie E (1999) Lidocaine loaded biodegradable nanospheres II. Modelling of drug release. *J Control Release* 60:169–177
 27. Liu Z, Robinson JT, Sun XM, Dai HJ (2008) PEGylated nanographene oxide for delivery of water-insoluble cancer drugs. *J Am Chem Soc* 130(33):10876–10877
 28. Cui T, Liang JJ, Chen H, Geng DD, Jiao L, Yang JY, Qian H, Zhang C, Ding Y (2017) Performance of doxorubicin-conjugated gold nanoparticles: regulation of drug location. *ACS Appl Mater Inter* 9(10):8569–8580
 29. Otsuka H, Nagasaki Y, Kataoka K (2003) PEGylated nanoparticles for biological and pharmaceutical applications. *Adv Drug Deliver Rev* 55(3):403–419
 30. Palanikumar L, Kim J, Oh JY, Choi H, Park MH, Kim C, Ryu JH (2018) Hyaluronic acid-modified polymeric gatekeepers on biodegradable mesoporous silica nanoparticles for targeted cancer therapy. *ACS Biomater Sci Eng* 4(5):1716–1722

31. Kreuter J (1983) Physicochemical characterization of polyacrylic nanoparticles. *Int J Pharm* 14(1):43–58
32. Magenheim B, Levy MY, Benita S (1993) A new in-vitro technique for the evaluation of drug-release profile from colloidal carriers – ultrafiltration technique at low-pressure. *Int J Pharm* 94:115–123
33. Wang XY, Cai XP, Hu JJ, Shao NM, Wang F, Zhang Q, Xiao JR, Cheng YY (2013) Glutathione-triggered “off-on” release of anticancer drugs from dendrimer-encapsulated gold nanoparticles. *J Am Chem Soc* 135(26):9805–9810
34. Wang SH, Xu T, Yang YH, Shao ZZ (2015) Colloidal stability of silk fibroin nanoparticles coated with cationic polymer for effective drug delivery. *ACS Appl Mater Inter* 7(38):21254–21262
35. Bollu VS, Barui AK, Mondal SK, Prashar S, Fajardo M, Briones D, Rodriguez-Dieguez A, Patra CR, Gomez-Ruiz S (2016) Curcumin-loaded silica-based mesoporous materials: synthesis, characterization and cytotoxic properties against cancer cells. *Mat Sci Eng C-Mater* 63:393–410
36. Kotcherlakota R, Barui AK, Prashar S, Fajardo M, Briones D, Rodriguez-Dieguez A, Patra CR, Gomez-Ruiz S (2016) Curcumin loaded mesoporous silica: an effective drug delivery system for cancer treatment. *Biomater Sci* 4(3):448–459
37. Gayathri T, Barui AK, Prashanthi S, Patra CR (2014) Singh SP: meso-Substituted BODIPY fluorescent probes for cellular bio-imaging and anticancer activity. *RSC Adv* 4(88):47409–47413
38. Barui AK, Nethi SK, Patra CR (2017) Investigation of the role of nitric oxide driven angiogenesis by zinc oxide nanoflowers. *J Mater Chem B* 5(18):3391–3403
39. Nagababu P, Barui AK, Thulasiram B, Devi CS, Satyanarayana S, Patra CR, Sreedhar B (2015) Antiangiogenic activity of mononuclear copper(ii) polypyridyl complexes for the treatment of cancers. *J Med Chem* 58(13):5226–5241
40. Modak A, Barui AK, Patra CR, Bhaumik A (2013) A luminescent nanoporous hybrid material based drug delivery system showing excellent theranostics potential for cancer. *Chem Commun* 49(69):7644–7646
41. Sau S, Agarwalla P, Mukherjee S, Bag I, Sreedhar B, Pal-Bhadra M, Patra CR, Banerjee R (2014) Cancer cell-selective promoter recognition accompanies antitumor effect by glucocorticoid receptor-targeted gold nanoparticle. *Nanoscale* 6(12):6745–6754
42. Quan QM, Xie J, Gao HK, Yang M, Zhang F, Liu G, Lin X, Wang A, Eden HS, Lee S, Zhang GX, Chen XY (2011) HSA coated iron oxide nanoparticles as drug delivery vehicles for cancer therapy. *Mol Pharm* 8(5):1669–1676
43. Mukherjee S, Dasari M, Priyamvada S, Kotcherlakota R, Bollu VS, Patra CR (2015) A green chemistry approach for the synthesis of gold nanoconjugates that induce the inhibition of cancer cell proliferation through induction of oxidative stress and their in vivo toxicity study. *J Mater Chem B* 3(18):3820–3830
44. Jain S, Hirst DG, O’Sullivan JM (2012) Gold nanoparticles as novel agents for cancer therapy. *Br J Radiol* 85:101–113
45. Libutti SK, Paciotti GF, Byrnes AA, Alexander HR, Gannon WE, Walker M, Seidel GD, Yuldasheva N, Tamarkin L (2010) Phase I and pharmacokinetic studies of CYT-6091, a novel pegylated colloidal gold-rhTNF nanomedicine. *Clin Cancer Res* 16(24):6139–6149
46. Aryal S, Grailer JJ, Pilla S, Steeber DA, Gong SQ (2009) Doxorubicin conjugated gold nanoparticles as water-soluble and pH-responsive anticancer drug nanocarriers. *J Mater Chem* 19(42):7879–7884
47. Brown SD, Nativo P, Smith JA, Stirling D, Edwards PR, Venugopal B, Flint DJ, Plumb JA, Graham D, Wheate NJ (2010) Gold Nanoparticles for the improved anticancer drug delivery of the active component of oxaliplatin. *J Am Chem Soc* 132(13):4678–4684
48. Kumar CS, Raja MD, Sundar DS, Antoniraj MG, Ruckmani K (2015) Hyaluronic acid co-functionalized gold nanoparticle complex for the targeted delivery of metformin in the treatment of liver cancer (HepG2 cells). *Carbohydr Polym* 128:63–74

49. Suarasan S, Focsan M, Potara M, Soritau O, Florea A, Maniu D, Astilean S (2016) Doxorubicin-incorporated nanotherapeutic delivery system based on gelatin-coated gold nanoparticles: formulation, drug release, and multimodal imaging of cellular internalization. *ACS Appl Mater Inter* 8(35):22900–22913
50. Benyettou F, Rezgui R, Ravaux F, Jaber T, Blumer K, Jouiad M, Motte L, Olsen JC, Platas-Iglesias C, Magzoub M, Trabolsi A (2015) Synthesis of silver nanoparticles for the dual delivery of doxorubicin and alendronate to cancer cells. *J Mater Chem B* 3(36):7237–7245
51. Li YH, Guo M, Lin ZF, Zhao MQ, Xiao MS, Wang CB, Xu TT, Chen TF, Zhu B (2016) Polyethylenimine-functionalized silver nanoparticle-based co-delivery of paclitaxel to induce HepG2 cell apoptosis. *Int J Nanomedicine* 11:6693–6702
52. Liang JM, Zeng F, Zhang M, Pan ZZ, Chen YZ, Zeng YN, Xu Y, Xu Q, Huang YZ (2015) Green synthesis of hyaluronic acid-based silver nanoparticles and their enhanced delivery to CD44(+) cancer cells. *RSC Adv* 5(54):43733–43740
53. Wang YL, Newell BB, Irudayaraj J (2012) Folic acid protected silver nanocarriers for targeted drug delivery. *J Biomed Nanotechnol* 8(5):751–759
54. Paramasivam G, Sharma V, Sundaramurthy A (2017) Polyelectrolyte multilayer film coated silver nanorods: an effective carrier system for externally activated drug delivery. In: *IOP conference series: materials science and engineering*, p 225
55. Cai XL, Luo YN, Zhang WY, Du D, Lin YH (2016) pH-Sensitive ZnO quantum dots-doxorubicin nanoparticles for lung cancer targeted drug delivery. *ACS Appl Mater Inter* 8(34):22442–22450
56. Cho NH, Cheong TC, Min JH, Wu JH, Lee SJ, Kim D, Yang JS, Kim S, Kim YK, Seong SY (2011) A multifunctional core-shell nanoparticle for dendritic cell-based cancer immunotherapy. *Nat Nanotechnol* 6(10):675–682
57. Chen T, Zhao T, Wei DF, Wei YX, Li YY, Zhang HX (2013) Core-shell nanocarriers with ZnO quantum dots-conjugated Au nanoparticle for tumor-targeted drug delivery. *Carbohydr Polym* 92(2):1124–1132
58. Ghaffari SB, Sarrafzadeh MH, Fakhroueian Z, Shahriari S, Khorramzadeh MR (2017) Functionalization of ZnO nanoparticles by 3-mercaptopropionic acid for aqueous curcumin delivery: synthesis, characterization, and anticancer assessment. *Mater Sci Eng C* 79:465–472
59. Han Z, Wang XH, Heng CL, Han QS, Cai SF, Li JY, Qi C, Liang W, Yang R, Wang C (2015) Synergistically enhanced photocatalytic and chemotherapeutic effects of aptamer-functionalized ZnO nanoparticles towards cancer cells. *Phys Chem Chem Phys* 17(33):21576–21582
60. Chen J, Shi M, Liu PM, Ko A, Zhong W, Liao WJ, Xing MMQ (2014) Reducible polyamidoamine-magnetic iron oxide self-assembled nanoparticles for doxorubicin delivery. *Biomaterials* 35(4):1240–1248
61. Park J, Kadasala NR, Abouelmagd SA, Castanares MA, Collins DS, Wei A, Yeo Y (2016) Polymer-iron oxide composite nanoparticles for EPR-independent drug delivery. *Biomaterials* 101:285–295
62. Nasongkla N, Bey E, Ren JM, Ai H, Khemtong C, Guthi JS, Chin SF, Sherry AD, Boothman DA, Gao JM (2006) Multifunctional polymeric micelles as cancer-targeted, MRI-ultrasensitive drug delivery systems. *Nano Lett* 6(11):2427–2430
63. Hwu JR, Lin YS, Josephraj T, Hsu MH, Cheng FY, Yeh CS, Su WC, Shieh DB (2009) Targeted paclitaxel by conjugation to iron oxide and gold nanoparticles. *J Am Chem Soc* 131(1):66
64. Li QN, Wang XM, Lu XH, Tian HE, Jiang H, Lv G, Guo DD, Wu CH, Chen BA (2009) The incorporation of daunorubicin in cancer cells through the use of titanium dioxide whiskers. *Biomaterials* 30(27):4708–4715
65. Kamari Y, Ghiaci P, Ghiaci M (2017) Study on montmorillonite/insulin/TiO₂ hybrid nanocomposite as a new oral drug-delivery system. *Mat Sci Eng C Mater* 75:822–828

66. Samadi S, Moradkhani M, Beheshti H, Irani M, Aliabadi M (2018) Fabrication of chitosan/poly (lactic acid)/graphene oxide/TiO₂ composite nanofibrous scaffolds for sustained delivery of doxorubicin and treatment of lung cancer. *Int J Biol Macromol* 110:416–424
67. Wang TY, Jiang HT, Wan L, Zhao QF, Jiang TY, Wang B, Wang SL (2015) Potential application of functional porous TiO₂ nanoparticles in light-controlled drug release and targeted drug delivery. *Acta Biomater* 13:354–363
68. Leon A, Reuquen P, Garin C, Segura R, Vargas P, Zapata P, Orihuela PA (2017) FTIR and Raman characterization of TiO₂ nanoparticles coated with polyethylene glycol as carrier for 2-methoxyestradiol. *Appl Sci* 7(1)
69. Chen JY, Chen SY, Zhao XR, Kuznetsova LV, Wong SS, Ojima I (2008) Functionalized Single-Walled Carbon nanotubes as rationally designed vehicles for tumor-targeted drug delivery. *J Am Chem Soc* 130(49):16778–16785
70. Li RB, Wu R, Zhao L, Wu MH, Yang L, Zou HF (2010) P-Glycoprotein antibody functionalized carbon nanotube overcomes the multidrug resistance of human leukemia cells. *ACS Nano* 4(3):1399–1408
71. Ren JF, Shen S, Wang DG, Xi ZJ, Guo LR, Pang ZQ, Qian Y, Sun XY, Jiang XG (2012) The targeted delivery of anticancer drugs to brain glioma by PEGylated oxidized multi-walled carbon nanotubes modified with Angiopep-2. *Biomaterials* 33(11):3324–3333
72. Zhang XK, Meng LJ, Lu QH, Fei ZF, Dyson PJ (2009) Targeted delivery and controlled release of doxorubicin to cancer cells using modified single wall carbon nanotubes. *Biomaterials* 30(30):6041–6047
73. Meng LJ, Zhang XK, Lu QH, Fei ZF, Dyson PJ (2012) Single walled carbon nanotubes as drug delivery vehicles: targeting doxorubicin to tumors. *Biomaterials* 33(6):1689–1698
74. Feng T, Ai XZ, An GH, Yang PP, Zhao YL (2016) Charge-convertible carbon dots for imaging guided drug delivery with enhanced in vivo cancer therapeutic efficiency. *ACS Nano* 10(4):4410–4420
75. Majumdar S, Krishnatreya G, Gogoi N, Thakur D, Chowdhury D (2016) Carbon-dot-coated alginate beads as a smart stimuli-responsive drug delivery system. *ACS Appl Mater Inter* 8(50):34179–34184
76. Chen HY, Zheng DW, Liu J, Kuang Y, Li QL, Zhang M, Ye HF, Qin HY, Xu YL, Li C, Jiang BB (2016) pH-Sensitive drug delivery system based on modified dextrin coated mesoporous silica nanoparticles. *Int J Biol Macromol* 85:596–603
77. de Oliveira LF, Bouchmella K, Goncalves KD, Bettini J, Kobarg J, Cardoso MB (2016) Functionalized silica nanoparticles as an alternative platform for targeted drug-delivery of water insoluble drugs. *Langmuir* 32(13):3217–3225
78. Palanikumar L, Choi ES, Cheon JY, Joo SH, Ryu JH (2015) Noncovalent polymer-gatekeeper in mesoporous silica nanoparticles as a targeted drug delivery platform. *Adv Funct Mater* 25(6):957–965
79. Palanikumar L, Kim HY, Oh JY, Thomas AP, Choi ES, Jeena MT, Joo SH, Ryu JH (2015) Noncovalent surface locking of mesoporous silica nanoparticles for exceptionally high hydrophobic drug loading and enhanced colloidal stability. *Biomacromolecules* 16(9):2701–2714
80. Oh JY, Kim HS, Palanikumar L, Go EM, Jana B, Park SA, Kim HY, Kim K, Seo JK, Kwak SK, Kim C, Kang S, Ryu JH (2018) Cloaking nanoparticles with protein corona shield for targeted drug delivery. *Nat Commun* 9:4548
81. Elsaesser A, Howard CV (2012) Toxicology of nanoparticles. *Adv Drug Deliver Rev* 64(2):129–137
82. Xia T, Kovochich M, Liong M, Madler L, Gilbert B, Shi HB, Yeh JI, Zink JI, Nel AE (2008) Comparison of the mechanism of toxicity of zinc oxide and cerium oxide nanoparticles based on dissolution and oxidative stress properties. *ACS Nano* 2(10):2121–2134

Index

A

Ablation, 208, 212, 221, 223
Abraxane, 245, 281
Absorption peak, 425
Accumulation wall, 117
ACE, *see* Affinity capillary electrophoresis (ACE)
Acoustic lens, 211
Acoustic modes, 87
Acoustic pressure, 208, 210, 217
Acoustic window, 211
Active, 245, 248, 266, 283
Active targeting, 249, 335
Adenocarcinoma, 260, 272
Adenosine triphosphate (ATP)
 encapsulation with liposomes, 401
 formulation analysis, 400
 nanoliposomes, 398
 preparation of ATP-Laden
 nanoliposomes, 404
Adipogenic cells, 25
AF4, *see* Asymmetric flow field flow
 fractionation
Affinity capillary electrophoresis (ACE),
 124, 136
AFM, *see* Atomic force microscopy
Agglomeration, 251
AgNPs, *see* Silver nanoparticles
Alginate, 28
Alternating magnetic field (AMF), 246, 247,
 272, 302, 304, 312, 323
Alveolar, 29
Alzheimer's disease, 408
Aminobenzoic acid, 317
Aminoterephthalic acid (ATA), 317, 323
Amniotic fluid progenitor cells, 12
Anaemia, 245
Analyte-membrane interactions, 120

Analyte retention, 119
Angiogenesis, 165
Anisotropy energy constant, 301
Antibodies, 249, 251, 278, 282, 354
Anticancer, 268, 270, 272
Anticancer drug, 445
Anti-drug discovery, 156
Apoptosis, 181, 300, 323, 436, 440
Apoptosis assay, 434
Apparent mobility, 121
Association, 120, 136, 137
Asymmetric flow field flow fractionation, 121,
 127, 129, 131, 133
Atomic force microscopy (AFM), 72, 115, 423
AuNPs, 425, 437
 See also Gold nanoparticles

B

Back-scattered electrons, 306
Ball-milling, 303
Bartlett assay, 341
BD vacutainer EDTA tubes, 343
Bilodeau formula, 92, 95
Binding cooperativity, 123
Biocompatibility, 335, 431, 444
Bioconjugated nanomaterials, 114, 116, 117,
 120, 126, 129, 131
Bioconjugated nanoparticles,
 see Bioconjugated nanomaterials
Biodegradation, 428
Biodistribution, 277, 281, 283, 312, 437
Biofilms, 101
Biological barriers, 336
Biological characterizations, 437
Biologically relevant environment, 355
Biomarkers, 152, 153, 160, 187, 189, 197
Biomechanics, 71

- Biomedical applications, 419, 449
Biomimetic materials, 70
Bioplotting, 33
Bioprinting, 8
Biosensors, 152, 154, 155, 183–187
Bleaching, 350
Blood-brain barrier (BBB), 173, 227, 228, 445
Blood clearance, 221, 224
Blood plasma, 336
BMP-2, 31
Bone marrow, 39
Bradford assay, 436
Breast cancer, 255, 256, 260, 261, 268, 270, 273, 276, 282
Breast cancer cells, 447
Bright-field images, 305, 306
Brillouin light scattering, 80, 81
Brillouin spectroscopy, 80
Brownian motion, 300, 309, 313, 340
Bulk and local stiffness, 93
- C**
- Calibration of HPLC for ATP, ADP, and AMP, 402
Calorimetric magnetic fluid hyperthermia (CMFH), 310–311
Cancer, 206–208, 223, 224, 229, 300, 302, 303, 311, 312, 321, 324, 437
Cancer cells, 436, 443, 446
Cancer chemotherapy, 177, 443
Cancer-on-a-chip (CoC), 152, 154, 156, 162, 172–196
Cancer theranostics, 242, 243, 270
Cancer therapy, 154, 247, 268, 281, 334, 419, 439
Capillary electrophoresis, 116, 123, 139
Capillary electrophoresis-chemiluminescence, 142, 143
Capillary zone electrophoresis, 123
Capping agents, 302
Capture efficiency, 190
Carbon dots (CDs), 446
Carbon nanotubes (CNTs), 14, 445–446
Carcinoma, 153, 171, 175, 177, 186, 247, 249, 272
Cardiac differentiation, 40
Cardiotoxicity, 179
Carrier fluid, 120
Cartilage, 29
Cavitation, 209, 211, 213, 225, 227–229, 231
CE, *see* Capillary electrophoresis
CE-CL, *see* Capillary electrophoresis-chemiluminescence
Cell counting, 388
Cell culture, 403–404
Cell pellet preparation for analysis, 404
Cellular internalization, 433–434
Cellular signaling pathways, 434
Cellular uptake, 433, 442
Cellulose nanocrystals, 18
Cell viability assay, 431–433
Ceramic cements, 29
Cetyl trimethylammonium bromide, 315
Characterization, 300, 304, 308, 324, 418, 421
Chemohyperthermia, 273, 274
Chemokine, 170, 171
Chemotherapeutics, 242, 244, 247, 248, 265, 268, 276, 279, 281, 284, 354
Chemotherapy, 206, 207, 212, 443
Chitin-silica hybrid nanocomposites, 79
Chitosan, 17
Cholesterol, 218
Chromatography, 115, 117, 124, 125
Chromogenic light microscopy, 407
Chylomicrons and extracellular vesicles (exosomes), 342
Circulating tumor cells (CTCs), 153, 167, 170, 172, 188–190, 192, 196, 197
Circulation half-life, 344
Classification, 364, 382, 384, 387, 389
Clinical trials, 242, 243, 245, 247, 250, 255, 257, 259, 261, 265, 266, 272, 273, 277, 281–284
c-Myc, 10
CNS disease conditions, 408
Cobalt, 303
Cobblestone area formation, 13
CoC, 192, 197
Coercivity, 301, 302
CoFe₂O₄, 317, 319
Collagen, 28, 93, 97
Collagen formation, 408
Colloidal stability, 430
Co-localization, 351
Colonization, 161, 170–172
Column Wash, 402
ComDet, 351
Computed tomography (CT), 153
Concave self-focusing transducer, 211
Confocal/total internal reflection fluorescence (TIRF) microscopy, 348
Confocal microscopy, 230, 257, 269, 433
Conjugates, *see* Bioconjugated nanomaterials
Contact mechanics, 71, 76

- Contact mode, AFM, 73, 74
Controlled-release, 248
Co-precipitation, 250, 252, 254, 302, 303
Co-solvent evaporation method, 215
Critical temperature, 222
Cryoprotection, 406
CTC, *see* Circulating tumor cells (CTCs)
Curcumin, 446
Cx 43, 40
Cytocompatibility, 300
Cytokines, 48
Cytotoxicity, 177, 192, 194, 268, 270, 275, 283, 322, 323, 442, 447
CZE, *see* Capillary zone electrophoresis
- D**
Dark-field images, 306
Daunoxome, 265
DDS, *see* Drug delivery system (DDS)
Dead time, 119
DEA, *see* *N, N'*-diethylenediamine (DEA)
Decafluorobutane, 225
Deep learning, 388
Derjaguin-Muller-Toporov model, 79
Dexamethasone, 31
Dextran, 248, 251, 252, 259, 266, 273
 D_h , 310
Diagnostics, 362–390
Dialysis, 340
Diaminobenzene, 317
Diaminobenzoic acid, 317, 320, 323
Dielectrophoresis (DEP), 187–189, 197
N, N'-Diethylenediamine (DEA), 229
Diethylene glycol (DEG), 320
Differential scanning calorimetry, DSC, 216
Diffusion, 429
Diffusion coefficient, 119, 125
Digital PCR (dPCR), 195
2-(Diisopropylamino)ethylamine (DIP), 229
DIP, *see* 2-(diisopropylamino)ethylamine (DIP)
1,2-Dipalmitoyl-sn-glycero-3-phosphate (DPPA), 230
1,2-Dipalmitoyl-sn-glycero-3-phosphocholine (DPPC), 217, 224, 230
Dispersion medium, 303, 309, 320, 321
Dissociation, 120, 121, 123, 129, 138, 141
 equilibrium constants, 123, 138, 141
 of FLLs, 334
1,2-Distearoyl-sn-glycero-3-phosphocholine (DSPC), 217, 219, 224
DLS, *see* Dynamic light scattering (DLS)
DNA, 114, 116, 142
Dodecane, 320
Donnan exclusion effect, 120
DOTA, 225
Doxil, 207, 224, 245, 265, 281, 335
Doxorubicin (DOX), 138, 140, 173, 207, 219, 221, 223, 228, 229, 231, 245, 268, 270, 279, 426
DPPA, *see* 1,2-Dipalmitoyl-sn-glycero-3-phosphate (DPPA)
DPPC, *see* 1,2-Dipalmitoyl-sn-glycero-3-phosphocholine (DPPC)
Drug carriers, *see* Drug delivery
Drug-conjugated lipid dissociation, 354
Drug-conjugated MNP, 242, 243, 246, 266, 267, 271
Drug conjugation, 243, 267, 275
Drug delivery, 114, 117, 134, 242, 246, 248, 261, 264, 266, 268, 270, 273, 275, 279, 283, 284, 440, 441, 443, 445
Drug delivery system (DDS), 417, 419, 428, 429, 433, 435, 437, 439, 446, 447
Drug discovery, 165, 172, 173, 196
Drug formulations, 177
Drug loading capacity, 420, 429, 440
Drug release, 206, 208, 212, 216, 218, 219, 221, 222, 225, 226, 230, 231, 428–429, 445
Drug screening platform, 175
Drug stability, 428–429
DSPC, *see* 1,2-Distearoyl-sn-glycero-3-phosphocholine (DSPC)
DSPE-PEG-2000.NH.folate, 230
Ductal carcinoma in situ (DCIS), 175
Dulbecco's modified eagle medium (DMEM), 320, 321
Duty cycle, 208, 230, 231
Dynamic light scattering (DLS), 115, 126, 133, 216, 305, 309–310, 420–421, 430
- E**
Egg L- α -phosphatidylcholine (Egg-PC), 218
Egg-PC, *see* Egg L- α -phosphatidylcholine (Egg-PC)
Elasticity of materials, 77
Elasticity of polymers, 90
Elastin, 98
Elastin like polypeptide (ELP), 223
Electrical field, 187
Electrical stimulation, 5
Electroosmotic flow, 122, 125
Electrophoresis, 115, 116, 121–126, 133–143
Electrophoretic mobility, 122, 124, 125, 137, 141

- Electrospinning, 6
ELP, *see* Elastin like polypeptide (ELP)
Energy barrier, 301
Engineered nanomaterials, *see* Nanoparticles
Enhanced permeability and retention (EPR)
 effect, 207, 208, 212, 223, 231, 418,
 419, 443
Enzymatic, 268
EOF, *see* Electroosmotic flow
Epicardial, 37
Epidermal growth factor receptors (EGFR), 335
Epi-fluorescence, 161, 181, 182
Epithelial-mesenchymal transition (EMT), 161
Epitope Retrieval 2, 407
Ethanol injection, 338
Ethylene glycol, 316, 320
Europium, 45
Extracellular matrix (ECM), 159–160, 162,
 164, 165, 167, 168, 173, 175, 179, 193,
 194, 197
Extravasation, 152, 161, 170, 171
Extrusion, 339
- F**
F4, *see* Flow field flow fractionation
Fe₃O₄, 302, 314, 318
Feraheme, 245, 265, 282, 284
Feridex, 252, 255, 260, 319
Ferri, 301, 302
Ferro, 301
Ferrofluids, 300, 303, 305, 311, 313, 320, 321
Fetal bovine serum (FBS), 311, 320, 321
FFF, *see* Field flow fractionation
Fibrin, 28
Fibrosis, 41
Field flow fractionation, 116–122, 132
Field of view, 351
Fiji (Image J), 351
Flow cytometry, 177, 336, 338, 433, 434
Flow field flow fractionation, 118, 127
Flow shaping, 383, 384, 387
Fluorescence activated cell separation
 (FACS), 189
Fluorescence correlation spectroscopy
 (FCS), 340
Fluorescence *in situ* hybridization (FISH), 195
Fluorescence mediated tomography, 257
Fluorescent, 257, 259, 262
Fluorescently labeled lipids (FLLs), 334
Fluorescently labeled lipids dissociation,
 353, 355
Fluorescent microscopy, 225, 227
Fluorochromes, 257, 259
Focal point, 210, 212, 227
Focused ultrasound (FUS), 196, 210, 232
Folic acid/folate, 249, 252, 280, 335
Force spectroscopy, AFM, 75, 76
Fourier transform infrared spectroscopy (FTIR),
 159, 305, 307, 424, 425
Fractionation ranges, 342
Freeze-dryer, 340
Freeze dry method, 215
Freeze-thaw cycles, 339
Freezing and thawing, 407
Frequency behavior of biological materials, 88
FRET, 352
Functionalization, 242–244, 249, 251, 256,
 267, 270, 272, 275, 279, 280, 423, 425
- G**
Gadolinium, 255, 259, 260
Gastromark, 252, 255
Gelatin, 36
Gel electrophoresis, 115, 142
Gemcitabine, 224
Genotoxicity, 48
Glassy materials, 89
Glioblastoma, 322
Glioblastoma multiforme (GBM), 172
Global public health problem, 398
Glycerol (GC), 320
Gold, 40, 261, 262, 265
Gold nanoparticles (AuNPs), 125, 127, 135,
 138, 426, 439–440
Gold nanorods, 22
Graded/in an all-at-once scenario, 348
Grain boundary, 219, 220
Graphene, 16
Graphene oxide (GO), 423
Green fluorescence protein (GFP), 195
- H**
Harvesting cells, 403
Healing process, 399
Heat-influencing parameters, 304
Heparin, 46
HepG2, 323
Herceptin, 323
Hexadecane, 320
HF5, *see* Hollow fiber flow field flow
 fractionation
High-density (HDL) lipoprotein, 342
High frequency ultrasound, 209

- High intensity focused ultrasound, 211
High performance liquid chromatography (HPLC), 117, 131, 341, 345, 400, 429
High speed photography, 227
High throughput screening (HTS), 156
Hill equation, 123, 137
Histology, 406–407
Histopathology, 437
HI-60, 268, 270
Hollow fiber flow field flow fractionation, 118, 127
HPLC, *see* High-performance liquid chromatography
HSPC, *see* Hydrogenated soy L- α -phosphatidylcholine (HSPC)
Human administration, 413
Hyaluronic acid, 20
Hybrid, 243, 257, 261, 263, 279
Hydrodynamic diameter, 309, 310
See also Hydrodynamic radius
Hydrodynamic radius, 117, 119, 122, 133, 141
Hydrogel, 94, 96, 142, 263, 265
Hydrogenated soy L- α -phosphatidylcholine (HSPC), 218, 224
Hyperthermia, 208, 210, 216, 217, 219, 220, 224, 226, 241, 242, 244, 246, 248, 250, 261, 270, 271, 274, 279, 280, 283, 302, 303
Hysteresis, 301, 303, 308, 309
- I**
ICP-MS, *see* Inductively coupled plasma mass
Image guided focused ultrasound, 212
Immunobiosensors, 187
Immunocytochemistry, 435
Immunofluorescence staining, 160
Immunohistochemistry, 406–407, 437, 438
with antibodies to CD68 and CD163, 407
and histological examinations, 409
staining, 411
Indentation, 75, 76
Inductively coupled plasma mass spectrometry (ICP-MS), 127, 128, 133, 135, 142, 341, 345, 437
Inertial cavitation, 213
Inflammation, 283
Inkjet, 8
Intermittent contact mode, AFM, 74
Intracellular, 247, 248, 266
Intramyocardial, 37
Intraperitoneal, 437
Intratatumoral, 246, 255, 265, 267, 270, 272, 273, 284
Intravasation, 161, 162, 165, 167, 169, 197
Intrinsic loss power (ILP), 303, 311, 313
In vitro, 300, 304, 311, 314, 322, 324
In vivo, 300, 304, 312, 322, 324, 336
Irinotecan, 207
Iron oxide, 241, 243, 245, 251, 254, 255, 258, 259, 264, 265, 273, 282, 283, 302, 303
Ischemia, 47
Isocratically, 341
- K**
Kinase, 41
Kinetics, 115, 120, 121, 123, 124, 131, 135, 136
Klf4, 10
Ko-precipitation, 254
hydrolytic basic, 254, 255
- L**
Lab-on-a-chip, 154
Lanthanide, 45
LCST, *see* Low critical solution temperature (LCST)
Leukemia, 268, 269, 281
Leukocytes, 266
Ligand-exchange, 252
Light sheet fluorescence microscopy (LSFM), 183
Limit of detection, 184
Lipids
exchange, 352
preparation and mixing of, 404
Liposomal distribution and targeting, 336
Liposomal nanocarriers, 334
Liposomes, 114, 126, 131, 133, 142, 264, 334
Liquid Chromatography Mass Spectrometry (LC-MS), 345
Lithography, 157, 158, 173
Low critical solution temperature (LCST), 221, 223
Low frequency ultrasound, 209
Luminescence, 25
Luna Column C18, 400
Lyophilized lipid mixtures, 337
Lysolipid, 206, 219, 221, 223
- M**
Machine learning, 362, 388
Macrophages, 257, 266
polarization, 411
Maghemite, 243, 250, 252, 302

- Magnagel, 265
- Magnetic-activated cell sorting (MACS), 189
- Magnetic drug carriers, 248, 249
- Magnetic drug targeting, 245
- Magnetic field, 245, 247, 248, 255, 265, 279
- Magnetic fluid hyperthermia (MFH), 247, 248, 300, 302–305, 311, 315, 317, 319, 321, 324
- Magnetic hyperthermia, 247, 248, 280
- Magnetic nanoparticles (MNPs), 300, 302, 303, 313, 324
- Magnetic resonance guided focused ultrasound (MRgFUS), 212
- Magnetic resonance imaging (MRI), 153, 243, 246
- contrast agent, 223
- focused ultrasound, 227, 232
- Magnetics, 241, 245, 247, 250, 252, 254, 261, 265, 270, 273, 275, 279, 280, 283, 284
- Magnetite, 250, 251, 253, 259, 260, 264, 283, 302
- Magnetization, 301, 303, 305, 308, 309
- Magneto-responsive, 241, 244, 263, 265, 283, 284
- Magnevist, 224
- Mag-TE, 263, 264
- MALS, *see* Multi-angle light scattering
- Manganese, 303
- Manufacture of liposomes, 405
- MCF-7, 268, 275, 322, 323
- MCF-10A, 268
- MDA-MB-231, 268
- Mean free path, 87
- Mechanical index, 226
- Mechanistic pathways, 434
- Membrane fluidity, 337
- Mesoporous silica nanoparticles (MSNs), 428, 446–448
- Metallic nanoparticles, 126, 128, 133, 135, 138, 140
- Metal organic framework materials, 129
- Metal oxide nanoparticles, 128, 130, 133, 138, 139, 141
- Metastasis, 153, 154, 161–173, 175, 183, 196, 245, 248, 261
- in cancer therapy, 408
- Methacrylate, 17
- Methotrexate, 275
- MFe₂O₄, 317, 319
- Micellar electrokinetic chromatography, 124, 125
- Microbubbles, 206, 215, 226, 229
- Microemulsion, 302, 303
- Microenvironment, 153, 154, 157, 162, 167, 170, 172, 173, 175, 176, 179, 183, 195, 197
- Microextrusion, 34
- Microfluidic systems, 152, 154–156, 158–161, 168, 170, 175, 177, 179, 181, 184, 186, 192, 194, 197
- platforms, 390
- MicroRNA, 43, 116, 120
- Microscopy, 336
- Microvasculature, 166, 195
- Microwave, 302
- Miniaturization, 116
- MIP NPs, *see* Molecularly-imprinted polymer
- miRNA, *see* microRNA
- MnFe₂O₄, 317, 319
- Model predictive control, 377, 381
- MOFs, *see* Metal organic framework materials
- Molecularly-imprinted polymer nanoparticles, 141
- Monochromator, 307
- Monocore, 322
- Monodisperse, 252, 253, 313, 314
- Morphology, 420, 421
- MPPC, *see* 1-Palmitoyl-2-hydroxy-sn-glycero-3-phosphocholine (MPPC)
- MSNs, *see* Mesoporous silica nanoparticles (MSNs)
- MSPC, *see* 1-Stearoyl-2-hydroxy-sn-glycero-3-phosphocholine (MSPC)
- MTT assay, 312, 431, 432
- Multi-angle light scattering, 116, 126, 127, 130, 131, 133
- Multicore, 319, 322
- Multi-domain, 301
- Multi drug resistance (MDR), 445
- Multi-lamellar, 339
- Multilayer, 390
- Multilayer microfluidic device, 377, 383
- Multimodal imaging, 255, 256, 259, 261, 263, 273, 274
- Multiparameter, 363, 383, 387, 388
- Myocardial infarction, 35
- N**
- Nanobubbles, 211, 215, 226, 229
- Nanocarriers, 249, 266, 268, 273, 275, 278, 284
- for drug delivery, 334
- Nanocolloids, 250, 254
- Nanoconjugated system, 432
- Nanoconstructs, 242, 265, 273
- Nanocrystals, 252, 253, 314

- Nanocubes, 314, 315
Nanodiscs, 314
NanoDrop spectrofluorometer, 345
Nanoemulsions, 230
Nanoflower, 314
Nanoformulations, 242, 243, 245, 259, 267, 268, 270, 281, 284
Nanog/Oct4/Sox2, 9
Nanoindentation, 71, 93
Nanomaterials, 433
 See also Nanoparticles
Nanomedicine, 242, 243, 245, 267, 275, 281, 418, 449
Nanoparticles, 114–117, 120, 121, 125, 128, 129, 131, 133, 136, 207, 243, 244, 253, 261, 422, 423, 430
Nanoparticle-protein, *see* Protein corona
Nanoparticle tracking analysis (NTA), 115, 340
Nanorods, 314, 315
Nanoscience, 300
Nanospheres, 322
Nanotechnology, 4, 242, 244, 245, 300, 418
Nano-theranostic, 223
Nanotherapeutics, 48, 266, 276, 284
NanoTherm, 248, 265, 282
Nano-toxicity, 448
Nanotubes, 16
Near infrared (NIR) fluorescence, 217, 224, 257, 259, 262, 265
Néel, 300, 313
Neonatal, 46
Neural network, 389
Neurodegenerative response, 411
NGC Explorer, 401
NMR, *see* Nuclear magnetic resonance spectroscopy
NP, *see* Nanoparticles
NRTIs, *see* Nucleoside reverse transcriptase inhibitors
NTA, *see* Nanoparticle tracking analysis
Nuclear magnetic resonance spectroscopy, 116, 424, 426
Nucleoside reverse transcriptase inhibitors, 129
- O**
Oct 4, 9
Octafluoropropane, 215, 225
Octahedral, 314
Octopod, 314
Oil-in-water emulsion method, 215
On-chip integration, 388
Open-channel separation, 114, 116, 129
Optimization, 120, 135, 143
Orbitals, 301, 306
Organometallic, 252
Organ-on-a-chip, 152, 154
Organ preservation, 408
Organs on a chip, 385–386
Osteoarthritis, 26
Osteoblasts, 29
Osteochondral tissue, 33
Osteogenic cells, 25
Osteomyelitis, 26
Osteoporosis, 26
- P**
Paclitaxel (PTX), 245, 275, 278
1-Palmitoyl-2-hydroxy-sn-glycero-3-phosphocholine, 219, 221, 224
Particle volume, 301
Passive targeting, 248, 266
Peakforce, 78
Peak resolution, 126
PEG-conjugated lipids, 354
PEGylated lipids, 219
PEGylated liposomes, 270, 278, 281, 282, 353
PEGylated surfactants, 221
Peptides, 249, 251, 257, 259, 276
Perfluorohexane, 230
Perfluoropentane, 230
Perfusion, 406
Permeability, 170
Personalized medicine, 152
Personalized treatment, 364
Pharmacokinetics, 449
Phase Analysis Light Scattering techniques (PALS), 341
Phase transition, 210, 216, 219, 222
Phosphate buffer saline (PBS), 320, 321
Phospholipids exchange, 352
Photo-crosslinking, 35
Photolithography, 157
Photomask, 157, 158
Photoresists, 157, 158
Photostability, 25
Physicochemical property, 300, 302, 305, 313, 324
Piezoelectric materials, 44
Plasmid, 6
Plate height number, 125
Platelet-derived growth factor (PDGF), 176
Plate reader, 343
Pluripotent, 8
Point of care, 363

- Poly ADP ribose polymerase (PARP)
protein, 436
- Polycaprolactone, 16, 31
- Polycarbonate membrane, 339
- Polydimethylsiloxane (PDMS), 157, 159, 162,
179, 181, 192, 195, 197
- Polydispersed, 313, 314
- Polyethylene glycol (PEG), 251, 280, 320,
323, 324
- Poly(ethylene glycol) diacrylate (PEGDA), 32
- Polymer, 249, 253, 265, 268, 279
- Polymeric micelles, 231
- Polymeric nanodroplet, 229
- Polymeric nanoparticles, 129, 131, 135, 141,
142, 230–232
- Polymer micelles, 215
- Polymer modified thermosensitive
liposomes, 206
- Polystyrene nanoparticles, 120, 129
- Poly (vinylpyrrolidone), 251, 315
- Porosity, 93
- Positron emission tomography (PET), 256, 258
- Post-insertion method, 214
- Probing mechanics with different
instruments, 88
- ProHance, 223
- Propidium iodide, 227
- Protein, 114, 117, 119, 123, 126, 130, 135,
136, 138
- Protein corona, 114, 115, 127, 129
- Protein corona shielding nanoparticles
(PCSN), 447
- Prussian blue, 312
- Pyromellitic acid (PMA), 317
- Q**
- Quantitate adenosine phosphates, 408
- Quantitative microscopy, 349
- Quantum dots, 24, 126, 133, 135, 142
- Quartz crystal microbalance, 353
- R**
- Rabbit kidney cells (RK-13), 401
- Raman, 7
- Ras homolog protein A (RhoA), 162
- Reactive oxygen species (ROS), 434, 435, 440
- Realtime, 364, 383, 387
- Regenerative M2 (CD68⁺ and CD163⁺)
macrophage, 398, 411
- Regenerative medicine, 4
- Relative recovery, 120
- Relaxation, 300, 303, 313
- Release of drugs, 441
- Resolution, 115, 117, 121, 122, 125, 138,
142, 143
- Resovist, 252, 255, 282
- Retention parameter, 119
- Retention time, 115, 119, 132
- Reticuloendothelial system, 266
- Rho-associated protein kinase (ROCK), 162
- S**
- Scanning electron microscopy (SEM), 305,
306, 340, 421–423
- Scanning probe microscopy (SPM), 72–79
- Scott model, 95
- SDS-polyacrylamide gel, 436
- SEC matrices, 342
- Secondary electrons, 306
- Selected area electron diffraction (SAED), 306
- Selenium nanoparticles, 127
- Self-assembly, 215
- Self-formed ectodermal autonomous multi-
zone (SEAM), 11
- Semi-permeable membrane, 215
- SEM, *see* Scanning Electron Microscopy
(SEM)
- SeNPs, *see* Selenium nanoparticles
- SentiMag, 256
- Separation efficiency, 125, 142, 189
- Serum stability, 430
- SF4, *see* Symmetric flow field flow
fractionation
- Shape, 300, 304, 305, 307, 313, 315, 319,
321, 324
- Short-lived reactive oxygen/nitrogen species
(ROS/RNS), 184
- Signal-to-noise ratio, 349
- Silica nanoparticles (SiNPs), 435, 436
- Silk, 17, 96
- Silver, 29
- Silver nanoparticles (AgNPs), 126, 128, 137,
140, 440–441
- Sinerem, 252, 255
- Single-domain, 301, 303
- Single liposome dissociation (SLiD) assay,
336, 347
- Single liposome microscopy, 334
- Size, 300, 301, 304, 305, 307, 309, 312, 315,
319, 321, 324
- Size distribution, 420
- Size exclusion chromatography (SEC), 334,
336, 341

- Sizes, 317
Sodium cholate, 315
Solvent evaporation method, 215
Solvothermal, 302
Somatic cell nuclear transfer (SCNT), 10
Sonication, 14, 340
Sonochemical, 302
Sonolysis, 231
Sonoporation, 211, 224, 226, 228, 231
SonoVue[®], 215
Sox 2, 9
Specific absorption rate (SAR), 303, 311, 313, 322
Spheroids, 34
Spinal cord, accelerated restoration, 411, 412
Spinal cord injury, 405–407
Spinel-ferrites, 303
SPIONS, *see* Superparamagnetic iron oxide nanoparticles
Spliceosome, 408
Stability, 428
Stability study, 420
Stable cavitation, 213
“Stealth” liposomes, 335
1-Stearoyl-2-hydroxy-sn-glycero-3-phosphocholine (MSPC), 219, 221
Stem cell, 177
Sterility, checking, 405
Stewart assay, 341
Stimulated emission depletion microscopy (STED), 183
Stimuli-responsive nanoparticles, 206, 208, 225, 268, 283
Stochastic optical reconstruction microscopy (STORM), 182
Structured illumination microscopy (SIM), 183
Subcellular compartments, 103
Sub-micron particles, 192
Sulfur hexafluoride, 225
Superparamagnetics (SPM), 243, 252, 255, 259, 271, 300, 302–303, 305, 310, 313–324
Superparamagnetic iron, 22
Superparamagnetic iron oxide nanoparticles, 128, 138, 244, 252, 265, 270, 273
Superparamagnetic (SPM) nanoparticles, 302, 305, 310, 313, 324
Super-resolution, 154, 181–183, 196, 197
Surface charge, 428
Surface coatings, 300, 304, 313, 316, 317, 319, 321, 324
Surface functionalization, 424–426
Surface plasma resonance, 20
Surfactants, 124, 125, 142, 302, 315, 317
Symmetric flow field flow fractionation, 118
Synergistic therapy, 442
- T**
T1 mapping, 224
T1 relaxation, 224
T1 relaxivity, 224
T1 weighted, 229
Tandem Fabry-Pérot interferometer, 84
Targeted, 243, 245, 247, 249, 257, 259, 267, 268, 272, 275, 277, 279, 282, 284
Targeted alpha (α)-particle therapy, 131
Targeted delivery, 421
Targeted drug delivery systems, 431, 437, 448, 449
Targeted drug delivery applications, 419
Targeting agent, 446
Targeting ligand, 354, 447
TAT, *see* Targeted alpha (α)-particle therapy
Taylor dispersion analysis, 142
Temozolomide, 279
Temporomandibular joint, 29
TEM, *see* Transmission Electron Microscopy (TEM)
Terephthalic acid (TA), 317
Tetracosane, 320
Theoretical plate number, 125
Theragnostic liposomes, 206
Theranostic nanoparticles, 212
Therapeutics, 241, 243, 248, 261, 264, 266, 267, 270, 272, 273, 279, 284
Therapeutic applications, 439–448
Therapeutic efficacy, 257, 267, 273, 279
Thermal decomposition, 250, 252, 253, 302
Thermal drift, 351
ThermoDox, 207, 221
Thermogravimetric analysis (TGA), 305, 308
Thermoresponsive polymers, 221
Thermosensitive liposomes, 206, 218–221, 224
Thermotherapy, 300, 321, 324
Thin-film hydration, 214
Thioctic acid, 137, 139
Thiomalic acid, 137, 139
TiO₂ nanoparticles, 445
Tissue engineering, 4, 70, 93, 243, 255, 263, 264
Tissue penetration, 209
Titanium, 29
Titanium oxide, 444–445
Topographical map, 423
Topotecan, 224, 226

- Total integrated fluorescence intensity, 351
Toxicology, 156
Transducers, 211, 212, 217
Transducer arrays, 211, 212
Transforming growth factor β (TGF β), 162
Transition temperature, 337
Transmission electron microscopy (TEM), 115, 305–306, 320, 340, 421
Transwell insert, 167
Traumatic spinal cord injury, 398
Treatment evaluation, 401
Triethylene glycol (TEG), 320
Trimesic acid (TMA), 317
Tumor, 245, 249, 257, 260, 265, 270, 272, 276, 279, 280, 283, 300, 312, 323
 microenvironment, 153, 162, 196
 targeting, 448
 volume regression, 448
 uptake, 223, 226
- U**
UCST, *see* Upper critical solution temperature (UCST)
Ultrasound, 206–232
Ultrasound intensity, 209
Ultrasound transducers, 208, 210
Unilamellar, 339
Upper critical solution temperature (UCST), 222
UV-Vis spectroscopy, 425, 426
- V**
Vaccinia virus complement control protein (VCP), 399
Vascular endothelial growth factor (VEGF), 42, 165
Very large scale integrated microfluidic systems (VLSIMS), 362
Very low-density lipoproteins (VLDL), 342
Vibration sample magnetometer (VSM), 305, 308–309
Virtually imaged phase array, 84
Visualization by transmission electron microscopy, 405
Vitronectin, 44
- W**
Whole blood analysis, 383–385
Wound healing, acceleration, 408
- X**
X-rays, 307
X-ray diffraction (XRD), 305, 307
X-ray photoelectron spectroscopy (XPS), 159
- Z**
Zeta (ζ) potential, 310, 340, 428
Zinc oxide (ZnO), 441–443
 nanoparticles, 443